Charm Production and QCD Analysis at HERA and LHC

Dissertation

zur Erlangung des Doktorgrades

an der Fakultät für

Mathematik, Informatik und Naturwissenschaften

Fachbereich Physik

der Universität Hamburg

vorgelegt von

Oleksandr Zenaiev

aus Mariupol/Kiew (Ukraine)

Hamburg

2015

Folgende Gutachter empfehlen die Annahme der Dissertation:	PD Dr. Achim Geiser Prof. Dr. Brian Foster Prof. Dr. Ronan McNulty
Tag der Disputation:	17. Februar 2015

Abstract

In this thesis the study of charm production in ep and pp collisions is presented. The heavy-quark masses provide a hard scale, allowing the application of perturbative QCD.

A measurement of D^+-meson production in deep inelastic scattering with the ZEUS detector at HERA is presented. The analysis was performed using a data sample with an integrated luminosity of $354\,\mathrm{pb}^{-1}$. Differential cross sections were measured as a function of virtuality Q^2, inelasticity y, transverse momentum and pseudorapidity of the D^+ mesons. Lifetime information was used to reduce the combinatorial background significantly. Next-to-leading-order QCD predictions in the fixed-flavour-number scheme were compared to the data.

This measurement was combined with other H1 and ZEUS measurements of charm production. The combination was performed at inclusive level for the reduced charm cross sections, which were obtained from the measured visible cross sections, extrapolated to the full phase space using the shape of the theoretical predictions in the fixed-flavour-number scheme. The combination method accounts for the correlations of the systematic uncertainties among the different datasets, thus allowing cross calibration of different measurements. The combined charm data were compared to QCD predictions in various heavy-flavour schemes and used together with the inclusive production data at HERA as input for QCD analyses to determine the charm running mass in the $\overline{\mathrm{MS}}$ renormalisation scheme and the optimal values of the charm-quark mass parameters in other heavy-flavour schemes.

An additional combination of the H1 and ZEUS D^{*+} visible cross sections was performed to provide the combined cross sections without theory-related uncertainties from the extrapolation procedure. This combination also provides differential cross sections as a function of the D^{*+} kinematic variables. Next-to-leading-order QCD predictions in the fixed-flavour-number scheme were compared to the combined D^{*+} cross sections and a 'customised' QCD calculation was introduced in order to improve the agreement between the central values of the theoretical predictions and the data.

While the HERA charm data are sensitive to the gluon distribution in the proton at the values of partonic fractions of the proton momenta $10^{-4} \lesssim x \lesssim 10^{-1}$, the production of charm quarks at LHCb probes the region $5 \times 10^{-6} \lesssim x \lesssim 10^{-4}$. The impact of recent LHCb measurements of heavy-flavour production on parton distribution functions was studied in a QCD analysis in the fixed-flavour-number scheme at next-to-leading order. Differential cross sections of charm and beauty production obtained by the LHCb experiment were used together with the combined inclusive and heavy-flavour production cross sections in deep inelastic scattering at HERA. The heavy-flavour data of the LHCb experiment impose constraints on the gluon and sea-quark distributions at very low partonic fractions of the proton momenta. This kinematic range is currently not covered by other experimental data in QCD fits.

As the technical part of this thesis, the ZEUS Event Display program has been modified in the context of the ZEUS data preservation project to become independent of the ZEUS Software. The new program is a pure ROOT application. While it provides the main functionalities that were available in the classic program, it does not require any maintenance.

Kurzfassung

In der hier vorgestellten Arbeit wurde die Charmproduktion in ep- und pp-Kollisionen untersucht. Die schweren Quarkmassen liefern eine harte Skala, die die Anwendung der perturbativen QCD ermöglicht.

Eine Messung der Produktion von D^+-Mesonen in der tief unelastischen Streuung wurde mit dem ZEUS-Detektor am HERA-Speicherring durchgeführt. Für diese Analyse wurde ein Datensatz mit einer integrierten Luminosität von $354\,\mathrm{pb}^{-1}$ benutzt. Differentielle Produktionswirkungsquerschnitte wurden gemessen als Funktion der Virtualität Q^2, der Inelastizität y, dem Transversalimpuls und der Pseudorapidität der D^+-Mesonen. Die Lebensdauerinformation wurde genutzt, um den kombinatorischen Untergrund signifikant zu reduzieren. QCD-Vorhersagen in nächstführender Ordnung im "Fixed-Flavour"-Schema werden mit den Daten verglichen.

Diese Messung wurde mit anderen H1- und ZEUS-Charmproduktionsmessungen kombiniert. Die Kombination wurde durchgeführt auf der Stufe der inklusiven reduzierten Charm-Produktionswirkungsquerschnitte, die aus den gemessenen sichtbaren Wirkungsquerschnitten abgeleitet wurden durch Extrapolation mit der Form der theoretischen Vorhersagen im "Fixed-Flavour"-Schema. Die Kombinationsmethode berücksichtigt die Korrelationen der systematischen Unsicherheiten zwischen verschiedenen Datensätzen und ermöglicht damit die wechselseitige Kalibration der verschiedenen Messmethoden. Die kombinierten Charm-Daten wurden mit QCD-Vorhersagen in verschiedenen schwere-Quark-Berechnungsschemata verglichen und zusammen mit inklusiven Datensätzen als Eingangsdatensätze für QCD-Analysen genutzt. Diese dienten der Bestimmung der laufenden $\overline{\mathrm{MS}}$-Charm-Quark-Masse und der optimalen Werte der Charm-Quark-Massenparameter in den verschiedenen schwere-Quark-Schemata.

Eine zusätzliche Kombination der sichtbaren H1- und ZEUS-D^{*+}-Wirkungsquerschnitte wurde durchgeführt, um kombinierte Wirkungsquerschnitte ohne theoriebezogene Unsichercheiten aus dem Extrapolationsverfahren zu erhalten. Diese Kombination liefert auch differentielle Wirkungsquerschnitte als Funktion der kinematischen D^{*+}-Variablen. QCD-Vorhersagen in nächstführender Ordnung im "Fixed-Flavour"-Schema wurden mit den kombinierten D^{*+}-Wirkungsquerschnitten verglichen und eine 'angepasste' QCD-Rechnung wurde eingeführt, um die Übereinstimmung zwischen den zentralen Werten der theoretischen Vorhersagen und den Daten zu verbessern.

Während die HERA-Charm-Daten sensibel sind auf die Gluon-Verteilung im Proton bei Werten des partonischen Impulsanteils des Protons von $10^{-4} \lesssim x \lesssim 10^{-1}$, sondiert die Produktion von Charm-Quarks in LHCb die Region $5 \times 10^{-6} \lesssim x \lesssim 10^{-4}$. Die Auswirkungen der neusten LHCb-Messungen von schweren Quarks auf die Parton-Verteilungsfunktionen wurden mit einer QCD-Analyse in nächstführender Ordnung im "Fixed-Flavour"-Schema untersucht. Differentielle Wirkungsquerschnitte der Charm- und Beauty-Produktion im LHCb-Experiment wurden verwendet zusammen mit den kombinierten inklusiven Wirkungsquerschnitten und den schwere-Quark-Produktionsquerschnitten in der tiefunelastischen Streuung bei HERA. Die schwere-Quark-Daten des LHCb-Experiments liefern Einschränkungen der Gluon- und See-Quark-Verteilungen bei sehr niedrigen partonischen Impulsanteilen des Protons. Dieser kinematische Bereich wurde bisher nicht durch andere experimentelle Daten in den QCD-Fits

abgedeckt.

Im technischen Teil dieser Arbeit wurde das ZEUS-Ereignisvisualisierungsprogramm im Rahmen des ZEUS-Datensicherungsprojekts so modifiziert, dass es von der ZEUS-Software unabhängig wurde. Das neue Programm ist eine reine ROOT-Anwendung. Während es die wichtigsten Funktionen bietet, die im klassischen Programm zur Verfügung standen, ist es nunmehr wartungsfrei.

Contents

CHAPTER 1

Introduction

The Standard Model is the widely accepted theory of elementary particle physics. It describes weak, electromagnetic and strong interactions of the particles. The most complicated and thus one of its most interesting parts is Quantum Chromodynamics (QCD), which describes strong interactions between quarks and gluons.

Nowadays the Standard Model is able to provide precise and robust predictions for many processes, measured in the high energy experiments. One of its most well-known recent successes was the observation of the Standard Model Higgs boson, predicted in the 60's of the XXth century and discovered at the Large Hadron Collider almost 50 years later. Other outstanding results of the Standard Model are, e.g. a successful description of inclusive jet production at the Tevatron over eight orders of magnitude in rate, or a consistent fit of a few hundred data points which represent H1 and ZEUS measurements of the proton structure function with only ten adjusted parameters.

One may ask the question, if the Standard Model is so well advanced and confirmed, why is yet another physics analysis on this topic of interest? The answer is, any pure theory by *itself*, including the Standard Model, cannot describe, and moreover predict, anything. Without any existing experimental data, a theorist, even being a genius in the Standard Model calculations, would not be able to predict any cross section, except making some very rough qualitative estimations. This is because the Standard Model (and QCD in particular) has a number of free parameters (masses of the particles, couplings etc.) which must be extracted experimentally and then used in the calculations to describe other measurements or predict new phenomena. In other words, free parameters can be rewritten in terms of observables which can be measured in the experiment. Once the number of measurements exceeds the number of free parameters, it becomes possible *to test the consistency* of the Standard Model. Moreover, there are still some corners where first-principle theory cannot be applied at the present time, and thus some phenomenology has to be used. Experimental data are the only constraint which can be used to resolve the ambiguity of various phenomenological approaches. Thus the discovery of the Higgs boson would not have been possible without many years of earlier measurements at other colliders, followed by a subsequent comprehensive comparison of data and theory. There

is a rather thin line between a measurement of the free parameters and a consistency test, since theoretical predictions require as input extremely precise values of the free parameters, which can only be obtained from another precise measurement. Therefore the Standard Model is then confirmed to the extent that these measurements from different physical sources agree with each other. The most prominent aspect is that after all the Standard Model became able to describe a great variety of physics processes, and more stringent tests are still to come.

This thesis is devoted to various aspects of heavy-flavour physics. The production of heavy quarks in electron–proton and hadronic collisions provides one of the most difficult tests of perturbative QCD. On the other hand, once the applicability of this theory is established, one can use these processes as an input to improve the precision of parameters of the Standard Model and thus its predictive power for other processes in other experiments. The current thesis is designed in this spirit of the given discussion: it is neither a pure experimental work, nor a theoretical contribution, but rather an amalgamation of the two. Briefly, it presents one new measurement of charm production at HERA, which is further combined with many other precise H1 and ZEUS charm measurements in order to obtain the most precise charm dataset from HERA. These combined data are extensively used in a comparison of data and theory and in a QCD analysis to extract the charm-quark mass. Another combination is performed at the more exclusive level of D^{*+} visible cross sections; in contrast to the previous one, it does not include theory-related uncertainties. Furthermore, charm and beauty measurements from LHCb are considered and included in a QCD analysis. They provide sensitivity to the gluon distribution at low values of partonic fractions of the proton momenta; this is a kinematic range that is currently completely unexplored in parton-distribution-function fits.

The thesis is organised in the following way. Chapter 2 introduces the theoretical concepts, relevant for the subsequent contents. Chapter 3 gives a description of the experimental set-up and existing measurements of heavy-flavour production at HERA and LHCb. Chapter 4 is devoted to the technical task: it describes the ZEUS Event Display program and the modification of this program in the context of the ZEUS data preservation project. Chapter 5 starts to deal with the physics results: it presents a measurement of D^{+}-meson production performed with the ZEUS detector at HERA. Chapter 6 describes a combination of charm measurements from H1 and ZEUS, performed at two levels: for D^{*+} visible cross sections and for inclusive charm reduced cross sections. Chapter 7 presents a QCD fit with the LHCb heavy-flavour data. Finally, Chapter 8 summarises the results presented in the previous four chapters.

CHAPTER 2

Theoretical overview

This Chapter introduces the theoretical concepts relevant for the analyses presented in this thesis. It starts with Section 2.1, which gives a description of deep inelastic ep scattering in terms of the quark-parton model. In Section 2.2 the most important aspects of Quantum Chromodynamics are introduced. Finally, Section 2.3 describes the current status of the theoretical calculations for heavy-quark production in ep and pp collisions.

2.1 Deep inelastic scattering

Deep inelastic ep scattering has two main strands of interest: it can be used to investigate the theory of strong interaction and to determine the momentum distributions of the partons within the proton. Section 2.1.1 explains the kinematics of ep scattering and gives a definition of deep inelastic scattering processes. Section 2.1.2 presents general expressions for the inclusive cross sections in terms of structure functions. Finally, Section 2.1.3 gives an interpretation of the structure functions in terms of the quark-parton model.

The review given in this Section is largely based on [1].

2.1.1 Kinematics

The generic electron–proton[1] scattering process, $ep \to l'X$, where l' is the scattered lepton and X is the hadronic final state, is shown in Fig. 2.1. It occurs via the exchange of an electroweak boson V^*[2] of two types:

- a neutral γ or Z^0 boson; these reactions are called *neutral current* (NC);
- a charged $W^\pm$ boson; these reactions are called *charged current* (CC).

[1] Both electrons and positrons are referred to as electrons, unless explicitly stated otherwise.
[2] The superscript * denotes a virtual particle.

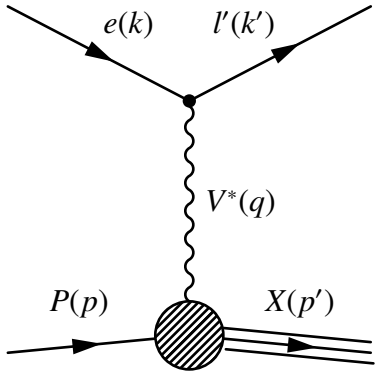

Figure 2.1: Schematic diagram of ep scattering.

Denoting the incoming electron and proton four-momenta with k and p, respectively, and the scattered-lepton four-momentum with k', the event kinematics can be described by the following Lorentz invariant variables:

$$\begin{aligned}
Q^2 &= -q^2 = (k - k')^2, && \text{virtuality of the exchanged boson,} \\
s &= (k + p)^2 \simeq 2k \cdot p, && \text{centre-of-mass energy squared,} \\
W^2 &= (p + q)^2, && \text{centre-of-mass energy squared of the boson-proton system,} \\
y &= \frac{p \cdot q}{p \cdot k} \simeq \frac{2p \cdot q}{s}, && \text{inelasticity,} \\
x &= \frac{Q^2}{2p \cdot q}, && \text{Bjorken variable.}
\end{aligned} \tag{2.1}$$

Neglecting the lepton and proton masses, they are connected by the following relation:

$$Q^2 = sxy. \tag{2.2}$$

Considering s fixed in the experiment, any other two variables fully determine the lepton scattering kinematics.

Virtuality Q^2 can be interpreted as the power with which the exchanged boson can resolve the proton structure. Depending on Q^2, the ep scattering phase space is divided into two regions:

- *deep inelastic scattering* (DIS), if $Q^2 \gtrsim 1\,\text{GeV}^2$;
- *photoproduction* (PHP), if $Q^2 \approx 0\,\text{GeV}^2$.

Inelasticity y defines the relative fraction of the electron energy transferred to the hadronic system in the proton rest frame, while the Bjorken variable x determines the relative fraction of the proton energy involved in the scattering process (this will be shown in Section 2.1.3).

2.1.2 Inclusive cross sections

The general form for the differential cross section for NC is given in terms of three structure functions, F_2, F_L, xF_3, as

$$\frac{\mathrm{d}^2\sigma^{\mathrm{NC}}(ep)}{\mathrm{d}x\mathrm{d}Q^2} = \frac{2\pi\alpha^2}{Q^4 x}[Y_+ F_2^{\mathrm{NC}}(x,Q^2) - y^2 F_L^{\mathrm{NC}}(x,Q^2) \mp Y_- x F_3^{\mathrm{NC}}(x,Q^2)], \tag{2.3}$$

where $Y_\pm = 1 \pm (1-y)^2$ and α is the electromagnetic coupling constant (the mass terms are ignored as appropriate at high Q^2). For Q^2 values much below that of the Z^0 mass squared, the parity-violating structure function xF_3 is negligible and the structure functions F_2, F_L are given purely by γ^* exchange.

The CC differential cross section mediated by $W^\pm$ bosons (where the lepton final state is a neutrino) is given by

$$\frac{\mathrm{d}^2\sigma^{\mathrm{CC}}(ep)}{\mathrm{d}x\mathrm{d}Q^2} = \frac{G_F^2}{4\pi x}\frac{M_W^4}{(Q^2+M_W^2)^2}[Y_+ F_2^{\mathrm{CC}}(x,Q^2) - y^2 F_L^{\mathrm{CC}}(x,Q^2) \mp Y_- x F_3^{\mathrm{CC}}(x,Q^2)] \tag{2.4}$$

and the correspondence to the NC case can be seen easily if the Fermi coupling constant G_F is expressed as

$$G_F = \frac{\pi\alpha}{\sqrt{2}\sin^2\theta_W M_W^2}, \tag{2.5}$$

where M_W is the $W^\pm$ mass and θ_W is the weak mixing angle (known also as the Weinberg angle). Hence at $Q^2 \ll M_W^2$ the CC cross section is largely suppressed relative to NC:

$$\frac{\sigma^{\mathrm{CC}}}{\sigma^{\mathrm{NC}}} \sim \frac{Q^4}{M_W^4}. \tag{2.6}$$

Fig. 2.2 shows the NC and CC inclusive cross sections measured by H1 and ZEUS as a function of Q^2 [2]. At low Q^2, the CC cross section is largely suppressed compared to NC, while in the region $Q^2 \sim M_W^2$ the CC and NC cross sections become similar, which can be considered as a manifestation of electroweak unification in spacelike scattering [3].

2.1.3 Quark-parton model

The quark-parton model (QPM) grew out of the scaling that had been predicted by Bjorken [4] and observed in the high energy DIS experiments at SLAC [5], where F_2 was observed to be independent of Q^2 for x values around $x \sim 0.3$. The model states that the nucleon is full of pointlike noninteracting scattering centers known as partons. The ep reaction cross section is approximated by an incoherent sum of elastic electron–parton scattering cross sections, shown in Fig. 2.3.

Neglecting the transverse component of the scattered-parton momentum[3] and its mass, the

[3] This approximation is known as the *infinite momentum frame*.

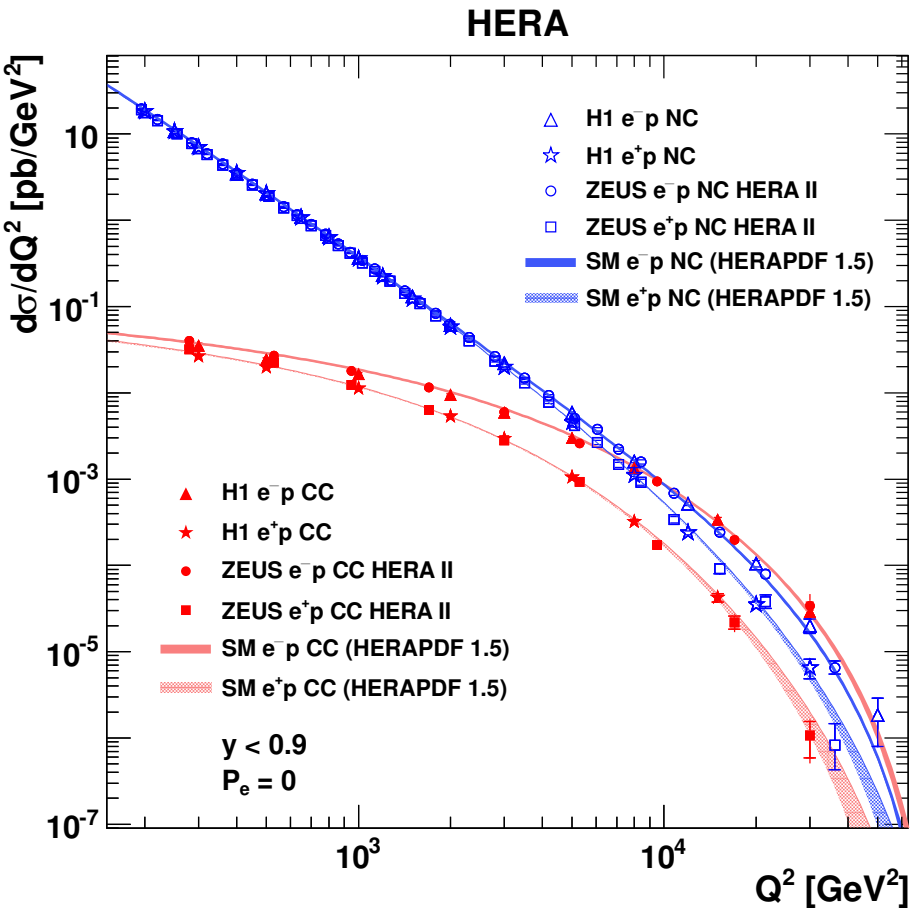

Figure 2.2: NC and CC inclusive cross section as a function of Q^2 as measured by H1 and ZEUS for electron and positron beams [2]. Predictions from the Standard Model are shown as bands.

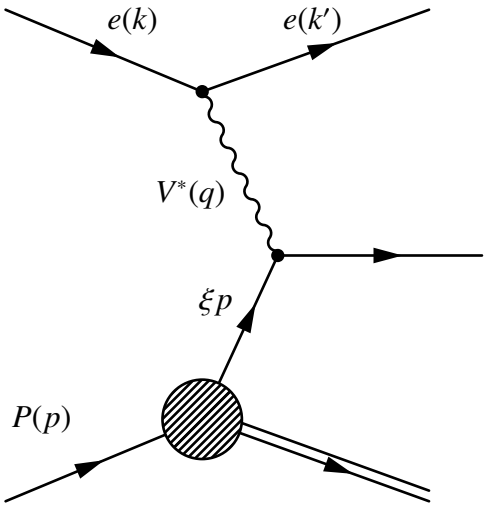

Figure 2.3: Schematic diagram of ep scattering in the QPM.

squared four-momentum of the outgoing parton is given by

$$0 \approx (\xi p + q)^2 = \xi^2 p^2 - Q^2 + 2\xi p \cdot q \Rightarrow \xi \approx \frac{Q^2}{2p \cdot q} = x. \tag{2.7}$$

This interprets the Bjorken variable x as the fraction of the proton momentum carried by the scattered parton, ξ.

The parton model had to be reconciled with the static quark model, which pictures a proton and other baryons as being made up of three constituent quarks (suggested earlier by Gell-Mann [6] for the classification of the existing hadrons), which give them their flavour properties. The reconciliation was effected in the QPM by considering the proton as being made of valence quarks, which give it its flavour properties, and a "sea" of quark-antiquark pairs which have no overall flavour. Both the valence quarks and the sea quarks and antiquarks are identified as partons.

The significance of the structure functions can be better understood by specifying them in terms of partons as follows:

$$F_2(x, Q^2) = F_2(x) = \sum_i e_i^2 [x q_i(x) + x\bar{q}_i(x)], \tag{2.8}$$

where the sum goes over the quark, xq_i, and antiquark, $x\bar{q}_i$, momentum distributions contained in the proton, multiplied by the corresponding quark charge squared, e_i^2. The spin 1/2-nature of the quarks implies that $F_L = 0$.

Fig. 2.4 [7] shows the proton structure function $F_2(x, Q^2)$ as measured by several collider and fixed-target experiments. For $x \approx 0.1$, F_2 is nearly independent of Q^2, thus confirming the scaling behaviour predicted by Bjorken, while at lower and higher x the dependence on Q^2 is clearly observed.

If quarks and antiquarks carry all of the momentum of the proton, the momentum sum rule must be obeyed:

$$\mathrm{I} = \int_0^1 \mathrm{d}x \, x \sum_i q_i(x) = 1. \tag{2.9}$$

This was not confirmed; the experimental measurement of $\mathrm{I} \approx 0.5$ [8] implied that there is more momentum in the proton, than that carried by the charged quarks and antiquarks, and gave impetus to the development of the theory of strong interactions, in which the deficit in momentum is carried by the gluons. This topic will be continued in Section 2.2.3.

2.2 Some aspects of Quantum Chromodynamics

Quantum Chromodynamics (QCD) is the quantum field theory of strong interactions between quarks and gluons. Quarks were originally proposed by Gell-Mann [6] as a classification scheme for hadrons. The idea that quarks carry a three-fold 'colour' charge was introduced to allow baryon wave-functions (e.g. the Δ^{++}) to have simultaneously the correct permutational symmetry and satisfy Fermi-Dirac statistics; the color charge is considered as very closely

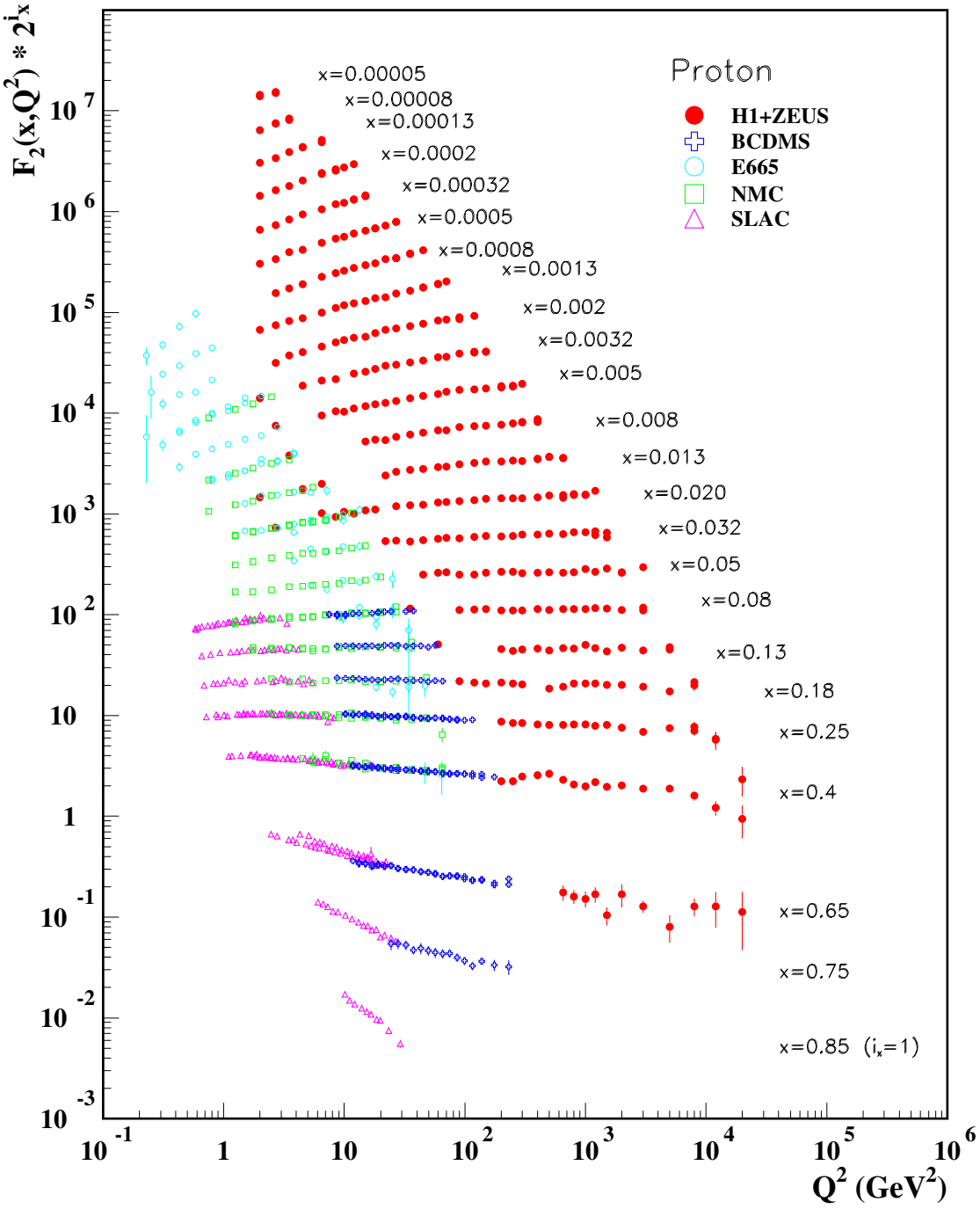

Figure 2.4: The proton structure function F_2 measured in electromagnetic scattering of electrons and positrons on protons (collider experiments H1 and ZEUS for $Q^2 \geq 2\,\mathrm{GeV}^2$), in the kinematic domain of the HERA data, and for electrons (SLAC) and muons (BCDMS, E665, NMC) on a fixed target. The data are plotted as a function of Q^2 in bins of fixed x. Some points have been slightly offset in Q^2 for clarity. The H1+ZEUS combined binning in x is used in this plot; all other data are rebinned to the x values of these data. For the purpose of plotting, F_2 has been multiplied by 2^{i_x} , where i_x is the number of the x bin, ranging from $i_x = 1$ ($x = 0.85$) to $i_x = 24$ ($x = 0.00005$). The plot is taken from [7].

analogous to the electric charge.

Section 2.2.1 introduces the basics of QCD, while in Sections 2.2.2 and 2.2.3 two important aspects of perturbative QCD are described: renormalisation and factorisation.

The review given in this Section is largely based on [1, 9].

2.2.1 Basics of QCD

QCD is a non-abelian gauge theory with quark-gluon interaction generated by the SU(3) group structure of the colour charges. The fermion wave-functions transform as

$$\psi(x) \rightarrow \psi'(x) = e^{ig(t\cdot\theta(x))}\psi(x), \tag{2.10}$$

where g is the constant representing the coupling strength and $(t \cdot \theta)$ represents the product of the colour group generators with a vector of space-time phase functions in colour space. The group generators t^a satisfy

$$[t^a, t^b] = if^{abc}t^c, \tag{2.11}$$

where f^{abc} are the structure constants. The gluon field-strength tensor is

$$F_a^{\mu\nu} = \delta^\mu A_a^\nu - \delta^\nu A_a^\mu + g f_{abc} A_b^\mu A_c^\nu, \tag{2.12}$$

where A_a (a = 1–8) are the gluon fields and the final term represents the interaction of the gluons amongst themselves as they also carry colour charges. The quark spinor fields ψ_i transform as triplets under SU(3) with i = 1–3 running over the three colour indices. The Lagrangian density is given by

$$\mathcal{L}_{\text{QCD}} = \sum_f \bar{\psi}_f^i (i\gamma_\mu D^\mu - m_f)_{ij}\psi_f^j - \frac{1}{4}F_a^{\mu\nu}F_{\mu\nu}^a, \tag{2.13}$$

where m_f are mass parameters, the covariant derivative D_{ij}^μ is

$$D_{ij}^\mu = \delta_{ij}\partial^\mu + ig(t^a)_{ij}A_a^\mu \tag{2.14}$$

and $(t^a)_{ij}$ are 3×3 hermitian matrices, which for the fundamental triplet representation of SU(3) are $(\lambda^a)_{ij}/2$, where λ_a are the Gell-Mann matrices.

Note that the same coupling constant g couples the gluon fields to themselves (in $F_a^{\mu\nu}$) and the gluon to the quark fields through the covariant derivative (D_{ij}^μ). This is the major difference between QCD and Quantum Electrodynamics (QED): in QCD the strong force quanta — the spin-1 massless gluons — also carry colour charges and thus couple to other gluons, while in QED the photon does not couple to other photons.

2.2.2 Perturbative calculations and renormalisation

In the approach of perturbative QCD (pQCD), any physical quantity, Γ, is given as a power series in the strong coupling constant, α_s (conventionally $\alpha_s = g^2/4\pi$):

$$\Gamma = \sum_{i=0}^{n} c_i \alpha_s^i, \tag{2.15}$$

where n is the order of the calculation and the coefficients c_i are determined using the Feynman rules. The derivation of Feynman rules from $\mathcal{L}_{\mathrm{QCD}}$ and their use, even at the tree-level, is non-trivial as non-Abelian gauge theories give rise to greater complications in handling quantisation and gauge invariance than QED. Most of the tree-level results can be derived from the QED calculation with the addition of colour factors, given by the summation over the involved states. However, in the tree approximation, the dynamical effect of QCD does not show up and the really important ingredient of QCD is hidden in the QCD radiative corrections to the tree amplitudes, which necessarily include the contributions of loop diagrams.

Contributions to the perturbative expansion of scattering amplitudes beyond the leading order (LO) are usually formally divergent because of the unrestricted integration over the momentum flowing around loops (ultraviolet divergencies). The way in which these divergences are regulated is known as *renormalisation*[4]. In the renormalisation procedure there exists an arbitrariness of how to define divergent pieces, i.e. how much of the finite pieces are to be subtracted together with the infinities; therefore different *renormalisation schemes* (RS) exist. Moreover, in subtracting the divergences in any RS, an arbitrary mass scale is introduced, known as the *renormalisation scale*, μ_r.

Because of this arbitrariness, there are many possible finite expressions for one physical quantity depending on the choice of the RS and scale, connected by a finite renormalisation. Since they are obtained for one physical quantity starting from the unique Lagrangian, they describe a unique physical phenomenon and hence have to be equivalent under a finite renormalisation. This requirement defines the renormalisation group equations, which express the response of renormalised parameters (e.g. coupling constant and masses) to the change of the renormalisation scale μ_r.

Most commonly the modified minimal subtraction scheme, $\overline{\mathrm{MS}}$, is used [10, 11]. Considering the important case of the renormalised coupling, g_r, the renormalisation group equation in the $\overline{\mathrm{MS}}$ scheme is given by

$$\mu_r \frac{\mathrm{d}g_r}{\mathrm{d}\mu_r} = \beta(g_r), \tag{2.16}$$

where β is known as the QCD β-function; it is currently calculated in the perturbative approach

[4] Although renormalisation is not necessarily directed to the elimination of divergences; there may be a finite renormalisation, discussed later.

to three loops [7]:

$$\begin{aligned}\beta(g_r) &= -\beta_0 g_r^3 - \beta_1 g_r^5 - \beta_2 g_r^7 + O(g_r^9),\\ \beta_0 &= \frac{1}{(4\pi^2)^2},\\ \beta_1 &= \frac{1}{4\pi^4}\left(102 - \frac{38}{3}n_f\right),\\ \beta_2 &= \frac{1}{(4\pi)^6}\left(\frac{2857}{2} - \frac{5033}{18}n_f + \frac{325}{54}n_f^2\right),\end{aligned} \tag{2.17}$$

where n_f is the number of quark flavours appearing in the loops. Keeping only the one-loop order, the running coupling is given by

$$g_r^2 = \frac{1}{\beta_0 \ln(\frac{\mu_r^2}{\Lambda_{\mathrm{QCD}}^2})}, \tag{2.18}$$

where a constant of integration, Λ_{QCD}, is introduced, since the boundary condition for Eq. 2.16 is not provided. Λ_{QCD} is often referred to as the QCD scale parameter; it has to be extracted from data and is the only adjustable parameter in QCD (except for the quark masses).

Two important notes have to be made concerning the QCD β-function:

1. the expansion parameters of the β-function, β_i, fully define the RS and can be used for labeling different RSs in the massless approach[5] [12];

2. β_0 and β_1 are RS-independent; this is a consequence of the requirement stated above that physical quantities must be RS-independent.

The latter means that the running of the coupling given by Eq. 2.18 is not an artefact of the given RS but is a property of QCD.

Due to the minus sign in the β-function expansion (Eq. 2.17) the renormalised coupling tends to decrease as the relevant momentum scale grows. This behaviour is known as *asymptotic freedom*; it represents the justification that perturbative calculations are applicable for large momentum scales (short distances). On the other hand, the coupling increases as the energy scale decreases (long distances) and at Λ_{QCD} the coupling diverges. Thus quarks and gluons are not observed as free particles, because, with increasing distance between them, at some point it is more energetically favourable for a new quark-antiquark pair to appear spontaneously; this phenomenon is known as *confinement*.

In determinations of the QCD coupling one usually quotes the value of α_s at the scale $\mu_r^2 = M_Z^2$. The following average was obtained from the different measurements [7]:

$$\alpha_s^{n_f=5}(M_Z) = 0.1185 \pm 0.0006. \tag{2.19}$$

[5] If mass terms are present, then different ways of renormalising the mass could also affect the calculations of physical quantities; while in massless theory different RSs mean only different variants of the renormalised coupling [12].

The measurements of α_s as a function of the energy scale are shown in Fig. 2.5 [7]. The running of α_s follows the expectation from pQCD.

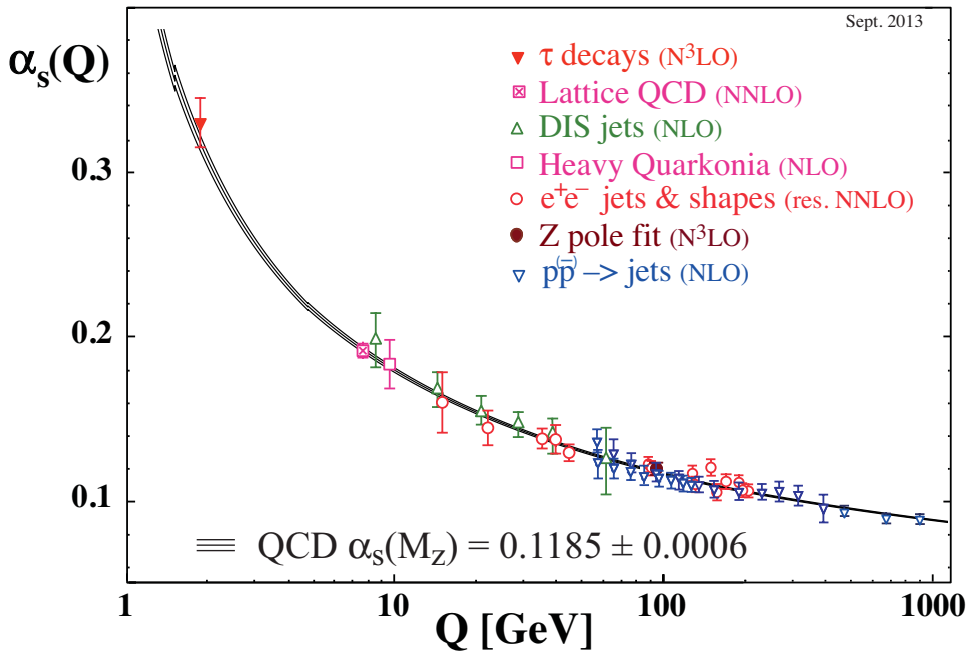

Figure 2.5: Summary of measurements of α_s as a function of the energy scale Q. The respective order of pQCD used in the extraction of α_s is indicated in brackets. The plot is taken from [7].

In the practical application of perturbation theory, the perturbative series 2.15 is truncated at a certain order N to obtain an approximate expression of the physical quantity, $[\Gamma]_N$; then the quantity $[\Gamma]_N$ itself turns out to be scheme-dependent in the order of $O(\alpha_s^{N+1})$ because of the neglected terms. This dependence is two-fold: the arbitrariness of choosing the RS and the arbitrariness in choosing the renormalisation scale. Just as the second arbitrariness is characterised by the scale parameter μ_r, it is also possible to give an explicit parametrisation for the first one by using suitable renormalisation parameters, e.g. the expansion parameters β_i [12]; both aspects will be referred to as the *scheme dependence* (although usually in practice the choice of μ_r is more interesting). This scheme dependence of perturbative predictions gives rise to serious complications in the phenomenological applications of pQCD and is discussed in the next Section 2.2.2.1.

2.2.2.1 Prescriptions on the scale choice

The scheme dependence mentioned in Section 2.2.2 is not a QCD problem, but rather a problem of approximation: this is the question how best to choose the RS and μ_r to achieve the ultimate convergence of the perturbative series [12][6].

[6] From this point of view the scheme dependence can be even thought of as a fortunate feature of the renormalisation procedure: there is a degree of freedom, which can be adjusted to obtain a more precise approximation at a given order.

A realistic way of circumventing this problem is to try to make the size of the neglected orders as small as possible by varying the RS and μ_r.[7] There are two general strategies:

1. to compare the calculated highest-order term with the lower-order ones and find the best μ_r for which this ratio is minimised, so that the fast convergence of the perturbation series is apparently guaranteed. This is also known as the *fastest apparent convergence* [13];

2. to require that an ideal truncated perturbative series $[\Gamma]_N$ has to share the property possessed by the full series, i.e. the property of RS-independence. In other words, the best RS is determined by the requirement that $[\Gamma]_N$ be least sensitive to a variation of the RS parameters. This is also known as the *principle of minimal sensitivity* [12, 14, 15].

In practice one usually chooses the renormalisation scale to be of the order of the energy involved in the hard process; e.g. for inclusive DIS the renormalisation scale is often set to the virtuality $\mu_r^2 = Q^2$ while for the production of heavy quarks in DIS and PHP, $\mu_r^2 = Q^2 + 4m_Q^2$ and $\mu_r^2 = \langle p_T^2 \rangle + m_Q^2$ are possible choices, respectively, where m_Q denotes the heavy-quark mass and $\langle p_T^2 \rangle$ is the average squared transverse momentum of the heavy quark and antiquark.

On the other hand, the scheme dependence can be used to estimate the missing higher orders, known also as perturbative uncertainties or scale uncertainties. For this purpose, one usually varies the renormalisation scale by some factor (conventionally a factor of 2) around the central value and assigns the difference as the uncertainty.

2.2.2.2 Quark masses

The key quantity of heavy-quark theory is the quark mass, m_Q. Since free quarks are unobservable, one can suggest different definitions of m_Q. One of the most popular choices is the pole quark mass, m_Q^{pole}, defined as the position of the pole in the quark propagator in perturbation theory. This quantity is introduced in a gauge invariant way and is well defined in each finite order of perturbation theory. This convenient feature has made it very popular and widely used in perturbative calculations, although it has an important drawback: any definition of this quantity suffers from an intrinsic uncertainty of order $\frac{\Lambda_{\text{QCD}}}{m_Q}$. The problem arises for the reason that the pole mass is sensitive to large-distance dynamics (infrared contributions).[8]

Alternative mass definitions offer a solution to this problem. The most prominent example is the $\overline{\text{MS}}$ mass, $m_Q(\mu_r)$, which is to be evaluated at the renormalisation scale μ_r, where $\mu_r \gg \Lambda_{\text{QCD}}$, and which is free of ambiguities of order Λ_{QCD}. One benefit of theory predictions using the $\overline{\text{MS}}$ mass is improved stability of the perturbative series with respect to scale variations as compared to the result in the pole-mass scheme [17]. The scale dependence of the running

[7] Although puristically there are no means for estimating the size of the neglected orders without calculating these terms.

[8] In other words, the pole mass is unobservable, because of confinement no free colored quarks exist. Perturbation theory itself produces clear evidence for this non-perturbative correction to m_Q^{pole}: the signal is the peculiar factorial growth of the high-order terms in the α_s expansion corresponding to a renormalon; for more details see, e.g. [16] and references therein.

mass at LO is given by

$$m_Q(\mu_r) = m_Q(m_Q)\left(1 - \frac{\alpha_s(\mu_r)}{\pi} \ln \frac{\mu_r^2}{m_Q^2}\right). \tag{2.20}$$

The scale dependence of the charm and beauty running masses has been measured at LEP and HERA [18–20] and is shown in Fig. 2.6. It is found to be consistent with the QCD expectation.

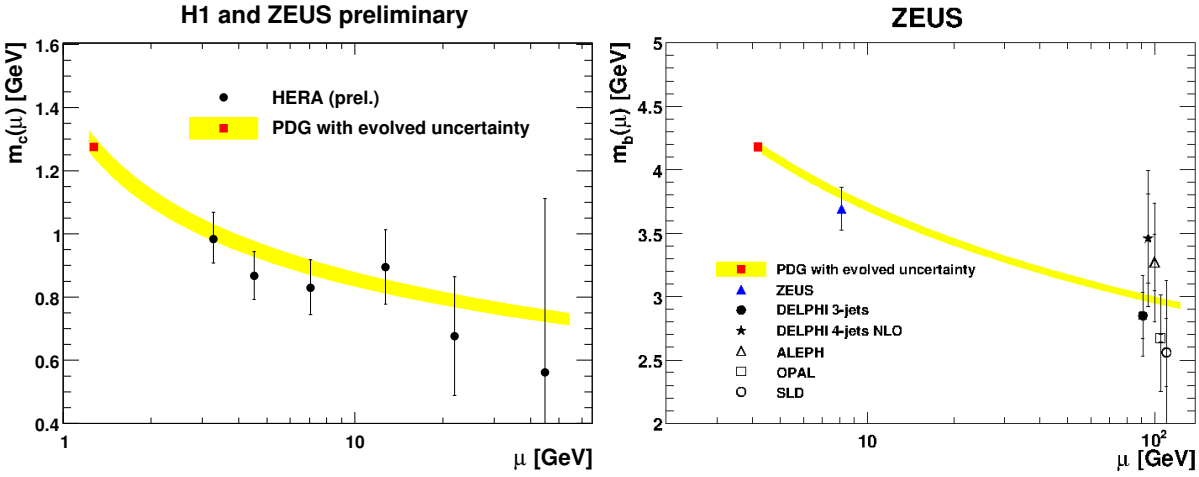

Figure 2.6: Measurements of the charm (left) and beauty (right) $\overline{\text{MS}}$ running masses as a function of the energy scale μ [18–20].

The relation between the pole mass m_Q^{pole} and the $\overline{\text{MS}}$ running mass $m_Q(m_Q)$, i.e. evaluated at the scale $\mu_r = m_Q$, is known to three loops [21–24]; at one-loop order it is given by

$$m_Q^{\text{pole}} = m_Q(m_Q)\left(1 + \frac{4\alpha_s(m_Q)}{3\pi}\right). \tag{2.21}$$

2.2.3 Factorisation and evolution of parton distribution functions

The field-theory realisation of the parton model is the theorem of the factorisation of the long-distance from the short-distance dependence for DIS [25]. This theorem states that the sum of all the diagrammatic contributions to the structure functions is a direct generalisation of the parton-model results, Eq. 2.8, given by

$$F_2(x, Q^2) = \sum_i \int_0^1 \mathrm{d}\xi C_2^i\left(\frac{x}{\xi}, \frac{Q^2}{\mu_r^2}, \frac{\mu_f^2}{\mu_r^2}, \alpha_s(\mu_r^2)\right) f_i(\xi, \mu_f^2), \tag{2.22}$$

where i denotes the sum over all partons (quarks, antiquarks and gluons), ξ is the momentum fraction of the parton i, C_2^i are the *coefficient functions* (known also as the hard-scattering functions, or matrix elements), f_i are the *parton distribution functions* (PDF) and μ_f is called

the *factorisation scale*. The factorisation scale serves to define the separation of short-distance from long-distance effects: any propagator that is off-shell by μ_f^2 or more will contribute to C_2^i, while below this scale it will be grouped into f_i. It appears in the definition of the PDFs in a fashion very similar to the way the renormalisation scale μ_r appears in renormalisation.

The substance of factorisation is contained in the following properties of the functions C_2^i and f_i:

- each coefficient function C_2^i is infrared safe and calculable in perturbation theory. It depends on the electroweak vector boson V^*, on the parton i, and on the renormalisation and factorisation scales, but it is independent of long-distance effects. In particular it is independent of the identity of the initial hadron; e.g. it is the same in the DIS from a proton and a neutron and, for that matter, from a pion or kaon;

- the PDF f_i, on the other hand, is specific to the hadron h. It is universal, that is, it is independent of the particular hard-scattering process which is treated. It is the same for the different structure functions F_2, F_L and F_3 and it depends on neither a boson V^*, nor even virtuality Q^2, unless the factorisation scale is set to $\mu_f^2 = Q^2$. It is a direct generalisation of the parton-model quark distribution.

The C_2^i may be calculated in perturbation theory but the f_i must be measured by comparing Eq. 2.22 to experiment, given explicit expressions for the C_2^i. Once enough data have been amassed to determine the PDFs from some standard set of cross sections, factorisation can be exploited to provide predictions for any factorisable process, and, in particular, for the evolution of a given process with μ_f.

Such a prescription obviously involves a degree of choice. A set of rules that makes these choices is called a *factorisation scheme* (e.g. $\overline{\text{MS}}$ [10, 11] or DIS [26]), by analogy to the RS (see Section 2.2.2). Such a scheme defines the hard-scattering functions and the PDFs simultaneously. Once this has been done, the PDFs have no particular meaning, since they are dominated by infrared effects and thus by infrared parameters that cannot be measured, although they can be extracted from data by comparing the theoretical calculation 2.22 with measured cross sections. The factorisation theorem ensures that the hard-scattering functions determined in this calculation are insensitive to infrared scales and parameters, and are applicable to cross sections calculated with phenomenologically determined PDFs.

A remarkable consequence of factorisation is that measuring PDFs for one scale μ_f allows their prediction for any other scale μ_f', as long as both μ_f and μ_f' are large enough that both $\alpha_s(\mu_f')$ and $\alpha_s(\mu_f)$ are small. The evolution of PDFs in μ_f is most often, and most conveniently, described in terms of integro-differential equations:

$$\mu_f^2 \frac{\mathrm{d}}{\mathrm{d}\mu_f^2} f_i(\xi, \mu_f^2) = \sum_i \int_x^1 \frac{\mathrm{d}\xi}{\xi} P_{ij}\left(\frac{x}{\xi}, \alpha_s\right) f_i(\xi, \mu_f^2). \tag{2.23}$$

These equations are known as the *Dokshitzer-Gribov-Lipatov-Altarelli-Parisi (DGLAP) equations* [27–32]. The *evolution kernels* $P_{ij}(x)$, also known as the *splitting functions*, are given by perturbative expansions, beginning with $O(\alpha_s)$; they represent the probability of a parton i to emit a parton j carrying a fraction $z = \frac{x}{\xi}$ of the momentum of the parton i. The tree-level and

one-loop terms in $P_{ij}(x)$ are independent of the factorisation scheme used to define the PDFs. The tree-level diagrams of the splitting functions are shown in Fig. 2.7.

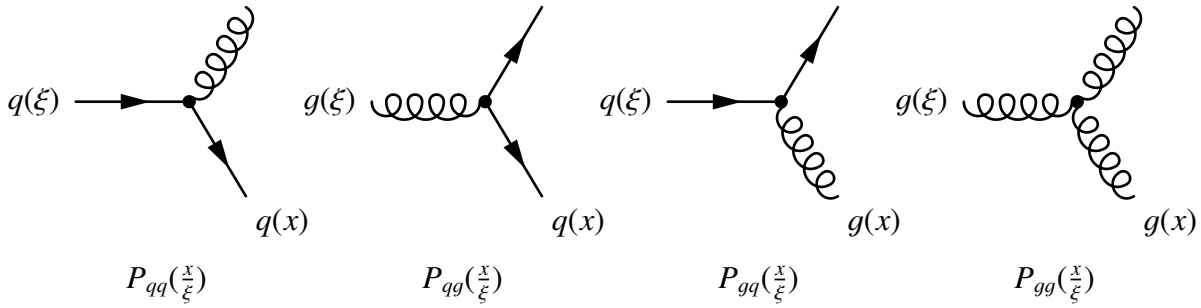

Figure 2.7: The tree-level DGLAP splitting functions.

Note that the integral on the right-hand side of Eq. 2.23 begins at x. Thus, it is only necessary to know $f_i(\xi, \mu_{f_0}^2)$ for $\xi > x$ at some starting value of the scale μ_{f_0}, in order to derive $f_i(x, \mu_f^2)$ at a higher value μ_f. This is a great simplification, since data at small x are hard to come by at moderate energies.

At very low values of x, terms proportional to $\alpha_s \ln(\frac{1}{x})$ may spoil the accuracy of the DGLAP approach; there other evolution schemes, e.g. BFKL [33–35] or CCFM [36–39], might be more appropriate to use. The difference between the schemes comes from the ordering of the emitted partons before entering the hard-scattering process.

Similar to the RS dependence (see Section 2.2.2), if the perturbative series is truncated at a certain order, the approximation is μ_f dependent in the neglected orders. The prescriptions how to choose the μ_r given in Section 2.2.2.1 can be applied for the μ_f also. In practice the two scales are often set to be equal, although it is not a requirement. To estimate the perturbative uncertainties of the neglected higher orders, the two scales are varied around the central values, simultaneously or independently.

2.3 Heavy-quark production in pQCD

The masses of the heavy quarks $m_Q \gg \Lambda_{\mathrm{QCD}}$ ($m_c \approx 1.5\,\mathrm{GeV}$, $m_b \approx 4.5\,\mathrm{GeV}$, $m_t \approx 170\,\mathrm{GeV}$) provide a hard scale for pQCD calculations. On the other hand they complicate calculations, since a new hard scale leads to appearance of terms proportional to $\ln(\frac{p_T^2}{m_Q^2})$ or $\ln(\frac{Q^2}{m_Q^2})$ (this is known as a *multi-scale problem*); an ambiguity exists also for the PDF evolution and α_s running, since they depend on the number of quark flavours assumed to be massless and appearing in loops and legs.

Section 2.3.1 overviews possible treatments of heavy-quark production. Sections 2.3.2 and 2.3.3 provide information on the current status of the calculations for heavy-quark production in different schemes in ep and pp collisions, respectively. Finally, Section 2.3.4 reviews an important non-perturbative aspect of heavy-flavour production: the fragmentation process of partons into hadrons.

The review given in this Section is largely based on [40] (Section 2.3.2), [41, 42] (Section 2.3.3) and [43] (Section 2.3.4).

2.3.1 Treatment of heavy flavours in pQCD

Several schemes exist for the treatment of heavy flavours in pQCD:

- In the *fixed-flavour-number scheme* (FFNS), heavy quarks are treated as massive at all energy scales, thus they do not appear in the PDF evolution and α_s running.[9] More precisely, the FFNS should be specified with the number of flavours that are assumed to be massless, e.g. in the FFNS with $n_f = 3$, only u, d and s quarks are treated as massless, while in the FFNS with $n_f = 4$ or $n_f = 5$, additionally c quarks, or c and b quarks, are treated as massless, respectively. This scheme is expected to be most precise in the threshold region $Q^2 \sim m_Q^2$ ($p_T^2 \sim m_Q^2$), while at high Q^2 (p_T^2) terms proportional to $\ln(\frac{Q^2}{m_Q^2})$ ($\ln(\frac{p_T^2}{m_Q^2})$) may spoil the convergence of the perturbative series.

- In the *variable-flavour-number scheme* (VFNS), heavy quarks are treated as massive or massless depending on the energy scale. Different variants of VFNS exist:
  - in the *zero-mass variable-flavour-number scheme* (ZM-VFNS) [46], heavy flavours are treated as infinitely massive (and thus fully vanishing) below a certain threshold and as massless above it. This scheme is expected to be appropriate at high Q^2, since the PDF evolution of the "heavy" quarks and the renormalisation of collinear and infrared singularities provides a resummation of terms proportional to $\ln \frac{Q^2}{m_Q^2}$.
  - in the *general-mass variable-flavour-number scheme* (GM-VFNS), an interpolation is made between the FFNS and the ZM-VFNS, avoiding double counting of common terms in the PDF evolution and coefficient functions. This scheme is expected to combine the advantages of the FFNS and ZM-VFNS, although some level of arbitrariness is unavoidably introduced in the treatment of the interpolation. Therefore, different variants of the GM-VFNS are available [47–58]. Moreover, this arbitrariness prevents a clear interpretation of the heavy-quark masses in terms of a specific scheme; therefore the heavy-quark masses in GM-VFNS can be treated as effective mass parameters.

In the present thesis in most cases the FFNS is used in comparisons of theory to the data and QCD analyses.

2.3.2 Heavy-quark production in ep collisions

Heavy-quark production in ep collisions serves as a stringent test of pQCD; moreover, it is directly sensitive to the gluon density of the proton and to the heavy-quark masses.

The fractions of the inclusive structure functions F_2, F_L, related to heavy-flavour production, are represented by the heavy-flavour structure functions, $F_2^{Q\bar{Q}}$, $F_L^{Q\bar{Q}}$ (Q stands for charm or beauty; top production is not accessible at HERA). The inclusive differential cross section of

[9] Note that in some variants of the FFNS, heavy quarks contribute to the loops in the PDF evolution and α_s running (see, e.g. [44]); sometimes these variants are called the *mixed-flavour-number scheme* [45].

heavy-flavour production is given in terms of these structure functions, analogously to Eq. 2.3, as

$$\frac{\mathrm{d}^2\sigma^{Q\bar{Q}}(ep)}{\mathrm{d}x\mathrm{d}Q^2} = \frac{2\pi\alpha^2}{Q^4 x}[Y_+ F_2^{Q\bar{Q}}(x,Q^2) - y^2 F_L^{Q\bar{Q}}(x,Q^2)], \tag{2.24}$$

where the term proportional to F_3 is neglected as appropriate at not too high Q^2. Often it is expressed in terms of the *reduced cross sections*:

$$\sigma_{\mathrm{red}}^{c\bar{c}} = \frac{\mathrm{d}^2\sigma^{c\bar{c}}}{\mathrm{d}x\mathrm{d}Q^2} \cdot \frac{xQ^4}{2\pi\alpha^2\,(1+(1-y)^2)} = F_2^{c\bar{c}} - \frac{y^2}{1+(1-y)^2} F_L^{c\bar{c}}. \tag{2.25}$$

The heavy-flavour structure functions $F_2^{Q\bar{Q}}$, $F_L^{Q\bar{Q}}$ are calculated in pQCD using the factorisation approach (Eq. 2.22).

The charm contribution to the inclusive structure function F_2 at HERA lies in the range 10–30% [59], thus necessitating its understanding for any global PDF fit based on HERA DIS data.

2.3.2.1 Calculations in FFNS

In the FFNS, the LO process ($O(\alpha_s)$) for heavy-flavour production in DIS is the boson–gluon-fusion (BGF) process, $g\gamma^* \to Q\bar{Q}$, shown in Fig. 2.8.

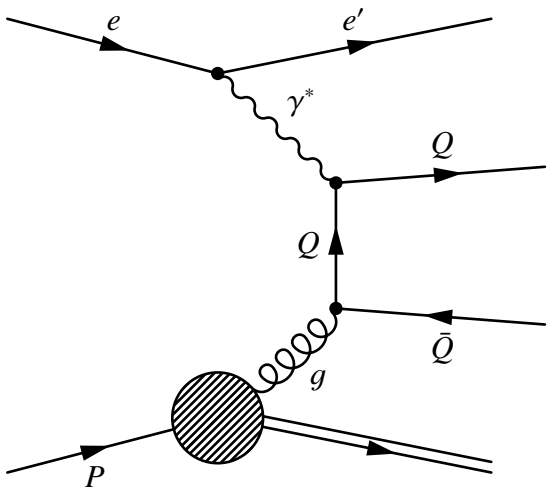

Figure 2.8: The BGF diagram.

Next-to-leading-order (NLO) corrections ($O(\alpha_s^2)$) were calculated in [60, 61]. They can be classified into three groups:

1. real corrections to the BGF process, i.e. all processes containing an extra gluon in the final state $g\gamma^* \to Q\bar{Q}g$;

2. virtual corrections to the BGF process coming from the interference of $O(\alpha_s)$ and $O(\alpha_s^3)$ terms;

3. a new process, when the virtual photon interacts with a light quark in the proton: $\gamma^* q(\bar{q}) \rightarrow Q\bar{Q}q(\bar{q})$.

The NLO predictions [60, 61] have been recalculated fully differentially in [62]; they are available in the HVQDIS program, which calculates double-particle inclusive cross sections. The pole-mass definition is used in these calculations.

In a recent variant of the FFNS from the ABM group the running-mass definition in the $\overline{\text{MS}}$ scheme is used instead [17]. This scheme has the advantage of improving the convergence of the perturbative series (see Section 2.2.2.2). These predictions are provided for inclusive quantities only, i.e. at the $F_2^{Q\bar{Q}}$ level.

At next-to-next-to-leading order (NNLO) ($O(\alpha_s^3)$) only approximate calculations are available; the most comprehensive results are given in [63], which contains combined approximate expressions for three kinematic limits: in the limit of high partonic centre-of-mass energy squared, $\hat{s} \gg m_Q^2$, in the threshold region, $\hat{s} \gtrsim 4m_Q^2$, and in the high-scale region $Q^2 \gg m_Q^2$.

2.3.2.2 Calculations in VFNS

In the VFNS, the LO process for heavy-flavour production in ep collisions is the QPM-like scattering (see Fig. 2.3) at order zero in α_s. At NLO, fully differential calculations exist only in the ZM-VFNS.

The main difference between the FFNS and ZM-VFNS mechanisms can be attributed to the fact that for heavy-quark production in the FFNS, two heavy particles appear in the final state instead of one as in the case of the intrinsic heavy-quark approach[10]. This reveals itself in the p_T-distribution where for the FFNS the quark and antiquark appear back to back in the Breit frame. The heavy-flavour data from HERA [64, 65] clearly confirm the p_T-spectrum predicted by the FFNS production mechanism.

Calculations in the GM-VFNS for heavy-flavour production in DIS exist only at the inclusive $F_2^{Q\bar{Q}}$ level. The two most popular GM-VFNS are the Thorne-Roberts (RT) [53, 54, 58] and Aivazis-Collins-Olness-Tung (ACOT) [47, 48, 50–52] schemes. The calculations are available at NLO and (approximate) NNLO orders. Predictions from various variants of GM-VFNS were compared to the combined HERA charm data in [66]; they are generally found to describe the data well in the region $Q^2 \gtrsim 5\,\text{GeV}^2$.

2.3.3 Heavy-quark production in pp collisions

Similar to the case of ep collisions, heavy-quark production in hadronic collisions is interesting either as a benchmark process for the study of pQCD or as a probe of the nucleon structure [41]. Some examples of the latter include:

- Inclusive heavy-flavour production at high energy mostly probes the gluon density of the proton, since the leading process is $gg \rightarrow Q\bar{Q}$. This covers a wide kinematic range, because a hard scale provided by the mass of heavy quarks allows applicability of pQCD even at low transverse momentum $p_T \sim \Lambda_{\text{QCD}}$.

[10] In this case the other heavy quark belongs to the proton remnant and thus is effectively integrated over.

- $W^{\pm} + c$ final states probe the strange content of the proton, since the leading production mechanism is $gs \rightarrow W^{\pm}c$.
- Associated production of $W^{\pm}$ and heavy-quark pairs is sensitive to gluon-splitting processes, since the dominant production process is the production of a $W^{\pm}$ and an off-shell gluon, which then decays to the heavy-quark pair: $q\bar{q}' \rightarrow W^{\pm}g^{*} \rightarrow W^{\pm}Q\bar{Q}$.

The understanding of heavy-quark production is also important for searches of possible new physics, where QCD-initiated heavy-quark final states provide large backgrounds for such analyses.

The cross sections for heavy-flavour production in pp collisions are calculated in pQCD using the factorisation approach, similar to Eq. 2.22:

$$\sigma^{Q\bar{Q}} = \sum_{i,j} \int_0^1 \int_0^1 \mathrm{d}x_1 \mathrm{d}x_2 f_i(x_1, \mu_f^2) f_j(x_2, \mu_f^2) \hat{\sigma}_{ij\rightarrow Q\bar{Q}}(x_1, x_2, \mu_f^2). \tag{2.26}$$

Here the sum in i, j goes over all partons, $\hat{\sigma}_{ij\rightarrow Q\bar{Q}}$ is the perturbatively calculated partonic cross section, independent of the initial hadrons, and f_i, f_j are the universal PDFs for the two protons, introduced in Section 2.2.3.

In the FFNS at LO two processes are responsible for heavy-quark production:

$$q\bar{q} \rightarrow Q\bar{Q} \quad \text{and} \quad gg \rightarrow Q\bar{Q}. \tag{2.27}$$

The corresponding diagrams are shown in Fig. 2.9.

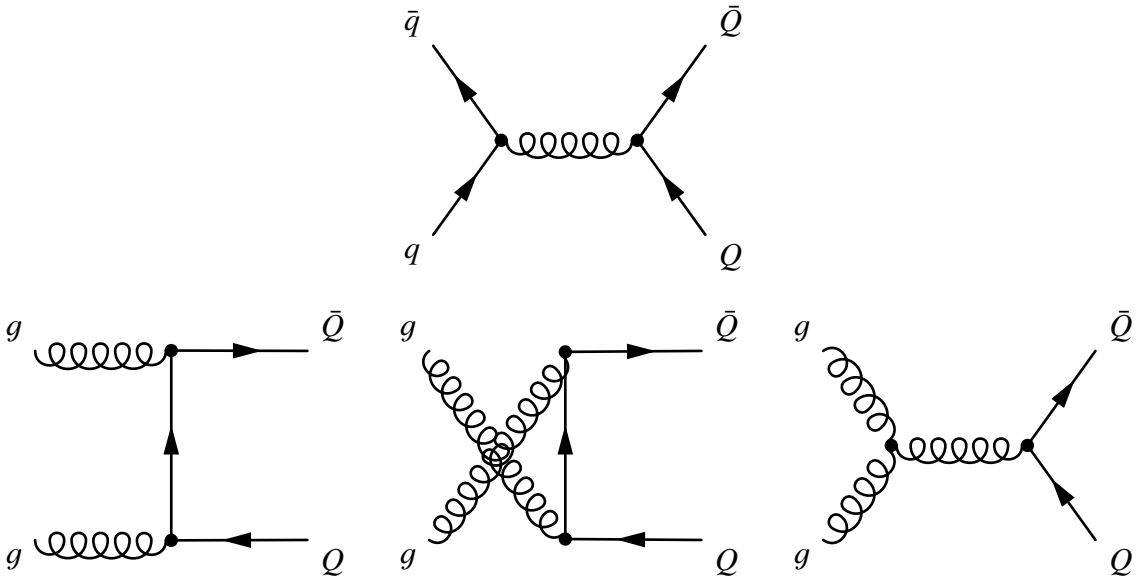

Figure 2.9: LO diagrams for heavy-quark production in pp collisions.

The total production cross section for heavy quarks is finite at LO, owing to the fact that m_Q^2 is the minimum virtuality exchanged in the t-channel, therefore no poles can develop in the intermediate propagators. This is not the case for light quarks: the total production cross

section for u or d quarks is not calculable in pQCD [41]. At large partonic centre-of-mass energy squared the $q\bar{q}$ rate reduces more quickly than gg. Additionally, threshold effects for the $q\bar{q}$ channel vanish very quickly as soon as $\hat{s} > 4m_Q^2$; this is related to the spin 1/2 of quarks [41].

2.3.3.1 MNR calculations

NLO corrections come from two sources of $O(\alpha_s^3)$ diagrams: real- and virtual-emission diagrams. In the first case, the corrections come from the square of the real-emission matrix elements; in the second case, from the interference of the virtual matrix elements (of $O(\alpha_s^4)$) with the tree-level ones (of $O(\alpha_s^2)$). Ultraviolet divergences in the virtual diagrams are removed by the renormalisation process. Infrared and collinear divergences, which appear both in the virtual diagrams and in the integration over the emitted parton in the real-emission processes, cancel each other or are absorbed in the PDFs. The complete calculations of NLO corrections to the production of heavy-quark pairs in hadro- and in photoproduction were done in [67, 68] (total hadroproduction cross sections), [69, 70] (one-particle inclusive distributions in hadroproduction), [71, 72] (total and one-particle inclusive distributions in ep PHP), [73] (two-particle inclusive distributions in hadroproduction) and [74] (two-particle inclusive distributions in ep PHP). They are known as MNR calculations and are available in the MNR program, which calculates double- or single-particle inclusive or total cross sections. The pole-mass definition is used in the calculations.

There are a few important remarks concerning the NLO calculations:

- no collinear singularities appear when gluons are emitted from the final-state heavy quarks, since they are screened by the heavy-quark mass. Therefore, contrary to the case of a light parton, the p_T distribution for a heavy quark is a well-defined quantity in NLO. For light partons, a collinear singularity would be encountered that requires the introduction of a fragmentation function, not calculable from first principles (see also Section 2.3.4);

- at large p_T, nevertheless, large $\ln(p_T/m_Q)$ factors appear, signalling the increased probability of collinear gluon emission. At large p_T, the massive quark looks in fact more and more like a massless particle. These logarithms can be resummed using the fragmentation-function formalism (see next Section 2.3.3.2);

- new processes appear at NLO which drastically change the $\hat{s}$ dependence of the cross sections and/or the kinematic distributions;

- there is evidence however that NLO is not sufficient to get accurate estimates, since a large scale dependence is still present. This is demonstrated in Fig. 2.10, which shows the scale dependence of the inclusive p_T distribution of b quarks at the Tevatron. Large scale dependence is a symptom of large NNLO corrections.

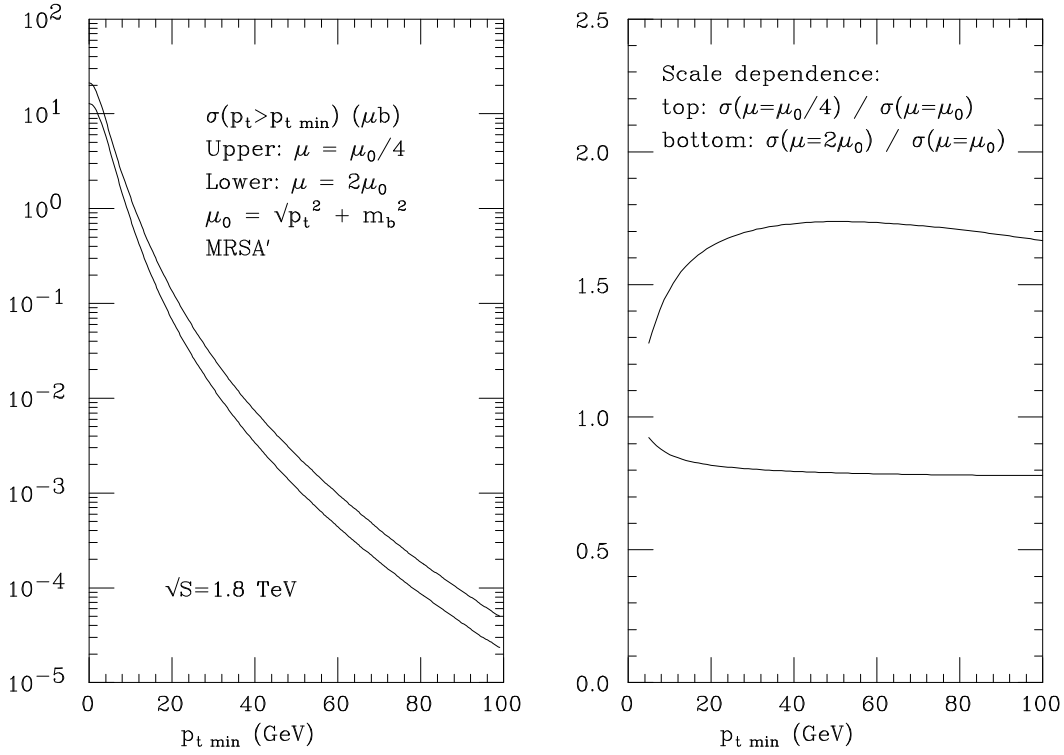

Figure 2.10: Scale dependence of the inclusive p_T distribution for b quarks, in $p\bar{p}$ collisions at $\sqrt{s}$ = 1.8 TeV. The plot is taken from [41].

2.3.3.2 FONLL calculations

The fixed-order plus next-to-leading-logarithms (FONLL) calculations [75] were developed for improving the large-p_T differential cross section for heavy-quark production in hadron–hadron collisions and then were extended to PHP in ep collisions [76]. This approach is a variant of GM-VFNS, based on the matching of NLO massive and massless calculations according to the prescription [42]:

$$\mathrm{d}\sigma_{\mathrm{FONLL}} = \mathrm{d}\sigma_{\mathrm{FO}} + (\mathrm{d}\sigma_{\mathrm{RS}} - \mathrm{d}\sigma_{\mathrm{FOM0}}) \times G(m_Q, p_T). \tag{2.28}$$

Here FO denotes the massive NLO cross section, where a heavy quark enters only in the partonic scattering through the flavour-creation processes, but not in the PDFs, and its mass is kept as a non-vanishing parameter. The NLO partonic cross section then includes terms proportional to $\ln \frac{p_T^2}{m_Q^2}$, where m_Q regularises the collinear singularity, e.g. of the splitting $Q \to Qg$, and where the logarithm becomes large when $p_T \gg m_Q$, thus spoiling the perturbative expansion in α_s. This part, which is singular in the massless limit, and the finite parts related to its different definition in dimensional and mass regularisation are denoted FOM0 and therefore resummed to next-to-leading-logarithm (NLL) order in the contribution denoted RS. The RS contribution is then added to the FO calculation, while the overlap FOM0 is subtracted to avoid double counting; this is controlled by the matching function $G(m_Q, p_T)$, which is discussed later.

The resummation relies on the perturbative fragmentation functions for the probability of a

heavy quark, gluon, or light parton to go into a heavy quark [77]. The perturbative fragmentation functions satisfy the DGLAP evolution equations and their initial values at the starting scale are calculable perturbatively. The perturbative fragmentation functions are evolved to the factorisation scale μ_f and convoluted with the NLO cross sections for massless partons, subtracted in the $\overline{\text{MS}}$ scheme, so that flavour-excitation processes are also included. These involve the heavy quark also as an active parton in the PDFs.

The matching function $G(m_Q, p_T)$ must tend to unity in the massless limit $p_T \gg m_Q$, where FO approaches FOM0 and the mass logarithms must be resummed. However, in FONLL its functional form is not simply unity, but rather

$$G(m_Q, p_T) = \frac{p_T^2}{p_T^2 + a^2 m_Q^2}. \tag{2.29}$$

While it fulfills the above condition, the matching is not exact away from the massless limit. This is justified by the observation that the difference RS − FOM0, although formally of NNLO order, turns out to be abnormally large below $p_T = 5m_Q$, so that the constant a is phenomenologically set to $a = 5$.[11]

Comparison of the NLO and FONLL calculations for beauty production at the Tevatron is shown in Fig. 2.11; uncertainty bands obtained from the scale variations are also shown. In summary, the resummation procedure indicates the presence of a small enhancement in the intermediate-p_T region, followed by a reduction of the cross section (and of the uncertainty band) at larger p_T [75]. Both uncertainty bands fully overlap in a wide p_T range.

FONLL predictions for the most recent LHC data are given in [78]; they can be also obtained using the public web interface [79].

2.3.3.3 Other GM-VFNS calculations

Other GM-VFNS calculations were originally performed in the massless limit, valid at high p_T, and therefore include flavour-creation, gluon-splitting and flavour-excitation processes [42]. Subsequently the calculations were improved by identifying the previously omitted finite-mass terms through a comparison with the massive NLO calculation, where together with the mass logarithms, finite terms were also subtracted in such a way that in the limit $m_Q \to 0$ the correct massless $\overline{\text{MS}}$ result was recovered [80]. This is necessary, since the PDFs and perturbative fragmentation functions that are convoluted with the partonic cross sections are defined in the ZM-VFNS. In the calculations in the S-ACOT scheme [51], heavy-quark mass terms in flavour-excitation processes are neglected, which corresponds to a specific choice of the scheme, but no loss in precision.

[11] The choice to control such terms by means of an *ad-hoc* function might seem a somewhat unpleasant characteristic of this approach; however, it simply portraits the freedom one has in performing the matching, and does not represent a shortcoming of the approach [43].

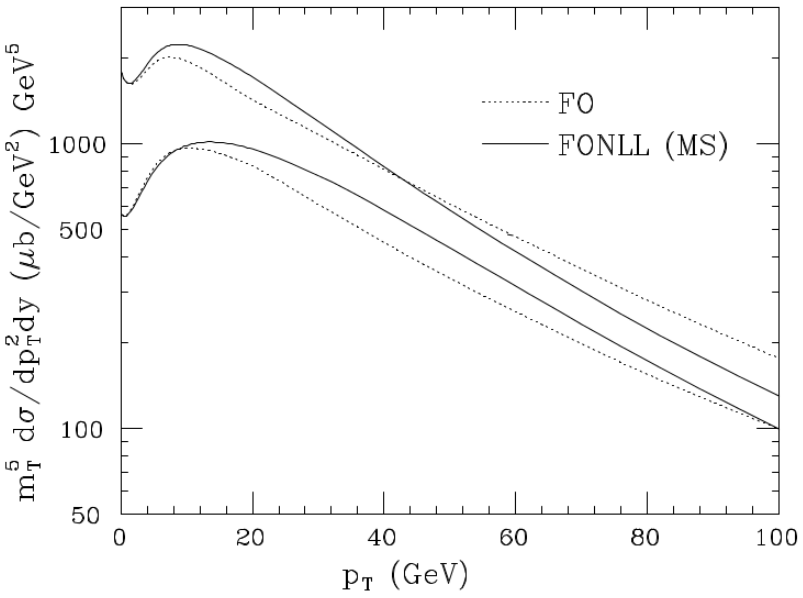

Figure 2.11: Comparison of the uncertainty bands from the scale variations of the NLO and FONLL calculations for beauty production at the Tevatron. The plot is taken from [75].

2.3.4 Fragmentation of heavy quarks

The production of hadrons in QCD can only be described by taking into account a non-perturbative hadronisation phase, i.e. the processes which transform objects amenable to a perturbative description (quarks and gluons) into real particles. In the case of light hadrons, the QCD factorisation theorem [25, 81–85] allows for factorisation of these non-perturbative effects into universal (but factorisation-scheme dependent) fragmentation functions:

$$\frac{\mathrm{d}\sigma_h}{\mathrm{d}p_T}(p_T) = \sum_i \int \frac{\mathrm{d}z}{z} \frac{\mathrm{d}\sigma_i}{\mathrm{d}p_T}\left(\frac{p_T}{z}, \mu\right) D_{i\to h}(z,\mu) + O\left(\frac{\Lambda_{\mathrm{QCD}}}{p_T}\right). \tag{2.30}$$

In this equation, valid up to higher-twist corrections of order $\frac{\Lambda_{\mathrm{QCD}}}{p_T}$, the partonic cross sections $\frac{\mathrm{d}\sigma_h}{\mathrm{d}p_T}$ for production of the parton i are calculated in pQCD, while the fragmentation functions, $D_{i\to h}(z,\mu)$, are usually extracted from fits to experimental data (not to be confused with the heavy-quark perturbative fragmentation functions, introduced in Section 2.3.3.2, which initial values at the starting scale are calculable perturbatively [77]). Due to their universality they can be used to make predictions for different processes. The factorisation scale μ is a reminder of the non-physical character of both the partonic cross sections and the fragmentation functions: it is usually taken of the order of the hard scale of the process (p_T), and $D_{i\to h}(z,\mu)$ are evolved from a low scale up to μ by means of the DGLAP evolution equations.[12]

This general picture becomes somewhat different for the production of heavy-flavoured hadrons. Owing to the large masses of the charm and bottom quarks, acting as a cut-off for the

[12] Note, that this scale μ it is not the μ_f, which was introduced in Section 2.2.3, although the argument for its introduction is the same: to separate long-distance effects. This scale may be called the fragmentation scale.

collinear singularities that appear in higher orders in perturbative calculations, the perturbative prediction for heavy-quark production can be calculated. Still, of course, the quark to hadron transition must be described. Mimicking the factorisation theorem given above, it has become customary to complement the perturbative calculation for heavy-quark production with a non-perturbative fragmentation function, $D^{\mathrm{np}}_{Q\to H}(z)$, accounting for its hadronisation into a meson:

$$\frac{\mathrm{d}\sigma_H}{\mathrm{d}p_T}(p_T) = \int \frac{\mathrm{d}z}{z} \frac{\mathrm{d}\sigma^{\mathrm{pert}}_Q}{\mathrm{d}p_T}\left(\frac{p_T}{z}, m_Q\right) D^{\mathrm{np}}_{Q\to H}(z). \tag{2.31}$$

It is worth noting that at this stage this formula is not the product of a rigorous theorem, but rather results from some sensible assumptions. Moreover, it will in general fail (or at least be subject to large uncertainties) in the region where the mass m_Q of the heavy quark is not much larger than its transverse momentum p_T, since the choice of the scaling variable, z, is no longer unique, and $O(m_Q/p_T)$ corrections cannot be neglected.

An important characteristic of the non-perturbative fragmentation function is that the average fraction of momentum lost by the heavy quark when hadronising into a heavy-flavoured hadron, $\langle z\rangle^{\mathrm{np}}$, is given by [86, 87]

$$\langle z\rangle^{\mathrm{np}} \simeq 1 - \frac{\Lambda_{\mathrm{QCD}}}{m_Q}. \tag{2.32}$$

Since (by definition) the mass of a heavy quark is much larger than the scale Λ_{QCD}, this amounts to saying that the non-perturbative fragmentation function for a heavy quark from Eq. 2.31 is very hard, i.e. the quark loses very little momentum when hadronising. This can also be seen with a very simplistic argument: a fast massive quark will lose very little speed (and hence momentum) when picking up a light quark of mass Λ_{QCD} from the vacuum to form a heavy meson.[13]

This basic behaviour is to be found as a common trait in all the non-perturbative heavy-quark fragmentation functions, derived from various phenomenological models. Among the most commonly used are the Kartvelishvili-Likhoded-Petrov [91], Bowler [92], Peterson-Schlatter-Schmitt-Zerwas [93] and Collins-Spiller [94] functions. These models all provide some functional form for the $D^{\mathrm{np}}_{Q\to H}(z)$ function and one or more free parameters that control its hardness. Such parameters are usually not predicted by the models (or only very roughly), and must be fitted to experimental data.

There are two important aspects concerning the fragmentation of heavy quarks:

1. a non-perturbative fragmentation function is designed to describe the transition from the heavy quark to the hadron, dealing with events mainly populated by soft gluons of energies of the order of Λ_{QCD}. However, if a heavy quark is produced in a high-energy event, it will initially be far off-shell: perturbative hard gluons will be emitted to bring it on-shell, reducing the heavy-quark momentum and yielding in the process large collinear logarithms. The amount of gluon radiation is related to the distance between the heavy-quark mass scale and the hard scale of the interaction, and is therefore process dependent. To

[13] More modern and more rigorous derivations of this result can be found in [88–90].

account for this dependency, different free parameters of the non-perturbative fragmentation function can be used at different centre-of-mass energies or transverse momenta (see, e.g. [95]), or the non-perturbative fragmentation function can be evolved directly by means of the DGLAP equations, hence including the perturbative collinear logarithms. However, this is not what non-perturbative fragmentation functions are meant for, and doing so spoils the validity of the relation in Eq. 2.32;

2. since only the final heavy hadron is observed, both the non-perturbative fragmentation function and the perturbative cross section for producing heavy quarks must be regarded as non-physical objects. The details of the fitted non-perturbative fragmentation function (e.g. the precise value(s) of its free parameter(s)) depend on those of the perturbative cross sections: different perturbative calculations (LO, NLO, FONLL etc.) and different perturbative parameters (heavy-quark masses, strong coupling etc.) lead to different non-perturbative fragmentation functions. These in turn will have to be used only with a perturbative description similar to the one within which they have been determined [96].

CHAPTER 3

Experimental set-up and measurements of heavy-flavour production

This Chapter introduces the experimental set-up and measurements of heavy-flavour production at HERA and LHC, which are relevant for the remainder of this thesis.

The overview starts with a description of the HERA accelerator in Section 3.1.1; it is largely based on [97]. Section 3.1.2 describes the two collider experiments at HERA, H1 and ZEUS; it is largely based on [97, 98]. Techniques of charm tagging at HERA are given in Section 3.1.3, as well as a description of selected measurements from H1 and ZEUS, which are used in Chapter 6 for a data combination. In Section 3.2 selected measurements of charm and beauty production from LHCb are described.

3.1 HERA collider, H1 and ZEUS experiments, measurements of charm production at HERA

The HERA collider was the culmination of 50 years of experimentation with electron, later also muon and neutrino, beams to explore the structure of the proton. HERA emerged from a series of electron–proton accelerator studies in the 70's as the highest energy ep collider possible.

3.1.1 HERA collider

HERA (German: Hadron-Elektron Ring Anlage), at DESY, Hamburg, was the first, and so far the only, accelerator complex in which electrons and protons were collided [99]. It was built in the 80's with the capability to scatter polarised electrons and positrons off protons, at an energy of the proton beam of initially 820 GeV until it was increased to 920 GeV, in 1998. Together with an electron energy of 27.5 GeV, this resulted in a centre-of-mass energy, $\sqrt{s}$, of about 320 GeV. The protons were accelerated and stored in a ring of superconducting magnets. The electron ring was normal conducting. A schematic view of the HERA accelerator ring and

preaccelerators is shown in Fig. 3.1.

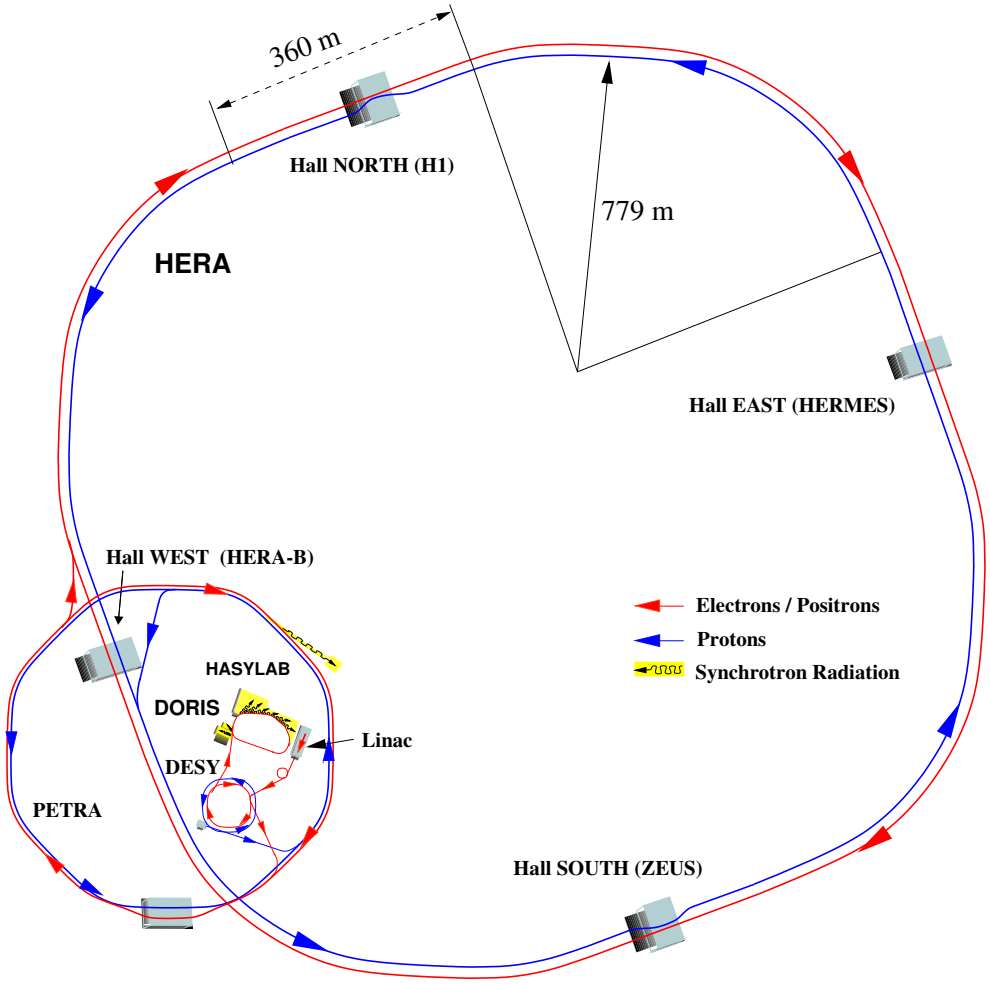

Figure 3.1: A schematic view of the HERA accelerator ring and preaccelerators. The plot is taken from [100].

Two general-purpose collider detectors with nearly 4π acceptance were proposed in 1985, H1 [101] and ZEUS [102]. They were operated over the 16 years of HERA operation. Two further experiments at HERA were built and run in the fixed-target mode. The HERMES experiment [103] (1994–2007) used the polarised electron beam to study spin effects in lepton–nucleon interactions using a polarised nuclear target. The HERA-B experiment [104] (1998–2003) was designed to investigate B-meson physics and nuclear effects in the interactions of the proton-beam halo with a nuclear wire target.

The first HERA data were taken in summer 1992. HERA had its first phase of operation (referred to as HERA-I) from 1992 through 2000. In this period, the collider experiments H1 and ZEUS each recorded data corresponding to integrated luminosities of approximately $120\,\mathrm{pb}^{-1}$ of e^+p and $15\,\mathrm{pb}^{-1}$ of e^-p collisions. The energy of the electron (positron) beam was about 27.5 GeV. The HERA collider was then upgraded to increase the specific luminosity by a factor of about four, as well as to provide longitudinally polarised lepton beams to the

collider experiments [105]. The second data-taking phase (referred to as HERA-II) began in 2003, after completion of the machine and detector upgrades, and ended in 2007. The H1 and ZEUS experiments each recorded approximately 200 pb^{-1} of e^+p and 200 pb^{-1} of e^-p data with electron (positron) energy of approximately 27.5 GeV and proton energy of 920 GeV. The lepton beams had an average polarisation of approximately ±30% with roughly equal samples of opposite polarities recorded. In the last three months of HERA operation, data with lowered proton-beam energies of 460 GeV (referred to as LER, Low Energy Run) and 575 GeV (referred to as MER, Middle Energy Run) were taken; each experiment recorded approximately 13 pb^{-1} and 7 pb^{-1} of the LER and MER data, respectively. The primary purpose of the LER and MER data was the measurement of the longitudinal proton structure function F_L.

HERA ceased operations in June 2007 after a long, successful data-taking period of 16 years. Analysis of these data still continue. HERA data have already had a great impact on the understanding of the partonic structure of the proton and on the development of QCD.

3.1.2 H1 and ZEUS experiments

The collider detectors H1 [101] and ZEUS [102] were designed primarily for DIS ep scattering at the highest virtuality Q^2 and large final-state energies. Thus, much attention was paid to the electromagnetic and hadron calorimeters. The H1 Collaboration chose liquid argon as active material for their main calorimeter to maximise long-term reliability. The ZEUS Collaboration chose scintillator active media and uranium as the absorber material to produce the desired equalisation of the calorimeter "$e\pi$" response to electrons and hadrons. The calorimeters were complemented by large-area wire chamber systems to measure muon momentum and the tail of hadron-shower energy. Because the electron- and proton-beam energies were very different, the detectors were asymmetric, with extended coverage of the forward (proton-beam) direction. Drift chambers inside the calorimeters, both in H1 and in ZEUS, were segmented into a forward and a central part. Later, in H1 starting in 1996 and in ZEUS from 2003 onwards, silicon detectors near the beampipe were installed for precision vertexing and tracking. Both apparatus were complemented with detector systems positioned near the beam axis in the accelerator tunnel, to measure backward photons and electrons, mainly for the determination of the interaction luminosity, and to tag leading protons and neutrons in the forward direction. Both experiments took data for the entire time of HERA's operation with efficiency of 70-80%.

The main components of the ZEUS detector are briefly described below in Section 3.1.2.1. A description of the H1 detector and its main sub-detectors can be found elsewhere [101, 106–109].

3.1.2.1 ZEUS detector

A schematic view of the ZEUS detector [102] along the beampipe and the main detector components are shown in Fig. 3.2. The ZEUS coordinate system is a right-handed Cartesian system, with the Z axis pointing in the proton-beam direction, referred to as the "forward direction", and the X axis pointing towards the centre of HERA. The coordinate origin is at the nominal interaction point. The pseudorapidity is defined as $\eta = -\ln\left(\tan\frac{\theta}{2}\right)$, where the polar angle, θ, is

measured with respect to the Z axis. The azimuthal angle, ϕ, is measured with respect to the X axis. The main detector components are briefly described below.

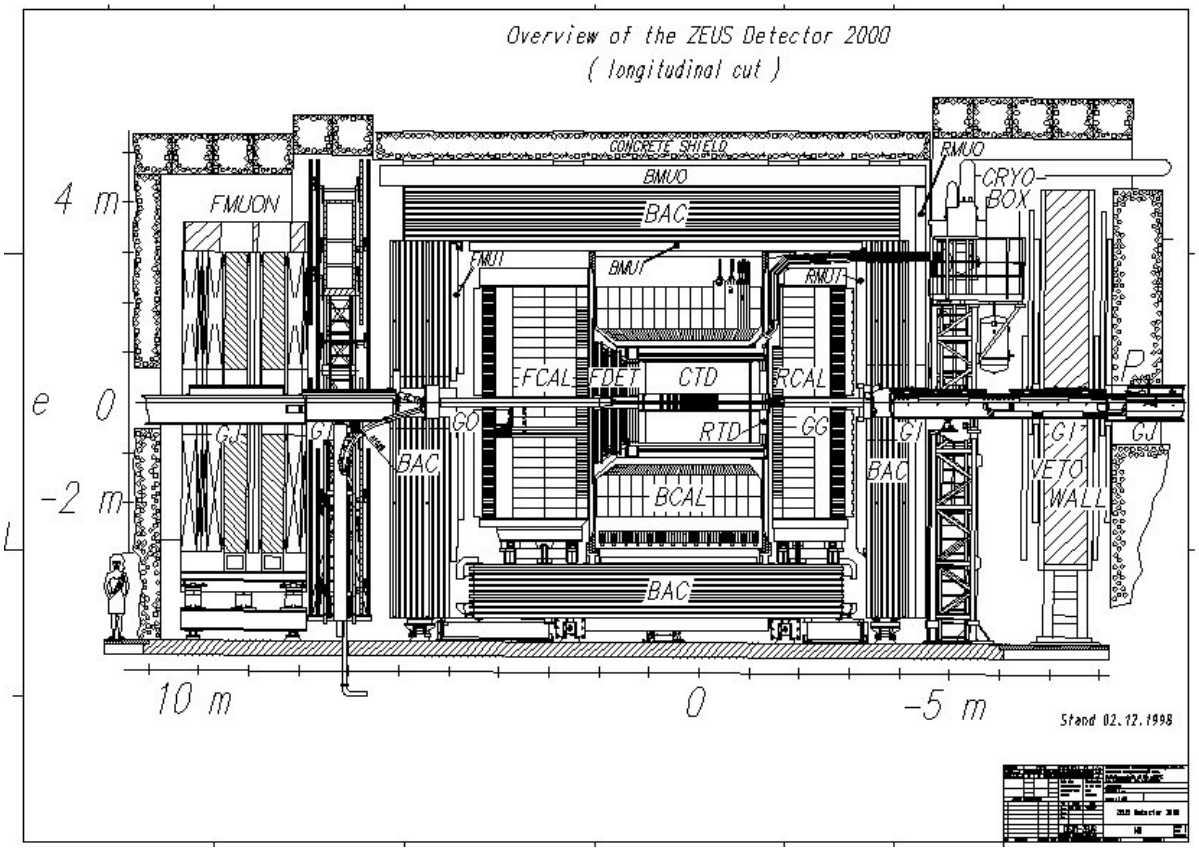

Figure 3.2: A schematic view of the ZEUS detector along the beampipe.

The most important sub-detector that measured energies was the calorimeter (CAL) [110–113]. The CAL was a sampling calorimeter consisting of plates of depleted uranium interleaved with plastic scintillator as active material. The ratio of absorber and scintillator thickness had been chosen to achieve equal signals from hadrons and electromagnetic showers, thereby producing the best possible resolution for hadrons. The CAL provided precise energy measurements for hadrons and jets, an angular resolution for jets better than 10 mrad, the ability to discriminate between hadrons and electrons using their different energy depositions, and a time resolution of 1 ns. The energy resolution for electrons and hadrons as determined under test-beam conditions was $18\%/\sqrt{E/\mathrm{GeV}}$ and $35\%/\sqrt{E/\mathrm{GeV}}$, respectively.

The CAL was mechanically subdivided in three parts:

- the Barrel Calorimeter (BCAL) covering polar angles from $36.7° < \theta < 129.1°$;
- the Forward Calorimeter (FCAL) covering polar angles from $2.2° < \theta < 39.9°$;
- the Rear Calorimeter (RCAL) covering polar angles from $128.1° < \theta < 176.5°$.

The three sections of the calorimeter were divided into modules, which were oriented perpendicularly to the beam axis in the BCAL and longitudinally to the beam axis in the FCAL and RCAL. Each module was subdivided into towers of dimensions $20 \times 20\,\mathrm{cm}^2$. Each tower had a longitudinal structure of one electromagnetic section (EMC) and two (only one in RCAL) hadronic sections (HAC1 and HAC2). Every EMC section consisted of four $5 \times 20\,\mathrm{cm}^2$ cells (two $10 \times 20\,\mathrm{cm}^2$ in RCAL) to give a fine segmentation for electron reconstruction. Each cell of the calorimeter was read out on two sides by wavelength shifters, which were coupled to photomultiplier tubes. The energy corresponds to the sum of both photomultiplier tubes and was therefore independent of the impact point of the particle on the cell. A comparison of both photomultiplier tubes allowed determining the position within a cell to be reconstructed.

The momenta of charged particles were measured by the Central Tracking Detector (CTD) [114–116] in the 1.43 T magnetic field of the solenoid [117]. The CTD was a cylindrical drift chamber measuring the direction, momentum and energy loss (dE/dx). It was filled with a gas mixture of argon, carbon dioxide and ethane. The CTD was made of 72 layers of wires, which were grouped in 9 superlayers. The angular coverage of the CTD was $15° < \theta < 164°$ and the momentum resolution for the full-length tracks in the HERA-I period was determined to be $\sigma(p_T)/p_T = 0.0058 \cdot p_T/\mathrm{GeV} \oplus 0.0065 \oplus 0.0014\,\mathrm{GeV}/p_T$[1] [118].

At the time of the HERA luminosity upgrade during the shutdown period 2000–2001, the tracking system of the ZEUS detector was upgraded with the Microvertex Detector (MVD) [119] (Fig. 3.3). The MVD was a silicon-strip vertex detector, mainly supposed to allow reconstruction of secondary vertices and track impact parameters from heavy-quark decays. The MVD consisted of two sections: barrel (BMVD) with an angular coverage $30° < \theta < 150°$ and forward (FMVD), which extended the coverage to 7°. The momentum resolution of the combined tracking system MVD+CTD for full-length tracks in the HERA-II period was determined to be $\sigma(p_T)/p_T = 0.0029 \cdot p_T/\mathrm{GeV} \oplus 0.0081 \oplus 0.0012\,\mathrm{GeV}/p_T$ [120], indicating an improved transverse momentum resolution, although the MVD material between the interaction point and the CTD increases the probability for multiple scattering.

The forward region of the ZEUS detector required enhanced tracking and particle identification capabilities due to the asymmetric beam energies. It consisted of the Forward Tracking Detector (FTD) and the Transition Radiation Detector (TRD). The purpose of the FTD was to reconstruct low-angle tracks of ionising particles whereas the TRD separated electrons from hadrons. During the HERA luminosity upgrade programme the TRD was replaced by the Straw Tube Tracker (STT) [121], which improved the tracking efficiency in events with high multiplicities. In the rear direction the Rear Tracking Device (RTD) was located. To determine the position of the scattered electron near the beampipe, the small-angle rear tracking detector (SRTD) [122] was used.

The Backing Calorimeter (BAC) was built to fulfill two tasks: to achieve a hermetic hadron jet-energy measurement and to aid the tracking of muons passing through the iron yoke of the detector. To measure the energy of hadron-shower leakages out of the CAL and to correct jet-energy measurements, the BAC was equipped with an analog readout, giving precise information on the deposited energy but only approximate information on the deposit position. To enable muon tracking in the iron yoke, a complementary digital readout was designed, giving

[1] The $\oplus$ sign indicates that the terms are added in quadrature.

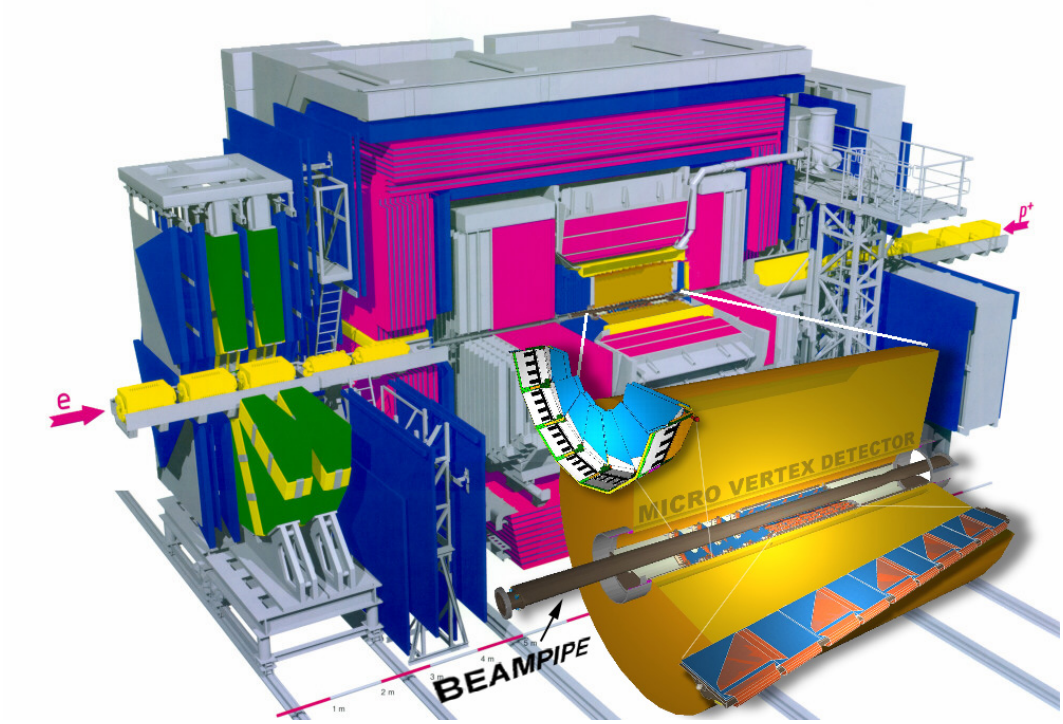

Figure 3.3: A schematic view of the ZEUS detector with installed MVD.

basically no information about the deposited energy, but exact position in two dimensions. This information was used for better positioning of shower leakages and for discrimination between leaking hadron cascades and muons. To identify muons, the forward muon detector (FMUON) was located in front of the magnet yoke and the barrel and rear muon detectors (BMUON, RMUON) [123] inside and outside the iron yoke.

The luminosity — a necessary ingredient for any cross-section measurement — was measured at ZEUS using the bremsstrahlung reaction $ep \to e'\gamma p$ [124] by a lead-scintillator calorimeter (PCAL) [125], located at $Z = -107\,\text{m}$, and (after the HERA upgrade) an independent magnetic spectrometer (SPEC) [126], located at $Z = -104\,\text{m}$. The best achieved relative uncertainty on the measured luminosity was 1.8%.

To reduce the event rate from the potential collision rate $\approx 10\,\text{MHz}$ to technically acceptable $\approx 10\,\text{Hz}$, a three-level trigger system was used at ZEUS. The First Level Trigger (FLT) [127, 128] consisted of hardware trigger systems in individual sub-detectors, which sent the information to the Global First Level Trigger (GFLT) to perform the decision. Events that passed the GFLT were processed further by the Second Level Trigger (SLT), based on software triggers, which used information on charged-particle tracks, the interaction vertex, calorimeter timing and global energy sums [129]. Events that passed the SLT were processed by the Third Level Trigger (TLT) [130], which took the decision based on the global information from an event. Finally, events that passed the TLT were written to tape to be fully reconstructed offline.

Some further information on the ZEUS experiment is provided in Section 4 in the context of the ZEUS Event Display program and in Section 5.1 in the context of the measurement of D^+-meson production with the ZEUS detector.

3.1.3 Measurements of charm production at HERA

This Section describes tagging techniques used to measure open[2] charm production at HERA and gives an overview of the measurements in DIS done by the H1 and ZEUS experiments. This overview is restricted to the measurements that are used for the charm combination, described in Chapter 6.

Charm-tagging techniques used at HERA include:[3]

- **reconstruction of D^{*+} mesons in the "golden" decay channel $D^{*+} \to D^0\pi_s^+$ and subsequently $D^0 \to K^-\pi^+$.** The π_s^+ denotes a "slow" pion with a low momentum in the D^{*+} centre-of-mass frame, since the mass of D^{*+} is only slightly above the sum of the masses of D^0 and π^+. This results in a narrow peak for the mass difference $\Delta M = M(K^-\pi^+\pi_s^+) - M(K^-\pi^+)$ near the threshold, accompanied with a not too large combinatorial background and hence the best signal-to-background ratio. This technique was proposed in [131] and widely used in different experiments (e.g. [59, 132–135]). The main shortcoming is that in practice D^{*+} mesons can be measured in the limited kinematic space $p_T(D^{*+}) \gtrsim 1.25\,\text{GeV}$ only, otherwise the transverse momentum of the slow pion is too small and its track cannot be reconstructed. Another limitation comes from the fact that all decay products have to be reconstructed in the tracking system, thus the production of D^{*+} mesons can be measured in the central region only, typically $|\eta(D^{*+})| \lesssim 1.8$. Also, the product of the branching ratios for the decay channels $D^{*+} \to D^0\pi_s^+$ and $D^0 \to K^-\pi^+$ is about 3% only [7]. However still the most precise measurements of open charm production at HERA were obtained using this technique; they are described in Section 3.1.3.1;

- **reconstruction of weakly decaying D mesons.** This technique exploits the long lifetime of weakly decaying charm hadrons. All final decay products must be charged particles reconstructed in the tracking system. Examples of such decay channels are $D^+ \to K^-\pi^+\pi^+$ and $D^0 \to K^-\pi^+$. Large combinatorial background can be significantly suppressed by applying a cut on lifetime information (e.g. track impact parameters or decay-length significance), although since the background rises steeply towards lower values of $p_T(D)$, a lower cut on $p_T(D)$ has to be applied; a cut on transverse momentum also improves the effectiveness of the lifetime information. Therefore the limitations of this technique are similar to those of the previous one: a measurement can be performed only in a fiducial transverse-momentum and pseudorapidity phase space and the branching ratios are small. Measurements performed using this technique are described in Section 3.1.3.2;

- **usage of semi-leptonic decays.** This technique is based on the separation of charm events with leptonic decays from light-flavour background using discriminating variables, e.g. the missing transverse momentum caused by a neutrino or the impact parameter of the lepton track. The measurements benefit from large branching ratios and a better pseudorapidity coverage at the cost of a worse signal-to-background ratio. Measurements performed using this technique are described in Section 3.1.3.3;

[2] When the measured final state contains only one charm quark.
[3] Charge conjugation is always implied for decay channels.

- **fully inclusive analysis.** In this technique, charm events are identified by reconstruction of displaced secondary vertices based on the lifetime information. The measurements benefit from the best phase-space coverage and largest statistics, since they are not limited by any particular branching ratio, although the signal-to-background ratio is usually worst. Measurements performed using this technique are described in Section 3.1.3.4.

The last two tagging techniques are often used for a simultaneous measurement of charm and beauty production, while in measurements using the first two, usually the sum of hadron production from charm and beauty processes are measured (dominated by charm). Techniques that rely on the usage of lifetime information require precise tracking and vertexing, thus can be fully exploited only with the data taken with the silicon detectors near the beampipe.

Results of precise charm measurements, which provide a double-differential cross section, are usually exploited to extract the inclusive cross section, i.e. the charm structure function $F_2^{c\bar{c}}$ or the reduced cross section $\sigma_{\text{red}}^{c\bar{c}}$. The extraction was based on the extrapolation procedure, which used the shape of theoretical predictions, thus measurements with larger transverse-momentum and pseudorapidity phase-space coverage are preferable (more details on the extrapolation procedure are provided in Section 6.2.3 in the context of data combination).

3.1.3.1 Reconstruction of D^{*+} mesons in the "golden" decay channel

Both the H1 and ZEUS experiments have measured the production of D^{*+} mesons using the "golden" decay channel using the HERA-I and HERA-II data [59, 64, 65, 134, 136, 137]. The best phase-space coverage was achieved in the HERA-II H1 measurement [65]: $p_T(D^{*+}) > 1.25\,\text{GeV}$, $|\eta(D^{*+})| < 1.8$.

Distributions of the reconstructed mass difference ΔM for the most precise H1 and ZEUS HERA-II measurements [65, 137] are shown in Fig. 3.5. Note that these measurements are performed in slightly different ranges of $p_T(D^{*+})$ and $\eta(D^{*+})$, therefore the ZEUS measurement has a better signal-to-background ratio and narrower peak at the cost of two times smaller statistics. Both experiments performed a subtraction of the background using the wrong-sign combinations, obtained by forming "D^0 candidates" by combining two tracks with the same sign.

The measured cross sections of D^{*+} production as a function of Q^2, y, x, $p_T(D^{*+})$, $\eta(D^{*+})$ and $z(D^{*+}) = (E(D^{*+}) - p_Z(D^{*+}))/(2E_e y)$, with E_e being the incoming electron energy, $E(D^{*+})$ and $p_Z(D^{*+})$ the energy and longitudinal momentum of D^{*+}, respectively, are shown in Fig. 3.5 and compared to the NLO predictions, obtained in the ZM-VFNS and FFNS (see Sections 2.3.1 and 2.3.2). The dominant experimental uncertainty is the systematic uncertainty on the tracking efficiency ($\approx 4\%$); in most of the bins the statistical uncertainty is smaller than the total systematical one. The FFNS predictions describe the data reasonably well within uncertainties, with a possible exception for the shape of the $z(D^{*+})$ distribution. The ZM-VFNS predictions describe the data significantly less well; in particular, they fail to describe the shape of $p_T(D^{*+})$, y and x distributions.

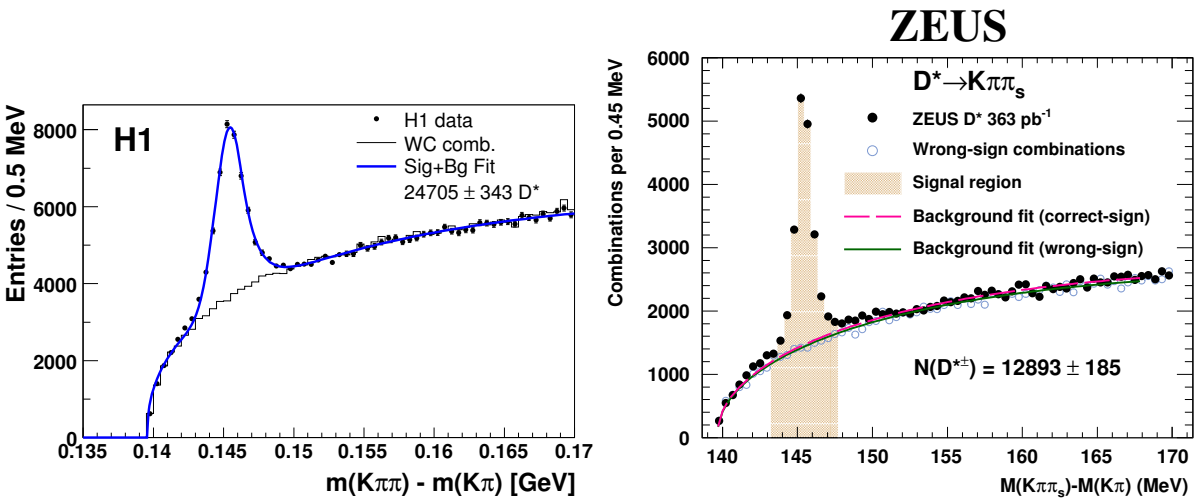

Figure 3.4: Distributions of the reconstructed mass difference ΔM from the H1 [65] (left) and ZEUS [137] (right) D^{*+} measurements, respectively.

3.1.3.2 Reconstruction of weakly decaying D mesons

ZEUS measured the production of D^0 [138] and D^+ [139] mesons using the weak decays $D^0 \to K^-\pi^+$ and $D^+ \to K^-\pi^+\pi^+$, respectively. The measurement of D^0 production was based on the 134 pb^{-1} of data from 2005 only, while the measurement of D^+ production used the full HERA-II data of 354 pb^{-1}.[4] Both measurements were performed in the phase space $p_T(D^+, D^0) > 1.5\,\text{GeV}$, $|\eta(D^+, D^0)| < 1.6$, $5 < Q^2 < 1000\,\text{GeV}^2$, $0.02 < y < 0.7$. Lifetime information was used to reduce combinatorial background substantially, applying a cut on the decay-length significance of the secondary vertex. This technique benefits from the MVD tracking and vertexing, that not feasible using the HERA-I data. The measurement of D^+ production is one of the physics results of this thesis, therefore it is described in detail in separate Chapter 5.

3.1.3.3 Usage of semi-leptonic decays

ZEUS measured charm and beauty production identified through their decays into muons [140]. The measurement was based on the 134 pb^{-1} of data from 2005. The measured observables were cross sections of muons originating from charm and beauty. The fractions of muons originating from charm, beauty and light flavours were extracted by exploiting three discriminating variables: the muon impact parameter, the muon momentum component transverse to the associated jet axis, and the missing transverse momentum, which is sensitive to the neutrino from semi-leptonic decays. The kinematic space of the measurement was $p_T(\mu) > 1.5\,\text{GeV}$, $-1.6 < \eta(\mu) < 2.3$, $Q^2 > 20\,\text{GeV}^2$ and $0.01 < y < 0.7$ (note an extended coverage of the forward region compared to D measurements).

Distributions of the discriminating variables are shown in Fig. 3.6. Contributions from charm and beauty production are separated from light flavours and from each other by using a global

[4] The D^+ measurement [139] superseded the previous measurement of D^+ production in [138], based on data from 2005.

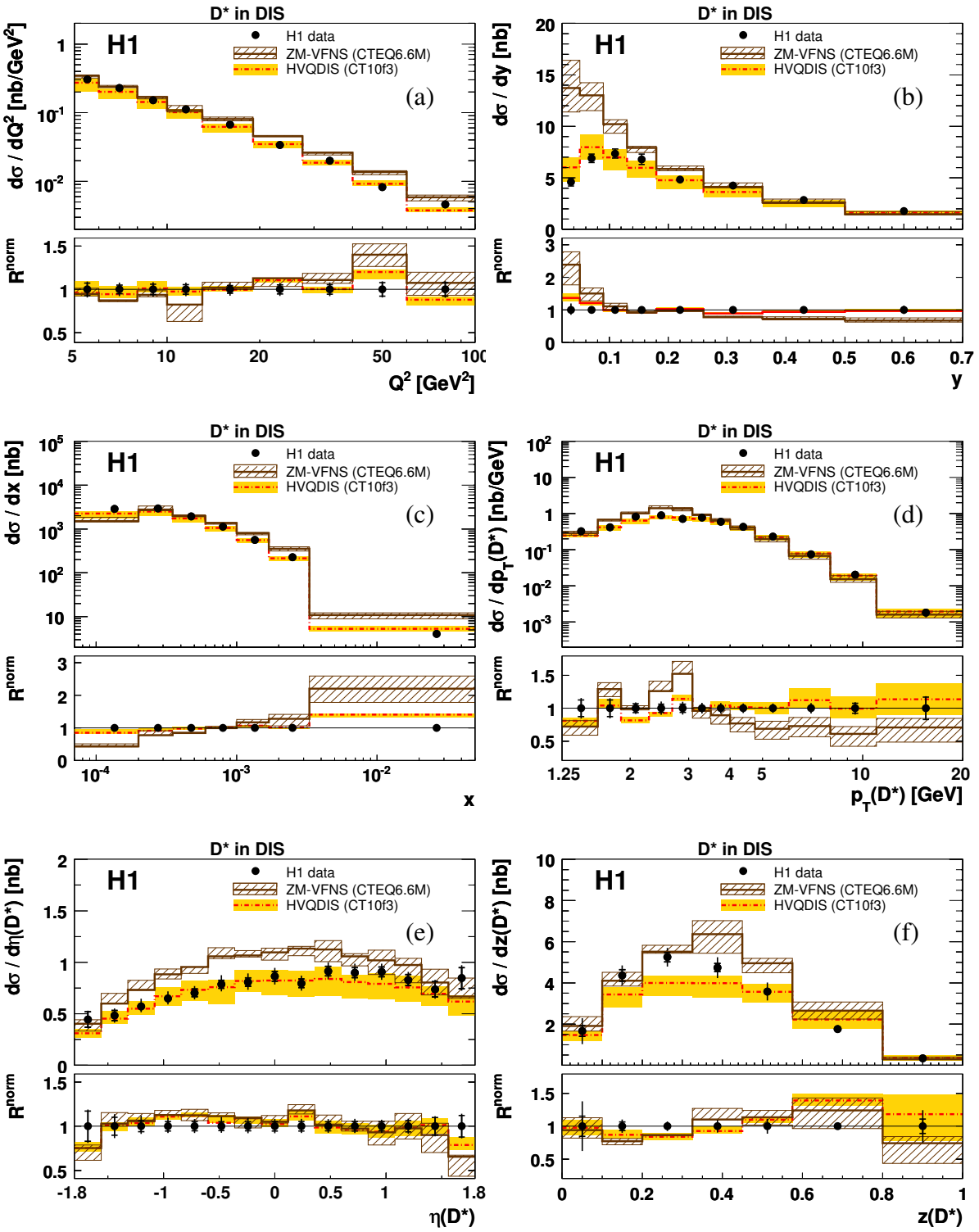

Figure 3.5: Differential D^{*+} cross sections as a function of Q^2 (a), y (b), x (c), $p_T(D^{*+})$ (d), $\eta(D^{*+})$ (e) and $z(D^{*+})$ (f), measured in [65]. The data are compared to NLO predictions obtained in the ZM-VFNS and FFNS (HVQDIS). In the lower part of the figures the normalised ratio, R^{norm}, of theory to data is shown, defined in Eq. 3 of [65], which has reduced normalisation uncertainties.

template fit to the Monte Carlo (MC) expectation. The measured muon differential cross sections as a function of $p_T(\mu)$, $\eta(\mu)$, Q^2 and x are shown in Fig. 3.7 and compared to the NLO predictions, obtained in the FFNS, and RAPGAP MC, normalised according to the result of the global fit. The NLO FFNS predictions describe the data well. The RAPGAP MC gives a good description of the shape of all the differential cross sections, although this cannot be interpreted as an independent data to theory comparison, but only as a justification of the validity of the fit results.

3.1.3.4 Fully inclusive analysis based on lifetime information

H1 measured inclusive charm and beauty cross sections using variables reconstructed by the vertex detector, including the impact parameter of tracks to the primary vertex and the position of the secondary vertex [141]. The measurement was based on the 189 pb^{-1} of data from 2006–2007. The phase space of the measurement was $5 < Q^2 < 2000\,\text{GeV}^2$ and $0.0002 < x < 0.05$. Similar to the technique used for measurements with semi-leptonic decays, described in Section 3.1.3.3, this measurement was based on the discrimination of charm and beauty contributions, performed with a neural network, using long-lifetime discriminating variables. Fig. 3.8 shows the distributions of the discriminating variables, used as input for the neural network. The measured quantities were the charm and beauty reduced cross sections as a function of Q^2 and x in the full p_T and η range. The measurement [141] was then combined with previous H1 measurements [142, 143] based on HERA-I data.

ZEUS measured the production of charm and beauty with at least one jet using the invariant mass of the charged tracks associated with secondary vertices and the decay-length significance of these vertices [19]. The measurement was based on the full HERA-II data of 354 pb^{-1}. The kinematic phase of the charm measurement was $E_T^{\text{jet}} > 4.2\,\text{GeV}$, $-1.6 < \eta^{\text{jet}} < 2.2$, $5 < Q^2 < 1000\,\text{GeV}^2$ and $0.02 < y < 0.7$, where E_T^{jet} is the transverse energy of the jet. Contributions from charm and beauty production were separated from light flavours and from each other by using a global template fit to the MC expectation. Fig. 3.9 shows the distributions of the decay-length significance for different bins of the secondary-vertex mass, m_{vtx}. All MC samples were normalised according to the scaling factors obtained from the fit. A good agreement between data and MC is observed. The first two mass bins corresponding to the region $1 < m_{\text{vtx}} < 2\,\text{GeV}$ are dominated by charm events. In the third mass bin, $2 < m_{\text{vtx}} < 6\,\text{GeV}$, beauty events are dominant at high values of the decay-length significance. The measured differential cross sections for inclusive jet production in charm events as a function of E_T^{jet}, η^{jet}, Q^2 and x are shown in Fig. 3.10 and compared to the NLO predictions obtained in the FFNS with different proton PDFs and to the predictions from the RAPGAP MC, scaled to the ratio of the measured visible cross section to the RAPGAP prediction. All measured cross sections are reasonably well described by the NLO FFNS and RAPGAP MC predictions. RAPGAP provides a worse description of the shape of the charm cross sections than the NLO FFNS calculations. The data are typically 20–30% above the NLO predictions, but in reasonable agreement within uncertainties. The differences between the NLO predictions using different proton PDFs are mostly very small.

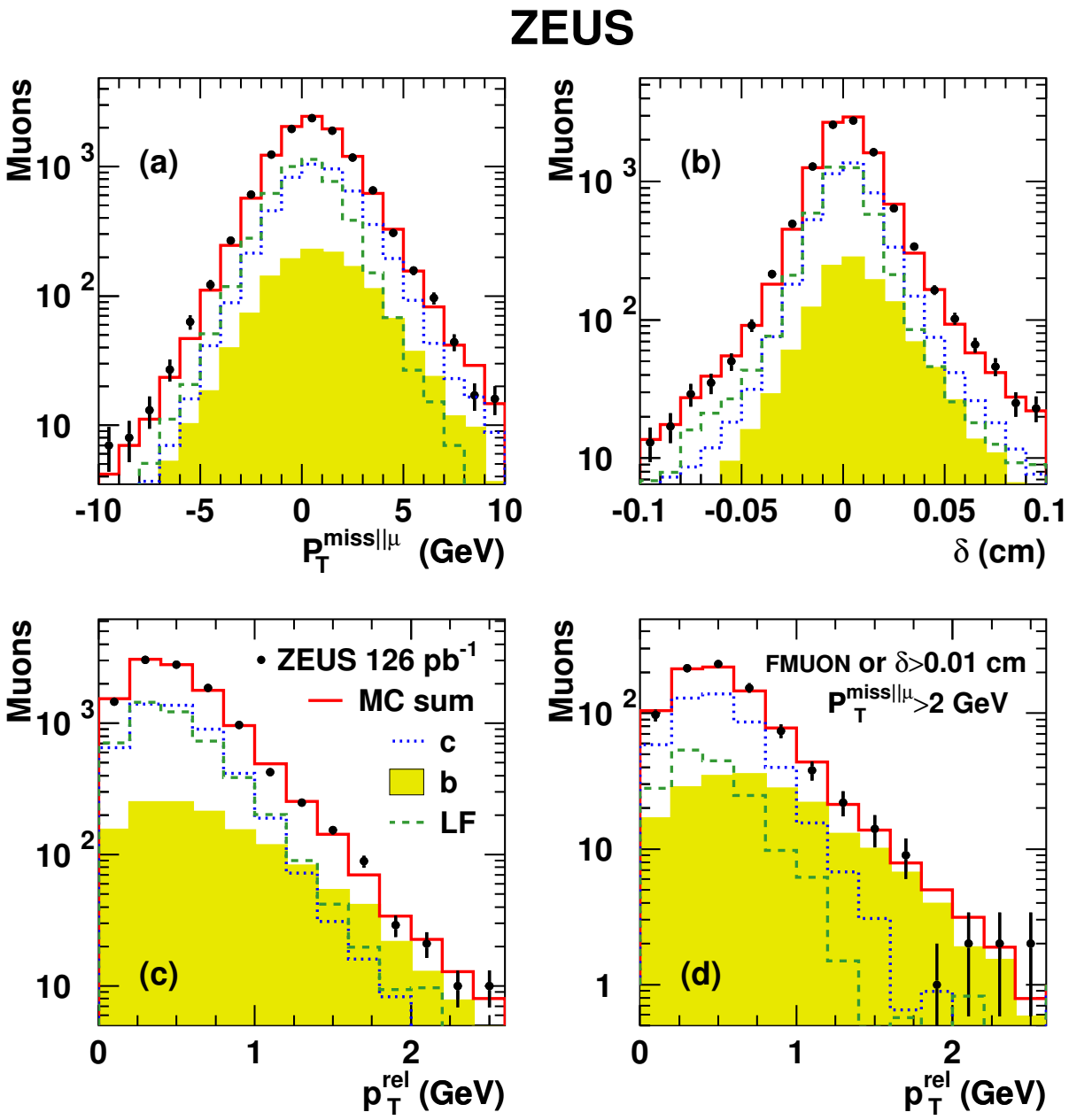

Figure 3.6: Distributions of the discriminating variables from ZEUS muon measurement [140]: the missing transverse momentum, $p_T^{\text{miss}||\mu}$, (a), muon impact parameter, δ, (b), muon momentum component transverse to the axis of the associated jet, p_T^{rel}, (c) and p_T^{rel} for a heavy-flavour-enriched sample (d). The data are compared to the MC expectation with the normalisation of the charm, beauty and light-flavour, LF, components obtained from the global fit. The charm, beauty and light-flavour contributions are shown separately.

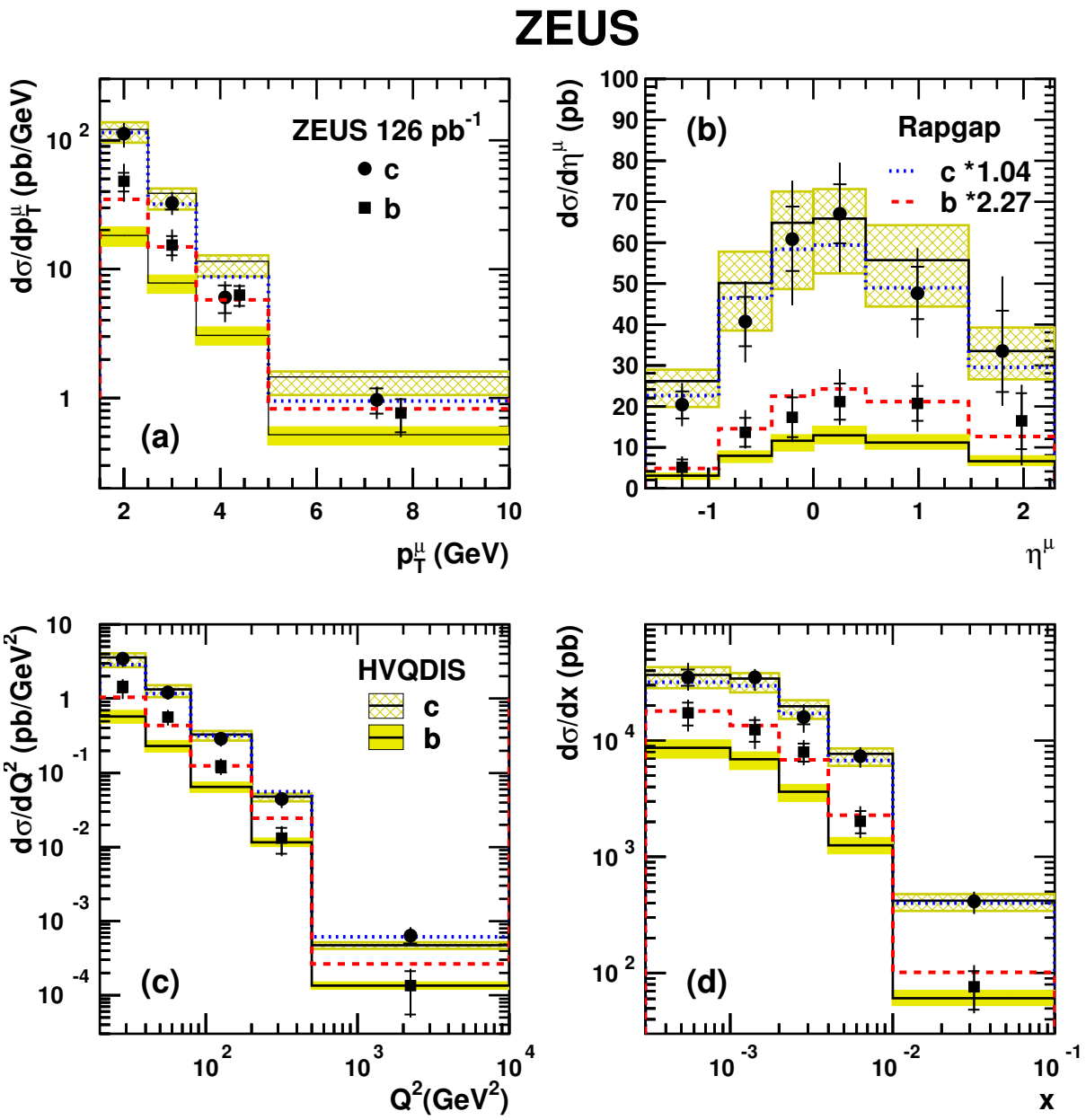

Figure 3.7: Differential muon cross section for charm and beauty production as a function of $p_T(\mu)$ (a), $\eta(\mu)$ (b), Q^2 (c) and y (d), measured in [140]. The data are compared to the NLO predictions obtained in the FFNS (HVQDIS) and to the predictions from MC RAPGAP.

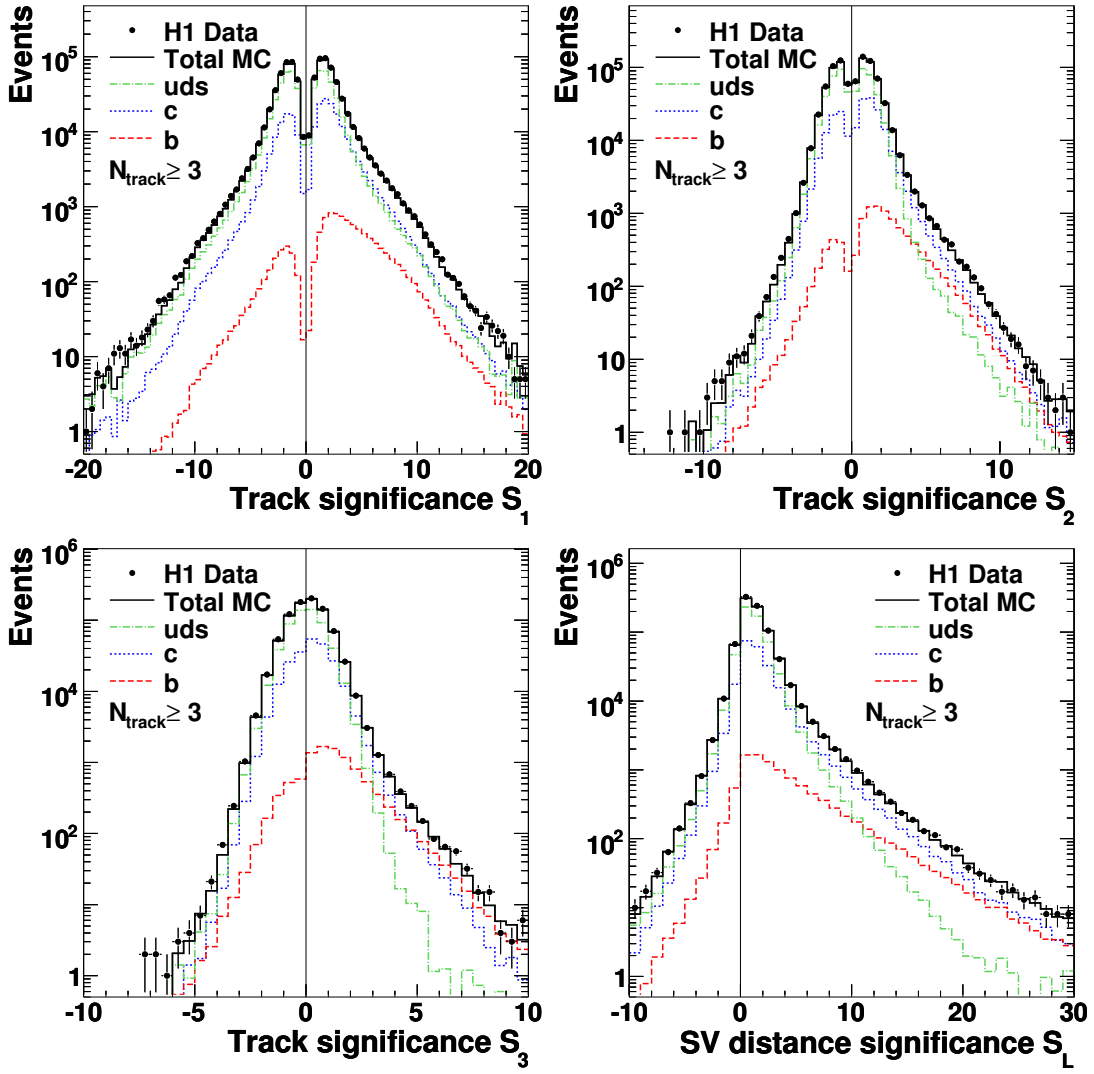

Figure 3.8: Distributions of discriminating variables from the H1 vertex measurement [141]: the impact-parameter significances, defined as the significance of the track with the highest, S_1, (top left), second highest, S_2, (top right) and third highest, S_3, (bottom left) absolute significances, respectively, and the secondary-vertex significance, S_L, (bottom right). The data are compared to the MC expectation, obtained after applying the scale factors from the fit to the complete data sample. The charm, beauty and light-flavour contributions are shown separately.

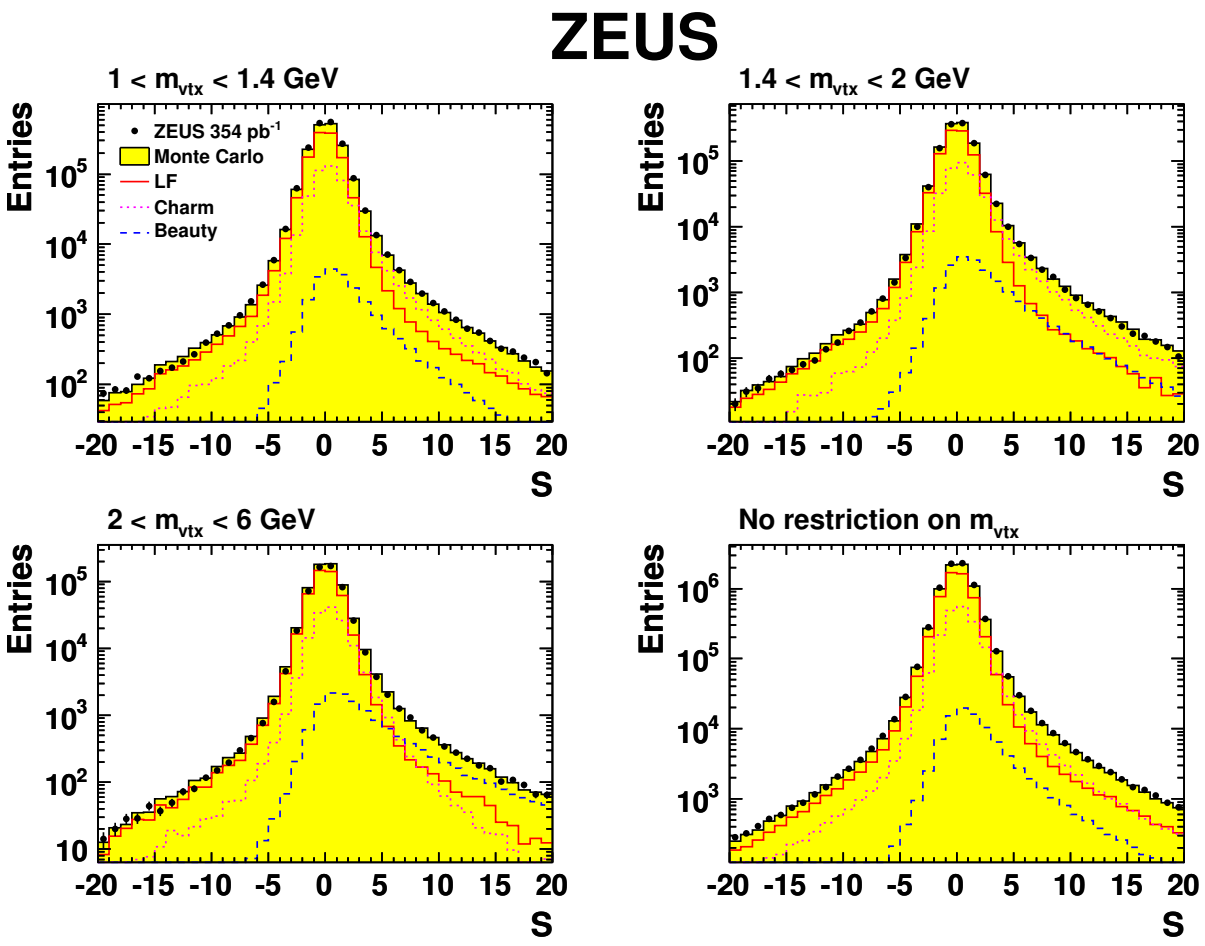

Figure 3.9: Distributions of the decay-length significance, S, for different bins of the secondary-vertex mass, m_{vtx}: $1 < m_{\text{vtx}} < 1.4\,\text{GeV}$ (top left), $1.4 < m_{\text{vtx}} < 2\,\text{GeV}$ (top right), $2 < m_{\text{vtx}} < 6\,\text{GeV}$ (bottom left) and no restriction on m_{vtx} (bottom right) from the ZEUS vertex measurement [19]. The data are compared to the sum of all MC distributions. The individual contributions from the beauty, charm and light-flavour MC subsamples are shown separately.

3.1.3.5 Summary

Different techniques have been used to measure open charm production in DIS at HERA. The most precise results were obtained in measurements of D^{*+} production using the "golden" decay channel. In all cases (except for the H1 vertex measurement [141]) the measured quantities were visible cross sections in a limited p_T (E_T^{jet}) and η phase space. The largest phase-space coverage was obtained in fully inclusive analysis based on lifetime information.

All measured cross sections were compared to the theoretical predictions obtained in different schemes. The NLO FFNS predictions provide a good description of the data within uncertainties in all cases, while the NLO ZM-VFNS predictions do not describe shape of some kinematic variables well. A direct comparison of measured visible cross sections to the GM-VFNS predictions is not possible, since the GM-VFNS calculations were done only for inclu-

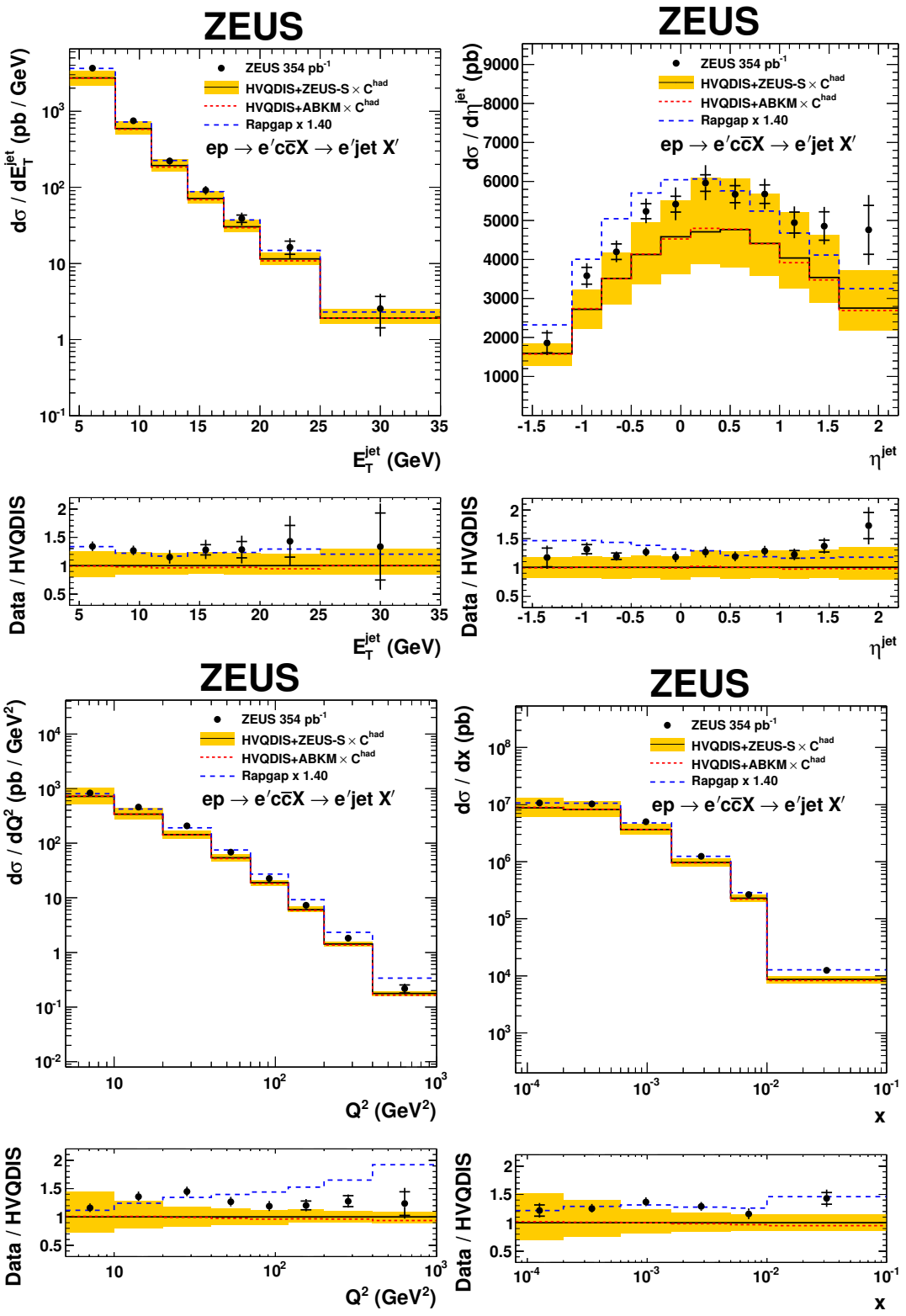

Figure 3.10: Differential cross section for inclusive jet production in charm events as a function of E_T^{jet} (top left), η^{jet} (top right), Q^2 (bottom left) and x (bottom right) measured in [19]. The data are compared to the NLO predictions obtained in the FFNS (HVQDIS) with different input PDFs and to the predictions from MC RAPGAP.

sive cross sections. Comparisons to MC predictions did not aim to check theory, since in these cases MC simulations were LO and parton showers, re-normalised to the data (more details on the technique of MC simulations are provided in Section 5.3.1). These comparisons mainly aimed to justify the validity of the template fit procedure or the acceptance corrections, which exploited MC.

In general, measurements performed using different methods are complementary to each other and thus can be combined to achieve the best precision. This is done in Chapter 6 (Section 6.5). Such combination requires an extrapolation of the visible cross sections to the full phase space using the shape of some theoretical calculations. Since the FFNS predictions are consistent with the data in all kinematic regions (including high Q^2), the NLO FFNS is considered as the best theoretical calculation for this extrapolation.[5] After extrapolation to the full phase space, the data can be compared to the GM-VFNS calculations (see Section 6.5).

3.2 LHC and LHCb experiment, measurements of charm and beauty production at LHCb

The Large Hadron Collider (LHC) is the world's largest and most powerful particle collider; its description can be found elsewhere [144]. The LHCb detector at the LHC provides unique access to the forward-rapidity region with a detector that is tailored for flavour physics.

The LHCb detector [145] (Fig. 3.11) is a single-arm forward spectrometer covering the pseudorapidity range $2 < \eta < 5$, designed for the study of particles containing b or c quarks. The right-handed coordinate system adopted has the Z axis along the beam. The detector includes a high-precision tracking system consisting of a silicon-strip vertex detector surrounding the pp interaction region, a large-area silicon-strip detector located upstream of a dipole magnet with a bending power of about 4 Tm, and three stations of silicon-strip detectors and straw drift-tubes placed downstream. The combined tracking system has a momentum resolution ($\delta p/p$) that varies from 0.4% at 5 GeV to 0.6% at 100 GeV and an impact-parameter resolution of 20 μm for tracks with high transverse momentum. Charged hadrons are identified using two ring-imaging Cherenkov detectors (RICH). The RICH system [146] of the LHCb experiment provides charged-particle identification over a wide momentum range, from 2 to 100 GeV[6]. It consists of two RICH detectors that cover between them the angular acceptance of the experiment, 15–300 mrad with respect to the beam axis. Photon, electron, and hadron candidates are identified by a calorimeter system consisting of scintillating-pad and pre-shower detectors, an electromagnetic calorimeter, and a hadronic calorimeter. Muons are identified by a system composed of alternating layers of iron and multi-wire proportional chambers.

[5] Although also it is the only one practically available NLO calculation for the fully differential cross sections.

[6] The typical momentum (in the laboratory frame) of the decay products in two-body B decays is about 50 GeV. The requirement of maintaining a high efficiency for the reconstruction of these decays leads to the need for particle identification up to at least 100 GeV. The lower momentum limit of about 2 GeV follows from the need to identify decay products from high-multiplicity B decays and also from the fact that particles below this momentum will not pass through the dipole magnetic field (4 Tm) of the LHCb spectrometer [146].

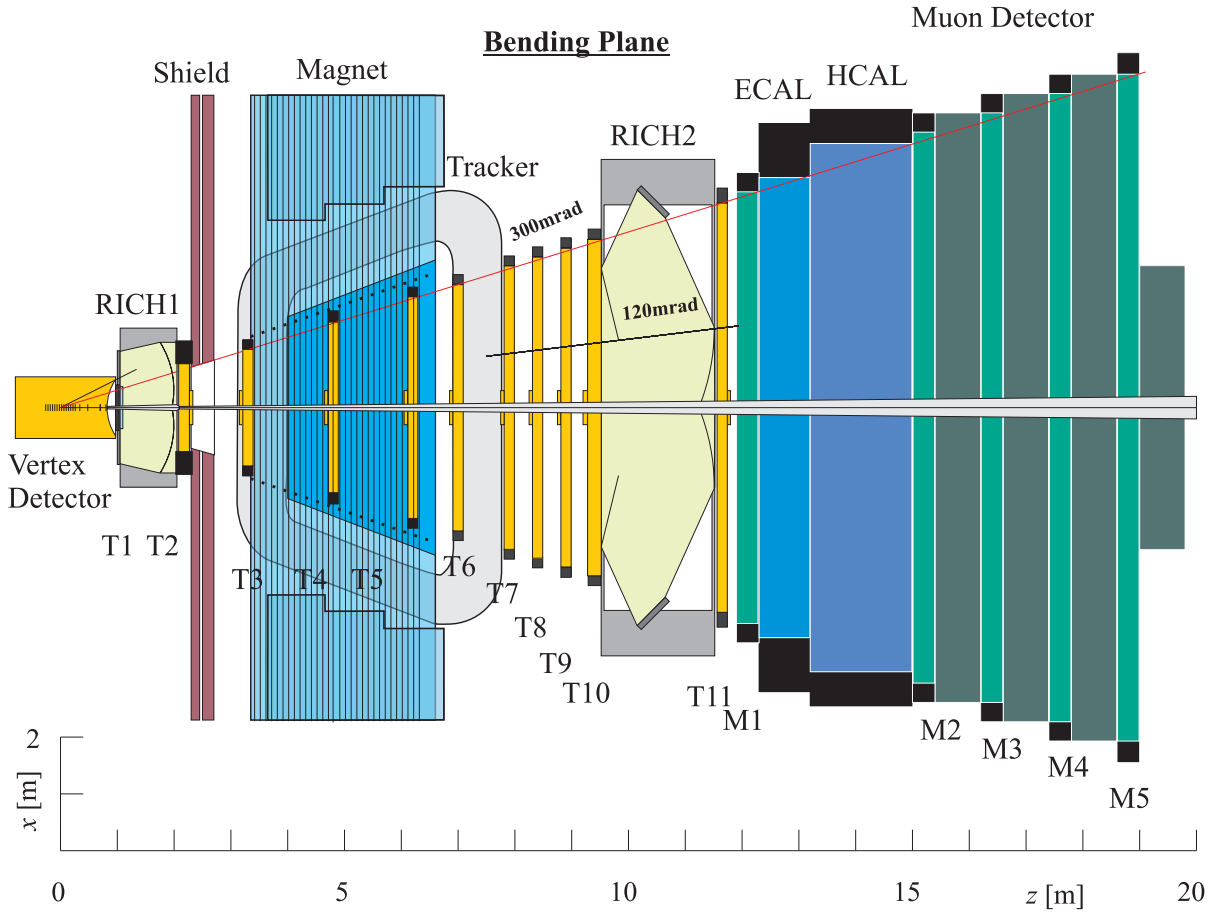

Figure 3.11: A schematic view of the LHCb detector along the beampipe.

3.2.1 Measurement of prompt charm production

LHCb measured D^0, D^+, D_s^+, D^{*+} and Λ_c^+ production using data corresponding to an integrated luminosity of 15 nb^{-1} in the region of rapidity $2.0 < y < 4.5$ and transverse momentum $0 < p_T < 8$ GeV in pp collisions at a centre-of-mass energy of 7 TeV [135]. The analysis was based on fully reconstructed decays of charmed hadrons in the following decay modes: $D^0 \to K^-\pi^+$, $D^+ \to K^-\pi^+\pi^+$, $D^{*+} \to D^0(K^-\pi^+)\pi^+$, $D_s^+ \to \phi(K^-K^+)\pi^+$ and $\Lambda_c^+ \to pK^-\pi^+$.

Charmed hadrons may be produced at the pp collision point either directly or as feed-down from the instantaneous decays of excited charm resonances. They may also be produced in decays of beauty hadrons. The first two sources (direct production and feed-down) are referred to as prompt. Charmed particles from beauty-hadron decays are called secondary charmed hadrons. The measurement reports the production cross sections of prompt charmed hadrons; secondary charmed hadrons were treated as background. The measurement was performed in two-dimensional bins of p_T and y. For the Λ_c^+ measurement, only single-differential cross sections as a function of p_T and y were measured. The prompt signal yields were selected using multi-dimensional extended maximum likelihood fits to the mass and $\log_{10}(\text{IP}\,\chi^2)$, where IP χ^2 is defined as the difference between the χ^2 of the primary vertex, reconstructed with and without

the considered particle (Fig. 3.12). The dominant systematic uncertainty is the uncertainty on the tracking efficiency, which is 3–4% per one final-state track, thus resulting in 6–10% for the measured cross sections.

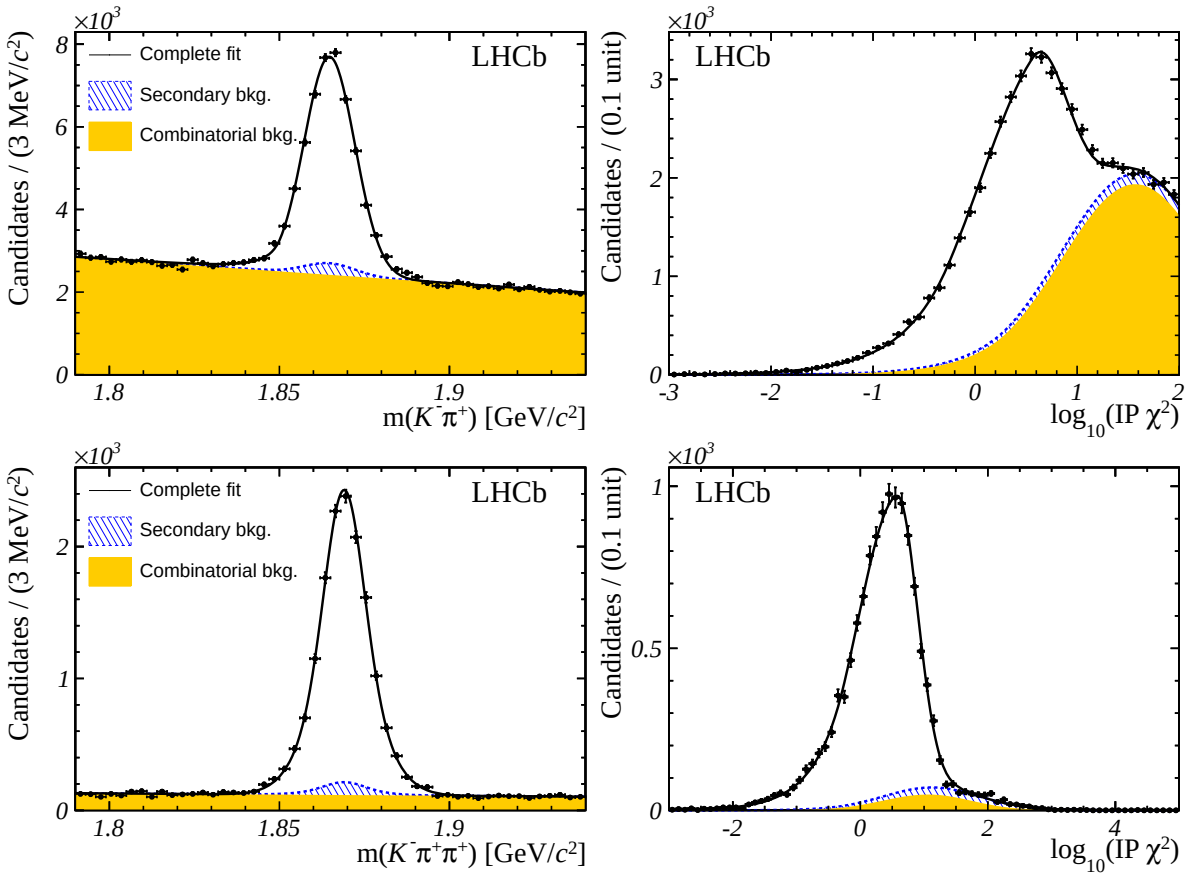

Figure 3.12: Mass and $\log_{10}(\mathrm{IP}\chi^2)$ distributions for selected $D^0 \to K^-\pi^+$ and $D^+ \to K^-\pi^+\pi^+$ candidates from the LHCb measurement of prompt charm production [135] showing the masses of the D^0 candidates (top left), $\log_{10}(\mathrm{IP}\,\chi^2)$ distribution of D^0 candidates (top right), masses of the D^+ candidates (bottom left) and $\log_{10}(\mathrm{IP}\,\chi^2)$ distribution of D^+ candidates (bottom right). Projections of likelihood fits to the full data samples are shown with components as indicated in the legends.

The measured double-differential cross sections of D^0, D^+, D_s^+ and D^{*+} production are shown in Fig. 3.13 and compared to the NLO predictions obtained in the FONLL and other GM-VFNS approach (see Sections 2.3.3.2 and 2.3.3.3). The GM-VFNS predictions are shown for $p_T > 3\,\mathrm{GeV}$. Predictions for D^0 mesons are also compared with the GM-VFNS calculations using PDFs with intrinsic charm [147][7]. As shown in Fig. 3.13, in the phase space of the present measurement the effect of intrinsic charm is predicted to be small. All theoretical calculations describe the data well, although their uncertainties of the order of a factor 2 significantly exceed

[7] Many non-perturbative models, particularly those based on the light-cone wave-function picture, expect an "intrinsic charm" component of the nucleon at an energy scale comparable to the charm-quark mass. This intrinsic-charm component, if present at a low-energy scale, will participate fully in QCD dynamics and evolve along with the other partons as the energy scale increases; for more details see, e.g. [147] and references therein.

the experimental uncertainties of the data.

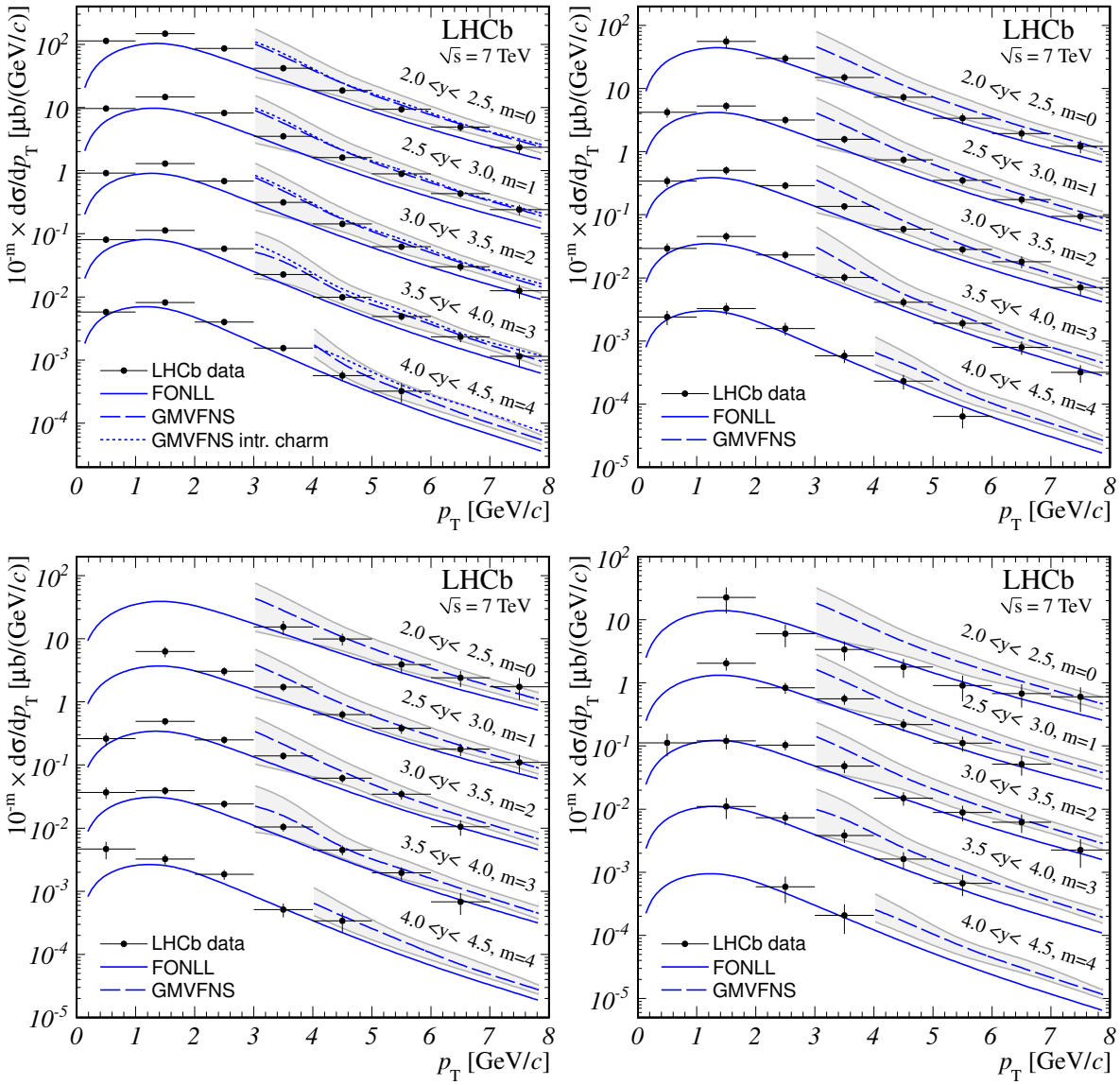

Figure 3.13: Differential cross sections for D^0 (top left), D^+ (top right), D^{*+} (bottom left) and D_s^+ (bottom right) from the LHCb measurement of prompt charm production [135] compared to theoretical predictions. The cross sections for different y regions are shown as functions of p_T. The y ranges are shown as separate curves and associated sets of points scaled by factors 10^{-m}, where the exponent m is shown on the plot with the y range.

3.2.2 Measurement of beauty production

LHCb measured B^+, B^0 and B_s^0 production using data corresponding to an integrated luminosity of 0.36 fb^{-1} in the region of rapidity $2.0 < y < 4.5$ and transverse momentum $0 < p_T < 40$ GeV

in pp collisions at a centre-of-mass energy of 7 TeV [148]. The analysis was based on fully reconstructed decays of beauty hadrons in the following decay modes: $B^+ \to J/\psi K^+$, $B^0 \to J/\psi K^{*0}$ and $B_s^0 \to J/\psi\phi$, with $J/\psi \to \mu^+\mu^-$, $K^{*0} \to K^+\pi^-$ and $\phi \to K^+K^-$. Similar to the charm measurement [135], this measurement was performed in two-dimensional bins of p_T and y.

The mass distributions of the selected candidates for one of the p_T and y bins are shown in Fig. 3.14. The dominant systematic uncertainty comes from the tracking (2–9%) and trigger (2–8%) efficiencies and finite size of the bins (0–19%); for B^0 and B_s^0 the branching-ratio uncertainties are also sizeable ($\approx 10\%$).

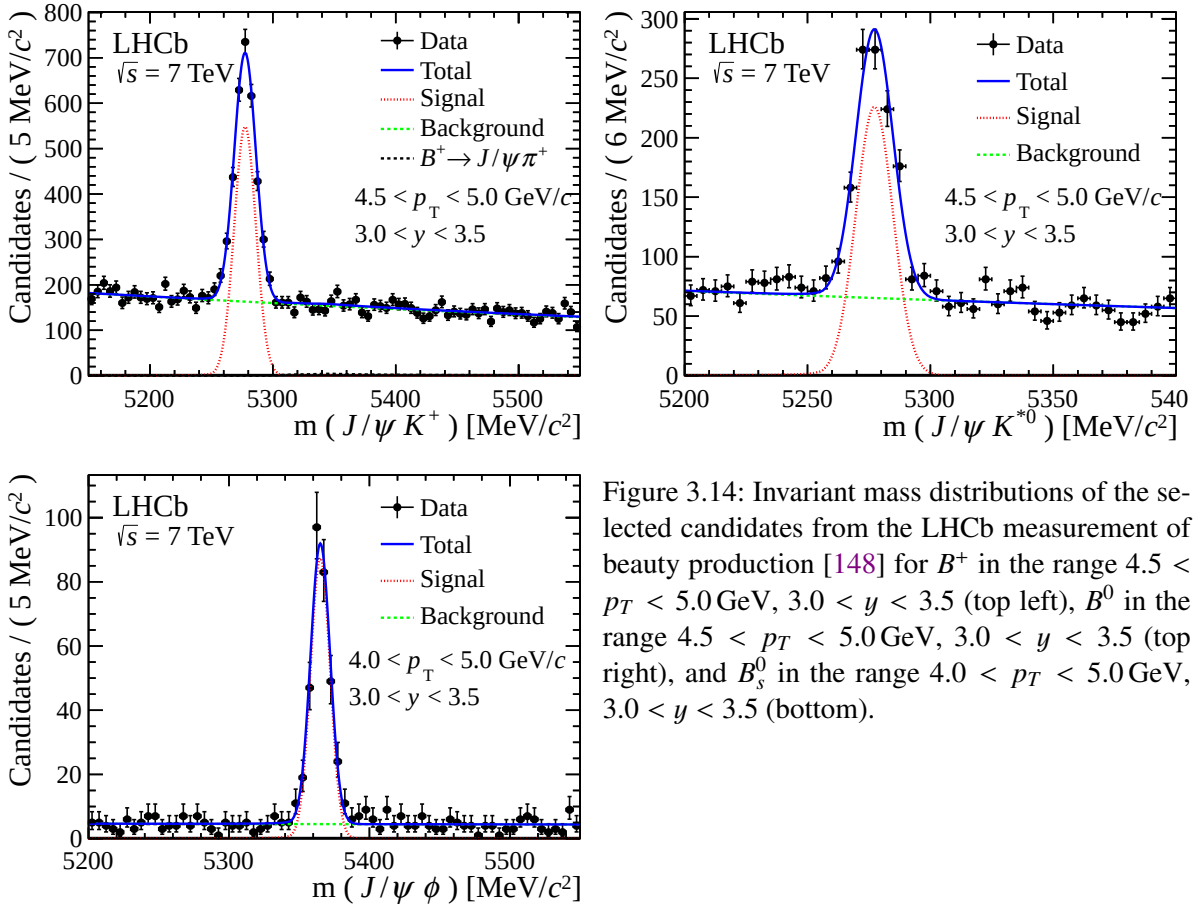

Figure 3.14: Invariant mass distributions of the selected candidates from the LHCb measurement of beauty production [148] for B^+ in the range $4.5 < p_T < 5.0\,\text{GeV}$, $3.0 < y < 3.5$ (top left), B^0 in the range $4.5 < p_T < 5.0\,\text{GeV}$, $3.0 < y < 3.5$ (top right), and B_s^0 in the range $4.0 < p_T < 5.0\,\text{GeV}$, $3.0 < y < 3.5$ (bottom).

The measured cross sections, integrated over p_T and y, are compared to the FONLL theoretical predictions in Figs. 3.15 and 3.16, respectively. Similar to the results of the charm measurement [135], the FONLL calculations describe the data well within large uncertainties.

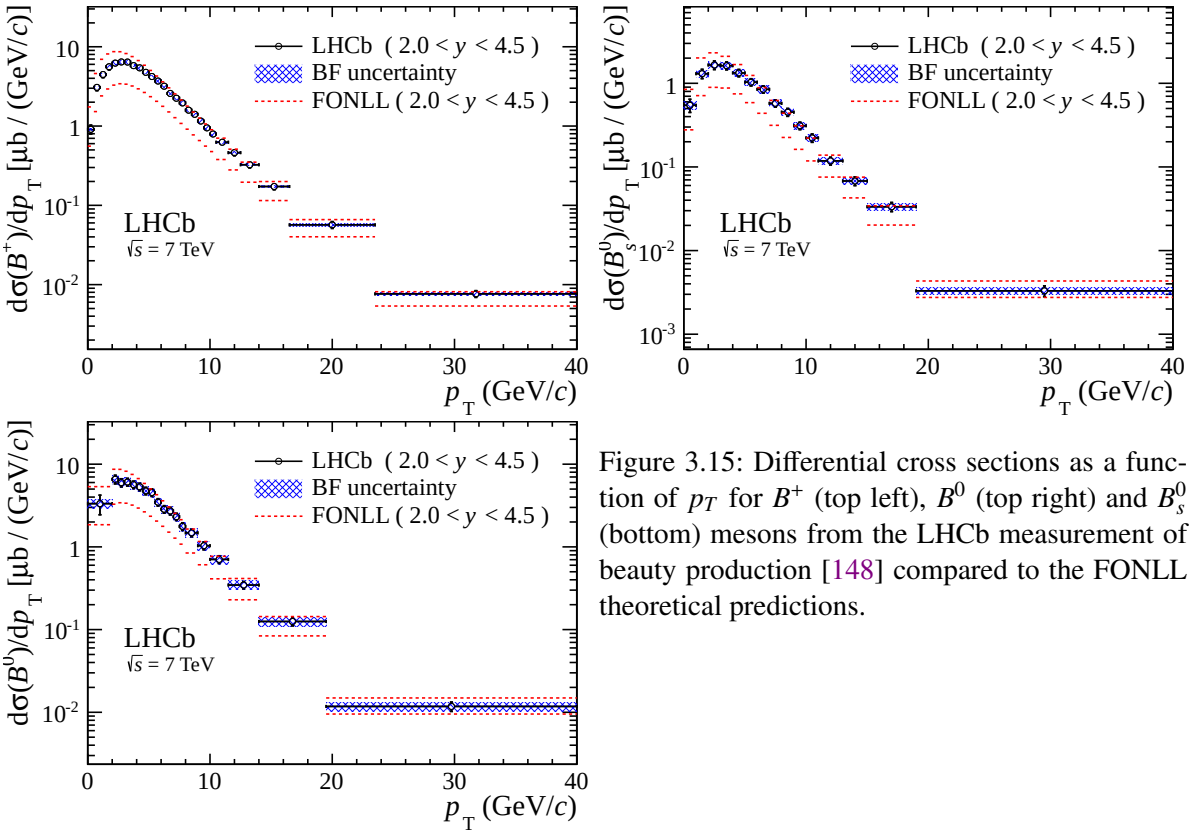

Figure 3.15: Differential cross sections as a function of p_T for B^+ (top left), B^0 (top right) and B_s^0 (bottom) mesons from the LHCb measurement of beauty production [148] compared to the FONLL theoretical predictions.

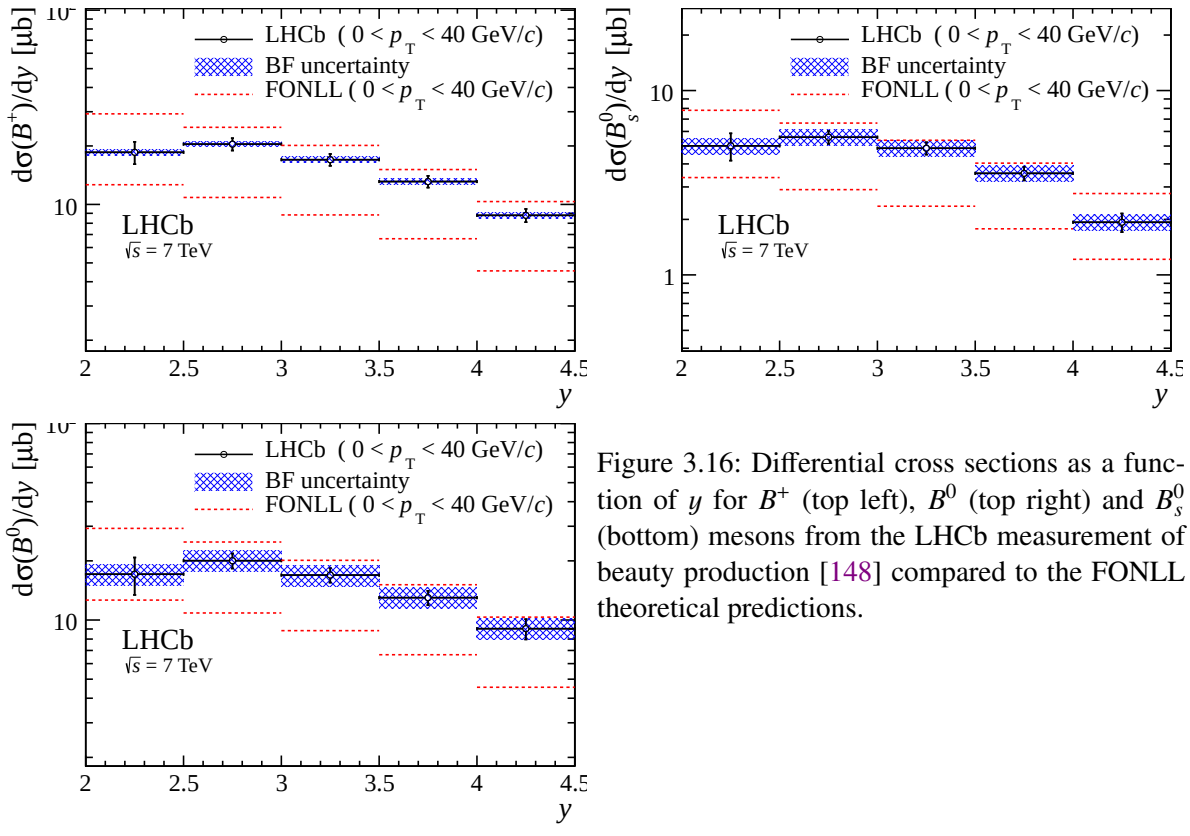

Figure 3.16: Differential cross sections as a function of y for B^+ (top left), B^0 (top right) and B_s^0 (bottom) mesons from the LHCb measurement of beauty production [148] compared to the FONLL theoretical predictions.

CHAPTER 4

Modification of the ZEUS Event Display

This Chapter describes the ZEUS Event Display (also referred to as Zeus Event Visualisation, ZeVis) program and the modification of this program in the context of the data preservation project at ZEUS. Section 4.1 gives an introduction to the purpose of the program. Section 4.2 explains the logic of the program. In Section 4.3 an example of the usage of ZeVis is given. In Section 4.4 the ZEUS data preservation project — the reason for the modification of ZeVis — is introduced; this overview is largely based on [149]. Section 4.5 contains a detailed overview of the Common Ntuples based ZeVis functionality and can be used as a program manual. Finally, Section 4.6 gives a short summary.

4.1 Introduction

ZeVis [150] is a program for the visualisation of ep collision data at ZEUS. The ZEUS experiment, as all modern high energy physics experiments, stored information about particle collisions in the format of *events*. Each event contains all signals from all sub-detectors and is supposed to correspond to a single ep collision. Recorded events are the basic units for all physics analyses done at ZEUS.

During its data-taking operation the ZEUS experiment stored about 500 million events. Such an enormous amount of data can be analysed only using automatic powerful pattern recognition techniques (sampling of events, reconstruction of basic physics objects like tracks, calorimeter clusters, combining information from different sub-detectors etc.). The event display is an efficient tool for adjusting and checking these techniques by looking at single typical events, although it is of course not able to produce a precise quantitative estimation of measurable physical quantities. Another purpose of the event display is producing pictures for talks and papers[1], which are intuitively understandable much better than sophisticated analysis techniques.

During the HERA-I period ZEUS used the Logical Access to ZEUS Events (LAZE) event display [153]. LAZE was written mostly in FORTRAN in monolithic architecture. Further-

[1] For instance, pictures obtained with ZeVis can be found in [151, 152].

more, it was a platform-dependent program not portable to Linux. The HERA-II period challenged the event-display development team with major changes in the ZEUS detector: new STT, MVD and beampipe (see Section 3.1.2.1 for the description of the ZEUS detector) needed to be visualised in the event display. A decision was taken to develop a new program: ZeVis.

4.2 Overview of ZeVis

ZeVis is written in C++ using ROOT libraries [154]. By its architecture it is a client-server application. A user launches a lightweight (and easily portable) Client which contacts the ZeVis Server to get information about the detector components and the requested events. Information from the Server to the Client is transmitted via the http protocol in the format of ROOT files. These ROOT files can be stored on the Client part and can be opened and re-displayed in subsequent sessions without contacting the Server again. The architecture of ZeVis is shown in Fig. 4.1; this program will be referred to as *classic ZeVis*.

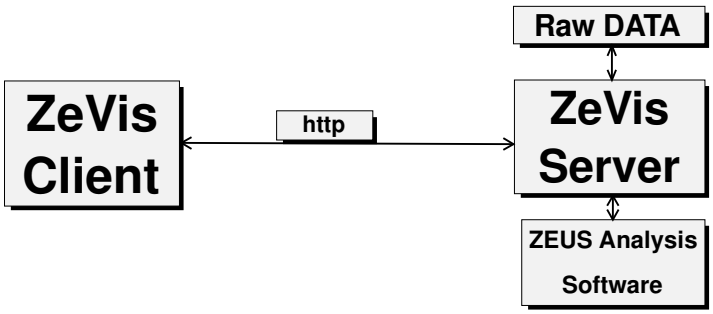

Figure 4.1: The architecture of classic ZeVis.

The main idea behind such a structure was to separate the database with information about detectors and stored events including the relevant routines for data access and basic reconstruction, known as the *ZEUS Software*, from the interactive visualisation part of the program. With this scheme, after a new release of the ZEUS Software, changes are only needed to the ZeVis Server, while the Client part of the program remains unchanged.

ZeVis can display:

- **main detector components** (Fig. 4.2; see Section 3.1.2.1 for the description of the ZEUS detector):
  - the tracking system: the MVD, CTD, FTD, RTD and STT;
  - the calorimeter system: the CAL consisting of the FCAL, BCAL and RCAL, and the BAC;
  - the muon system: the MUON, BMUON and RMUON;
  - the beampipe;
- **"low-level" analysis information**:
  - hits in the tracking detectors (Fig. 4.3);

  - energy deposits in the calorimeter (Fig. 4.4);
  - hits in the muon chambers (Fig. 4.5);
- **"high-level" analysis information** (typically several kinds of these objects, reconstructed using different analysis techniques, are available):
  - tracks and vertices (Fig. 4.3);
  - ZEUS Unidentified Flying Objects (ZUFOs) and jets (Fig. 4.4);
  - muons (Fig. 4.5).

4.3 Analysing events with ZeVis: example from ZEUS Z^0-boson analysis

As an example of how ZeVis can be used for visualisation of analysis techniques, the ZEUS analysis "Production of Z^0 bosons in elastic and quasi-elastic ep collisions at HERA" [155] can be considered. Although the expected rate of events is low, it is a good benchmark process for testing the Standard Model. Moreover, this was the first observation of Z^0 production in ep collisions.

The selected process is $ep \to eZ^0p^{(*)}$, where $p^{(*)}$ stands for a proton (elastic process) or a low-mass nucleon resonance (quasi-elastic process). The production of Z^0 bosons was measured in the hadronic decay mode. Fig. 4.6 shows a LO diagram of the process. There were 3 main event-selection criteria:

- at least two jets with $E_T > 25\,\text{GeV}$ and $|\Delta\phi_j| > 2\,\text{rad}$ were required, where E_T is the jet transverse energy and $\Delta\phi_j$ is their azimuthal difference (since the two leading jets from the Z^0-boson decays are expected to be nearly back-to-back in the XY plane);
- to select elastic (where the proton stays intact) or quasi-elastic (where it is transformed into a nucleon resonance p^*) processes, the cut $\eta_{\max} < 3.0$ was used, where $\eta_{\max}$ is the pseudorapidity of the energy deposit in the calorimeter closest to the proton-beam direction with energy greater than 400 MeV (noise cut);
- to suppress low-Q^2 NC and direct-PHP backgrounds, the RCAL veto cut $E_{\text{RCAL}} < 2\,\text{GeV}$ was used, where E_{RCAL} is the total energy deposit in the RCAL.

To measure the cross section, the invariant mass, M_{jets}, distribution was calculated and fitted to the sum of the signal and background templates. A more detailed description of the analysis can be found in [155].

From all HERA data, 54 events were selected. They were all checked and studied in ZeVis. One of the selected events is shown in Fig. 4.7. Two back-to-back high-E_T jets are clearly recognised from the $E_T(\eta, \phi)$ distribution in the CAL cells; furthermore, they are also visible on the ZR view (different projections available in ZeVis are described in Section 4.5.1). The CAL layout on the ZR view allows for a clear recognition of the gap in the forward direction and the energy veto in the RCAL. This demonstrates the principle of the effective usage of ZeVis in physics analises.

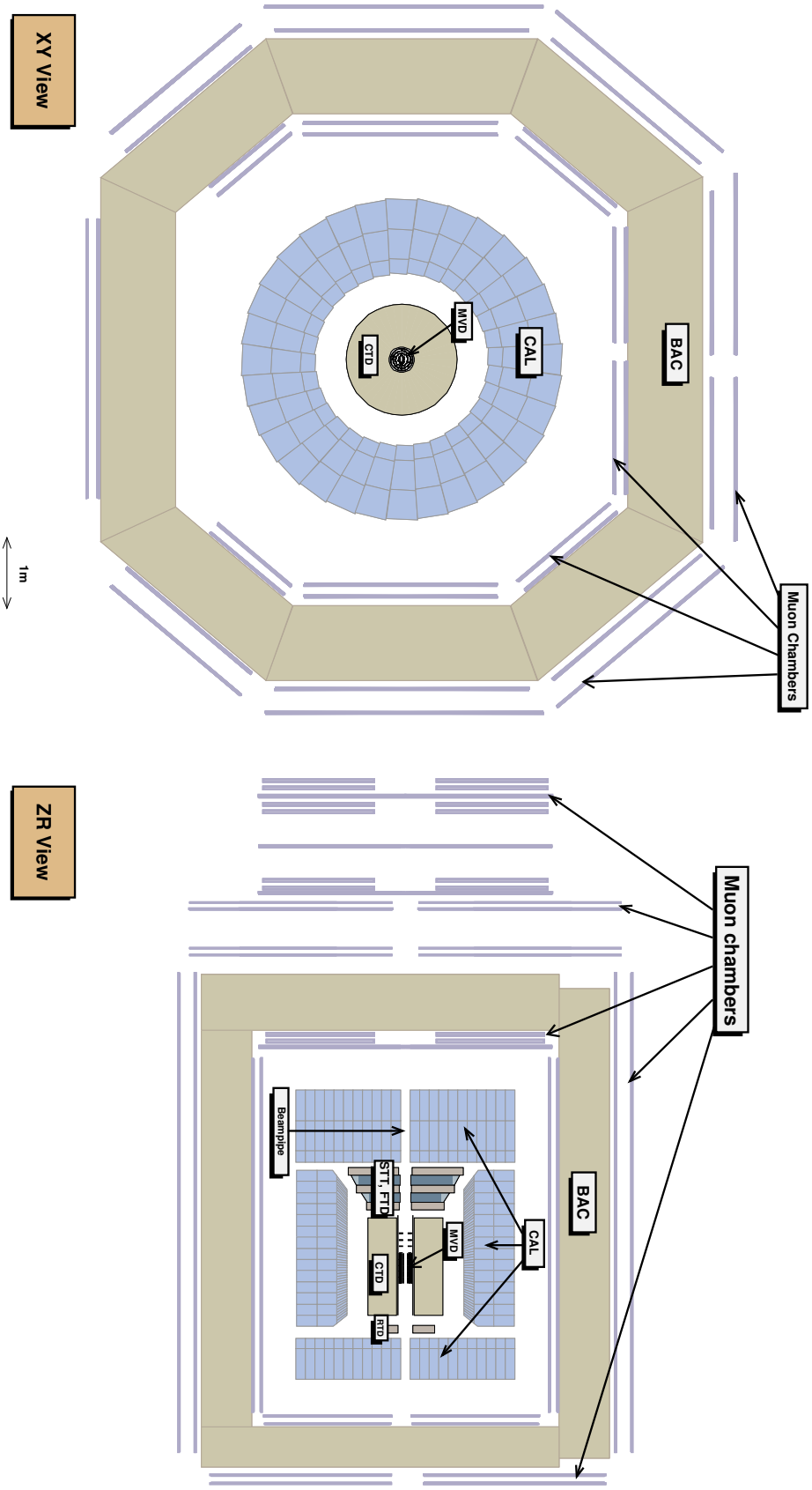

Figure 4.2: The ZEUS detector components displayed in ZeVis.

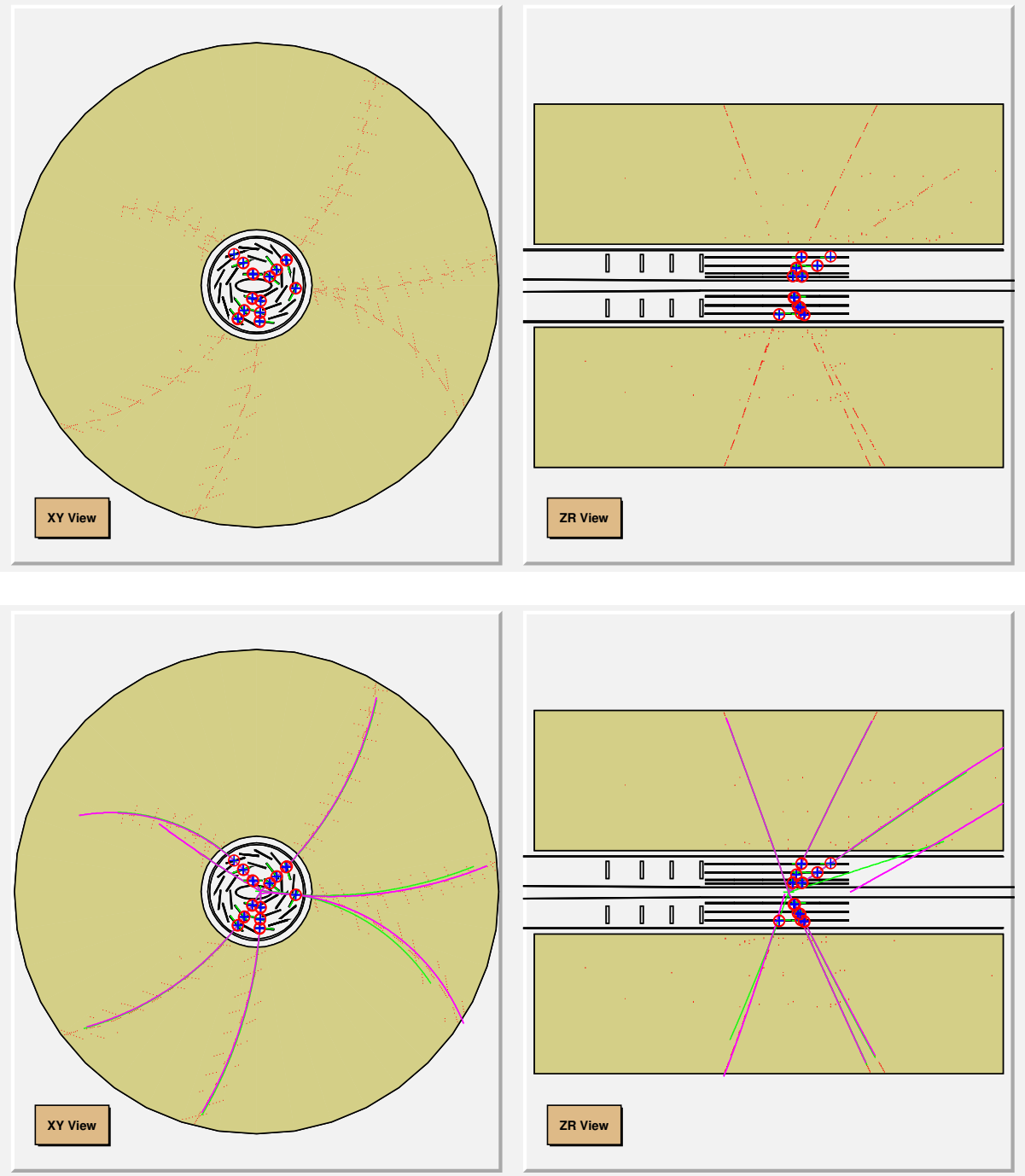

Figure 4.3: CTD and MVD hits (top) and tracks (bottom) displayed in ZeVis.

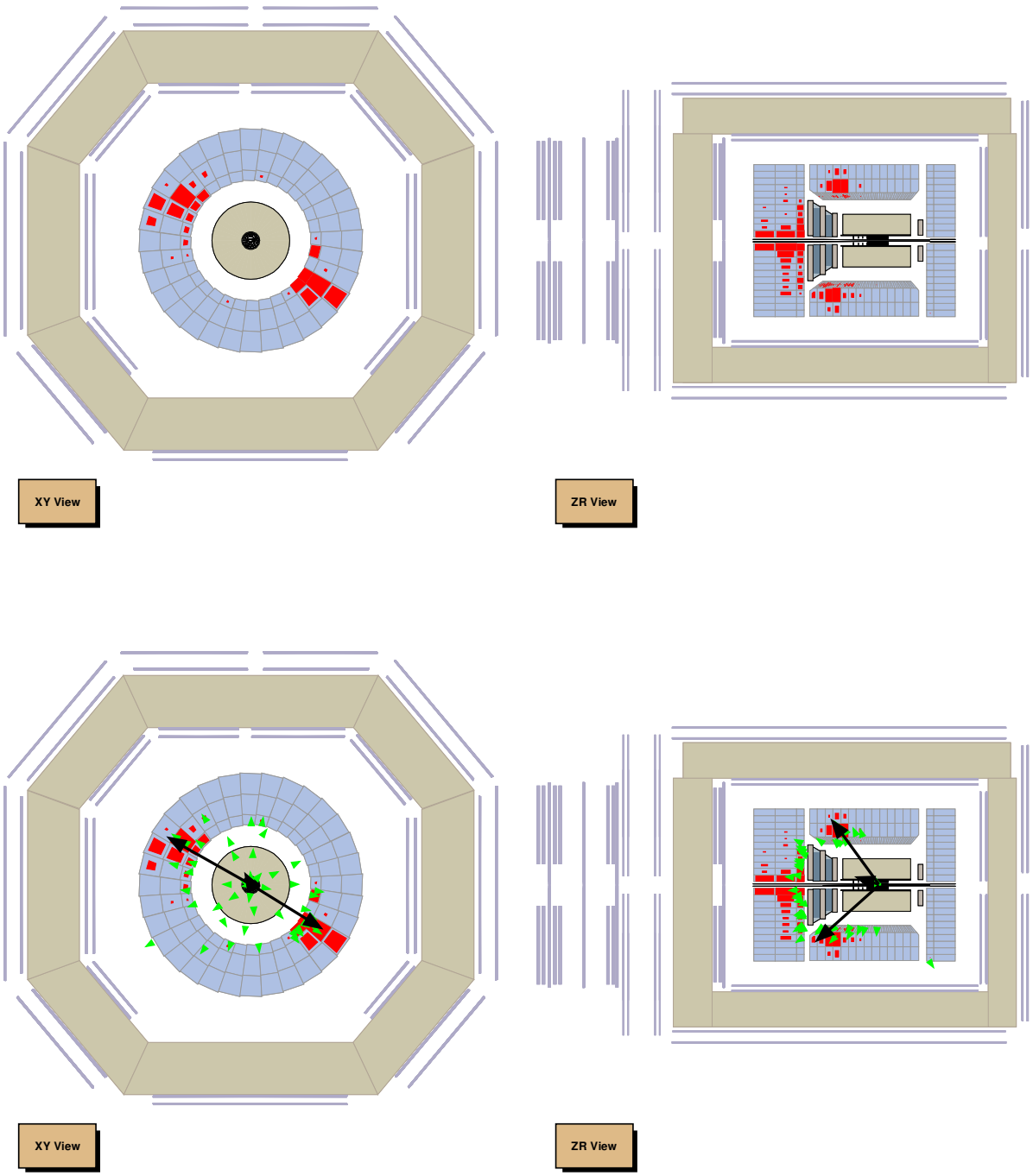

Figure 4.4: CAL hits (top) and ZUFOs and jets (bottom) displayed in ZeVis.

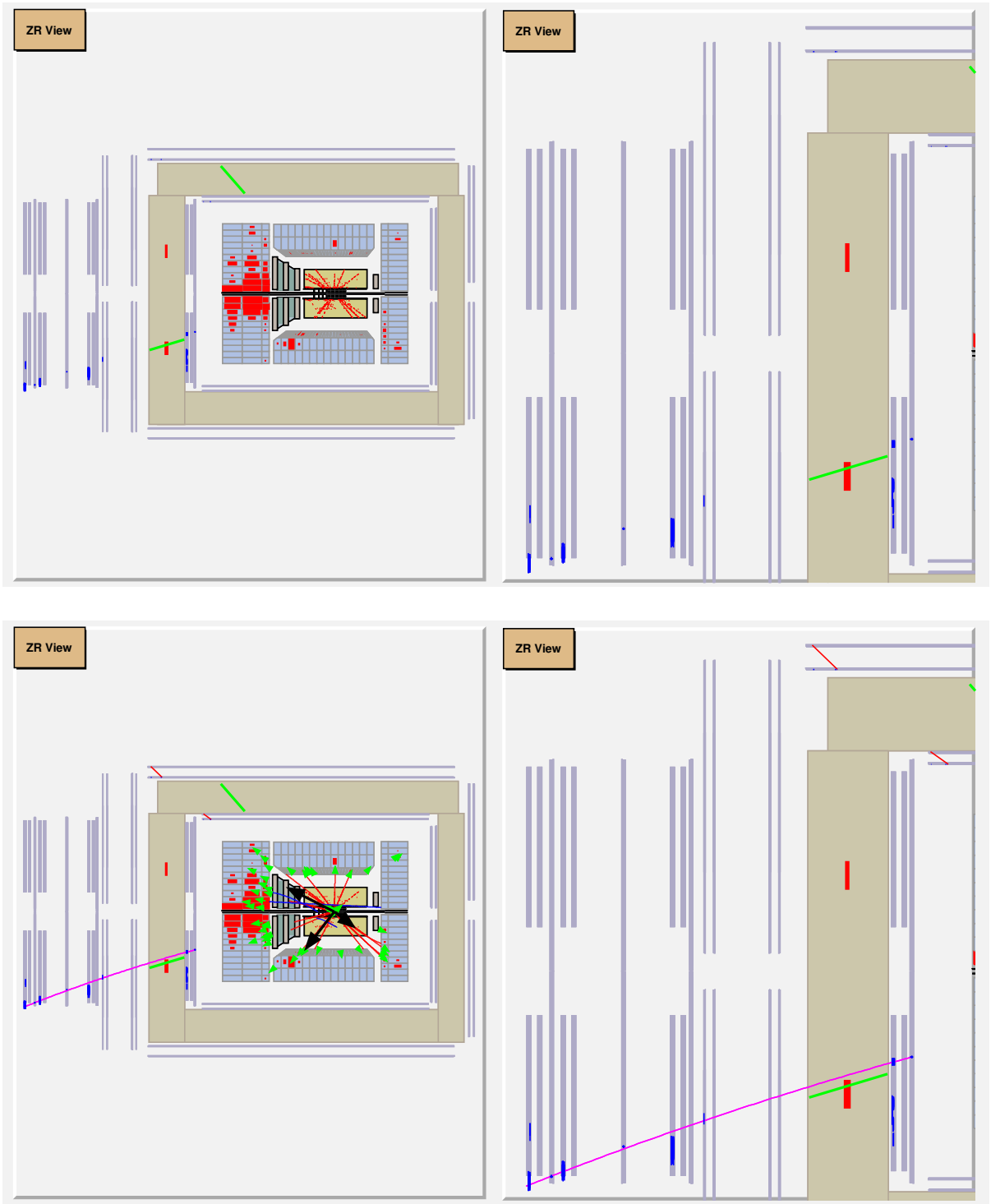

Figure 4.5: Muon hits (top) and muons (bottom) displayed in ZeVis.

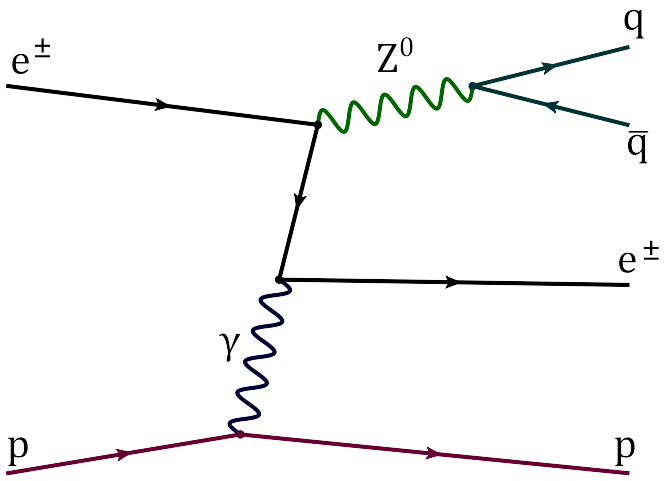

Figure 4.6: Example of a LO diagram of Z^0-boson production and subsequent hadronic decay (into quark q and antiquark $\bar{q}$) in $ep \to eZ^0p$.

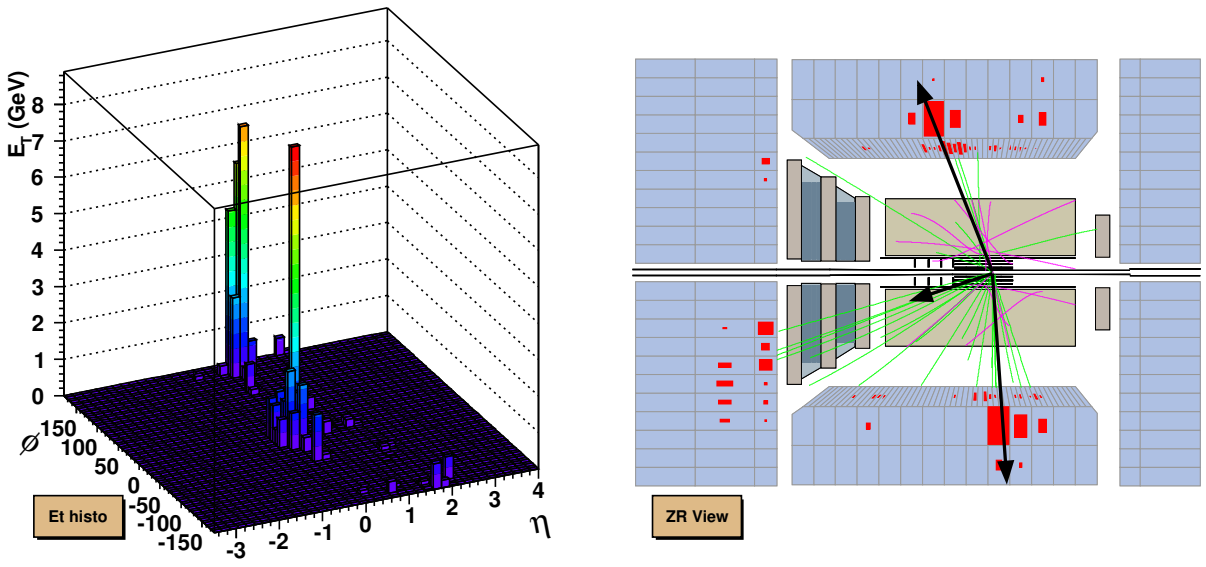

Figure 4.7: One of the selected events from the Z^0-boson analysis [155]. The transverse energy distribution $E_T(\eta, \phi)$ in the CAL sells (left) and ZR event view (right) are shown.

4.4 ZEUS data preservation project

The data collected by high energy physics experiments are crucial for the understanding of particle physics. Among the many high energy physics projects HERA holds a special place, since so far it was the world's only ep collider. All of the HERA experiments were recently consolidating their respective data analysis models, including finalising the data formats for preservation of the full HERA data [149]. The DESY Data Preservation Group (DESY-DPHEP) was established in 2009, shortly after the global DPHEP initiative was launched[2]. The data preservation effort aims to ensure long-term availability of the data after the end of the experimental Collaborations. Data preservation increases the physics potential of experiments, allowing a long-term data analysis, re-using and re-analyzing the data, combining results between experiments and using the data for education, training and outreach purposes.

The different data preservation models established by the DPHEP group, organised in levels of increasing benefits, complexity and cost, are shown in Table 4.1 [149].

Preservation Model	Use Case
1. Additional information	Publication related information
2. Provide data in simplified format	Outreach, training
3. Preserve the analysis-level software and data format	Full scientific analysis possible, based on existing reconstruction
4. Preserve the full simulation and reconstruction software as well as the basic-level data	Retain the full potential of the experimental data

Table 4.1: The DPHEP preservation modes listed in order of increasing complexity. The table is taken from [149].

The ZEUS concept fits into the preservation models 3 and 4. The ZEUS analysis model before the end of 2012 has been based on Mini Data Summary Tapes (MDST) and contained a lot of external dependencies, therefore it was not intended to be maintained when the available manpower was reduced. Therefore the ZEUS analysis software was used to create common-usage ntuples (real and MC data). The ROOT-based Common Ntuple (CN) content has been iterated over the last few years. By their structure CN are simple ROOT files with TTree objects only. They contain the necessary information to perform all ongoing and planned future analyses; all ongoing and most of the recently published analyses actively use them. Some low-level information for unplanned new analysis approaches is also included. The resulting total ntuple size is 10–20% of the size of the MDST data. Additionally a stand-alone MC package using existing, frozen executables is also being provided to generate small additional MC sets in the future, foreseeing developments in theory [149].

[2] For more details about the DPHEP study group see [156, 157]

4.5 ZeVis based on Common Ntuples

In the context of the ZEUS data preservation project described in the previous Section 4.4 the ZeVis program must fulfill the following requirements:

- it must be independent of the ZEUS Software;
- it must read information from the CN.

This in turn means that:

- the Server part is not needed anymore;
- ZeVis becomes a pure ROOT application.

The architecture of ZeVis based on the CN (referred to as *CN-ZeVis*) is shown in Fig. 4.8.

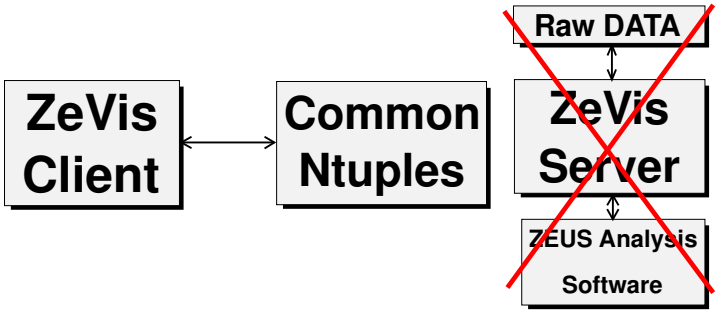

Figure 4.8: The architecture of CN-ZeVis.

Since the CN does not contain all information that was in the MDST files, CN-ZeVis also cannot display some things available in classic ZeVis. A list of information which can be displayed in CN-ZeVis is provided in Appendix A.1. A standalone version of CN-ZeVis is available also; it is described in Appendix A.2.

4.5.1 Overview

A user can start CN-ZeVis with the command `zevis-cn` (production version) or `zevis-cn-dev` (development version). ZeVis works by having one main window (Fig. 4.9) which contains a Canvas and several tabs. The Canvas is divided into two subpads supposed to display two different event views. The tabs allow a user to interact with ZeVis: specify an event to display, change the way how it is displayed, switch on/off different ingredients of the detector or event content. Additionally interaction with the program is possible using the context menu (available with a right-button mouse click on the Canvas) and `File`, `Edit`, `View_Option`, `Special_Viewers` and `Option` menus.

The purpose of the `Events` tab (Fig. 4.10) is to set an event to display. There are two ways to specify an event:

- to specify the run number, event number and CN version (for DATA only);

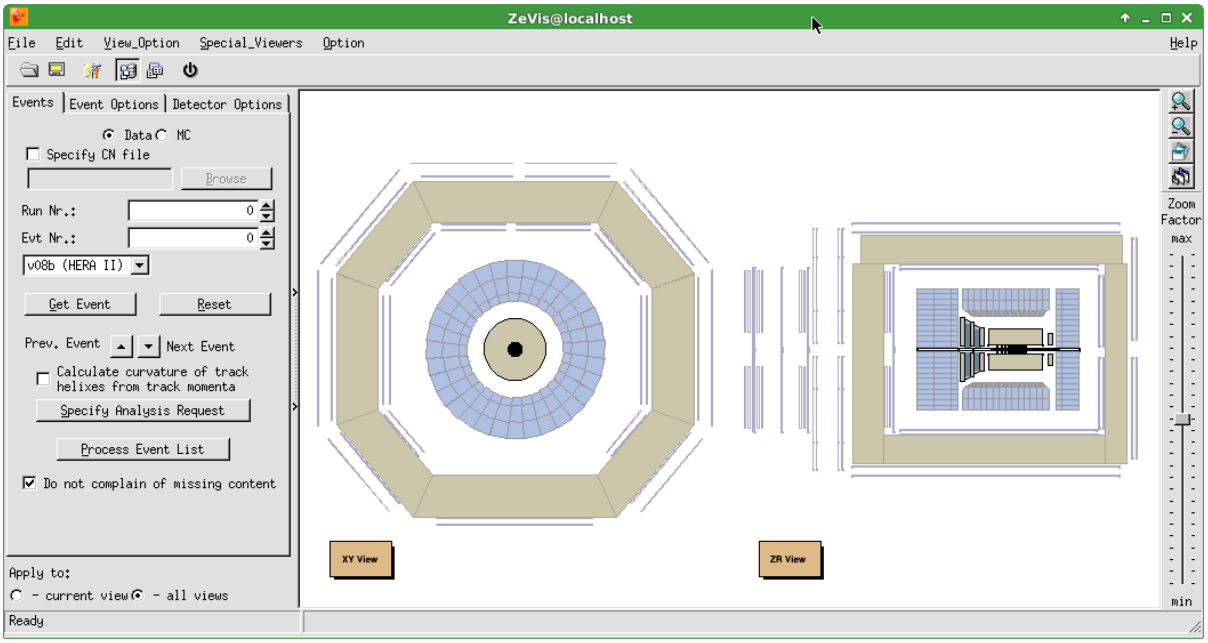

Figure 4.9: The CN-ZeVis main window.

- to specify the run number, event number and CN file (both for DATA and MC).

In the ZeVis Client a user can switch between these two regimes by using the `Specify CN file` check button[3]. There are two suitable buttons `Next Event` and `Prev. Event` to display either a next/previous available event with a larger/lower event number (if a CN file was not specified) or a next/previous event in the specified CN file.

There are several projections available in ZeVis (Fig. 4.11) (the description of the ZEUS coordinate system is given in Section 3.1.2.1):

- `ViewXY`: projection on the cartesian plane XY;
- `ViewZR`: projection Z vs. R, where R is defined as $\mathrm{R} = \pm\mathrm{R} = \pm\sqrt{\mathrm{X}^2 + \mathrm{Y}^2}$ with the sign depending on the azimuthal angle ϕ of the object to be drawn: $\mathrm{R} = +\mathrm{R}$ if $\phi_1 < \phi < \phi_2$ and $\mathrm{R} = -\mathrm{R}$ otherwise;[4]
- `View3D`: three-dimensional view;
- `FishEye`: projection on the cartesian plane $\mathrm{X}_F\mathrm{Y}_F$, where the cartesian coordinates X_F, Y_F are calculated from the transformed spherical coordinates ρ_F, ϕ_F after the transformation $\rho_F = \frac{\rho}{1+a\rho}$, $\phi_F = \phi$; here $a > 1$ is a predefined parameter.

A user can switch between different projections for each subpad using the context menu or the `Special_Viewers` menu.

[3] For MC it is mandatory to set the run number to 1. If one wants to display an event from MC it is recommended to switch to the MC regime using the `DATA-MC` radio buttons: in this case the run number input field will be set to 1 automatically and become inactive.

[4] ϕ_1 and ϕ_2 can be specified with the `SetPhiRange` entry from the context menu.

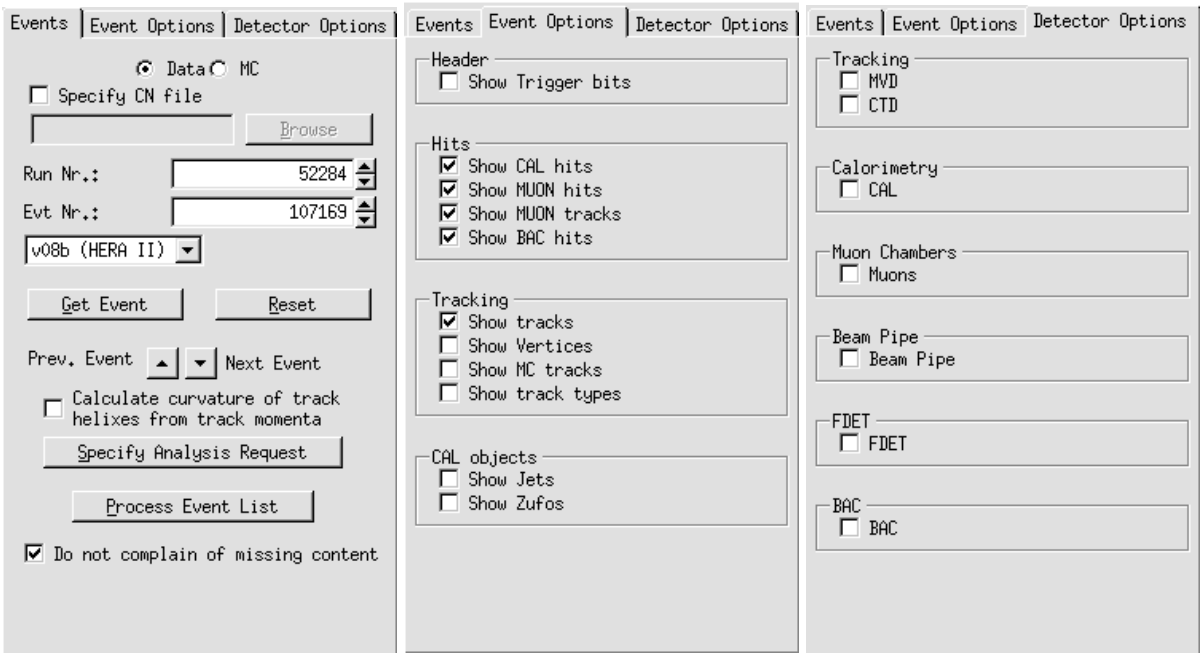

Figure 4.10: The `Events` (left), `Event Options` (middle) and `Detector Options` (right) tabs.

There are also some special projections to display the content of the CAL cells:

- `Eta-Phi Energy Distribution` (`ViewET`): pseudorapidity η vs. azimuthal angle ϕ energy distribution in the cells;
- `Forward Theta-Phi`.

They can be selected from the `Special_Viewers` menu.

To specify the information to be displayed a user uses the `Event Options` and `Detector Options` (Fig. 4.10) tabs and/or the `View_Option` menu and/or the `Event Settings` button (the last one will open a new `Easy Tool` window), which are self-explanatory. The changes can be applied either to the current subpad or to the both subpads of the Canvas depending on the `Apply to:` radio button. There is a small additional tab on the right from the main Canvas suited for changing the zooming.

4.5.2 New features

In addition to the classic ZeVis functionality, several new features have been implemented in CN-ZeVis by the author:

- processing an event list;
- batch mode;
- support for “private mini-ntuples”;
- analysis-specific tracks and vertices;

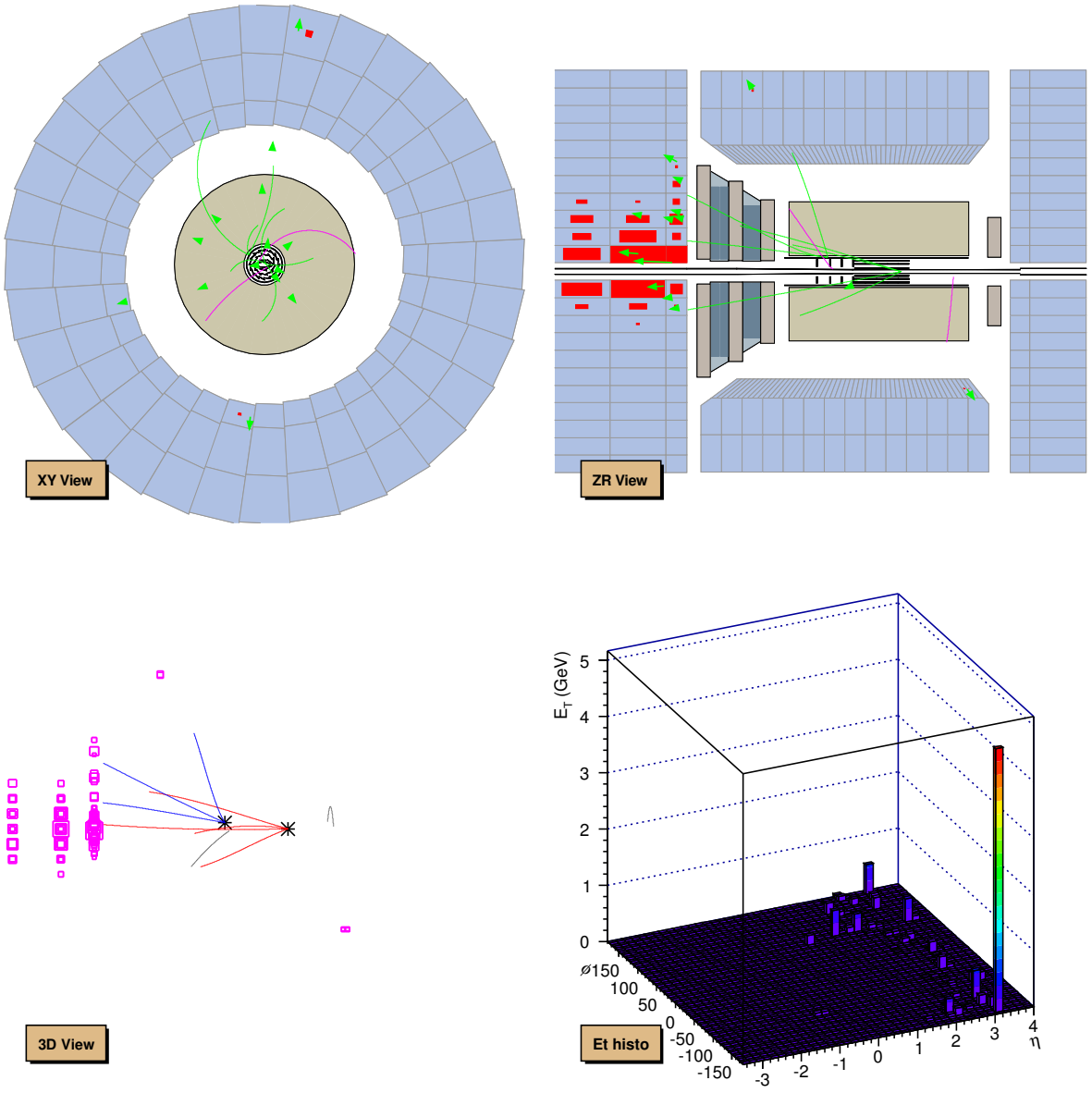

Figure 4.11: Different projections available in ZeVis: `ViewXY` (top left), `ViewZR` (top right), `View3D` (bottom left), `Eta-Phi Energy Distribution` (bottom right).

- MVD standalone TRKMSA tracks;
- using a constant magnetic field for displaying track helices;
- possibility to change the ZeVis style;
- zooming of the selected area;
- access CN on dCache from outside DESY using a Grid proxy.

They are described in Appendix A.3.

4.6 Summary

The ZeVis program has been modified in the context of the ZEUS data preservation project to become independent of the ZEUS Software. The new CN-ZeVis, based on Common Ntuples, is a pure ROOT application. While CN-ZeVis provides the main functionalities, which were available in classic ZeVis, it does not require any maintenance. In addition, several new features have been implemented in CN-ZeVis.

CHAPTER 5

Measurement of D^+ production

This Chapter is devoted to the measurement of D^+-meson production with the ZEUS detector at HERA. This is one of the charm-tagging techniques (see Section 3.1.3), based on the full reconstruction of final-state charm hadrons, which crucially depends on the precise tracking and vertexing near the beampipe. Combinatorial background can be significantly suppressed by applying a cut on lifetime information. The previous ZEUS measurement of D^+ production [138] was performed using 134 pb^{-1} of data from 2005. It has demonstrated the high potential of this tagging method, although was not really competitive in precision to other ZEUS charm measurements, e.g. [136]. The present measurement benefits from $\approx$ 2.5 times larger data sample and improved tracking allignment.

Results presented in this Chapter were obtained by the author as the second analysis (a cross check, independent from the primary analysis) in the ZEUS Collaboration. Partially these results were described in the previous master diploma [158] of the author and, independently, in the PhD dissertation [159] of the primary analyser. The results were published by the ZEUS Collaboration [139]. Finalisation of the analysis was part of the work for this thesis.

Section 5.1 explains general aspects of the event reconstruction in ZEUS, relevant for the present analysis; because the author was not involved in the development of any of these reconstruction techniques, it has rather an overview style and is largely based on [98, 159]. Section 5.2 describes the selection of DIS events. Section 5.3 introduces the technique of MC simulations and provides information on MC samples, used in the analysis. Section 5.4 describes the reconstruction and selection of D^+ candidates, while Section 5.5 explains the procedure of the separation of these candidates into the D^+ signal and background. Section 5.6 describes the cross-section determination procedure and all applied corrections. Details of the theoretical calculations are given in Section 5.7. Finally, results of the measurement are reported in Section 5.8, while Section 5.9 gives conclusions.

5.1 Event reconstruction

Each single ep collision is referred to as an *event*. Events passed the TLT were written to tape as raw data in the form of signals from all sub-detectors (see Section 3.1.2.1 for the description of the ZEUS detector). These data were used offline to reconstruct general characteristics of events which correspond to signatures of physical objects (particles, jets etc.). Below the reconstruction of tracks (Section 5.1.1), vertices (Section 5.1.2), hadronic final-state system (Section 5.1.3) and DIS kinematic variables (Section 5.1.4) is described.

5.1.1 Tracking

A track is the trajectory of a charged particle in the detector. It depends not only on the inhomogeneous magnetic field, but also on energy loss and multiple scattering in the material; thus the reconstruction of tracks is a complicated task. The approach adopted in ZEUS made use of the Kalman filter [160] and offered a rigorous treatment of all factors which affect particle trajectories [161].

5.1.1.1 Kalman filter algorithm

The Kalman filter algorithm [160] is an iterative procedure for the reconstruction of tracks from the measured hits[1]. It reconstructs tracks from the outermost point of the tracking system to the origin. Unlike other global methods which fit all the measurements to a single set of track parameters, the Kalman filter causes the track to "follow the measurements" through the detector [163]. A detailed description of the procedure can be found in [160] and an extended review of its properties and advantages can be found in [163]. Briefly summarising the most important features [163]:

- the Kalman filter method uses *all* the information and cannot, if used correctly, give poorer track parameters by adding more measurements. Including additional hits would not result in an increase in the uncertainty of the track parameters, unlike many other track fitting methods;
- because the algorithm traces the track backwards, the parameters on the outer part of the track are much more poorly determined than the ones on the inner part. Although this benefits the analysis since accuracy at the production vertex is vital, it means that the projection of the track to the outer region can be unreliable;
- the method can easily deal with gaps in which there are no measurements;
- the iterative nature of this procedure allows tracks to be fitted in pieces, e.g. tracks can be found and fitted in the drift chambers and then projected to the silicon detector with the full covariance matrix so that the silicon hits can be added to the fit trivially without having to redo the entire fit.

[1] Description of the ZEUS hit reconstruction procedure can be found in [162].

5.1.1.2 ZTT tracks

In this analysis the so-called *ZTT tracks* were used, which combined the information from the CTD and MVD and therefore are the most precise [159]. Tracks were reconstructed in two stages:

- **pattern recognition.** The first stage was performed in multiple steps by the VCTRACK package [162, 164]. It started from the outermost tracking detector layer, which was the 9th CTD superlayer for the central region, where the track density was lower than close to the interaction point. Combinations of three CTD hits from axial CTD superlayers formed the tracking *seeds*. A track seed was extrapolated inward, gathering additional hits with increasing precision as the trajectory parameters were updated. A very broad "virtual" hit was added at the beam line to guide the trajectory. After a "road" of hits from the CTD through the MVD to the interaction point has been created, a least-squares fit of the track was done using the selected hits on the road in order to determine the helix parameters at the beginning of the helix. In general the tracking reconstruction was not restricted to tracks with hits in all tracking devices; the so-called *CTD-only* and *MVD-only* tracks have hits in only one sub-detector;

- **trajectory refinement.** A track fit was performed with the Kalman filter to improve the precision of the helix parameters in the vicinity of the interaction point. As input it took the fit output from the pattern recognition stage. The track fit was applied recursively in three steps: *prediction*, *filtering* and *smoothing*. At the prediction step, the present state i hits (i.e. hits that have already been used for the trajectory estimation) was used to predict the position of the next $(i+1)^{\text{th}}$ hit on the next detector sensor (which could be a CTD wire or an MVD sensor). At the following filtering step the predicted and the measured values for the $(i+1)^{\text{th}}$ hit positions were combined. At the last step a smoothing of the whole trajectory was performed and the covariance matrix was updated.

The Kalman filter examines the hits individually, whereas the least-squares fit evaluates all hits simultaneously. Removing wrong hits from the least-squares fit requires all fits to be redone from the start, which results in a large calculation time as the number of hits increases. Therefore the effect of multiple scattering on a trajectory was easier to incorporate in the Kalman filter fit. Detailed information on the mathematical framework of the track fitting with the ZEUS detector is provided in [161]. The parametrisation of tracks, used in ZEUS, is described in Appendix B.3.

5.1.2 Vertexing

A vertex is the point where an interaction or decay happened. The evaluation of vertices serves two purposes [165]. The first is to evaluate the position of the primary ep interaction point and to calculate the appropriate track momenta at that point with improved precision due to the vertex constraint. The second purpose of using vertices is to estimate the probability that the tracks originate from a certain vertex. This probability might be estimated from the vertex fit quality (e.g. the χ^2 of the vertex fit) and used for the event selection. The essential information that is used in the fit consists of track parameters and their covariance matrices.

Proper identification of both the primary point of interaction and the D^+ decay vertex in an event was of particular importance for this analysis. Their position was reconstructed first with the VCTRACK package and further refinement was applied later [159].

The vertex pattern recognition started with a loose constraint that the primary vertex should be found along the proton-beam line. Track pairs, that were compatible with this soft constraint as well as with a common vertex, were combined with other track pairs. The final choice of the primary-vertex position after the pattern recognition stage was the vertex with the best overall χ^2. To improve the precision of the vertex-position measurement, the Deterministic Annealing Filter (DAF) [166] was used. The main feature of the DAF algorithm is that tracks with the best quality get the largest weight in the fit, while tracks that are far from the vertex get the smallest weight in the fit [165]. In the chosen approach the vertex position was measured iteratively by calculating a weighted sum of the χ^2 contributions from individual tracks to the vertex [159].

For the primary-vertex fit, a further improvement in precision was possible by the introduction of a constraint on the vertex position to be close to the averaged interaction point, the *beamspot*. The beamspot was defined as the overlap region of the colliding beams. It had a width of roughly $80 \times 20\,\mu\text{m}$ in the XY plane [167], but it was too large in the Z direction to use this information as a constraint [159].

In the case of secondary vertices, e.g. the D^+-decay vertex, the fit was made with the same algorithm skipping the step of the pattern recognition, since the combination of tracks was chosen based on its compatibility with the D^+ mass. For each secondary vertex, the corresponding reduced primary vertex was recalculated removing the secondary-vertex tracks and repeating the standard primary-vertex fit [159].

5.1.3 Hadronic final states

To get the most precise hadronic energy measurement, information from the calorimeter and the tracking detectors was combined into the so-called *ZEUS Unidentified Flying Objects* (ZUFOs) [168].[2] Ideally each ZUFO was supposed to represent one final-state particle. The energy resolution of the CAL developed for higher particle energies as $\sigma(E)/E \sim 1/E$, while the tracking momentum resolution, parametrised by $\sigma(p_T)/p_T = ap_T \oplus b \oplus c/p_T$, gave a better energy estimate for lower particle momenta (see Section 3.1.2.1). For neutral particles, only CAL information could be used, whereas for charged particles the tracking information was mainly used below 10 GeV while calorimeter energy was used for higher energies.

ZUFOs were constructed in the following steps:

- CAL cells were clustered into two-dimensional *cell islands*. A cell with lower energy deposit was connected to a cell with higher energy. The combination algorithm provided a unique association of a cell to its highest energy neighbour. This algorithm was run in each calorimeter part separately;

- the cell islands from the previous stage were used as an input to clustering in (θ, ϕ) space. The procedure started from the outermost layer of the CAL and went inward by calculating the angular separation between neighbouring cell islands. The separation was

[2] ZUFOs are also referred to as Energy Flow Objects (EFOs) in ZEUS publications.

used to associate the input islands together to form three-dimensional energy clusters called *cone islands*. The position of a cone island was determined by the logarithmic centre-of-gravity of the energy deposit;[3]

- charged tracks, that have been fitted to a vertex and passed certain requirements, were extrapolated to the surface of the CAL taking into account the magnetic field. The selected tracks should fulfill the following requirements:
  - $0.1 < p_T < 20\,\text{GeV}$ for tracks with hits in at least 4 CTD superlayers;
  - $0.1 < p_T < 25\,\text{GeV}$ for tracks with hits in at least 7 CTD superlayers.

  A track and a cluster were matched if either the distance of the closest approach between the track and the position of the cone island was less than 20 cm or the track was within the area of the island. As a result of this procedure, groups of cone islands and tracks — ZUFOs — were formed;

- the combination of the information from the CAL and the tracking system was carried out in the following way:
  - if one track has been matched to one cone island, the ZUFO energy was taken either from the CAL cluster or from the matched track momentum, depending on which measurement had better resolution;
  - for good tracks that have not been associated to islands, the energy was derived from the momentum measurement with the assumption that the particle was a charged pion;
  - cone islands that have not been matched to any track were treated as neutral particles and the CAL energy was used;
  - cone islands with more than three associated tracks were treated as jets and the energy was taken from the CAL;
  - if a track has been matched to multiple islands or two tracks have been matched to one or two islands, the algorithm was similar to the one-to-one matching, but using the sum of energies or momenta instead.

Further corrections were applied to account for the material budget of the detector, the inefficiency in the regions of cracks between the CAL sections, the presence of muons[4] and the imbalance in the compensation effect for low momentum ($\sim 1\,\text{GeV}$) hadrons. Detailed information on the ZUFO reconstruction can be found in [168]. In this analysis the reconstructed ZUFOs have been used to determine the kinematics of the hadronic system as well as DIS kinematic variables (see Section 5.1.4).

[3] Using logarithmic weights instead of the linear sum took into account the exponential falloff of the transverse shower energy distribution from the shower maximum.

[4] Muons did not release all their energy in the CAL, thus if the CAL information was used the energy would be underestimated.

5.1.4 Scattered-electron identification and reconstruction of kinematic variables

The identification of the scattered electron is essential for the NC DIS event selection. The scattered electron leaves a clear signature which differentiates the NC DIS events from the CC DIS, where the neutrino escapes undetected, and PHP, where the scattered electron escapes through the beam hole. There have been two main electron finders developed in ZEUS: the neural-network-based SINISTRA95 (also referred to just as SINISTRA) [169] and the probabilistic EM [170]. The former was tuned for the kinematic region of the measurement presented in this thesis, whereas the latter was better for the high-Q^2 region, where the electron was reconstructed in the BCAL.

A scattered electron passing through the CAL created an electromagnetic shower, therefore most of its energy was measured in the EMC with a small leakage in the HAC. SINISTRA started from the search of the cells with maximum energy deposits to form candidate clusters. These clusters were formed using the next-to-nearest neighbour algorithm on CAL towers to produce islands and then merging the islands from different CAL sections; this algorithm allowed diagonal associations in contrast to the nearest neighbour algorithm used for ZUFOs (see Section 5.1.3). The position of the energy deposit within a cell was reconstructed from the imbalance of the two readout photomultipliers in the cell. These energy deposits were used to calculate the longitudinal- and transverse-energy distributions in the original shower and this information was passed to the neural network. The neural network had been trained using MC simulated hadronic and electromagnetic clusters in the RCAL. As an output SINISTRA returned a number between 0 and 1, which represents the probability of the cluster to be the scattered electron. In the following only the candidate with the highest probability was considered. The identified electron was assigned the energy of the reconstructed CAL cluster.

After the reconstruction of the scattered electron and the hadronic system in an event, the kinematic variables Q^2, x and y, introduced in Section 2.1.1, can be calculated. There were several methods, described below.

5.1.4.1 Electron method

The *electron method* (el) used only the electron energy and scattering angle. The kinematic variables were calculated as follows:

$$\begin{aligned} Q^2_{\text{el}} &= 2E_e E'_e(1+\cos\theta_e), \\ y_{\text{el}} &= 1 - \frac{E'_e}{2E_e}(1-\cos\theta_e), \\ x_{\text{el}} &= \frac{Q^2_{\text{el}}}{s y_{\text{el}}}, \end{aligned} \tag{5.1}$$

where E_e is the incoming electron energy (which is known *a priori*), E'_e and θ_e are the scattered-electron energy and angle, respectively. This method relies strongly on the measurement of the electron energy and position. Because of the characteristics of the ZEUS detector it is more precise in the rear region, therefore it is optimal at low Q^2. In addition this method is strongly

affected by initial- and final-state photon radiation, which spoils the measurement of the lepton energy and leads to deterioration of the results.

5.1.4.2 Jacquet-Blondel method

The *Jacquet-Blondel method* (JB) relied exclusively on the reconstruction of the hadronic final state [171]. The kinematic variables were calculated as follows:

$$\begin{aligned} y_{\mathrm{JB}} &= \frac{\delta_{\mathrm{had}}}{2E_e}, \\ Q^2_{\mathrm{JB}} &= \frac{P^2_{T\ \mathrm{had}}}{1 - y_{\mathrm{JB}}}, \\ x_{\mathrm{JB}} &= \frac{Q^2_{\mathrm{JB}}}{s y_{\mathrm{JB}}}, \end{aligned} \tag{5.2}$$

where $P_{T\ \mathrm{had}}$ and δ_{had} are given by

$$\begin{aligned} P_{T\ \mathrm{had}} &= \sqrt{\sum_i (P^i_{x\ \mathrm{had}})^2 + (P^i_{y\ \mathrm{had}})^2}, \\ \delta_{\mathrm{had}} &= \sum_i (E^i_{\mathrm{had}} - P^i_{z\ \mathrm{had}}), \end{aligned} \tag{5.3}$$

where $(P^i_{x\ \mathrm{had}}, P^i_{y\ \mathrm{had}}, P^i_{z\ \mathrm{had}}, E^i_{\mathrm{had}})$ is the four-momentum of each hadronic final state and the sum goes over all hadronic energy, excluding the scattered electron, if any. The advantage of this method is that it does not require the scattered electron to be detected and thus can be used in PHP or CC events, although it has poor Q^2 resolution in DIS events.

5.1.4.3 Double-angle method

The *double-angle method* (DA) combined information from the scattered electron and the hadronic system [172, 173]. The kinematic variables were calculated as follows:

$$\begin{aligned} Q^2_{\mathrm{DA}} &= 4E_e^2 \frac{\cot(\theta_e/2)}{\tan(\theta_e/2) + \tan(\theta_{\mathrm{had}}/2)}, \\ y_{\mathrm{DA}} &= \frac{\tan(\theta_{\mathrm{had}}/2)}{\tan(\theta_e/2) + \tan(\theta_{\mathrm{had}}/2)}, \\ x_{\mathrm{DA}} &= \frac{Q^2_{\mathrm{DA}}}{s y_{\mathrm{DA}}}, \end{aligned} \tag{5.4}$$

where θ_{had} is the hadronic angle, defined as

$$\tan(\theta_{\mathrm{had}}/2) = \frac{\delta_{\mathrm{had}}}{P_{T\ \mathrm{had}}}. \tag{5.5}$$

This method exploits the fact that the angular resolution for the hadronic system is usually better than the angular resolution for the scattered electron, while for energy it is *vice versa*. Thus the DA method leads to a more precise measurement of the kinematic variables in a large part of the phase space and was chosen as the main one for the present analysis [159].

5.2 DIS event selection

The measurement used the full HERA-II data with an integrated luminosity $354\,\text{pb}^{-1}$. Both electron–proton and positron–proton data were used, because the charm NC DIS cross sections at not too high Q^2 are invariant with respect to the lepton charge. The DIS kinematic region of the measurement was restricted to $5 < Q^2 < 1000\,\text{GeV}^2$ and $0.02 < y < 0.7$, where reliable reconstruction of the scattered electron was possible with the ZEUS detector after the HERA-II high-luminosity upgrade [105].

The selected events had to be triggered online by one of the inclusive DIS TLT slots:

- SPP02 for the 2004–2005 data period, or
- SPP09, or HFL17, or HPP31 for the 2006–2007 data period.

A detailed description of the TLT slots can be found in [174]. Furthermore to ensure selection of good DIS events, the following cuts were applied offline:

- $5 < Q^2_{\text{DA}} < 1000\,\text{GeV}^2$, $0.02 < y_{\text{DA}} < 0.7$. These criteria selected the considered DIS phase space;
- $E'_e > 10\,\text{GeV}$. The requirement ensured high efficiency of SINISTRA and rejected possible background PHP events with "fake" scattered electrons;
- $E^{\text{cone}}_{\text{non }e} < 5\,\text{GeV}$, where $E^{\text{cone}}_{\text{non }e}$ is the energy deposit in the CAL in the cone centered around the scattered electron with a radius of 0.8 in the (η, ϕ) plane, not originating from it. This cut is known as the *electron isolation* and was supposed to improve further the quality of the scattered-electron reconstruction;
- $\text{prob}_{\text{SINISTRA}} > 0.9$, where $\text{prob}_{\text{SINISTRA}}$ is the output of the SINISTRA neural network.[5] This selection further ensured high efficiency in SINISTRA;
- $y_{\text{JB}} > 0.02$. This requirement rejected events with the poorly reconstructed hadronic system, for which the DA method was not precise;
- $40 < \delta_{\text{had}} < 65\,\text{GeV}$. The lower cut reduced the PHP contamination (when the scattered electron was not detected) and the upper cut rejected events initiated by cosmic-ray particles;[6]

[5] Despite the notation, it is not the probability in its mathematical meaning.
[6] For a fully contained NC event, $\delta_{\text{had}} = 2E_e = 55\,\text{GeV}$.

- $-30 < Z_{\text{vtx}} < 30\,\text{cm}$, where Z_{vtx} is the Z coordinate of the primary vertex. This requirement rejected events initiated by beam-gas and satellite-bunch interactions;

- a set of cuts on the geometric position of the scattered electron in the CAL ($x_{e'}$, $y_{e'}$, $z_{e'}$), to remove events, in which the scattered electron passed through the regions of the CAL poorly simulated in Monte Carlo; note that these cuts are quoted as exclusion cuts, i.e. the events were removed if they satisfied any of the criteria:
  - $|x_{e'}| < 13\,\text{cm}$ and $|y_{e'}| < 13\,\text{cm}$. This requirement is known as the *box cut* and removed the edges of the CAL;
  - $\sqrt{x_{e'}^2 + y_{e'}^2} > 175\,\text{cm}$. This cut rejected the region between the RCAL and BCAL;
  - $-104 < z_{e'} < -98.5\,\text{cm}$ or $164 < z_{e'} < 174\,\text{cm}$. This requirement is known as the *super-crack cut* and removed the regions of cracks between the RCAL, BCAL and FCAL;
  - $6.5 < x_{e'} < 12\,\text{cm}$ and $y_{e'} > 0$, or $-14 < x_{e'} < -8.5\,\text{cm}$ and $y_{e'} < 0$. This requirement is known as the *module-gap cut* and removed the region of gaps between halves of the RCAL;
  - $|x_{e'}| < 12\,\text{cm}$ and $y_{e'} > 80\,\text{cm}$. This requirement is known as the *chimney cut* and removed the region of the RCAL where cooling tubes and supply cables for the solenoid were mounted;
  - in addition, for a subset of the data with the run ranges 59600–60780, 61350–61580, 61800–63000 the region $11 < x_{e'} < 27\,\text{cm}$ and $10.5 < y_{e'} < 27\,\text{cm}$ was removed, which was not described by the Monte Carlo simulations.

5.3 Monte Carlo simulations

Any detector has its own response to underlying physics processes. This results in a limited acceptance, which should be taken into account for any measured cross section. To model a detector response the Monte Carlo (MC) [175] method is widely used.

5.3.1 Technique of MC simulations

MC simulations are performed in two stages:

1. **simulation of underlying physics.** This stage is performed using some MC generator, which produces a list of all particles in the final state, which are considered to be stable;[7]

2. **simulation of detector response.** At this stage the simulated particles pass through a detector simulation.

[7] i.e. which reach the detector and interact with its material.

5.3.1.1 Simulation of underlying physics

In the generation of MC events the QCD factorisation theorem [25, 81–85] is exploited to separate short- and long-distance effects. In Fig. 5.1 it is illustrated considering an example of a BGF event (see also Fig. 2.8 for the BGF diagram):

- **simulation of the hard scattering.** Usually it is calculated at LO;
- **radiation corrections** (referred to also as *parton showers*) are modelled using some phenomenological models. The difference between the fixed-order NLO calculation and LO accompanied by parton showers is that the latter better reproduces the whole final state (the *event shape*), which is important for the correct simulation of the detector response, while the former gives a better description of inclusive quantities;[8]
- **hadronisation** is the non-perturbative QCD process of the formation of colourless hadrons from coloured partons. It is performed by using some phenomenological models;
- **particle decays.** Decays of unstable particles are simulated accordingly to supplied decay tables.[9]

Examples of event generators commonly used in ZEUS are PYTHIA [176], ARIADNE [177], RAPGAP [178] etc.

5.3.1.2 Simulation of detector response

After the simulation of underlying physics processes, final-state particles are passed through a simulated detector. Simulation of the ZEUS detector was performed in the MOZART program, which is based on GEANT 3.21 [180]. Furthermore, generated events were passed through the simulated ZEUS trigger system and the reconstruction program ZEPHYR. More details on the ZEUS MC production system can be found in [159]. Finally, MC events were written to tape as regular data and processed by the same reconstruction and selection algorithms, although they contain additional information on generated particles, referred to as *generated*, or *true* information. However, the procedure of matching between generated particles and reconstructed ones has some complications (see Section 5.6.1.2).

5.3.2 MC samples

In the present analysis the following MC samples have been used:

- the RAPGAP charm DIS MC sample was the main sample used to determine acceptance corrections. MC events were simulated with the RAPGAP 3.00 [178] program, interfaced with HERACLES 4.6.1 [181] to incorporate first-order electroweak corrections. The CTEQ5L [182] PDFs were used for the proton;

[8] NLO calculations are much more complicated to be matched with parton showers. NLO accompanied by parton showers MC generators were never used in ZEUS.

[9] Some relatively long-lived particles (typically pions, kaons, muons) are usually considered as stable in an MC generator, since they interact with a detector directly.

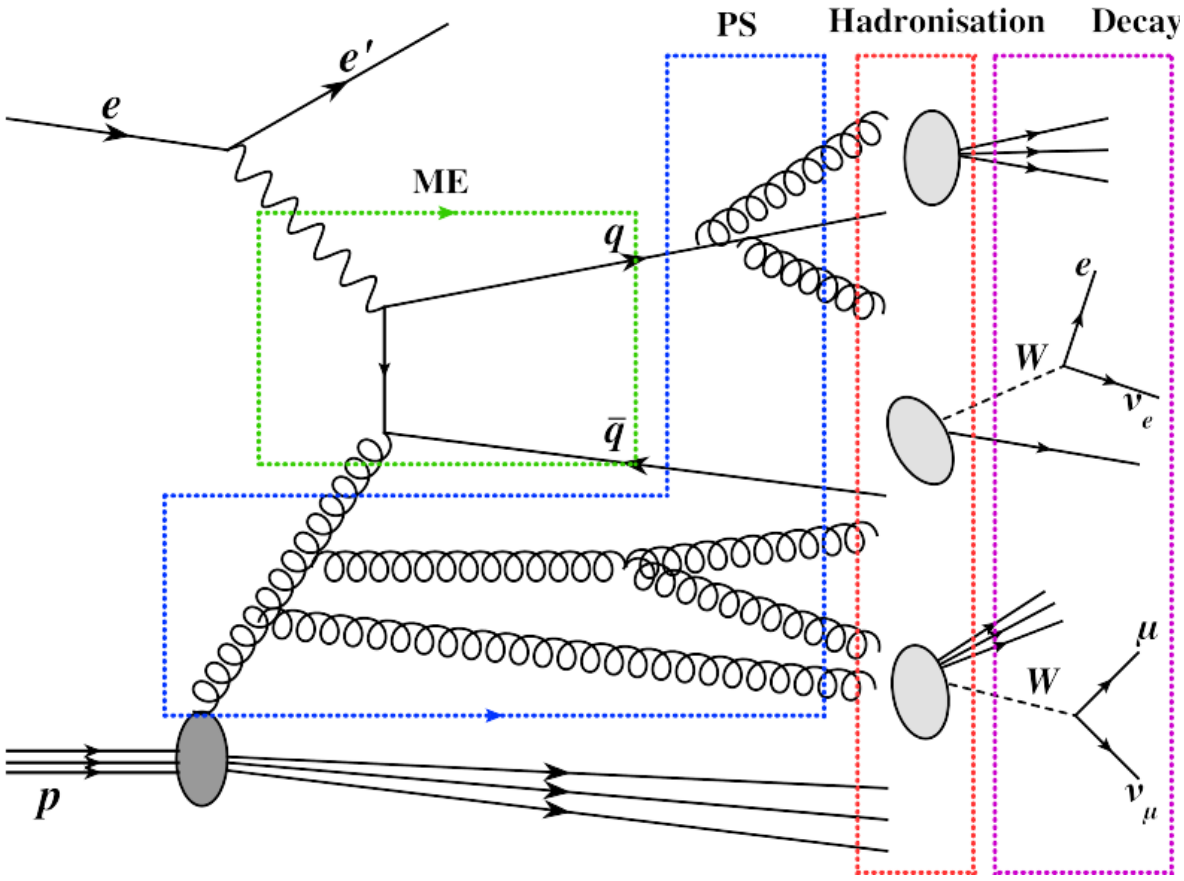

Figure 5.1: Stages of physics simulation in MC for the BGF process. The figure was taken from [179].

- the RAPGAP beauty DIS MC sample, similar to the previous one, was used to estimate the contribution to D^+ production from decays of beauty hadrons;
- the RAPGAP charm DIS MC without QED radiation was used to correct the measured cross sections to the QED Born level;
- the ARIADNE inclusive MC sample was used for simulation of combinatorial background and optimisation of selection cuts;
- the PYTHIA PHP MC sample was used to estimate the contribution from PHP events.

5.4 Reconstruction and selection of D^+ candidates

The D^+ mesons were reconstructed in the decay channel $D^+ \to K^-\pi^+\pi^+$. The underlying principle of a full final-state reconstruction is to make combinations of all tracks with proper charges, reconstruct, if possible, the secondary vertex (a place where the decay happened), refit the considered tracks to this vertex, thus improving their reconstruction, and to calculate the invariant mass, $M(K\pi\pi)$, using the energy and momentum conservation rules, implying a given

mass hypothesis; if it is found to be close to the mass of the analysed hadron, the combination is considered as a *candidate*. The tracks from the selected combinations are referred to as *daughter* tracks.

Inherently such a method leads to the presence of large combinatorial background, which is initiated from combinations of tracks not originating from the analysed hadron channel (or from wrongly combined daughter tracks). In order to suppress this background, additional cuts on the parameters of the daughter tracks and the quality of the secondary-vertex reconstruction can be applied.

The measurement was performed in the D^+ phase space $1.5 < p_T(D^+) < 15\,\text{GeV}$, $|\eta(D^+)| < 1.6$. At lower values of $p_T(D^+)$ the combinatorial background increases drastically, making the signal determination impossible, while at higher values of $p_T(D^+)$ the production cross section becomes too small to be measured with the available integrated luminosity.[10] The $\eta(D^+)$ range is determined by the coverage of the tracking system, since all daughter tracks have to be detected and well reconstructed.

This Section starts from a description of the selection of the secondary vertices (Section 5.4.1); then all selection criteria for D^+ candidates are given (Section 5.4.2).

5.4.1 Selection of secondary vertices

The relatively long lifetime of D^+ mesons, $c\tau(D^+) = 311.8 \pm 2.1\,\mu\text{m}$ [183], makes it possible to reconstruct their secondary vertices with the MVD. Important characteristics of the reconstructed secondary vertices (Fig. 5.2) include:

- χ^2 of the secondary-vertex fit, $\chi^2_{\text{sec vtx}}$;
- the decay length, defined as the distance between the primary and secondary vertices;
- the uncertainty on the decay length;
- the collinearity of the directions from the primary to the secondary vertex and the D^+ momentum.

The most efficient way of using the lifetime information is to combine the last three quantities into the *projected decay-length significance* (also referred to as just the *decay-length significance*), S_l, defined as the ratio of the decay length, projected on the XY plane and on the D^+ momentum, to the uncertainty on this quantity:

$$S_l = \frac{l_{\text{XY}}}{\sigma_{l_{\text{XY}}}}, \tag{5.6}$$

where l_{XY} is the projected decay length, defined as

$$l_{\text{XY}} = \frac{(\vec{S}_{\text{XY}} - \vec{P}_{\text{XY}}) \cdot \vec{p}(D^+)}{p_T(D^+)} \tag{5.7}$$

[10] An extension of the D^+ measurement to the kinematic region $p_T(D^+) < 1.5\,\text{GeV}$ is presented in Appendix B.2

and $\sigma_{l_{\mathrm{XY}}}$ is the uncertainty on l_{XY}. Here $\vec{P}_{\mathrm{XY}}$ and $\vec{S}_{\mathrm{XY}}$ are the vectors pointing to the primary and secondary vertices, respectively, and the $\cdot$ sign denotes a scalar product. The projection on the XY plane was used because the resolution of the vertex position was most precise in the transverse plane.

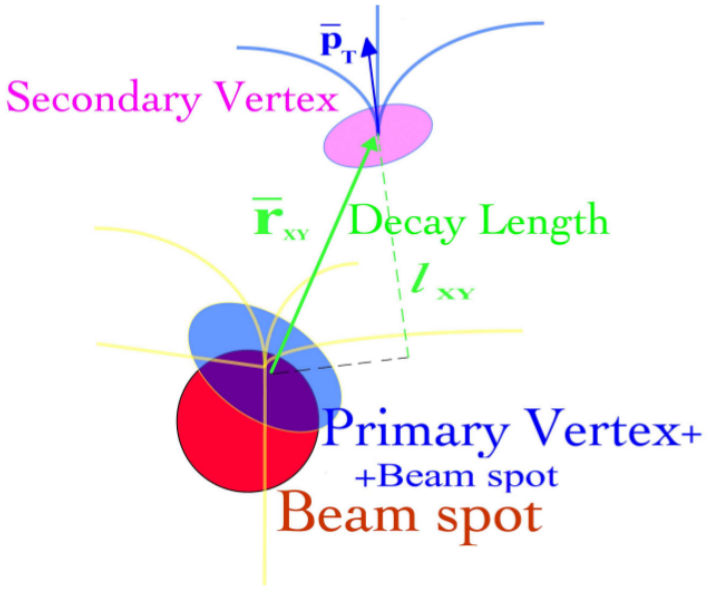

Figure 5.2: Production and decay of a D^+ meson. The figure was taken from [159].

The optimal cuts on S_l and $\chi^2_{\text{sec vtx}}$ were determined by maximising the statistical significance of the mass peak, S_P, defined as the ratio of the signal to its statistical uncertainty, assuming a Poisson distribution:

$$S_P = \frac{S}{\sqrt{S + Bg}}, \tag{5.8}$$

where S is the number of candidates in the signal peak and Bg is the number of candidates in the background, where the region of the signal peak is defined within three standard deviations. The study was performed on the inclusive ARIADNE MC sample. The dependence of S_P on a lower cut on S_l and an upper cut on $\chi^2_{\text{sec vtx}}$ is shown in Fig. 5.3. The determined optimal cuts are:

- $S_l > 4$,
- $\chi^2_{\text{sec vtx}} < 10$.

5.4.2 Selection of D^+ candidates

To ensure the selection of well reconstructed D^+ candidates and to improve the signal-to-background ratio, the following cuts were applied:

- $1.5 < p_T(D^+) < 15\,\text{GeV}$, $|\eta(D^+)| < 1.6$, to select the D^+ phase space;

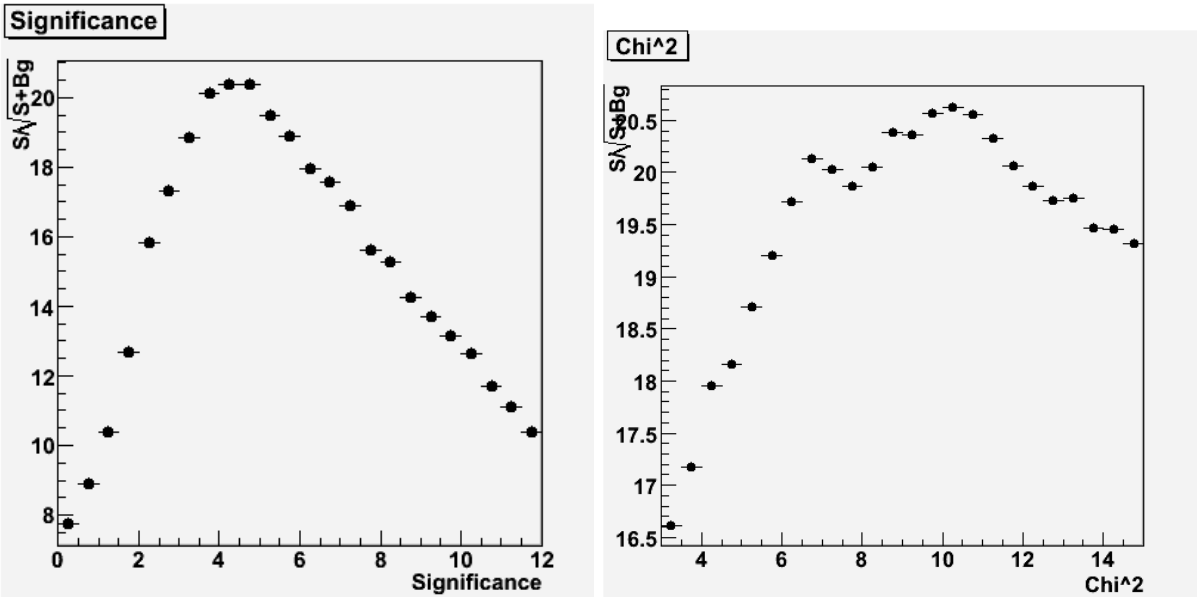

Figure 5.3: The statistical significance of the mass peak as a function of a lower cut on the decay-length significance (left) and χ^2 of the secondary vertex (right).

- $S_l > 4$, $\chi^2_{\text{sec vtx}} < 10$, to reduce the combinatorial background, as explained in Section 5.4.1;
- $l_{\text{XY}} < 1.5\,\text{cm}$, to ensure that selected secondary vertices were inside the beampipe, thus did not originate from interactions with the beampipe or detector material;
- $p_T(K) > 0.5\,\text{GeV}$, $p_T(\pi) > 0.35\,\text{GeV}$, to further reduce combinatorial background while still keeping the detector acceptance at a reasonable level at low $p_T(D^+)$;
- $|\eta(K,\pi)| < 1.75$, to ensure the selection of well reconstructed daughter tracks;
- each track should have at least two MVD hits in both the Z and ϕ directions and pass through at least three CTD superlayers, to improve further the quality of the daughter tracks;
- the mass difference $\Delta M = M(K\pi\pi) - M(K\pi)$ should not be within $0.143 < \Delta M < 0.148\,\text{GeV}$, to reduce background from D^{*+} mesons decaying in the "golden" channel (see Section 3.1.3), which result in identical final states;
- the invariant mass of a combination of the kaon and any of two pion daughter tracks assuming that they are kaons, $M(KK)$, should not be within $1.0115 < M(KK) < 1.0275\,\text{GeV}$. This cut reduced background from D_s^+ mesons decaying in the channel $D_S^+ \to \phi\pi^+$ with subsequent $\phi \to K^-K^+$, which result in similar final states with an asymmetric mass peak (a so-called *reflection*).

An example of an event with a selected D^+ candidate, displayed in ZeVis, can be found in Appendix A (Fig. A.2 top).

5.5 Extraction of D^+ signal

Fig. 5.4 shows the invariant mass distribution $M(K\pi\pi)$ of the selected D^+ candidates. For comparison, the same distribution selected without the cuts on the decay-length significance and χ^2 of the secondary vertex is also shown. The applied cuts on S_l and $\chi^2_{\text{sec vtx}}$ improved the statistical significance by a factor of 3 (a similar conclusion can also be drawn from Fig. 5.3). To extract the number of reconstructed D^+ mesons, the mass distribution was fitted with a function

$$F(M) = F_{\text{signal}}(M) + F_{\text{background}}(M), \tag{5.9}$$

where the signal component, $F_{\text{signal}}(M)$, is given by a modified Gaussian function:

$$F_{\text{signal}}(M) = C \exp[-0.5X^{1+1/(1+\beta X)}], \quad X = \frac{M - M_0}{\sigma_M}, \quad \beta = 0.5 \tag{5.10}$$

and the background component, $F_{\text{background}}(M)$, is given by a second-order polynomial. The signal position, M_0, the peak width, σ_M, as well as the signal normalisation parameter, C, and parameters of the background component were free parameters in the fit. The fit was performed using the least-squares method as implemented in the MINUIT package [184]. As the expectation values in the χ^2-function, the integrals of the fit function within each bin of M were used. To account for possible non-linearities, the fit uncertainty was calculated as the average of the positive and negative fit uncertainty, obtained with the MINOS algorithm [185].

The number of D^+ mesons yielded by the fit is $N(D^+) = 8356 \pm 198$. The fitted position of the peak is $M_0 = 1868.97 \pm 0.26$ MeV, where only the statistical uncertainty is quoted, consistent with the PDG value of 1869.62 ± 0.15 MeV [183]. The peak width is $\sigma = 12.2 \pm 0.3$ MeV, driven by the momentum resolution of the detector.

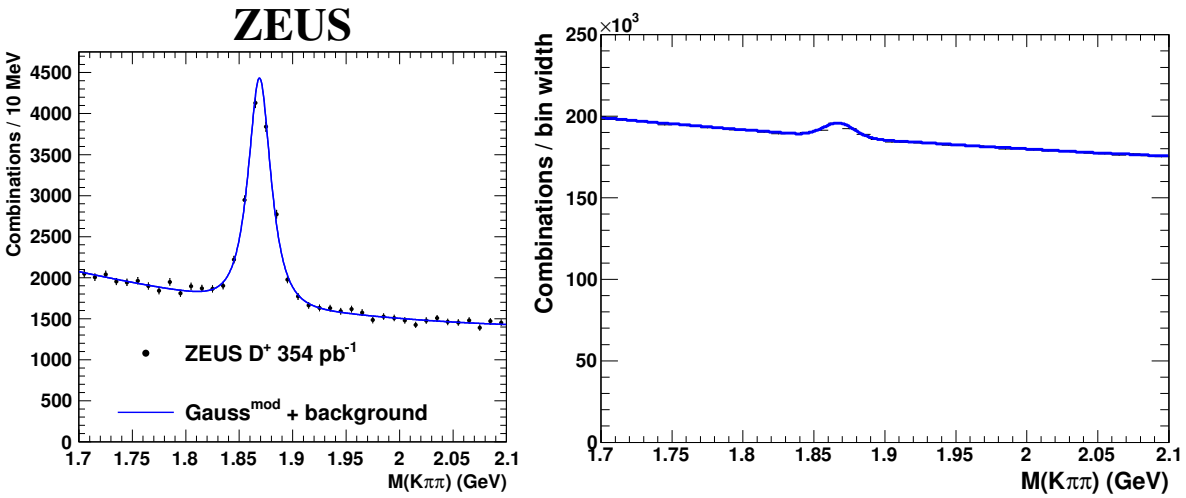

Figure 5.4: Mass distribution of the reconstructed D^+ candidates after final selection (left), and without the cuts on the decay-length significance and χ^2 of the secondary vertex (right). The solid curve represents a fit to the sum of a modified Gaussian for the signal and a second-order polynomial for the background.

5.6 Cross-section determination

By definition, the cross section for a given process, σ, is determined as the ratio of the number of events, N, to the integrated luminosity, $\mathcal{L}$:

$$\sigma = \frac{N}{\mathcal{L}}. \tag{5.11}$$

In the present measurement, further corrections to the definition 5.11 come from the branching ratio, $\mathcal{B}(D^+ \to K^-\pi^+\pi^+) = 9.13 \pm 0.19\%$ [183], the acceptance correction, $\mathcal{A}$, the radiative correction, C^{rad}, and the contribution from beauty-hadron decays:

$$\sigma = \frac{N_{\text{DATA}} - N^{\text{reco}}_{\text{MC } b}}{\mathcal{A}\mathcal{L}\mathcal{B}} \cdot C^{\text{rad}}, \tag{5.12}$$

where N_{DATA} is the number of the reconstructed D^+ mesons in the data and $N^{\text{reco}}_{\text{MC } b}$ is the number of D^+ mesons from beauty-hadron decays, as predicted by RAPGAP. The latter was additionally scaled by 1.6, an average value which was estimated from previous ZEUS measurements [186–188] of beauty production in DIS. The radiative corrections were applied to correct the measured cross sections to the QED Born level; more details on their calculations can be found in [159]. The determination of the acceptance corrections is described in Section 5.6.1.

The differential cross section as a function of a given observable, Y, in the i^{th} bin was determined as

$$\frac{\mathrm{d}\sigma}{\mathrm{d}Y} = \frac{N_{\text{DATA}} - N^{\text{reco}}_{\text{MC } b}}{\mathcal{A}\mathcal{L}\mathcal{B}\Delta Y_i} \cdot C^{\text{rad}}, \tag{5.13}$$

where ΔY_i is the width of the i^{th} bin.

5.6.1 Acceptance correction

MC simulations were used to determine efficiency, $\mathcal{E}$, purity, $\mathcal{P}$, and acceptance $\mathcal{A}$. For the i^{th} bin these quantities are defined as

$$\begin{aligned} \mathcal{E}_i &= \frac{N_i^{\text{gen}} \bigcap N_i^{\text{rec}}}{N_i^{\text{gen}}}, \\ \mathcal{P}_i &= \frac{N_i^{\text{gen}} \bigcap N_i^{\text{rec}}}{N_i^{\text{rec}}}, \\ \mathcal{A}_i &= \frac{\mathcal{E}_i}{\mathcal{P}_i} = \frac{N_i^{\text{rec}}}{N_i^{\text{gen}}}, \end{aligned} \tag{5.14}$$

where N_i^{gen} and N_i^{rec} are the numbers of the signal events, generated and reconstructed in the i^{th} bin, respectively. The notation $N_i^{\text{gen}} \bigcap N_i^{\text{rec}}$ in the numerators means that events must be generated and reconstructed in the same bin. Therefore, the efficiency is the portion of events generated in a given bin, that were also reconstructed in the same bin; it determines the dependence of the measurement on the MC simulations. The purity is the portion of events

reconstructed in a given bin, that were also generated in the same bin; it determines the level of migrations of events to different bins. Finally, the acceptance determines the correction from detector to generator level required to calculate the cross section.

5.6.1.1 Comparison of data to MC

To get the correct acceptance, the MC simulations must describe the shapes of all kinematic variables in the data. Indeed, the acceptance determined from the MC and integrated over some variable, x, is given by:

$$\begin{aligned} \mathcal{A} &= \frac{1}{\sigma^{\text{tot}}} \int \mathcal{A}(x) \frac{\mathrm{d}\sigma}{\mathrm{d}x} \mathrm{d}x, \\ \sigma^{\text{tot}} &= \int \sigma(x) \mathrm{d}x, \end{aligned} \tag{5.15}$$

where the integration is performed over the full range of the variable x, $\mathcal{A}(x)$ is the acceptance at a fixed value of x and $\frac{\mathrm{d}\sigma}{\mathrm{d}x}$ is the differential cross section as a function of x. The correct detector simulation guarantees the correct value of $\mathcal{A}(x)$, although $\frac{\mathrm{d}\sigma}{\mathrm{d}x}$ is the generator-level cross section, thus even for correct $\mathcal{A}(x)$ at all x, incorrect $\frac{\mathrm{d}\sigma}{\mathrm{d}x}$ will lead to an incorrect total acceptance $\mathcal{A}$.

Therefore the differential distributions of kinematic variables from the MC simulations and from the data were compared to each other; these comparison plots are referred to as *control plots*. Since the MC simulations usually describe the shapes of kinematic distributions reasonably, but not the normalisation, and moreover acceptance does not depend on the MC normalisation, the MC distributions are re-normalised to the data. To estimate the goodness of the description, for each control plot the χ^2/n_{dof} were calculated as follows:

$$\chi^2/n_{\text{dof}} = \frac{1}{n_{\text{dof}}} \sum_i \frac{(N_i^{\text{DATA}} - N_i^{\text{MC}})^2}{\sigma_i^{\text{DATA}\,2} + \sigma_i^{\text{MC}\,2}}, \tag{5.16}$$

where the sum goes over all bins, N_i^{DATA} and N_i^{MC} are the number of signal events in the i^{th} bin in the data and MC, respectively, σ_i^{DATA} and σ_i^{MC} are the corresponding statistical uncertainties on N_i^{DATA} and N_i^{MC}, respectively, and n_{dof} is the number of bins minus one[11].

Fig. 5.5 shows the control plots for $p_T(D^+)$, $\eta(D^+)$, Q^2 and y. The data are compared to the sum of charm and beauty MC; the beauty contribution was scaled by 1.6 [186–188], while the charm contribution was re-normalised to the difference between the data and re-scaled MC beauty.[12] The beauty contribution is shown separately; typically it is below 5%. More control plots can be found in Appendix B (Fig. B.3). The MC does not describe well the shapes of $p_T(D^+)$, $\eta(D^+)$ and Q^2, thus the generator-level MC cross sections had to be reweighted.[13] The reweighting procedure is described in Section 5.6.1.3.

[11] Because of re-normalisation of MC to the data.

[12] This procedure corresponds to the measurement of charm production, when the beauty contribution is assumed to be known *a priori*.

[13] For a single correction one should say rather "weighting", but the term "reweignting" is much more convenient and will be used in this work. Moreover, this is not a single correction applied to MC in the analysis.

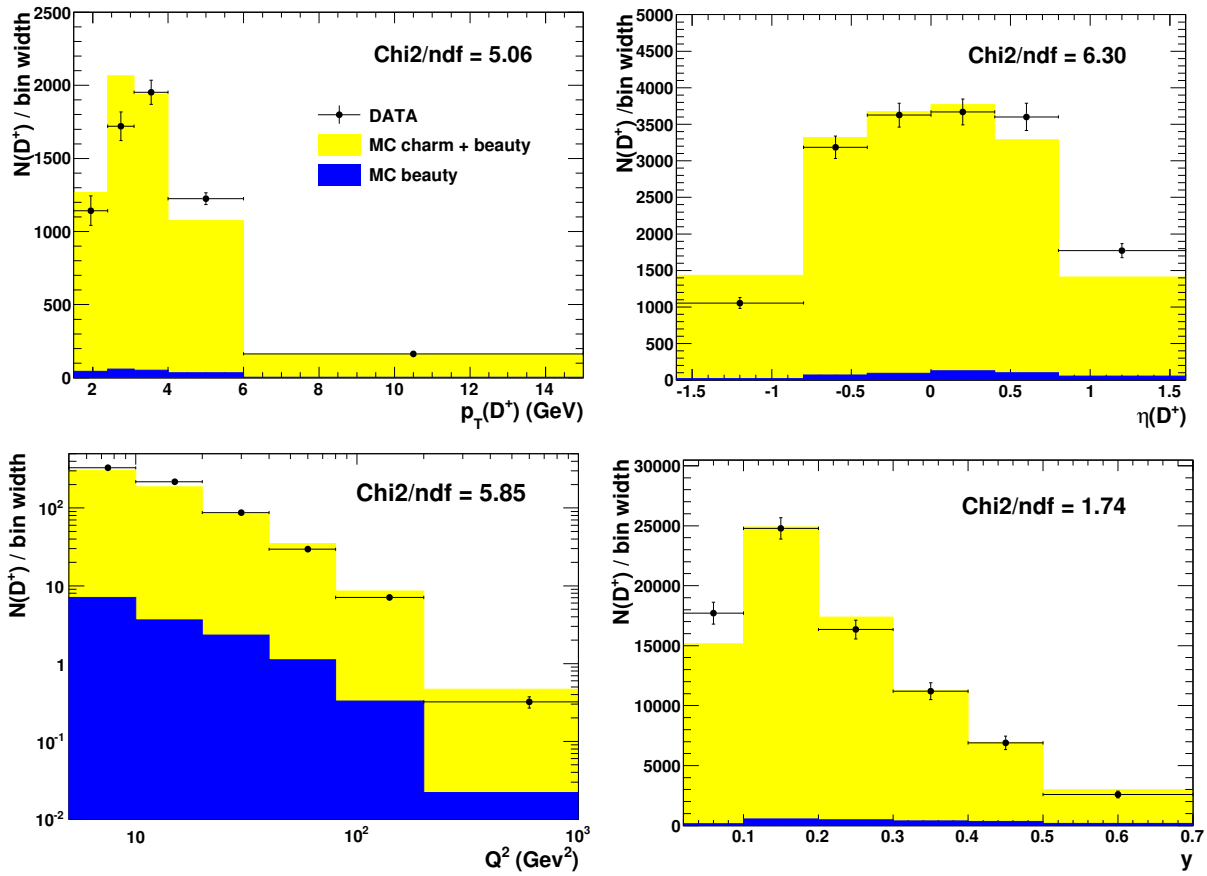

Figure 5.5: Control plots for $p_T(D^+)$ (top left), $\eta(D^+)$ (top right), Q^2 (bottom left) and y (bottom right). The data are shown as points, with bars representing the statistical uncertainty. The sum of charm and beauty MC is shown as the light shaded area; the beauty contribution is shown separately as the dark shaded area.

Fig. 5.6 shows control plots for S_l and $\chi^2_{\text{sec vtx}}$, obtained before applying the cuts on these quantities. MC simulations describe these distributions well. This fact is of crucial importance, because the detector acceptance steeply depends on the cuts applied on S_l and $\chi^2_{\text{sec vtx}}$, so that an incorrect simulation of their shape would lead to large systematic uncertainty; this was the dominant systematic uncertainty in the previous analysis [138], performed with an inferior tracking alignment and calibration.

5.6.1.2 Data to MC matching

A general rule of the MC reweighting approach is that the kinematic weights must be applied at the generator level only. This is straightforward for reweighting in inclusive event quantities, e.g. Q^2, although it becomes complicated if the shapes of D^+ kinematic variables should be corrected (namely $p_T(D^+)$ and $\eta(D^+)$), because:

- in each MC event there may be more than one generated D^+ mesons;

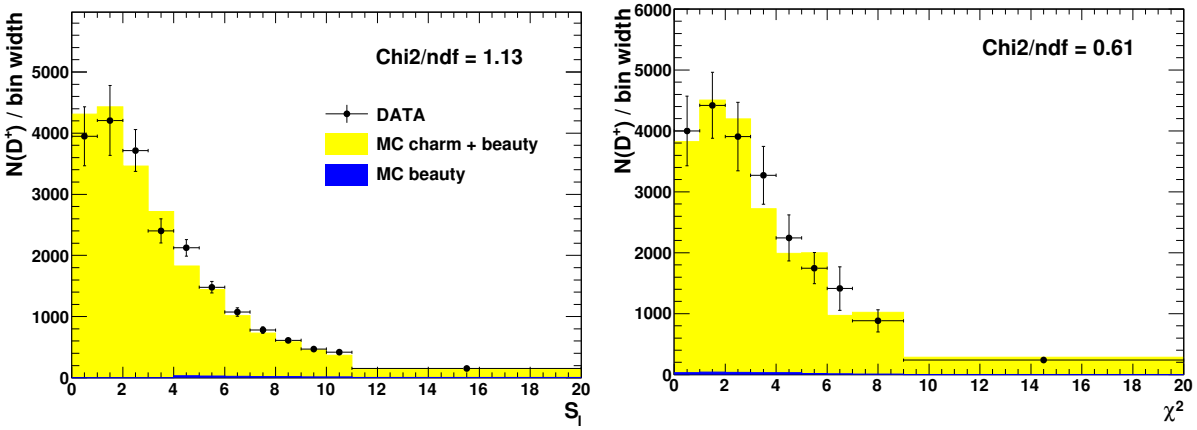

Figure 5.6: Control plots for S_l (left) and $\chi^2_{\text{sec vtx}}$ (right). The data are shown as points, with bars representing the statistical uncertainty. The sum of charm and beauty MC is shown as the light shaded area; the beauty contribution is shown separately as the dark shaded area.

- the efficiency of the D^+ reconstruction in the present analysis is not very high ($\mathcal{E}$ = 1.5–15% depending on $p_T(D^+)$; see Fig. B.2 in Appendix B), thus for a large fraction of events, the reweighting of all generated D^+ mesons will result in a reweighting of the combinatorial background, which does not make sense and potentially may introduce an additional systematic uncertainty.

These complications arise from the fact that according to the general rule weights must be applied for *events*, while the control plots allow their determination for *candidates* only. If applied for events, weights are unique for both generator and reconstructed level, while if applied for candidates, the uniqueness is lost.

Therefore in the present analysis the procedure of *matching* between true and reconstructed D^+ candidates was developed. It contained two steps:

1. for each daughter track the corresponding generator-level particle was matched, if the following criteria (motivated by the resolution of the tracking system) were fulfilled:
   - $|\Delta p_T| = |p_T^{\text{gen}} - p_T^{\text{rec}}| < 0.2\,\text{GeV}$, where p_T^{gen} and p_T^{rec} are the transverse momenta of the generated and reconstructed particles, respectively, and
   - $\Delta R = \sqrt{(\phi^{\text{gen}} - \phi^{\text{rec}})^2 + (\eta^{\text{gen}} - \eta^{\text{rec}})^2} < 0.035$, where ϕ^{gen} and ϕ^{rec} are the azimuthal angles of the generated and reconstructed particles, respectively, and η^{gen} and η^{rec} are the pseudorapidities of the generated and reconstructed particles, respectively;
2. if all daughter tracks were successfully matched to generator-level particles and if the generator-level particles originated from a D^+ meson in the considered decay channel[14], the reconstructed D^+ candidate was considered to be successfully matched to the generator-level one.

[14] The indirect decay channel $D^+ \to \tilde{K}^{*0}(892)\pi^+$ with subsequent $\tilde{K}^{*0}(892) \to K^-\pi^+$ was simulated in the MC and considered in the matching procedure.

The efficiency of this matching procedure was found to be very close to 100% [158].[15] Note that the matching procedure is needed also to determine purity and efficiency (the numerators in 5.14), although it is not needed for the accpetance determination).

5.6.1.3 MC reweighting

Since transverse momentum $p_T(D^+)$ and virtuality Q^2 are significantly correlated, reweighting in these two variables was performed simultaneously, while the cross section in pseudorapidity $\eta(D^+)$ was reweighted independently. In both cases step functions determined from the control plots as the ratios of the number of signal events in the data to the number of signal events in the charm MC were used as reweighting functions. The beauty MC contribution was subtracted from the data and reweighting was applied only to the charm MC. The reweighting functions are shown in Fig. 5.7. For the reweighting in $p_T(D^+)$ and $\eta(D^+)$ only the matched D^+ candidates, as explained in Section 5.6.1.2, were reweighted at the reconstruction level, because the reweighting of non-reconstructed D^+ effectively would result in a meaningless reweighting of combinatorial background, thus producing additional statistical fluctuations. For the acceptance calculation according to Eq. 5.14, all D^+ were reweighted at the generator level (for the N_i^{gen} calculation).[16]

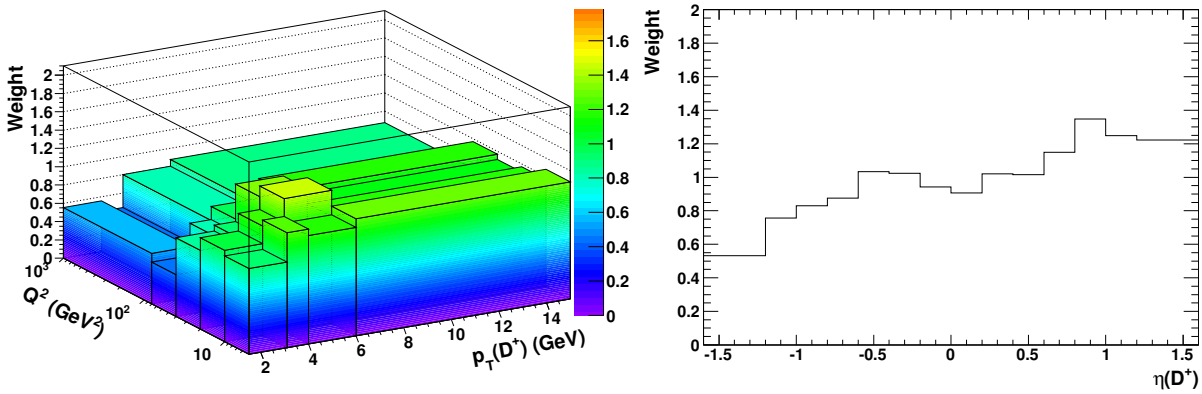

Figure 5.7: Step functions used for MC reweighting in $p_T(D^+)$–Q^2 (left) and $\eta(D^+)$ (right).

The control plots for $p_T(D^+)$, $\eta(D^+)$ and Q^2 after reweighting are shown in Fig. 5.8. The reweighted MC simulations describe the data well and were used to determine acceptance corrections. The acceptance as a function of $p_T(D^+)$, $\eta(D^+)$, Q^2 and y is shown in Fig. 5.9. It is not high, mainly because of the strong cut applied on the decay-length significance in order to

[15] The efficiency of the matching procedure is defined as the ratio of the number of matched particles to the number of candidates in the fitted signal. This quantity is not to be confused with the efficiency defined in Eq. 5.14.

[16] Note that this procedure does not guarantee that the same weights have been applied at both levels (generator and reconstruction), and therefore cannot *a priori* guarantee consistency for the determined acceptance. In order to check it, the $p_T(D^+)$–Q^2 reweighting was performed by applying the same weight, derived from the "best" D^+ (with highest $p_T(D^+)$), on both levels. The difference between the two procedures was found to be less than 0.5%.

reduce combinatorial background, varying from 1.5% at low $p_T(D^+)$ to 15% at high $p_T(D^+)$. The same plots for purity and efficiency are provided in Appendix B (Fig. B.1 and B.2).

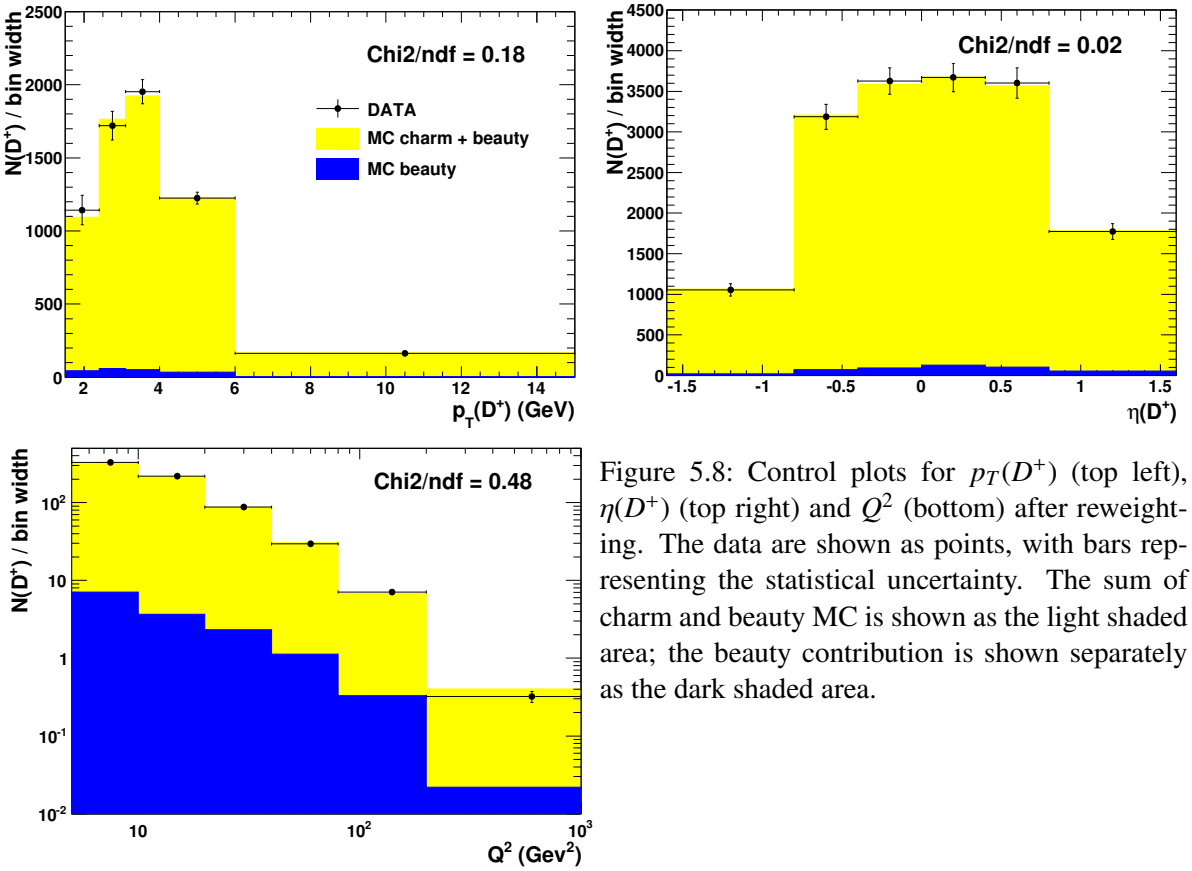

Figure 5.8: Control plots for $p_T(D^+)$ (top left), $\eta(D^+)$ (top right) and Q^2 (bottom) after reweighting. The data are shown as points, with bars representing the statistical uncertainty. The sum of charm and beauty MC is shown as the light shaded area; the beauty contribution is shown separately as the dark shaded area.

5.6.2 Additional corrections

Additional corrections were applied in the MC simulations: a correction for the FLT inefficiency (Section 5.6.2.1); a correction for the tracking inefficiency (Section 5.6.2.2); and a correction to the distribution of the decay-length significance (Section 5.6.2.3); they are briefly described below.

5.6.2.1 FLT-inefficiency correction

Most of the FLT bits used in this analysis had some requirements on the track multiplicity in the events. The efficiency of these criteria was measured [159] using a trigger without track requirements and the detector simulation was tuned to match the data. The trigger-inefficiency corrections for the MC simulations were between 1–10% for different tracking requirements. The corrections changed the overall efficiency of the triggers used in the analysis by a negligible amount for medium-Q^2 values and up to $\sim 2\%$ for the low- and high-Q^2 regions. More details on this study can be found in [159].

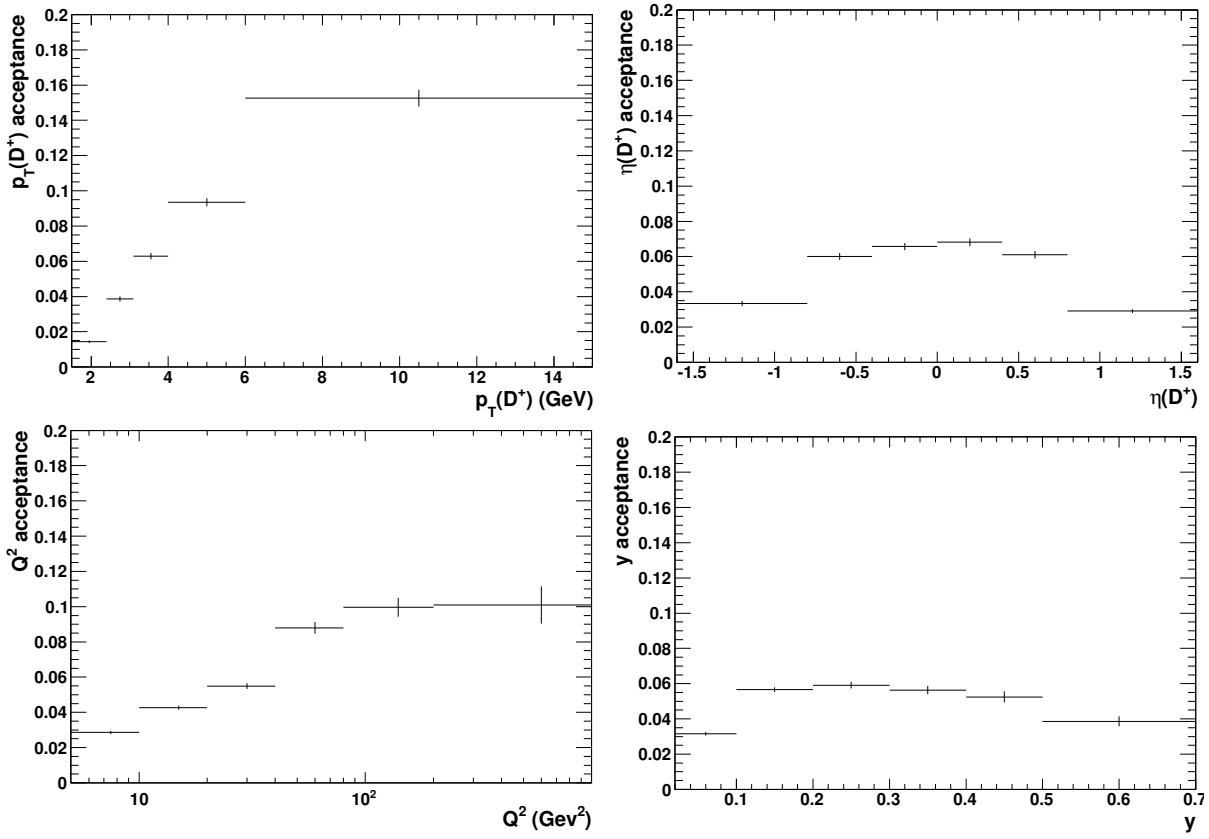

Figure 5.9: Acceptance as a function of $p_T(D^+)$ (top left), $\eta(D^+)$ (top right), Q^2 (bottom left) and y (bottom right). Error bars represent the statistical uncertainty.

5.6.2.2 Tracking-inefficiency correction

A special study [189] was performed to assess the tracking inefficiency for charged pions due to hadronic interactions in the detector material and how well the MC simulations reproduce these interactions. The MC simulations were found to underestimate the interaction rate by about 40% for $p_T < 1.5\,\text{GeV}$ and to agree with the data for $p_T > 1.5\,\text{GeV}$; more details can be found in [189] and references therein. A corresponding correction was applied to the MC simulations. The effect of the correction on the D^+-production cross section was found to be about 3%. The effect of the correction on the D^+ differential cross sections is provided in Appendix B (Fig. B.4).

5.6.2.3 Decay-length smearing

The S_l distribution was found to be asymmetric [159] with respect to zero, with charm mesons dominating in the positive tail. Detector resolution effects cause the negative tail, which is dominated by light-flavour events. A smearing was applied to the decay length of a small fraction of the MC events in order to reproduce the negative decay-length data. The parameters of the smearing had to be tuned to describe the data. The effect of the smearing is typically below 3%. More details on this correction can be found in [159].

5.6.3 Systematic uncertainties

The systematic uncertainties were determined by changing the analysis procedure or varying parameter values within their estimated uncertainties and repeating the extraction of the signals and the cross-section calculations. The following sources of systematic uncertainties were considered with the typical effect on the cross sections given in parentheses:

- the cut on the positions $|x_{e'}|$ and $|y_{e'}|$ of the scattered electron in the RCAL was varied by ±1 cm in both the data and the MC simulations, to account for potential imperfections of the detector simulation near the inner edge of the CAL (±1%);
- the reconstructed electron energy was varied by ±2% in the MC only, to account for the uncertainty in the electromagnetic energy scale (< 1%);
- the energy of the hadronic system was varied by ±3% in the MC only, to account for the uncertainty in the hadronic energy scale (< 1%);
- the FLT tracking-efficiency corrections for the MC were varied within their estimated uncertainties (< 1%);[17]
- uncertainties due to the signal-extraction procedure were estimated by repeating the fit in both the data and the MC using:
  - an exponential function for the background parametrisation (< 1%);
  - a signal parametrisation changed by simultaneously varying the β parameter of the modified Gaussian function in the data and MC by $^{+0.1}_{-0.2}$ from the nominal value 0.5. The range was chosen to cover the values which give the best description of the mass peaks in the data and MC simulations in bins of the differential cross sections ($^{+0.7\%}_{-1.5\%}$);
- uncertainties due to the decay-length smearing procedure were estimated by varying it ±50% (±1%)[17]. As a further cross check, the cut on the decay-length significance was varied between 3 and 5. The resulting variations of the cross sections were compatible with the variation of the decay-length smearing and were therefore omitted to avoid double counting;
- the scaling factor for the MC beauty-production cross sections was varied by ±0.6 from the nominal value 1.6. This was done to account for the range of the RAPGAP beauty-prediction normalisation factors extracted in various analyses [186–188] (±2%);
- the uncertainties due to the model dependence of the acceptance corrections were estimated by varying the shapes of the kinematic distributions in the charm MC sample in a range of good description of the data:
  - the shape of the $\eta(D^+)$ reweighting function (±2%);
  - the shape of the $p_T(D^+)$–Q^2 reweighting function (±4%);

[17] This study was performed by Mykhailo Lisovyi; more details can be found in [159].

- the uncertainty of the pion track inefficiency due to nuclear interactions was evaluated by varying the correction applied to the MC by its estimated uncertainty of ±50% of its nominal size (±1.5%);

- the contribution from the PHP processes was estimated using the PYTHIA MC sample and found to be < 0.5%, therefore it was neglected;

- overall normalisation uncertainties:
  - the simulation of the MVD hit efficiency (±0.9%);[18]
  - the effect of the imperfect description of $\chi^2_{\text{sec vtx}} < 10$ was checked by multiplying $\chi^2_{\text{sec vtx}} < 10$ for D^+ candidates in the MC simulations by a factor 1.1 to match the distribution in the data (+2%); [18]
  - the branching-ratio uncertainty (±2.1%);
  - the measurement of the luminosity (±1.9%).

  The size of each systematic effect was estimated bin-by-bin except for the overall normalisation uncertainties. The overall systematic uncertainty was determined by adding the above uncertainties in quadrature. The normalisation uncertainties due to the luminosity measurement and that of the branching ratio were not included in the systematic uncertainties on the differential cross sections.

5.7 Theoretical calculations

NLO QCD predictions were obtained in the FFNS with the HVQDIS program [62] (see Section 2.3.2.1).[19] The renormalisation and factorisation scales were set to $\mu_r = \mu_f = \sqrt{Q^2 + 4m_c^2}$ and the charm-quark pole mass to $m_c = 1.5\,\text{GeV}$. The FFNS variant of the ZEUS-S NLO QCD PDF fit [190] to inclusive DIS data was used as the parametrisation of the proton PDFs. The same charm mass and choice of scales were used in the fit as in the HVQDIS calculation. The strong coupling constant was set to $\alpha_s^{n_f=3}(M_Z) = 0.105$, corresponding to $\alpha_s^{n_f=5}(M_Z) = 0.116$.

To calculate D^+ observables, events at the parton level were interfaced with a fragmentation model based on the Kartvelishvili function [91]. The fragmentation was performed in the $\gamma^* p$ centre-of-mass frame. The Kartvelishvili parameter, α_K, was parametrised [159] as a smooth function of the invariant mass of the $c\bar{c}$ system, $M_{c\bar{c}}$, to fit the measurements of the D^{*+} fragmentation function by ZEUS [191] and H1 [95]: $\alpha_K(M_{c\bar{c}}) = 2.1 + 127/(M^2_{c\bar{c}} - 4m_c^2)$, with m_c and $M_{c\bar{c}}$ in GeV). In addition, the mean value of the fragmentation function was scaled down by 0.95 since kinematic considerations [192] and direct measurements [193] show that, on average, the momentum of D^+ mesons is 5% lower than that of D^{*+} mesons; this is due to some of the D^+ mesons originating from D^{*+} decays. For the fragmentation fraction, $f(c \to D^+)$, the value 0.2297 ± 0.0078 was used [194].

The uncertainties on the theoretical predictions were estimated as follows:

[18] This study was performed by Mykhailo Lisovyi; more details can be found in [159].
[19] The theoretical predictions were obtained by Mykhailo Lisovyi; more details can be found in [159].

- the renormalisation and factorisation scales were independently varied up and down by a factor of 2;
- the charm-quark mass was consistently changed in the PDF fits and in the HVQDIS calculations by ±0.15 GeV;
- the proton PDFs were varied within the total uncertainties of the ZEUS-S PDF fit;
- the fragmentation function was varied by changing the functional dependence of the parametrisation function $\alpha(M_{c\bar{c}})$ within uncertainties [159];
- the fragmentation fraction was varied within its uncertainties.

The total theoretical uncertainty was obtained by summing in quadrature the effects of the individual variations. The dominant contributions originate from the variations of the charm-quark mass and the scales. In previous studies [66] the uncertainty due to the variation of $\alpha_s^{n_f=3}(M_Z)$ was found to be insignificant and therefore it was neglected here.

5.8 Results

The production of D^+ mesons in the process $ep \to e'c\bar{c}X \to e'D^+X$ (i.e. not including D^+ mesons from beauty decays) was measured in the kinematic range:

$$\begin{aligned} &5 < Q^2 < 1000\,\text{GeV}^2, \\ &0.02 < y < 0.7, \\ &1.5 < p_T(D^+) < 15\,\text{GeV}, \\ &|\eta(D^+)| < 1.6. \end{aligned} \tag{5.17}$$

The differential cross sections are defined according to Eq. 5.13. The measured cross sections in bins of $p_T(D^+)$, $\eta(D^+)$, Q^2 and y are listed in Table 5.1 and shown in Fig. 5.10. The cross section falls by about three orders of magnitude over the measured Q^2 range and one order of magnitude in y; it also falls with the transverse momentum $p_T(D^+)$, but is only mildly dependent on the pseudorapidity $\eta(D^+)$. The measured cross sections are compared to the results of the previous ZEUS D^+ measurement [138][20], based on a subset of the HERA-II data. The present measurement has significantly smaller uncertainties and supersedes the previous results. The NLO QCD predictions, calculated in the FFNS, provide a good description of the data. The experimental uncertainties are smaller than the theoretical uncertainties, apart from the high-Q^2 region, where statistics is limited.

The measured cross sections as a function of y in five Q^2 ranges are listed in Table 5.2 and shown in Fig. 5.11. The data are well reproduced by the HVQDIS calculation. The effects of individual sources of systematic uncertainties (described in Section 5.6.3) on the cross sections in bins of Q^2 and y can be found in [139]. The measured double-differential cross section as

[20] The contribution of D^+ mesons from beauty decays was subtracted using the scaled RAPGAP MC predictions [186–188].

$p_T(D^+)$ [GeV]	$d\sigma/dp_T(D^+)$ [nb/GeV]	Δ_{stat}	Δ_{syst}	C_{rad}	$d\sigma_b/dp_T(D^+)$ [nb/GeV]
1.5 : 2.4	2.40	±0.26	$^{+0.14}_{-0.12}$	1.016	0.07
2.4 : 3	1.44	±0.12	$^{+0.07}_{-0.05}$	1.020	0.05
3 : 4	1.00	±0.05	$^{+0.04}_{-0.04}$	1.023	0.03
4 : 6	0.396	±0.017	$^{+0.014}_{-0.013}$	1.029	0.011
6 : 15	0.0349	±0.0018	$^{+0.0011}_{-0.0010}$	1.054	0.0011

$\eta(D^+)$	$d\sigma/d\eta(D^+)$ [nb]	Δ_{stat}	Δ_{syst}	C_{rad}	$d\sigma_b/d\eta(D^+)$ (nb
−1.6:−0.8	1.04	±0.09	$^{+0.06}_{-0.06}$	1.034	0.02
−0.8:−0.4	1.67	±0.10	$^{+0.06}_{-0.06}$	1.025	0.05
−0.4: 0.0	1.70	±0.10	$^{+0.07}_{-0.05}$	1.023	0.05
0.0 : 0.4	1.63	±0.10	$^{+0.07}_{-0.07}$	1.017	0.06
0.4 : 0.8	1.84	±0.12	$^{+0.07}_{-0.08}$	1.013	0.06
0.8 : 1.6	1.81	±0.16	$^{+0.09}_{-0.09}$	1.016	0.05

Q^2 [GeV^2]	$d\sigma/dQ^2$ [nb/GeV^2]	Δ_{stat}	Δ_{syst}	C_{rad}	$d\sigma_b/dQ^2$ [nb/GeV^2]
5 : 10	0.382	±0.022	$^{+0.027}_{-0.017}$	1.018	0.007
10 : 20	0.150	±0.007	$^{+0.008}_{-0.010}$	1.016	0.003
20 : 40	0.047	±0.003	$^{+0.003}_{-0.004}$	1.020	0.002
40 : 80	0.0108	±0.0008	$^{+0.0008}_{-0.0009}$	1.025	0.0006
80 : 200	0.00192	±0.00020	$^{+0.00014}_{-0.00016}$	1.042	0.00016
200:1000	0.000088	±0.000021	$^{+0.000006}_{-0.000007}$	1.113	0.000013

y	$d\sigma/dy$ [nb]	Δ_{stat}	Δ_{syst}	C_{rad}	$d\sigma_b/dy$ [nb]
0.02: 0.1	16.9	±0.9	$^{+0.9}_{-0.8}$	1.038	0.1
0.1 : 0.2	13.4	±0.6	$^{+0.5}_{-0.5}$	1.022	0.3
0.2 : 0.3	8.5	±0.5	$^{+0.4}_{-0.4}$	1.025	0.3
0.3 : 0.4	6.2	±0.5	$^{+0.3}_{-0.3}$	1.016	0.3
0.4 : 0.5	4.0	±0.4	$^{+0.3}_{-0.2}$	1.008	0.2
0.5 : 0.7	2.2	±0.3	$^{+0.2}_{-0.2}$	0.999	0.2

Table 5.1: Differential cross sections for D^+ production in bins of $p_T(D^+)$, $\eta(D^+)$, Q^2 and y. The statistical and systematic uncertainties, Δ_{stat} and Δ_{syst}, are presented separately. Normalisation uncertainties of 1.9% and 2.1% due to the luminosity and the branching-ratio measurements, respectively, were not included in Δ_{syst}. The correction factors to the QED Born level, C_{rad}, are also listed. For reference, the beauty cross sections predicted by RAPGAP and scaled as described in the text, σ_b, are also shown.

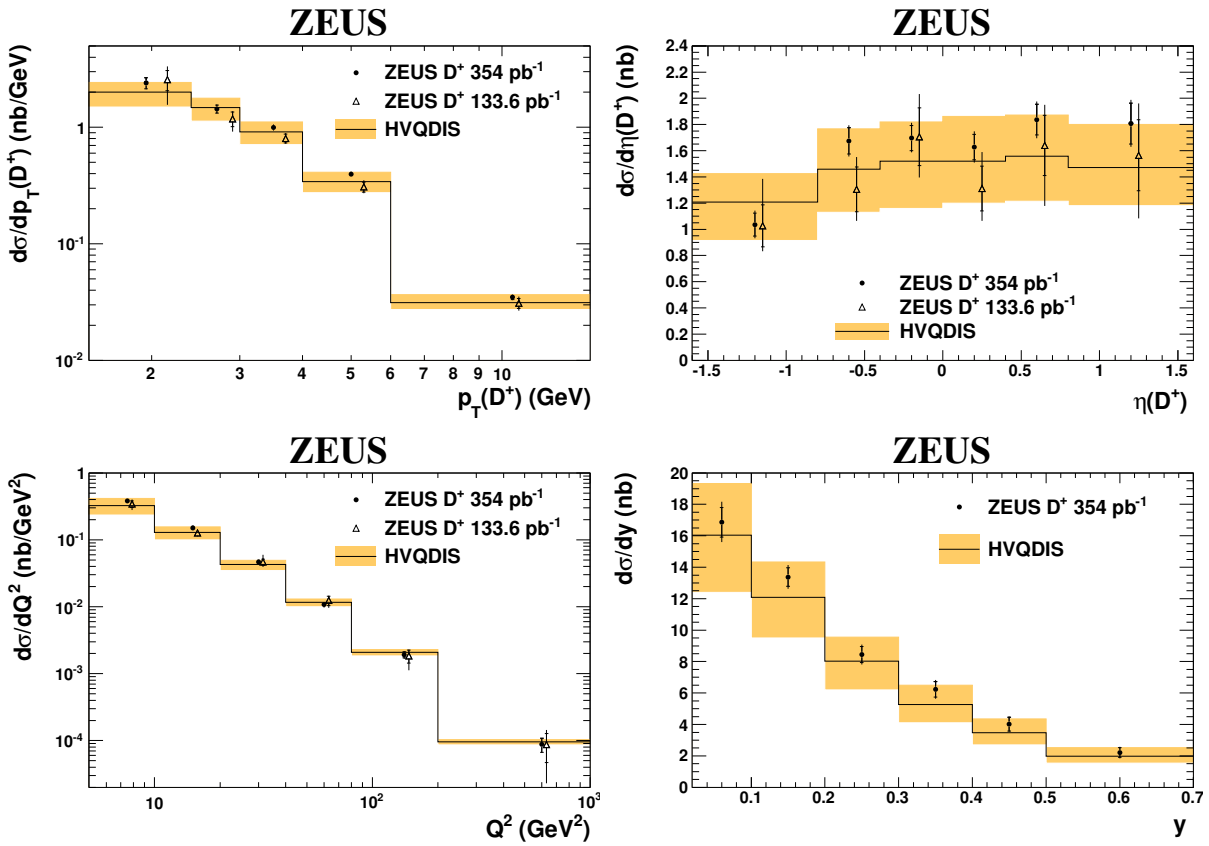

Figure 5.10: Differential cross sections for D^+ production as a function of $p_T(D^+)$ (top left), $\eta(D^+)$ (top right), Q^2 (bottom left) and y (bottom right). The results obtained in this analysis are shown as filled circles. The inner error bars correspond to the statistical uncertainty, while the outer error bars represent the statistical and systematic uncertainties added in quadrature. For the cross section as a function of $p_T(D^+)$, $\eta(D^+)$ and Q^2, the results of the previous ZEUS measurement are also shown (open triangles). The solid lines and the shaded bands represent the NLO QCD predictions in the FFNS with estimated uncertainties.

a function of Q^2 and y has been used to extract the charm contribution to the proton structure function $F_2^{c\bar{c}}$; the results can be found in [139]. This part of the analysis is not covered in the present chapter, but is described in Chapter 6 in the context of the charm combination (Section 6.5).

5.9 Summary

The production of D^+ mesons has been measured in DIS at HERA in the kinematic region $5 < Q^2 < 1000\,\text{GeV}^2$, $0.02 < y < 0.7$, $1.5 < p_T(D^+) < 15\,\text{GeV}$ and $|\eta(D^+)| < 1.6$. The present results supersede the previous ZEUS D^+ measurement, based on a subset of the data, and exhibit significantly better precision. The improvement in precision comes from the larger data sample, used in the present analysis and from a better control of experimental systematic

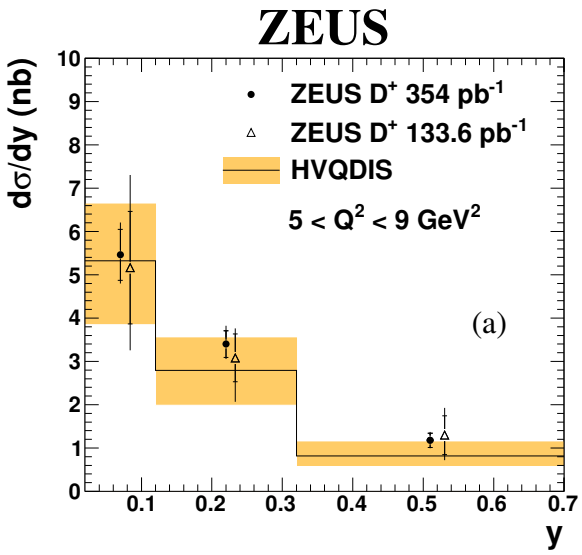

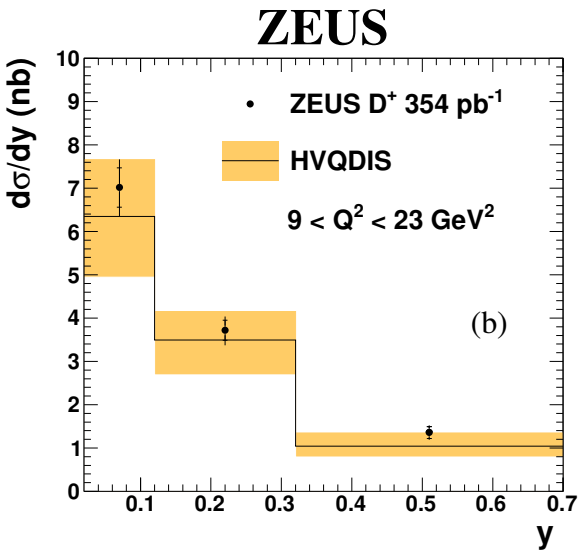

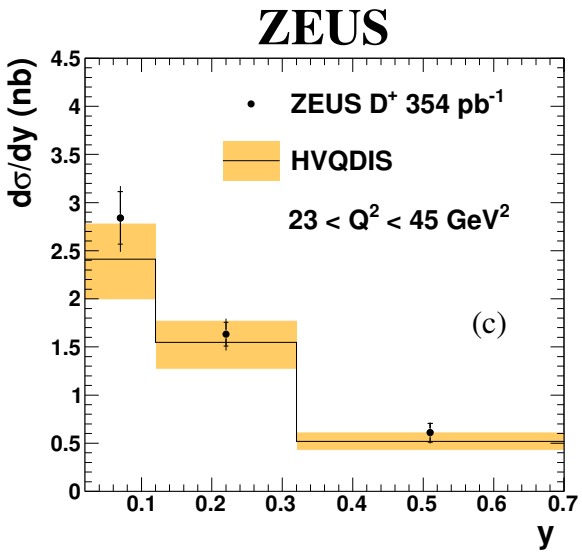

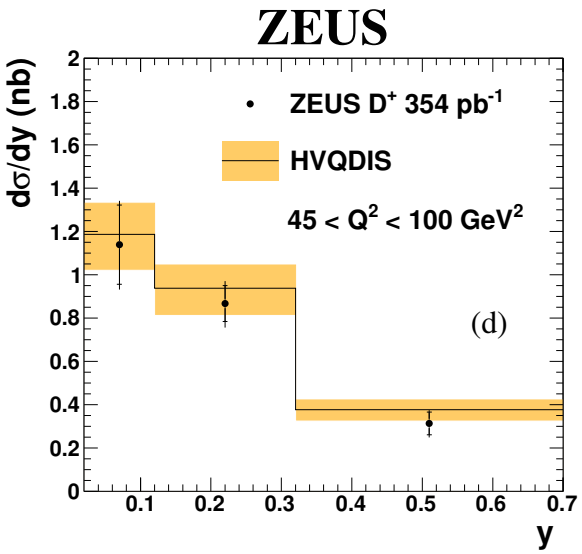

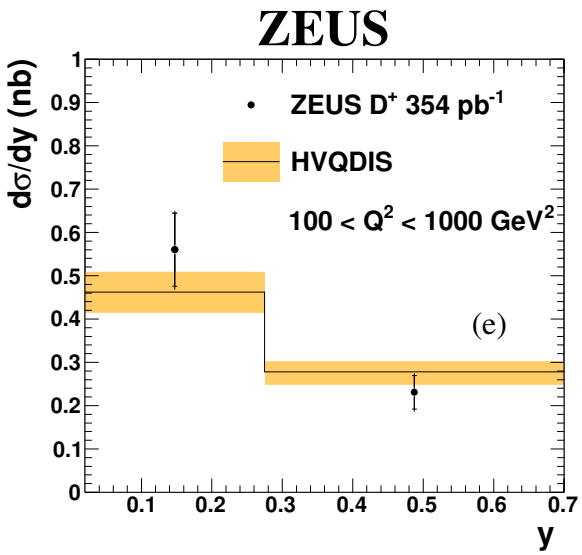

Figure 5.11: Differential cross sections for D^+ production as a function of y in different Q^2 ranges: $5 < Q^2 < 9\,\text{GeV}^2$ (a), $9 < Q^2 < 23\,\text{GeV}^2$ (b), $23 < Q^2 < 45\,\text{GeV}^2$ (c), $45 < Q^2 < 100\,\text{GeV}^2$ (d) and $100 < Q^2 < 1000\,\text{GeV}^2$ (e). The results obtained in this analysis are shown as filled circles. The inner error bars correspond to the statistical uncertainty, while the outer error bars represent the statistical and systematic uncertainties added in quadrature. For the Q^2 range $5 < Q^2 < 9\,\text{GeV}^2$, the results of the previous ZEUS measurement are also shown (open triangles). The solid lines and the shaded bands represent the NLO QCD predictions in the FFNS with estimated uncertainties.

Bin	Q^2 [GeV^2]	y	$d\sigma/dy$	Δ_{stat} [nb]	Δ_{syst}	C_{rad}	$d\sigma_b/dy$ [nb]
1	5 : 9	0.02 : 0.12	5.46	±0.59	$^{+0.46}_{-0.30}$	1.026	0.04
2		0.12 : 0.32	3.40	±0.31	$^{+0.29}_{-0.16}$	1.022	0.06
3		0.32 : 0.7	1.18	±0.17	$^{+0.10}_{-0.08}$	1.006	0.04
4	9 : 23	0.02 : 0.12	7.02	±0.45	$^{+0.46}_{-0.49}$	1.028	0.05
5		0.12 : 0.32	3.72	±0.23	$^{+0.21}_{-0.26}$	1.017	0.09
6		0.32 : 0.7	1.36	±0.14	$^{+0.09}_{-0.10}$	0.998	0.06
7	23 : 45	0.02 : 0.12	2.84	±0.27	$^{+0.19}_{-0.22}$	1.040	0.03
8		0.12 : 0.32	1.63	±0.12	$^{+0.10}_{-0.12}$	1.020	0.05
9		0.32 : 0.7	0.609	±0.097	$^{+0.047}_{-0.053}$	1.009	0.035
10	45 : 100	0.02 : 0.12	1.14	±0.18	$^{+0.09}_{-0.10}$	1.046	0.03
11		0.12 : 0.32	0.867	±0.083	$^{+0.063}_{-0.074}$	1.024	0.050
12		0.32 : 0.7	0.313	±0.052	$^{+0.032}_{-0.037}$	1.012	0.033
13	100 : 1000	0.02 :0.275	0.560	±0.085	$^{+0.031}_{-0.038}$	1.117	0.033
14		0.275: 0.7	0.231	±0.039	$^{+0.020}_{-0.022}$	1.030	0.035

Table 5.2: Differential cross sections for D^+ production as a function of y in five regions of Q^2. The cross sections are given in the kinematic region $5 < Q^2 < 1000\,\text{GeV}^2$, $0.02 < y < 0.7$, $1.5 < p_T(D^+) < 15\,\text{GeV}$ and $|\eta(D^+)| < 1.6$. The statistical and systematic uncertainties, Δ_{stat} and Δ_{syst}, are presented separately. Normalisation uncertainties of 1.9% and 2.1% due to the luminosity and the branching-ratio measurements, respectively, were not included in Δ_{syst}. The correction factors to the QED Born level, C_{rad}, are also listed. For reference, the beauty cross sections predicted by RAPGAP and scaled as described in the text, σ_b, are also shown.

uncertainties, owing to improved tracking alignment and calibration. Predictions from NLO QCD in the FFNS describe the measured cross sections well. The results presented here are of similar or higher precision than measurements of charm production, previously published by ZEUS[21]. The new precise data provide an improved check of pQCD and have the potential to constrain the PDFs in the proton. Chapter 6 uses these data for the HERA charm combination (Section 6.5).

[21] At the moment when the results were being published (February 2013).

CHAPTER 6

Combination of the HERA charm measurements

This Chapter is devoted to a combination of the open charm measurements at HERA in DIS. Section 6.1 explains the motivation and gives an overview of general aspects of the procedure. Section 6.2 describes the procedure of cross-section averaging, the extrapolation to a common phase space and the treatment of experimental uncertainties. Details of the theoretical calculations in the FFNS, which were used in the combination procedure for phase-space corrections and for the comparison with the combined data, are given in Section 6.3. In Sections 6.4 and 6.5 the main results are presented: a combination of visible D^{*+} cross sections and charm reduced cross sections, respectively. Finally, Section 6.6 gives a summary of the obtained results.

6.1 Introduction

Measurements of open charm production at HERA provide an important input for stringent tests of QCD. As explained in Section 2.3.2, charm quarks in ep collisions are predominantly produced by the boson–gluon-fusion process, $\gamma g \to c\bar{c}$, thus charm production is sensitive to the gluon distribution in the proton, and charm measurements are a valuable input for global PDF fits and for the extraction of the charm-quark mass.

The motivation to perform a data combination is the following [195]. Modern QCD fit procedures (see, e.g. [54, 196–198]) use data from a number of individual experiments to extract the PDFs. All modern programs use both the central values and uncertainties of measured cross sections as well as information about the correlations among the experimental data points. This extraction procedure has some drawbacks. Firstly the number of input datasets is large consisting of many individual publications. The data points are correlated through common systematic uncertainties, within and also across the publications. Handling of the experimental data without additional expert knowledge often becomes very difficult. In addition, the treatment of the correlations produced by the systematic errors is not unique [199]. These difficulties lead to a situation in which some global QCD analyses have to use non-statistical criteria to estimate the

resulting uncertainties, $\Delta\chi^2 \gg 1$ (see, e.g. [200, 201]). This is driven by apparent discrepancies between different experiments which are often difficult to quantify without a consistency check, independent of any theory.

These drawbacks can be significantly reduced by averaging of the input data in a model-independent way before performing a QCD analysis of that data. One combined dataset of DIS charm cross-section measurements is much easier to handle compared to a scattered set of individual experimental measurements, overviewed in Section 3.1.3, while retaining the full correlations between data points. The averaging method used here is unique and removes the drawback of the offset method [202], which fixes the size of the systematic uncertainties. In the averaging procedure the correlated systematic uncertainties are floated coherently, allowing in some cases a reduction of the uncertainty. In addition, a study of the global χ^2/n_{dof} of the average and the distribution of the pulls allows a model-independent consistency check between the experiments. In case of a discrepancy between the input datasets, a localised enlargement of the uncertainties for the average can be performed.

Summarising, the main goal of a data combination is to obtain a single consistent dataset for a given physical process; additionally it serves as a consistency cross-check of the input measurements. Note that a combination is not supposed to provide new information[1]; nominally it serves as a tool which allows for the simplification of the usage of information already contained in the input measurements, i.e. reduce the number of input datasets and the number of uncertainty sources, e.g. by combining in quadrature independent (uncorrelated) uncertainties in one source.

6.1.1 Combination of the HERA charm measurements: general strategy

A combination requires input data in the same bins covering the same phase space. Considering the existing charm measurements at HERA, there are two strategies for the combination:

- to combine a limited number of measurements that closely fulfill the above requirement;
- to combine all relevant measurements extrapolated to a common phase space and common bins.

The former provides a model-independent combination (or with minimised model dependency) which delivers most of originally measured information; this strategy is followed in the combination of the visible D^{*+} cross sections (Section 6.4). The latter gains from a big number of input measurements, thus on one hand has ultimate accuracy, but on the other hand is not anymore model independent and has a sizeable theoretical uncertainty from the extrapolation procedure; this strategy is followed in the combination of the charm reduced cross sections (Section 6.5).

[1] Although it is possible that a combination will give an extra reduction of correlated uncertainties due to usage of information from the phase-space corners which normally would not be used in analyses or theory fits.

6.2 Combination procedure

In this Section common aspects of the combination procedure are described: the combination method, needed to average quantities given in a common phase space (Section 6.2.1), the treatment of systematic uncertainties of input quantities in the combination method (Section 6.2.2), and phase-space corrections, needed to translate the input quantities to a common phase space (Section 6.2.3).

6.2.1 Combination method

This Section describes the combination method used for the H1 and ZEUS data combination. The HERAverager package [203][2] is used for the combination of the charm data. It is an averaging tool developed for the H1 and ZEUS data combination. The combination method is based on the minimisation of the χ^2-function which includes correlated systematic uncertainties using the nuisance-parameter technique (known also as the Hessian method [204]).

Section 6.2.1.1 describes the method of averaging itself and the next Section 6.2.1.2 presents and explains the χ^2-function. Additional technical details on the minimisation procedure are provided in Appendix C.

6.2.1.1 Average of several measurements

Initially consider the simplest case. Suppose there is a set of N_m measurements μ_i of some quantity μ. Each measurement μ_i has an associated uncertainty σ_i. Errors on measurements are generally well described by a Gaussian (also called normal) distribution, and the probability density for each measurement is given by [205]

$$P(\mu_i, \sigma_i; m) = \frac{1}{\sigma_i \sqrt{2\pi}} e^{-(m-\mu_i)^2/2\sigma_i^2}, \tag{6.1}$$

where m is the true value of the quantity μ, referred to as a true parameter. For some sources of uncertainties (e.g. statistical fluctuations) this is due to their nature[3], while for others it is usually argued as a consequence of the Central Limit Theorem [205]. If all μ_i are independent and their uncertainties σ_i are Gaussian, the best estimation (consistent, unbiased and efficient) of the average, $\overline{\mu}$, and the associated uncertainty, $\Delta\overline{\mu}$, is given by

$$\begin{aligned} \overline{\mu} &= \frac{\sum_{i=1}^{N_m} \mu_i/\sigma_i^2}{\sum_{i=1}^{N_m} 1/\sigma_i^2}, \\ \Delta\overline{\mu} &= \frac{1}{\sqrt{\sum_{i=1}^{N_m} 1/\sigma_i^2}}. \end{aligned} \tag{6.2}$$

[2] HERAverager is based on the earlier program F2averager introduced in [195] and used, e.g. for the previous HERA charm combination [66].

[3] Of course, statistical fluctuations actually obey a Poisson distribution, but for a large enough sample it tends to a Gaussian one [205].

This can be shown from the principle of maximum likelihood, or from the principle of least squares (LS), or from the law of combination of erros, or just from the definitions of the mean and the variance [205]. However for the future discussion of a more general (and complicated) situation it is convenient to stick with one of the methods; in this case the LS one will be followed.

6.2.1.2 χ^2 definition

The quantity χ^2 is the squared difference between the observed values and their theoretical predictions, suitably weighted by the errors of the measurements [205]; in the considered case it is

$$\chi^2(m) = \sum_{i=1}^{N_m} \frac{(\mu_i - m)^2}{\sigma_i^2}. \tag{6.3}$$

The minimum of the χ^2 quantity, χ_0^2, with respect to the parameter m of the true distribution provides the best average value, $\overline{\mu}$:

$$\chi_0^2 = \chi^2(\overline{\mu}) \tag{6.4}$$

and its variation by 1 gives the associated uncertainty, $\Delta\overline{\mu}$ [205]:

$$\chi_0^2 + 1 = \chi^2(\overline{\mu} + \Delta\overline{\mu}). \tag{6.5}$$

So with the LS method the results of Eq. 6.2 can be found by solving the equation:

$$\frac{d\chi^2}{dm} = 0 \tag{6.6}$$

(since the χ^2 expression is a positive quadratic form of the true parameter μ, its extremum gives a minimum).

The χ^2-distribution depends on the number of degrees of freedom, n_{dof}, which is the number of points in the sum, N_m, minus the number of variables that have been adjusted to minimise χ^2 (the true parameters). The χ^2-distribution has mean, $\overline{\chi^2}$:

$$\overline{\chi^2} = n_{\text{dof}} \quad [4] \tag{6.7}$$

and variance, $\overline{\left(\chi^2 - \overline{\chi^2}\right)^2}$:

$$\overline{\left(\chi^2 - \overline{\chi^2}\right)^2} = 2n_{\text{dof}}. \tag{6.8}$$

Thus one expects a χ^2 per degree of freedom, χ^2/n_{dof}, of roughly one.

So far it was assumed that each measurement μ_i has only one individual (independent from the others) source of uncertainty. Real measurements have many sources of systematic uncertainties which may be correlated (shared) between several or all data points. As mentioned in Section 6.1, there is no unique way to treat the correlations produced by the systematic

[4] But note, that n_{dof} is neither the mode (the most probable value) nor the median (the value separating the higher half from the lower half) of the χ^2-distribution, although they tend to it when n_{dof} becomes large [205].

uncertainties. In the present combination the Hessian method [204] using nuisance parameters is exploited. Consider N_e sets of measurements of N_m quantities μ_i (e.g. from different experiments or from one experiment, but obtained in different analises), μ_i^e. Each measurement has one uncorrelated uncertainty, σ_i^e, and N_s correlated, $\Gamma_i^{e,j}$ ($1 \le i \le N_m$, $1 \le e \le N_e$, $1 \le j \le N_s$). All correlated uncertainties are assumed to be Gaussian. Thus each measurement can be written as

$$\mu_i^e = m_i + \sigma_i^e a_i^e - \sum_{j=1}^{N_s} \Gamma_i^{e,j} b^{e,j}, \tag{6.9}$$

where a_i^e and $b^{e,j}$ are independent variables distributed according to the unit Gaussian distribution around zero. Note that $b^{e,j}$ are independent of i; that is, the uncertainties $\Gamma_i^{e,j}$ are 100% correlated for all data points denoted with the same e. The $b^{e,j}$ are called nuisance parameters of correlated uncertainties. Then the generalised χ^2 can be written as

$$\chi^2(\mathbf{m}, \mathbf{b}) = \sum_{e=1}^{N_e} \sum_{i=1}^{N_m} \frac{\left(m_i - \sum_{j=1}^{N_s} \Gamma_i^{e,j} b^{e,j} - \mu_i^e\right)^2}{\sigma_i^{e\,2}} + \sum_{j=1}^{N_s} b^{e,j\,2}, \tag{6.10}$$

where the vectors $\mathbf{m}$ and $\mathbf{b}$ denote the true parameters m_i and nuisance parameters $b^{e,j}$, respectively. Here the first term is a generalisation of 6.3, taking into account the effects of the shifts of the correlated uncertainties; the second term is a penalty for the correlated uncertainty shifts from their nominal (zero) values. The uncorrelated uncertainties σ_i^e are the total uncorrelated uncertainties which may consist of several independent components (e.g. a statistical uncertainty and several different systematic ones, assumed to be uncorrelated between the data points) added in quadrature, according to the law of combination of errors [205]. Note, that some of $\Gamma_i^{e,j}$ may be equal to 0 if the measurement μ_i^e is insensitive to the systematic source j. A formal derivation of the χ^2 expression 6.10 from the assumption 6.9 can be found in [206]. The averaging problem is solved by minimising $\chi^2(\mathbf{m}, \mathbf{b})$ w.r.t $\mathbf{m}$ and $\mathbf{b}$, providing the average values $\overline{\mathbf{m}}$ and the fitted nuisance parameters $\overline{\mathbf{b}}$; a variation of $\chi^2(\mathbf{m}, \mathbf{b})$ by 1 provides the uncertainties on these values. The formulas for these quantities are obtained in Appendix C.1.

So far the form of the correlated uncertainties $\Gamma_i^{e,j}$ was not specified. It is useful to define the relative correlated systematic uncertainties by the ratio

$$\gamma_i^{e,j} = \frac{\Gamma_i^{e,j}}{\mu_i^e}. \tag{6.11}$$

Usually the relative, not absolute, systematic uncertainties are provided by the measurements. Two types of uncertainty treatment can be considered:

- the *multiplicative* treatment, when the systematic uncertainties are proportional to the *true* values:
$$\Gamma_i^{e,j} = m_i \gamma_i^{e,j}; \tag{6.12}$$
- the *additive* treatment, when the systematic uncertainties are independent of the true value; then they are considered to be proportional to the *measured* values, i.e. by the

definition 6.11, or independent of either:

$$\Gamma_i^{e,j} = \mu_i \gamma_i^{e,j} \tag{6.13}$$

(in other words they are constant and not changed in the combination procedure).

The same options exist for the treatment of the uncorrelated uncertainties in the denominator of 6.10. The additive treatment is appropriate for background-dominated uncertainties, which do not depend on the true value $\mathbf{m}$, while the multiplicative treatment is appropriate for all others.[5]

For the charm measurements at HERA the statistical uncertainties are mainly dominated by background, so in the combination they were treated additively. The systematic uncertainties are predominantly proportional to the central values and thus treated multiplicatively. So the final χ^2-function, used in the present combination, is given by

$$\chi^2(\mathbf{m}, \mathbf{b}) = \sum_{e=1}^{N_e} \sum_{i=1}^{N_m} \frac{\left(m_i - \sum_{j=1}^{S} \gamma_i^{e,j} m_i^e b^{e,j} - \mu_i^e\right)^2}{\delta_{stat,i}^e \mu_i^{e\,2} + \delta_{uncor,i}^e m_i^{e\,2}} + \sum_{j=1}^{N_s} b^{e,j\,2}, \tag{6.14}$$

where in the denominator the statistical and uncorrelated systematic uncertainties are added in quadrature; $\delta_{stat,i}^e$ and $\delta_{uncor,i}^e$ are the relative statistical and uncorrelated systematic uncertainties, respectively, defined similar to 6.11:

$$\begin{aligned} \delta_{stat,i}^e &= \frac{\sigma_{stat,i}^e}{\mu_i^e}, \\ \delta_{uncor,i}^e &= \frac{\sigma_{uncor,i}^e}{\mu_i^e}, \end{aligned} \tag{6.15}$$

where $\sigma_{stat,i}^e$ and $\sigma_{uncor,i}^e$ are the absolute statistical and uncorrelated systematic uncertainties, respectively. In the previous round of the combination of the charm reduced cross sections [66] the sensitivity of the result to the treatment of the uncertainties was studied and procedural uncertainties were assigned; however they turned out to be much smaller than the other ones (on average below 0–10% of the total uncertainty, reaching up to 40% only at few combined points [66]) and are neglected in the present combination.

6.2.2 Treatment of systematic uncertainties

As explained in Section 6.2.1.2, in the combination procedure uncertainties are treated either as fully uncorrelated or fully correlated between the data points of certain measurements. Neither of these is most conservative in general. Experimental uncertainties of the input measurements

[5] A special case is the signal-dominated statistical uncertainties, which obey the Poisson statistics. Their values are scaled with the suqare root of m_i:

$$\Gamma_i^{e,j} = \sqrt{\mu_i m_i} \gamma_i^{e,j}.$$

consist of statistical and systematic uncertainties. The statistical component of uncertainties was always treated as uncorrelated between all data points.[6]

The systematic component of uncertainties, in general, may have mixed nature: it may be partially correlated between the data points; moreover, the level of correlation may differ in different corners of a phase space. In the current combination procedure the following "common sense" strategy was applied:

- normalisation uncertainties (reported as a single number) were treated as correlated (e.g. luminosity and branching ratios); they are marked as 'N';
- those uncertainties that have smooth behaviour in the phase space were also treated as correlated (typically these are different kinds of corrections, reweightings, inefficiencies etc., evaluated using studies based on MC); they are marked as 'S';
- theory-related uncertainties that arose from the phase-space corrections (see Sections 6.2.3) were treated as correlated; they are marked as 'T';
- all other uncertainties were treated as uncorrelated (typically these are uncertainties estimated using cut variations in data, which are subject to statistical fluctuations).

Explicit information on the sources that were treated as correlated is given in relevant combination Sections 6.4.1.1, 6.4.2.1 and 6.5.1.

Many of the experimental systematic uncertainties are originally asymmetric and must be symmetrised before performing a combination. For the newly included measurements [19, 137, 139] symmetrisation was performed by taking the largest deviation; no corrections to the central values were applied. For those measurements that have been included in the previous charm combination [66], the symmetrisation remains the same.[7]

6.2.3 Phase-space correction

Whenever the quantities to be averaged are measured in different phase spaces, they have to be corrected before performing a combination. Assume that there is a measured quantity (e.g. a cross section) in the phase space 1, σ_1^{meas}, which needs to be translated into the phase space 2. The correction procedure is called *extrapolation* and is based on usage of theoretical calculations:

$$\sigma_2^{extr} = \sigma_1^{meas} \frac{\sigma_2^{th}}{\sigma_1^{th}}. \tag{6.16}$$

[6] In fact small correlations exist between inclusive measurements and those where full final states were reconstructed (e.g. between the measurement [19], where information from secondary vertices from all charm-hadron decays was used, and [137], where D^{*+} mesons were reconstructed in the $D^{*+} \to D^0(K^-\pi^+)\pi_s^+$ decay channel), but since the corresponding branching ratios are much smaller than 1, phase-space cuts differ and statistical uncertainties in heavy-flavour measurements are usually dominated by background, such correlations have been neglected.

[7] It was found in [66] that the results are insensitive to the details of the symmetrisation procedure.

Here σ_1^{th} and σ_2^{th} are the predicted quantities in the phase spaces 1 and 2, respectively. The closer the phase spaces 1 and 2 (the more they overlap), the less model dependency the extrapolated quantity, σ_2^{extr}, has. In order to estimate the remaining model dependence, the parameters of the theoretical calculations are varied; the resulting uncertainty is called the *extrapolation uncertainty*. Naturally, in addition to the extrapolation uncertainty the extrapolated quantity σ_2^{extr} has an original uncertainty of σ_1^{meas} (which, for instance, may consist of statistical and systematic uncertainties of the experimental measurement).

It is important to distinguish between "small" extrapolations to another region of a measured phase space (these can be thought of rather as interpolations), known also and referred to in the future as *swimming*, e.g. when a quantity is translated into a different binning scheme, and actual extrapolation to an "extra" (unmeasured) phase space, referred to in the future just as *extrapolation*. In the first case it is important that the original measurement in general covers all the phase space where the swimming is performed, so the predictions can be compared to the measurements in order to check the adequacy of the swimming. In contrast, in the second case the results of the extrapolation depend on theoretical predictions in unmeasured phase-space corners; thus in general the adequacy of the results cannot be verified unless there are other measurements in the uncovered regions. Note that in both cases the corrections do not depend on common normalisation factors, like a branching ratio or a fragmentation fraction. For the combinations presented in this thesis, the combination of D^{*+} cross sections requires only swimming, while the combination of charm reduced cross sections requires extrapolation.

For the charm combination presented here, phase-space corrections were always done using the theory introduced in Section 2.3.2.1: the NLO QCD calculations ($O(\alpha_s^2)$) in the 3-flavour FFNS obtained with the HVQDIS program [62]. Details of the theoretical calculations (including the variations which are used to estimate the extrapolation uncertainties) are given in the next Section 6.3.

6.3 Theoretical calculations in FFNS

This Section describes the set-up of the FFNS theoretical calculations which were used for two purposes:

- for the extrapolation and swimming corrections (Sections 6.4.1.1, 6.4.2.1, 6.5.1.3);
- for the comparison of the combined data with theory (Sections 6.4.1.3, 6.4.1.4, 6.4.2.3, 6.5.3) and QCD fits (Section 6.5.3.1).

Note that this Section describes the calculations in the FFNS only; they were always used for extrapolation and swimming, although in the comparison of the combined charm reduced cross sections to theory and in the QCD fits different variants of VFNS were involved; details of these calculations are provided later.

NLO QCD predictions in the FFNS were obtained with the HVQDIS program [62]. The parameters used in the calculations, together with the corresponding variations which were used to estimate the uncertainties, are described below.[8] In the combination procedure each extrap-

[8] The settings were mainly inherited from [66], although there are some differences (see also Section 6.5.1.3).

olation uncertainty was treated as correlated between all points and all measurements. Most of the extrapolation uncertainties (except the fragmentation fraction uncertainties) were originally asymmetric and must be symmetrised before performing a combination. Symmetrisation was performed by taking the largest deviation; no corrections to the central values were applied. For the data to theory comparison, to obtain total theoretical uncertainties, all the variations were added in quadrature; in this case the summation was performed separately for positive and negative variations.

6.3.1 Parton-level cross sections

The parton-level cross sections were calculated using the following settings:

- **the renormalisation and factorisation scales** were set to $\mu_r = \mu_f = \sqrt{Q^2 + 4m_c^2}$ and varied up and down by a factor of two. The variations were performed independently if the theoretical predictions were used for comparison with data, or simultaneously if they were used for extrapolation or swimming corrections (which are sensitive only to the shape of the predictions);
- **the pole mass of the charm quark** $m_c = 1.50 \pm 0.15$ GeV [66]; since the renormalisation and factorisation scale definitions include the charm-quark mass, varying this also slightly affected the two scales;
- **the strong coupling constant** $\alpha_s^{n_f=3}(M_Z) = 0.105 \pm 0.002$, corresponding to the value $\alpha_s^{n_f=5}(M_Z) = 0.116 \pm 0.002$;
- **the PDFs** were described by a series of 3-flavour FFNS variants of the HERAPDF1.0 set [207] at NLO, similar to those used for the cross-section extrapolations in the previous charm combination paper [66], evaluated for $m_c = 1.5 \pm 0.15$ GeV, for $\alpha_s^{n_f=3}(M_Z) = 0.105 \pm 0.002$, and for different scales. Charm measurements were not included in the determination of these PDF sets. For each of the parameter variations above, a different respective PDF set was used. By default, the scales for the charm contribution to the inclusive data in the PDF determination were chosen to be consistent with the factorisation scale used in HVQDIS, while the renormalisation scale in HVQDIS was decoupled from the PDF scales, except in the cases where the factorisation and renormalisation scales were varied simultaneously. As a cross check, instead of fitting the PDFs from inclusive data, 3-flavour NLO variants of the ABM [197] and MSTW [200] PDFs were also used to evaluate the cross sections. For MSTW, the variant with $m_c = 1.5$ GeV was chosen. The differences were found to be much smaller compared to those from other parameter variations, therefore the PDF uncertainties are neglected; the plots are provided in Appendix D (Fig. D.32).

6.3.2 Fragmentation

The fragmentation model described in the previous publication [66] was used to provide hadron cross sections, if needed. It is based on the measurements by H1 [95] and ZEUS [191] using

the production of D^{*+} mesons, with and without associated jets, in DIS and PHP. This model uses the fragmentation function of Kartvelishvili et al. [91], controlled by the parameter α_K, to describe the longitudinal fraction of the charm momentum transferred to the D^{*+} mesons. The fragmentation was performed in the photon-proton centre-of-mass frame by rescaling the quark three-momentum, then the energy of the produced hadron was calculated and the hadron was boosted to the lab frame. The calculation of the hadron energy and the Lorentz boost were done by using the hadron mass.[9] Different values of α_K [66] were used for different bins in the photon-parton centre-of-mass-frame squared energy, $\hat{s}$, and for different hadrons. Since ground-state D mesons partly originate from decays of D^{*+} and other excited mesons, the corresponding charm fragmentation function is softer than that measured using D^{*+} mesons. From kinematic considerations [192], supported by experimental measurements [193], the expectation value for the fragmentation function of c quarks into $D^{0,\text{ not }D^{*+}}$[10], D^+ and in the mix of charm hadrons decaying into muons, has to be reduced by $\approx 5\%$ with respect to that for D^{*+} mesons. The values of α_K for the fragmentation into ground-state hadrons, used for the $D^{0,\text{ not }D^{*+}}$, D^+ and μ measurements, have been re-evaluated accordingly [66] and are reported in Table 6.1. The model also implements a transverse fragmentation component by assigning to the charm hadron a transverse momentum, k_T, with respect to the charm-quark direction, with $\langle k_T \rangle = 0.35 \pm 0.15$ GeV. If needed (for the phase-space corrections for the ZEUS muon measurement [140]), the charm-hadron cross sections were accompanied by the semi-leptonic decays from [208]. Fragmentation fractions were taken from [183, 194] and are listed in Table 6.2.

$\hat{s}$ range	$\alpha_K(D^{*+})$	α_K(g.s.)	Measurement
$\hat{s} \leq \hat{s}_1$	6.1 ± 0.9	4.6 ± 0.7	[95] D^{*+}, DIS, no-jet sample
$\hat{s}_1 < \hat{s} \leq \hat{s}_2$	3.3 ± 0.4	2.7 ± 0.3	[95] D^{*+}, DIS, jet sample
$\hat{s} > \hat{s}_2$	2.67 ± 0.31	2.19 ± 0.24	[191] D^{*+} jet PHP

Table 6.1: The α_K parameters used for the longitudinal fragmentation into D^{*+} mesons and in ground-state (g.s.) charmed hadrons. The first column shows the $\hat{s}$ range in which a particular value of α_K is used, with $\hat{s}_1 = 70 \pm 40$ GeV^2 and $\hat{s}_2 = 324$ GeV^2. The variations of α_K are given in the second and third column. The parameter $\hat{s}_2$ was not varied, since the corresponding uncertainty is already covered by the α_K variations.

In total, the following uncertainties were assigned to the fragmentation:

- the variation of α_K (the upward and downward variations were performed simultaneously for all $\hat{s}$ bins and for all hadrons[11]);

[9] As explained in Section 2.3.4, a phenomenological fragmentation model should be applied exactly in the same way as it was measured. Here the fragmentation model follows the original H1 and ZEUS measurements [95, 191].

[10] $D^{0,\text{ not }D^{*+}}$ refers to D^0 that do not originate from decays of D^{*+}.

[11] The values of α_K, determined in [95, 191], are only partially correlated (the two values from [95]) or rather fully uncorrelated (the values from [95] and [191]), nevertheless their simultaneous variation is the most conservative way to estimate the uncertainty.

$f(c \to D^{*+})$	0.2287 ± 0.0056
$f(c \to D^{+})$	0.2256 ± 0.0077
$f(c \to D^{0,\text{not}D^{*+}})$	0.409 ± 0.014
$B(c \to \mu)$	0.096 ± 0.004

$f(b \to D^{*+}, D^{*-})$	0.173 ± 0.020
$f(b \to D^{+}, D^{-})$	0.233 ± 0.017
$f(b \to D^{0}, \bar{D}^{0})$	0.598 ± 0.029

Table 6.2: Charm fragmentation fractions to charmed mesons and the charm branching fraction to muons (left), and beauty branching fractions to charmed mesons (right).

- the variation of $\hat{s}_1$[12];
- the variation of $\langle k_T \rangle$[13];
- the uncertainties on the fragmentation fractions (do not enter extrapolation and swimming uncertainties, since they cancel for this purpose).

6.3.3 Beauty contribution

Most of the charm measurements report the cross sections of charm hadrons which are produced either directly or in decays of beauty hadrons. For the combination of charm reduced cross sections the beauty contribution needed to be subtracted, while for the data to theory comparison for D^{*+}-production cross sections it must be added to the charm theoretical predictions. In previous H1 and ZEUS charm analyses the beauty contribution had been obtained from the RAPGAP MC [178], with the normalisation rescaled to dedicated beauty measurements. Typical normalisation factors vary from 1.0 to 2.0 [19, 186–188, 209], thus an uncertainty $\sim 50\%$ has to be assigned to the beauty contribution. Propagated to the uncertainty on charm and beauty production, this results in an uncertainty of $\sim 5\%$ and thus becomes a dominant uncertainty at high Q^2, where the perturbative calculations are quite accurate. Moreover, conceptually this scheme provides predictions at LO accompanied by parton showers, re-normalised to measured data.

In contrast, in the present study the beauty contribution was obtained exactly at NLO: from the NLO QCD predictions for beauty hadrons with subsequent decays into charm hadrons.

A non-trivial ingredient of these calculations is the decay kinematics of charm to beauty hadrons, which, since many individual decay channels are involved, has to be obtained from some MC generator. In Fig. 6.1 the distributions of D-meson momenta in the B-hadron rest frame as obtained from the PYTHIA [176] and EvtGen [210] MC generators are compared with the data from CLEO [133] and ARGUS [211]. The shape from EvtGen describes the data reasonably well, therefore it was used for the predictions.

The parameters for the beauty contribution calculations and uncertainties were:

[12] In the case of extrapolation uncertainties, α_K and $\hat{s}_1$ variations were added in quadrature and treated as one source, referred to as 'longitudinal fragmentation'.

[13] In the case of extrapolation uncertainties this source is referred to as 'transverse fragmentation'.

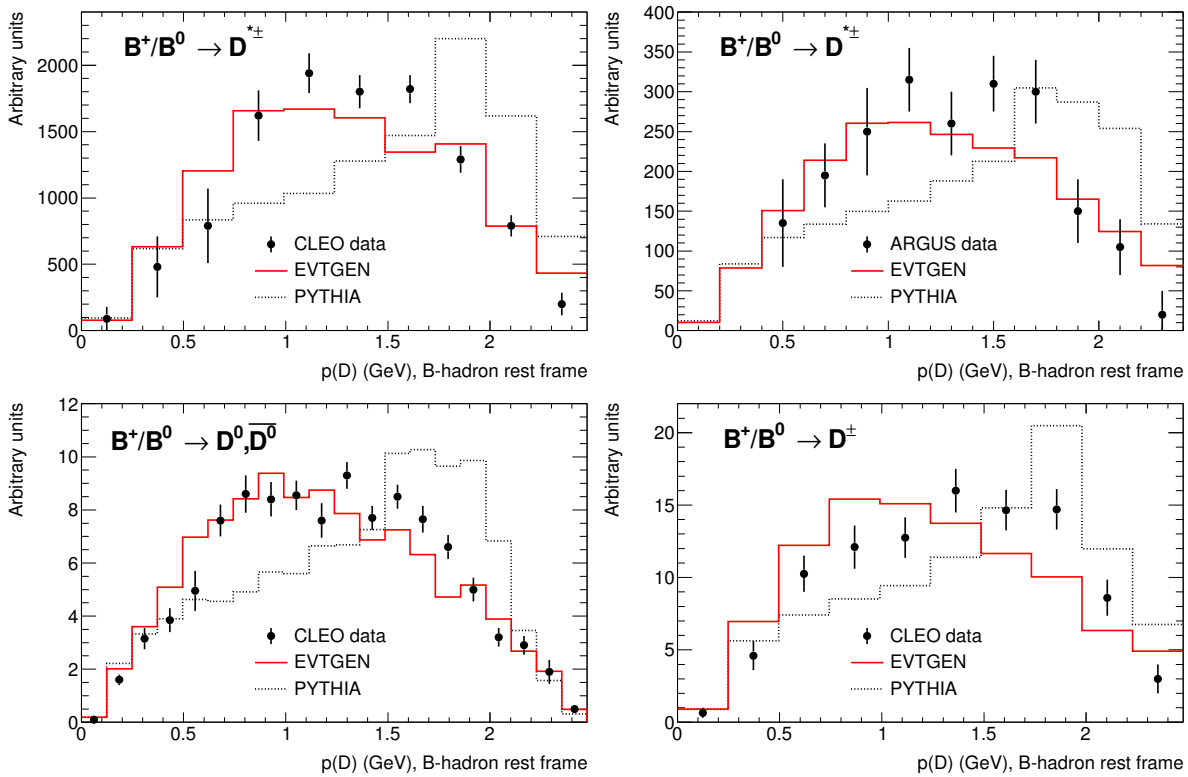

Figure 6.1: Distributions of D^{*+} (top left and top right), D^0 (bottom left) and D^+ (bottom right) momenta in the B-hadron rest frame as obtained from the PYTHIA [176] and EvtGen [210] MC generators compared with the data from CLEO [133] (top left, bottom left and bottom right) and ARGUS [211] (top right). The distributions from the event generators are normalised to the data.

- **the renormalisation and factorisation scales** $\mu_r = \mu_f = \sqrt{Q^2 + 4m_b^2}$, varied as for charm. The variations for charm and beauty were applied simultaneously;
- **the pole mass of the beauty quark** $m_b = 4.75 \pm 0.25$ GeV;
- **the fragmentation model for beauty quarks** based on the Peterson et al. [93] parametrisation with $\epsilon_b = 0.0035 \pm 0.0020$ [212];
- **the fraction of beauty hadrons decaying into charm hadrons** was taken from [183] and listed in Table 6.2;
- **the PDFs**, described by the same set (the 3-flavour FFNS) as the one used for the corresponding charm prediction.

The dominant uncertainty comes from the variation of the fraction of beauty hadrons decaying into D^{*+} mesons; although it reaches only $\approx 2\%$ in the highest Q^2 bins. Since the beauty contribution itself is small (varies from 1% at low Q^2 to 7% at high Q^2), all other uncertainties are almost negligible.

6.4 Combination of visible D^{*+} cross sections

This Section describes a combination of the HERA charm production measurements at the level of visible cross sections of D^{*+}-meson production in DIS. The primary aim of the analysis was to obtain one consistent dataset which presents (as close as possible) a directly experimentally measured quantity, thus minimising dependency on the theory model used in the combination. This needs data with the same final state covering preferentially the same visible phase space, as explained in Section 6.1.

Among all techniques used at HERA to measure open charm production (see Section 3.1.3), measurements of D^{*+} production have the best signal-to-background ratio and hence are the most precise. ZEUS and H1 have recently published single- and double-differential D^{*+} cross sections for inclusive D^{*+}-meson production in DIS from their respective final HERA-II datasets [64, 65, 137]. The measurements have been performed in very similar phase spaces and used very similar binning schemes[14] thus fulfilling the requirement stated above for a combination with minimised theory dependence.

The phase space of HERA-II measurements in DIS is restricted compared to that of HERA-I measurements. Due to beam-line modifications related to HERA-II high-luminosity running [105] the visible phase space of these D^{*+} cross sections at HERA-II is restricted to virtualities $Q^2 > 5\,\mathrm{GeV}^2$. This fact prevents straightforward combination with HERA-I measurements for most of the single-differential D^{*+} cross sections, although in the case of the single- or double-differential D^{*+} cross sections as a function of Q^2, the above restriction does not apply and the kinematic range can be extended to lower Q^2 using earlier HERA-I measurements. In fact only the double-differential D^{*+} cross sections as a function of Q^2 and y can be combined with HERA-I measurements without applying extensive swimming corrections.[15] For this reason the description of the visible D^{*+} cross section combination consists of two parts: a combination of single-differential D^{*+} cross sections, described in Section 6.4.1, and a combination of the double-differential cross section, described in Section 6.4.2. While the common method and strategy for both parts remain the same, the input measurements and phase spaces differ.

All measurements to be combined for the single- and double-differential D^{*+} cross sections are already corrected to the QED Born level with a running fine-structure constant and include both the charm and beauty contributions to D^{*+} production.

Results reported in this Section present a first combination of the H1 and ZEUS measurements of visible D^{*+} cross sections. The results have been approved by the H1 and ZEUS

[14] An agreement on the phase space and binning schemes was achieved between the H1 and ZEUS Collaborations before performing the measurements.

[15] Although the single-differential D^{*+} cross sections as a function of Q^2, in principle, also can be combined with HERA-I measurements without applying swimming corrections, this combination is not provided, because

- information on the single-differential D^{*+} cross sections as a function of Q^2 can be obtained from the double-differential D^{*+} cross sections as a function of Q^2 and y, provided in 6.4.2;
- to keep consistency between all the combined single-differential D^{*+} cross sections, which requires the same input data.

Collaborations as preliminary [213]; currently their publication is being prepared.[16]

6.4.1 Combination of single-differential D^{*+} cross sections

This Section describes the combination of D^{*+} single-differential cross sections. Section 6.4.1.1 describes the input measurements, defines the combination phase space and describes details of the combination procedure which includes all necessary corrections needed to transform the input data to the common phase space. Section 6.4.1.2 presents and discusses the results of the combination, the consistency of the input data and gives the combined D^{*+} cross sections. Section 6.4.1.3 presents a comparison of NLO QCD predictions to the combined data. Finally, Section 6.4.1.4 presents a detailed comparison of data and theory and introduces a 'customised' theoretical calculation.

6.4.1.1 Input measurements, phase space and combination details

Table 6.3 presents the datasets used for this combination together with their visible phase space regions and integrated luminosities. Note that the H1 Collaboration has published D^{*+} cross-section measurements separately for $5 < Q^2 < 100$ GeV^2 (dataset I) [65][17] and for $100 < Q^2 < 1000$ GeV^2 (dataset II) [64] because different sub-detectors had to be employed for the detection and measurement of the scattered electron in these two regions. Thus the overall phase space for the combined D^{*+} cross sections is given by

$$\begin{aligned} &5 < Q^2 < 1000\,\text{GeV}^2, \\ &0.02 < y < 0.7, \\ &p_T(D^{*+}) > 1.5\,\text{GeV}, \\ &|\eta(D^{*+})| < 1.5. \end{aligned} \tag{6.17}$$

The combination was done for single-differential D^{*+} cross sections as a function of the D^{*+} transverse momentum, $p_T(D^{*+})$, pseudorapidity, $\eta(D^{*+})$, and inelasticity, $z(D^{*+}) = (E(D^{*+}) - p_Z(D^{*+}))/(2E_e y)$, with E_e being the incoming electron energy, $E(D^{*+})$ and $p_Z(D^{*+})$ the energy and longitudinal momentum of D^{*+}, respectively, as well as of the DIS kinematic variables Q^2 and y.[18]

Since the H1 datasets I and II are complementary to each other and give the combined phase space 6.17, their differential D^{*+} cross sections should be summed up on a bin-by-bin basis and enter the combination as a single dataset. However, due to the limited statistics at high Q^2 a coarser binning scheme in $p_T(D^{*+})$, $\eta(D^{*+})$, $z(D^{*+})$ and y had to be used in dataset II compared

[16] After the disputation during the final preparation of this thesis for printing, the results have been publicly released by the Collaborations [214].

[17] From the two sets of measurements in [65], the one compatible with the cuts on $p_T(D^{*+})$ and $\eta(D^{*+})$ quoted in Table 6.3, which are compatible with the phase space of the ZEUS measurement [137], was chosen and referred as dataset I.

[18] Although all input measurements from Table 6.3 report also the single-differential cross section as a function of the Bjorken variable x, the binning differs significantly, preventing a combination without large swimming corrections.

Dataset	Kinematic range				$\mathcal{L}$
	Q^2 [GeV^2]	y	$p_T(D^{*+})$ [GeV]	$\eta(D^{*+})$	[pb^{-1}]
I: H1 D^{*+} HERA-II (medium Q^2) [65]	5 : 100	0.02 : 0.70	1.5 : ∞	−1.5 : 1.5	348
II: H1 D^{*+} HERA-II (high Q^2) [64]	100 : 1000	0.02 : 0.70	1.5 : ∞	−1.5 : 1.5	351
III: ZEUS D^{*+} HERA-II [137]	5 : 1000	0.02 : 0.70	1.5 : 20.0	−1.5 : 1.5	363

Table 6.3: Datasets used in the combination of the visible D^{*+} single-differential cross sections. For each dataset the respective kinematic region and the integrated luminosity, $\mathcal{L}$, are given.

to dataset I. This made a straightforward summation of the differential D^{*+} cross sections from the two measurements impossible. Therefore the cross section in a bin i of a given observable integrated in the range $5 < Q^2 < 1000$ GeV^2 was calculated according to

$$\begin{aligned}\sigma_i(5 < Q^2/\text{GeV}^2 < 1000) &= \sigma_i(5 < Q^2/\text{GeV}^2 < 100) \\ &+ \sigma_i^{NLO}(100 < Q^2/\text{GeV}^2 < 1000) \cdot \frac{\sigma_{int}(100 < Q^2/\text{GeV}^2 < 1000)}{\sigma_{int}^{NLO}(100 < Q^2/\text{GeV}^2 < 1000)}.\end{aligned} \tag{6.18}$$

Here σ_{int} denotes the integrated visible cross section and *NLO* stands for the NLO predictions obtained from HVQDIS.[19] In this calculation both the experimental uncertainties of the visible cross section at high Q^2 and the theoretical uncertainties (described in Section 6.2.3) were included. The contribution from the region $100 < Q^2 < 1000$ GeV^2 to the full Q^2 range amounts to 4% on average and reaches up to 50% at the highest $p_T(D^{*+})$; the extrapolation uncertainty is negligible in most of the bins compared to the corresponding experimental uncertainty; only at the two highest $p_T(D^{*+})$ bins it approaches 35% of the experimental uncertainty. Thus in the combination procedure the extrapolation uncertainties from all theoretical parameter variations were added in quadrature and treated as an uncorrelated uncertainty. The sensitivity of the shape to the beauty contribution was found to be negligible and therefore was ignored.

For the single-differential D^{*+} cross sections as a function of Q^2, the procedure described above was not needed. However the binning schemes used for these D^{*+} cross sections differ between datasets I–II and dataset III. At low Q^2 this was solved by combining the cross-section measurements of the first two bins of dataset I into a single bin. For $Q^2 > 100$ GeV^2 no consistent binning scheme could be defined from the single-differential cross-section measurements $\mathrm{d}\sigma/\mathrm{d}Q^2$ itself. However, the measurements of the double-differential D^{*+} cross section $\mathrm{d}^2\sigma/\mathrm{d}y\mathrm{d}Q^2$ have been performed in a common binning scheme. By integrating these D^{*+} cross sections in y, single-differential D^{*+} cross sections in Q^2 were obtained at $Q^2 > 100$ GeV^2 from datasets II, III which were used directly in the combination. The contribution to dataset III from the range $p_T(D^{*+}) > 20$ GeV was found to be negligible ($\ll 1\%$).

Applying the procedure described above provided exactly two input measurements for each

[19] Since the normalisation was taken from another measurement, not from theory predictions, this is swimming, as explained in Section 6.2.3.

combined bin: one from H1 (datasets I–II) and one from ZEUS (dataset III). Thus n_{dof} is equal to the number of combined bins. Since the data are statistically correlated between the different distributions, each distribution was combined separately.

The branching ratios for datasets I, II were updated to the latest PDG value [183]. A full list of considered correlated sources is provided in Appendix D (Table D.13); also input data tables used for the combination are provided (Tables D.5 to D.9). All systematic uncertainties were treated as uncorrelated between the H1 and ZEUS measurements, except for the branching-ratio uncertainty; since the latter is fully correlated between all datasets, it is not changed in the combination and technically was not included in the combination but applied as an external uncertainty on the results.

6.4.1.2 Combined D^{*+} cross sections

The results of combining the HERA-II measurements [64, 65, 137] as a function of $p_T(D^{*+})$, $\eta(D^{*+})$, $z(D^{*+})$, Q^2 and y are given in Table 6.4, together with their uncorrelated and correlated uncertainties. The total uncertainties were obtained by adding the uncorrelated and correlated uncertainties in quadrature. A detailed breakdown of the correlated uncertainties can be found in Appendix D (Tables D.14 to D.15).

The individual datasets as well as the results of the combination are shown in Fig. 6.2. The consistency of the datasets as well as the reduction of the uncertainties are illustrated further for the steeply falling D^{*+} cross sections as a function of $p_T(D^{*+})$ and Q^2 in the bottom parts. The input H1 and ZEUS datasets are similar in precision. The values of χ^2, n_{dof} and the corresponding χ^2-probabilities for the combinations of the different distributions are reported in Table 6.5. The combinations in the different variables have the χ^2-probability varying between 15% and 87%, i.e. the datasets are consistent. The pull distributions are shown in Fig. 6.3. Considering a relatively small number of input points, the pulls are reasonably similar to unit Gaussians. Although Fig. 6.2 indicates that the H1 data points lie on average below the ZEUS points, the pulls in Fig. 6.3 show an overall symmetric spread of the H1 and ZEUS input data around the combined results; this is explained by taking into account shifts of the correlated systematic uncertainties. The shifts and reductions of the correlated sources are consistent for the combinations of the D^{*+} cross sections in different variables; they can be found in Appendix D (Table D.13).

The combined D^{*+} cross sections exhibit significantly reduced uncertainties. While the effective doubling of the statistics of the combined result reduces the uncorrelated uncertainties (inner error bars in Fig. 6.2), the correlated uncertainties (quadratic difference of the outer and inner error bars) of the combined D^{*+} cross sections are significantly reduced through cross-calibration effects between the two experiments. Typically, both effects contribute about equally to the reduction of the total uncertainty.

6.4.1.3 Comparison with theoretical predictions

The combined D^{*+} cross sections as a function of $p_T(D^{*+})$, $\eta(D^{*+})$, $z(D^{*+})$, Q^2 and y are compared to the NLO QCD predictions in the FFNS (described in Section 6.3) in Fig. 6.4; there is also a dotted line referred as 'customised' NLO QCD predictions shown there, which will

$p_T(D^{*+})$ (GeV)	$\frac{d\sigma}{dp_T(D^{*+})}$ (nb/GeV)	δ_{unc} (%)	δ_{cor} (%)	δ_{tot} (%)
1.50 : 1.88	2.35	6.4	4.7	8.0
1.88 : 2.28	2.22	4.9	4.2	6.4
2.28 : 2.68	1.98	3.7	4.0	5.5
2.68 : 3.08	1.55	3.5	3.7	5.1
3.08 : 3.50	1.20	3.7	3.5	5.1
3.50 : 4.00	9.29×10^{-1}	3.2	3.4	4.7
4.00 : 4.75	6.14×10^{-1}	3.0	3.5	4.6
4.75 : 6.00	3.19×10^{-1}	3.1	3.3	4.5
6.00 : 8.00	1.15×10^{-1}	3.8	3.7	5.3
8.00 : 11.00	3.32×10^{-2}	5.4	3.7	6.5
11.00 : 20.00	3.80×10^{-3}	10.4	6.4	12.2

Q^2 (GeV^2)	$\frac{d\sigma}{dQ^2}$ (nb/GeV^2)	δ_{unc} (%)	δ_{cor} (%)	δ_{tot} (%)
5 : 8	4.74×10^{-1}	4.0	5.0	6.4
8 : 10	2.96×10^{-1}	4.3	3.8	5.8
10 : 13	2.12×10^{-1}	3.8	4.0	5.6
13 : 19	1.24×10^{-1}	3.2	3.8	5.0
19 : 28	7.26×10^{-2}	3.5	3.6	5.0
28 : 40	3.97×10^{-2}	3.7	4.0	5.5
40 : 60	1.64×10^{-2}	4.4	4.7	6.4
60 : 100	7.45×10^{-3}	5.2	3.9	6.5
100 : 158	2.08×10^{-3}	7.2	5.3	9.0
158 : 251	8.82×10^{-4}	7.6	5.0	9.1
251 : 1000	7.50×10^{-5}	12.0	6.7	13.3

$\eta(D^{*+})$	$\frac{d\sigma}{d\eta(D^{*+})}$ (nb)	δ_{unc} (%)	δ_{cor} (%)	δ_{tot} (%)
-1.50 : -1.25	1.36	5.8	4.3	7.2
-1.25 : -1.00	1.52	4.6	4.0	6.1
-1.00 : -0.75	1.59	4.6	4.0	6.1
-0.75 : -0.50	1.79	3.8	3.5	5.2
-0.50 : -0.25	1.83	3.8	3.3	5.1
-0.25 : 0.00	1.89	3.8	3.7	5.3
0.00 : 0.25	1.86	4.0	3.4	5.2
0.25 : 0.50	1.88	4.0	3.6	5.4
0.50 : 0.75	1.91	4.1	3.5	5.4
0.75 : 1.00	1.92	4.3	4.0	5.9
1.00 : 1.25	2.08	4.7	4.0	6.1
1.25 : 1.50	1.81	6.3	4.8	7.9

y	$\frac{d\sigma}{dy}$ (nb)	δ_{unc} (%)	δ_{cor} (%)	δ_{tot} (%)
0.02 : 0.05	12.13	5.8	9.1	10.8
0.05 : 0.09	18.84	3.9	4.6	6.0
0.09 : 0.13	16.99	3.4	4.3	5.5
0.13 : 0.18	13.35	3.7	4.2	5.6
0.18 : 0.26	11.19	3.4	3.7	5.0
0.26 : 0.36	7.65	3.7	4.2	5.6
0.36 : 0.50	4.78	4.0	5.3	6.6
0.50 : 0.70	2.65	5.6	6.4	8.5

$z(D^{*+})$	$\frac{d\sigma}{dz(D^{*+})}$ (nb)	δ_{unc} (%)	δ_{cor} (%)	δ_{tot} (%)
0.00 : 0.10	3.28	9.5	5.9	11.2
0.10 : 0.20	7.35	4.8	6.3	7.9
0.20 : 0.32	8.61	3.5	4.6	5.7
0.32 : 0.45	8.92	2.7	3.9	4.7
0.45 : 0.57	8.83	1.8	4.0	4.3
0.57 : 0.80	4.78	2.4	5.1	5.6
0.80 : 1.00	6.31×10^{-1}	8.1	10.2	13.0

Table 6.4: The combined single-differential D^{*+} cross sections as a function of $p_T(D^{*+})$, $\eta(D^{*+})$, $z(D^{*+})$, Q^2 and y, with their uncorrelated (δ_{unc}), correlated (δ_{cor}) and total (δ_{tot}) uncertainties.

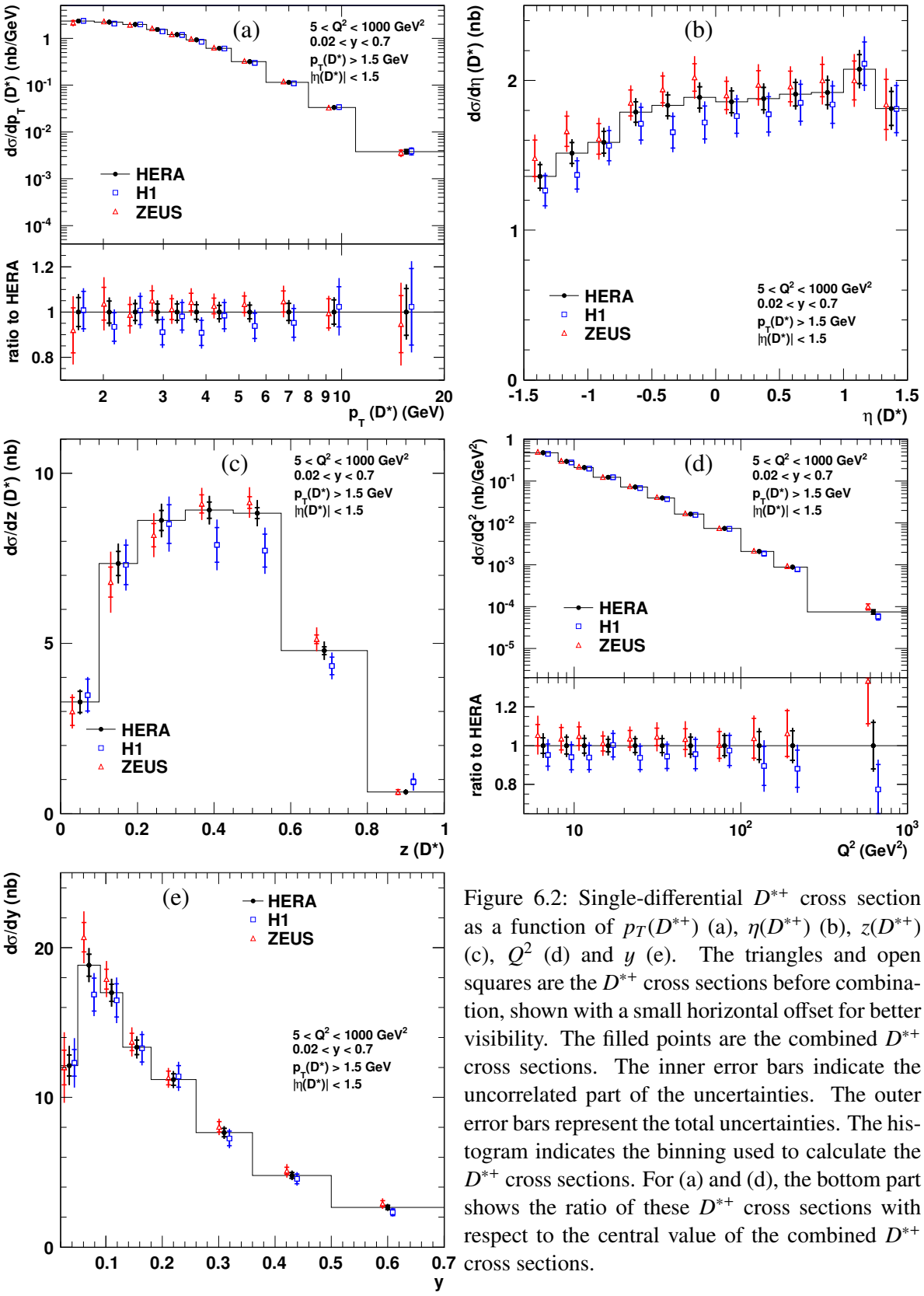

Figure 6.2: Single-differential D^{*+} cross section as a function of $p_T(D^{*+})$ (a), $\eta(D^{*+})$ (b), $z(D^{*+})$ (c), Q^2 (d) and y (e). The triangles and open squares are the D^{*+} cross sections before combination, shown with a small horizontal offset for better visibility. The filled points are the combined D^{*+} cross sections. The inner error bars indicate the uncorrelated part of the uncertainties. The outer error bars represent the total uncertainties. The histogram indicates the binning used to calculate the D^{*+} cross sections. For (a) and (d), the bottom part shows the ratio of these D^{*+} cross sections with respect to the central value of the combined D^{*+} cross sections.

Cross section	n_{dof}	χ^2	p(χ^2,n_{dof})
$\mathrm{d}\sigma/\mathrm{d}p_T(D^{*+})$	11	6.9	81%
$\mathrm{d}\sigma/\mathrm{d}\eta(D^{*+})$	12	7.8	80%
$\mathrm{d}\sigma/\mathrm{d}z(D^{*+})$	7	10.9	15%
$\mathrm{d}\sigma/\mathrm{d}Q^2$	11	6.1	87%
$\mathrm{d}\sigma/\mathrm{d}y$	8	5.8	67%

Table 6.5: The values of χ^2, n_{dof} and the corresponding χ^2-probabilities for the combinations of the single-differential D^{*+} cross sections as a function of different variables.

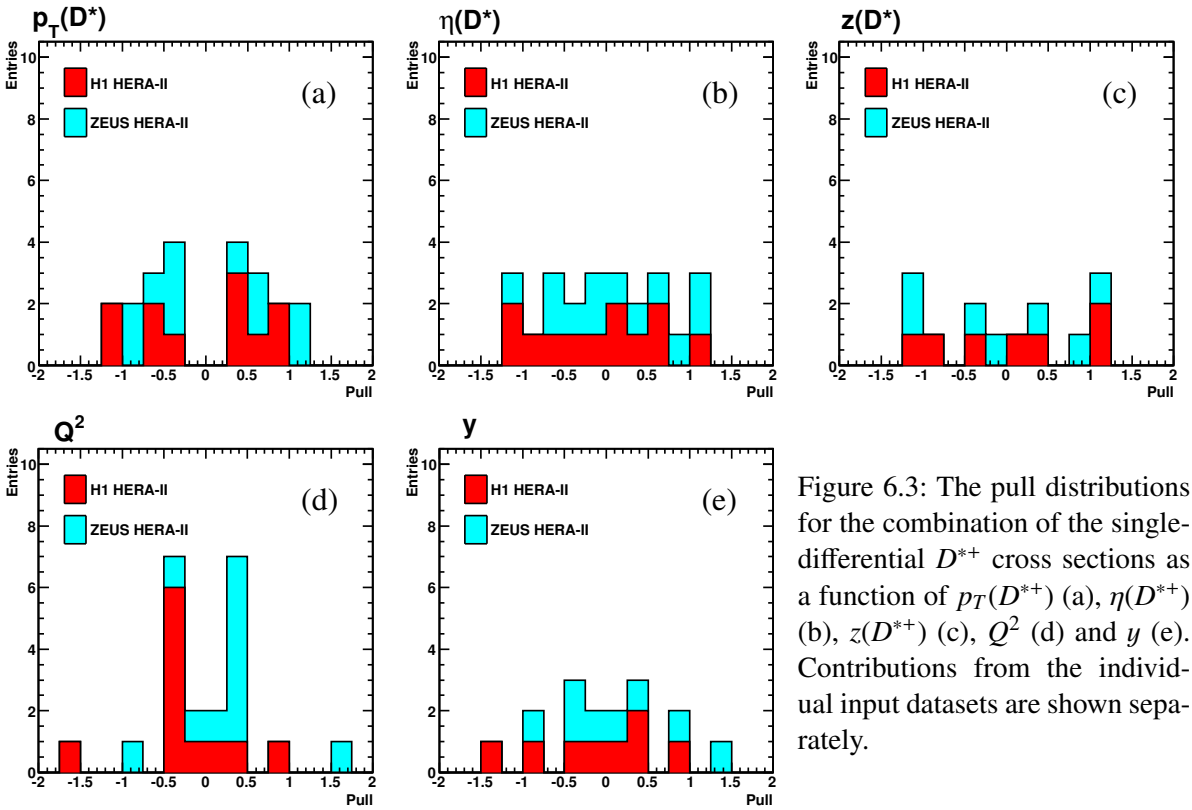

Figure 6.3: The pull distributions for the combination of the single-differential D^{*+} cross sections as a function of $p_T(D^{*+})$ (a), $\eta(D^{*+})$ (b), $z(D^{*+})$ (c), Q^2 (d) and y (e). Contributions from the individual input datasets are shown separately.

be discussed in the next Section 6.4.1.4. In general the predictions describe the data well. The data reach a precision of about 5% over a large fraction of the measured phase space, while the typical theory uncertainty ranges from 30% at low Q^2 to 10% at high Q^2. The data points between the different distributions are statistically and systematically correlated, so they can be quantitatively compared to theory only on a one-by-one basis.

The theoretical predictions describe the combined data rather well within the corresponding uncertainty band, while the central theoretical curves underestimate the data normalisation. The central theoretical prediction shows a somewhat softer y distribution than the data. The central prediction for $z(D^{*+})$ is a bit wider than the measured distribution.

6.4.1.4 'Customised' theoretical predictions

As mentioned in the previous Section 6.4.1.3, the theoretical uncertainties are usually larger than the corresponding uncertainties of the combined data. Since the theoretical uncertainties are combined from several correlated sources, it is rather difficult to make a strong statement about agreement between the theory and the data from Fig. 6.4 itself.

In order to study the impact of the current theory uncertainties in more detail, the effect of each separate theory variation on the predictions was studied. The most conclusive variations on the predictions are shown separately in Fig. 6.5, compared to the same data as in Fig. 6.4. Plots with all the variations are in Appendix D (Figs. D.27 to D.31).

The NLO prediction as a function of $p_T(D^{*+})$ (Fig. 6.5a) describes the data better if either

- the charm-quark pole mass is reduced to 1.35 GeV; or
- the renormalisation scale is reduced by a factor 2; or
- the factorisation scale is increased by a factor 2.

Simultaneous variation of both scales will largely compensate and will therefore have a much smaller effect.

The prediction for the $z(D^{*+})$ distribution (Fig. 6.5d) describes the shape of the data noticeably better if the fragmentation parameters are adjusted such that the bin boundary $\hat{s}_1$ between the two lowest fragmentation bins [66] is varied from the default of 70 GeV^2 to its lower boundary of 30 GeV^2. This also slightly improves the shape of the y distribution (Fig. 6.5b).

The preference for a reduced renormalisation scale already observed for $p_T(D^{*+})$ is confirmed by the $z(D^{*+})$ distribution (Fig. 6.5c). However, the shape of the $z(D^{*+})$ distribution rather prefers variations of the charm mass and the factorisation scale in the opposite direction to those found for the $p_T(D^{*+})$ distribution. The other kinematic variables do not contribute any additional information to these findings.

As stated before, within the large uncertainties indicated by the theory bands in Fig. 6.4, all distributions are reasonably described. However, the above study shows that the different contributions to these uncertainties do not only affect the normalisation but also change the shape of different distributions in different ways. It is therefore nontrivial that a variant of the prediction which gives a good description in one variable will also give a good description in another.

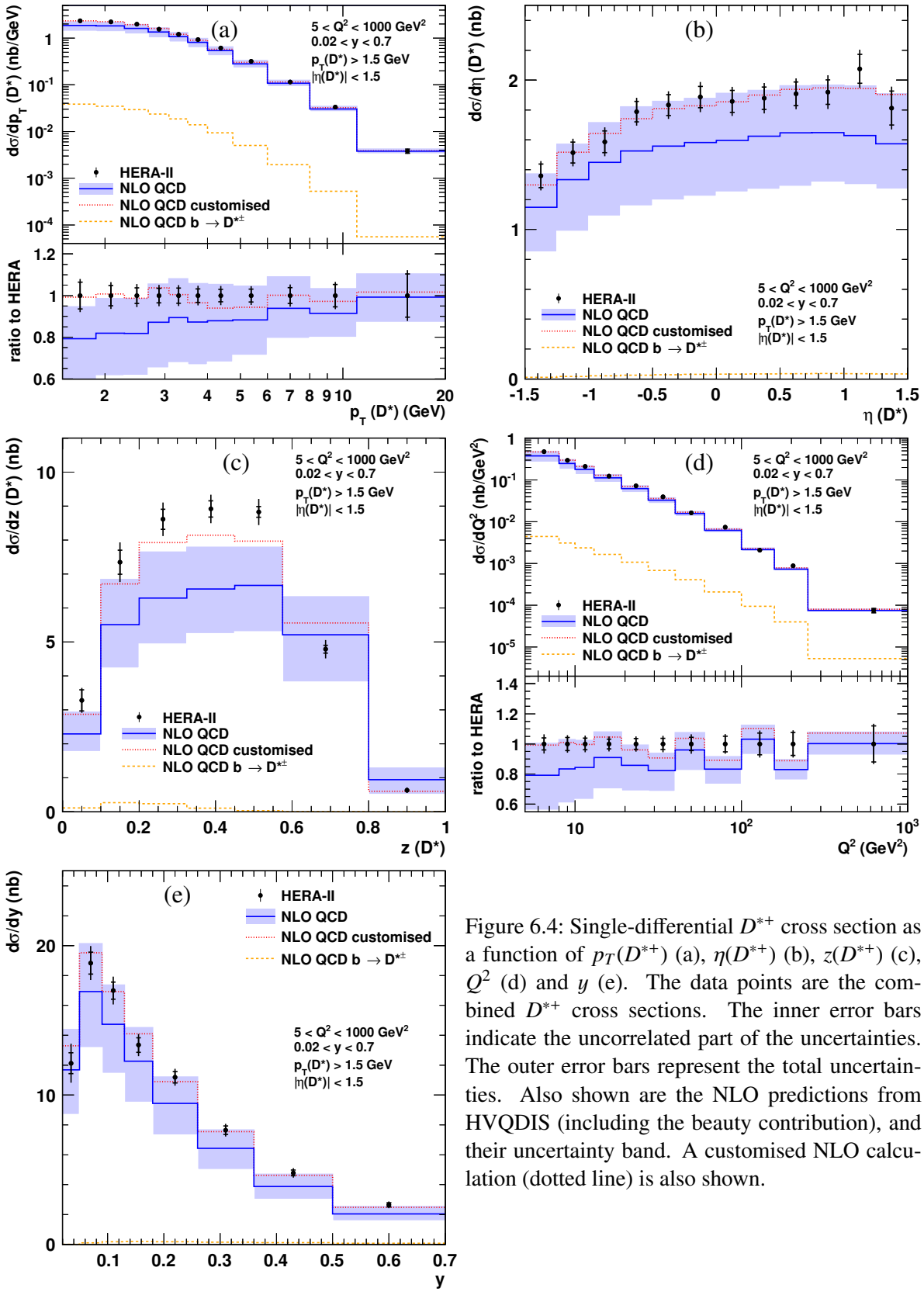

Figure 6.4: Single-differential D^{*+} cross section as a function of $p_T(D^{*+})$ (a), $\eta(D^{*+})$ (b), $z(D^{*+})$ (c), Q^2 (d) and y (e). The data points are the combined D^{*+} cross sections. The inner error bars indicate the uncorrelated part of the uncertainties. The outer error bars represent the total uncertainties. Also shown are the NLO predictions from HVQDIS (including the beauty contribution), and their uncertainty band. A customised NLO calculation (dotted line) is also shown.

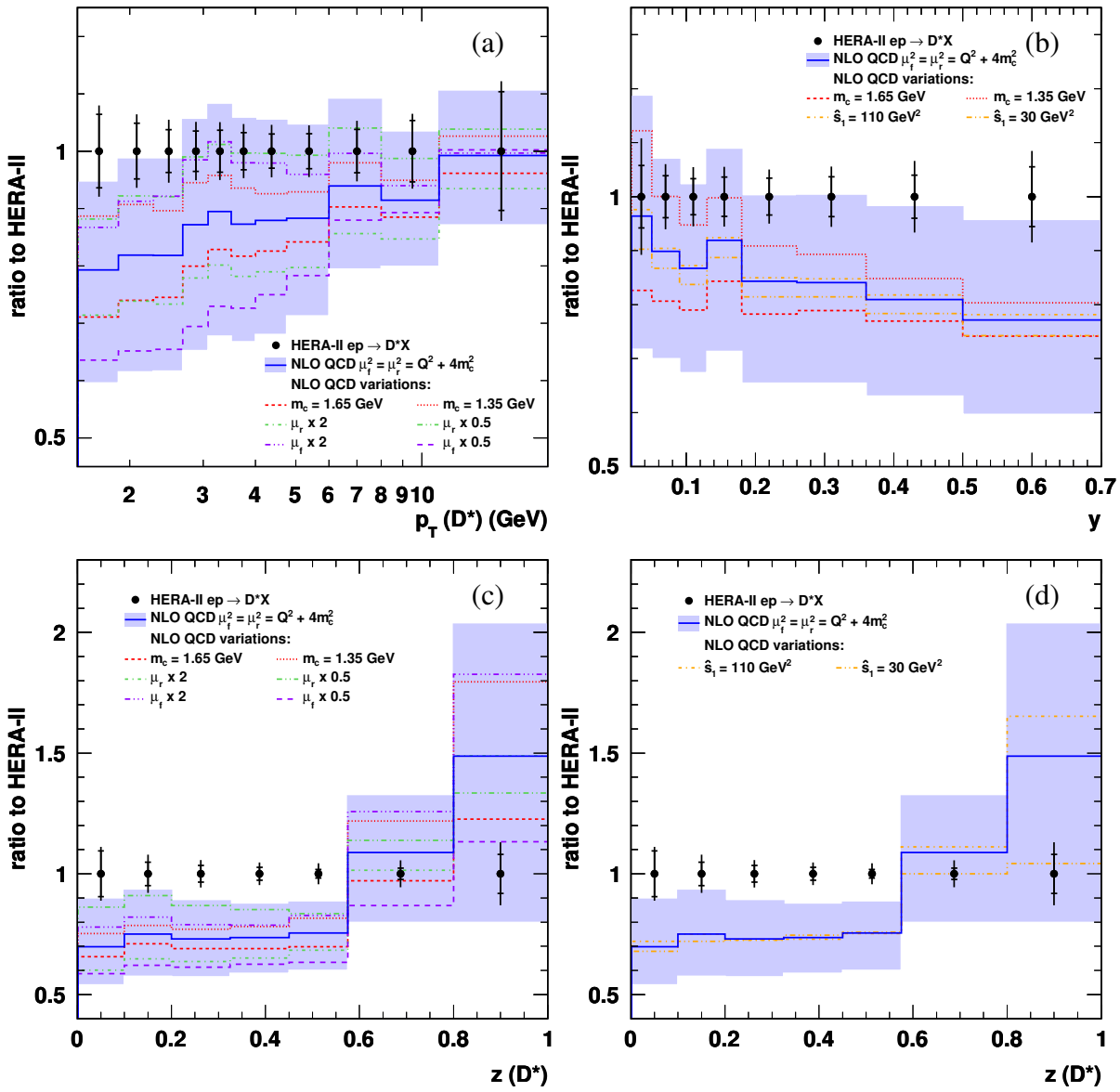

Figure 6.5: Single-differential D^{*+} cross section as a function of $p_T(D^{*+})$ (a), y (b) and $z(D^{*+})$ (c,d) compared to NLO predictions with different variations: charm-quark mass m_c, renormalisation scale μ_r, factorisation scale μ_f and fragmentation bin boundary $\hat{s}_1$.

Based on the above study, a 'customised' calculation was hence performed with the goal to demonstrate that it is possible to obtain an acceptable description of the data in all variables at the same time, for both shape and normalisation, within the theoretical uncertainties quoted in Section 6.3.[20] For this calculation

- the renormalisation scale was reduced by a factor 2, with the factorisation scale unchanged;
- the change of the fragmentation parameter $\hat{s}_1 = 30\,\text{GeV}^2$ was applied;
- at this stage, the resulting distributions were still found to underestimate the data normalisation. As the renormalisation and factorisation scales are recommended to differ by at most a factor of two [43], the only significant remaining handle is the charm-quark pole mass. This mass was set to 1.4 GeV, a value which was also found to be compatible with the partially overlapping data used for a previous dedicated study [66] of the charm-quark mass;
- all other parameters, which were found to have a much smaller impact than those treated above, were left at their central settings as described in Section 6.3.

The result of this customised calculation is indicated as a dotted line in Fig. 6.4. Indeed a reasonable agreement with the data is achieved in all variables at the same time. This *a posteriori* adjustment of theory parameters is not a prediction, but it can be taken as a hint in which direction theoretical and phenomenological developments might need to proceed:

- the strong improvement of the description of the data relative to the central prediction through the customisation of the renormalisation scale indicates that NNLO calculations, which might reduce the scale-related uncertainties to a level which matches the data precision, should be very helpful to obtain a more stringent statement concerning the agreement of the pQCD predictions with the data;
- the improvement from the customisation of one of the fragmentation parameters and the still not fully satisfactory description of the $z(D^{*+})$ distribution indicate that further dedicated experimental and theoretical studies of the fragmentation treatment, such as the introduction of a perturbative heavy-quark fragmentation scale in the pQCD calculations, might be helpful.

In general, the precise single-differential distributions resulting from the combination, in particular those as a function of $p_T(D^{*+})$, $\eta(D^{*+})$ and $z(D^{*+})$, are sensitive to theoretical and phenomenological parameters in a way which complements the sensitivity of more inclusive variables like Q^2 and y.

[20] Since several of the theory parameters (e.g. the renormalisation and factorisation scales) are not physical parameters, and hence their "uncertainties" have no physical relevance, a "proof of existence" rather than a detailed fit will suffice to clarify this point. Another reason not to perform a detailed fit is that the data are statistically correlated between the different distributions, therefore all the distributions must not be fitted simultaneously.

Dataset	Kinematic range				$\mathcal{L}$	$\sqrt{s}$
	Q^2 [GeV^2]	y	$p_T(D^{*+})$ [GeV]	$\eta(D^{*+})$	[pb^{-1}]	[GeV]
I: H1 D^{*+} HERA-II (med. Q^2) [65]	5 : 100	0.02 : 0.70	1.5 : ∞	−1.5 : 1.5	348	318
II: H1 D^{*+} HERA-II (high Q^2) [64]	100 : 1000	0.02 : 0.70	1.5 : ∞	−1.5 : 1.5	351	318
III: ZEUS D^{*+} HERA-II [137]	5 : 1000	0.02 : 0.70	1.5 : 20.0	−1.5 : 1.5	363	318
IV: ZEUS D^{*+} HERA-I 98–00 [136]	1.5 : 1000	0.02 : 0.70	1.5 : 15.0	−1.5 : 1.5	82	318
V: ZEUS D^{*+} HERA-I 96–97 [59]	1 : 600	0.02 : 0.70	1.5 : 15.0	−1.5 : 1.5	37	300
VI: H1 D^{*+} HERA-I [134]	2 : 100	0.05 : 0.70	1.5 : 15.0	−1.5 : 1.5	47	318

Table 6.6: Datasets considered for the combination of the visible D^{*+} double-differential cross section. For each dataset the respective kinematic region, the integrated luminosity, $\mathcal{L}$, and the centre-of-mass energy, $\sqrt{s}$, are given.

6.4.2 Combination of double-differential cross section

This Section describes a combination of the D^{*+} double-differential cross section as a function of Q^2 and y. Section 6.4.2.1 describes the selection of the input measurements, defines the combination phase space and gives details of the combination. Section 6.4.2.2 presents and discusses the results of the combination, the consistency of the input data and gives the combined D^{*+} cross sections. Section 6.4.2.3 presents a comparison of NLO QCD predictions to the combined data.

6.4.2.1 Input measurements, phase space and combination details

Since for the combination of the double-differential cross section as a function of Q^2 and y the restriction to the same phase space in Q^2 does not apply, HERA-I D^{*+} measurements can be included in the combination.

Table 6.6 presents the datasets considered for the combination of the visible D^{*+} double-differential cross section.[21] Comparing to Table 6.3, Table 6.6 is extended with the three most precise HERA-I measurements; it also has an additional column which reports the centre-of-mass energy, since the latter differs for one of the HERA-I measurements.

Inclusion of HERA-I measurements in the combination allows an extension of the kinematic range down to lower Q^2. Although all three HERA-I measurements have different lower Q^2 boundaries, a reasonable compromise between them was to choose the lower Q^2 equal to Q^2 =

[21] Same as in Table 6.3, from the two sets of measurements in [65], the one compatible with the quoted cuts on $p_T(D^{*+})$ and $\eta(D^{*+})$, which are compatible with the phase space of the ZEUS measurement [137], was chosen and referred to as dataset I.

$1.5\,\text{GeV}^2$. Thus the overall phase space for the combined D^{*+} cross sections is given by

$$\begin{aligned} &1.5 < Q^2 < 1000\,\text{GeV}^2, \\ &0.02 < y < 0.7, \\ &p_T(D^{*+}) > 1.5\,\text{GeV}, \\ &|\eta(D^{*+})| < 1.5, \\ &\sqrt{s} = 318\,\text{GeV}. \end{aligned} \tag{6.19}$$

Some of the HERA-I measurements from Table 6.6 have a slightly different phase space and are performed at a different centre-of-mass energy. Moreover, their binning scheme for the double-differential cross section significantly differ from that which has been used for datasets I–III; dataset VI reports the double-differential cross section not as a function of Q^2 and y but as a function of Q^2 and x. Thus inclusion of HERA-I measurements in the combination necessarily required applying swimming corrections.

A dedicated study was done to select those HERA-I measurements which are reasonably compatible with the HERA-II ones. At first a common binning scheme had to be chosen. Since the HERA-II measurements still remain the most precise in the combination, the double-differential cross section as a function of Q^2 and y was selected with the binning scheme which is based on datasets I–III (although slightly revised to improve consistency with the HERA-I measurements). It was extended at low Q^2 with the binning scheme based on the most precise HERA-I dataset IV. The new binning will be given together with the combined D^{*+} cross sections in Table 6.8. D^{*+} cross sections in the new bins (also referred to as *destination*, or *output*, bins) were obtained from the original bins (referred to also as *input* bins) using the swimming procedure described in Section 6.2.3. For each swum bin the following quantities were calculated:

- the fraction of the cross section of the original bin contained in the new one, *efficiency*, E;
- the fraction of the cross section of the new bin contained in the original one, *purity*, P;
- the ratio of the swimming uncertainty to the experimental uncorrelated uncertainty in the corresponding bin, R.

Definition of purity, efficiency, and swimming factor, F_{sw}, which were used to translate the differential cross section from the original bin to the destination one, is illustrated in Fig. 6.6. Note that in some cases for a given original bin there can be several candidates for destination bins; in this case a destination bin with maximum P, E, and minimum R was chosen. Sometimes it was profitable to combine two input bins before swimming.

The overlap of the binning schemes for the double-differential cross section from all input measurements and the new binning scheme is shown in Fig. 6.7. All results on the swimming procedure are provided in Appendix D (Figs. D.1 to D.26 and Tables D.2 to D.4). Fig. 6.8 shows P vs. E, and R vs. its denominator, the experimental uncorrelated uncertainty, for all considered datasets. Since the binning scheme was chosen to be based on the HERA-II measurements, for all bins from datasets I–III purity, efficiency and the ratio satisfy $P, E > 80\%$

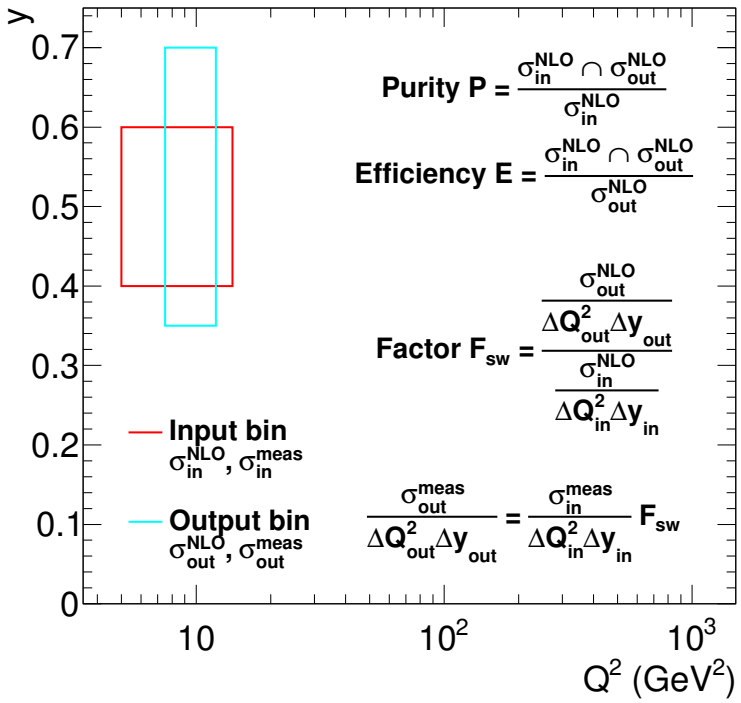

Figure 6.6: Definition of purity, efficiency and swimming factors.

and $R < 10\%$ (note that in most bins $P = E = 100\%$ and $R = 0\%$, since the original and destination bins exactly coincide).

Since the purpose of the combination is to provide the visible D^{*+} cross sections, P and E should not be too low and R not too large. Thus it is natural to introduce cuts on these quantities. Several possible values for the cuts on P and E are presented in Table 6.7 together with the number of input bins which survive the cuts. A reasonable cut was chosen to be $P, E > 50\%$. Then most of the input bins from dataset IV (29 of 31) survive this selection, although it eliminates most of the bins from datasets V and VI.[22] Therefore a decision was taken to include in the combination from the HERA-I measurements only dataset IV. In addition the cut $R < 30\%$ was introduced. This eliminated 3 other input bins from dataset IV, so finally 26 of 31 original bins were kept. The data points removed from dataset IV mainly correspond to the low-y region where larger bins were used for the HERA-I data; additionally they suffer more from the swimming uncertainties, since the NLO QCD predictions at low y have a large mass dependence. All input bins from datasets I–III survived the above cuts on P, E and R and were kept. The swimming procedure includes the contribution to dataset IV from the range $p_T(D^{*+}) > 15\,\text{GeV}$. Similar to the case of the single-differential cross-section combination (Section 6.4.1.1), the sensitivity of the shape to the beauty contribution was found to be negligible and thus was ignored.

The branching ratios for datasets I, II and IV were updated to the latest PDG value [183].

[22] For dataset V the input bins are too large, while for dataset VI the main problem is the original differential cross section as a function of Q^2 and x.

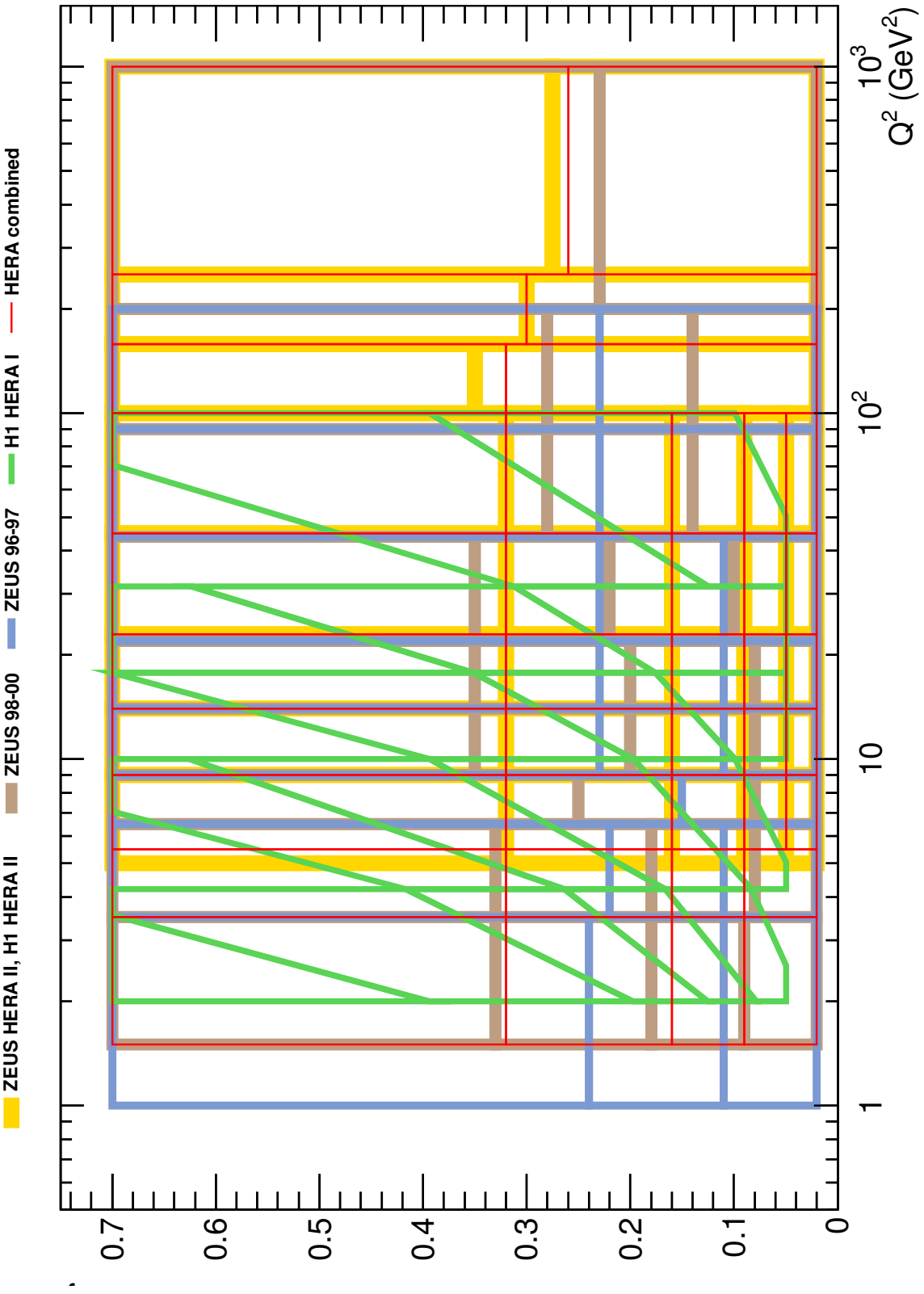

Figure 6.7: Overlap of the binning schemes for the D^{*+} double-differential cross section from input measurements and the new binning scheme.

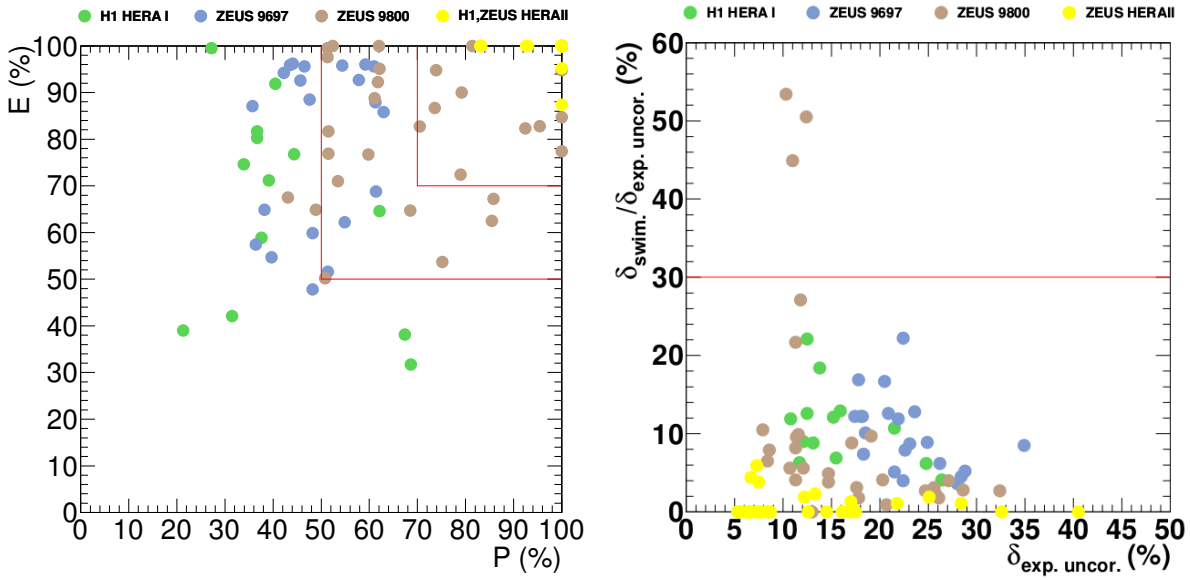

Figure 6.8: Purity vs. efficiency (left) and the ratio of the swimming uncertainty to the experimental uncorrelated uncertainty vs. the latter (right) for combination of the double-differential D^{*+} cross section. Contributions from the individual input datasets are shown separately. The solid lines show cuts $P, E > 50\%$ and $P, E > 70\%$ for (a) and $R < 30\%$ for (b).

min(P,E) (%)	H1 HERA-I	ZEUS 96–97	ZEUS 98–00	H1,ZEUS HERA-II
0	17	21	31	31
30	15	21	31	31
40	5	17	31	31
50	2	9	29	31
60	2	4	20	31
70	0	0	12	31
80	0	0	6	31

Table 6.7: Possible values for the cuts on P and E together with numbers of input bins from different measurements which survive these cuts.

A full list of considered correlated sources is provided in Appendix D (Table D.13); also input data tables used for the combination are provided (Tables D.10 to D.12). Similar to the case of the single-differential D^{*+} cross sections, all systematic uncertainties were treated as uncorrelated between H1 and ZEUS measurements, except for the branching-ratio uncertainty; although since the latter is fully correlated between all datasets, it is not changed in the combination and technically was not included in the combination but applied as an external uncertainty on the results.

6.4.2.2 Combined D^{*+} cross sections

The combined double-differential cross section with the uncorrelated, correlated and total uncertainties as a function of Q^2 and y is given in Table 6.8. The total uncertainties were obtained by adding the uncorrelated and correlated uncertainties in quadrature. A detailed breakdown of the correlated uncertainties can be found in Appendix D (Table D.16).

The individual datasets as well as the results of the combination are shown in Fig. 6.9. The combined D^{*+} cross sections exhibit significantly reduced uncertainties. The input HERA-II H1 and ZEUS datasets are similar in precision. The precision of the ZEUS HERA-I data is smaller; however this sample also provides valuable input in some bins. In the first two Q^2 bins, the combination is based on the HERA-I data only; note that the uncertainty on the combined data in these bins is a bit reduced comparing to the original one because of reduction of the correlated systematic uncertainties.

The combination has $\chi^2/n_{\text{dof}} = 38/48$; the corresponding probability is 85%, indicating consistency of the input measurements and, possibly, some overestimation of the experimental systematic uncertainties. The pull distribution is shown in Fig. 6.10. It is reasonably similar to a unit Gaussian distribution. As was seen in the results of the single-differential cross section combination (Section 6.4.1.2), although Fig. 6.9 indicates that the H1 data points lie on average below the ZEUS points, the pull distribution in Fig. 6.10 shows an overall symmetric spread of all input data around the combined results. The shifts and reductions of the correlated sources can be found in Appendix D (Table D.13).

6.4.2.3 Comparison with theoretical predictions

The combined cross section is compared to the NLO QCD predictions in the FFNS (described in Section 6.3) in Fig. 6.11. The customised calculation (see Section 6.4.1.4) is also shown. In general the predictions describe the data well. As seen before from the single-differential y cross section (Section 6.4.1.3), the central theory prediction shows a somewhat softer y distribution than the data, in particular at low Q^2. The data reach a precision of about 5–10% over a large fraction of the measured phase space, while the typical theory uncertainty ranges from 30% at low Q^2 to 10% at high Q^2, so higher-order calculations would be very helpful to match the data precision. As well as the single-differential distributions, this double-differential distribution gives extra input to test further theory improvements.

Q^2 (GeV^2)	y	$\frac{d^2\sigma}{dQ^2dy}$ (nb/GeV^2)	δ_{unc} (%)	δ_{cor} (%)	δ_{tot} (%)
1.5 : 3.5	0.02 : 0.09	4.76	12.9	2.5	13.2
	0.09 : 0.16	5.50	11.3	2.6	11.5
	0.16 : 0.32	3.00	12.0	2.6	12.3
	0.32 : 0.70	9.21×10^{-1}	20.5	2.5	20.7
3.5 : 5.5	0.02 : 0.09	2.22	11.3	2.8	11.6
	0.09 : 0.16	1.98	7.9	2.7	8.3
	0.16 : 0.32	1.09	20.2	2.7	20.4
	0.32 : 0.70	3.47×10^{-1}	14.6	2.6	14.8
5.5 : 9	0.02 : 0.05	1.06	12.3	4.4	13.1
	0.05 : 0.09	1.46	7.8	4.1	8.8
	0.09 : 0.16	1.32	5.4	4.3	6.9
	0.16 : 0.32	7.73×10^{-1}	4.9	3.9	6.3
	0.32 : 0.70	2.51×10^{-1}	5.6	4.2	7.0
9 : 14	0.02 : 0.05	5.20×10^{-1}	13.0	6.6	14.6
	0.05 : 0.09	7.68×10^{-1}	6.6	3.9	7.7
	0.09 : 0.16	5.69×10^{-1}	4.6	2.8	5.4
	0.16 : 0.32	4.12×10^{-1}	4.6	3.1	5.6
	0.32 : 0.70	1.51×10^{-1}	5.6	4.0	6.9
14 : 23	0.02 : 0.05	2.29×10^{-1}	11.4	6.3	13.0
	0.05 : 0.09	3.78×10^{-1}	6.5	4.1	7.7
	0.09 : 0.16	2.90×10^{-1}	4.8	3.3	5.8
	0.16 : 0.32	1.86×10^{-1}	5.0	3.4	6.0
	0.32 : 0.70	6.92×10^{-2}	6.2	4.4	7.7
23 : 45	0.02 : 0.05	6.91×10^{-2}	14.8	8.2	16.7
	0.05 : 0.09	1.23×10^{-1}	5.9	3.6	6.9
	0.09 : 0.16	1.14×10^{-1}	4.4	3.0	5.3
	0.16 : 0.32	7.42×10^{-2}	4.3	3.0	5.2
	0.32 : 0.70	3.21×10^{-2}	5.2	3.7	6.4
45 : 100	0.02 : 0.05	6.16×10^{-3}	33.5	11.1	35.3
	0.05 : 0.09	2.70×10^{-2}	11.0	4.4	11.8
	0.09 : 0.16	2.05×10^{-2}	8.0	3.7	8.8
	0.16 : 0.32	1.99×10^{-2}	5.4	3.2	6.3
	0.32 : 0.70	7.84×10^{-3}	6.9	4.0	7.9
100 : 158	0.02 : 0.32	4.12×10^{-3}	8.2	4.1	9.2
	0.32 : 0.70	2.18×10^{-3}	11.1	4.1	11.9
158 : 251	0.02 : 0.30	1.79×10^{-3}	10.2	4.4	11.1
	0.30 : 0.70	9.28×10^{-4}	11.6	4.6	12.5
251 : 1000	0.02 : 0.26	1.31×10^{-4}	14.5	4.7	15.3
	0.26 : 0.70	1.18×10^{-4}	12.7	5.0	13.6

Table 6.8: The combined double-differential D^{*+} cross section as a function of Q^2 and y, with its uncorrelated (δ_{unc}), correlated (δ_{cor}) and total (δ_{tot}) uncertainties.

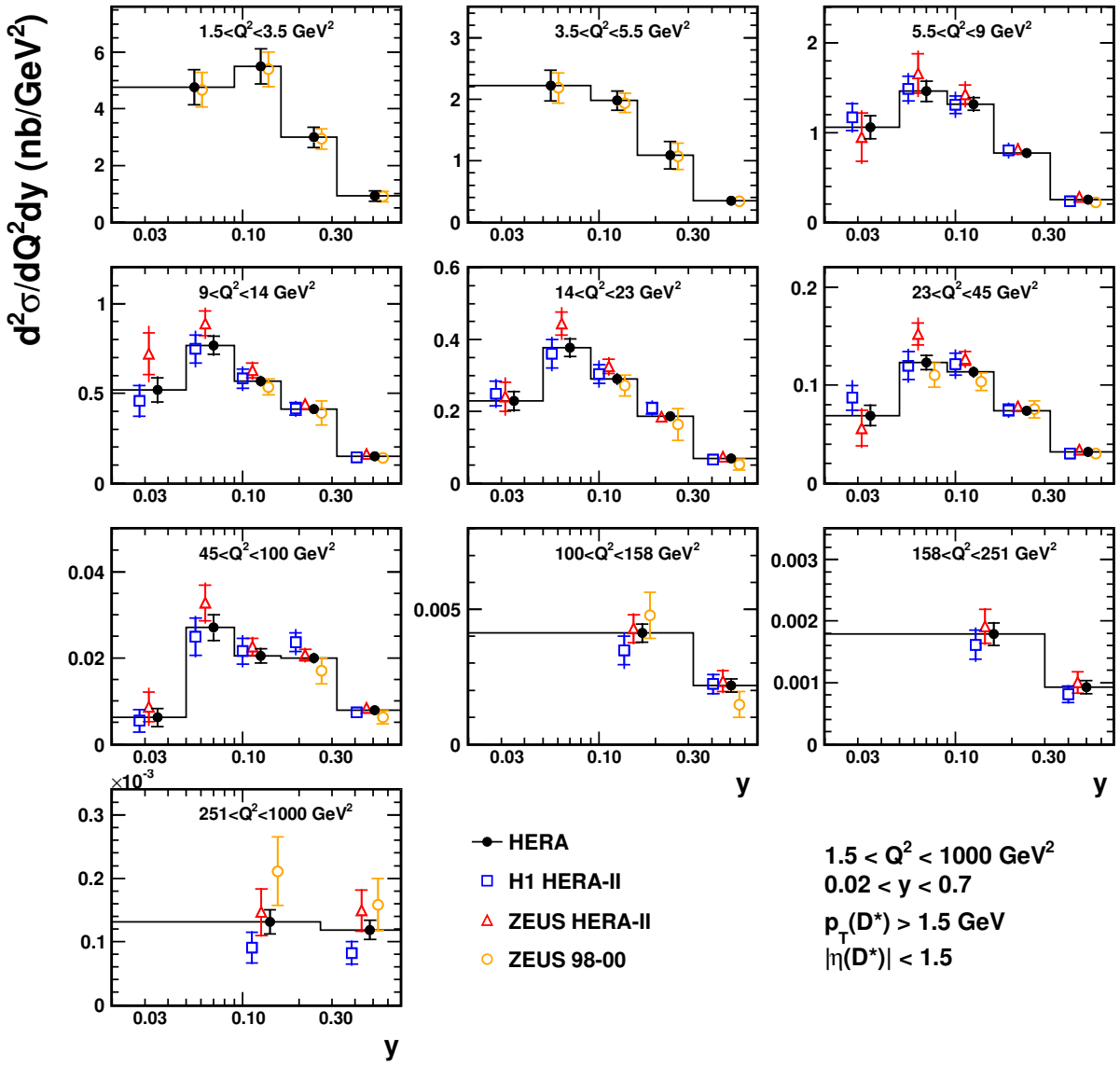

Figure 6.9: Double-differential D^{*+} cross sections as a function of Q^2 and y. The triangles, open squares and open circles are the D^{*+} cross sections before combination, shown with a small horizontal offset for better visibility. The filled points are the combined D^{*+} cross sections. The inner error bars indicate the uncorrelated part of the uncertainties. The outer error bars represent the total uncertainties. The histogram indicates the binning used to calculate the D^{*+} cross sections.

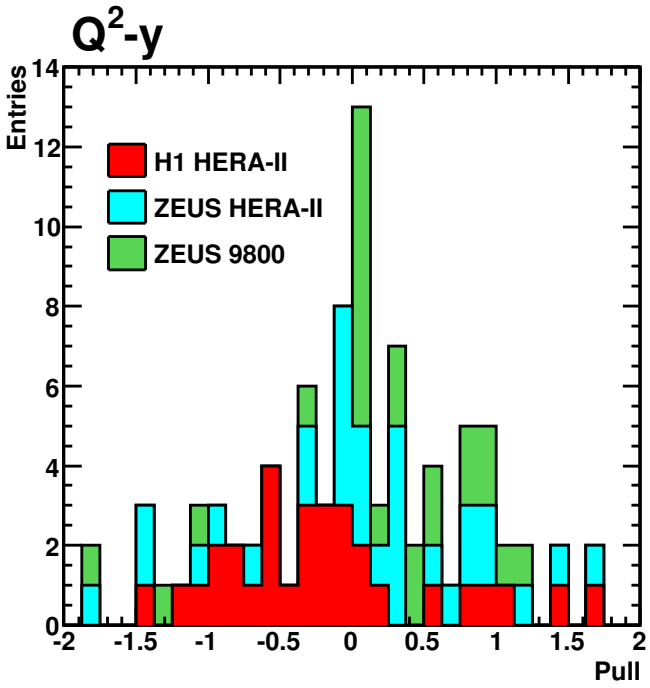

Figure 6.10: The pull distribution for the combination of the double-differential D^{*+} cross sections as a function of Q^2 and y. Contributions from the individual input datasets are shown separately.

6.5 Combination of charm reduced cross sections

This Section describes a combination of HERA charm-production measurements in DIS at the level of the reduced cross sections. The primary aim of the analysis was to obtain one consistent dataset which provides information on charm production in DIS in the full phase space, integrated over p_T and η of a charm quark, because most theoretical predictions exist only for this inclusive quantity. Since all methods used to measure charm production at HERA, introduced in Section 3.1.3, have limited phase-space coverage and thus should be corrected to the full phase space using theory, there are no reasons to restrict this combination to a specific phase space and binning scheme, and all datasets from H1 [64, 65, 134, 141] and ZEUS [19, 59, 136–140] were included for which the necessary information on systematic uncertainties needed for the combination is available and which have not been superseded.

The results reported in this Section represent an extension of the previous combination of H1 and ZEUS charm measurements [66] with three recent ZEUS datasets [19, 137, 139] which appeared after the combination [66] has been performed. The intention was to keep the procedure as close as possible to [66] to allow for a consistent comparison with the published results.

Subsection 6.5.1 introduces the combination details: the input datasets and treatment of their experimental uncertainties (Section 6.5.1.1), definition of the reduced cross sections and the combination Q^2–x grid (Section 6.5.1.2) and extraction of the reduced cross sections from the visible ones, needed to put the input measurements into the common grid (Section 6.5.1.3). In Section 6.5.2 the results of the combination are presented and compared to the results

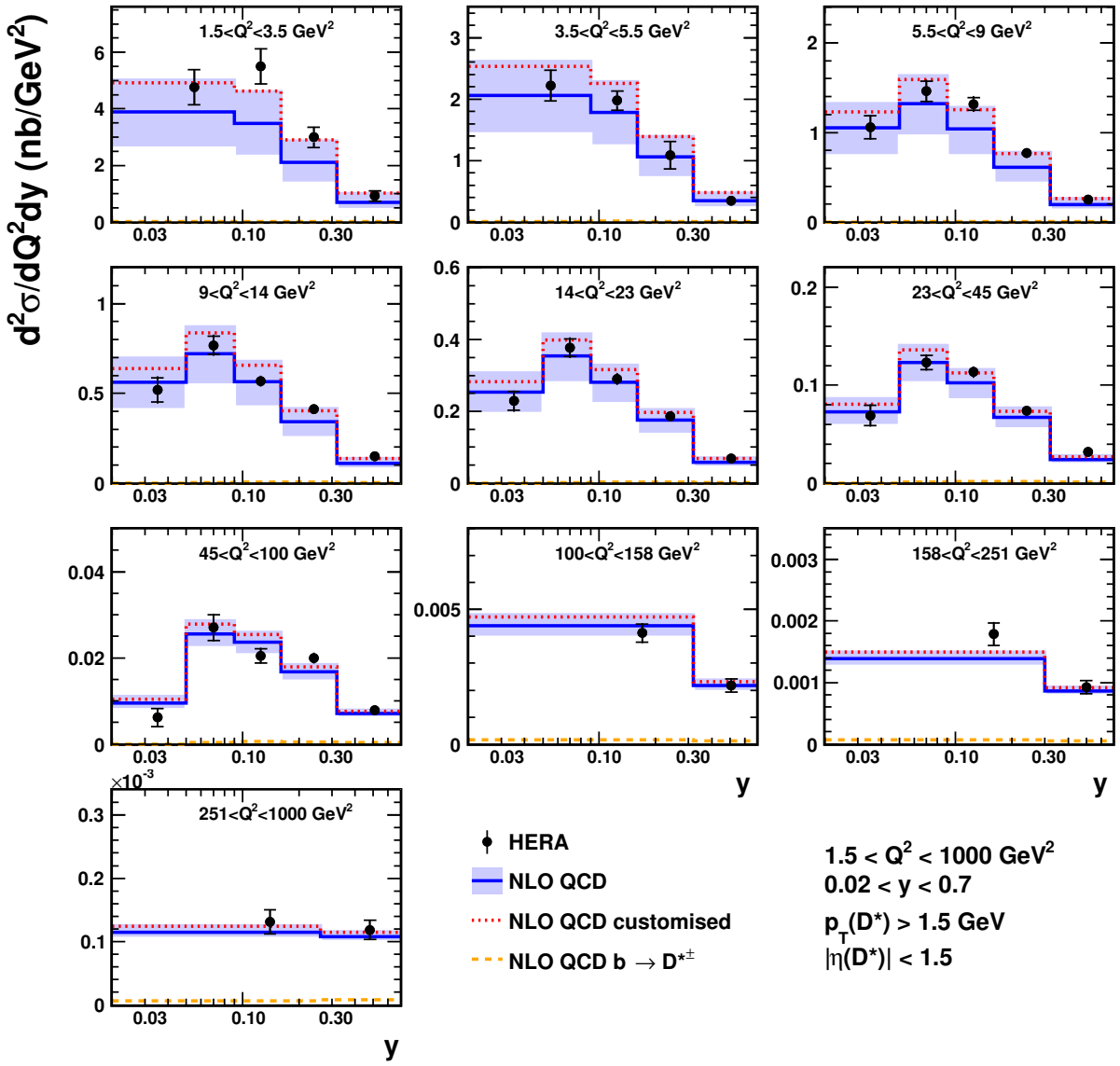

Figure 6.11: Double-differential D^{*+} cross section as a function of Q^2 and y. The data points are the combined D^{*+} cross sections. The inner error bars indicate the uncorrelated part of the uncertainties. The outer error bars represent the total uncertainties. Also shown are the NLO predictions from HVQDIS (including the beauty contribution), and their uncertainty band. A customised NLO calculation (dotted line) is also shown.

from [66]. In Section 6.5.3 the combined data are compared to the theoretical predictions in the FFNS and the running and pole charm masses are extracted from the data, while Section 6.5.4 is devoted to a comparison with the theoretical predictions in different VFNS and a determination of optimal charm-quark mass parameters for these schemes.

6.5.1 Combination details

The combination procedure closely follows the one used for the previous HERA charm combination [66], referred to as 'HERA 2012'.

6.5.1.1 Input data samples

The datasets included in the combination are listed in Table 6.9 and correspond to 209 different cross-section measurements[23] [24] . The combination includes measurements of charm production performed using different tagging techniques: the reconstruction of particular decays of D-mesons (datasets 2–7, 9, 10), the inclusive analysis of tracks exploiting lifetime information (datasets 1, 11) and the reconstruction of muons from charm semi-leptonic decays (dataset 8).

Datasets 1–8 have been used in the previous 'HERA 2012' combination, while datasets 9–11 were newly included. Note that dataset 9 replaced one of the datasets from 'HERA 2012', which is its subset.

Correlations between systematic uncertainties of different measurements were accounted for as explained in Section 6.2.2. All experimental systematic uncertainties were treated as independent between H1 and ZEUS. A full list of considered correlated sources is provided in Appendix E (Tables E.1 to E.2). The total uncorrelated systematic uncertainties were obtained by adding individual ones in quadrature.[25]

6.5.1.2 Reduced cross sections and common Q^2–x grid

The quantities to be combined are the charm reduced cross sections, defined as follows:

$$\begin{aligned} \sigma_{\text{red}}^{c\bar{c}} &= \frac{\mathrm{d}^2\sigma^{c\bar{c}}}{\mathrm{d}x\mathrm{d}Q^2} \cdot \frac{xQ^4}{2\pi\alpha(Q^2)^2\,(1+(1-y)^2)} \\ &= F_2^{c\bar{c}} - \frac{y^2}{1+(1-y)^2} F_L^{c\bar{c}}. \end{aligned} \tag{6.20}$$

The superscript $c\bar{c}$ indicates the presence of a $c\bar{c}$ pair in the final state, including all possible QCD production processes. The cross section $\mathrm{d}^2\sigma^{c\bar{c}}/\mathrm{d}x\mathrm{d}Q^2$ is given at the Born level without

[23] From the two sets of measurements in [65], the one in the wider $p_T(D^{*+})$ and $\eta(D^{*+})$ range was chosen and referred to as dataset I; this is another dataset from the one that was used in the combination of the D^{*+} cross sections, described in Section 6.4.

[24] A misprint was found in Table 3 of [136]: for the rows 22 and 23 the y ranges should read 0.22 – 0.10 and 0.10 – 0.02, respectively. Another misprint was found in Table 2 of [140]: the Q^2 range in the last row should be 400 : 10000 GeV^2.

[25] For dataset 11 an additional uncorrelated systematic uncertainty was considered: an uncertainty of 100% on $\Delta_{\text{had}} = C_{\text{had}} - 1$ (Table 6 of [19]).

Dataset	Tagging method	Q^2 range [GeV^2]	N	$\mathcal{L}$ [pb^{-1}]	$\sqrt{s}$ [GeV]
1 H1 VTX [141]	Inclusive track lifetime	5 – 2000	29	245	318
2 H1 D^{*+} HERA-I [134]	D^{*+}	2 – 100	17	47	318
3 H1 D^{*+} HERA-II (med. Q^2) [65]	D^{*+}	5 – 100	25	348	318
4 H1 D^{*+} HERA-II (high Q^2) [64]	D^{*+}	100 – 1000	6	351	318
5 ZEUS D^{*+} 96-97 [59]	D^{*+}	1 – 200	21	37	300
6 ZEUS D^{*+} 98-00 [136]	D^{*+}	1.5 – 1000	31	82	318
7 ZEUS D^0 2005 [138]	$D^{0,\text{no}D^{*+}}$	5 – 1000	9	134	318
8 ZEUS μ 2005 [140]	μ	20 – 10000	8	126	318
9 ZEUS D^+ HERA-II [139]	D^+	5 – 1000	14	354	318
10 ZEUS D^{*+} HERA-II [137]	D^{*+}	5 – 1000	31	363	318
11 ZEUS VTX HERA-II [19]	Inclusive track lifetime	5 – 1000	18	354	318

Table 6.9: Datasets used in the combination of the charm reduced cross sections. For each dataset the charm tagging method, the Q^2 range, the number of cross-section measurements, N, the integrated luminosity, $\mathcal{L}$, and the centre-of-mass energy, $\sqrt{s}$, are given. The dataset with the $D^{0,\,\text{no}\,D^{*+}}$ tagging method is based on an analysis of D^0 mesons not originating from detectable D^{*+} decays.

QED and electro-weak radiative corrections, except for the running electromagnetic coupling, $\alpha(Q^2)$.

The reduced cross sections (and not the structure functions $F_2^{c\bar{c}}$) were chosen for the combination because they are proportional to the directly measured double-differential cross sections. Despite the fact that $F_2^{c\bar{c}}$ and $F_L^{c\bar{c}}$ depend only on Q^2 and x, the presence of y in definition 6.20 leads to dependence of $\sigma_{\text{red}}^{c\bar{c}}$ on the centre-of-mass energy, $\sqrt{s}$. Following the majority of the datasets listed in Table 6.9, $\sigma_{\text{red}}^{c\bar{c}}$ were defined in the combination at the centre-of-mass energy $\sqrt{s} = 318\,\text{GeV}$.

The values of $\sigma_{\text{red}}^{c\bar{c}}$ for individual measurements were determined at the 52 (Q^2, x) points of a common grid, chosen such that they are close to the centre-of-gravity in Q^2 and x of the corresponding bins, taking advantage of the fact that the binning schemes used by the H1 and ZEUS experiments are similar (the grid points were kept the same as in the 'HERA 2012' combination). For all but three grid points, at least 2 measurements entered into the combination; for points in the medium Q^2 bins, the number of input measurements reached 7. The phase space of the combined cross sections is given by

$$\begin{aligned} 2.5 \leq Q^2 \leq 2000\,\text{GeV}^2, \\ 3 \times 10^{-5} \leq x \leq 5 \times 10^{-2}. \end{aligned} \tag{6.21}$$

6.5.1.3 Extrapolation and corrections

The results of the inclusive lifetime analysis (dataset 1) were directly taken from the original measurement in the form of $\sigma_{\mathrm{red}}^{c\bar{c}}$. For all other measurements the inputs to the combination were visible cross sections, $\sigma_{\mathrm{vis,bin}}$, defined as the D-, μ- or jet-production cross sections in a particular p_T and η range, in bins of Q^2 and y or x.

The reduced cross sections $\sigma_{\mathrm{red}}^{c\bar{c}}$were obtained from the visible cross sections $\sigma_{\mathrm{vis,bin}}$ measured in a limited phase space using a common theory according to the procedure described in Section 6.2.3: the reduced charm cross section at a reference (x, Q^2) point is given by

$$\sigma_{\mathrm{red}}^{\mathrm{c\bar{c}}}(x, Q^2) = \sigma_{\mathrm{vis,bin}} \frac{\sigma_{\mathrm{red}}^{\mathrm{c\bar{c},th}}(x, Q^2)}{\sigma_{\mathrm{vis,bin}}^{\mathrm{th}}}. \tag{6.22}$$

To calculate $\sigma_{\mathrm{red}}^{\mathrm{c\bar{c},th}}(x, Q^2)$ and the visible cross sections $\sigma_{\mathrm{vis,bin}}^{\mathrm{th}}$, the NLO QCD FFNS theory set-up was used, consistent with the previous 'HERA 2012' combination.[26] This set-up is almost identical to the one described in Section 6.3, except for the following minor changes:

1. in the fragmentation process, calculation of the hadron energy and Lorentz boost were done by using the charm-quark mass[27];

2. if it needed to be subtracted, the beauty contribution was evaluated using the estimates of the corresponding papers (based on MC re-normalised to data).

The extrapolation factors, $R = \sigma_{\mathrm{bin}}^{\mathrm{th}}/\sigma_{\mathrm{vis,bin}}^{\mathrm{th}}$, where $\sigma_{\mathrm{bin}}^{\mathrm{th}}$ is the cross section in the full p_T, η phase space, vary in a wide range: from $R \gtrsim 1$ at high Q^2 to $R \sim 5$ at low Q^2 and high x. For dataset 5 the extrapolation procedure includes also the centre-of-mass energy correction.

The extrapolation uncertainties were estimated from the variations described in Section 6.3, and were treated as correlated between datasets 2-11[28]. For dataset 1 the extrapolation uncertainties (except for the longitudinal fragmentation) do not appear explicitly and were covered by the experimental systematic uncertainties. The dominant contributions arise from the variation of the renormalisation and factorisation scales (average 5–6%, reaching 15% at lowest Q^2) and from the variation of the fragmentation function (average 3–5%).

Prior to the combination, datasets 1 and 11 were transformed, when needed, from the grids used in the original papers to the common grid using the NLO FFNS calculation. The corrections were always smaller than 25% and the associated uncertainties, obtained by varying the charm mass, the scales and the PDFs, were negligible. All D-meson cross sections were updated using the most recent branching ratios [183].

[26] The fully consistent theory set-up allowed for using existing input tables for $\sigma_{\mathrm{red}}^{c\bar{c}}$for datasets 1–8, available from [66], and straightforward comparison of new results of the combination with the 'HERA 2012' results; also note that two of three newly included ZEUS measurements (datasets 10 and 11) already published $\sigma_{\mathrm{red}}^{c\bar{c}}$extracted from the visible cross sections using exactly this theoretical set-up.

[27] Except for dataset 8.

[28] The PDF uncertainties were neglected for the newly included datasets 9-11, since for the other ones they were found to be negligibly small (1% on average) [66].

6.5.2 Combined charm cross sections

In total, 209 measurements were combined to 52 reduced cross-section measurements. The data show good consistency with $\chi^2/n_{\text{dof}} = 117/157$; the corresponding probability is 99.3%, indicating conservative estimation of the experimental systematic uncertainties of the input measurements.[29] The pull distribution is shown in Fig. 6.12. It is reasonably similar to a unit Gaussian distribution.

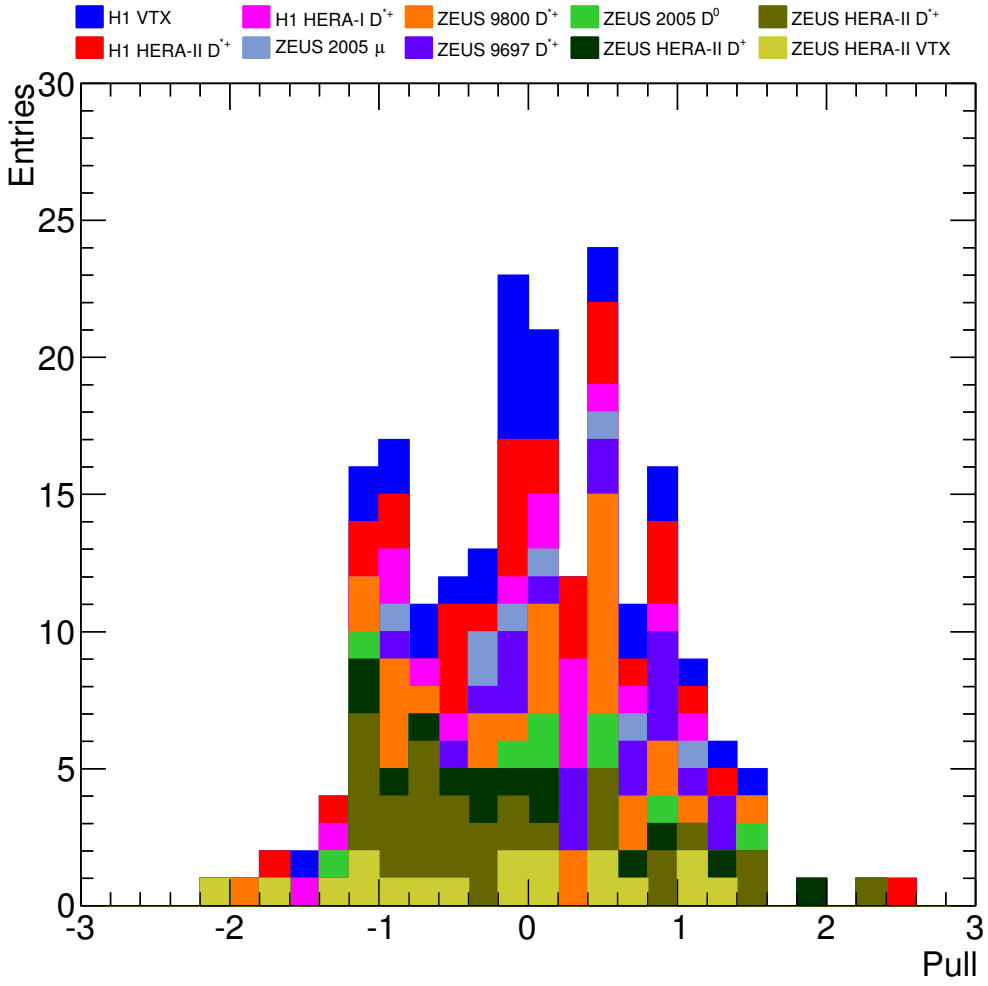

Figure 6.12: The pull distribution for the combination of the charm reduced cross sections. Contributions from the individual input datasets are shown separately.

The values of the combined cross section $\sigma_{\text{red}}^{c\bar{c}}$ together with uncorrelated, correlated and total uncertainties are given in Table 6.10. A detailed breakdown of the correlated uncertainties can be found in Appendix E (Tables E.3 to E.4).

The individual datasets as well as the results of the combination are shown in Fig. 6.13.[30] The combined cross sections exhibit significantly reduced uncertainties. The input H1 and ZEUS

[29] In this case also the uncertainties on the combined results from χ^2 variation of 1 must be conservative.
[30] The same plots, but separately for each Q^2 bin, are available in Appendix E (Figs. E.1to E.12).

Q^2 (GeV^2)	x	$\sigma_{\text{red}}^{c\bar{c}}$	δ_{unc} (%)	δ_{cor} (%)	δ_{tot} (%)
2.5	0.00003	0.1215	13.5	8.2	15.8
2.5	0.00007	0.1144	8.7	8.2	11.9
2.5	0.00013	0.0940	9.6	7.8	12.4
2.5	0.00018	0.0966	9.2	7.2	11.7
2.5	0.00035	0.0586	8.6	6.5	10.8
5	0.00007	0.1568	14.9	7.7	16.8
5	0.00018	0.1594	8.0	6.0	10.0
5	0.00035	0.1208	6.9	5.6	8.9
5	0.00100	0.0839	9.2	5.2	10.6
7	0.00013	0.2333	5.5	6.7	8.7
7	0.00018	0.2088	8.7	7.1	11.2
7	0.00030	0.1833	3.7	5.2	6.3
7	0.00050	0.1673	3.5	4.7	5.8
7	0.00080	0.1249	6.1	4.4	7.5
7	0.00160	0.0958	5.3	4.7	7.1
12	0.00022	0.3279	5.8	5.9	8.3
12	0.00032	0.3041	4.5	5.6	7.2
12	0.00050	0.2470	3.3	4.1	5.3
12	0.00080	0.1882	3.0	3.9	4.9
12	0.00150	0.1586	4.2	4.3	6.0
12	0.00300	0.1106	5.5	4.9	7.3
18	0.00035	0.3306	6.3	5.4	8.3
18	0.00050	0.3030	4.0	5.7	7.0
18	0.00080	0.2685	3.1	3.6	4.7
18	0.00135	0.2134	2.6	3.8	4.6
18	0.00250	0.1723	2.7	3.7	4.5
18	0.00450	0.1314	5.9	5.2	7.8
32	0.00060	0.4348	14.6	4.9	15.4
32	0.00080	0.3778	3.5	4.4	5.6
32	0.00140	0.2874	2.7	3.2	4.2
32	0.00240	0.2241	3.3	3.3	4.7
32	0.00320	0.2136	5.3	3.8	6.5
32	0.00550	0.1610	4.7	3.8	6.0
32	0.00800	0.1022	9.8	5.4	11.2
60	0.00140	0.3380	4.6	3.8	5.9
60	0.00200	0.3440	3.9	2.6	4.7
60	0.00320	0.2709	3.5	3.0	4.6
60	0.00500	0.1993	3.6	3.0	4.7
60	0.00800	0.1712	6.0	3.0	6.7
60	0.01500	0.1014	9.9	4.2	10.8
120	0.00200	0.3560	6.5	4.0	7.6
120	0.00320	0.3619	9.5	2.7	9.9
120	0.00550	0.2309	5.2	3.3	6.2
120	0.01000	0.1605	4.7	2.9	5.5
120	0.02500	0.0888	13.9	3.7	14.4
200	0.00500	0.2510	6.6	3.9	7.7
200	0.01300	0.1773	5.5	3.3	6.4
350	0.01000	0.2264	8.1	4.0	9.0
350	0.02500	0.1079	10.0	4.1	10.8
650	0.01300	0.2124	9.5	5.6	11.1
650	0.03200	0.0993	11.4	7.9	13.9
2000	0.05000	0.0655	26.3	12.9	29.3

Table 6.10: The combined reduced cross sections of charm production with their uncorrelated (δ_{unc}), correlated (δ_{cor}) and total (δ_{tot}) uncertainties.

data in total are similar in precision and contribute roughly equally to the averaged results. The combined data are significantly more precise than any of the individual input datasets. The uncertainty of the combined results is about 8% on average and reaches 4% in the region of small x and medium Q^2. This is an improvement of about a factor of 2.5 with respect to each of the most precise datasets in the combination.

There are in total 78 sources of correlated systematic uncertainty, including global normalisations, characterising the separate datasets. The shifts and the reduction of the correlated uncertainties can be found in Appendix E (Tables E.1 to E.2). None of these systematic sources shifted by more than 1.3 standard deviation of the nominal value in the averaging procedure. The influence of several correlated systematic uncertainties was reduced by more than a factor of two, while on average the reduction factors are about 20% of the nominal standard devia-

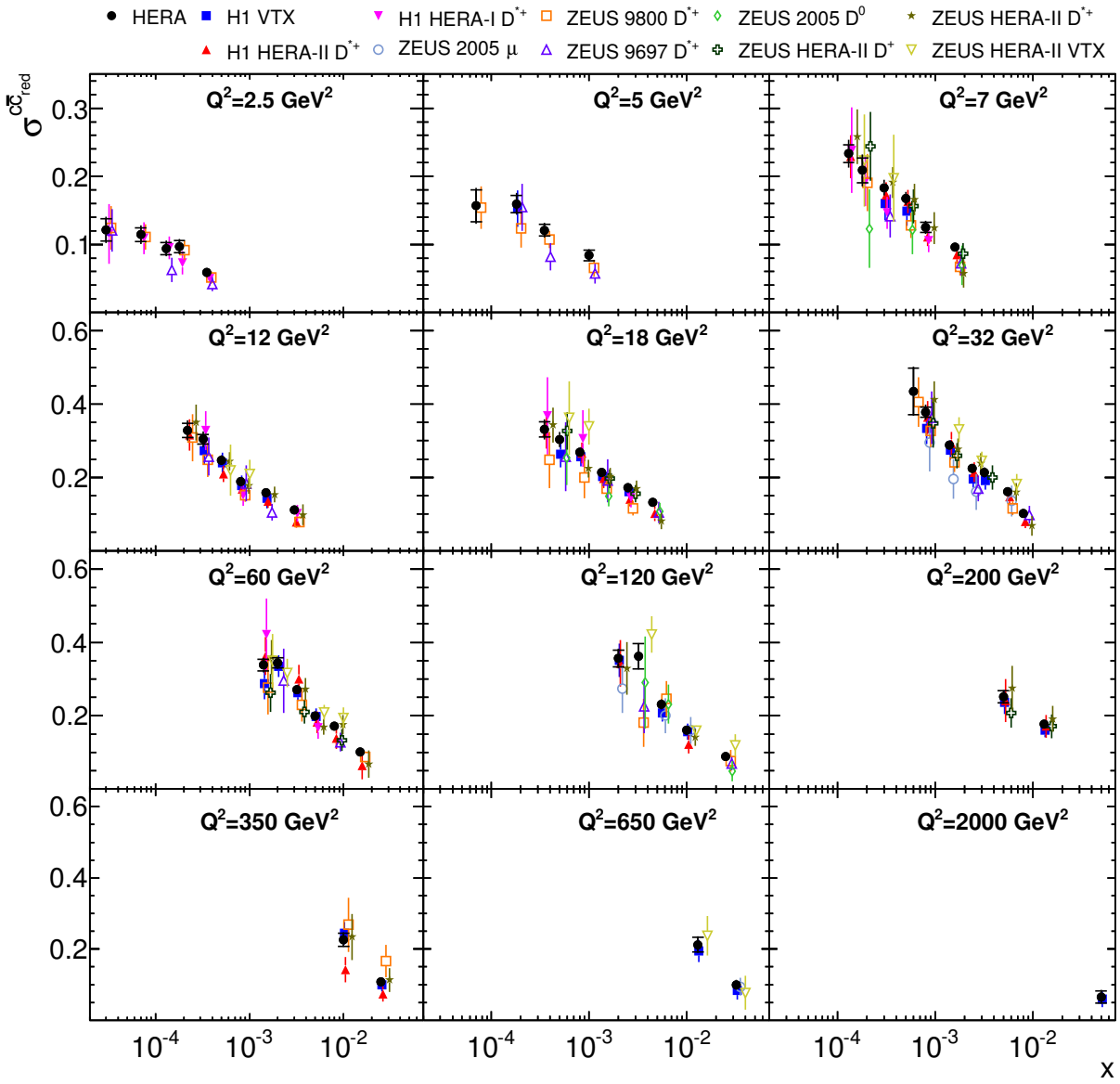

Figure 6.13: Combined measurements of $\sigma_{red}^{c\bar{c}}$ (closed circles) shown as a function of x for given values of Q^2. The input measurements are also shown with different markers. For the combined data, the inner error bars indicate the uncorrelated part of the uncertainties and the outer error bars represent the total uncertainties. For presentation purposes each individual measurement is shifted in x.

tion. The reductions can be traced mainly to the different charm-tagging methods, and to the requirement that different measurements probe the same cross section at each (x, Q^2) point. The reduction of systematic uncertainties propagated to the other average points, including those which are based solely on the less precise measurements. Due to this propagation the uncertainty on the combined data in the points, to which only one input measurement contributes, was also reduced compared to the original one.

6.5.2.1 Comparison to previous combination

Comparing $\chi^2/n_{\text{dof}} = 117/157$ to the 'HERA 2012' result, $\chi^2/n_{\text{dof}} = 62/103$, the individual contributions from the newly included measurements are 11/14, 30/31 and 18/18 for datasets 9, 10 and 11, respectively, and the total contribution from all three datasets is 59/63, thus the new measurements are perfectly consistent.

The combined data are compared to the 'HERA 2012' results in Fig. 6.14; for a more detailed comparison Fig. 6.15 shows the same results normalised to the 'HERA 2012' and Fig. 6.16 shows the comparison of the relative uncertainties. The new results are consistent with the previously published ones, although on average they lie slightly above. This is explained by taking into account the changes in the shifts of correlated systematic uncertainties, which affect all points simultaneously (mainly the theory-related sources and luminosity uncertainties, see Tables E.1 to E.2 in Appendix E).

The new combined cross sections exhibit reduced uncertainties. Typically, the reduction of the uncorrelated and correlated uncertainties contribute about equally to the total improvement. At medium Q^2, where the new measurements contribute directly, the improvement is on average of the order of 20% of the 'HERA 2012' uncertainties, reaching 35% in several points, and in the low and very high Q^2 bins the improvement is 5–15% owing to the reduction of the correlated uncertainties only.

6.5.3 Comparison to theoretical predictions and QCD analysis in FFNS

Fig. 6.17 presents a comparison of the NLO QCD predictions in the FFNS, calculated as described in Section 6.3, to the combined data. This is more clearly seen in the ratio to the theoretical predictions, shown in Fig. 6.18. The predictions describe the data well within the uncertainties in the whole kinematic range of the combination, although the central theoretical curve underestimates the data normalisation, as observed also in the combination of the D^{*+} cross sections (Sections 6.4.1.3, 6.4.1.3). The 'customised' NLO calculation (Section 6.4.1.4), while it was determined mainly from the exclusive D^{*+} quantities in the restricted phase space, provides an improved description of the reduced cross-section normalisation, although it does not improve the description of the x shape.

In Fig. 6.19 the data are compared to the predictions by the ABM group in the FFNS at NLO and NNLO, based on the running-mass scheme [17, 215]. The uncertainties on the predictions include the uncertainties on the charm mass, which dominate at small Q^2. The predictions at NLO and NNLO are very similar and describe the data well in the whole kinematic range of the measurement.

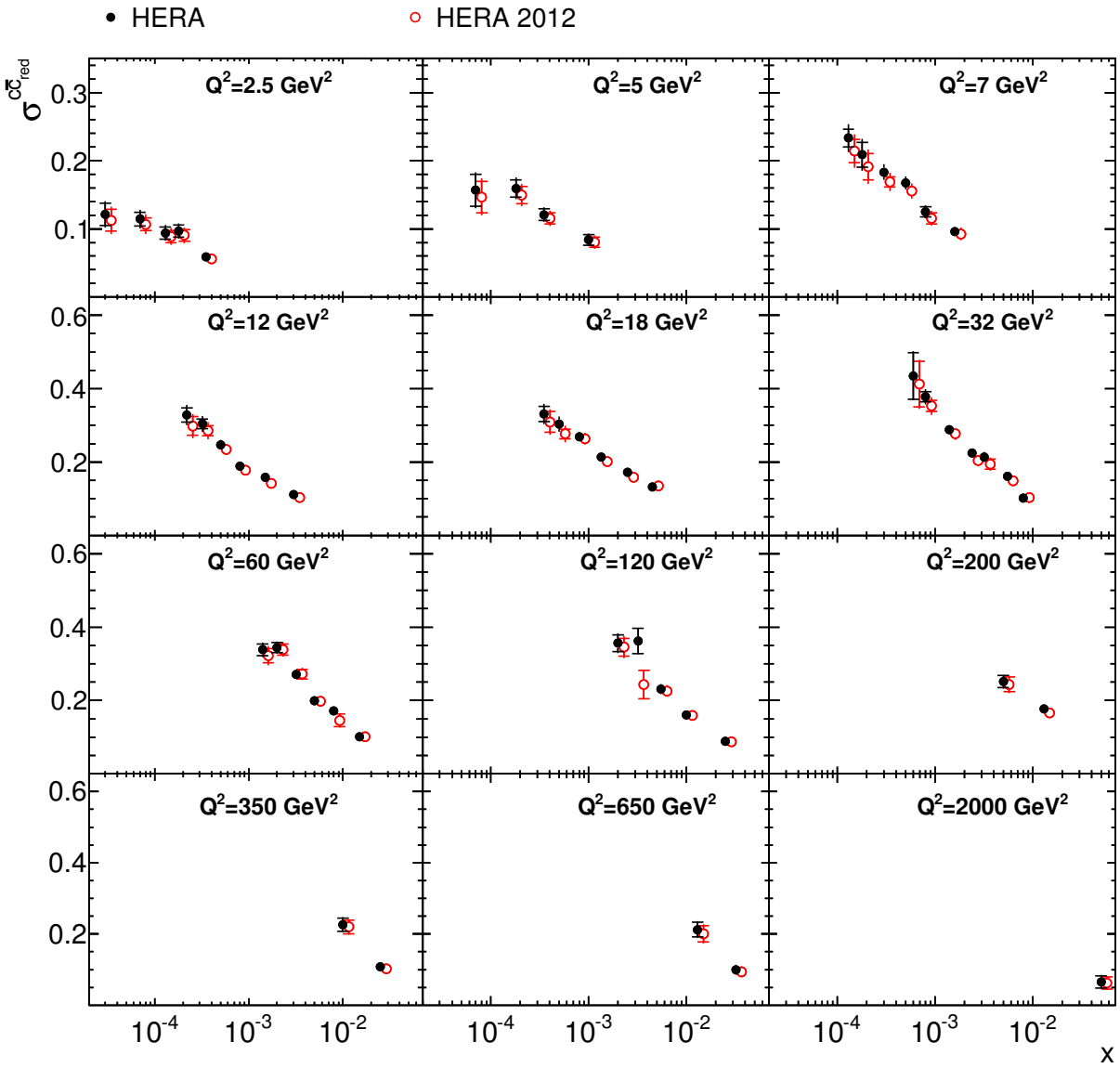

Figure 6.14: Combined charm reduced cross sections (closed circles) shown as a function of x for given values of Q^2, compared to the 'HERA 2012' results (open circles). The error bars represent the total uncertainty. The inner error bars indicate the uncorrelated part of the uncertainties. For presentation purposes, the 'HERA 2012' results are slightly shifted in x.

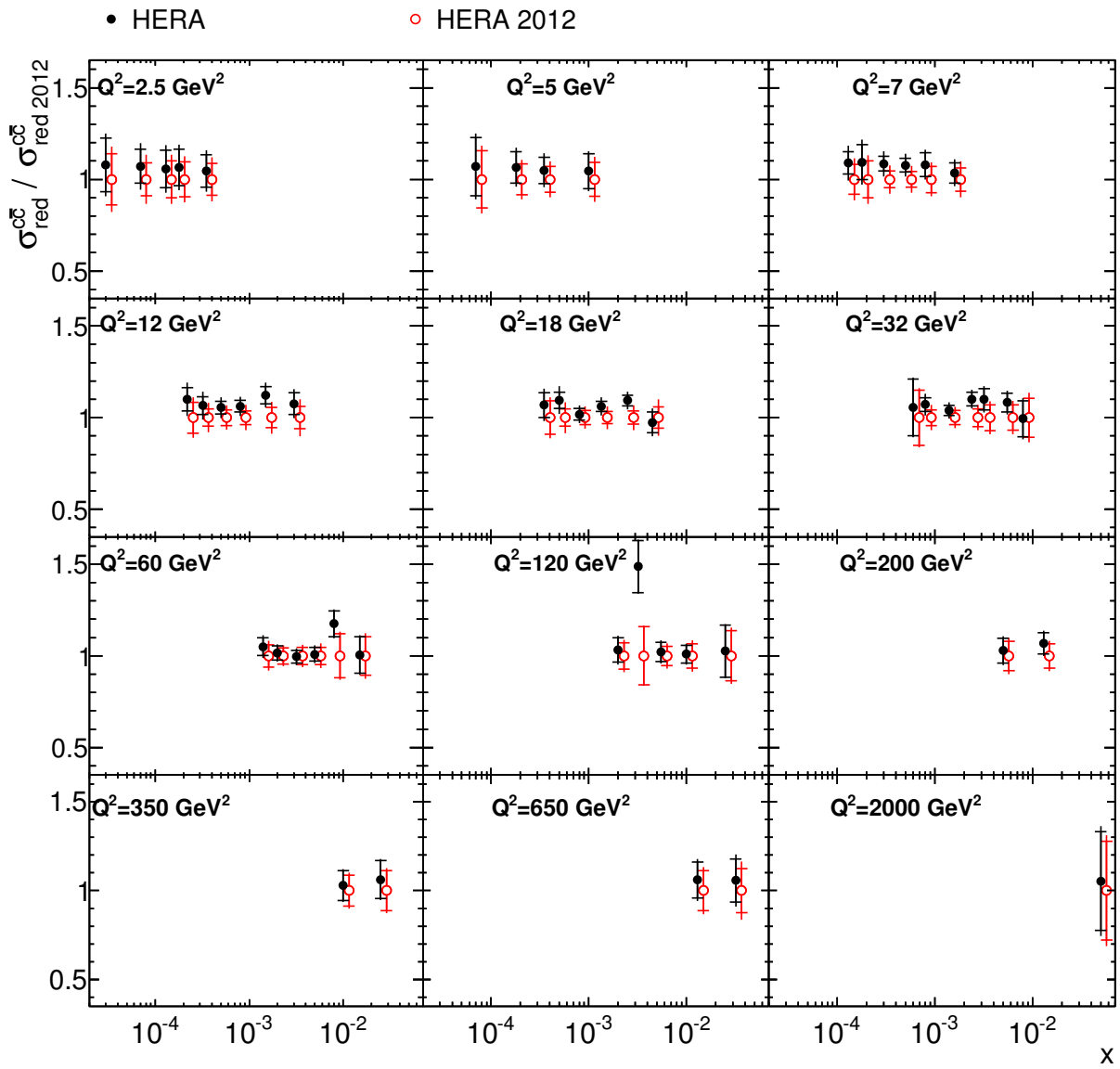

Figure 6.15: Combined charm reduced cross sections (closed circles) shown as a function of x for given values of Q^2, normalised to the 'HERA 2012' results (open circles). The error bars represent the total uncertainty. The inner error bars indicate the uncorrelated part of the uncertainties. For presentation purposes the 'HERA 2012' results are slightly shifted in x.

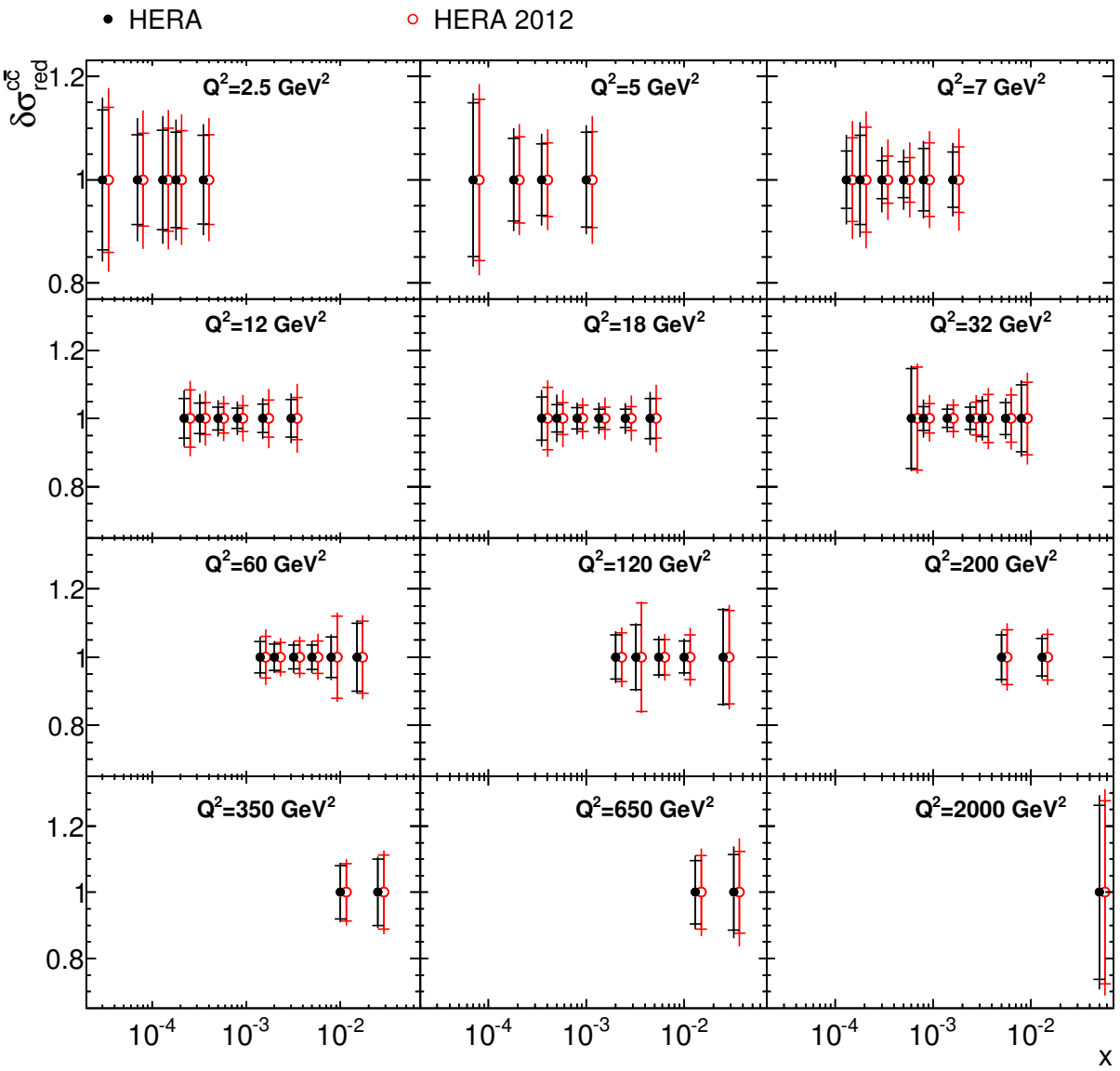

Figure 6.16: The relative uncertainties of the combined charm reduced cross sections (closed circles) shown as a function of x for given values of Q^2, compared to the 'HERA 2012' results (open circles). The error bars represent the total uncertainty. The inner error bars indicate the uncorrelated part of the uncertainties. For presentation purposes the 'HERA 2012' results are slightly shifted in x.

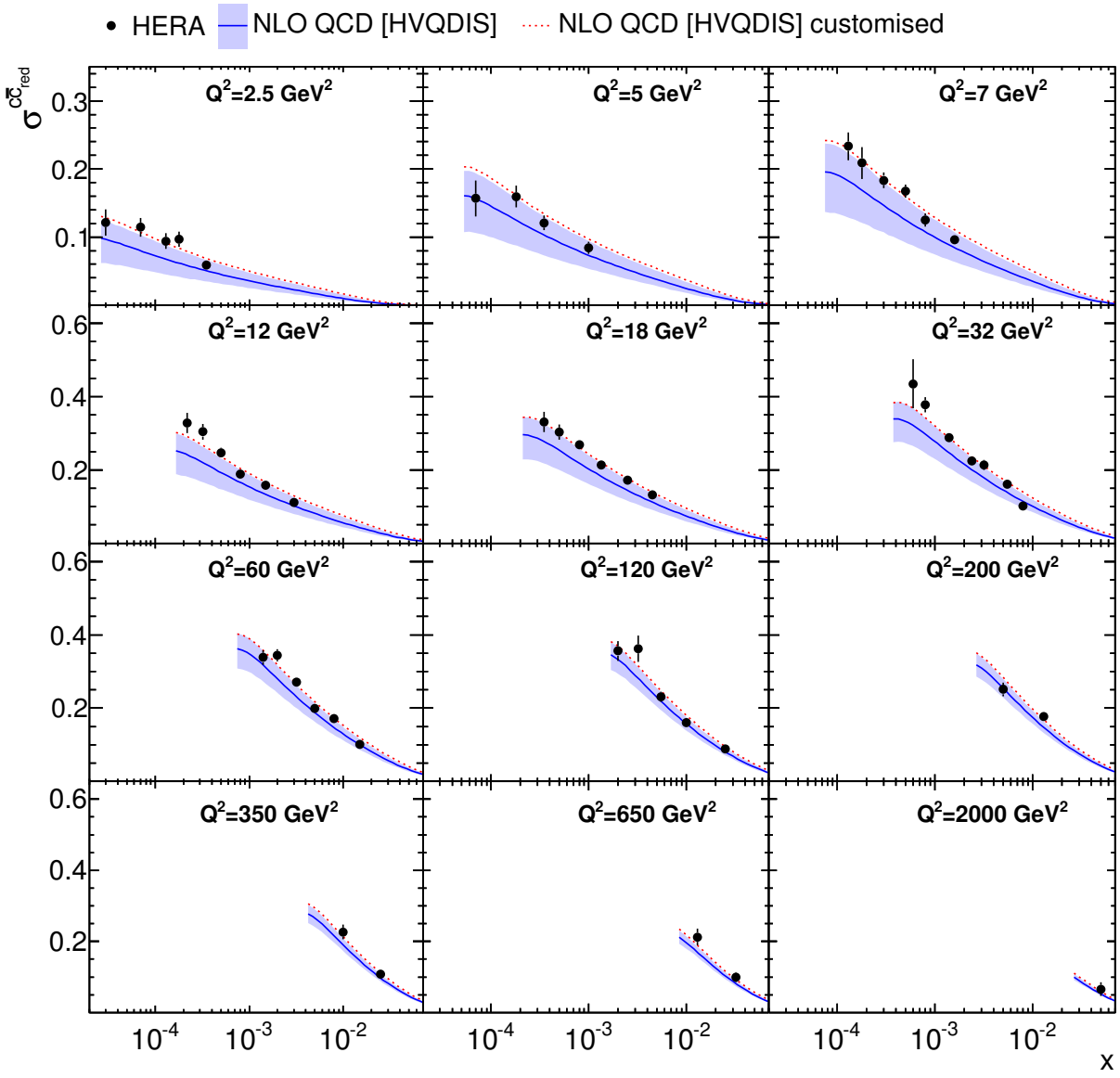

Figure 6.17: Combined measurements of $\sigma^{c\bar{c}}_{red}$ (closed circles) shown as a function of x for given values of Q^2, compared to the NLO QCD FFNS theoretical predictions (a solid line with a band). The customised NLO calculation (a dotted line) is also shown.

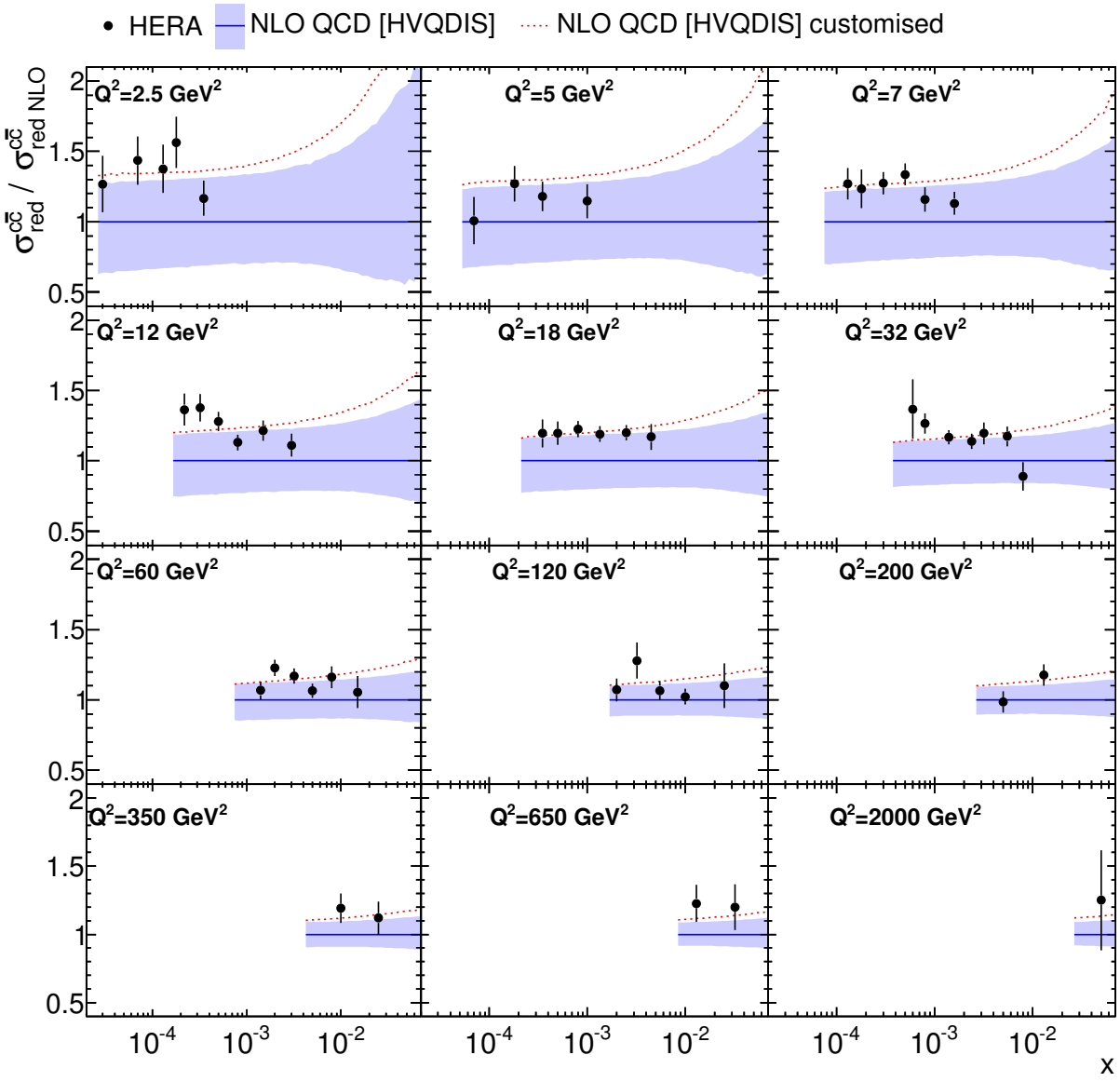

Figure 6.18: Combined measurements of $\sigma_{red}^{c\bar{c}}$ (closed circles) shown as a function of x for given values of Q^2, normalised to the NLO QCD FFNS theoretical predictions (a solid line with a band). The customised NLO calculation is also shown (a dotted line).

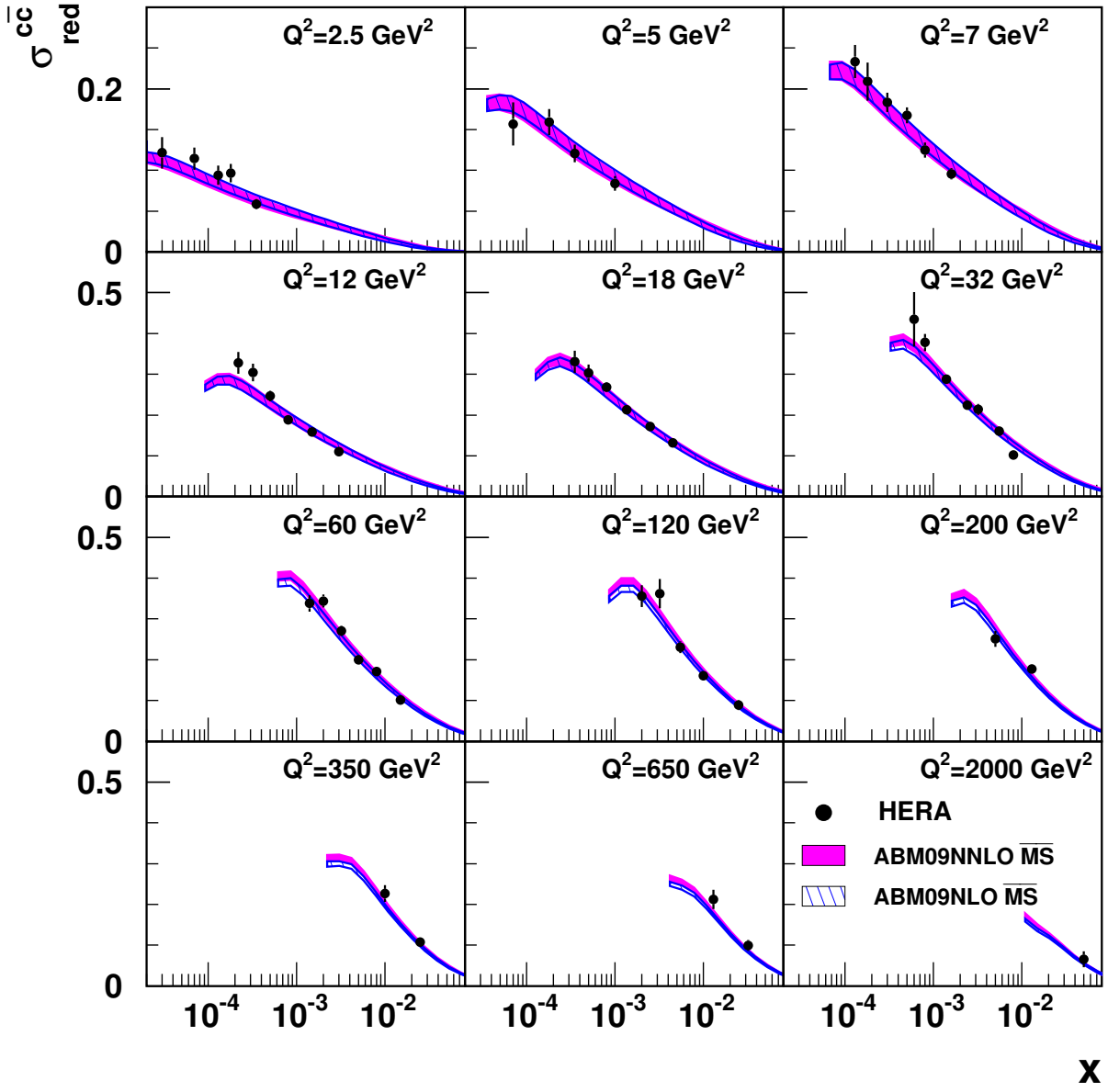

Figure 6.19: Combined measurements of $\sigma_{red}^{c\bar{c}}$ (closed circles) shown as a function of x for particular Q^2, compared to the prediction by the ABM group at NLO (hashed band) and NNLO (shaded band) in the FFNS using the $\overline{\text{MS}}$ definition for the charm-quark mass.

6.5.3.1 Extraction of pole and running charm mass

The strong sensitivity of the theoretical predictions to the charm mass suggests that a QCD fit to determine the preferred value from the data should be carried out.

The analysis was performed with the HERAFitter program [216, 217] , which is based on the NLO DGLAP evolution scheme [27–32] as implemented in QCDNUM [45]. The strategy of the HERAPDF1.0 fit [66, 207] was followed. The combined H1 and ZEUS inclusive ep NC and CC DIS cross sections [207] were used to constrain the PDFs. The analysis was restricted to the inclusive data with $Q^2 > Q^2_{min} = 3.5\ \mathrm{GeV}^2$ to ensure the applicability of pQCD calculations; for the charm data this cut was not applied[31]. Theoretical predictions were obtained at NLO using the FF ABM and FF ABM RUNM scheme for the heavy-quark pole- and running-mass treatment, respectively, as implemented in OPENQCDRAD [218]. The factorisation and renormalisation scales were set to $\mu_f = \mu_r = Q$ for the light quarks and to $\mu_f = \mu_r = \sqrt{Q^2 + 4m_Q^2}$ for the heavy quarks. The number of active flavours in PDFs and α_s evolution was set to $n_f = 3$. The strong coupling constant was set to $\alpha_s^{n_f=3}(M_Z) = 0.105$, corresponding to the value $\alpha_s^{n_f=5}(M_Z) = 0.116$. The beauty mass was set to $m_b^{\mathrm{pole}} = 4.75\,\mathrm{GeV}$ and $m_b(m_b) = 4.18\,\mathrm{GeV}$ [183] for the pole- and running-mass treatments, respectively.[32]

The following independent combinations of PDFs were chosen in the fit procedure at the initial scale of the QCD evolution $Q_0^2 = 1.4\ \mathrm{GeV}^2$: the valence-quark distributions $xu_v(x)$, $xd_v(x)$, the gluon distribution $xg(x)$ and the u-type and d-type anti-quark distributions (note that they are identical to the sea-quark distributions), $x\overline{U}(x)$, $x\overline{D}(x)$, where $x\overline{U}(x) = x\bar{u}(x)$ and $x\overline{D}(x) = x\bar{d}(x) + x\bar{s}(x)$. At the scale Q_0, the PDFs are represented by

$$
\begin{aligned}
xg(x) &= A_g x^{B_g}(1-x)^{C_g} - A'_g x^{B'_g}(1-x)^{C'_g},\\
xu_v(x) &= A_{u_v} x^{B_{u_v}}(1-x)^{C_{u_v}}(1 + D_{u_v}x + E_{u_v}x^2),\\
xd_v(x) &= A_{d_v} x^{B_{d_v}}(1-x)^{C_{d_v}},\\
x\overline{U}(x) &= A_{\overline{U}} x^{B_{\overline{U}}}(1-x)^{C_{\overline{U}}}(1 + D_{\overline{U}}x),\\
x\overline{D}(x) &= A_{\overline{D}} x^{B_{\overline{D}}}(1-x)^{C_{\overline{D}}}(1 + D_{\overline{D}}x).
\end{aligned}
\tag{6.23}
$$

The normalisation parameters A_{u_v}, A_{d_v}, A_g were determined by the QCD sum rules, the parameters B are responsible for the small-x behaviour of the PDFs, and the parameters C describe the shape of the distribution as $x \to 1$. A flexible form for the gluon distribution was adopted with the choice of $C'_g = 25$ motivated by the approach of the MSTW group [53, 54]. The s-quark distribution is expressed as x-independent strangeness fraction, f_s, of the d-type sea, $x\bar{s} = f_s x\overline{D}$ at Q_0^2, where $f_s = 0.31$ as in the analysis of [54]. Additional constraints $B_{\overline{\mathrm{U}}} = B_{\overline{\mathrm{D}}}$ and $A_{\overline{\mathrm{U}}} = A_{\overline{\mathrm{D}}}(1 - f_s)$ were imposed, with $x\bar{u} \to x\bar{d}$ as $x \to 0$. The parameters D_{u_v}, $D_{\bar{U}}$ and $D_{\bar{D}}$ were set to 0 for the nominal variant of the fit. In a compact way, these constraints can be

[31] For the charm data the applicability of pQCD calculations is ensured by the presence of a massive charm quark-antiquark pair in the final state; see also the scale choices.

[32] For the calculation of the beauty contribution to the inclusive cross sections.

summarised as

$$
\begin{aligned}
&A_{\overline{U}} = A_{\overline{D}}(1 - f_s),\ f_s = 0.31,\\
&B_{\overline{U}} = B_{\overline{D}},\\
&C'_g = 25,\\
&D_{u_v} = D_{\overline{U}} = D_{\overline{D}} = 0,\\
&\int_0^1 [\textstyle\sum_i (q_i(x) + \overline{q}_i(x)) + g(x)]xdx = 1,\\
&\int_0^1 [u(x) - \overline{u}(x)]dx = 2,\\
&\int_0^1 [d(x) - \overline{d}(x)]dx = 1.
\end{aligned}
\tag{6.24}
$$

The analysis was performed by fitting the remaining 13 free parameters in 6.23[33]. The charm mass was left free in the fit.

The free parameters are determined in HERAFitter by minimisation of a χ^2-function as implemented in the MINUIT package [184] taking into account correlated and uncorrelated measurement uncertainties [217]. Systematic uncertainties are assumed to be proportional to the central prediction values, whereas statistical uncertainties scale with the square root of the predictions. Correlated uncertainties are treated using nuisance-parameter representation [217]. To minimise biases arising from the likelihood transition to χ^2 when the scaling of the errors is applied, a logarithmic correction is added to the χ^2-function [219].

The uncertainties were evaluated following the strategy of [66, 207]. These include:

- a fit uncertainty was evaluated using the Hessian method [204, 217] from a χ^2 variation of 1;[34]
- model uncertainties from variation of theory model parameters:
  - f_s was varied in the range $0.23 < f_s < 0.38$;
  - m_b^{pole} and $m_b(m_b)$ were varied in the ranges $4.50 < m_b^{\text{pole}} < 5.00\,\text{GeV}$ and $4.00 < m_b(m_b) < 4.40\,\text{GeV}$ for the pole- and running-mass treatments, respectively;
  - Q^2_{min} was varied in the range $2.5 < Q^2_{min} < 5.0\,\text{GeV}^2$;
  - $\alpha_s^{n_f=3}(M_Z)$ was varied in the range $0.103 < \alpha_s^{n_f=3}(M_Z) < 0.107$, corresponding to $0.114 < \alpha_s^{n_f=5}(M_Z) < 0.118$;
  - μ_f and μ_r for heavy-flavour production were varied simultaneously by a factor of two (the framework allows only their simultaneous variation); the largest differences in this range were taken;
- parametrisation uncertainties:
  - Q_0^2 was varied in the range $1.0 < Q_0^2 < 1.9\,\text{GeV}^2$;
  - the parameter D_{u_v} was released;
  - the parameter $D_{\overline{U}}$ was released;
  - the parameter $D_{\overline{D}}$ was released.

[33] Note that a negative gluon distribution was allowed at the parametrisation scale.
[34] For the charm-quark mass, the fit uncertainty was determined with the MINOS algorithm [185].

The fitted values of the pole and running charm masses are

$$\begin{aligned} m_c^{\text{pole}} &= 1.334\ ^{+0.039}_{-0.043}(\text{fit})\ ^{+0.013}_{-0.005}(\text{mod})\ ^{+0.008}_{-0.011}(\alpha_s)\ ^{+0.005}_{-0.001}(\text{scale})\ ^{+0.020}_{-0.001}(\text{par})\ \text{GeV}, \\ m_c(m_c) &= 1.225\ ^{+0.034}_{-0.034}(\text{fit})\ ^{+0.008}_{-0.001}(\text{mod})\ ^{+0.009}_{-0.007}(\alpha_s)\ ^{+0.009}_{-0.005}(\text{scale})\ ^{+0.015}_{-0.000}(\text{par})\ \text{GeV}. \end{aligned} \tag{6.25}$$

For the model uncertainties the f_s, m_b and Q^2_{min} variations were added in quadrature, while the α_s and scale uncertainties are quoted separately. For the parametrisation uncertainties, the largest differences of all variations was taken. The χ^2/n_{dof} values are $\chi^2/n_{\text{dof}} = 656/630$ and $\chi^2/n_{\text{dof}} = 653/630$ for the pole- and running-mass treatments, respectively; the partial contribution from the combined charm data is $\chi^2/n_{\text{dof}} = 66/52$ in both fits. These values indicate a good consistency of the fit, although they are slightly larger than obtained in the previous analysis [66] with the 'HERA 2012' combined data (total $\chi^2/n_{\text{dof}} = 628/626$ and charm $\chi^2/n_{\text{dof}} = 44/47$ for the running-mass treatment). This might indicate that the more precise charm data require a somewhat more flexible PDF parametrisation.

The determined $m_c(m_c)$ value is consistent with the 'HERA 2012' result $m_c(m_c) = 1.26 \pm 0.05(\text{fit}) \pm 0.03(\text{mod}) \pm 0.02(\text{par}) \pm 0.02(\alpha_s)$ and has a better accuracy owing to the more precise combined charm data used in the fit and to the usage of all Q^2 bins[35]. The reduction of the model, α_s and scale uncertainties is attributed partially to the usage of all Q^2 bins and partially to a more stable fit result. This value also agrees reasonably well with the other analyses of the 'HERA 2012' charm data performed at NLO and partial NNLO [220, 221][36]:

$$\begin{aligned} &m_c(m_c) = 1.15 \pm 0.04(\text{exp})\ ^{+0.04}_{-0.00}(\text{scale})\ \text{GeV} && \text{NLO } O(\alpha_s^2)\ \text{(Alekhin)}, \\ &m_c(m_c) = 1.24 \pm 0.03(\text{exp})\ ^{+0.03}_{-0.02}(\text{scale})\ ^{+0.00}_{-0.07}(\text{theory})\ \text{GeV} && \text{approx. NNLO } O(\alpha_s^3)\ \text{(Alekhin)}, \\ &m_c(m_c) = 1.19\ ^{+0.08}_{-0.15}\ \text{GeV} && \text{NNLO } O(\alpha_s^2)\ \text{(CTEQ)}. \end{aligned} \tag{6.26}$$

Some differences between the results are attributed to different theoretical settings and procedures of uncertainty estimation (for more details see [220, 221] and references therein). The determined $m_c(m_c)$ value is also consistent with the world average of $m_c(m_c) = 1.275 \pm 0.025$ GeV [183] defined at two-loop QCD, based on lattice calculations and measurements of time-like processes.

Finally, note that the fitted running-mass value $m_c(m_c) = 1.225$ GeV corresponds to $m_c^{\text{pole}} = m_c(m_c)(1 + 4\alpha_s(m_c)/3\pi) = 1.417$ GeV, calculated using the appropriate one-loop relation 2.21, which is reasonably consisted with the fitted value for $m_c^{\text{pole}} = 1.334$ GeV, although the latter differs significantly from the world-average pole mass $m_c^{\text{pole}} = 1.67 \pm 0.07$ GeV [183], calculated from the world-average running mass using the three-loop relation. This illustrates one of the possible caveats in determination and usage of the pole mass in applications of pQCD, mentioned in Section 2.2.2.2. Since no attempt has been made to estimate the non-perturbative theoretical uncertainty on m_c^{pole}, the presented result should be considered as extraction of the

[35] Note, that for the previous 'HERA 2012' result the lowest Q^2 bin of the charm data has not been included in the fit; repeating the fit with the 'HERA 2012' data with the lowest Q^2 bin gives the closer value $m_c(m_c) = 1.228\ ^{+0.048}_{-0.038}(\text{fit})\ ^{+0.024}_{-0.000}(\text{mod})\ ^{+0.022}_{-0.006}(\alpha_s)\ ^{+0.025}_{-0.010}(\text{scale})\ ^{+0.015}_{-0.000}(\text{par})$ GeV.

[36] One of the four variants of the fitted $m_c(m_c)$ from [220] is quoted.

value, which is optimal for these particular data, rather than a measurement.

6.5.4 Comparison to theoretical predictions and QCD analysis in VFNS

In Figs 6.20 and 6.21 the combined cross sections are compared with predictions of the MSTW group in the GM-VFNS at NLO and NNLO, respectively, using the RT-standard [53, 54] and the RT-optimised [58] interpolation procedure of the cross section at the charm-production threshold. At NLO, the optimised prediction tends to describe the data better than the standard one at lower Q^2. The description of the data is improved at NNLO compared to NLO.

In Fig. 6.22 the data are compared to the NLO predictions based on HERAPDF1.5 [222] extracted in the RT standard scheme using as inputs the published HERA-I [207] and the preliminary HERA-II combined inclusive DIS data. For the central PDF set a charm-quark mass parameter $M_c = 1.4$ GeV is used. The uncertainty bands of the predictions reflect the full uncertainties on the HERAPDF1.5 set. They are dominated by the uncertainty on M_c which is varied between 1.35 GeV and 1.65 GeV [207]. Within these uncertainties the HERAPDF1.5 predictions describe the data well. The central predictions are very similar to those of the MSTW group for the same scheme.

In Fig. 6.23 the data are compared to the predictions in the GM-VFNS by the NNPDF Collaboration. Both the NNPDF FONLL-A [55] and FONLL-B [56, 57] predictions describe the data fairly well at higher Q^2, while they fail to describe the data at lower Q^2. The description of the data at lower Q^2 is improved in the FONLL-C [56, 57] scheme.

In Fig. 6.24 the data are compared to the predictions in the GM-VFNS by the CTEQ Collaboration. The CT predictions [201, 223] are based on the S-ACOT-χ heavy-quark scheme. The NLO prediction, which is very similar to the FONLL-A scheme, describes the data well for $Q^2 > 5$ GeV^2 but fails to describe the data at lower Q^2. Similar to the FONNL-C case, the description of the data improves significantly at NNLO.

In summary, conclusions similar to [66] can be drawn. The best description of the data is achieved by the predictions including partial $O(\alpha_s^3)$ corrections (MSTW NNLO), however they do not fully describe the Q^2 slope of the data at low Q^2 ($2.5 < Q^2 < 5.0$ GeV^2). The predictions including $O(\alpha_s^2)$ terms in all parts of the calculation (NNPDF FONLL C, CT NNLO) as well as the MSTW NLO optimal scheme also agree with the data reasonably well. The largest deviations are observed for predictions based on $O(\alpha_s)$ terms only (NNPDF FONLL A and CT NLO). As investigated in the next Section 6.5.4.1, further differences can be partially explained by the different choices for the value of the respective charm-quark mass parameter M_c.

6.5.4.1 Extraction of charm-mass parameters

Similar to the extraction of the charm-quark mass in the FFNS, described in Section 6.5.3.1, the combined charm data were used to determine the effective parameters of the individual VFNS.

The following implementations of the VFNS were considered: ACOT full [47, 48] as used for the CTEQHQ releases of PDFs; S-ACOT-χ [50–52] as used for the latest CTEQ releases of PDFs, and for the FONLL-A scheme [55] used by NNPDF; the RT standard scheme [53,

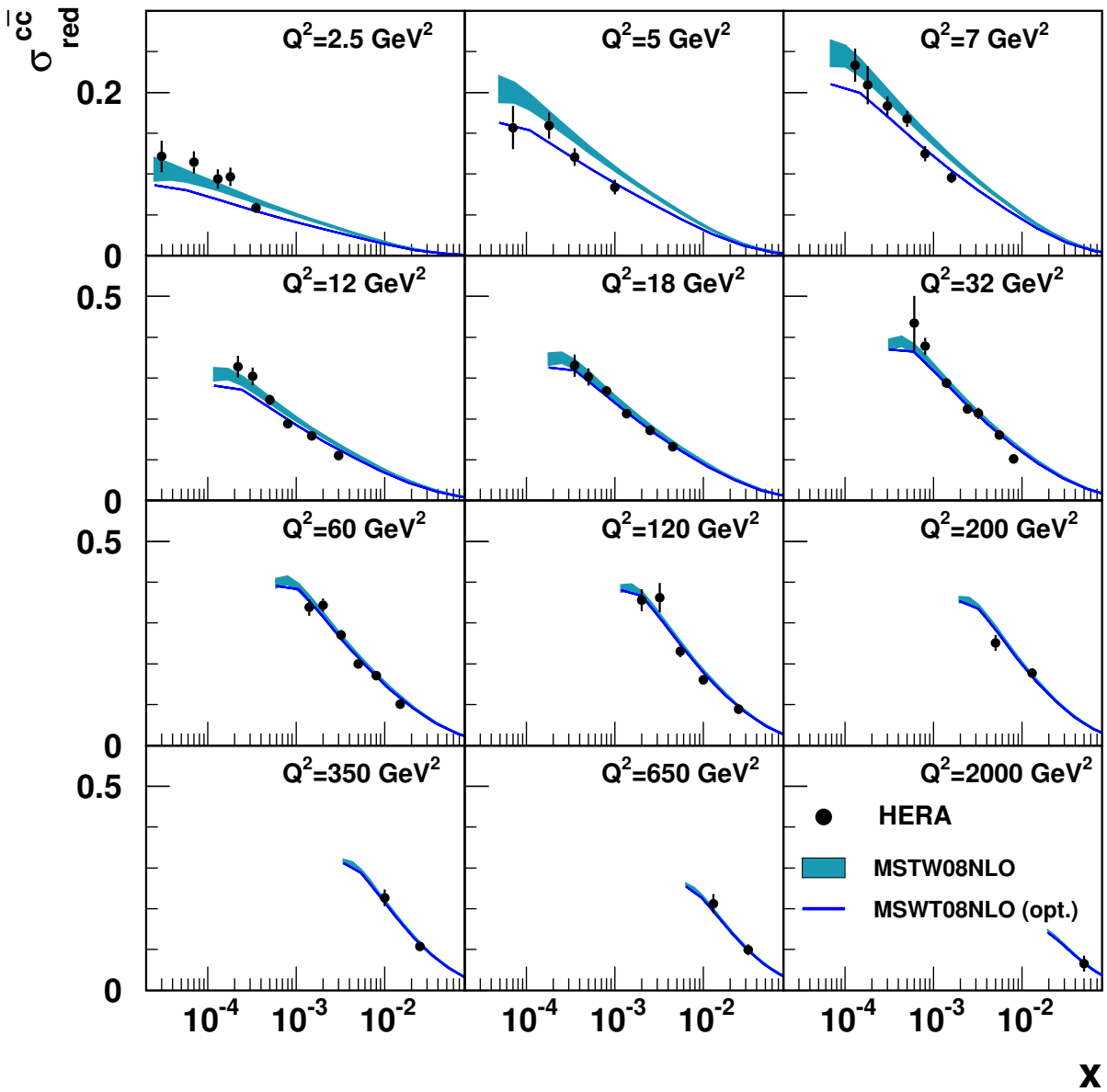

Figure 6.20: Combined measurements of $\sigma_{red}^{c\bar{c}}$ (closed circles) shown as a function of x for particular Q^2, compared to the prediction by MSTW at NLO. The predictions obtained using the standard (optimised) parametrisation are represented by the shaded bands (solid lines). The uncertainties for the optimised parametrisation are not evaluated by the authors of the predictions but are expected to be of same size as those for the standard parametrisation.

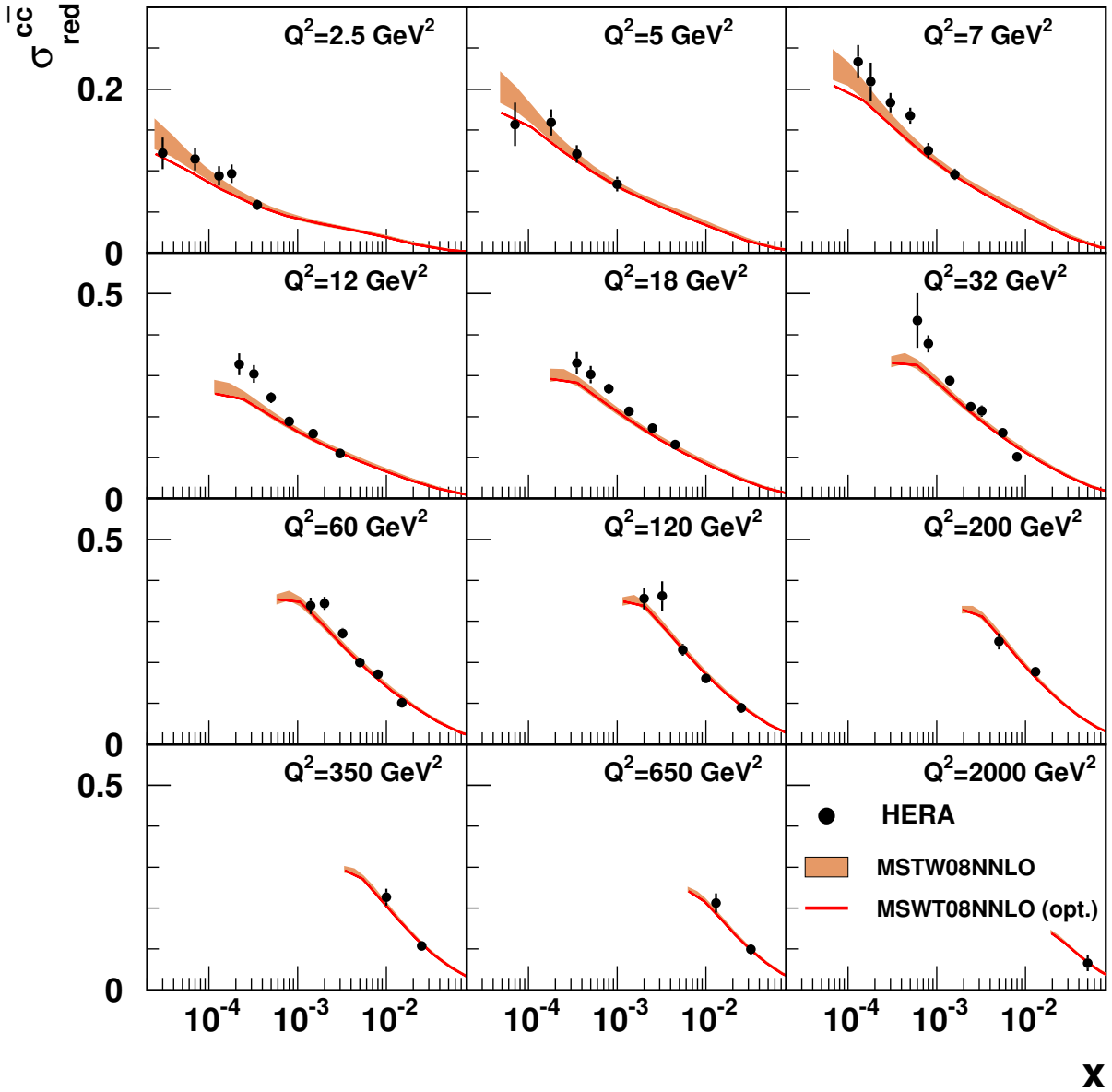

Figure 6.21: Combined measurements of $\sigma_{red}^{c\bar{c}}$ (closed circles) shown as a function of x for particular Q^2, compared to the prediction by MSTW at NNLO. The predictions obtained using the standard (optimised) parametrisation are represented by the shaded bands (solid lines). The uncertainties for the optimised parametrisation are not evaluated by the authors of the predictions but are expected to be of same size as those for the standard parametrisation.

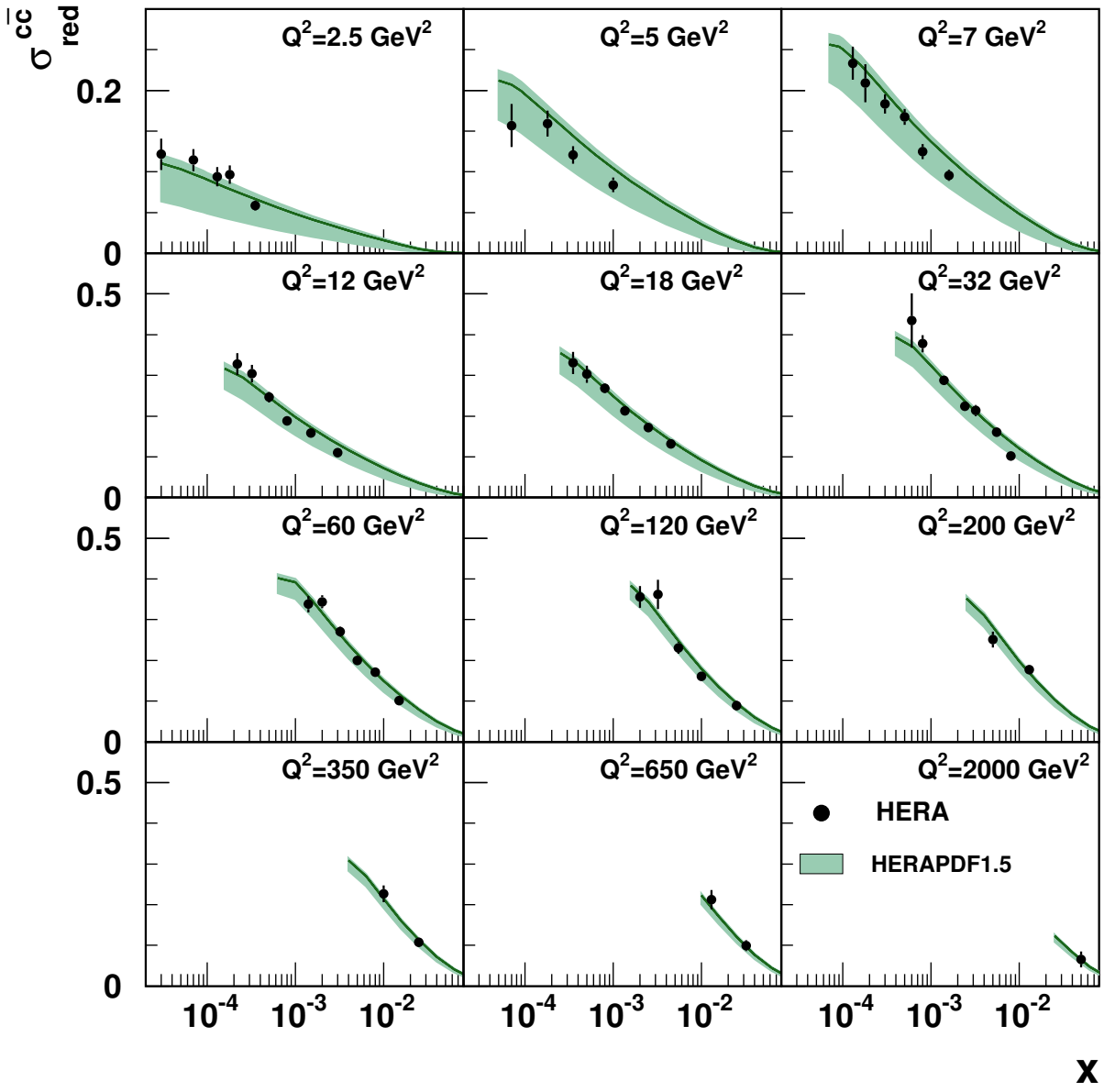

Figure 6.22: Combined measurements of $\sigma_{red}^{c\bar{c}}$ (closed circles) shown as a function of x for particular Q^2, compared to the NLO predictions based on HERAPDF1.5 extracted in the RT standard scheme. The line represents the prediction using $M_c = 1.4$ GeV. The uncertainty band shows the full PDF uncertainty which is dominated by the variation of M_c.

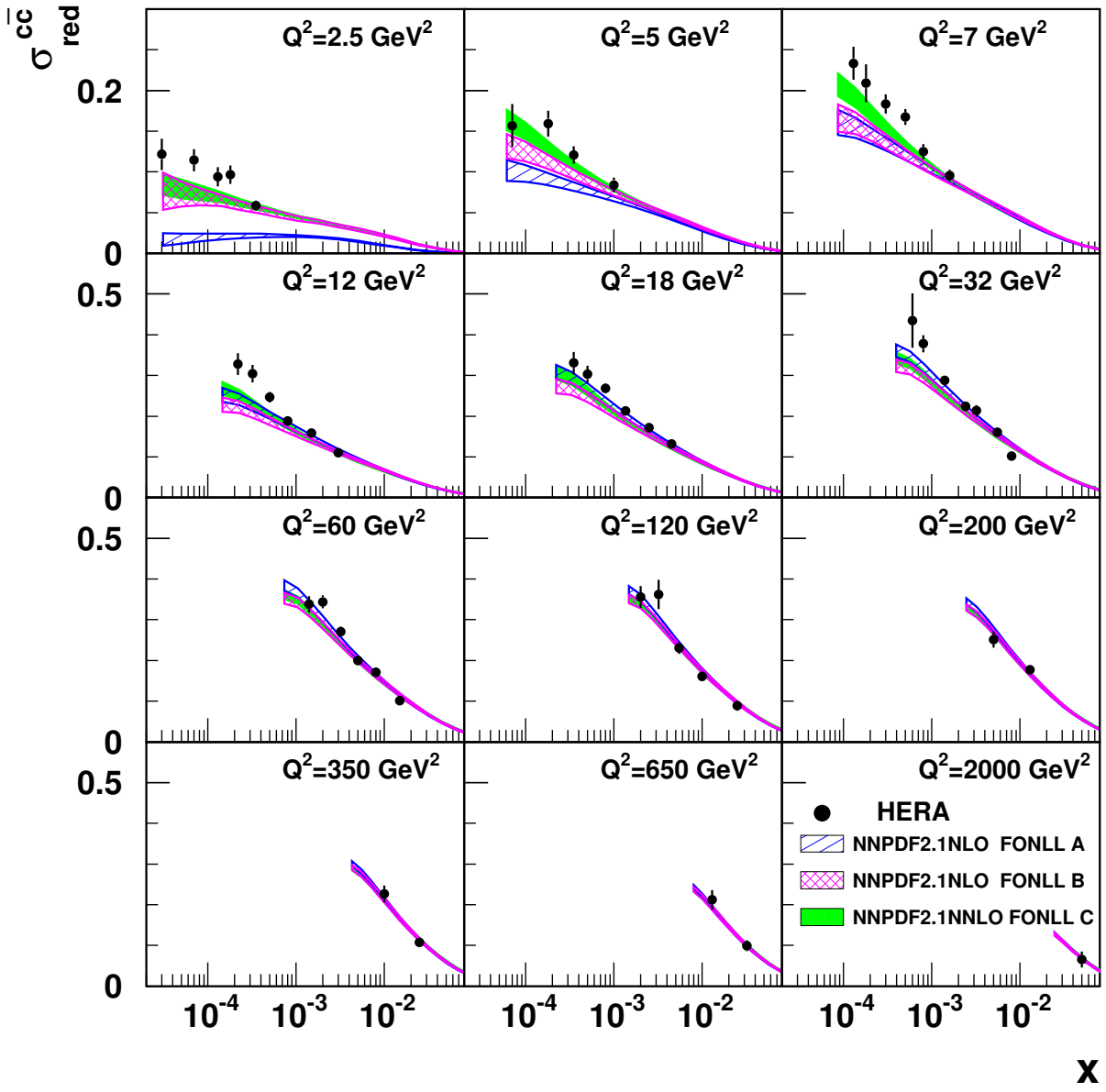

Figure 6.23: Combined measurements of $\sigma_{red}^{c\bar{c}}$ (closed circles) shown as a function of x for particular Q^2, compared to the predictions by NNPDF. The predictions from NNPDF2.1 in FONNL-A, -B and -C schemes are available with their uncertainties and are represented by bands with different hatch styles.

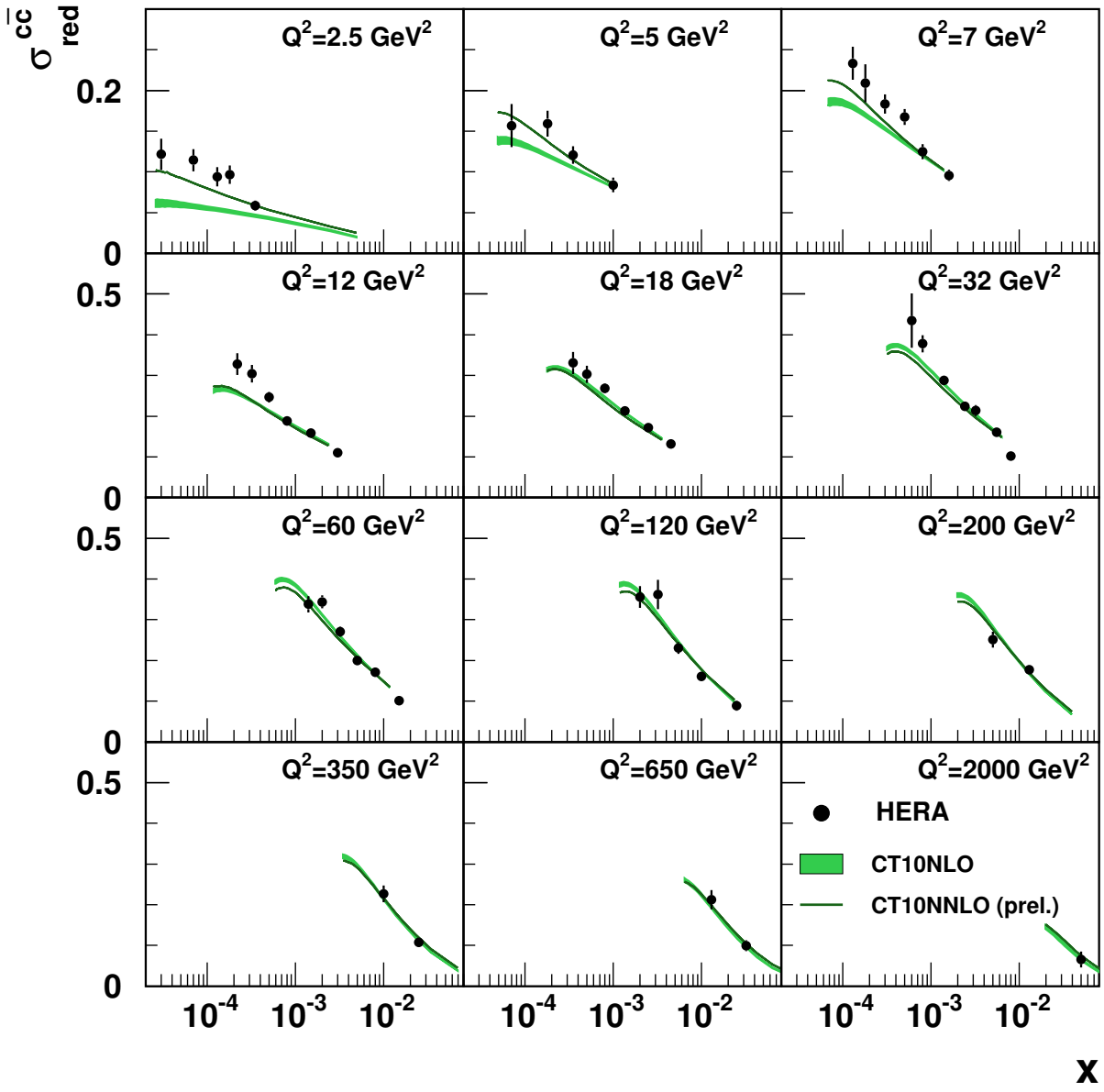

Figure 6.24: Combined measurements of $\sigma_{red}^{c\bar{c}}$ (closed circles) shown as a function of x for particular Q^2, compared to the predictions by CTEQ. The CT10 NLO prediction with its uncertainties is shown by the shaded bands. The uncertainties on the CT10 NNLO (prel.) predictions are not shown.

54] as used for the MRST and MSTW releases of PDFs, as well as the RT optimised scheme providing a smoother behaviour across thresholds [58]. The ZM-VFNS as implemented by the CTEQ group [47, 48] was also used for comparison. In all schemes, the onset of the heavy-quark PDFs is controlled by the parameter M_c, in addition to the kinematic constraints.

The fitting procedure was the same as in the FFNS fit, described in Section 6.5.3.1, except:

- since most of the considered VFNS at $O(\alpha_s^2)$ fail to describe the Q^2 slope of the data in the range of $2.5 < Q^2 < 5.0\,\mathrm{GeV}^2$, the first Q^2 bin was excluded from the fit;
- the strong coupling constant was chosen $\alpha_s^{n_f=5}(M_Z) = 0.1176 \pm 0.0020$;
- the renormalisation and factorisation scales for the heavy quarks were set to $\mu_f = \mu_r = Q$ and not varied, since it is not technically possible in the framework;
- the preferred mass parameters were obtained from the scan, since the implementation of the calculations does not allow for their changes in the PDF fitting procedure. The step size 0.01 GeV was used.

In Fig. 6.25 the χ^2 values as a function of M_c are shown for all schemes considered. Similar minimal χ^2-values are observed for the different schemes, albeit at quite different optimal values of the charm-mass parameter, M_c^{opt}. In the cases of the ACOT full and S-ACOT-χ schemes the dependence of χ^2 on M_c has small discontinuities since these schemes are implemented using K-factors.[37] A smooth curve can be obtained by fitting the points with a parabolic function, although this will not significantly change the preferred M_c^{opt} values.

In Table 6.11 the resulting values of M_c^{opt} are given together with the uncertainties and the χ^2/n_{dof} values; for comparison the 'HERA 2012' results are also given. For ACOT full and S-ACOT-χ schemes the uncertainties are not evaluated, since due to the present discontinuities in the χ^2 curves they can be misleading. The RT optimised scheme yields the best global χ^2. The fit in the S-ACOT-χ scheme results in a very low value of M_c^{opt} as compared to the other schemes. In general the predictions of the different schemes become very similar for $Q^2 \geq 5\,\mathrm{GeV}^2$ and describe the data well, once the charm-mass parameters are set to the preferred values. Note, that even the ZM-VFNS, which includes mass effects only indirectly [47, 48], yields a reasonably good description of the combined charm data for $Q^2 \geq 5\ \mathrm{GeV}^2$ (although it predicts a zero cross section in the lowest Q^2 bin), however ~ 20 units of χ^2 worse than the other schemes.

Similar to the fit in the FFNS, all fitted M_c^{opt} values are consistent with those which have been determined in the previous analysis [66] with the 'HERA 2012' combined data. Those variants, for which the uncertainties are determined, exhibit improved precision.

Using different charm-mass parameters adjusted to the HERA data allows for a reduction of the theoretical uncertainty due to the choice of the heavy-flavour scheme for $W^{\pm}$ and Z production at the LHC, as was demonstrated in [66].

[37] From a calculation point of view, the theoretical model consists of the numerical integration of an integro-differential equation and multiple convolution integrals that are evaluated mostly by adaptive algorithms (K-factors). Change of a parameter (M_c in this case) results in the appearance of an uncontrolled numerical noise. Some details can be found also in [224].

Scheme	HERA		HERA 2012	
	M_c^{opt} [GeV]	χ^2/n_{dof}	M_c^{opt} [GeV]	χ^2/n_{dof}
RT standard	$1.49 \pm 0.04(\mathrm{fit}) \,^{+0.03}_{-0.01}(\mathrm{mod}) \,^{+0.02}_{-0.02}(\mathrm{par}) \,^{+0.01}_{-0.00}(\alpha_s)$	647/626	$1.50 \pm 0.06(\mathrm{fit}) \pm 0.06(\mathrm{mod}) \pm 0.01(\mathrm{par}) \pm 0.003(\alpha_s)$	631/626
RT optimised	$1.37 \pm 0.04(\mathrm{fit}) \,^{+0.02}_{-0.00}(\mathrm{mod}) \,^{+0.02}_{-0.00}(\mathrm{par}) \,^{+0.01}_{-0.00}(\alpha_s)$	641/626	$1.38 \pm 0.05(\mathrm{fit}) \pm 0.03(\mathrm{mod}) \pm 0.01(\mathrm{par}) \pm 0.01(\alpha_s)$	624/626
ACOT-full	≈ 1.46	643/626	$1.52 \pm 0.05(\mathrm{fit}) \pm 0.12(\mathrm{mod}) \pm 0.01(\mathrm{par}) \pm 0.06(\alpha_s)$	607/626
S-ACOT-χ	≈ 1.23	652/626	$1.15 \pm 0.04(\mathrm{fit}) \pm 0.01(\mathrm{mod}) \pm 0.01(\mathrm{par}) \pm 0.02(\alpha_s)$	613/626
ZM-VFNS	$1.62 \pm 0.04(\mathrm{fit}) \,^{+0.04}_{-0.00}(\mathrm{mod}) \,^{+0.02}_{-0.02}(\mathrm{par}) \,^{+0.02}_{-0.01}(\alpha_s)$	665/626	$1.60 \pm 0.05(\mathrm{fit}) \pm 0.03(\mathrm{mod}) \pm 0.05(\mathrm{par}) \pm 0.01(\alpha_s)$	632/626

Table 6.11: The values of the charm-mass parameter M_c^{opt} as determined from the M_c scans in different VFNS, with their uncertainties and the corresponding χ^2/n_{dof} values. The results of the present study ('HERA') are shown together with the previous 'HERA 2012' results from [66].

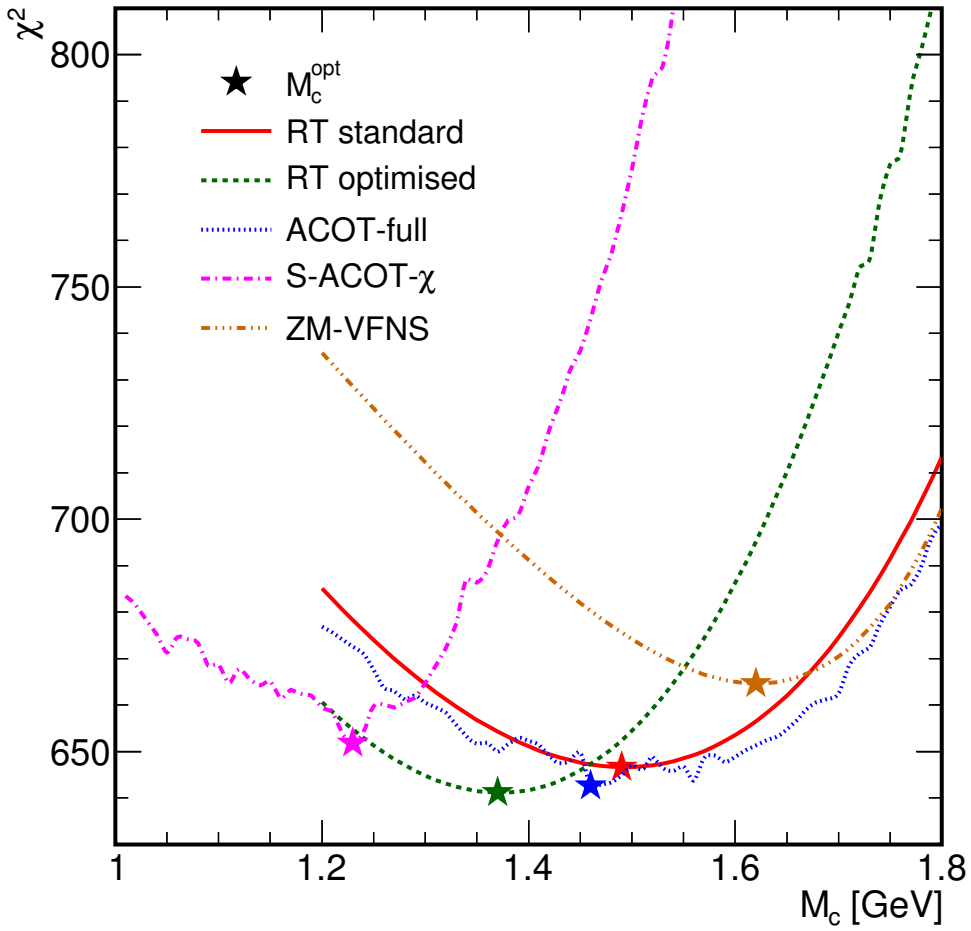

Figure 6.25: The values of $\chi^2(M_c)$ for the PDF fit to the combined HERA inclusive DIS and charm measurements in different VFNS, presented by lines with different styles. The values of M_c^{opt} for each scheme are indicated by the stars.

6.6 Summary

Measurements of charm production by the H1 and ZEUS experiments were combined. The combination was done separately for the single- and double-differential visible D^{*+} cross sections, and for all available measurements of open charm production extrapolated to the full phase space. The combination was performed in the kinematic region $1.5 < Q^2 < 1000\,\text{GeV}^2$ ($5 < Q^2 < 1000\,\text{GeV}^2$ for the single-differential cross sections), $0.02 < y < 0.7$, $p_T(D^{*+}) > 1.5\,\text{GeV}$ and $|\eta(D^{*+})| < 1.5$ for the visible D^{*+} cross sections, and in the region $2.5 \leq Q^2 \leq 2000\,\text{GeV}^2$ and $3 \times 10^{-5} \leq x \leq 5 \times 10^{-2}$ for the charm reduced cross sections. The procedure takes into account detailed information on correlations of the systematic uncertainties. For both combinations, the data were found to be consistent, and the combined sets exhibit significantly reduced uncertainties. The combination of visible D^{*+} cross sections does not induce significant theory-related uncertainties, while the combination of the charm reduced cross sections

presents the most precise charm dataset from HERA, although is affected by the theory-related uncertainties from the extrapolation procedure.

For the visible D^{*+} cross sections, the combination was performed separately for the single-differential cross sections using the HERA-II data only, and for the double-differential cross section using the HERA-I and HERA-II data. Inclusion of the HERA-I data allowed an extension of the kinematic region in Q^2. The combined D^{*+} data were compared to NLO QCD predictions in the FFNS. The predictions describe the data well within their uncertainties. Because the uncertainties of the combined data are smaller than the theoretical uncertainties, higher-order calculations and an improved treatment of the fragmentation process would be helpful to reduce the theory uncertainty to a level comparable with the data precision. These combined data can be used further as the most precise purely experimental charm measurement from HERA for stringent tests of pQCD and phenomenological approaches, e.g. of the fragmentation process.

The combined charm reduced cross sections are consistent with the previous H1 and ZEUS charm combination and have an improved precision owing to the inclusion of new ZEUS measurements. The combined data were compared to NLO QCD predictions in the FFNS and various VFNS. Most of the predictions describe the data well within their uncertainties. Similar to the D^{*+} combination, the uncertainties of the combined data are smaller than the theoretical uncertainties, thus further improvement in the theoretical calculations would be helpful to match the data precision. The best description of the data in the whole kinematic range is provided by the approximate NNLO FFNS predictions of the ABM group. The combined charm reduced cross sections were used as input for the QCD analysis to determine the optimal values of the $\overline{\text{MS}}$ running charm mass and charm-quark mass parameters in different VFNS. The extracted value of the $\overline{\text{MS}}$ running charm mass is consistent with the world-average value and has competitive precision to other individual determinations in pQCD. These data can be used further as the most precise inclusive charm measurement from HERA for stringent tests of pQCD and in QCD analyses to constrain the gluon distribution and to determine the charm-quark mass.

CHAPTER 7

PDF fit with LHCb heavy-flavour data

This Chapter describes a QCD analysis (PDF fit) with recent LHCb heavy-flavour forward data and the impact of this data on PDFs. Results presented in this Section have been approved by the PROSA Collaboration as preliminary [225]; currently their publication is being prepared.[1]

Section 7.1 gives an introduction to the subject and motivation for the study. Section 7.2 describes details of the theoretical calculations for the LHCb heavy-flavour data. In Section 7.3 a PDF fitting framework is described. Section 7.4 presents results of the fit, while in Section 7.5 the impact of the new data on the PDFs is discussed together with possible applications of the study as well as further improvements.

7.1 Introduction

As introduced in Section 2.2.3, PDFs are a necessary ingredient for QCD predictions in any process with incoming hadrons. Since they are not currently calculable from first principles, they should be extracted from data. At the present time several groups determine PDFs (see, e.g. [196, 197, 200, 201, 227]).

In Fig. 7.1 the gluon distributions from several modern PDF sets [56, 197, 200, 227] are compared at the scale $Q^2 = 10\,\text{GeV}^2$.[2] The FFNS variants of the fits with the number of active flavours $n_f = 3$ were chosen. While being consistent with each other and well constrained in the region of medium x, they have a significant spread between the central values and large uncertainties in the low-x region[3], since so far no data sensitive to gluons in this region are included in the PDF fits. Note also that within the uncertainty bands, some of the sets predict a negative gluon distribution in the region $x \lesssim 5 \times 10^{-5}$.

[1] After the disputation during the final preparation of this thesis for printing, the results have been publicly released by the Collaboration [226].

[2] Unlike the rest of this thesis, in this Chapter Q^2 denotes the PDF factorisation scale and not the virtuality of ep scattering, x denotes the longitudinal fraction of the proton momentum and not the Bjorken variable, y denotes rapidity and not inelasticity, unless otherwise stated explicitly.

[3] The region $x \lesssim 10^{-4}$ will be referred as *low* x.

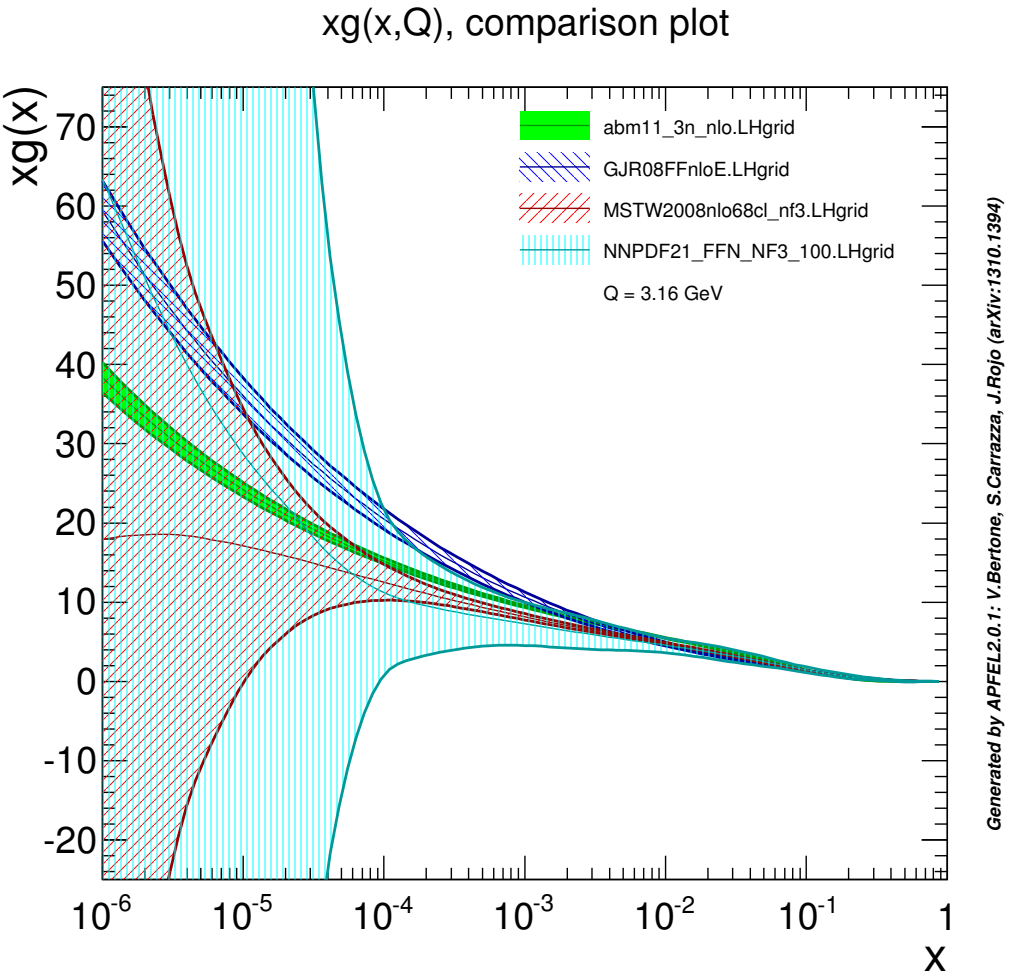

Figure 7.1: Gluon distributions at $Q^2 = 10\,\text{GeV}^2$ from PDF groups [56, 197, 200, 227] with their uncertainties, represented by bands with different hatch styles. The plot is obtained with the APFEL program [228].

The LHCb Collaboration has recently measured charm and beauty production in the forward rapidity region $2.0 < y < 4.5$ at the centre-of-mass energy $\sqrt{s} = 7\,\text{TeV}$ [135, 148]. The results are reported as hadron-level cross sections in the p_T ranges $0 < p_T < 8\,\text{GeV}$ and $0 < p_T < 40\,\text{GeV}$ for the charm and beauty measurements, respectively. Since the dominant process for heavy-flavour production in pp collisions at these energies is gluon–gluon fusion (see Section 2.3.3), these data are sensitive to gluons at low x. To illustrate this, in Fig. 7.2 the kinematic regions which are covered by different HERA and LHCb data are plotted. The precise HERA DIS data [207] are only indirectly sensitive to gluons, so they constrain the gluon distribution well only in the region $10^{-3} \lesssim x \lesssim 10^{-1}$. The HERA heavy-flavour data [19, 66] cover the region $10^{-4} \lesssim x \lesssim 10^{-2}$, while the LHCb data extend the coverage up to $x \lesssim 5 \times 10^{-6}$ (low-p_T forward charm) and up to $x \lesssim 1$ (high-p_T forward beauty).[4] Note that the LHCb data

[4] The quoted regions are qualitatively determined in the following way. For the HERA DIS data, the x range is indicated, where the gluon HERAPDF1.0 [207] uncertainty at $Q^2 = 10\,\text{GeV}^2$ is less than 10%. For the HERA

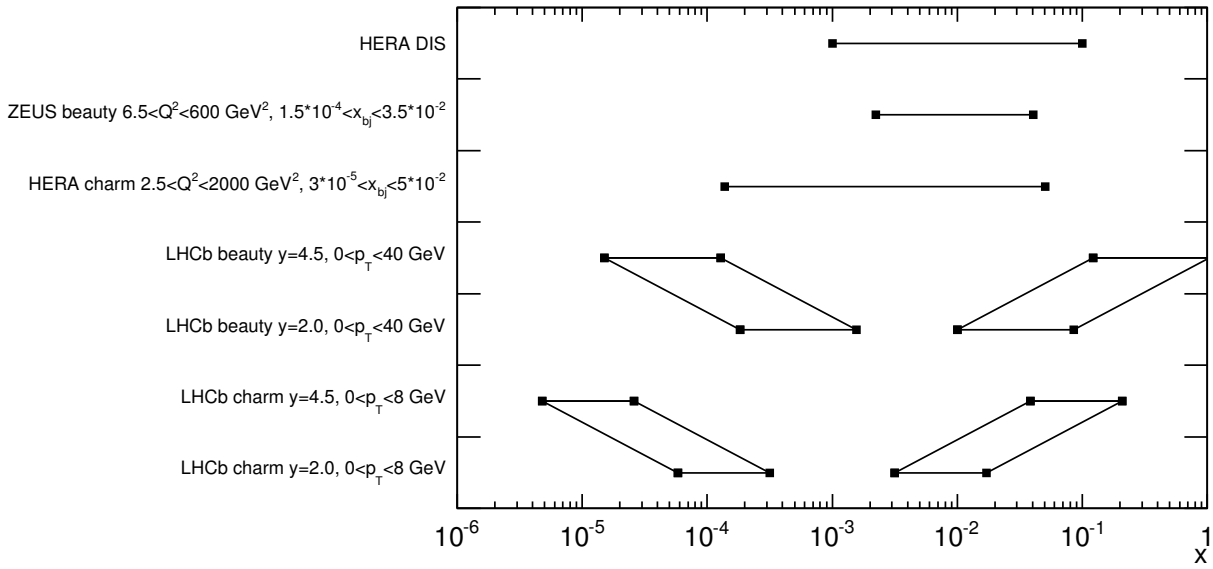

Figure 7.2: Kinematics in the gluon x space as covered by the different HERA and LHCb data.

are sensitive to the product of gluon densities in two non-overlapping regions: forward and medium; since the latter is already well constrained by other data, the LHCb data should have an impact mainly on the former.

It is worth noting that using PDFs with strongly negative gluons at low x results in negative predicted cross sections for the forward region of the LHCb charm data. To demonstrate this, two sets of HERAPDF1.5 [222] are used: the nominal one and a variation obtained with a negative gluon parametrisation.[5] The corresponding predictions for the LHCb charm measurement in the most forward y bin are shown in Fig. 7.3. The variation with negative gluons results in non-physical negative predicted cross sections for the lowest p_T bins. This motivates the inclusion of the LHCb data in a PDF fit to constrain gluons at low x.

The general strategy of the study was to perform a PDF fit with the HERA-only data, obtaining results close to HERAPDF1.0 [207], and then repeat the fit with the LHCb data included,

charm and beauty data, the LO formula $x = x_{\mathrm{bj}}(1 + 4m_Q^2/Q^2)$ is used, where x_{bj} is the Bjorken variable, Q^2 is boson virtuality and m_Q is the heavy-quark mass. For the LHCb charm and beauty data, the LO formula with the assumption $p_z = 0$ of the produced heavy quark in the parton-parton rest frame $x = e^{\pm y}\frac{\sqrt{p_T^2+m_Q^2}}{E_p}$ is used, where y and p_T are the transverse momentum and rapidity of the heavy quark and E_p is the energy of the proton beam.

[5] The fact that HERAPDF1.5 were determined using the GM-VFNS is ignored, since at the scales $Q^2 \sim m_c^2$ they should be reasonably valid also in the FFNS.

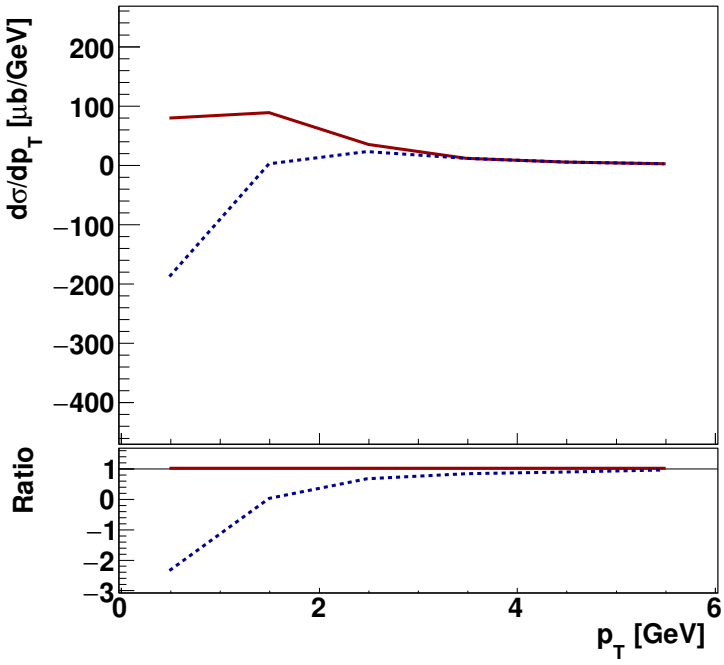

Figure 7.3: Predictions for the LHCb measurement of D^0-meson production in the bin $4.0 < y < 4.5$ obtained with the two sets of HERAPDF1.5: nominal (a solid line) and with a negative gluon parametrisation (a dotted line). The bottom pad shows the ratio to the nominal set.

thus studying potential constraints from these data.

7.2 Theoretical predictions

Theoretical predictions for the charm and beauty data were obtained using the massive NLO $O(\alpha_s^3)$ calculations in the FFNS [67, 69, 73] (see Section 2.3.3.1) using the MNR code [229], implemented in the HERAFitter package [216, 217] by the author. Technical details of the implementation are described in Appendix F.1. The parameters used in the calculations and the corresponding variations used to estimate the uncertainties are described below in Section 7.2.1.

7.2.1 Details of MNR calculations

7.2.1.1 Parton-level cross sections

The parton-level cross sections were calculated using the one-particle inclusive option of the MNR calculations [69] with the following settings:

- **the factorisation and renormalisation scales** were parametrised as $\mu_f = A_f^c \sqrt{p_T^2 + m_c^2}$, $\mu_r = A_r^c \sqrt{p_T^2 + m_c^2}$ for charm production and similarly $\mu_f = A_f^b \sqrt{p_T^2 + m_b^2}$, $\mu_r = A_r^b \sqrt{p_T^2 + m_b^2}$

for beauty, where m_c and m_b refer to the charm- and beauty-quark masses, respectively. The conventional choice for the coefficients $A^{c,b}_{f,r}$ is $A^c_f = A^b_f = A^c_r = A^b_r = 1$ and the variations within the range [0.5;2] (independently or simultaneously). Since the scale dependence of the predictions is of the order of a factor of 2, the choice of the coefficients $A^{c,b}_{f,r}$ is crucial for a successful data description and has to be carefully studied; the explicit details are given in Section 7.3;

- **the pole mass of the charm and beauty quarks** m_c and m_b were left free in the fit;
- **strong coupling constant** $\alpha_s^{n_f=3}(M_Z) = 0.1059 \pm 0.0005$, corresponding to the PDG value $\alpha_s^{n_f=5}(M_Z) = 0.1185 \pm 0.0006$ [183];
- **the PDFs** were left free in the fit; their parametrisation is described in Section 7.3.2.

7.2.1.2 Fragmentation

Non-perturbative fragmentation functions for charm and beauty were extracted from e^+e^- and ep data (see, e.g. [95, 191, 212, 230, 231]). So far no fragmentation measurements were done in pp collisions. Universality of the fragmentation is often assumed; however it holds only if the perturbative part of the calculations is the same (see Section 2.3.4). Moreover, e.g. in [95] the fragmentation-function parameters were shown to be different for two different kinematic regions.

Since the kinematic region of the LHCb charm measurement is close to the HERA region where measurements were done by H1 [95] and ZEUS [191], the Kartvelishvili function [91] with $\alpha_k = 4.4 \pm 1.7$ was used for the charm fragmentation, which covers the spread of the measurements [95, 191]. The fragmentation was performed in the laboratory frame by rescaling the quark three-momentum, then the energy of the produced hadron was calculated using the hadron mass. The prescription described above was used for D^{*+}, D_s^+ mesons and Λ_c^+ hadrons, while for D^0 and D^+ mesons the contribution from D^{*+} and D^{*0} mesons was treated as described in [232]. For beauty no fragmentation measurements at HERA exist; therefore the value $\alpha_k = 11 \pm 4$ was used, extracted from measurements at LEP [212]. All beauty hadrons were treated equally. The fragmentation fractions for charm hadrons were taken from [194] and for beauty from [148].

7.2.2 Kinematics of low-p_T region

The dominant channel for heavy-flavour production at LHC is gg. Fig. 7.4 shows the two-dimensional x distribution of the two incoming gluons, as predicted for the LHCb data by the calculations described above.[6] It qualitatively confirms the rough LO estimation (see Fig. 7.2): the main contribution comes from the two separated regions $x_1 \approx 10^{-4.5}$, $x_2 \approx 10^{-1.5}$ for charm and $x_1 \approx 10^{-4.0}$, $x_2 \approx 10^{-1.2}$ for beauty; although for charm an additional concentrated region is observed at $x_1 \approx x_2 \approx 10^{-2.0}$-$10^{-1.5}$.

[6] For these particular predictions the FFNS variant of the HERAPDF1.0 set [207] was used, the factorisation and renormalisation scale were set to $\mu_f = \mu_r = \sqrt{m_Q^2 + p_T^2}$ and the heavy-quarks masses chosen to be $m_c = 1.5\,\text{GeV}$, $m_b = 4.75\,\text{GeV}$, although the kinematics do not strongly depend on the settings.

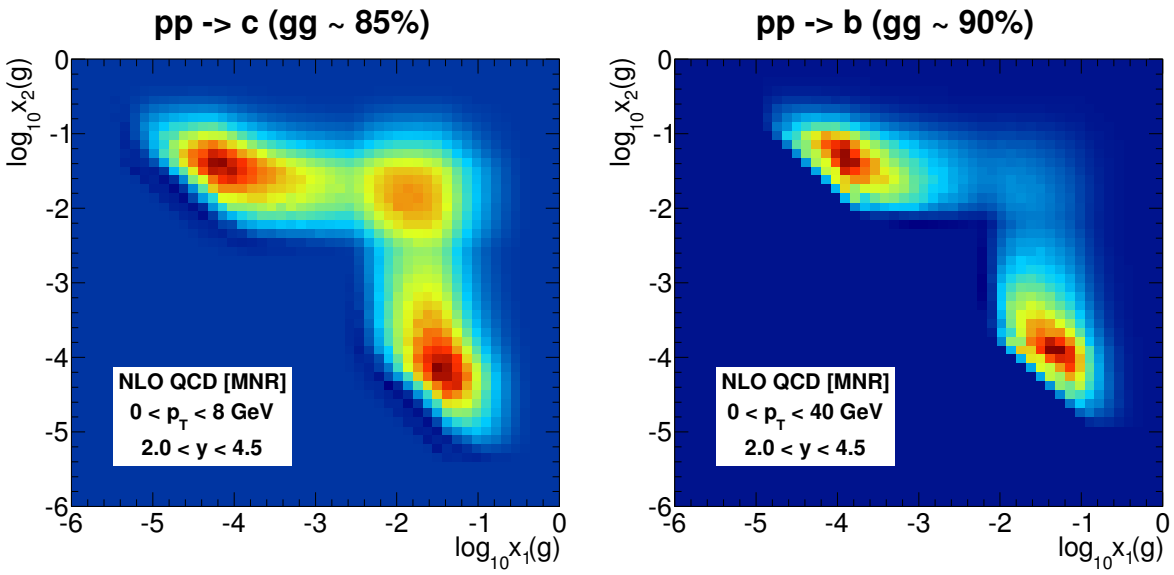

Figure 7.4: The two-dimensional x distribution of the two incoming gluons for charm (left) and beauty (right) production at LHCb via the gg channel.

The enhancement at medium x comes from a class of $O(\alpha_s^3)$ corrections, given by the flavour-excitation diagrams (an example is given in Fig. 7.5), which can be thought of as initial-state gluon-splitting processes [41]. The relevant region of the phase space in this case is the one with the heavy-quark propagator close to the mass shell (the low-p_T region). In GM-VFNS approaches these effects are reabsorbed in the evolution of the PDFs by defining a heavy-quark density inside a proton. The use of the $gQ \to gQ$ process allows the higher-order effects included in the evolution equations to be captured, while the use of the NLO flavour-excitation diagrams reproduces instead more faithfully the exact kinematics and correlations of the flavour-creation process in the region close to the threshold [41].

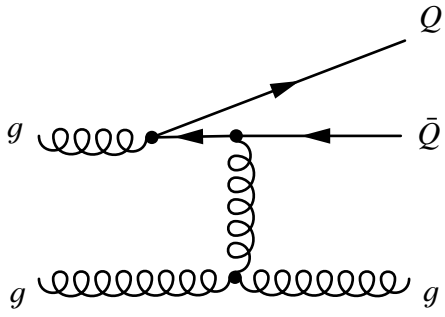

Figure 7.5: An example of the flavour-excitation diagram.

The corrections from the flavour-excitation diagrams should in no way be thought of as a problem of the FFNS calculations, but rather as an important correction to the LO kinematics of the process. In order to study this, Fig. 7.6 shows the median of the centre-of-mass energy in the parton-parton rest frame, $\sqrt{\hat{s}}$, vs. transverse momentum and rapidity of the heavy quark for the charm and beauty LHCb data. While in the case of beauty, the $\sqrt{\hat{s}}$ median smoothly

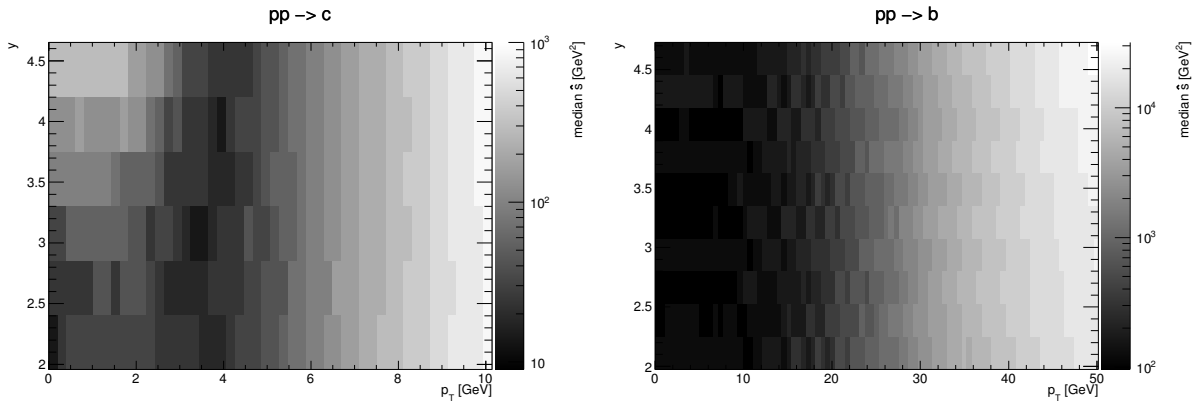

Figure 7.6: The median of the centre-of-mass energy $\sqrt{\hat{s}}$ in the parton-parton rest frame vs. transverse momentum p_T and rapidity y of the heavy quark for the charm (left) and beauty (right) LHCb data.

increases with increasing p_T independently of y, for charm in threshold region $0 < p_T \lesssim 2\,\text{GeV}$ a strong increase of the $\sqrt{\hat{s}}$ median with increasing y is observed. This indicates that the statement about the sensitivity of charm production at low p_T and forward y to the low-x gluon region should be taken with some caution: in fact, about 50% of contribution in the corner region $p_T \lesssim 2\,\text{GeV}$, $y \gtrsim 3.5$ does not come from low-x gluons.

7.2.3 Comparison to FONLL calculations

As mentioned in Section 2.3.3, one of the state of the art calculations for heavy-flavour production in hadron collisions is the FONLL approach [75]. Briefly reminding, the FONLL approach merges the massive NLO calculations (MNR) with massless ones using a phenomenologically chosen matching function. Owing to resummation of the NLL part the FONLL calculations are expected to have improved convergence of the perturbative expansion at high p_T.

In Fig. 7.7 the NLO predictions obtained with MNR as described in Section 7.2.1 are compared to the FONLL ones obtained using the public web interface [79][7] for parton-level charm and beauty cross sections at LHCb. For the relevant regions of transverse momentum in the charm and beauty data, $0 < p_T(c) \lesssim 8\,\text{GeV}$, $0 < p_T(b) \lesssim 40\,\text{GeV}$[8] the maximum deviations of the order of 20% in the region $p_T \approx 3m_Q$ are observed. Note that these changes are well within the uncertainties from the scale variations.

It is also instructive to look at Fig. 2.11 (Section 2.3.3.2), taken from the original FONLL paper [75], which shows the bands obtained from the scale variations for the NLO and FONLL calculations for beauty production at the Tevatron. Although the central values are not shown, the behaviour of the bands in Fig. 2.11 is very similar to the change of the central values shown in Fig. 7.7. Note that in Fig. 2.11 a significant reduction of the uncertainty band starts only at $p_T \gtrsim 40\,\text{GeV}$. Thus the considered p_T ranges of the LHCb data are not the high-p_T region

[7] The 'FONLL' option of the FONLL program was used; the settings consistently used in MNR and FONLL calculations were: PDFs set is MSTW2008nlo68cl [200], $\mu_f = \mu_r = \sqrt{m_Q^2 + p_T^2}$, $m_c = 1.5\,\text{GeV}$, $m_b = 4.75\,\text{GeV}$.

[8] The fragmentation effects do not change significantly p_T regions, since the heavy-flavour fragmentation functions are peaked near the scaling variable $z = 1$ and the cross sections are steeply falling with increasing p_T.

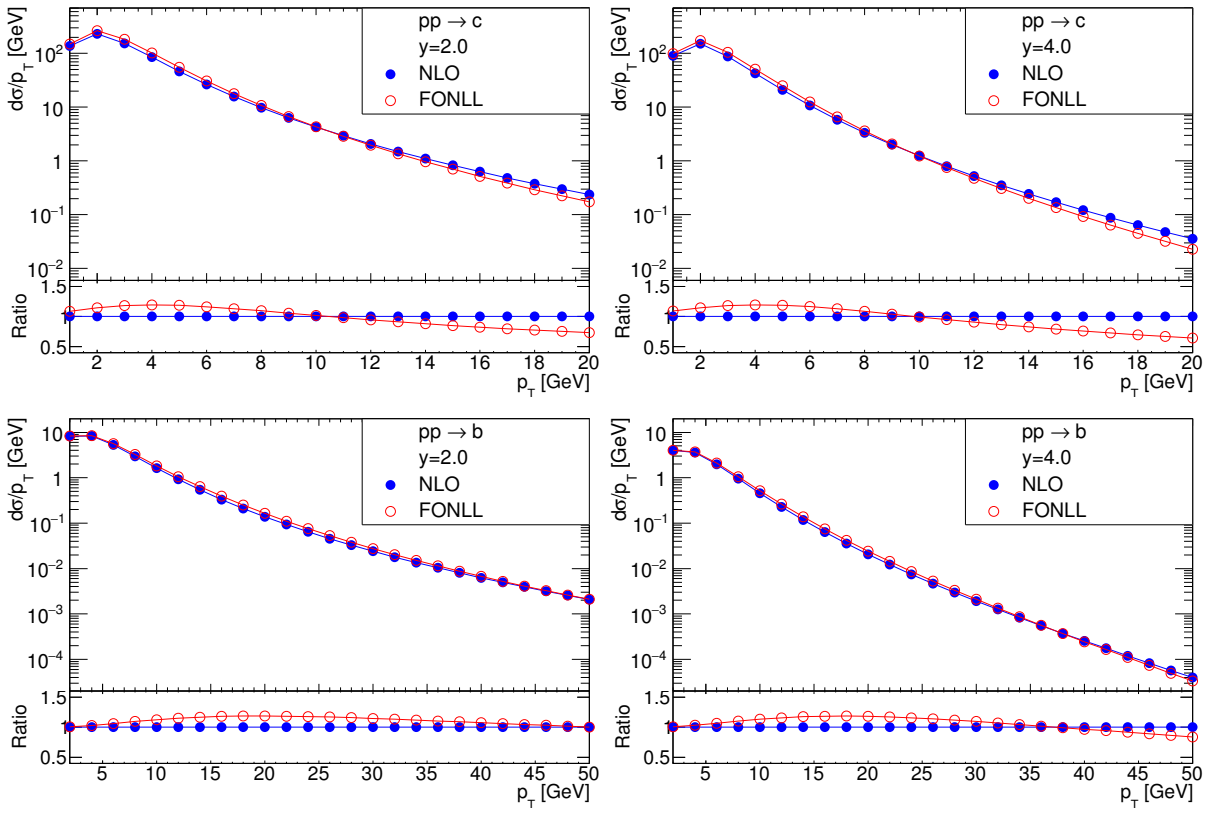

Figure 7.7: Comparison of NLO and FONLL predictions for the differential cross sections as a function of p_T, $\mathrm{d}\sigma/\mathrm{d}p_T$, for charm at rapidity $y = 2$ (top left) and $y = 4$ (top right), and beauty at rapidity $y = 2$ (bottom left) and $y = 4$ (bottom right) at LHCb. The bottom pads shows the ratio to the NLO predictions.

where the effects of the FONLL calculations become relevant. This justifies the usage of the NLO FFNS calculations in the present study as one of the best currently available theories for the considered kinematic region.

Theorists are continuously making progress, and very recently[9] the approximate NNLO $O(\alpha_s^4)$ predictions in the gg and $q\bar{q}$ channels for differential cross sections for heavy-flavour production at hadron colliders became available [233]. A prospect of their usage for an extension of this study is given in Appendix F.3.

7.3 PDF fitting framework

7.3.1 Input data

The datasets used in the PDF fit are listed in Table 7.1. The purpose of their inclusion is the following:

[9] In fact simultaneously with the moment when this thesis was being written.

Dataset		
1	NC $e^- p$	HERA-I DIS [207]
2	NC $e^+ p$	
3	CC $e^- p$	
4	CC $e^+ p$	
5	HERA DIS Charm [66]	
6	ZEUS Vertex DIS Beauty [19]	
7	D^0	LHCb Charm [135]
8	D^+	
9	D^{*+}	
10	D_s^+	
11	Λ_c^+	
12	B^+	LHCb Beauty [148]
13	B^0	
14	B_s	

Table 7.1: Datasets used in the PDF fit. Similar entries are grouped together.

- the combined HERA-I inclusive ep NC and CC DIS cross sections [207] (datasets 1–4) were used to constrain the core of the PDFs; the analysis is restricted to the inclusive data with virtuality $Q^2 > Q^2_{min} = 3.5\,\text{GeV}^2$ to ensure the applicability of pQCD;
- the combined HERA charm data [66] and ZEUS beauty [19] data (datasets 5–6) were used to constrain the gluon PDF and the charm and beauty masses;
- the LHCb charm [135] and beauty [148] data (datasets 7–14) — the main objects of the study — were used to constrain the gluon PDF at low x.

The HERA data (datasets 1–6) were treated in the same way as they have been treated in the original papers [19, 66, 207].[10]

For the LHCb data (datasets 7–14), the double-differential cross sections as a function of p_T and y, $\frac{\mathrm{d}^2\sigma}{dp_T dy}$, were used as published in [135, 148][11]. The correlations between the systematic uncertainties were taken into account as described in Section 3.3 of [135] and Section 4 of [148], treating as correlated those which are reported as single values for all (p_T, y) bins.[12]

[10] Except that for dataset 5 in contrast to [66] all Q^2 bins were used including the lowest one $Q^2 = 2.5\,\text{GeV}^2$; the applicability of pQCD for the charm data is ensured by the presence of a massive charm quark-antiquark pair in the final state; see also the scale choices in Section 7.3.2.

[11] For the Λ_c^+ measurement from [135], where no double-differential distribution is available, the single-differential cross sections $\frac{\mathrm{d}\sigma}{dp_T}$ and $\frac{\mathrm{d}\sigma}{dy}$ were used for the 'LHCb Abs' and 'LHCb Norm' approaches (see Section 7.3.3), respectively.

[12] Except that for the sources 'Bin size', 'Trigger efficiency', 'Tracking efficiency', 'Muon identification' and 'Angular distribution' from the beauty measurement the lowest boundaries from the respective ranges reported

The uncorrelated systematic uncertainty for each bin was obtained by subtracting all correlated sources from the total uncertainty, reported in the original papers. The 3.5% luminosity uncertainty was treated as correlated between the charm and beauty measurements. Additionally to the experimental uncertainties, the correlated fragmentation-fraction uncertainties were technically assigned to the data.

7.3.2 Details of PDF fit

The PDF fitting framework is similar to that which has been used for the FFNS fit with the HERA charm combined data, described in Section 6.5.3.1. Briefly recapping, the study was performed with the HERAFitter [216, 217] program, which is based on the NLO DGLAP evolution scheme [27–32] as implemented in QCDNUM [45]. Theoretical predictions for the HERA data were obtained at NLO using the FF ABM scheme in the pole-mass variant, as implemented in OPENQCDRAD [218]. For the HERA data, the factorisation and renomalisation scales were set to $\mu_f = \mu_r = Q$ for the light quarks and to $\mu_f = \mu_r = \sqrt{Q^2 + 4m_Q^2}$ for the heavy quarks, where Q^2 is boson virtuality. The number of active flavours in the PDFs and in the α_s evolution was set to $n_f = 3$. The strong coupling constant was set to $\alpha_s^{n_f=3}(M_Z) = 0.1059$, corresponding to $\alpha_s^{n_f=5}(M_Z) = 0.1185$ [183]. The PDFs were described at the parametrisation scale $Q_0^2 = 1.4\,\text{GeV}^2$ using the HERAPDF parametrisation style with 13 free parameters (Eq. 6.23, 6.24). The charm and beauty masses were left free in the fit and determined in HERAFitter by minimisation of a χ^2-function. Afterwards, the following uncertainties were evaluated:

- a fit uncertainty was evaluated using the Hessian method [204, 217] from a χ^2 variation of 1;
- model uncertainties from variations of theory model parameters:
  - f_s was varied in the range $0.23 < f_s < 0.38$;
  - Q_{min}^2 was varied in the range $2.5 < Q_{min}^2 < 5.0\,\text{GeV}^2$;
  - $\alpha_s^{n_f=3}$ was varied in the range $0.1059 < \alpha_s^{n_f=3} < 0.1069$;
  - μ_f and μ_r for heavy-flavour production in ep were varied simultaneously by a factor of 2 (the framework allows only their simultaneous variation);
- parametrisation uncertainties:
  - Q_0^2 was varied to $Q_0^2 = 1.9\,\text{GeV}^2$;
  - the parameter D_{u_v} was released;
  - the parameter $D_{\overline{U}}$ was released;
  - the parameter $D_{\overline{D}}$ was released.

in Table 1 of [148] were taken as a correlated part of the uncertainties.

For the model uncertainties, all variations were added in quadrature, while for those of parametrisation, the largest deviation of all variations was taken.

In variants of the fit with the LHCb heavy-flavour data additional uncertainties were evaluated, which are related to the uncertainties of the respective theoretical calculations; they are referred to as the 'MNR uncertainties':

- variations of the fragmentation and renormalisation scales, as described later in Section 7.3.3, and
- variations of the fragmentation parameters $\alpha_k = 4.4 \pm 1.7$ for charm and $\alpha_k = 11 \pm 4$ for beauty.

The MNR uncertainties were obtained by adding these variations in quadrature.

7.3.3 Strategy of QCD analysis

The strategy of the QCD analysis was to perform several PDF fits, with and without the LHCb data, and then compare the results. The two approaches of fitting the LHCb data were studied: fitting the absolute cross section or the cross section normalised in y; they are described below.

7.3.3.1 Fitting absolute LHCb cross sections

In this approach, the absolute double-differential cross sections $\frac{\mathrm{d}^2\sigma}{\mathrm{d}p_T\mathrm{d}y}$ were fitted. These quantities contain the maximum information and therefore are sensitive to all physical and non-physical parameters of the theoretical calculations: the PDFs, heavy-quark mass, fragmentation function and especially factorisation and renormalisation scales. The scale dependence of the predictions is of the order of a factor of 2, thus much exceeding the experimental data uncertainties, although the PDF uncertainties from the modern groups at very low x and low Q^2 are even larger (see Fig. 7.1)[13]. This fact makes the study rather complicated: in order to account for the uncertainties of the perturbative predictions, the scales should be varied, but these external variations change the description of the data and the fit results drastically, and thus are hard to control.

For this variant of the fit, the scale parameters A_f^c, A_r^c, A_f^b and A_r^b were therefore fitted for the nominal (central) results, while for the estimation of the scale uncertainties the following procedure was used: the factorisation and renormalisation scales were varied independently one at a time in the ranges [0.50;2.00] and [0.25;1.00][14], respectively, while the other scale was being refitted. More explicitly, the scale uncertainties include the following four variations:

- $A_f^c = A_f^b = 2.00$ with A_r^c, A_r^b free;
- $A_f^c = A_f^b = 0.50$ with A_r^c, A_r^b free;
- $A_r^c = A_r^b = 1.00$ with A_f^c, A_f^b free;

[13] Truly speaking, the PDF uncertainties in this region should be considered as infinitive.

[14] The 'common' range for the variations [0.50;2.00] for μ_r is discarded, since the χ^2/n_{dof} for $A_r^c = A_r^b = 2.00$ variation was found to be unacceptably large ($\chi^2/n_{\mathrm{dof}} = 2497/1089$).

- $A_r^c = A_r^b = 0.25$ with A_f^c, A_f^b free.

In addition, for the variation $A_f^c = A_f^b = 0.50$, the cut $p_T > 2\,\text{GeV}$ was applied for the charm LHCb data to ensure that the factorisation scale is above $1\,\text{GeV}^2$, since this is technically required in the framework.[15] Note that in this procedure, each scale is varied independently by a factor of 2, although still the whole concept is strongly data dependent. This sophisticated procedure was necessary to give a reasonable description of the data for all variations of the fit.

7.3.3.2 Fitting normalised LHCb cross sections

In this approach, the y shape of the cross-section ratio $\frac{\mathrm{d}\sigma}{\mathrm{d}y} / \frac{\mathrm{d}\sigma}{\mathrm{d}y_0}$ in each p_T bin was fitted, where $\frac{\mathrm{d}\sigma}{\mathrm{d}y_0}$ is the cross section in the central rapidity bin $3.0 < y_0 < 3.5$. The virtue is that the observable defined in this way has a much reduced scale dependence, while it is still very sensitive to the PDFs, namely to their x shape. This can be understood very easily: the change in the production rate in neighboring bins of y is driven mainly by the change in the input PDFs, while the hard-scattering process remains essentially the same. Hence the μ_r dependence is reduced to $\sim 1\%$ and the μ_f to ~ 5–10% (the renormalisation scale affects the matrix elements only, while the factorisation scale affects both the matrix elements and the PDFs). Reduction of the scale dependence is illustrated in Appendix F.4 (Figs. F.1, F.2). In addition, the dependence on the heavy-quark mass and the fragmentation function is also significantly reduced. For the mass, it is reduced almost to zero, while the fragmentation effects are still sizeable at low transverse momentum, since the fragmentation is performed by rescaling the quark three-momentum and thus it changes the rapidity of a massive particle.

To illustrate that the strong PDF dependence still remains in the normalised cross sections, in Fig. 7.8 the two sets of the predictions obtained from the PDFs, based on the HERA-only data, are shown for the most forward y bin of the LHCb charm data: the first is the nominal fit with the HERA data only and the second is the variation that results in one of the dominant uncertainties for gluons in the low-x and low-Q^2 region. The latter is clearly disfavoured by the data, since it predicts negative cross sections in bins with large y.

Owing to greatly reduced dependence on the scales, in this variant of the fit the 'common' scale choice and variations were used: for the nominal fit, the scale parameters were set to $A_f^c = A_f^b = A_r^c = A_r^b = 1$ and varied independently one at a time in the range [0.5;2.0]. More explicitly, the scale uncertainties include the following four variations:

- $A_f^c = A_f^b = 2.0$, $A_r^c = A_r^b = 1.0$;
- $A_f^c = A_f^b = 0.5$, $A_r^c = A_r^b = 1.0$;
- $A_f^c = A_f^b = 1.0$, $A_r^c = A_r^b = 2.0$;
- $A_f^c = A_f^b = 1.0$, $A_r^c = A_r^b = 0.5$.

Similar to the previous approach, for the variation $A_f^c = A_f^b = 0.50$, the cut $p_T > 2\,\text{GeV}$ was applied for the charm LHCb data to ensure that the factorisation scale is above $1\,\text{GeV}^2$.

[15] The QCDNUM package performs PDF evolution only in the region $Q^2 \geq 1\,\text{GeV}^2$.

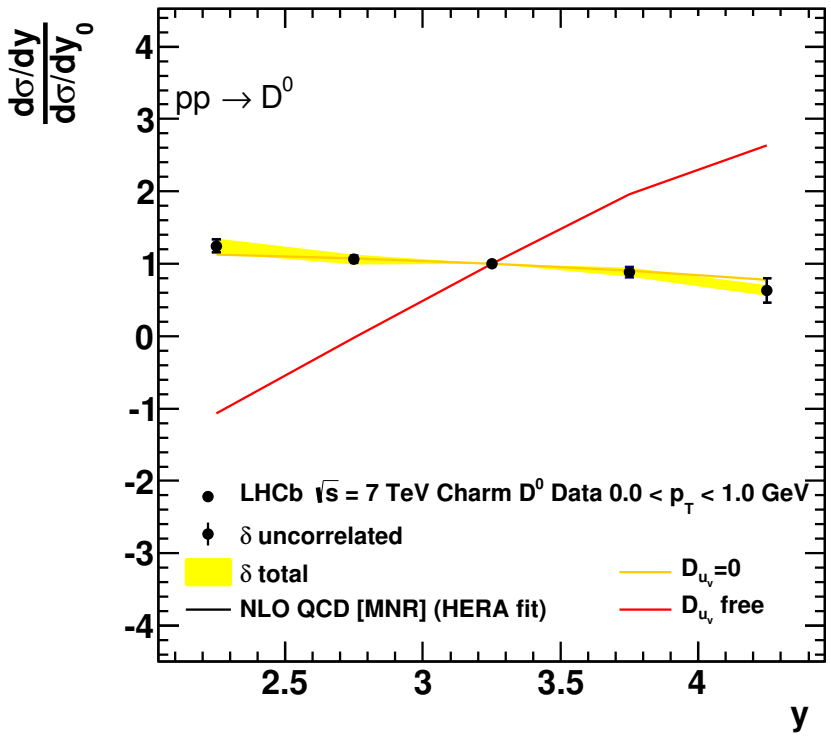

Figure 7.8: Predictions for the normalised cross sections from the LHCb measurement of D^0-meson production in the bin $0 < p_T < 1\,\text{GeV}$, obtained with two different PDF fits to the HERA-only data as explained in the text.

All correlated experimental systematic uncertainties and the fragmentation fractions cancel for the normalised cross sections, whilst for a given p_T bin the uncorrelated uncertainty of the central $\frac{\mathrm{d}\sigma}{\mathrm{d}y_0}$ bin was treated as correlated between the remaining y bins (because the cross sections in the remaining y bins were divided by the same $\frac{d\sigma}{dy_0}$).

7.4 Fit results

In this Section the results of three fits are presented and discussed:

- the fit with the HERA-only data, referred to as 'HERA only' (Section 7.4.1);
- the fit with the HERA and LHCb data using the absolute LHCb cross sections, referred to as 'LHCb Abs' (Section 7.4.2);
- the fit with the HERA and LHCb data using the normalised LHCb cross sections, referred to as 'LHCb Norm' (Section 7.4.3).

The direct comparison of all fitted PDFs and final conclusions are given in the next Section 7.5.

Dataset	χ^2/n_{dof}		
	HERA only	LHCb Abs	LHCb Norm
NC DIS HERA-I combined e^-p	108 / 145	108 / 145	108 / 145
NC DIS HERA-I combined e^+p	407 / 379	419 / 379	419 / 379
CC DIS HERA-I combined e^-p	22 / 34	26 / 34	26 / 34
CC DIS HERA-I combined e^+p	37 / 34	39 / 34	41 / 34
$c\bar{c}$ DIS HERA combined	50 / 52	78 / 52	47 / 52
$b\bar{b}$ DIS ZEUS Vertex	12 / 17	16 / 17	12 / 17
LHCb D^0		68 / 38	17 / 30
LHCb D^+		53 / 37	18 / 29
LHCb D^{*+}		50 / 31	19 / 22
LHCb D_s^+		24 / 28	11 / 20
LHCb Λ_c^+		5 / 6	5 / 3
LHCb B^+		99 / 135	81 / 108
LHCb B^0		66 / 95	35 / 76
LHCb B_s^0		78 / 75	23 / 60
Correlated uncertainties	9	73	49
Logarithmic correction	2	−129	48
Total χ^2/n_{dof}	647 / 646	1073 / 1087	958 / 994
p(χ^2,n_{dof})	49%	61%	79%

Table 7.2: χ^2/n_{dof} for all datasets for three variants of the fit. The contributions from correlated sources and logarithmic correction, total χ^2/n_{dof} and the corresponding probability values are also given.

7.4.1 'HERA only'

Here the results of the fit with the HERA-only data (datasets 1–6) are presented. The total χ^2 per degree of freedom for the fit is $\chi^2/n_{\text{dof}} = 647/646$ indicating perfect consistency of the data. The partial χ^2/n_{dof} for all datasets are given in Table 7.2. The fitted values for the heavy-quark pole masses are $m_c = 1.34 \pm 0.06\,\text{GeV}$, $m_b = 4.31 \pm 0.16\,\text{GeV}$ (the quoted uncertainties are the fit uncertainties only; note that this study does not aim to measure the heavy-quark masses).

The individual contributions to the uncertainties of the gluon, sea and valence-quark distributions at the scale $Q^2 = 10\,\text{GeV}^2$ are shown in Fig. 7.9. For better visibility also the relative individual uncertainties are shown in Fig. 7.10.[16] Note the gluon uncertainties in the low-x region: since this region is not covered directly by the HERA data, the dominant uncertainties are the parametrisation ones, namely those which come from releasing the $D_{\bar{U}}$ parameter. This is illustrated in Fig. 7.11, where all parametrisation variations are shown separately. Qualitatively

[16] The same plots for $Q^2 = 100\,\text{GeV}^2$ are available in Appendix F.4 (Figs. F.3, F.4).

it can be understood in the following way: since gluons in this region are not constrained by the data, they are constrained only via sum rules for certain distributions of all other partons; when the parametrisation for other partons is changed, a new solution results in a completely different distribution for gluons in the low-x region. This also explains the large spread of the results obtained by the different PDF groups, which was observed in Fig. 7.1: since the different groups use different parametrisations and none of them uses data which constrain gluons at low x, they obtain different gluon distributions in this region. Later when the impact of the LHCb data is studied, the parametrisation variations will be used as the 'litmus test': a first indication of whether constraints in the low-x region are present.

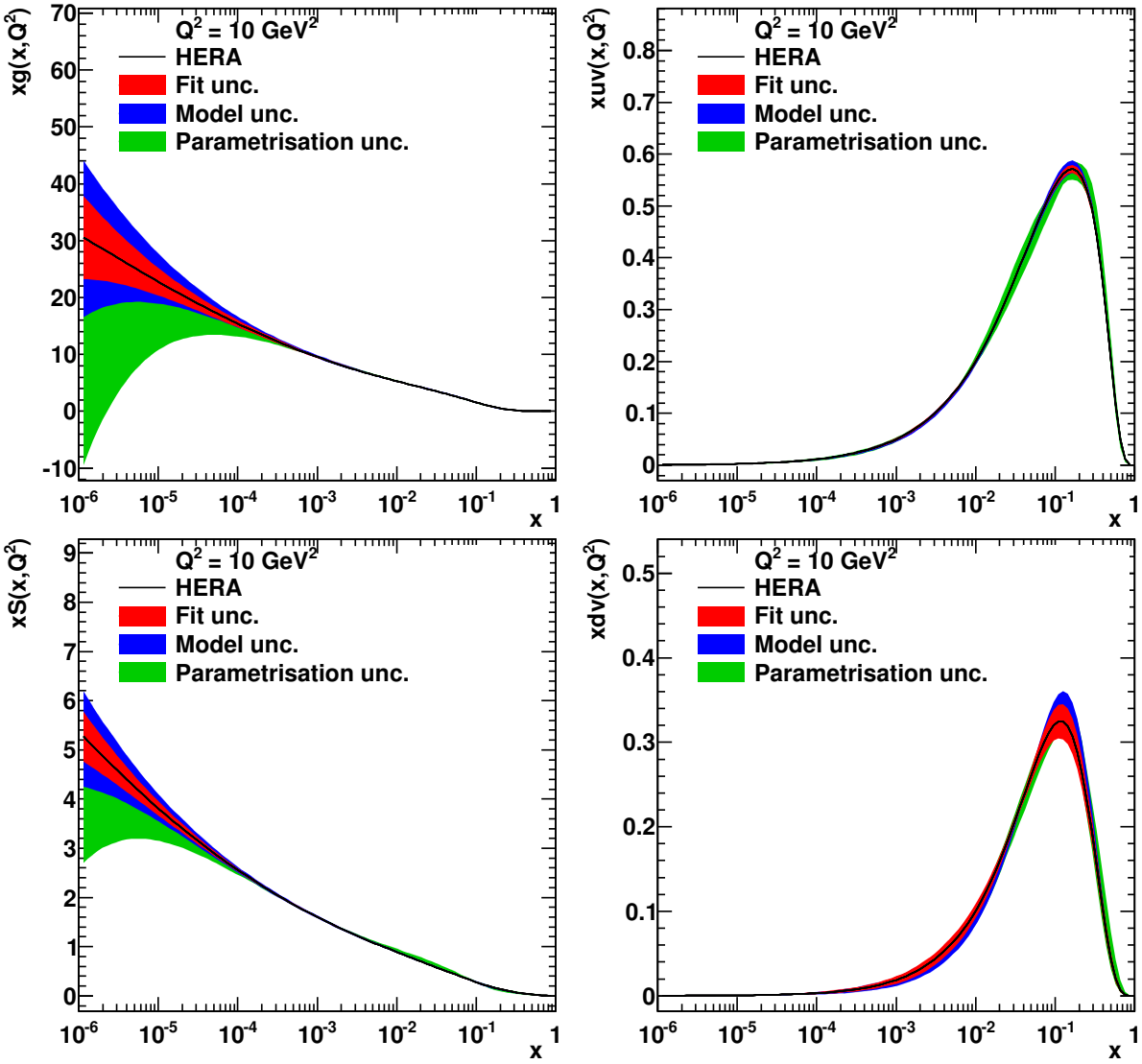

Figure 7.9: The individual contributions to the uncertainties of the gluon (top left), u-valence (top right), sea (bottom left) and d-valence (bottom right) distributions at $Q^2 = 10\,\mathrm{GeV}^2$ obtained in the fit with the HERA-only data.

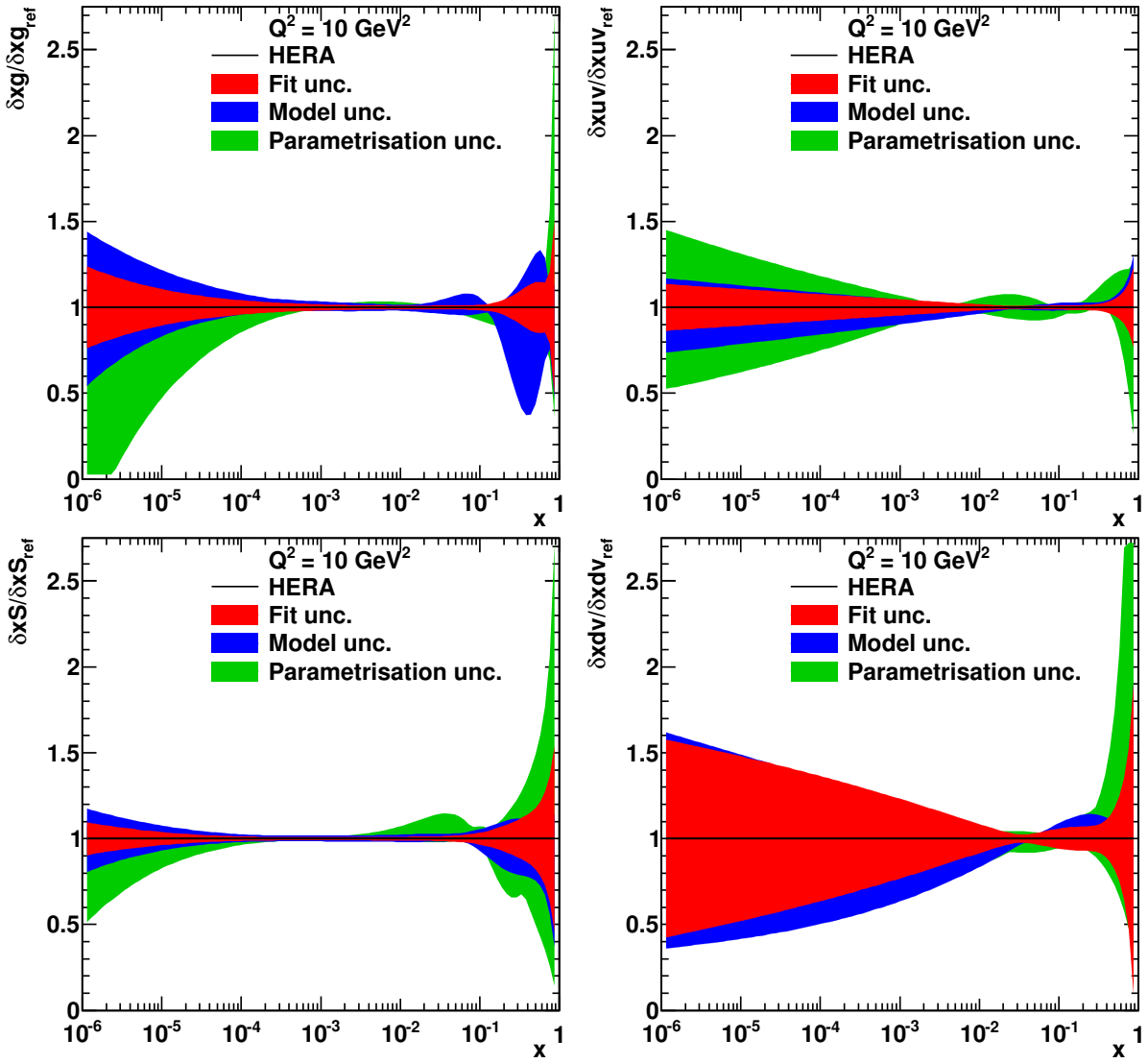

Figure 7.10: The individual contributions to the relative uncertainties of the gluon (top left), u-valence (top right), sea (bottom left) and d-valence (bottom right) distributions at $Q^2 = 10\,\text{GeV}^2$ obtained in the fit with the HERA-only data.

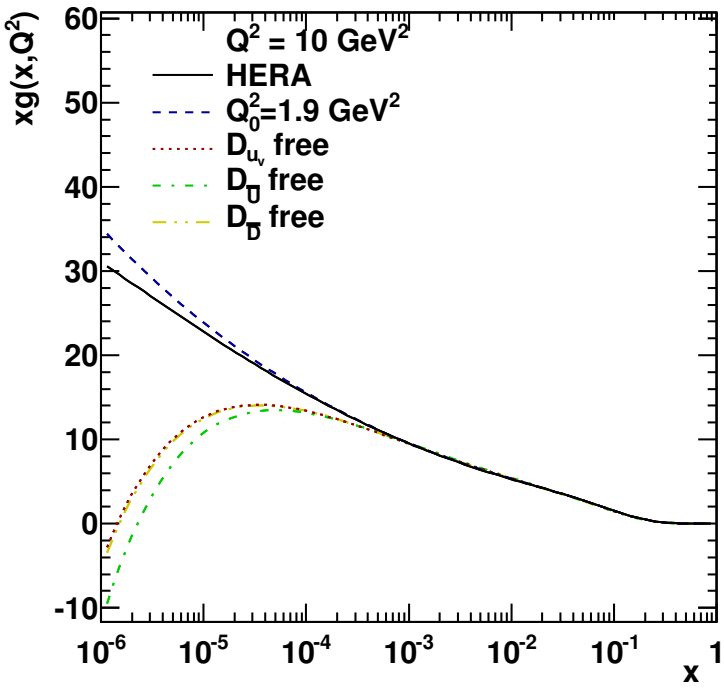

Figure 7.11: The parametrisation variations for the gluon distribution at $Q^2 = 10\,\mathrm{GeV}^2$ in the fit with the HERA-only data.

7.4.2 'LHCb Abs'

Here the results of the fit with the HERA and LHCb data (datasets 1–14) using the 'LHCb Abs' approach are presented. The total χ^2 per degree of freedom is $\chi^2/n_{\mathrm{dof}} = 1073/1087$. The partial χ^2/n_{dof} for all datasets are given in Table 7.2. For the LHCb charm and beauty datasets they vary from 0.9 to 1.8 and from 0.7 to 1.0, respectively, indicating an overall reasonable description of the charm data and a perfect one of the beauty data. As an example of the data description in the fit, in Fig. 7.12 the cross sections for D^0 and B^+ mesons for one of the y bins are shown.

The fitted values for the scale parameters are:

$$\begin{aligned} A_f^c &= 0.66, \\ A_r^c &= 0.44, \\ A_f^b &= 0.26, \\ A_r^b &= 0.33. \end{aligned} \tag{7.1}$$

Note that all values are within the range [0.25;1.00]; also note the significant difference between the fitted scales for charm and beauty. Additionally, as expected, a positive correlation was found between A_f^c, A_r^c and A_f^b, A_r^b, respectively.

The results of the 'litmus test' — the parametrisation variations — are shown in Fig. 7.13 (top left). As expected, in contrast to the results obtained with the HERA-only data, gluons are now strongly constrained in the low-x region.

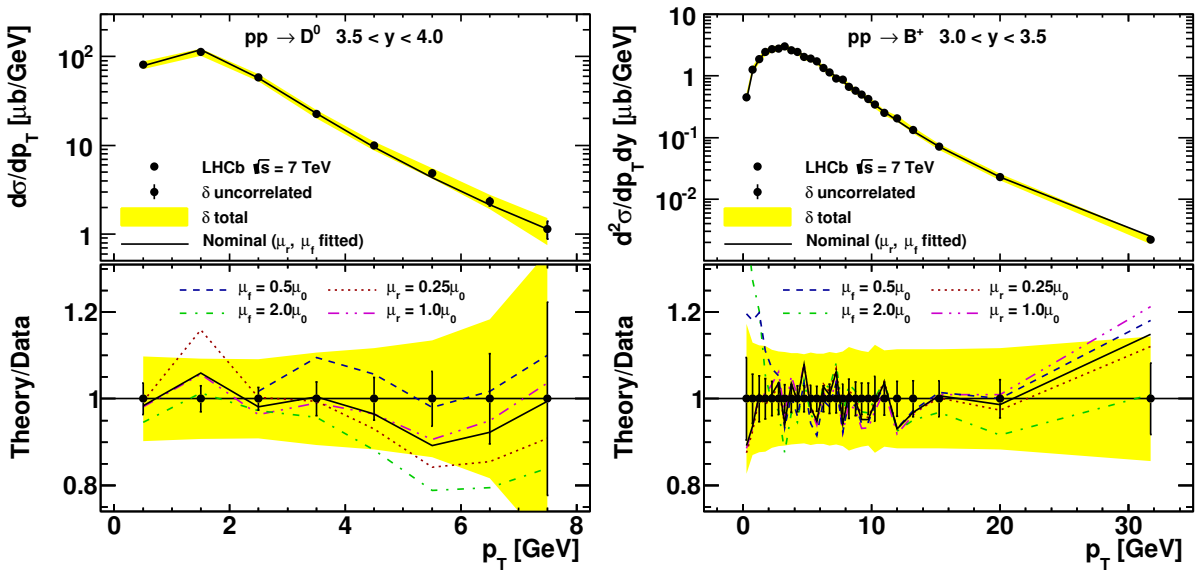

Figure 7.12: Data to theory comparison for a representative subset of the LHCb absolute cross sections: D^0 mesons, bin $3.5 < y < 4.0$ (left); B^+ mesons, bin $3.0 < y < 3.5$ (right). In the bottom panels the ratios theory/data for the nominal variant of the fit and the scale variations are shown. For demonstration purpose, correlated shifts for data points obtained in the fit using nuisance parameters are applied to theoretical predictions. Uncorrelated uncertainties for data points are shown as they are rescaled in the fit, while total uncertainties are shown as not rescaled.

The effect of scale variations on the predictions in the fit is shown in Fig. 7.12 and their effect on the fitted PDFs is shown in Fig. 7.13 (top right). The scale uncertainties are much larger than the parametrisation ones, however comparing to the fit with the HERA-only data they are a factor of 3 smaller than the total uncertainties. Another interesting observation from Figs. 7.12 and 7.13 (top right) is that the changes for the predictions from the scale variations are predominantly changes in their normalisation (see also Figs. F.1, F.2 in Appendix F.4); the fit handles them by adjusting the other scale and making large shifts for the correlated uncertainties of the data. This often results in a formally very bad χ^2 value (from the probability point of view), however the PDFs are affected less and remain reasonable, especially comparing to the huge total 'HERA only' uncertainty at low x.

In addition, variations of the fragmentation-function parameters were performed, as described in 7.2.1.2. The effect on the fitted PDFs is shown in Fig. 7.13 (bottom). All fragmentation variations result in a good description of the data, since relatively small changes of the p_T shape are easily compensated by adjusting the scales. The resulting uncertainties are much smaller compared to the scale variations. However, for charm a strong tendency was observed: the LHCb charm data prefer a harder fragmentation function; this is discussed in more detail in Appendix F.2.

Finally, all individual contributions to the uncertainties are shown in Fig. 7.14 and the relative uncertainties are shown in Fig. 7.15.[17] The dominant uncertainties in the low-x region become the MNR ones, in particular coming from the scale variations.

[17] The same plots for $Q^2 = 100\,\text{GeV}^2$ are available in Appendix F.4 (Figs. F.5, F.6).

Afterwards, since the fit with the new data might be more sensitive to the gluon parametrisation, a more flexible variant for gluons was considered:

$$xg(x) = A_g x^{B_g}(1-x)^{C_g}(1 + D_g + E_g x^2 + F_g x^3) - A'_g x^{B'_g}(1-x)^{C'_g} \tag{7.2}$$

and the fit repeated with the parameters D_g, E_g, F_g and C'_g released one at a time. The obtained changes in the PDFs were negligible.

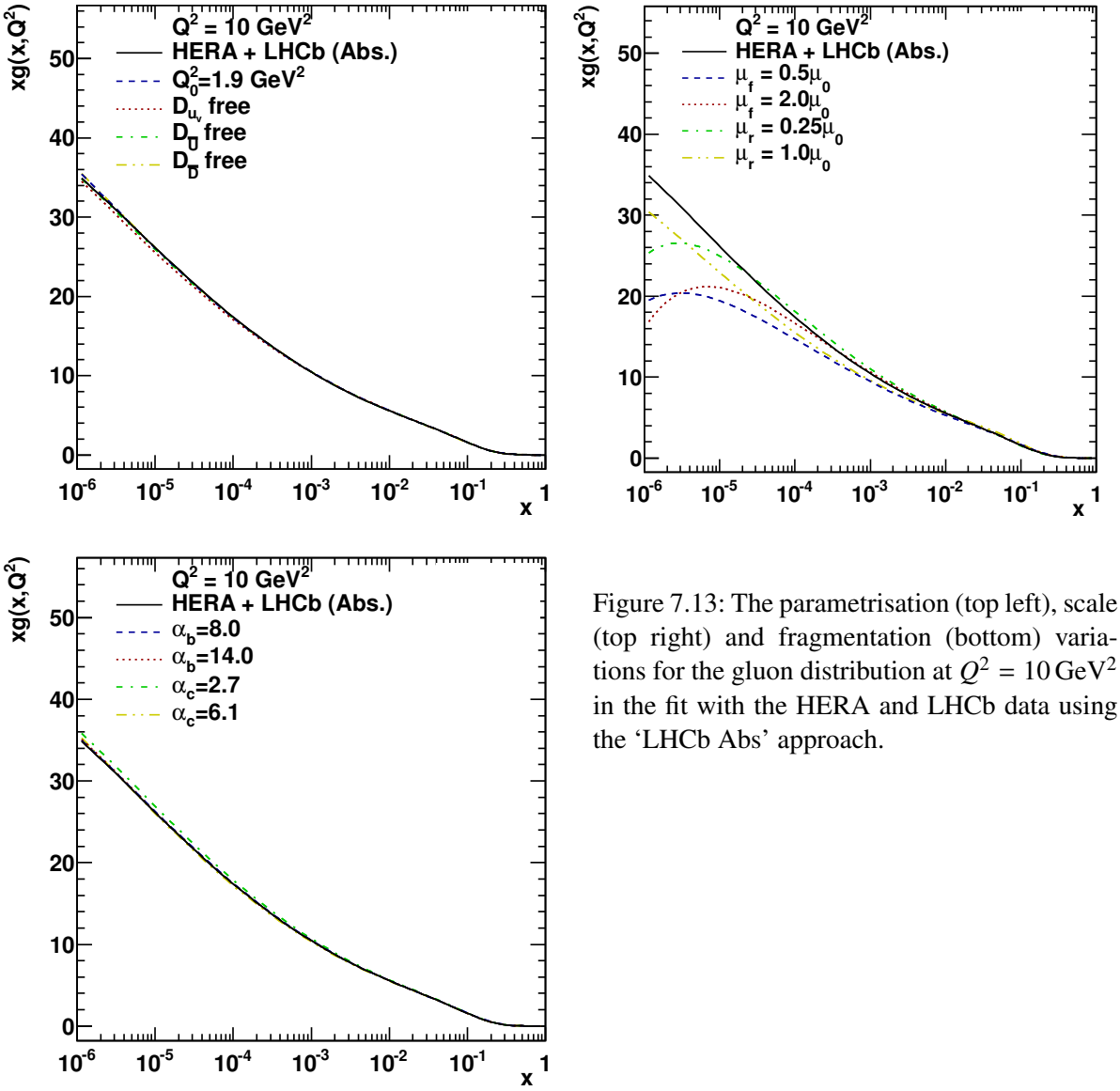

Figure 7.13: The parametrisation (top left), scale (top right) and fragmentation (bottom) variations for the gluon distribution at $Q^2 = 10\,\text{GeV}^2$ in the fit with the HERA and LHCb data using the 'LHCb Abs' approach.

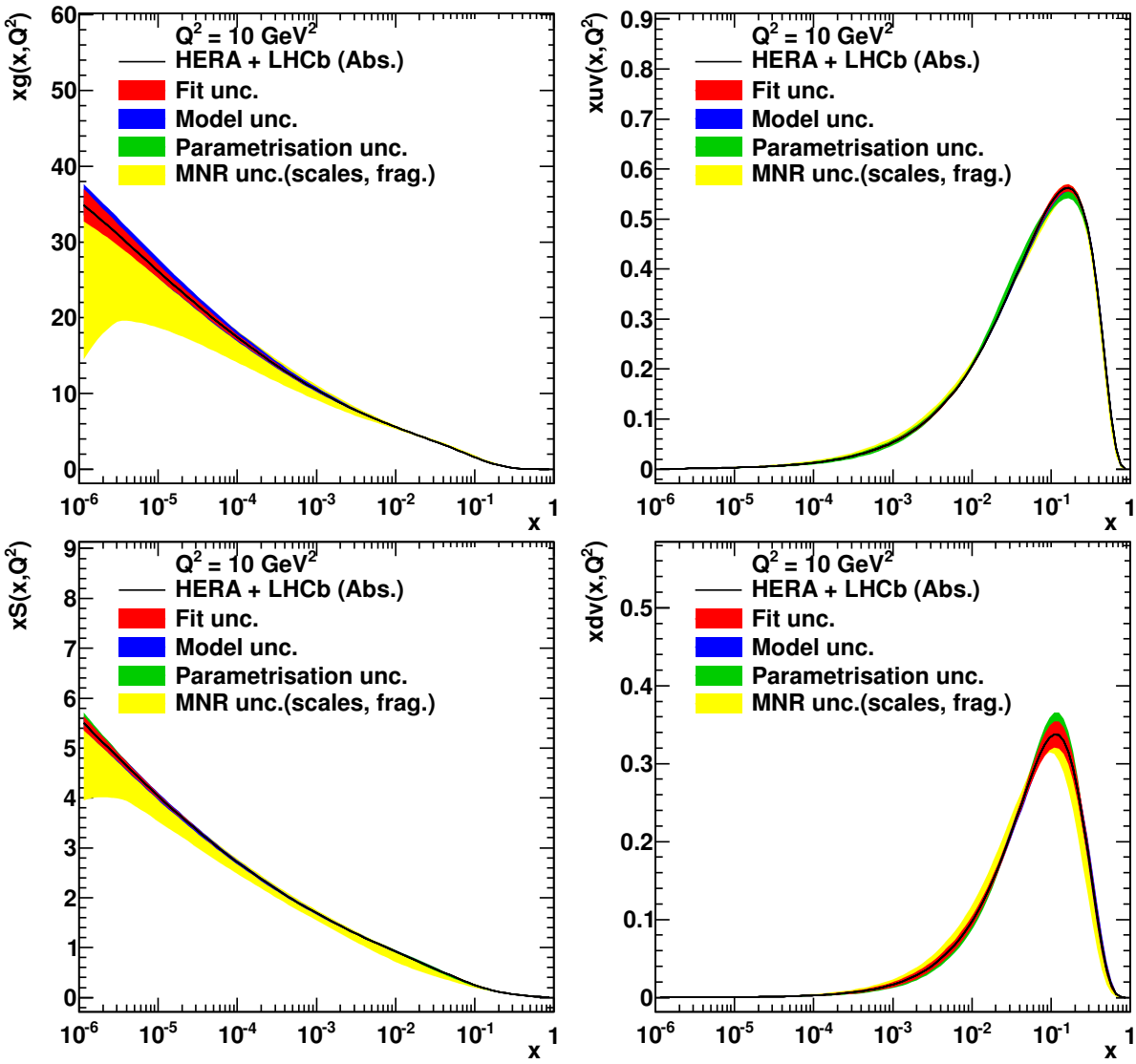

Figure 7.14: The individual contributions to the uncertainties of the gluon (top left), u-valence (top right), sea (bottom left) and d-valence (bottom right) distributions at $Q^2 = 10\,\text{GeV}^2$ obtained in the fit with the HERA and LHCb data using the 'LHCb Abs' approach.

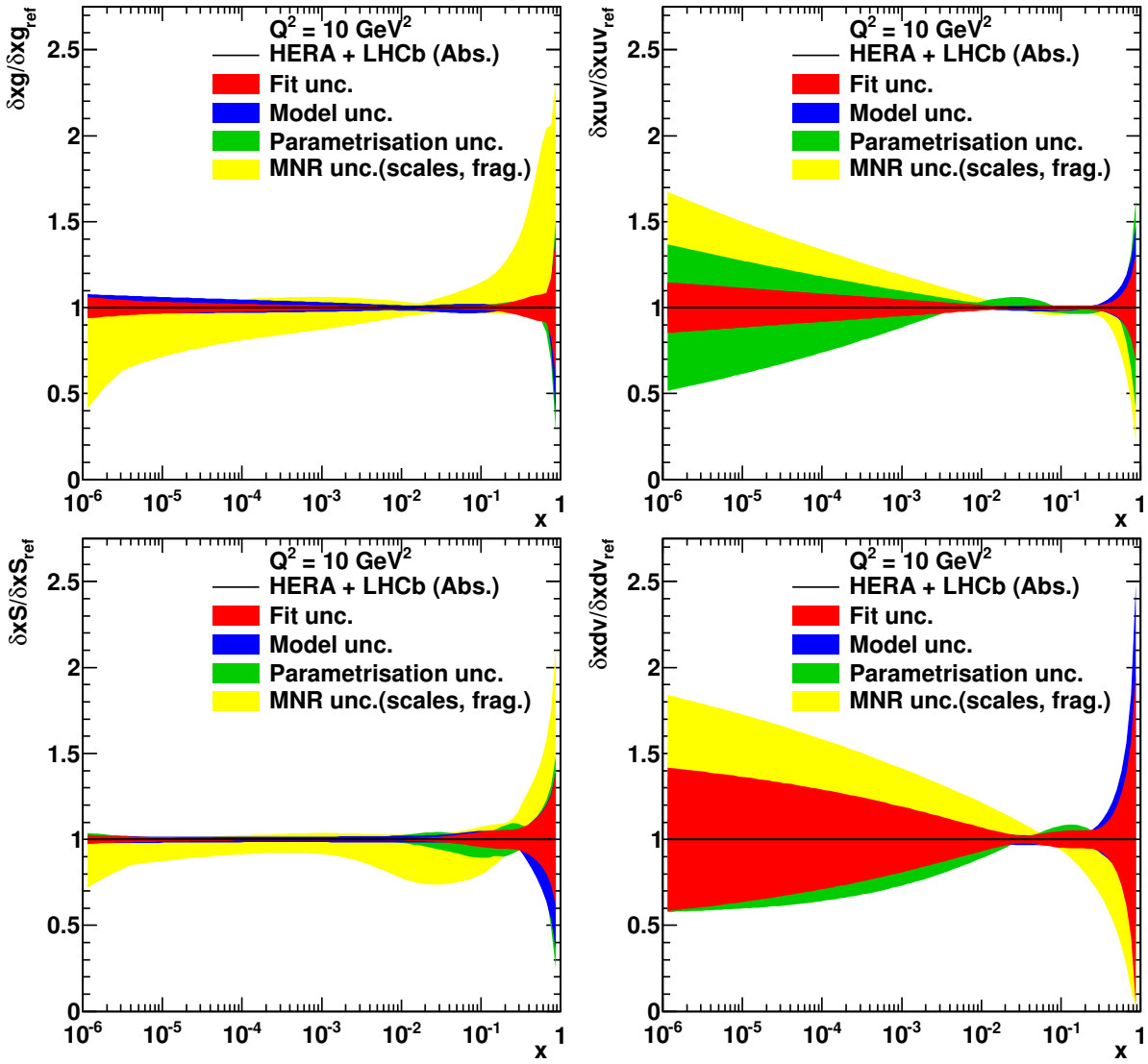

Figure 7.15: The individual contributions to the relative uncertainties of the gluon (top left), u-valence (top right), sea (bottom left) and d-valence (bottom right) distributions at $Q^2 = 10\,\text{GeV}^2$ obtained in the fit with the HERA and LHCb data using the 'LHCb Abs' approach.

7.4.3 'LHCb Norm'

Here the results of the fit with the HERA and LHCb data (datasets 1–14) using the 'LHCb Norm' approach are presented. The total χ^2 per degree of freedom is $\chi^2/n_{\text{dof}} = 958/994$. The partial χ^2/n_{dof} for all datasets are given in Table 7.2. For the LHCb charm and beauty datasets they vary from 0.4 to 0.9[18], indicating perfect description of the data and possible overestimation of the uncorrelated experimental uncertainties for the y shape (this can be thought of rather as an underestimation of correlations of the systematics). As an example of the data description in the fit, in Fig. 7.16 the cross sections for D^0 and B^+ mesons for one of the y bins are shown.

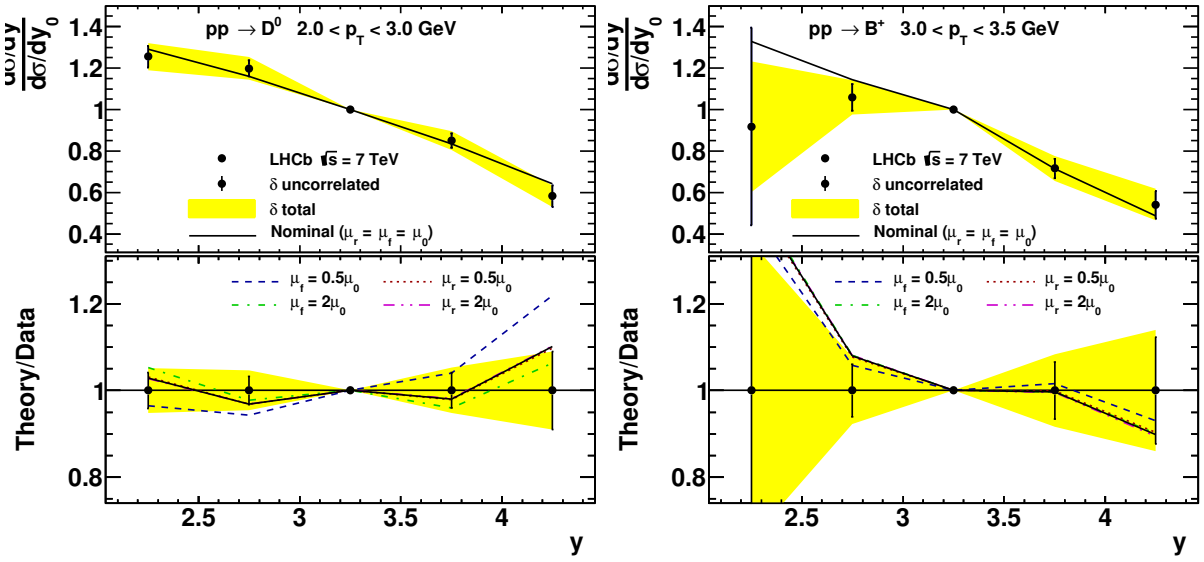

Figure 7.16: Data to theory comparison for a representative subset of the LHCb normalised cross sections: D^0 mesons, bin $2.0 < p_T < 3.0$ GeV (left); B^+ mesons, bin $3.0 < p_T < 3.5$ GeV (right). The central rapidity bins are fixed to 1 by the definition of the normalised cross sections. In the bottom panels the ratios theory/data for the nominal variant of the fit and the scale variations are shown. For demonstration purpose, correlated shifts for data points obtained in the fit using nuisance parameters are applied to theoretical predictions. Uncorrelated uncertainties for data points are shown as they are rescaled in the fit, while total uncertainties are shown as not rescaled.

The results of the 'litmus test' are shown in Fig. 7.17 (top left). Gluons in the low-x region remain constrained, although somewhat weaker than in the 'LHCb Abs' approach, but still drastically comparing to the 'HERA only' results.

The effect of the scale variations on the predictions in the fit is shown in Fig. 7.16 and their effect on the fitted PDFs is shown in Fig. 7.17 (top right). The effect of the fragmentation variations on the PDFs is shown in Fig. 7.17 (bottom). Note that fragmentation uncertainties obtained in this approach are larger than in the 'LHCb Abs' one, since the fragmentation effects are not reabsorbed in the refitted scales. All these variations result in a reasonable data description.

[18] Except for the low-statistics Λ_c^+ dataset, where $\chi^2/n_{\text{dof}} = 4.9/3$.

Finally, all individual contributions to the uncertainties are shown in Fig. 7.18 and the relative uncertainties are shown in Fig. 7.19.[19] The dominant uncertainties in the low-x and low-Q^2 region still remain the MNR ones, although they are comparable in size with the uncertainties from other sources.

Similar to the 'LHCb Abs' case, the study of the gluon parametrisation was performed by releasing the D_g, E_g, F_g and $C_g^{'}$ parameters (see Eq. 7.2). The obtained changes in the PDFs were negligible.

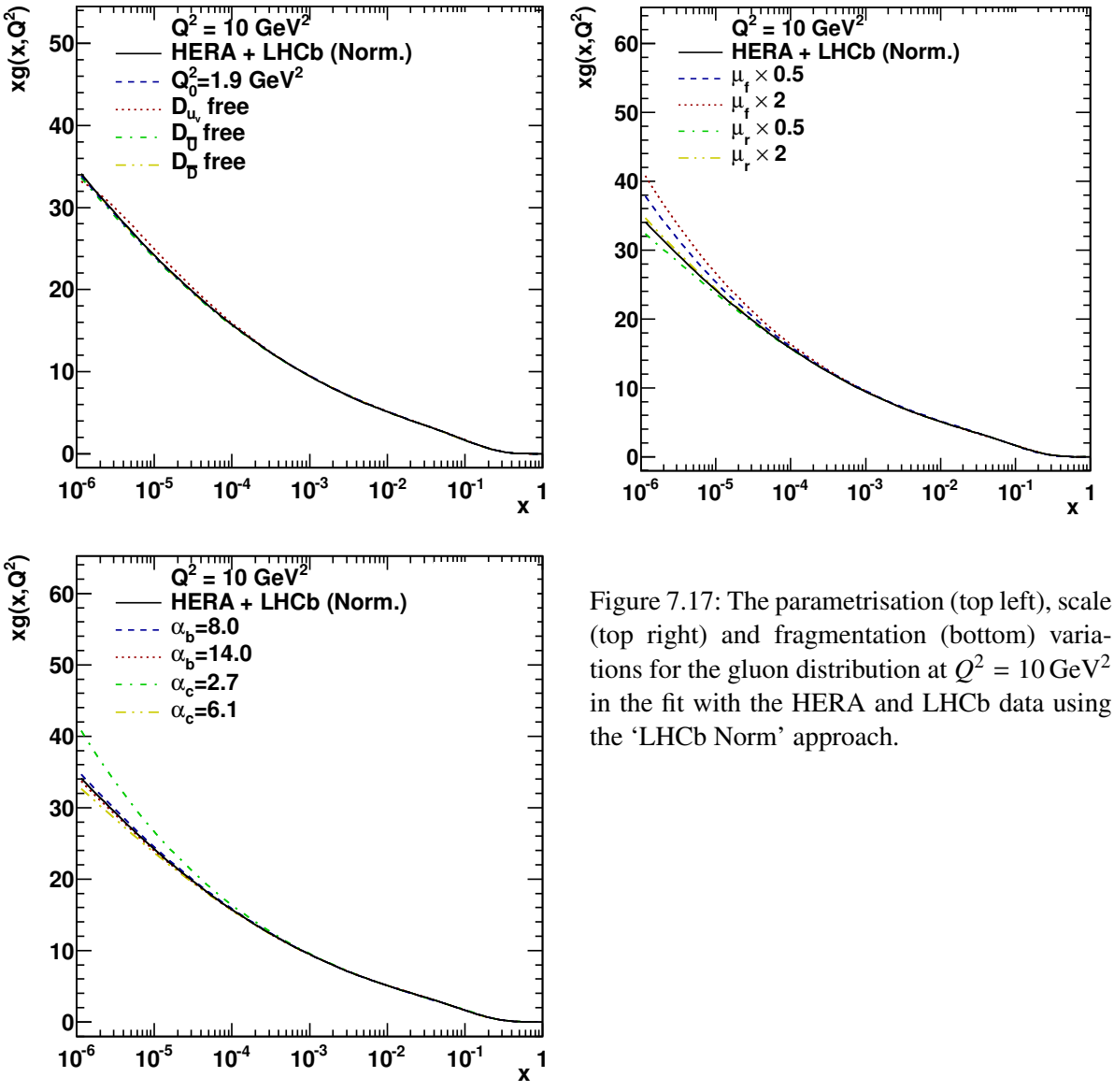

Figure 7.17: The parametrisation (top left), scale (top right) and fragmentation (bottom) variations for the gluon distribution at $Q^2 = 10\,\text{GeV}^2$ in the fit with the HERA and LHCb data using the 'LHCb Norm' approach.

[19] The same plots for $Q^2 = 100\,\text{GeV}^2$ are available in Appendix F.4 (Figs. F.7, F.8).

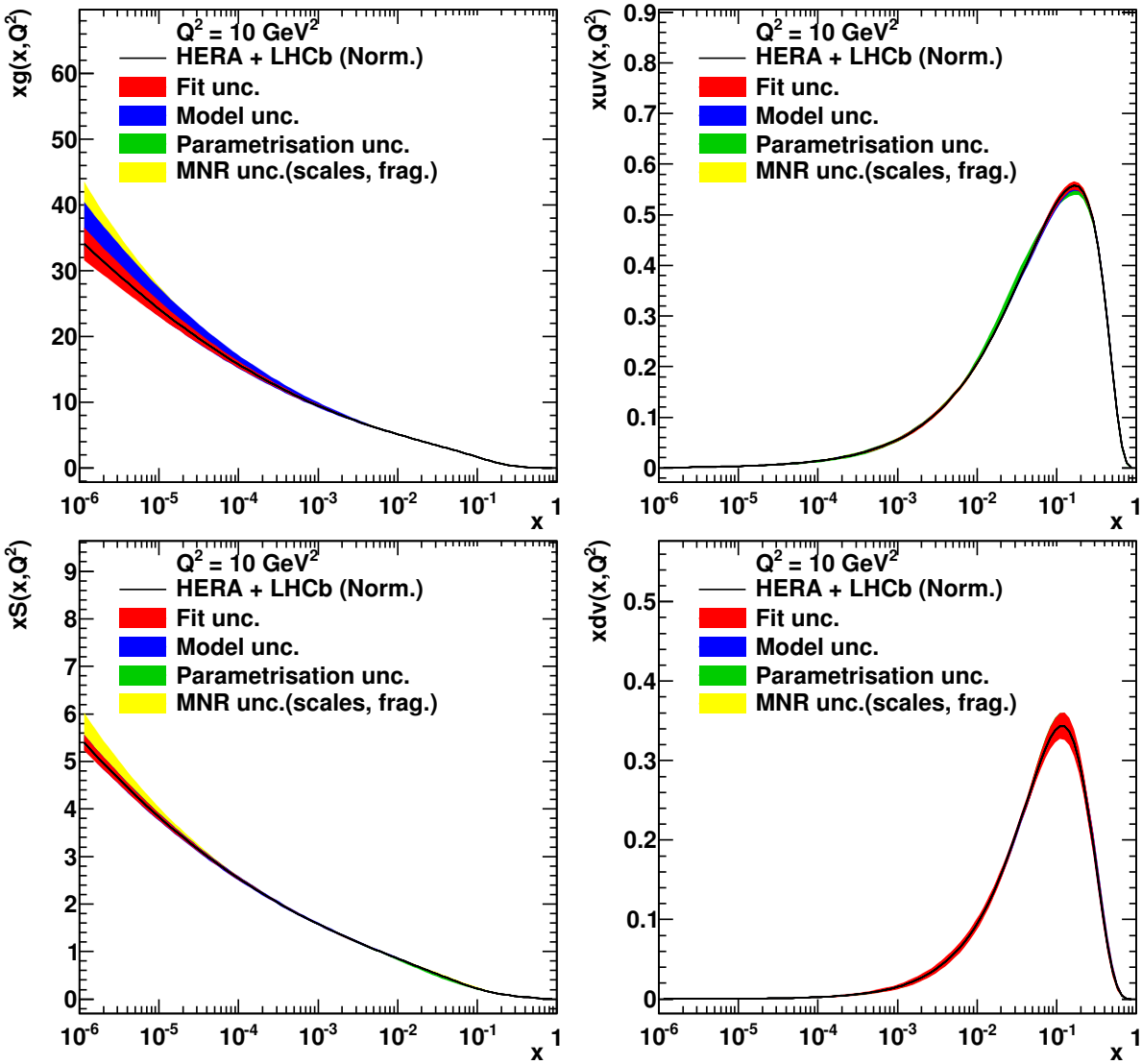

Figure 7.18: The individual contributions to the uncertainties of the gluon (top left), u-valence (top right), sea (bottom left) and d-valence (bottom right) distributions at $Q^2 = 10\,\text{GeV}^2$ obtained in the fit with the HERA and LHCb data using the 'LHCb Norm' approach.

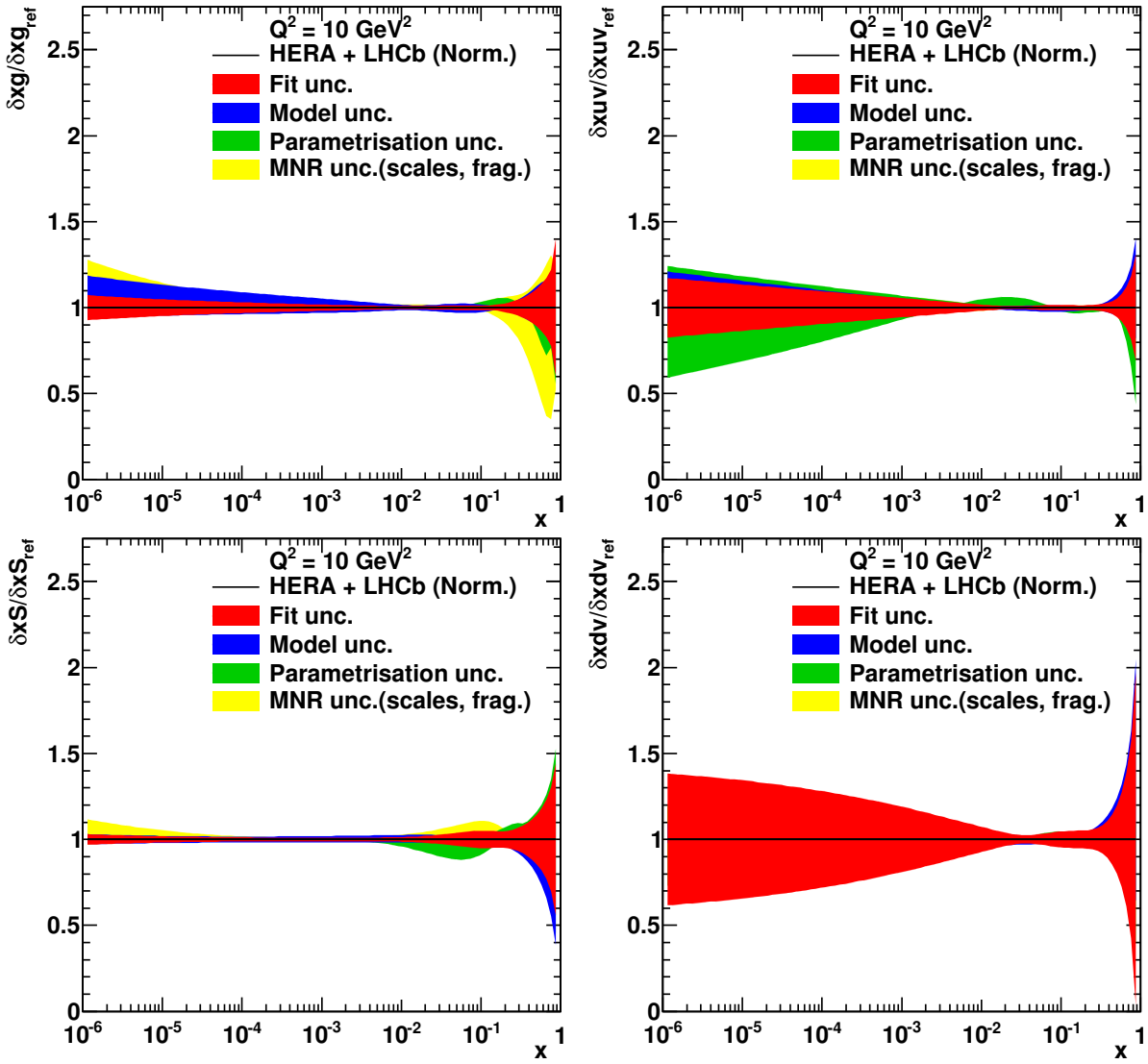

Figure 7.19: The individual contributions to the relative uncertainties of the gluon (top left), u-valence (top right), sea (bottom left) and d-valence (bottom right) distributions at $Q^2 = 10\,\text{GeV}^2$ obtained in the fit with the HERA and LHCb data using the 'LHCb Norm' approach.

7.5 Impact of LHCb heavy-flavour data on PDFs

The PDFs obtained obtained in the 'HERA only', 'LHCb Abs' and 'LHCb Norm' fits are compared at the scales $Q^2 = 10\,\text{GeV}^2$ and $Q^2 = 100\,\text{GeV}^2$ in Figs. 7.20 and 7.21, respectively. Their relative uncertainties are compared in Figs. 7.22 and 7.23.

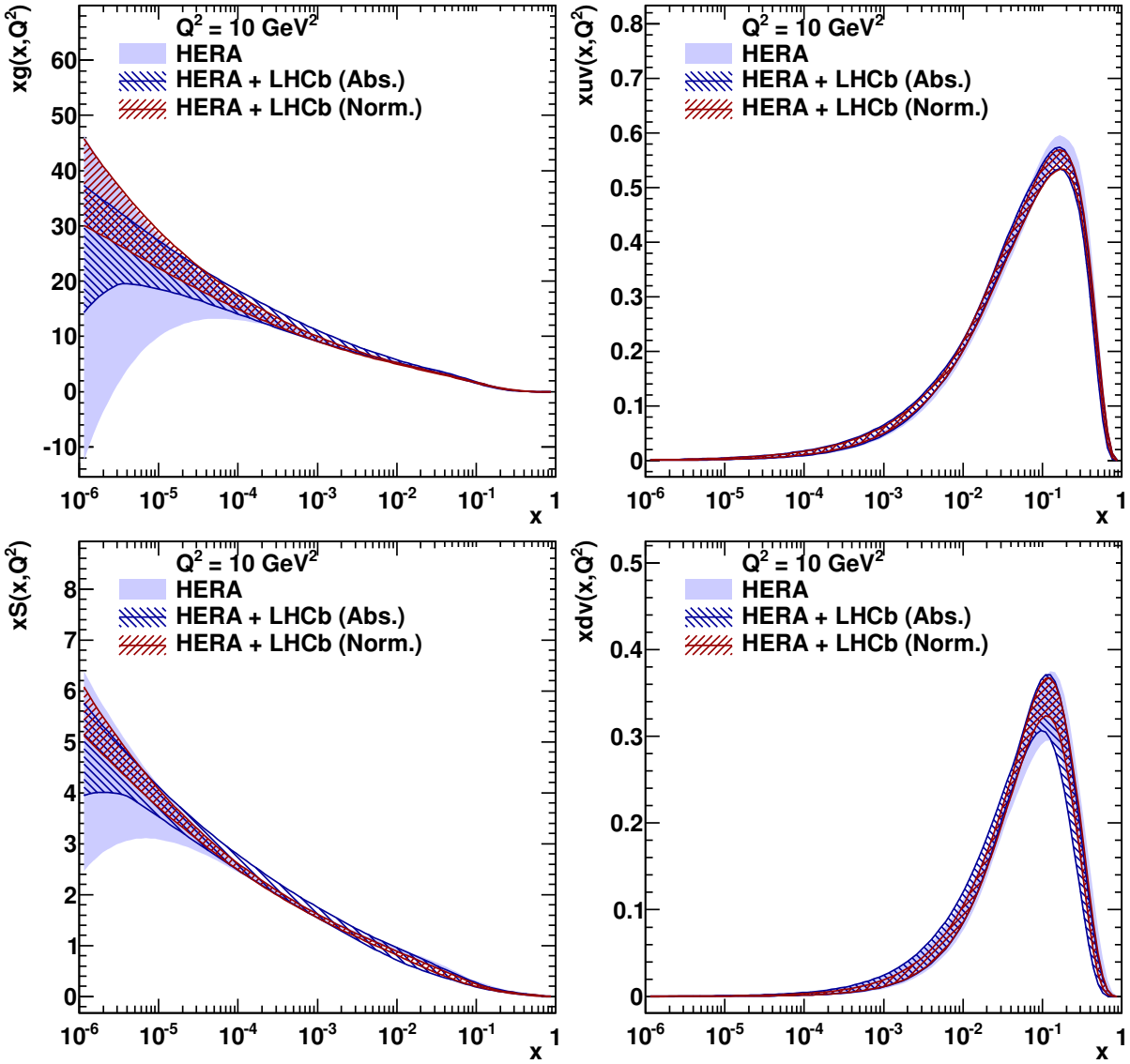

Figure 7.20: The gluon (top left), u-valence (top right), sea (bottom left) and d-valence (bottom right) distributions at $Q^2 = 10\,\text{GeV}^2$ obtained in the fit with the HERA-only, HERA and LHCb absolute, and HERA and LHCb normalised data. The widths of the bands represent the total uncertainties.

The two approaches of fitting the LHCb data result in similar constraints on low-x gluons, observed at both considered scales. Improvement is also observed for the sea density, while the valence-quark distributions remain essentially the same. Improvement of the sea distribution comes mainly from the connection of gluons and sea quarks via the PDF evolution equations.

Quantitatively, on average, reduction of the total uncertainty for gluons and sea quarks in the region $10^{-6} < x < 10^{-4}$, observed up to the scales $Q^2 \sim 1000\,\text{GeV}^2$, is of the order of a factor of 1.5–4. The gluon distribution remains positive in the region directly covered by the data $x \gtrsim 10^{-5.5}$, $Q^2 \gtrsim m_c^2 \approx 2\,\text{GeV}^2$.

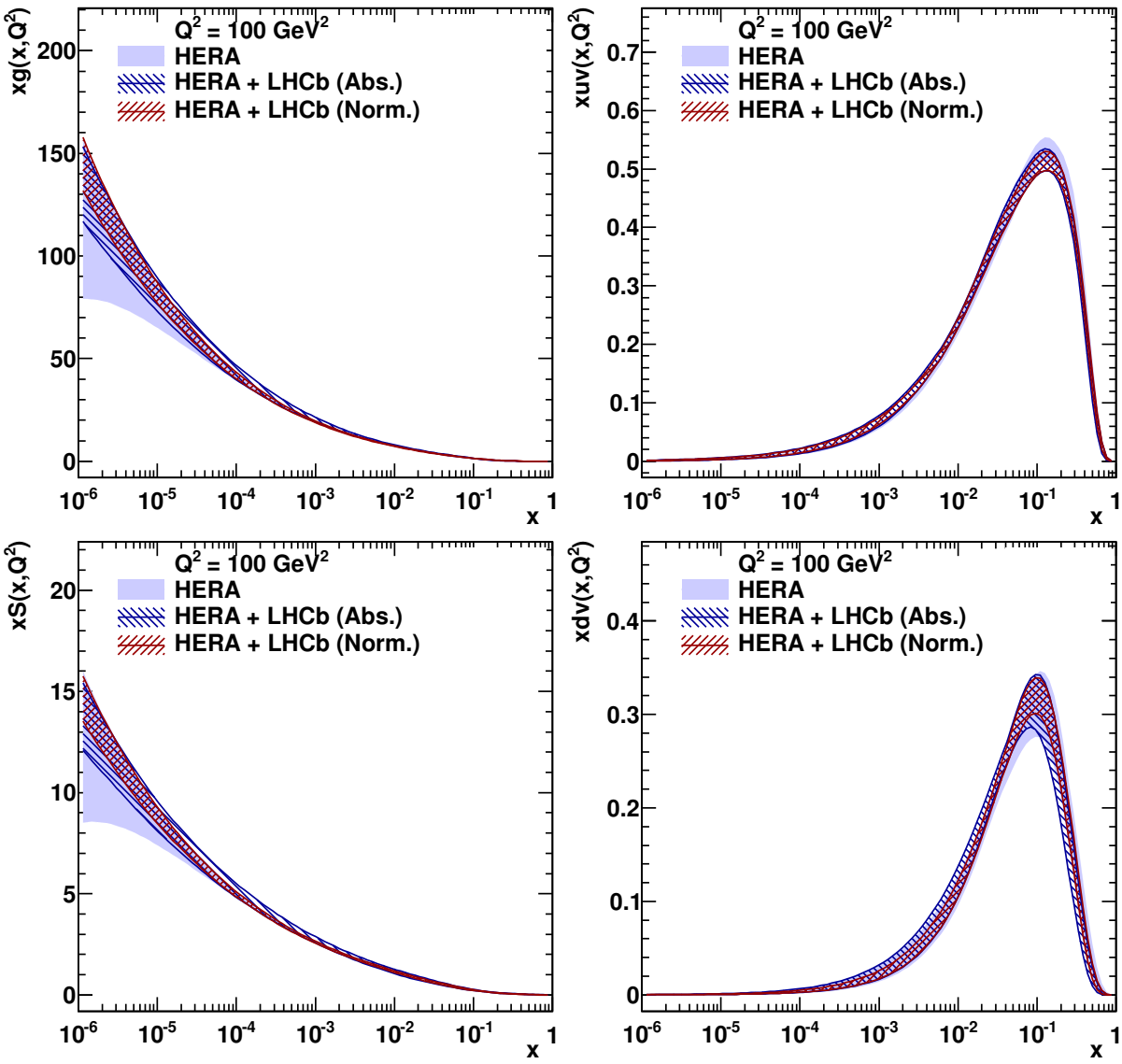

Figure 7.21: The gluon (top left), u-valence (top right), sea (bottom left) and d-valence (bottom right) distributions at $Q^2 = 100\,\text{GeV}^2$ obtained in the fit with the HERA-only, HERA and LHCb absolute, and HERA and LHCb normalised data. The widths of the bands represent the total uncertainties.

The distributions at medium x mainly remain unchanged, although in the 'LHCb Abs' approach some enlargement of the uncertainty is observed, explained by the inclusion of the scale uncertainties, most of which do not really describe the data. No such effect is observed in the 'LHCb Norm' approach, where all variations describe the data well.

In addition, a noticeable improvement is observed for all partons in the region of high x.

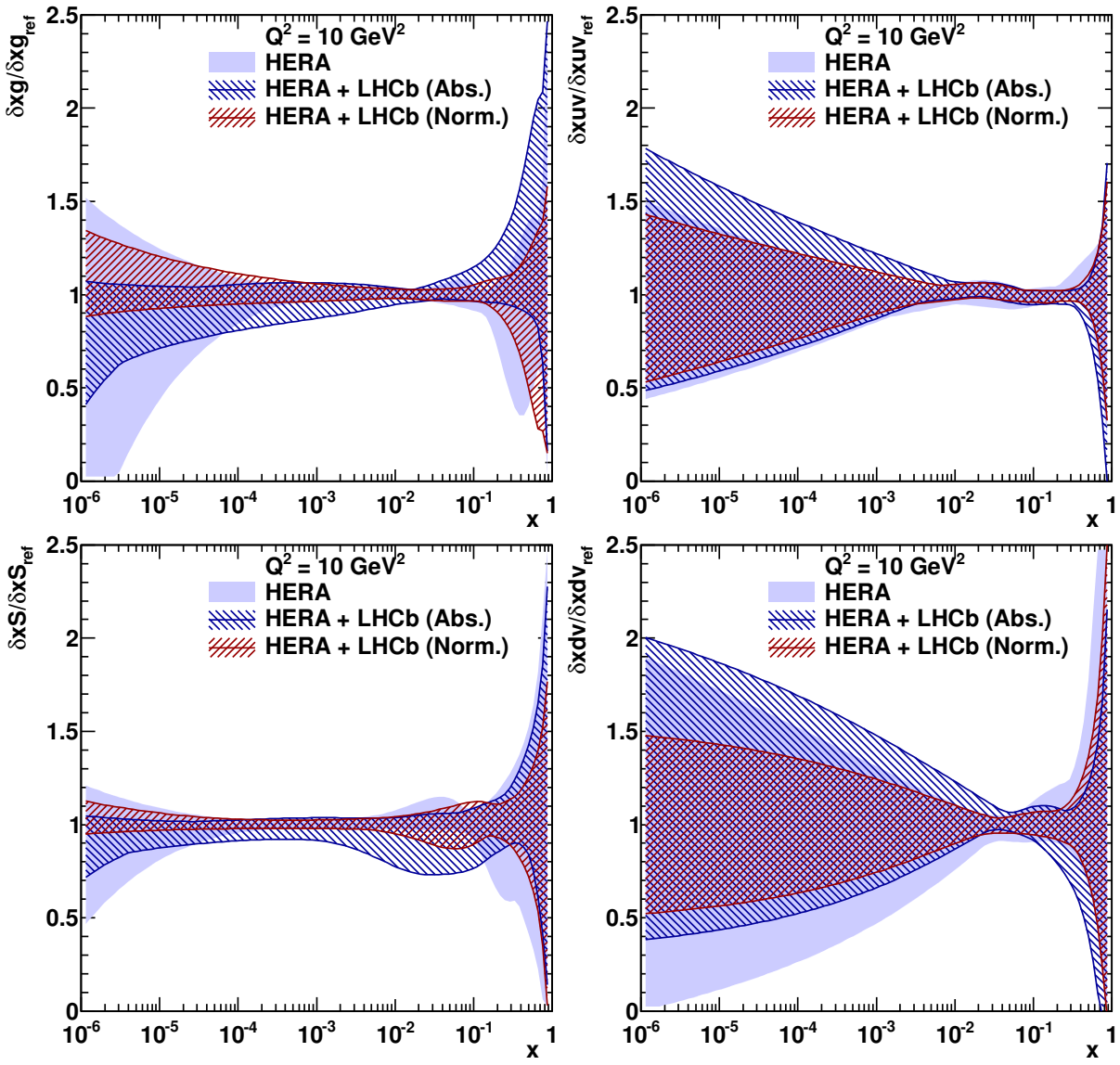

Figure 7.22: The gluon (top left), u-valence (top right), sea (bottom left) and d-valence (bottom right) distributions at $Q^2 = 10\,\mathrm{GeV}^2$ obtained in the fit with the HERA-only, HERA and LHCb absolute, and HERA and LHCb normalised data, normalised to one for a direct comparison of the uncertainties. The widths of the bands represent the total uncertainties.

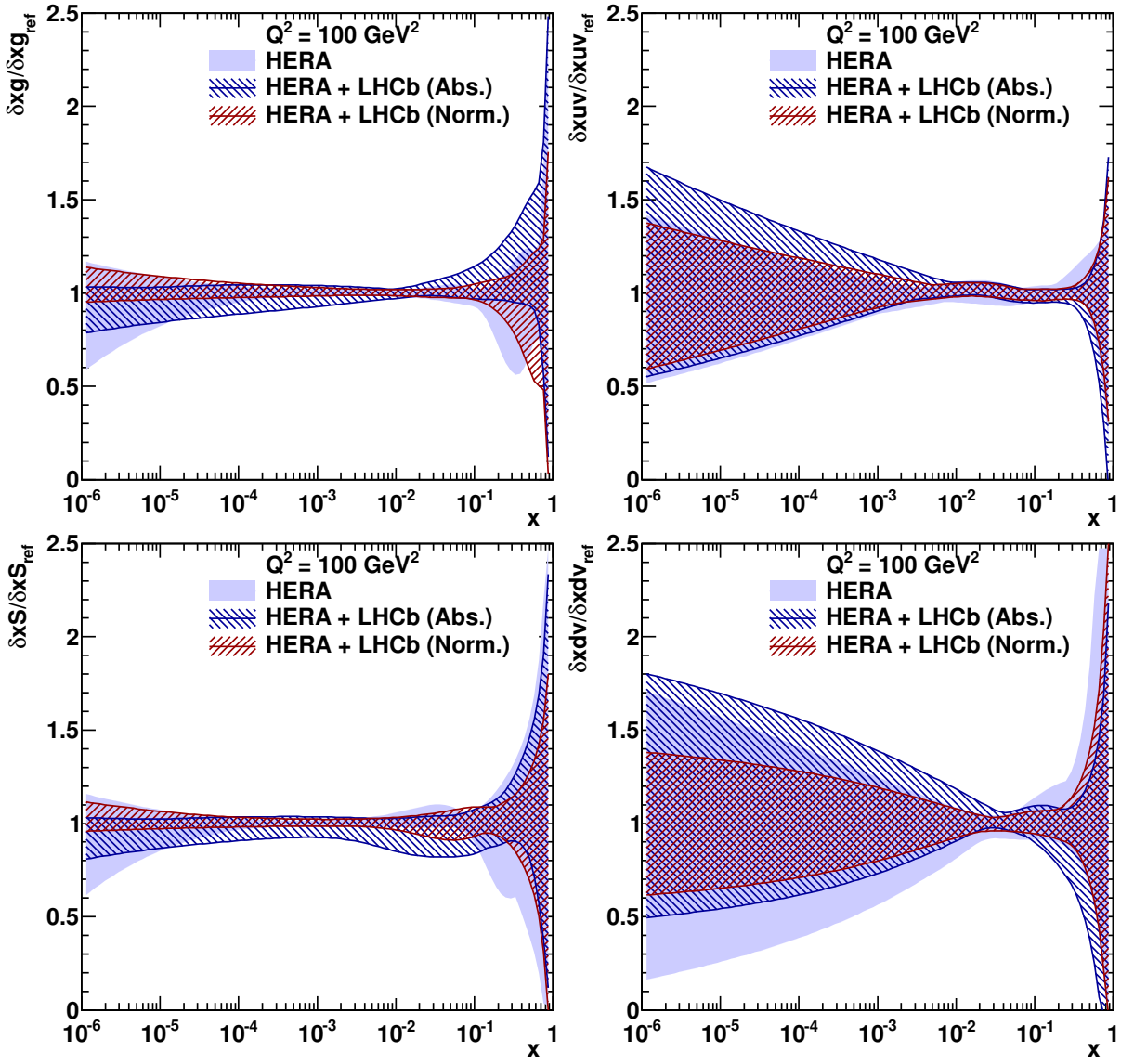

Figure 7.23: The gluon (top left), u-valence (top right), sea (bottom left) and d-valence (bottom right) distributions at $Q^2 = 100\,\text{GeV}^2$ obtained in the fit with the HERA-only, HERA and LHCb absolute, and HERA and LHCb normalised data, normalised to one for a direct comparison of the uncertainties. The widths of the bands represent the total uncertainties.

This might be constraints of the beauty LHCb data (see Fig. 7.2) which cover this region, as well as a side effect of the improvement at low x, transmitted via the momentum sum rule. The PDF distributions in linear x scale are available in Appendix F.4 (Figs. F.9, F.10, F.11, F.12).

Obviously, in the fit with the absolute cross sections, more information was used to constrain the gluons: the absolute cross sections constrain the normalisation of the product of the gluon PDFs at low and medium x, leading to the calibration of the low-x region to the medium one. However the uncertainty of this calibration is of the order of a factor 2, propagated from the scale uncertainties of the absolute cross sections.

In the fit with the normalised cross sections only the y shape of the cross sections was used and gluons at low x are calibrated to the medium-x range by the ratio of the cross sections in the most forward y bin to the least forward one. Doing so for all p_T bins and for both charm and beauty data effectively "builds a bridge" and calibrates low-x gluons to the medium x range, similar to the 'LHCb Abs' approach, although less directly. In this approach therefore, the final impact of the LHCb data crucially depends on the presence of any x region where the gluon density is very well constrained by other data (preferably at $x \sim 10^{-4}$–10^{-3}). Despite the reduced sensitivity, significantly smaller theoretical uncertainties were obtained owing to the reduced scale dependence of the normalised cross sections, so the final results are more precise than in the 'LHCb Abs' approach. Moreover, the whole theory concept is much more conventional and data independent in this case.

The observed impact of the heavy-flavour LHCb data suggests that these data might be a useful addition to the existing global PDF fits, although the study also demonstrates that the provided constraints are subject to sizeable theoretical uncertainties. Currently none of the PDF fitting groups estimate perturbative uncertainties of theoretical predictions (e.g. uncertainties from scale variations). In this context the 'LHCb Norm' approach should look more attractive since the uncertainties from the scale variations are not very crucial, while in the 'LHCb Abs' approach, results without the scale uncertainties will be obviously untrustworthy. On the other hand, nowadays the inclusion of perturbative theoretical uncertainties in the PDF fits is becoming a pressing issue. Once a general strategy is developed, both considered approaches of fitting the LHCb heavy-flavour data can be used in the global fits.

Any improvements in the theoretical predictions, both for the perturbative and non-perturbative parts, are very desirable to match the data precision (see also Appendix F.3). Having the scale uncertainties under control will provide a possibility to use the LHCb heavy-flavour data also for a precise measurement of the charm and beauty masses.

The final remark concerns the 'LHCb Norm' approach. As previously mentioned, the constraints at low x obtained in this approach crucially depend on the presence of any medium-x region already constrained by other data. In this context, the inclusion in the PDF fit of further datasets sensitive to gluons, e.g. jet measurements, should be very interesting. Another possible improvement may come from heavy-flavour measurements at LHC in the complementary rapidity region (e.g. [234, 235]), which will extend the fitted y shape to the central region $0 < y < 2$ and therefore to the medium range of gluon x.

CHAPTER 8

Conclusions and outlook

In this thesis a study of charm production in ep and pp collisions is presented. The production of heavy quarks is one of the strongest tests of QCD, because the heavy-quark masses provide a hard scale, allowing the application of perturbative calculations even at low scales $Q \sim \Lambda_{\mathrm{QCD}}$.

The production of D^+ mesons has been measured in DIS at HERA in the kinematic region $5 < Q^2 < 1000\,\mathrm{GeV}^2$, $0.02 < y < 0.7$, $1.5 < p_T(D^+) < 15\,\mathrm{GeV}$ and $|\eta(D^+)| < 1.6$. Differential cross sections were measured as a function of Q^2, y, $p_T(D^+)$ and $\eta(D^+)$. The present results supersede the previous ZEUS D^+ measurement, based on a subset of the data, and exhibit significantly better precision. The improvement in precision comes from the larger data sample used in the present analysis and from a better control of the experimental systematic uncertainties, owing to improved tracking alignment and calibration. Predictions from NLO QCD in the FFNS describe the measured cross sections well. The new precise data provide an improved check of pQCD and have the potential to constrain the PDFs in the proton.

This measurement was combined with all other available H1 and ZEUS measurements of open charm production, extrapolated to the full phase space using the shape of the theoretical predictions in the FFNS. The combination was performed in the kinematic region $2.5 \leq Q^2 \leq 2000\,\mathrm{GeV}^2$ and $3 \times 10^{-5} \leq x \leq 5 \times 10^{-2}$. The procedure takes into account detailed information on correlations of the systematic uncertainties, thus allowing for their cross calibration and significant reduction. The combined charm reduced cross sections are consistent with the previous H1 and ZEUS charm combination and have an improved precision owing to the inclusion of new ZEUS measurements. The combined data were compared to NLO QCD predictions in the FFNS and various VFNS. The best description of the data in the whole kinematic range is provided by the approximate NNLO FFNS predictions of the ABM group. The strong sensitivity of the theoretical predictions to the charm-quark mass allows its determination using the precise combined data. The charm reduced cross sections were used as input for a QCD analysis together with the inclusive production data at HERA to determine the optimal values of the pole and $\overline{\mathrm{MS}}$ running charm masses, as well as the charm-quark mass parameters in various VFNS. The extracted value of the $\overline{\mathrm{MS}}$ running charm mass is consistent with the world-average value and has competitive precision to other individual determinations

in pQCD.

The combination of many different charm measurements described above provides the ultimately precise one charm dataset from HERA, although it is affected by theory-related uncertainties, arising from the extrapolation procedure. In order to have a combination without this drawback, the single- and double-differential visible D^{*+} cross sections measured by H1 and ZEUS were combined. The combination was performed in the kinematic region $1.5 < Q^2 < 1000\,\mathrm{GeV}^2$ ($5 < Q^2 < 1000\,\mathrm{GeV}^2$ for the single-differential cross sections), $0.02 < y < 0.7$, $p_T(D^{*+}) > 1.5\,\mathrm{GeV}$ and $|\eta(D^{*+})| < 1.5$. This combination does not induce significant theory-related uncertainties, taking advantage of the fact that the phase spaces and binning schemes of the H1 and ZEUS measurements are very similar, and provides differential cross sections as a function of D^{*+} kinematic variables also. The input datasets were found to be consistent, and the combined data exhibit significantly reduced uncertainties. NLO QCD predictions in the FFNS were compared to the combined D^{*+} cross sections and a 'customised' QCD calculation was introduced in order to improve the agreement between the central values of the theoretical predictions and the data.

For both combinations, the uncertainties of the combined data are smaller than the theoretical uncertainties, thus higher-order calculations and an improved treatment of the fragmentation process would be helpful to reduce the theory uncertainty to a level comparable with the data precision. The combined D^{*+} data can be used further as the most precise purely experimental charm measurement from HERA for stringent tests of pQCD and phenomenological approaches, e.g. of the fragmentation process, while the combined charm reduced cross sections — the most precise inclusive charm measurement from HERA — also be used for stringent tests of pQCD and in QCD analyses to constrain the gluon distribution and to determine the charm-quark mass.

While the HERA charm data are sensitive to the gluon distribution in the proton at the values of partonic fractions of the proton momenta $10^{-4} \lesssim x \lesssim 10^{-1}$, the production of charm quarks at LHCb probes the region $5 \times 10^{-6} \lesssim x \lesssim 10^{-4}$. The sensitivity of heavy-quark production in pp collisions to the low-x gluon distribution was studied in a comprehensive QCD analysis at NLO. The measurements of charm and beauty production at the LHCb experiment were included into a PDF fit together with inclusive and heavy-quark production measurements in DIS at HERA. FFNS theory was used for predictions of heavy-quark production in ep and pp collisions. Two approaches to the use of the LHCb data were studied. Although the absolute differential cross-section measurements contain more information, the resulting PDFs suffer from large theoretical uncertainty due to uncalculated higher-order corrections, estimated by the variation of the pQCD scales. By using only the rapidity shape information, this uncertainty was significantly reduced. In both approaches a significant reduction of the parametrisation uncertainty of the gluon distribution at low x was observed, as compared to the result of the PDF fit using only HERA DIS data. The present analysis has illustrated the high potential of the LHCb heavy-flavour measurements to constrain the gluon distribution at low x. Further improvements in the theoretical calculations of heavy-flavour production in pp collisions, as well as new experimental measurements in the complementary phase space, are expected to fully exploit these constraints.

HERA data have already had a great impact on the understanding of the partonic structure of the proton and on the development of QCD. The analysis of these data still continues and

will continue in the future. In order to ensure the long-term availability of the ZEUS data after the end of the experimental Collaboration, as a part of the ZEUS data preservation project, the ZeVis program has been modified to become independent of the ZEUS Software. The new CN-ZeVis, based on Common Ntuples, is a pure ROOT application. While CN-ZeVis provides the main functionality that was available in classic ZeVis, it does not require any maintenance. In addition, several new features were implemented in CN-ZeVis.

Appendix

APPENDIX A

Modification of ZEUS Event Display: additional details

In this Appendix additional information on the modification of the ZEUS Event Display program (Section 4) is provided.

A.1 Available information

Since the CN does not contain all information that was in the MDST files, CN-ZeVis also cannot display some things available in classic ZeVis. Here is a list of information which can be displayed in CN-ZeVis:

- tracks:
  - ZTT for HERA-II or VCT for HERA-I (both vertex-fitted and off-vertex tracks are available);
  - analysis-specific tracks;
  - GTT;
  - TRKMSA;
  - MC tracks;
- vertices:
  - ZTT for HERA-II or VCT for HERA-I;
  - analysis-specific vertices;
  - GTT;
  - beamspot;
- jets:

  - all possible kT jets (from A to Z);
  - cone jets;
- ZUFOs;
- CAL hits;
- muons:
  - BAC hits;
  - muon tracks;
- event header:
  - run and event number;
  - date and time;
  - CAL information;
  - SINISTRA and EM information;
  - CC JB information;
  - trigger bits.

There are some limitations depending on the CN version, listed in Table A.1.

CN version	v02	v06	v07	v08
CAL hits	no	yes	yes	yes
Vertex-fitted tracks before vertexing	no	yes	yes	yes
TRKMSA tracks	no	yes	yes	yes
GTT tracks	no	yes	yes	yes
Analysis-specific SECVTX for different vertex types	ktJETS_A only	yes	yes	yes
Correct magnetic field for track helices	no	yes	yes	yes
Date and time	no	no	no	yes

Table A.1: CN-ZeVis limitations in different CN versions.

A.2 Standalone version

Information about the standalone version is available at:
http://www-zeus.desy.de/~zevis/new_oz/README
Note, that with CN-ZeVis, it is possible to access CN on dCache from outside DESY using a Grid proxy.

A.3 Description of new features

In addition to the classic ZeVis functionality, several new features have been implemented in CN-ZeVis:

- **processing an event list** (Fig. A.1):
  - if a user has a lot of events to display, one does not need to specify each event manually. Instead one can create an event list containing information about all events in the special format, and process it with CN-ZeVis "in one shot";
  - to use this feature a user should start ZeVis, press the `Process Event List` button and select an event-list file;
  - an event-list file is a text file where each line contains information about one event; each line must contain `run=...`, `event=...` and (optionally) `file=...` entries separated by an arbitrary number of spaces;
  - if the `file=...` entry is provided, ZeVis will search for the requested event in this CN file using the specified run and event numbers;
  - if there is no `file=...` entry, ZeVis will assume that the requested event is DATA and will search for it in the CN version specified in the main Client window. Therefore a user should consider to select the correct CN version before processing an event list;
  - a user must specify the run number equal to 1 for MC;
  - a user should be aware that ZeVis will take all settings concerning event reconstruction from the main Client window (the setting of using a constant magnetic field for building track helices and the settings for analysis-specific tracks and vertices) and should not forget to select the correct ones;
  - there is a limitation that an event list cannot contain more than 300 events;
  - lines in the event list may contain additional information suitable for users (e.g. Q^2, p_T etc.) which will be ignored by ZeVis;
  - after processing the event list a user can save the events in a ZeVis ROOT file (`File -> Save Event File as...`) and then work with this file in subsequent ZeVis sessions;
  - examples of event lists with typical events from the D^+ in DIS analysis (see Section 5) for DATA and MC are available at `http://www-zeus.desy.de/~zevis/new_oz/eventlists/eventlist_dch_data` and `http://www-zeus.desy.de/~zevis/new_oz/eventlists/eventlist_dch_mc`;
- **batch mode**:
  - ZeVis can be run on a system without a graphical environment;
  - there are basically two uses of this mode:

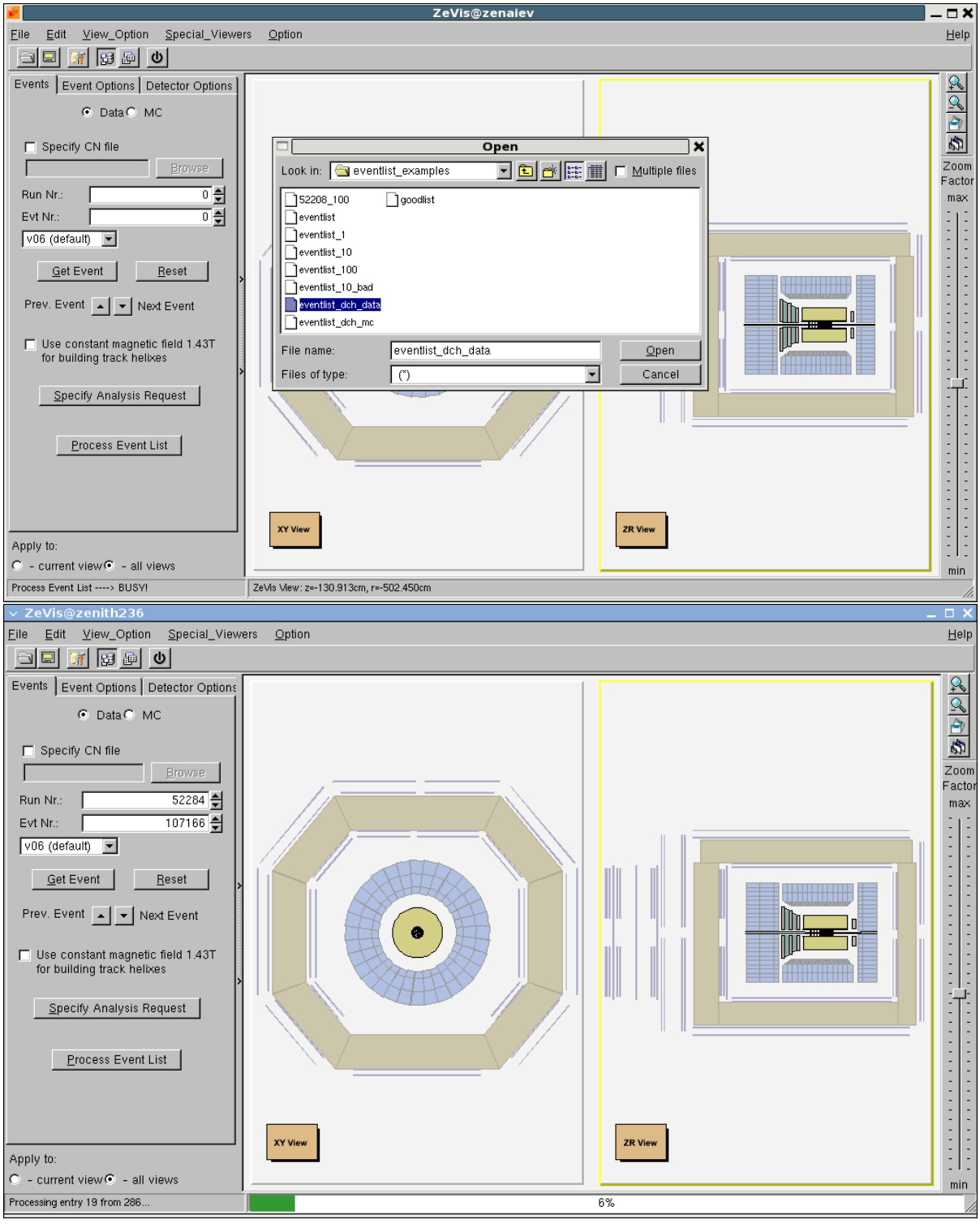

Figure A.1: Selecting (top) and processing (bottom) an event list.

    - to test and validate ZeVis on a new system (another operating system, compiler, ROOT version etc.);
    - to get some pictures even if there is no graphical interface (SSH session with very slow connection etc.);
  - a user should prepare event list and run a command:
    `zevis-cn-dev -b <event list> <output dir> <picture format 1> ...`
    The arguments `<picture format 1>, ...` are optional and can be ps, eps, png or any other formats supported by ROOT (see TPad::Print() for more details);
  - in the output directory the following items will be created:
    - the ZeVis ROOT file zevis.root with all processed events (can be correctly opened only with ZeVis);
    - the text file zevis.txt with the dump of all objects;
    - the pictures in the specified format(s) for each processed event;

- **support for "private mini-ntuples"**:
  - CN-ZeVis can display information from "private mini-ntuples"[1];
  - to work with "private mini-ntuples" a user should check the `Specify CN file` button and provide a path to the file (the same for processing event list: specify the files with `file=...` entries);
  - ZeVis checks the content of the input file before building the event: if some branches are missing, ZeVis prints a warning message in the console output ("Warning during building event: information about ... is not available due to missing branch(es): ..."");
  - a user should be aware that ZeVis does not build (and display) some stuff if at least one of the necessary branches is not available in the "private mini-ntuple" (e.g. tracks will not be available even if only the `Trk_layinner` branch is missing);

- **analysis-specific tracks and vertices** (Fig. A.2):
  - CN-ZeVis can display special analysis-specific ("analysis-level") tracks and vertices from decays of charm hadrons (information comes from ORANGE blocks `DCH`, `DSTAR1`, `DSTAR2`, `DZERO`, `DSS`, `DLA` and `SECVTX`);
  - to use this option, a user should press the `Specify Analysis Request` button and specify the settings in a new `Analysis Request` window;
  - a user should be aware that ZeVis can reconstruct only one combination of such tracks and vertices, e.g. only one D^{+}-, or D^{*+}-, or some other D-meson candidate (except for the `SECVTX` block). This limitation is a consequence of the fact that different combinations can have common tracks, and therefore displaying them together will be inconsistent; moreover each combination has its own reduced primary vertex. So before requesting the event one should specify in this window which

[1] CN which are produced by a user for certain purpose and may have reduced content of information (branches).

type of analysis-specific information is needed (from which ORANGE block) and either a certain number of the candidate or "the best one" with some cuts ("the best one" means with minimal decay-length significance for DCH and with largest p_T for DSTAR1, DSTAR2, DZERO, DSS and DLA; this information is available in the tooltips for the corresponding check buttons);

- after specifying (or changing) all settings a user requests an event and observes the analysis-specific tracks and vertices (if they are present in the event; otherwise one should check the console output for messages like "No Dch candidate" etc.);
- a user can switch them on/off from the `Tracks & Vertexes` tab of the `Easy Tool` window or from the menu bar;
- analysis-specific vertices contain both secondary and reduced primary vertex; in the description of a secondary vertex there is information about the mass of the candidate, decay-length significance (for some ORANGE blocks) etc.;
- tracks from different particles can be displayed with different colors (according to the mass hypothesis). For this option one should check the `Show track types` button in the `Event Options` tab;

- **MVD standalone TRKMSA tracks** (Fig. A.3):
  - CN-ZeVis can display MVD standalone TRKMSA tracks, which are not part of the normal tracking and vertexing structure;
  - a user can switch them on/off with the `MVD standalone tracks (TRKMSA)` check button in the `Extra options` tab of the `Easy Tool` window or from the menu bar (`View Options -> Tracks -> Non Vertex-Fitted Tracks -> MVD standalone tracks (TRKMSA)`);
  - ZeVis can display these tracks either within the MVD or extrapolate them to the CTD outer radius (check the `Extrapolate to outer CTD radius (TRKMSA)` button in the `Extra options` tab of the `Easy Tool` window or from the menu bar `View Options -> Tracks -> Tracking options -> Extrapolate to outer CTD radius (TRKMSA)`);

- **using a constant magnetic field for displaying track helices**:
  - since CN version v02 does not contain information about track helices before vertexing (see Table A.1), tracks with this version can be built only assuming a constant value of the magnetic field in the ZEUS detector;
  - for backward compatibility with other CN versions, there is an option in CN-ZeVis to build all tracks using this assumption;
  - to build tracks with the constant value of the magnetic field (1.43 T) a user should check the `Use constant magnetic field 1.43 T for building track helices` button in the `Events` tab;
  - if one selects the v02 version of CN in the `Events` tab, this option will be switched on automatically;

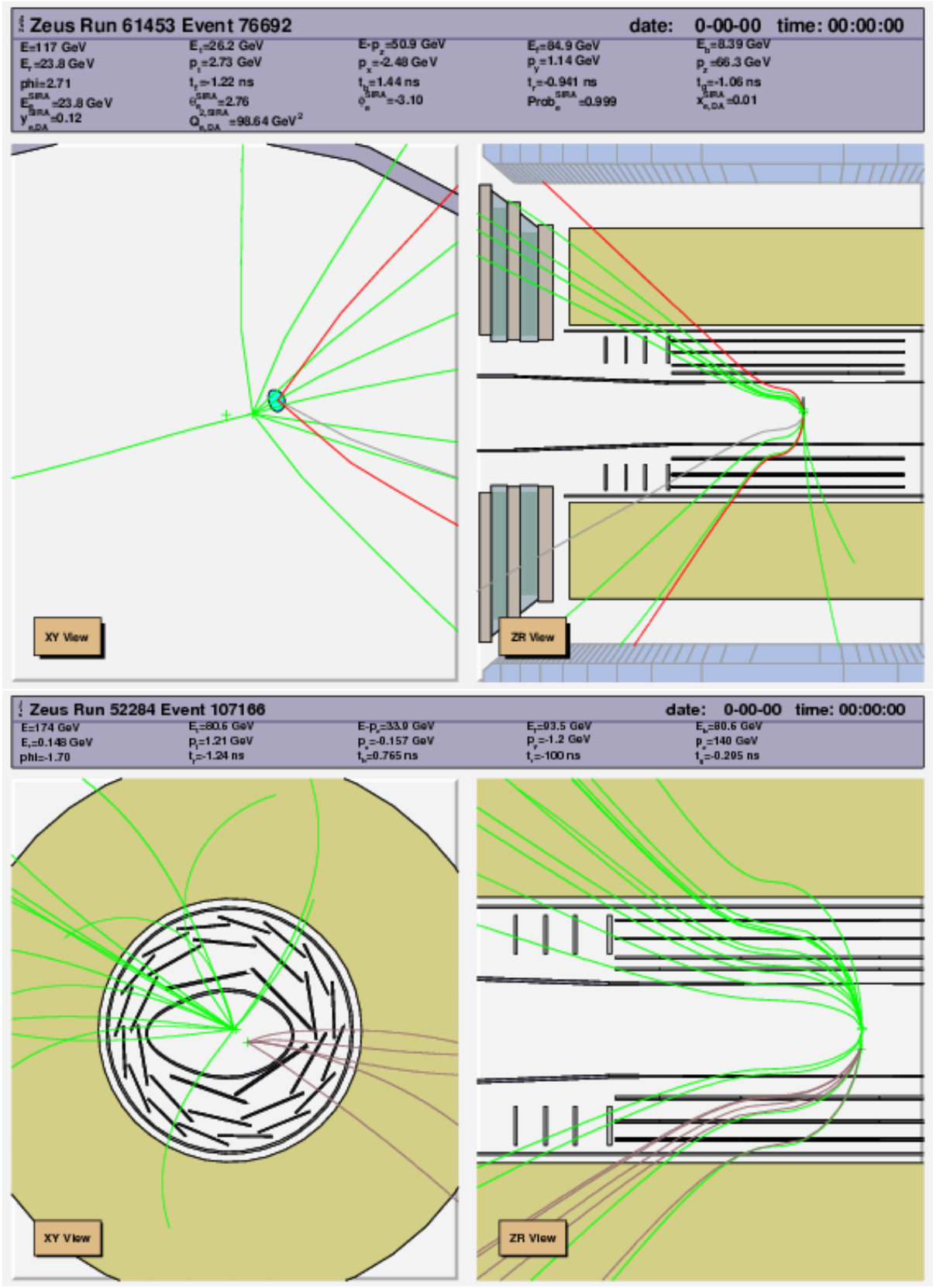

Figure A.2: Example of events with a $D^+ \to K^-\pi^+\pi^+$ candidate from the DCH block (top) and with an inclusive secondary vertex from the SECVTX block (bottom).

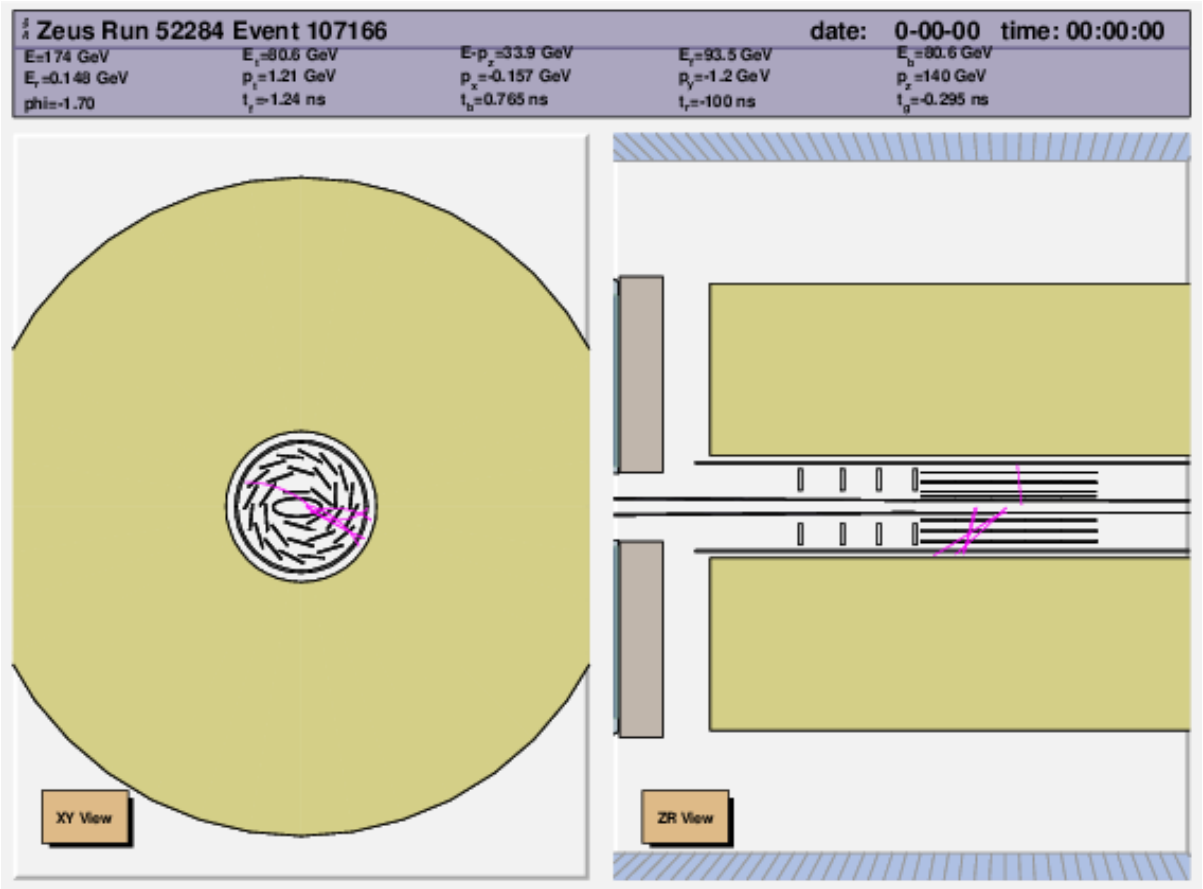

Figure A.3: TRKMSA tracks in ZeVis.

  - if one works with "private mini-ntuples" without information about track helices before vertexing (the `Trk_helpar` and `Trk_helmom` branches) and did not switch this option on, tracks nevertheless will be built assuming the constant magnetic field and a warning message will be displayed in the console output;

- **possibility to change the ZeVis style** (Fig. A.4):
  - there are two available style schemes in CN-ZeVis (`Edit -> Style Scheme`):
    - "Standard" is hardcoded and is the default one;
    - "User" is flexible and can be modified; it is stored in the `.zevis.rsc` file in the user's home directory;
  - there are two ways to modify the "User" scheme:
    - manual modification of the `.zevis.rsc` file;
    - interactively a user can apply new settings either to the currently selected object only or to all objects (need to request event again to see the effect); in the second case actually the ZeVis style is changed and settings can be stored with `File`

`-> Save Settings` (one should remember to switch to the User style before doing all these operations);

- for some objects (jets, CAL hits and vertex error ellipses) only the manual method works;

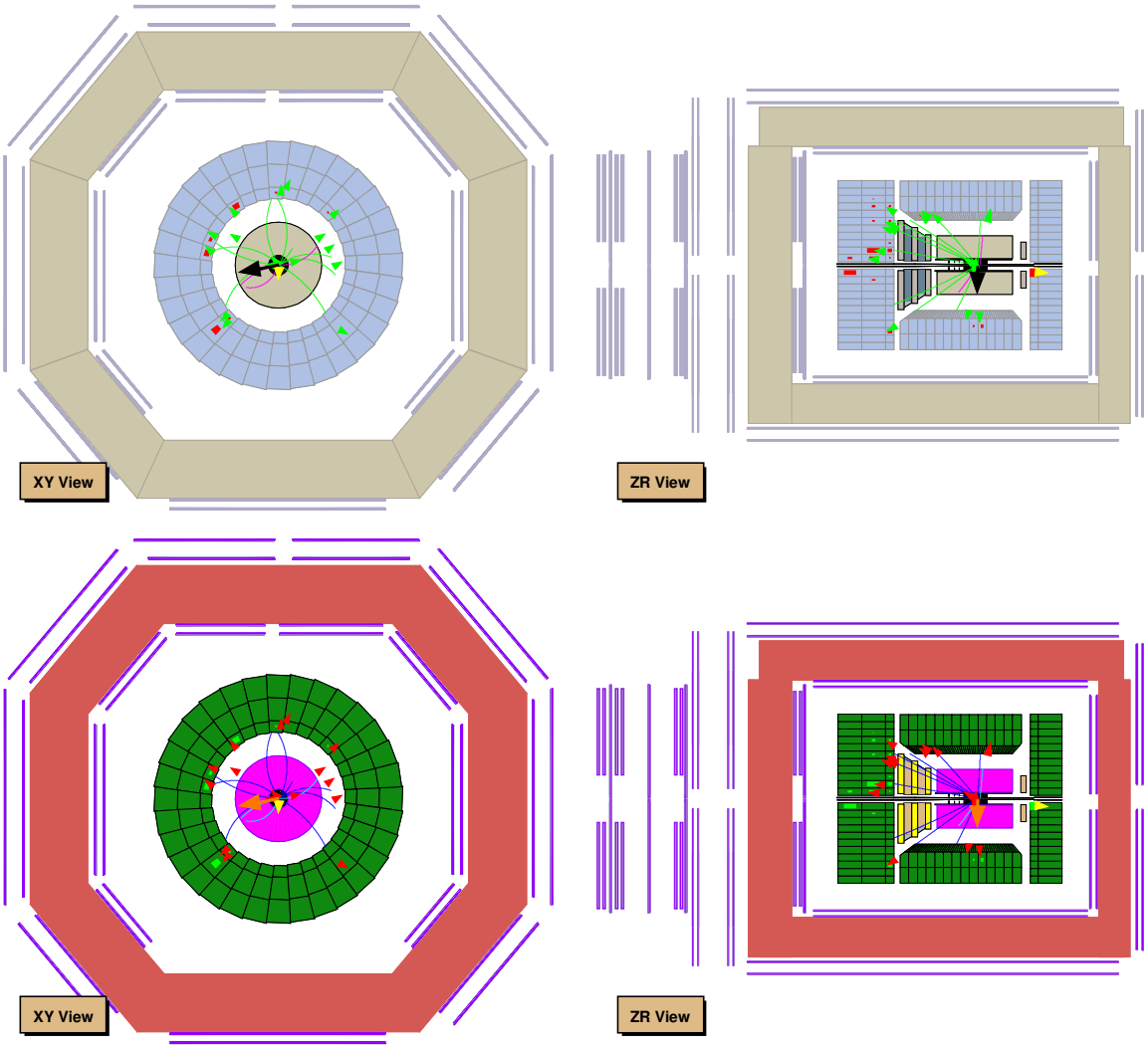

Figure A.4: The "Standard" (top) and modified "User" (bottom) styles in CN-ZeVis.

- **zooming of the selected area** (Fig. A.5):
  - select area to expand with the right mouse button;
- **access CN on dCache from outside DESY using a Grid proxy**:
  - information is provided on: `http://www-zeus.desy.de/~zevis/new_oz/README`.

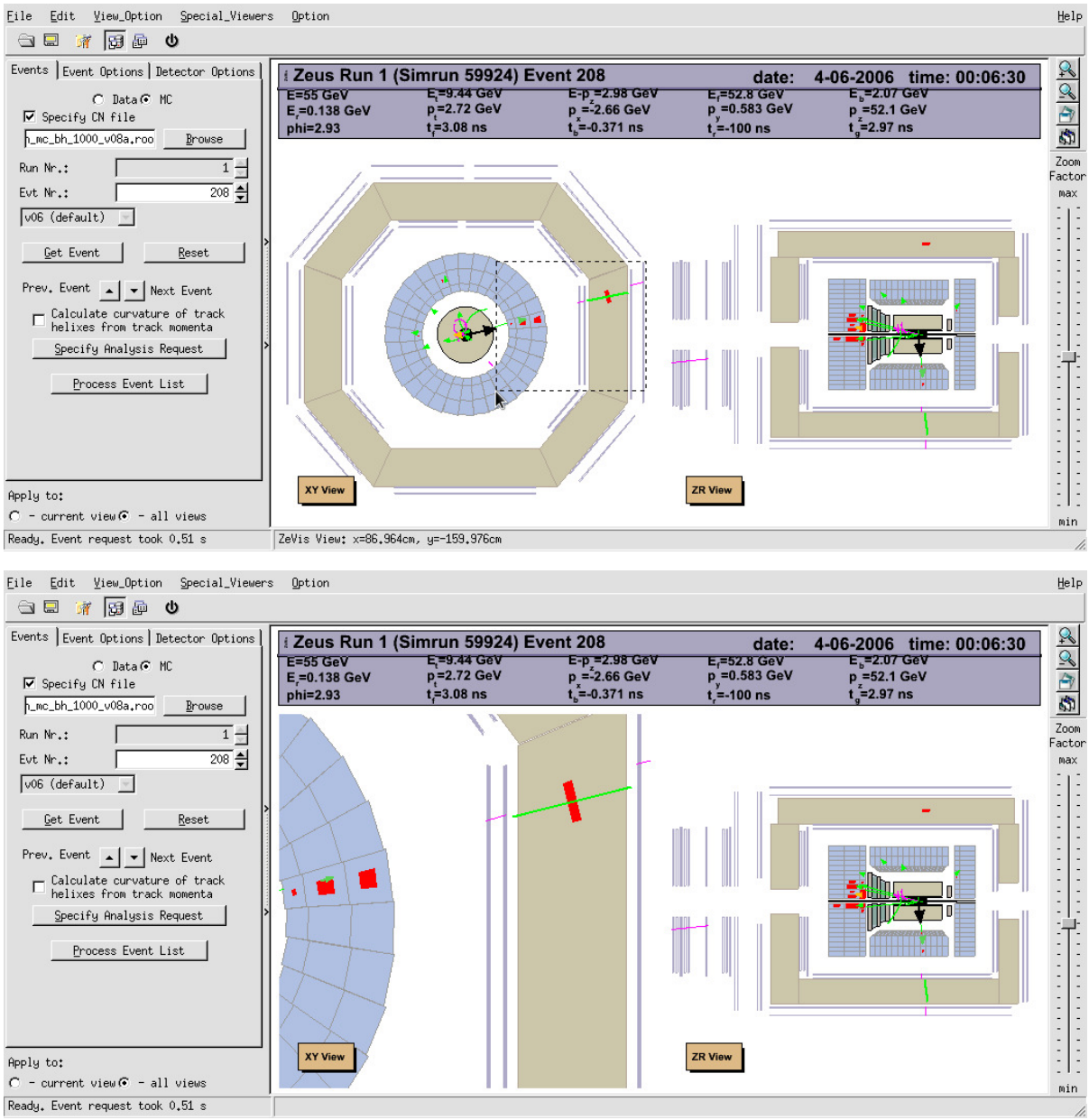

Figure A.5: Zooming of the selected area in CN-ZeVis: selecting the area to zoom (top) and the resulting view (bottom).

APPENDIX B

Measurement of D^+ production: additional information

In this Appendix additional information on the measurement of D^+ production (see Chapter 5) is provided.

B.1 Additional plots

Fig. B.1 shows purity as a function of $p_T(D^+)$, $\eta(D^+)$, Q^2 and y.

Fig. B.2 shows efficiency as a function of $p_T(D^+)$, $\eta(D^+)$, Q^2 and y.

Fig. B.3 shows control plots for E'_e, polar angle of the scattered electron, x, δ_{had} and Z_{vtx}.

Fig. B.4 shows effect of the tracking inefficiency correction as a function of $p_T(D^+)$, $\eta(D^+)$, Q^2 and y

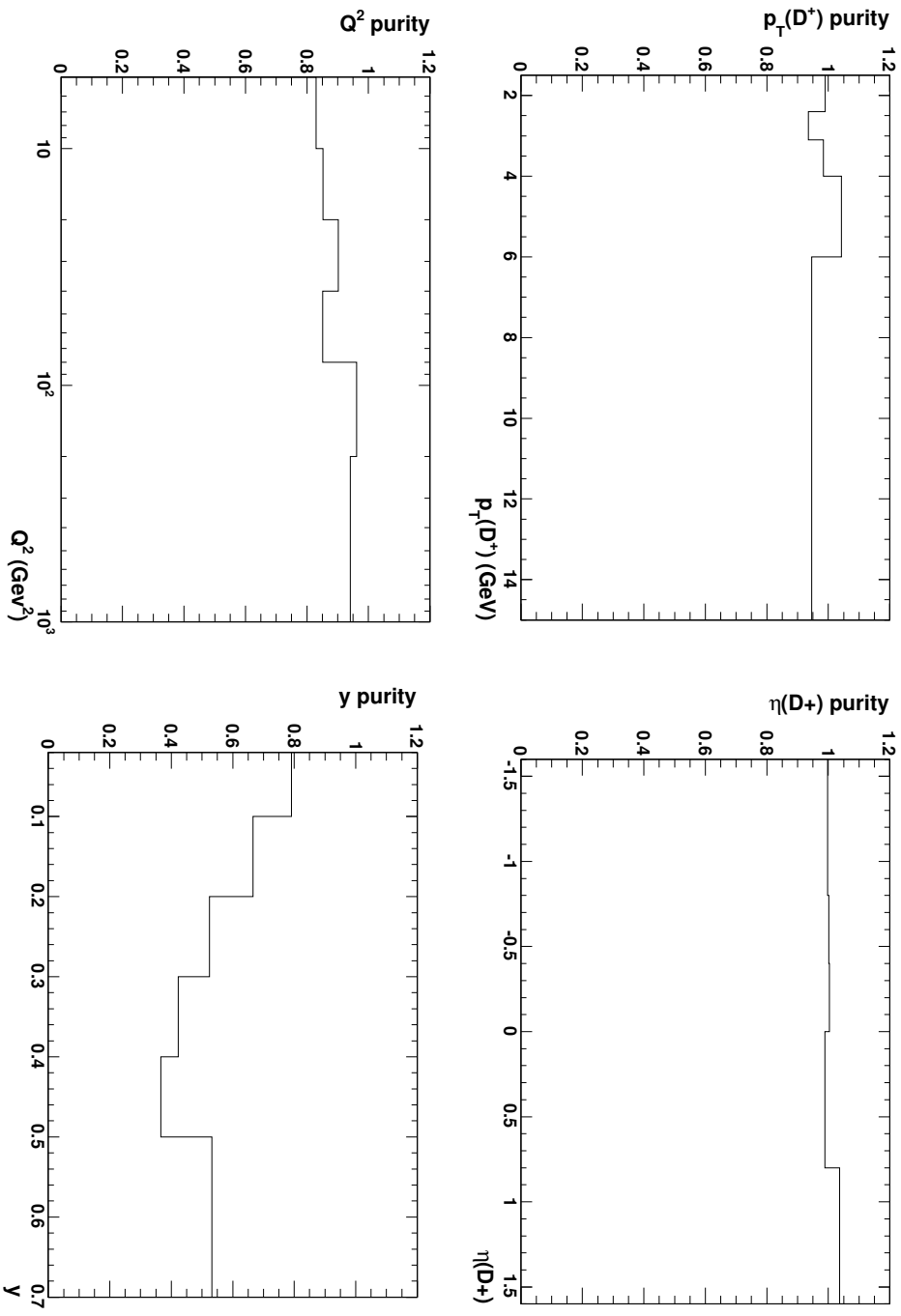

Figure B.1: Purity as a function of $p_T(D^+)$ (top left), $\eta(D^+)$ (top right), Q^2 (bottom left) and y (bottom right).

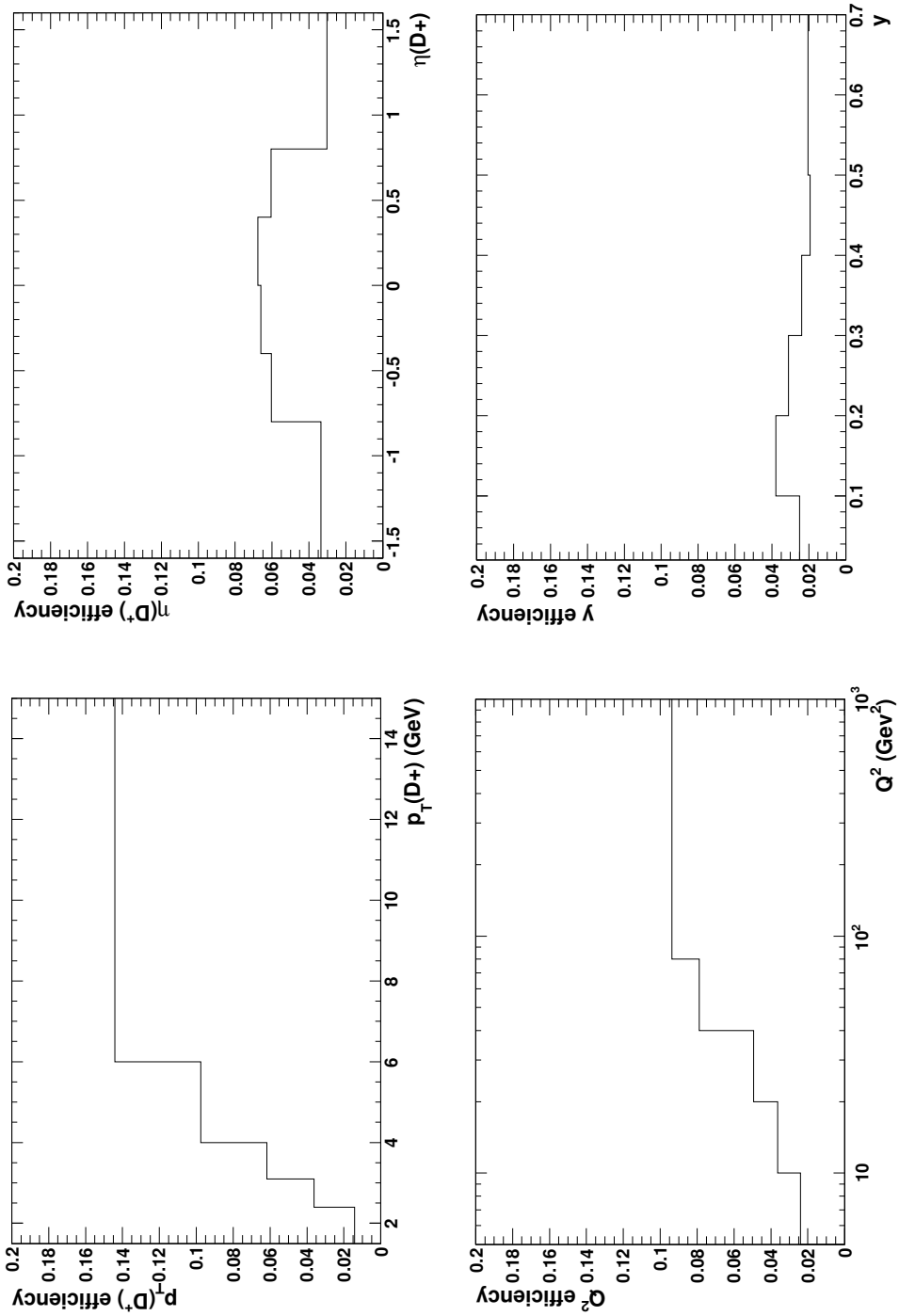

Figure B.2: Efficiency as a function of $p_T(D^+)$ (top left), $\eta(D^+)$ (top right), Q^2 (bottom left) and y (bottom right).

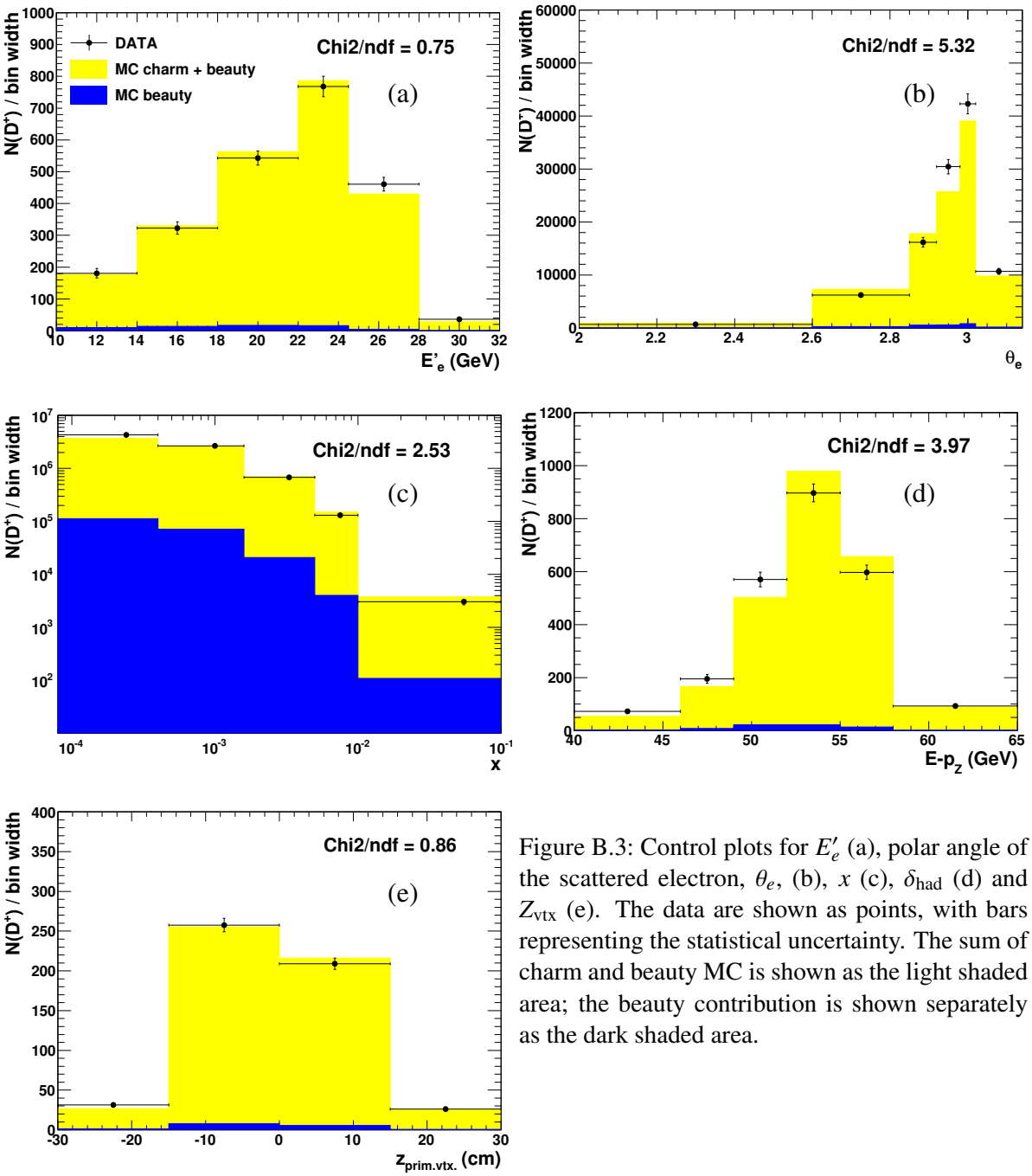

Figure B.3: Control plots for E'_e (a), polar angle of the scattered electron, θ_e, (b), x (c), δ_{had} (d) and Z_{vtx} (e). The data are shown as points, with bars representing the statistical uncertainty. The sum of charm and beauty MC is shown as the light shaded area; the beauty contribution is shown separately as the dark shaded area.

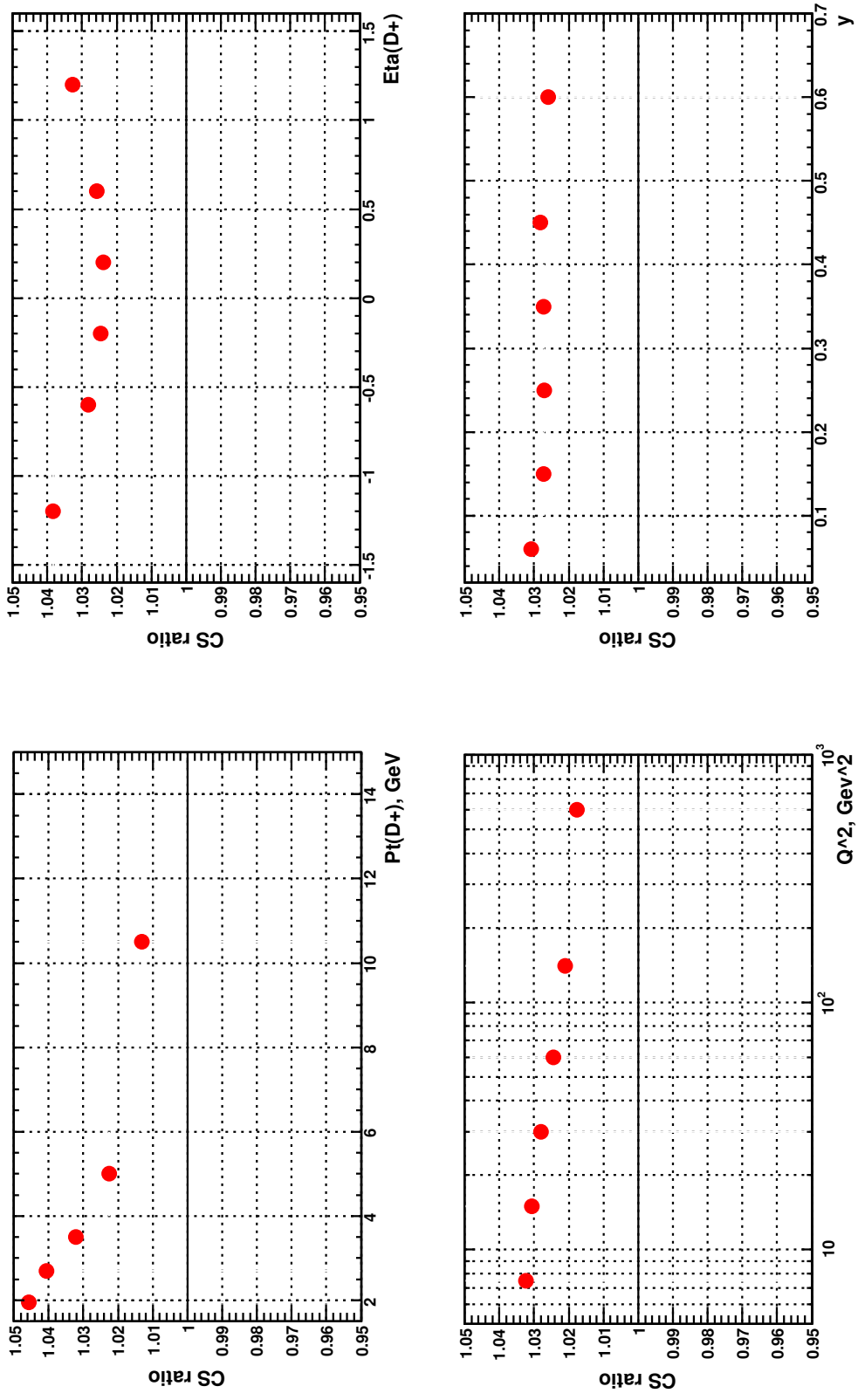

Figure B.4: Effect of the tracking inefficiency correction as a function of $p_T(D^+)$ (top left), $\eta(D^+)$ (top right), Q^2 (bottom left) and y (bottom right).

B.2 Extension of analysis to low-$p_T(D^+)$ region

This Section describes the extension of the D^+ measurement to the kinematic region $p_T(D^+) < 1.5\,\text{GeV}$. Section B.2.1 contains an introduction and motivation for this study, as well as an overview of existing measurements in this region. Sections B.2.2 and B.2.3 present results of the measurement in two decay channels, $D^+ \to K^0_S(\pi^+\pi^-)\pi^+$ and $D^+ \to K^-\pi^+\pi^+$, respectively. Finally, in Section B.2.4 comparison of the obtained results is presented, as well as a summary and prospects of possible further improvements.

B.2.1 Introduction

Most of the measurements of the charm contribution to the proton structure function $F_2^{c\bar{c}}$ (or in terms of the charm reduced cross section $\sigma_{\text{red}}^{c\bar{c}}$, see Section 2.3.2), performed at HERA, were done extrapolating results of the measurements in a visible (by the detector) phase space, typically very limited in p_T and η.[1] This extrapolation involves usage of the p_T and η shape from some theoretical predictions and results in appearance of the theory-related uncertainties on the extracted $F_2^{c\bar{c}}$ (see Section 6.2.3 for more details). Therefore, an additional measurement of charm production, even not competitively precise, in the region which is not accessible for other most precise measurements, can serve as a cross-check of the extrapolation procedure. Moreover, it will provide a self-independent crucial test of pQCD.

So far at HERA only one measurement was done in the region $p_T < 1.25\,\text{GeV}$ by ZEUS [236]. D^+ and Λ_c^+ production has been measured using $120\,\text{pb}^{-1}$ of the HERA-I data in DIS in the kinematic region $0 < p_T(D^+, \Lambda_c^+) < 10\,\text{GeV}$, $|\eta(D^+, \Lambda_c^+)| < 1.6$, $1.5 < Q^2 < 1000\,\text{GeV}^2$ and $0.02 < y < 0.7$. The charm hadrons were reconstructed in the decay channels $D^+ \to K^0_S(\pi^+\pi^-)\pi^+$, $\Lambda_c^+ \to pK^0_S(\pi^+\pi^-)$, $\Lambda_c^+ \to \Lambda(p\pi^-)\pi^+$ (note that no explicit lower cut on the transverse momenta of the reconstructed charmed hadrons was applied). The presence of a neutral strange hadron in the final state reduced the combinatorial background thus allowing the extention of the measured sensitivity into the low-p_T region. The differential cross section as a function of $p_T^2(D^+)$ is shown and compared to the NLO QCD FFNS predictions in Fig. B.5. The predictions describe the data reasonably, although at low $p_T(D^+)$ they differ by about two standard deviations. The experimental uncertainty of the data in the lowest bin $0 < p_T^2(D^+) < 2.25\,\text{GeV}^2$ is $\approx 30\%$, mainly driven by the statistical uncertainty.

Using the HERA-II data, there are two possibilities for a measurement of charm production at low $p_T(D^+)$:[2]

1. measurement in the decay channel $D^+ \to K^0_S\pi^+$ with subsequent $K^0_S \to \pi^+\pi^-$, similarly how it was done in [236] using the HERA-I data. Presence of the MVD on one hand allows the reconstruction of the D^+ secondary vertices, but on the other hand additional material leads to a significant suppression of acceptance at low $p_T(D^+)$. Additionally,

[1] Formally the H1 vertex measurement [141] is an exception, although its results also contain sizeable theory-related uncertainties, which means that the extrapolation to the full phase space has been performed implicitly.

[2] Measurement of D^{*+} production using the "golden" decay channel (see Section 3.1.3) is not feasible at very low $p_T(D^{*+})$, because the transverse momentum of the slow pion would be too small and its track cannot be reconstructed.

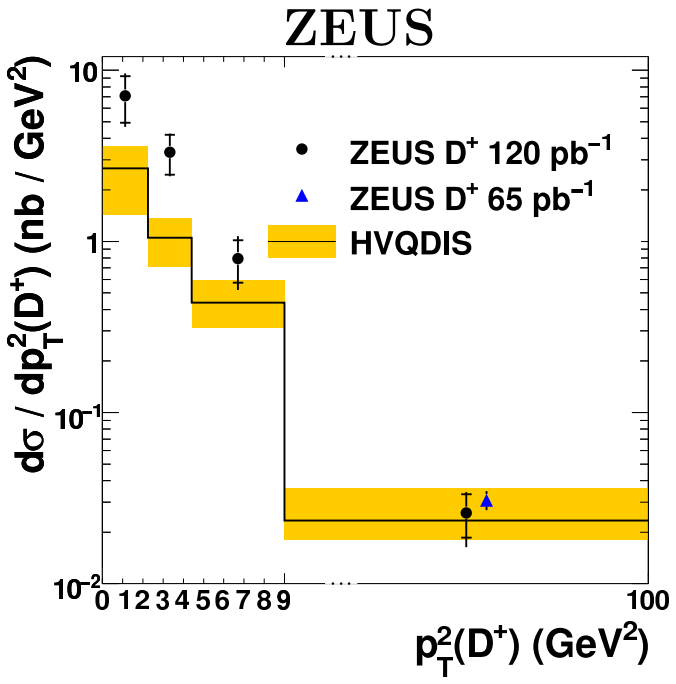

Figure B.5: Differential D^+ cross sections as a function of $p_T^2(D^+)$, as measured by ZEUS [236], compared to the NLO QCD calculation (HVQDIS). The measured cross section is shown as dots and the triangle represents the previous ZEUS result [237]. The X-axis is broken. The inner error bars show the statistical uncertainties and the outer error bars show the statistical and systematic uncertainties added in quadrature. The band shows the estimated theoretical uncertainty of the HVQDIS calculation.

Q^2 range at HERA-II is limited to $Q^2 > 5\,\mathrm{GeV}^2$, that leads to an additional acceptance suppression at low $p_T(D^+)$. Expected advantages and disadvantages of this decay channel can be summarised as follows:

(+) relatively small combinatorial background (almost clean K^0_S signal, combined with one additional charged track);

(−) small branching ratio ($\mathcal{B}(D^+ \to K^0_S\pi^+) = 1.5\%$, $\mathcal{B}(K^0_S \to \pi^+\pi^-) = 69.2\%$ [183]).

Measurement in this decay channel is described in Section B.2.2;

2. measurement in the decay channel $D^+ \to K^-\pi^+\pi^+$, similarly how it is described in Chapter 5. Expected advantages and disadvantages of this decay channel can be summarised as follows:

(+) larger branching ratio ($\mathcal{B}(D^+ \to K^-\pi^+\pi^+) = 9.1\%$ [183]);

(+) better reconstruction of the D^+ secondary vertices owing to the presence of three charged daughter tracks;

(−) larger combinatorial background due to the same fact of the presence of three charged daughter tracks.

Measurement in this decay channel is described in Section B.2.3.

B.2.2 Reconstruction of D^+ mesons in decay channel $D^+ \to K^0_S(\pi^+\pi^-)\pi^+$

The event reconstruction and selection was exactly the same as described in Chapter 5 (Sections 5.1 and 5.2).

B.2.2.1 Vertex fit

The vertex fit procedure was implemented by the author and is based on [238]. Both secondary vertices, D^+ and K^0_S, were reconstructed in a simultaneous fit (Fig. B.6). An additional constraint was applied to ensure that the direction from the D^+ to K^0_S vertex is collinear to the K^0_S momentum, while the D^+ momentum was independent from the D^+ direction, reconstructed from the vertices, thus providing an input for the calculation of the decay-length significance.

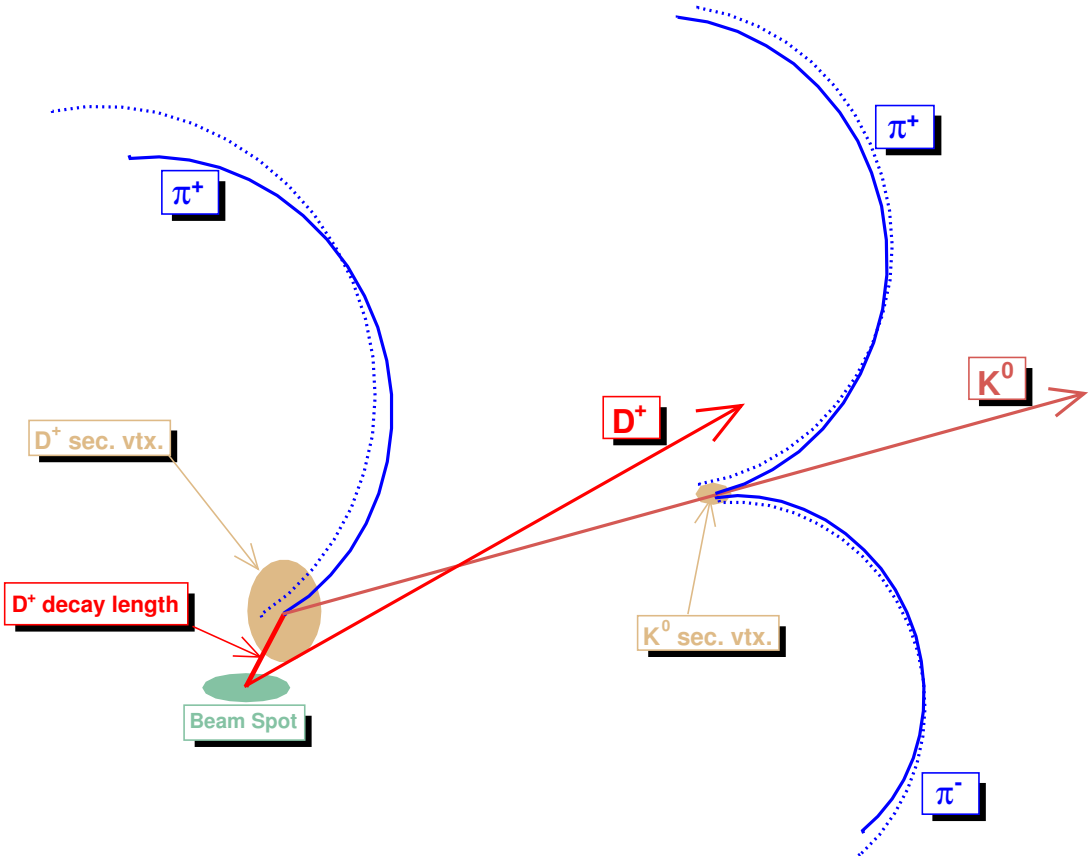

Figure B.6: Illustration of the simultaneous fit of the D^+ and K^0_S secondary vertices. Tracks before the fit are shown as dotted curves. Tracks after the fit are shown as solid curves.

There are 15 measured parameters in the fit (3 final-state tracks, each parametrised with 5 helix parameters), 15 free parameters (2 secondary vertices, each has 3 coordinates, and 3 momenta of the final-state tracks at the vertices, each has 3 components), and 2 additional

constraints (K^0_S direction), therefore the number of degrees of freedom is $n_{\text{dof}} = 2$. The fit yields the global χ^2 quantity, referred to as χ^2_{fit}, and allows usage of the D^+ lifetime information.

Similar to the previous analysis (Section 5.4.1), the most efficient way of using the lifetime information is the D^+ projected decay-length significance, S_l:

$$S_l = \frac{l_{\text{XY}}}{\sigma_{l_{\text{XY}}}}, \tag{B.1}$$

where l_{XY} is the projected decay length, defined as

$$l_{\text{XY}} = \frac{(\vec{S}_{\text{XY}} - \vec{P}_{\text{XY}}) \cdot \vec{p}(D^+)}{p_T(D^+)} \tag{B.2}$$

and $\sigma_{l_{\text{XY}}}$ is the uncertainty on l_{XY}. Here $\vec{P}_{\text{XY}}$ and $\vec{S}_{\text{XY}}$ are the vectors pointing to the primary and secondary vertices, respectively, and $\cdot$ sign denotes a scalar product. Projection on the XY plane was used because the resolution of the vertex position was most precise in the transverse plane.

B.2.2.2 K^0_S selection

This Section describes the selection of K^0_S done before performing the global vertex fit, described in the previous Section B.2.2.1. The selection closely follows [239]:

- $p_T(K^0_S) > 0.4\,\text{GeV}$;
- $p_T(\pi) > 0.12\,\text{GeV}$;
- $|\eta(\pi)| < 1.75$;
- each track should not belong to the primary vertex;
- each track should have at least two MVD hits in both the Z and ϕ directions and pass through at least three CTD superlayers;
- $\text{DCA}_{\text{K}^0_\text{S}} < 2\,\text{cm}$, where $\text{DCA}_{\text{K}^0_\text{S}}$ is the closest distance between the helices of the daughter tracks (distance of the closest approach) before the K^0_S vertex fit;
- $\chi^2_{\text{sec vtx K}^0_\text{S}} < 5$. This cut ensures good consistency of the hypothesis that two daughter tracks passed through the same secondary vertex;
- $\theta_{3D} < 0.3$, where θ_{3D} is the three-dimensional collinearity angle between the line, connecting the primary vertex and the secondary vertex of K^0_S, and the reconstructed K^0_S momentum;
- $\theta_{2D} < 0.12$, where θ_{2D} is the two-dimensional (in the XY plane) collinearity angle between the line, connecting the primary vertex and the secondary vertex of K^0_S, and the reconstructed K^0_S momentum;

- $M(e^+e^-) > 0.05\,\text{GeV}$, where $M(e^+e^-)$ is the invariant mass of the daughter tracks assuming that they are an electron and positron. This requirement eliminates background from photon conversion;
- $M(p\pi) > 1.121\,\text{GeV}$, where $M(p\pi)$ is the invariant mass of the daughter tracks assuming that they are a proton and pion. This requirement eliminates background from $\Lambda \to p\pi^-$ decays;
- $l_{\text{XY},K^0_S} > 0.5\,\text{cm}$, where l_{XY,K^0_S} is the two-dimensional (projected on the XY plane) decay length of the K^0_S secondary vertex.

The invariant-mass distribution of the reconstructed K^0_S candidates, $M(K^0_S)$, is shown in Fig. B.7. It is fitted to the sum of a Gaussian function describing the signal and first order polynomial describing the background. The fit was performed using the least-squares method as implemented in the MINUIT package [184]. As the expectation values in the χ^2-function, the integrals of the fit function within each bin of M were used. The number of K^0_S mesons yielded by the fit is $N(K^0_S) = 1379939 \pm 1250$. The fitted position of the peak is $M_0 = 497.513 \pm 0.005\,\text{MeV}$, where only the statistical uncertainty is quoted, reasonably consistent with the PDG value of $497.614 \pm 0.024\,\text{MeV}$ [183]. The peak width is $\sigma = 4.088 \pm 0.004\,\text{MeV}$, driven by the momentum resolution of the detector.

B.2.2.3 D^+ selection

The selection criteria were optimised on the sum of the charm RAPGAP (for the signal component) and inclusive ARIADNE MC (for combinatorial background) samples by maximising the peak significance as described in Section 5.4.1. The selection criteria for D^+ mesons were:

- $|\eta(D^+)| < 1.6$;
- $p_T(K^0_S) > 0.4\,\text{GeV}$;
- $p_T(\pi) > 0.4\,\text{GeV}$;
- $|\eta(K^0_S, \pi)| < 1.75$;
- the π track should have at least two MVD hits in both the Z and ϕ directions and pass through at least three CTD superlayers;
- $0.477 < M(K^0_S) < 0.517\,\text{GeV}$. This requirement selects K^0_S candidates in the peak region only;
- $\chi^2_{\text{fit}} < 10$;
- the cut on the D^+ decay-length significance depended on the D^+ transverse momentum:
  - $S_l > -2$, if $0 < p_T(D^+) < 1\,\text{GeV}$;
  - $S_l > -1$, if $1 < p_T(D^+) < 1.5\,\text{GeV}$;
  - $S_l > 0$, if $1.5 < p_T(D^+) < 15\,\text{GeV}$;

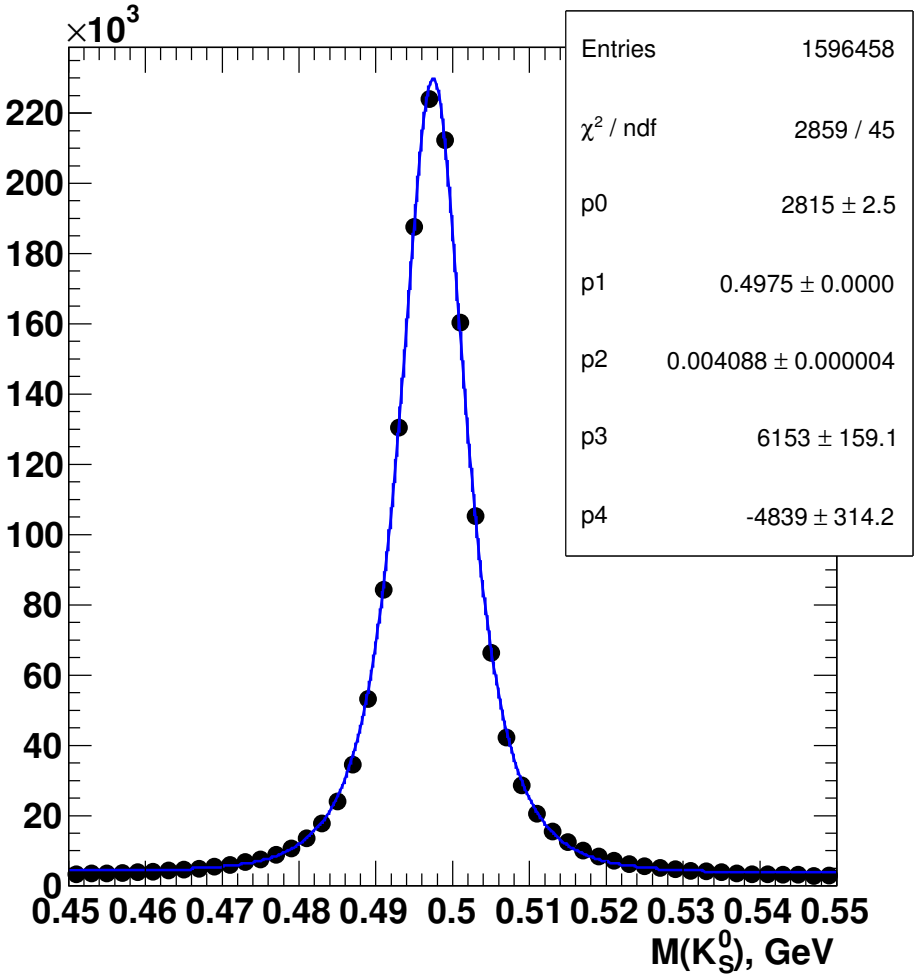

Figure B.7: The invariant-mass distribution of the reconstructed K^0_S candidates. The solid curve represents a fit by the sum of a Gaussian for the signal and a first-order polynomial for the background.

- $l_{\mathrm{XY},D^+} < 1.5\,\mathrm{cm}$, where l_{XY,D^+} is the two-dimensional (projected on the XY plane) decay length of the D^+ secondary vertex. This requirement ensured that selected D^+ secondary vertices were inside the beampipe, thus did not originate from interactions with the beampipe or detector material.

B.2.2.4 Verification of vertex fit

The vertex-fit procedure was verified on the MC simulations. The charm RAPGAP MC sample was used for this purpose and only matched D^+ candidates were used for the study. The matching was performed as explained in Section 5.6.1.2.

Distributions of the residuals for the D^+ secondary-vertex coordinates are shown in Fig. B.8. The residual is defined as the difference between the generated and reconstructed vertex positions. All residual distributions are approximately centered around zero. Spatial resolution

of the D^+ secondary-vertex reconstruction is $\approx 400\,\mu m$ in each direction.[3] Distributions of the pulls for the D^+ secondary-vertex coordinates are shown in Fig. B.9. The pull is defined as the residual divided by the uncertainty on the reconstructed secondary-vertex coordinate. All pull distributions are reasonably close to centered around zero unit Gaussians. Distributions of the residuals and pulls for the fitted parameters of all daughter tracks are provided in Section B.2.5 (Figs. B.18 to B.23). These plots confirm the absence of biases in the fit procedure and adequacy of the uncertainty estimation.

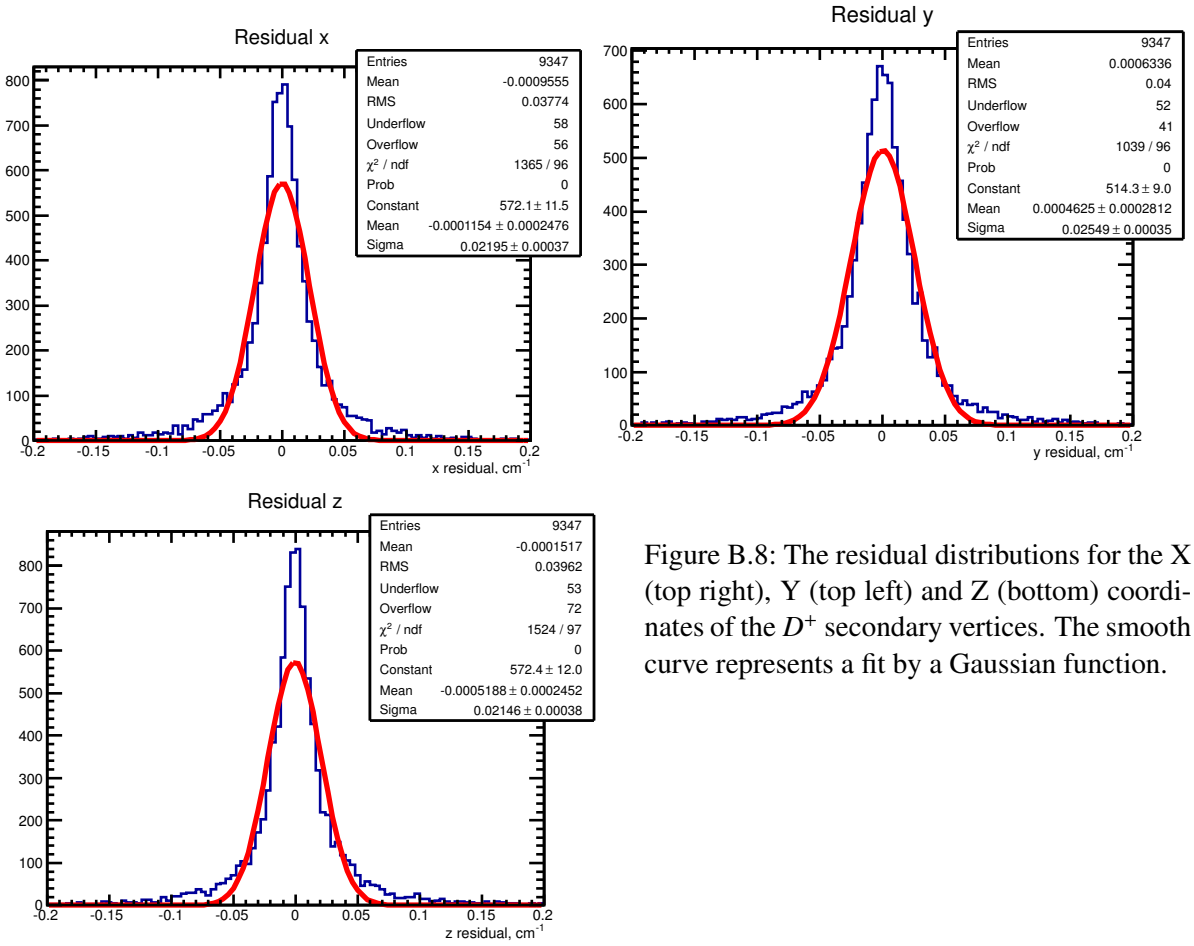

Figure B.8: The residual distributions for the X (top right), Y (top left) and Z (bottom) coordinates of the D^+ secondary vertices. The smooth curve represents a fit by a Gaussian function.

A distribution of $\chi^2_{\rm fit}$ values is shown in Fig. B.10. As expected, it has the mean value reasonably close to $n_{\rm dof} = 2$.

Finally, a distribution of the calculated S_l is shown in Fig. B.11. It is assymetric with respect to zero in the direction of positive values, as expected.

[3] For the D^+ secondary vertices reconstructed in the $D^+ \to K^-\pi^+\pi^+$ decay channel spatial resiolution is better, $\approx 200\,\mu m$, owing to the presence of three tracks originating from one vertex.

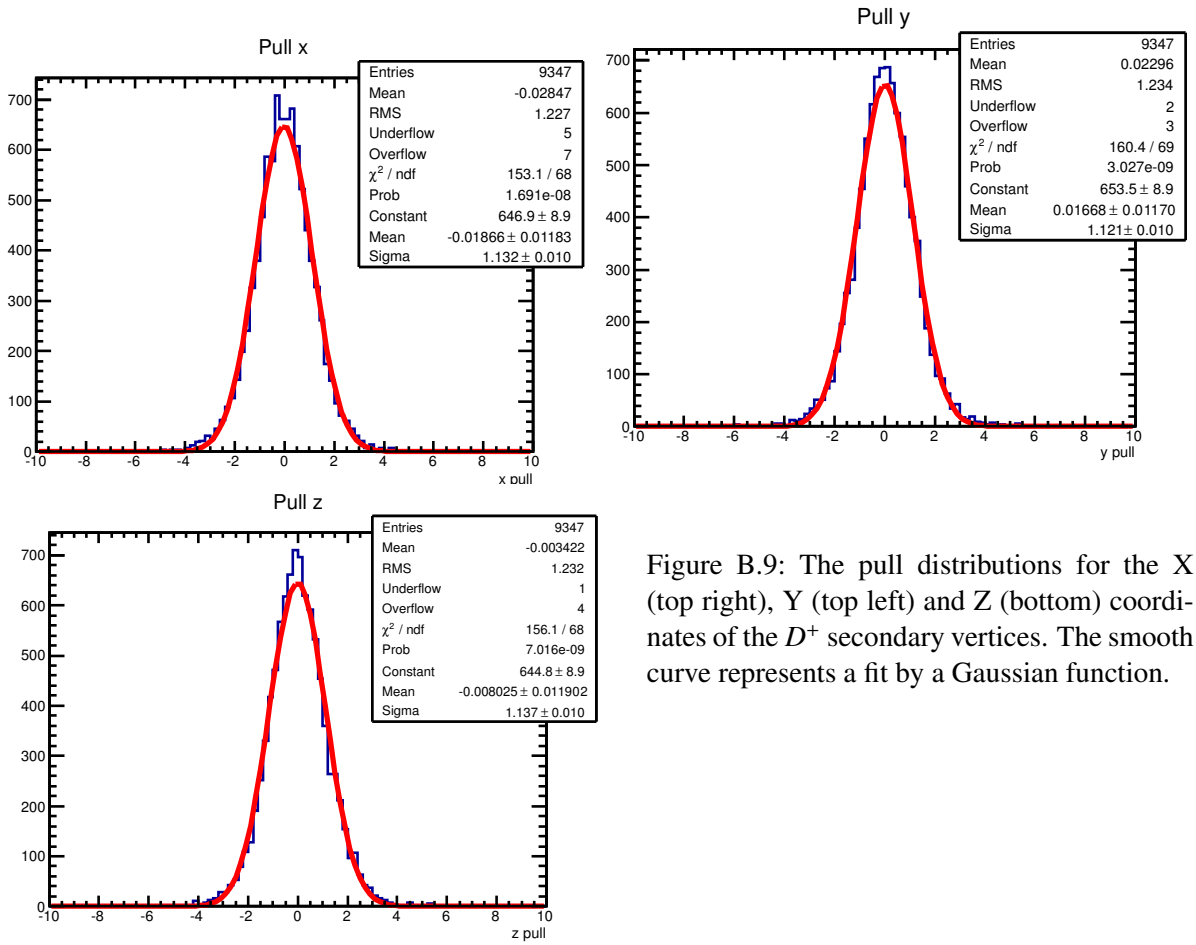

Figure B.9: The pull distributions for the X (top right), Y (top left) and Z (bottom) coordinates of the D^+ secondary vertices. The smooth curve represents a fit by a Gaussian function.

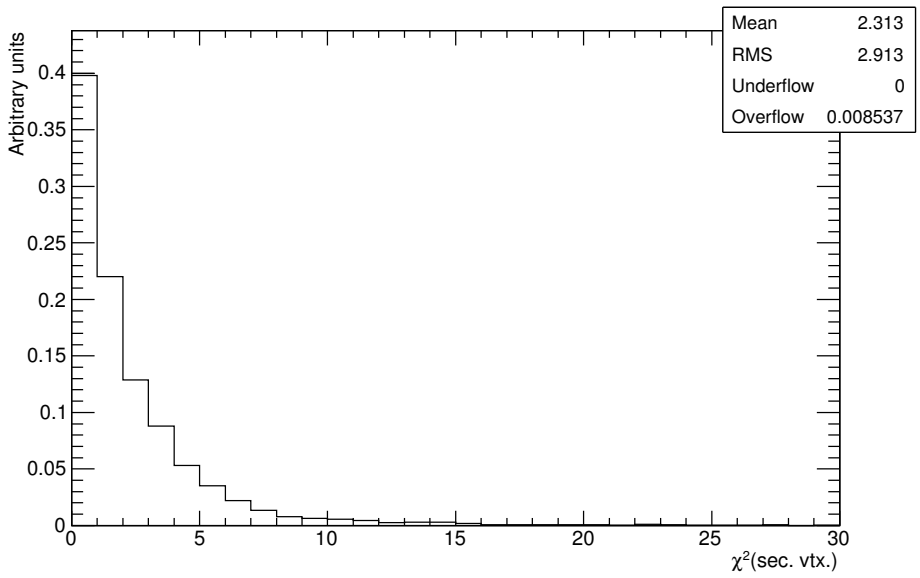

Figure B.10: The distribution of χ^2_{fit} for the simultaneous fit of the D^+ and K^0_S vertices.

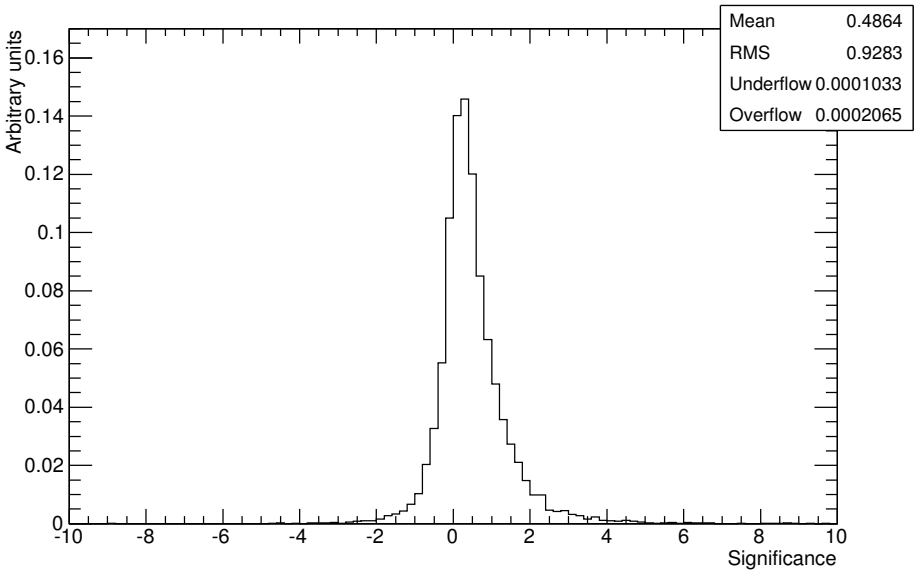

Figure B.11: The distribution of the D^+ decay-length significance for the simultaneous fit of the D^+ and K^0_S vertices.

B.2.2.5 Extraction of D^+ signal

The invariant-mass distribution of the D^+ candidates, $M(K^0_S\pi)$, is shown in Fig. B.12. It was fitted to the function:

$$F(M) = N(D^+) \cdot (F_{\text{signal}}(M) + R \cdot F_{\text{reflection}}(M)) + F_{\text{background}}(M), \tag{B.3}$$

where the signal component, $F_{\text{signal}}(M)$, is given by a Gaussian function:

$$F_{\text{signal}}(M) = \frac{1}{\sqrt{2\pi}\sigma} \exp \frac{-(M - M_0)^2}{2\sigma^2}, \tag{B.4}$$

the background component, $F_{\text{background}}(M)$, is given by a second-order polynomial and the reflection component, $F_{\text{reflection}}(M)$, takes into account the contribution from $D^+_s \to K^0_S K^+$ decays, which results in a distorted peak in the region of D^+ mass, as shown in Fig. B.13. The shape of the reflection contribution was obtained from the charm RAPGAP MC simulations and renormalised to the data with the coefficient in front, $N(D^+) \cdot R$, where $N(D^+)$ is the number of D^+ in the signal and R is given by

$$R = \frac{f(c \to D^+_s)}{f(c \to D^+)} \cdot \frac{\mathcal{B}(D^+_s \to K^0_S K^+)}{\mathcal{B}(D^+ \to K^0_S \pi^+)} \cdot \frac{\mathcal{A}(D^+_s)}{\mathcal{A}(D^+)}, \tag{B.5}$$

where $f(c \to D^+_s)$ and $f(c \to D^+)$ are the fragmentation fractions taken from [194], $\mathcal{B}(D^+_s \to K^0_S K^+)$ and $\mathcal{B}(D^+ \to K^0_S \pi^+)$ are the branching ratios taken from [183], and $\mathcal{A}(D^+_s)$ and $\mathcal{A}(D^+)$ are acceptance for the D^+_s and D^+ reconstruction, respectively, obtained from MC. Thus $N(D^+)$

gives the number of D^+ in the signal.

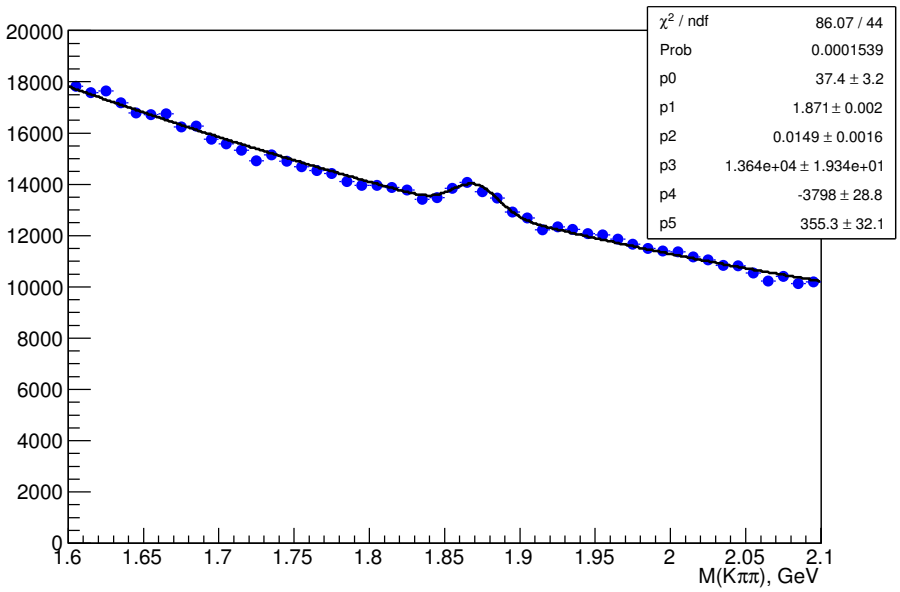

Figure B.12: The invariant-mass distribution of the reconstructed $D^+ \to K^0_S(\pi^+\pi^-)\pi^+$ candidates. The solid curve represents a fit as explained in the text.

The number of D^+ mesons yielded by the fit is $N(D^+) = 3998 \pm 352$. The fitted position of the peak is $M_0 = 1871 \pm 2\,\text{MeV}$, where only the statistical uncertainty is quoted, consistent with the PDG value of $1869.62 \pm 0.15\,\text{MeV}$ [183]. The peak width is $\sigma = 16.1 \pm 2.1\,\text{MeV}$, driven by the momentum resolution of the detector.

B.2.2.6 D^+ mass spectra in $p_T(D^+)$ bins

The invariant-mass distributions of the D^+ candidates in the bins of $p_T(D^+)$ are shown in Fig. B.14. In order to extract the D^+ signal in the bins of $p_T(D^+)$, the invariant-mass distributions in all bins were fitted simultaneously, using the same mass M_0 for all bins and ratios of the peak widthes σ fixed to the corresponding ratios from the MC simulations. This procedure improves statistical precision of the results.

The fit yields in $\chi^2/n_{\text{dof}} = 430/366$. The signal in the first $p_T(D^+)$ bin, $0 < p_T(D^+) < 0.5\,\text{GeV}$, is not accessible, while the statistical precision of the fitted D^+ yields in the bins $0.5 < p_T(D^+) < 1\,\text{GeV}$ and $1 < p_T(D^+) < 1.5\,\text{GeV}$ is $\approx 35\%$ and $\approx 20\%$, respectively. These results are quite encouraging, compared to the statistical precision $\approx 30\%$ in the bin $0 < p^2_T(D^+) < 2.25\,\text{GeV}^2$, obtained at HERA-I [236].

B.2.3 Reconstruction of D^+ mesons in decay channel $D^+ \to K^-\pi^+\pi^+$

The event reconstruction and selection was exactly the same as described in Chapter 5 (Sections 5.1 and 5.2).

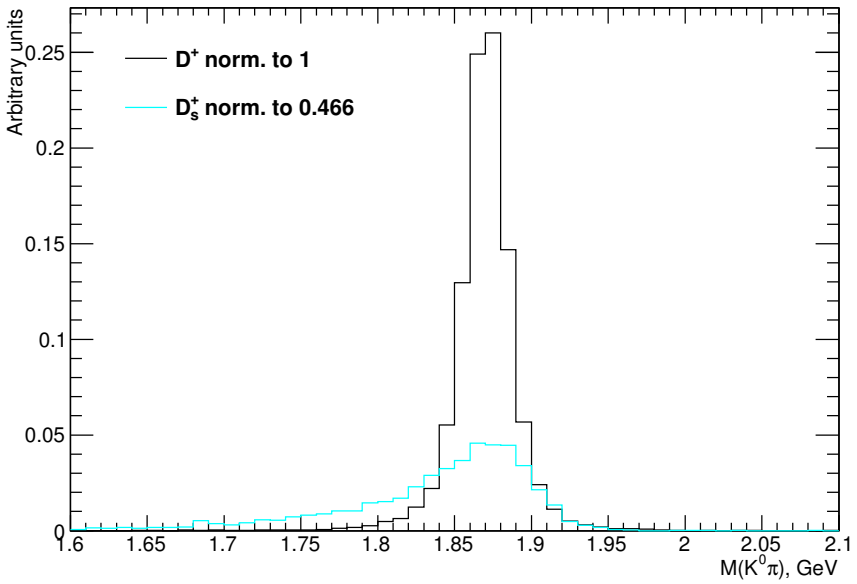

Figure B.13: The invariant-mass distributions of the matched candidates $D^+ \to K^0_S\pi^+$ and $D^+_s \to K^0_S K^+$.

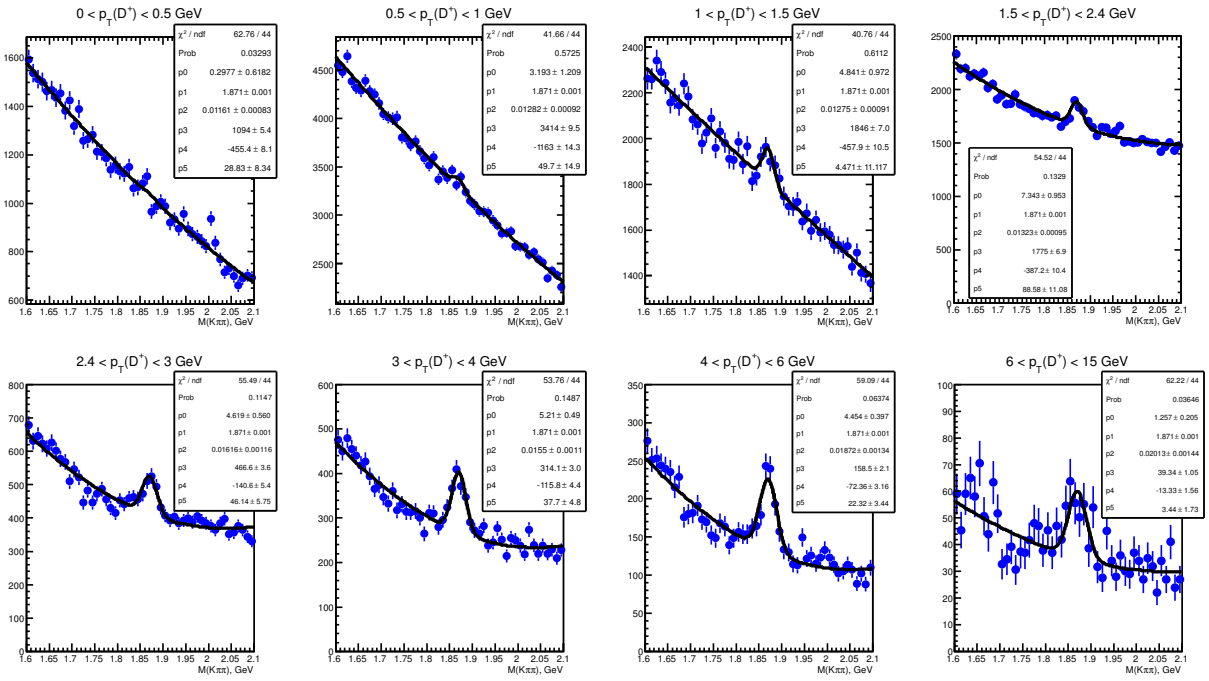

Figure B.14: The invariant-mass distribution of the reconstructed $D^+ \to K^0_S(\pi^+\pi^-)\pi^+$ candidates in the bins of $p_T(D^+)$. The solid curves represent a fit as explained in the text.

B.2.3.1 D^+ selection

The selection criteria are based on the given in Section 5.4.2, although they were slightly re-optimised to maximise the peak significance in the low-$p_T(D^+)$ region:

- $p_T(D^+) > 0.5\,\text{GeV}$. This requirement comes from the pre-selection, performed at the CN level (see Section 4.4);
- $|\eta(D^+)| < 1.6$;
- each track should have at least two MVD hits in both the Z and ϕ directions and pass through at least three CTD superlayers;
- $p_T(\pi) > 0.25\,\text{GeV}$;
- $p_T(K) > 0.35\,\text{GeV}$;
- $\chi^2_{\text{sec vtx}} < 10$;
- the cut on the D^+ decay-length significance depended on the D^+ transverse momentum:
  - $S_l > -2$, if $0.5 < p_T(D^+) < 1\,\text{GeV}$;
  - $S_l > 2$, if $1 < p_T(D^+) < 1.5\,\text{GeV}$;
  - $S_l > 4$, if $1.5 < p_T(D^+) < 15\,\text{GeV}$;
- $l_{\text{XY},D^+} < 1.5\,\text{cm}$, where l_{XY,D^+} is the two-dimensional (projected on the XY plane) decay length of the D^+ secondary vertex.

B.2.3.2 D^+ mass spectra in $p_T(D^+)$ bins

The invariant-mass distributions of the D^+ candidates, $M(K\pi\pi)$, in the bins of $p_T(D^+)$ are shown in Fig. B.15. To extract the number of reconstructed D^+ mesons, the mass distribution was fitted with a function

$$F(M) = F_{\text{signal}}(M) + F_{\text{background}}(M), \tag{B.6}$$

where the signal component, $F_{\text{signal}}(M)$, is given by a Gaussian function:

$$F_{\text{signal}}(M) = N(D^+) \cdot \frac{1}{\sqrt{2\pi}\sigma} \exp \frac{-(M - M_0)^2}{2\sigma^2} \tag{B.7}$$

and the background component, $F_{\text{background}}(M)$, is given by a second-order polynomial. Analogously to the case of the D^+ signal extraction in the $D^+ \to K^0_S(\pi^+\pi^-)\pi^+$ decay channel, all $p_T(D^+)$ bins were fitted simultaneously, using the same mass M_0 and ratios of the peak widthes σ fixed to the corresponding ratios from the MC simulations.

The fit results in $\chi^2/n_{\text{dof}} = 333/250$. The statistical precision of the fitted D^+ yields in the bins $0.5 < p_T(D^+) < 1\,\text{GeV}$ and $1 < p_T(D^+) < 1.5\,\text{GeV}$ is $\approx 25\%$ and $\approx 30\%$, respectively. This result is competitive to what was obtained using the $D^+ \to K^0_S(\pi^+\pi^-)\pi^+$ decay channel in Section B.2.2.6.

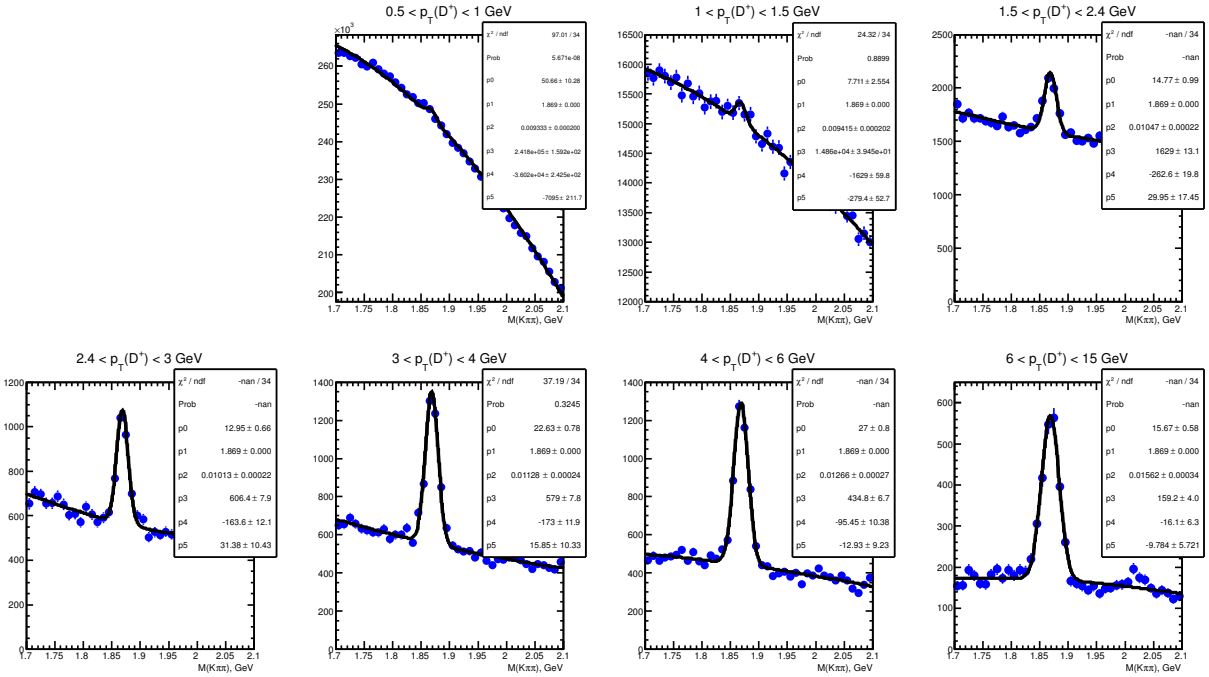

Figure B.15: The invariant-mass distribution of the reconstructed $D^+ \to K^-\pi^+\pi^+$ candidates in the bins of $p_T(D^+)$. The solid curves represent a fit as explained in the text.

B.2.4 Comparison of results from two decay channels

The kinematic region of the measurement is given by

$$\begin{aligned} &5 < Q^2 < 1000\,\text{GeV}^2, \\ &0.02 < y < 0.7, \\ &0.5 < p_T(D^+) < 15\,\text{GeV}, \\ &|\eta(D^+)| < 1.6. \end{aligned} \tag{B.8}$$

The differential cross section as a function of $p_T(D^+)$ in the i^{th} bin was determined as

$$\frac{\mathrm{d}\sigma}{\mathrm{d}Y} = \frac{N_{\text{DATA}}}{\mathcal{A}\mathcal{L}\mathcal{B}\Delta Y_i}, \tag{B.9}$$

where N_{DATA} is the number of the reconstructed D^+ mesons in the data, $\mathcal{A}$ is the acceptance correction, determined using the charm RAPGAP MC sample, $\mathcal{L}$ is the integrated luminosity, $\mathcal{B}$ is the branching ratio, taken from [183] and ΔY_i is the width of the i^{th} bin of $p_T(D^+)$ (see Section 5.6 for more details).

Acceptance as a function of $p_T(D^+)$ for two decay channels is shown in Fig. B.16. It is on average $\approx$ 15% and $\approx$ 8% for the $D^+ \to K^0_S(\pi^+\pi^-)\pi^+$ and $D^+ \to K^-\pi^+\pi^+$ decay channels, respectively. Because of the selection tuned for the low-$p_T(D^+)$ region, for both decay channels it reaches the minimum at $p_T(D^+) \approx 2\,\text{GeV}$ and grows at lower and higher $p_T(D^+)$. Note, that

for the acceptance determination no corrections to the MC simulations have been applied.

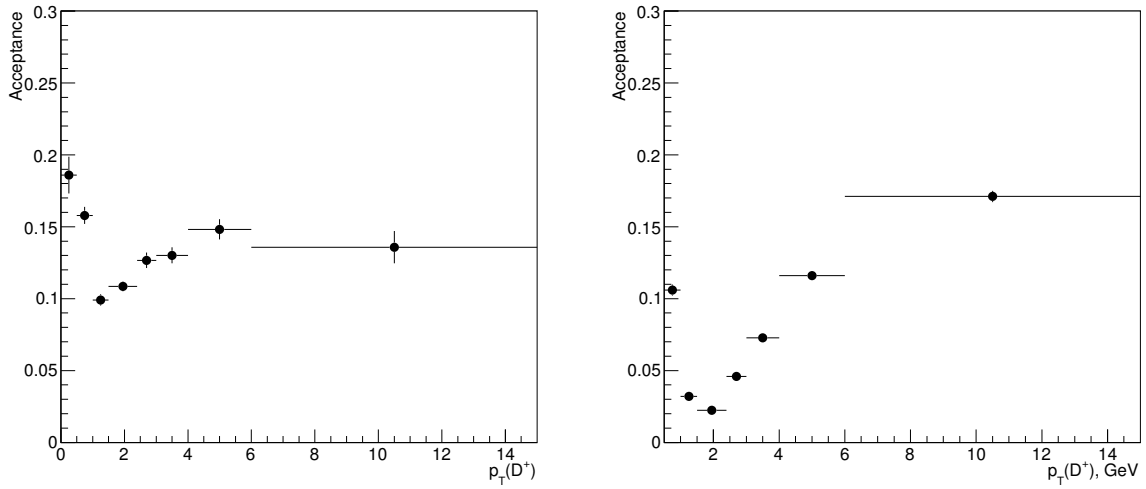

Figure B.16: Acceptance as a function of $p_T(D^+)$ for the $D^+ \to K^0_S(\pi^+\pi^-)\pi^+$ (left) and $D^+ \to K^-\pi^+\pi^+$ (right) decay channels. Error bars represent the statistical uncertainty.

Fig. B.17 shows the differential cross section as a function of $p_T(D^+)$, determined using the $D^+ \to K^0_S(\pi^+\pi^-)\pi^+$ and $D^+ \to K^-\pi^+\pi^+$ decay channels. The results from two decay channels have similar precision at low $p_T(D^+)$ and are consistent in all $p_T(D^+)$ range.

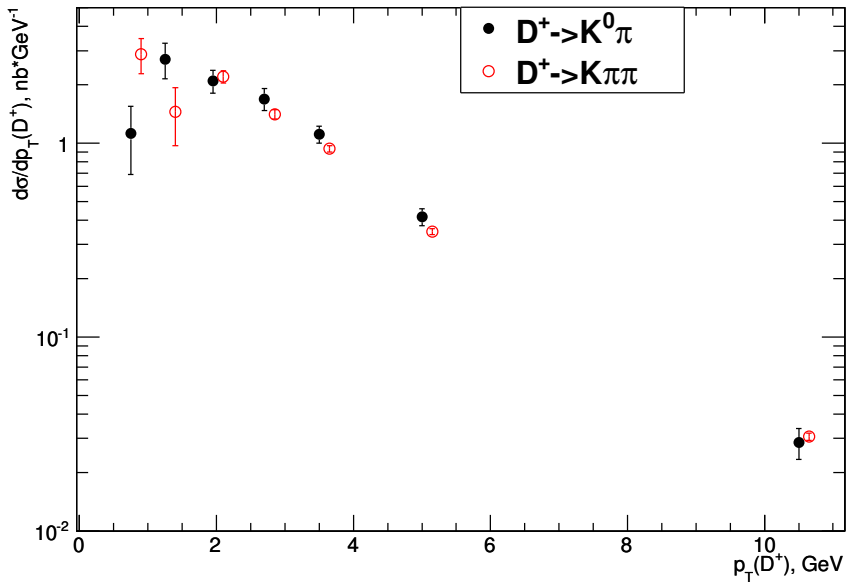

Figure B.17: The differential cross section as a function of $p_T(D^+)$, determined using decay channels $D^+ \to K^0_S(\pi^+\pi^-)\pi^+$ (filled circles) and $D^+ \to K^-\pi^+\pi^+$ (empty circles), shown with a small horizontal offset for better visibility.

By combining the results from two decay channels, it might be expected to obtain statistical precision $\approx$ 15–20% in the bins $0.5 < p_T(D^+) < 1\,\text{GeV}$ and $1 < p_T(D^+) < 1.5\,\text{GeV}$, about

two times better than was achieved with the HERA-I data [236] for the wider lowest bin $0 < p_T^2(D^+) < 2.25\,\text{GeV}^2$. Although these results need evaluation of systematic uncertainties also, the latter are not expected to become dominant in the low-$p_T(D^+)$ region.

Further potential improvement of the measurement includes:

- improvement of the vertex-fit procedure for the $D^+ \to K_S^0(\pi^+\pi^-)\pi^+$ decay channel:
  - perform a $M(K_S^0)$-constrained fit, i.e. require the mass of K_S^0 to be fixed in the fit;
  - fit the position of the primary vertex also (with possible usage of the beamspot position), requiring collinearity fot $p(D^+)$ and its decay length; further this will allow a $M(D^+)$-constrained fit;
- use a cut on the decay-length significance as a smooth function of $p_T(D^+)$;
- use the energy-loss information for kaon identification for the $D^+ \to K^-\pi^+\pi^+$ decay channel.

B.2.5 Residuals and pulls for fitted track parameters

Figs. B.18, B.20, B.22 and Figs. B.19, B.21, B.23 show residual and pull distributions, respectively, for the fitted a_1, a_2 and a_5 parameters of the D^+ daughter tracks (see Section B.3 for the description of the ZEUS track parametrisation).

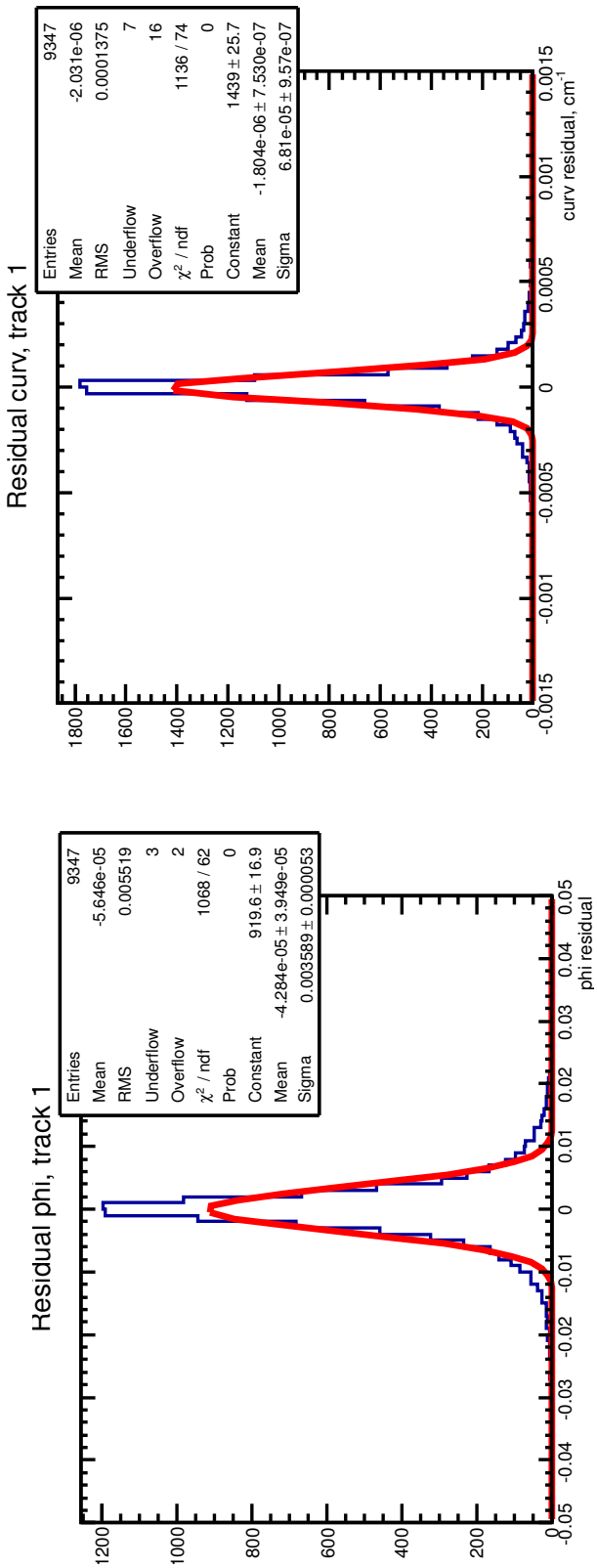

Figure B.18: The residual distributions for the parameters of the π track from D^+: a_1 (top right), a_2 (top left) and a_5 (bottom). The smooth curve represents a fit by a Gaussian function.

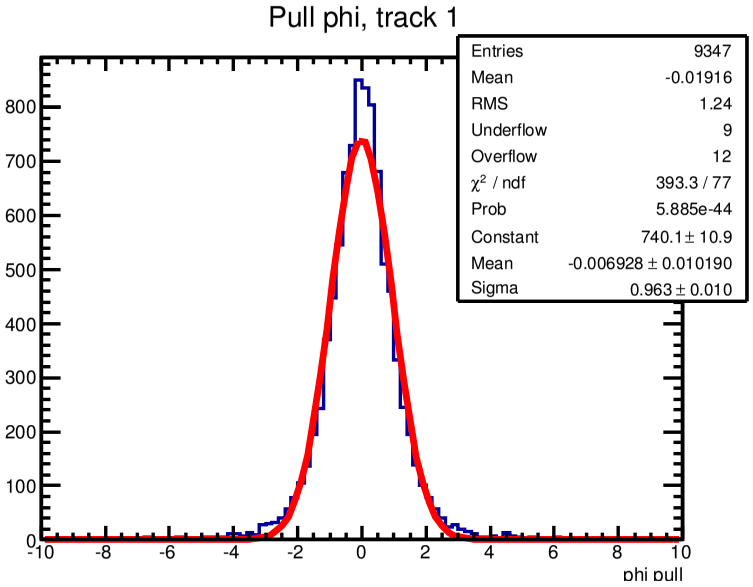

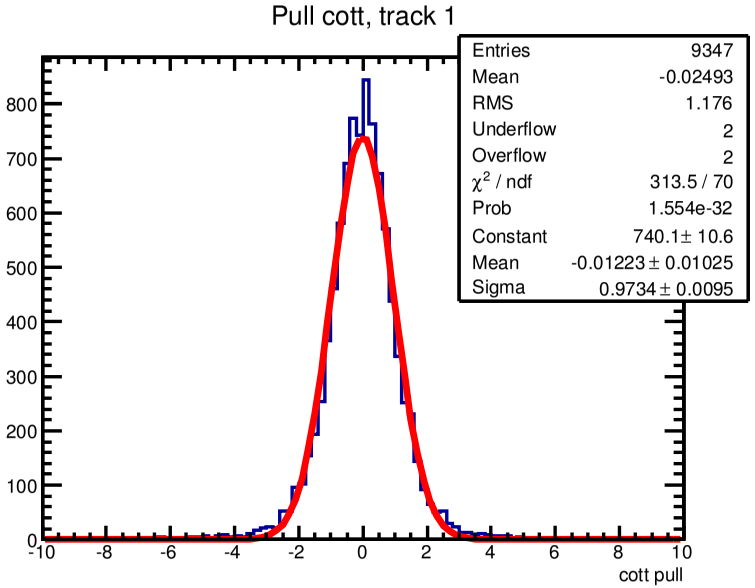

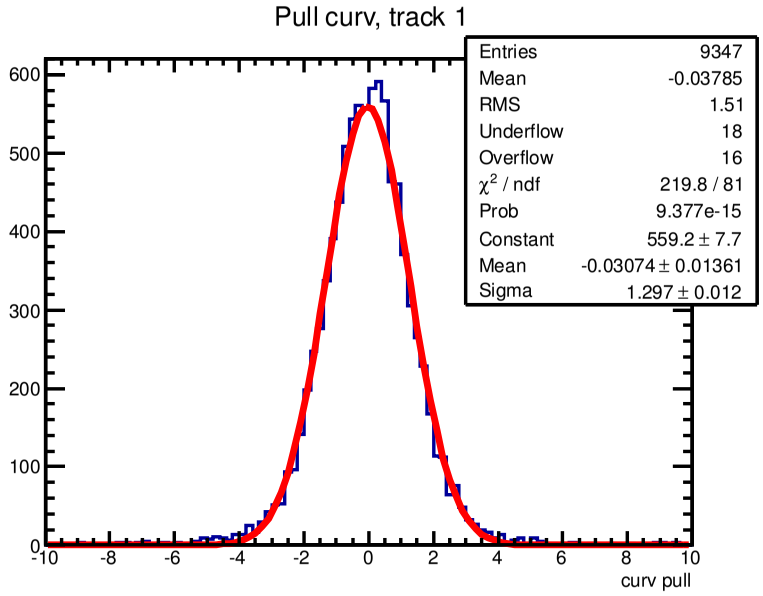

Figure B.19: The pull distributions for the parameters of the π track from D^+: a_1 (top right), a_2 (top left) and a_5 (bottom). The smooth curve represents a fit by a Gaussian function.

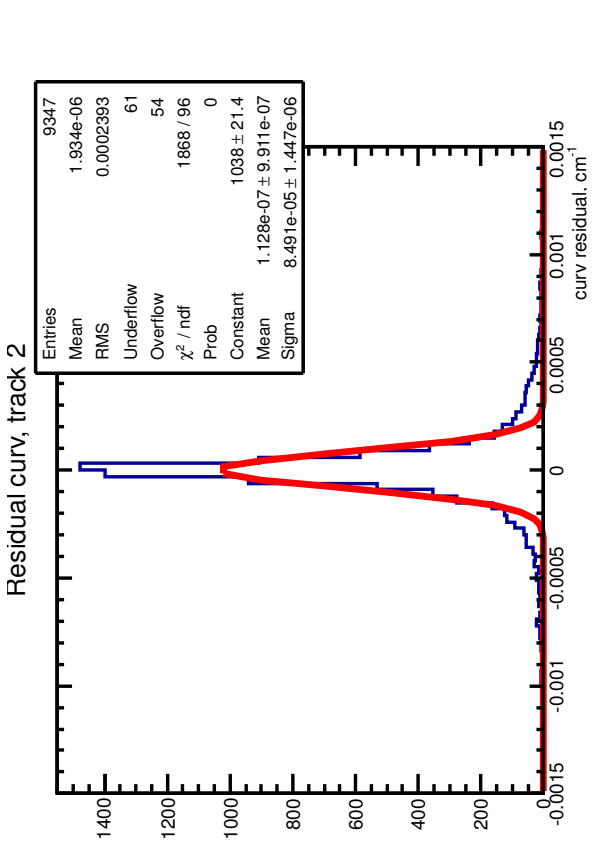

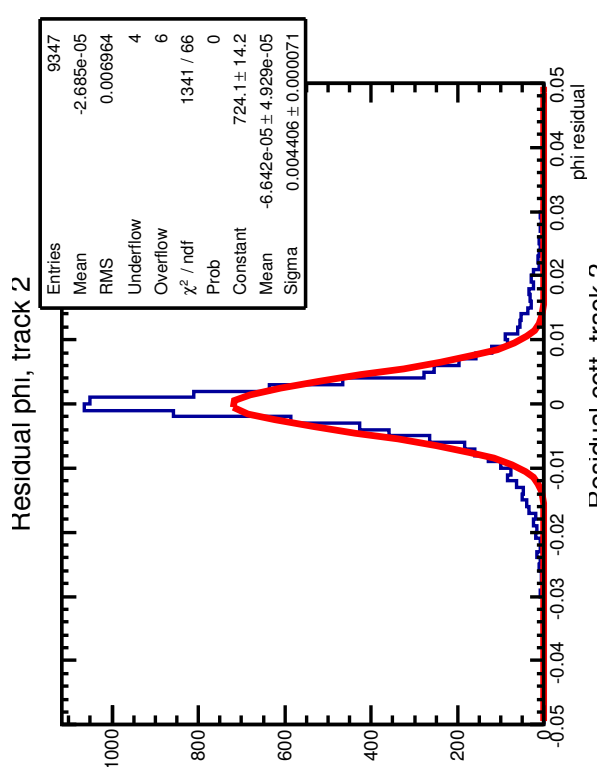

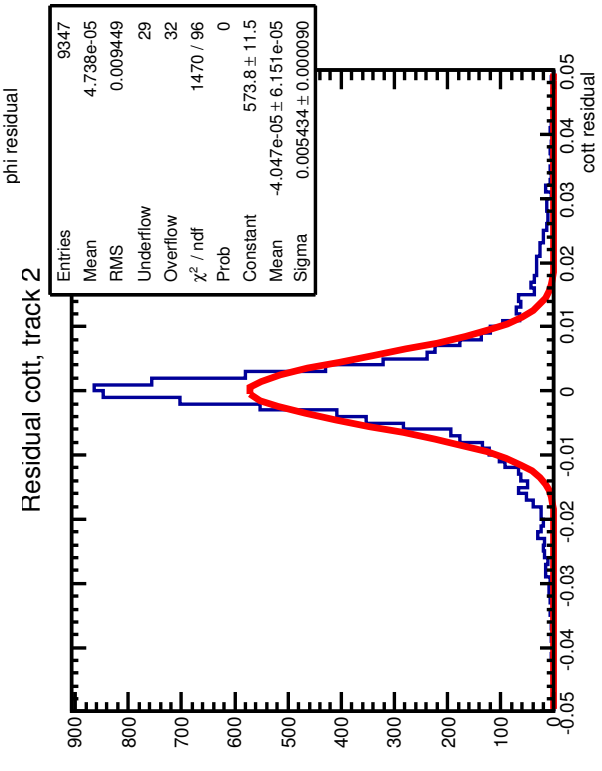

Figure B.20: The residual distributions for the parameters of the first π track from K^0_S: a_1 (top right), a_2 (top left) and a_5 (bottom). The smooth curve represents a fit by a Gaussian function.

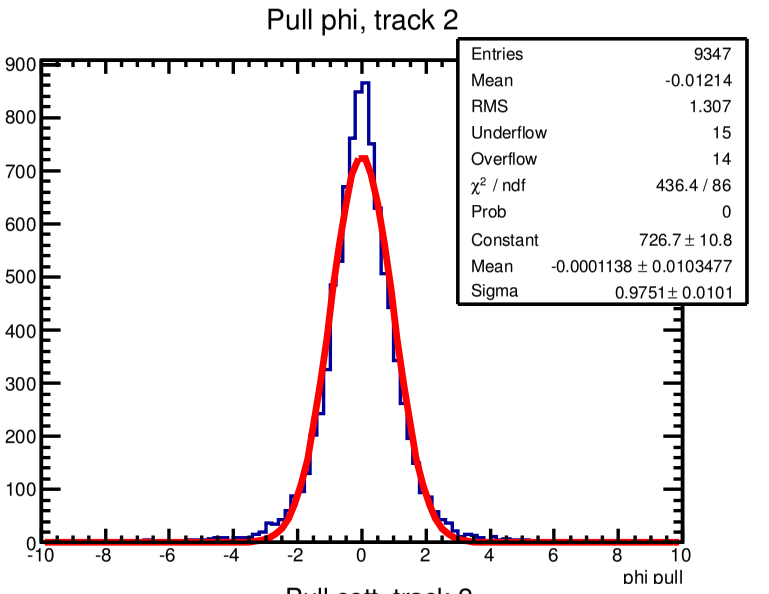

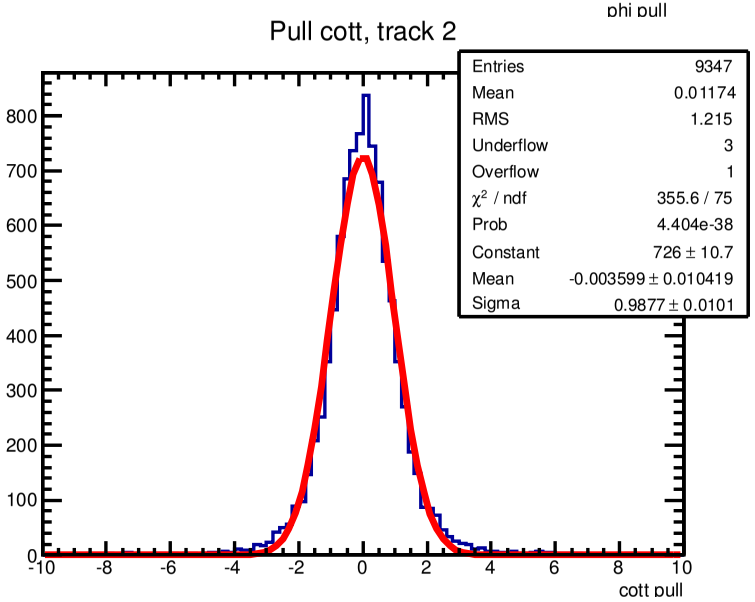

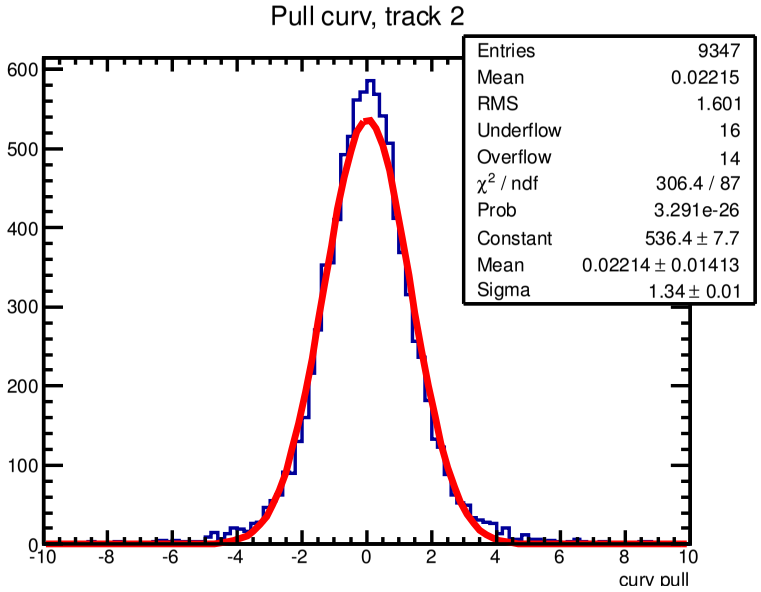

Figure B.21: The pull distributions for the parameters of the first π track from K^0_S: a_1 (top right), a_2 (top left) and a_5 (bottom). The smooth curve represents a fit by a Gaussian function.

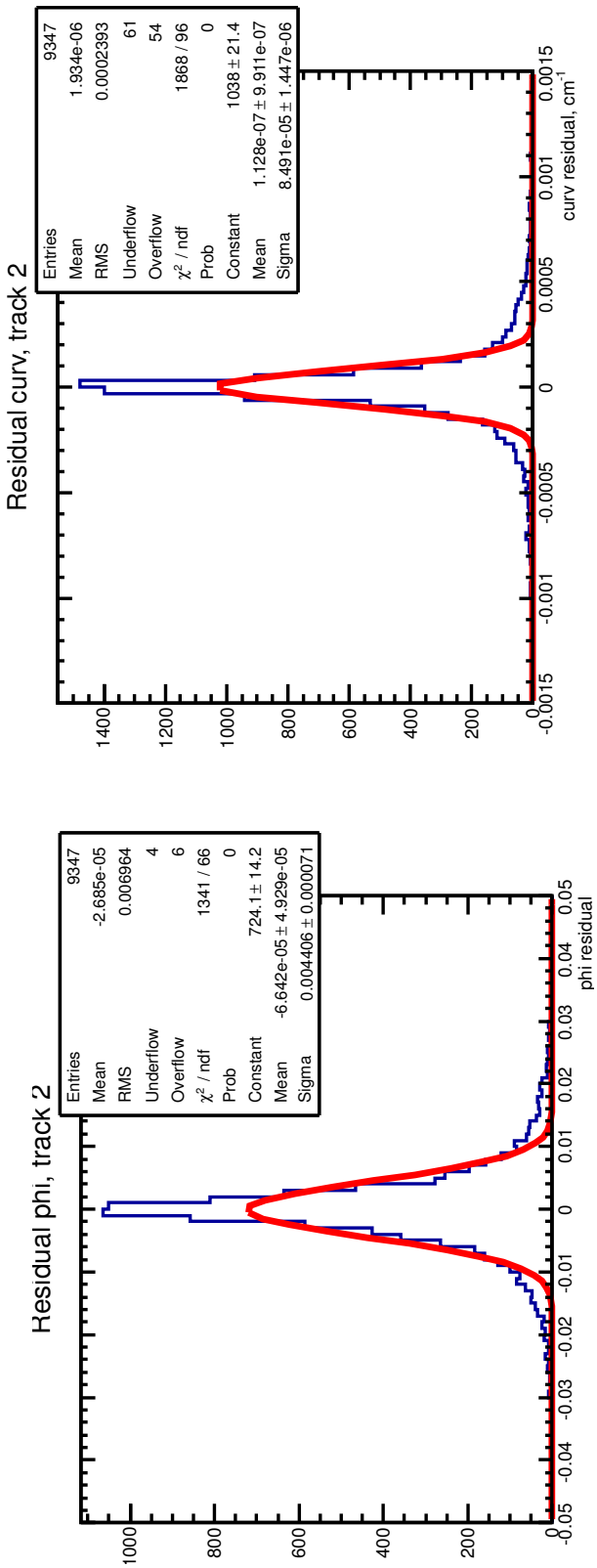

Figure B.22: The residual distributions for the parameters of the second π track from K^0_S: a_1 (top right), a_2 (top left) and a_5 (bottom). The smooth curve represents a fit by a Gaussian function.

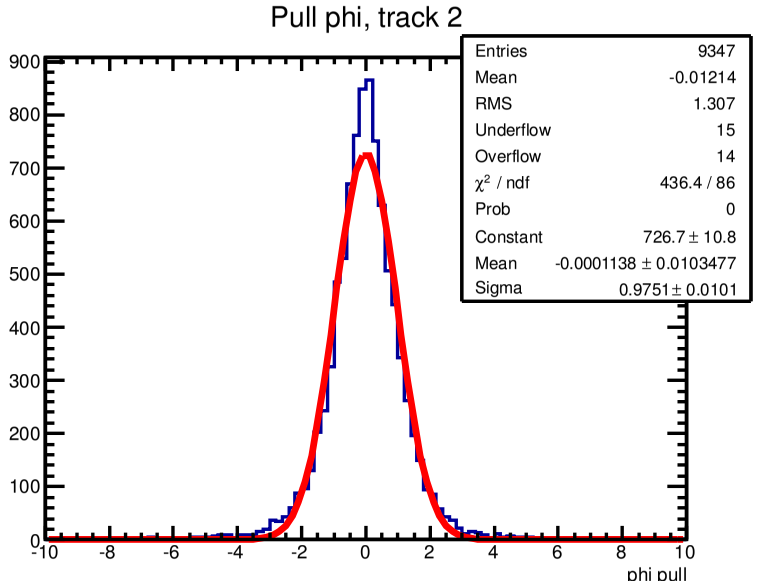

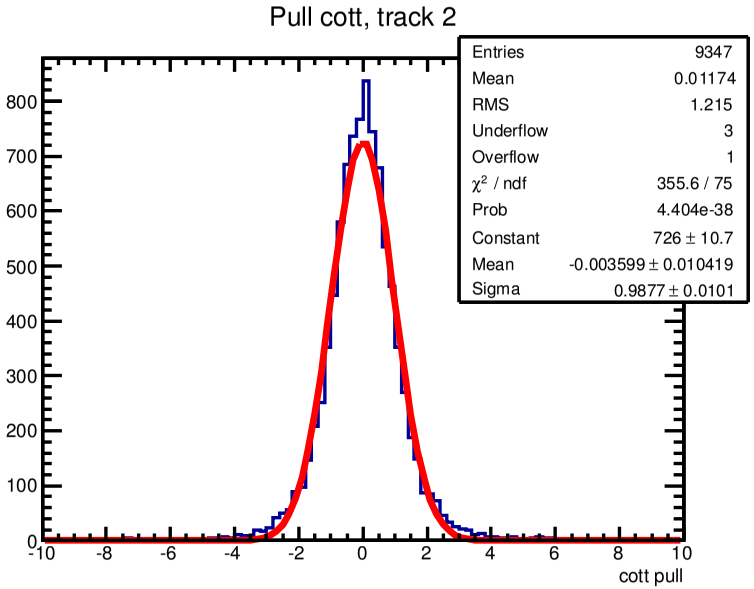

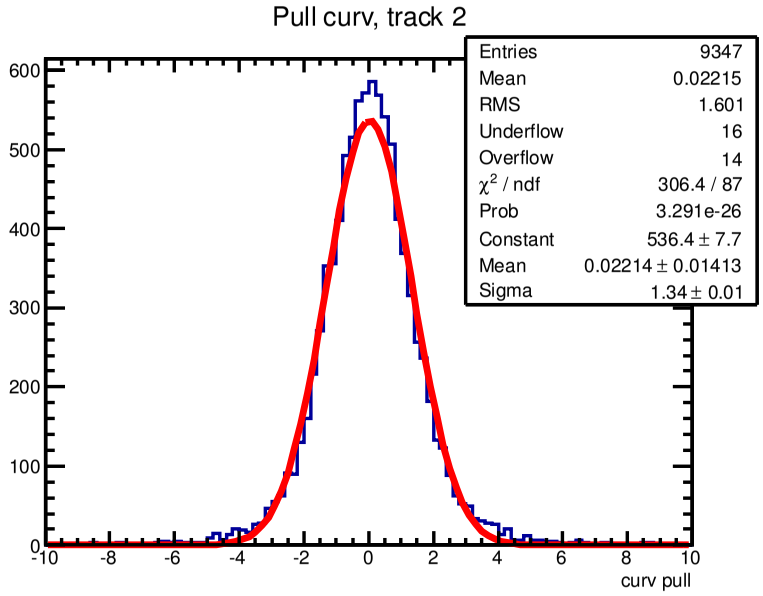

Figure B.23: The pull distributions for the parameters of the second π track from K^0_S: a_1 (top right), a_2 (top left) and a_5 (bottom). The smooth curve represents a fit by a Gaussian function.

B.3 ZEUS track parametrisation

Tracks are approximated by helices and are parametrised with 5 parameters and arbitrary two-dimensional reference point (X_{ref}, Y_{ref}) (Fig. B.24):

- $a_1 = \phi_H$ (angle tangent to the helix in the XY plane at the point of the closest approach to the reference point);
- $a_2 = Q/R$ (Q is the charge, R is the local radius);
- $a_3 = QD_H$ (D_H is called the *impact parameter*; it connects the helix to the reference point in the XY plane);
- $a_4 = Z_H$;
- $a_5 = \cot\theta$.

This is the *perigee parametrisation*.

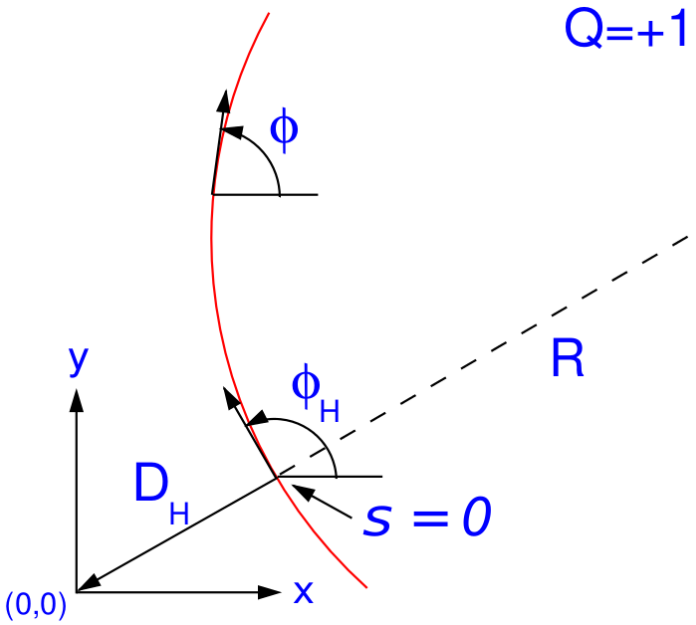

Figure B.24: Parametrisation of the track helix.

Any point of the helix can be expressed as a function of the outbound path length in the XY plane:

$$s(\phi) = QR(\phi - \phi_H), \tag{B.10}$$

where ϕ is the outbound tangent angle in the XY plane. The coordinate components are given by:

$$\begin{aligned} X &= X_H + QR(\sin\phi - \sin\phi_H), \\ Y &= Y_H + QR(\cos\phi_H - \cos\phi), \\ Z &= Z_H + s(\phi)\cot\theta, \end{aligned} \tag{B.11}$$

where $(X_H,\ Y_H,\ Z_H)$ are the coordinates of the point of the closest approach to the reference point:

$$\begin{aligned} X_H &= X_{\text{ref}} + QD_H \sin\phi_H, \\ Y_H &= Y_{\text{ref}} - QD_H \cos\phi_H, \\ Z_H &= Z_{\text{ref}}. \end{aligned} \tag{B.12}$$

APPENDIX C

Combination procedure: additional details

In this Appendix additional information on the combination procedure (Section 6.2) is provided.

C.1 Minimisation method

The minimisation method described below [240, 241] is applicable if the uncertainties of the measurements do not depend on the central values (the additive treatment); in the case of the multiplicative treatment this method is extended with an iteration procedure described in the next Section C.2. In this case the χ^2-function 6.10 can be considered. Since χ^2 in 6.10 is a quadratic form of $\mathbf{m}$ and $\mathbf{b}$, it may be rearranged such that it takes a simpler form similar to equation 6.3. To show this explicitly, χ^2 can be written as a Taylor series up to its second derivatives near the minimum, $(\mathbf{m_0}, \mathbf{b_0})$:

$$\chi^2(\mathbf{m},\mathbf{b}) = \sum_{e=1}^{N_e}\sum_{i=1}^{N_m} \frac{\left(m_i - \sum_{j=1}^{N_s} \Gamma_i^{e,j} b^{e,j} - \mu_i^e\right)^2}{\sigma_i^{e\,2}} + \sum_{j=1}^{N_s} b^{e,j\,2} = \chi^2\Big|_0 + \left.\frac{\partial\chi^2}{\partial\mathbf{m}}\right|_0 (\mathbf{m}-\mathbf{m_0}) + \left.\frac{\partial\chi^2}{\partial\mathbf{b}}\right|_0 (\mathbf{b}-\mathbf{b_0}) + \frac{1}{2}\left.\frac{\partial^2\chi^2}{\partial\mathbf{m}^2}\right|_0 (\mathbf{m}-\mathbf{m_0})^2 + \frac{1}{2}\left.\frac{\partial^2\chi^2}{\partial\mathbf{b}^2}\right|_0 (\mathbf{b}-\mathbf{b_0})^2 + \left.\frac{\partial^2\chi^2}{\partial\mathbf{m}\partial\mathbf{b}}\right|_0 (\mathbf{m}-\mathbf{m_0})(\mathbf{b}-\mathbf{b_0}). \tag{C.1}$$

Notation $|_0$ indicates that the expression is evaluated at $\mathbf{m} = \mathbf{m_0}$, $\mathbf{b} = \mathbf{b_0}$. Note, that this is an *exact* expression, because χ^2 is a quadratic form; moreover the second derivatives are constant, i.e. $\left.\frac{\partial^2\chi^2}{\partial\mathbf{m}^2}\right|_0 = \frac{\partial^2\chi^2}{\partial\mathbf{m}^2}$, $\left.\frac{\partial^2\chi^2}{\partial\mathbf{b}^2}\right|_0 = \frac{\partial^2\chi^2}{\partial\mathbf{b}^2}$, $\left.\frac{\partial^2\chi^2}{\partial\mathbf{m}\partial\mathbf{b}}\right|_0 = \frac{\partial^2\chi^2}{\partial\mathbf{m}\partial\mathbf{b}}$.

It is useful to give explicit expressions for the second derivatives and to introduce the fol-

lowing matrix notations:

$$\begin{aligned}
\frac{\partial^2\chi^2}{\partial m_i \partial m_j} &= 2\delta_{ij}\sum_{e=1}^{N_e}\frac{1}{\sigma_i^{e\,2}} = 2[\mathbf{A_M}]_{ij}, \quad 1 \le i,j \le N_m, \\
\frac{\partial^2\chi^2}{\partial b_i \partial b_j} &= 2\left(\delta_{ij} + \sum_{e=1}^{N_e}\sum_{k=1}^{N_m}\frac{\Gamma_k^{e,i}\Gamma_k^{e,j}}{\sigma_k^{e\,2}}\right) = 2[\mathbf{A_S}]_{ij}, \quad 1 \le i,j \le N_s, \\
\frac{\partial^2\chi^2}{\partial m_i \partial b_j} &= -2\sum_{e=1}^{N_e}\frac{\Gamma_i^{e,j}}{\sigma_i^{e\,2}} = 2[\mathbf{A_{SM}}]_{ij}, \quad 1 \le i \le N_m, \quad 1 \le j \le N_s,
\end{aligned} \tag{C.2}$$

where δ_{ij} is the Kronecker delta.

The minimum $\chi^2_{\min} = \chi^2\big|_0$ is found by solving a system of linear equations:

$$\begin{aligned}
\left.\frac{\partial\chi^2}{\partial\mathbf{m}}\right|_0 = 0 &\Longrightarrow \mathbf{A_M m_0} + \mathbf{A_{SM} b_0} - \mathbf{C_M} = 0, \\
\left.\frac{\partial\chi^2}{\partial\mathbf{b}}\right|_0 = 0 &\Longrightarrow \mathbf{A_{SM}}^T\mathbf{m_0} + \mathbf{A_S b_0} - \mathbf{C_S} = 0,
\end{aligned} \tag{C.3}$$

where

$$\begin{aligned}
[\mathbf{C_M}]_i &= \sum_{e=1}^{N_e}\frac{\mu_i^e}{\sigma_i^{e\,2}}, \\
[\mathbf{C_S}]_i &= -\sum_{e=1}^{N_e}\sum_{j=1}^{N_m}\frac{\mu_j^e\Gamma_j^{e,i}}{\sigma_j^{e\,2}}.
\end{aligned} \tag{C.4}$$

System of linear equations C.3 can be written in a form of one matrix equation:

$$\begin{pmatrix} \mathbf{A_M} & \mathbf{A_{SM}} \\ \mathbf{A_{SM}}^T & \mathbf{A_S} \end{pmatrix}\begin{pmatrix} \mathbf{m_0} \\ \mathbf{b_0} \end{pmatrix} = \begin{pmatrix} \mathbf{C_m} \\ \mathbf{C_s} \end{pmatrix}. \tag{C.5}$$

Although solving of this system can be performed directly by inversion of the whole matrix, it is more convenient to take an advantage of the diagonal structure of the block $\mathbf{A_M}$ and solve the system using the method of the Schur complement:

$$\begin{aligned}
\mathbf{b_0} &= \mathbf{A'_S}^{-1}(\mathbf{C_S} - \mathbf{A_{SM}}^T\mathbf{A_M}^{-1}\mathbf{C_M}), \\
\mathbf{m_0} &= \mathbf{A_M}^{-1}(\mathbf{C_M} - \mathbf{A_{SM}}\mathbf{b_0}),
\end{aligned} \tag{C.6}$$

where

$$\mathbf{A'_S} = \mathbf{A_S} - \mathbf{A_{SM}}^T\mathbf{A_M}^{-1}\mathbf{A_{SM}}. \tag{C.7}$$

This method benefits from the fact, that the only non-trivial inversion to be performed is the inversion of the block $\mathbf{A'_S}$. The size of this block is $N_s \times N_s$ and usually much smaller than the total size of the system C.5, $(N_m + N_s) \times (N_m + N_s)$, therefore this method is preferable for

computation.

Obtained solution ($\mathbf{m_0}$,$\mathbf{b_0}$) solves the minimisation problem for the central values. To find the uncertainties on ($\mathbf{m_0}$,$\mathbf{b_0}$), the χ^2 expansion in Eq. C.1 can be written, taking into account that ($\mathbf{m_0}$,$\mathbf{b_0}$) is its minimum:

$$\chi^2(\mathbf{m},\mathbf{b}) = \chi^2_{\min} + \langle \mathbf{m}-\mathbf{m_0}|\mathbf{A_M}|\mathbf{m}-\mathbf{m_0}\rangle + 2\,\langle \mathbf{m}-\mathbf{m_0}|\mathbf{A_{SM}}|\mathbf{b}-\mathbf{b_0}\rangle + \langle \mathbf{b}-\mathbf{b_0}|\mathbf{A_S}|\mathbf{b}-\mathbf{b_0}\rangle\,. \tag{C.8}$$

Denoting $\mathbf{m}-\mathbf{m_0} = \tilde{\mathbf{m}}$, $\mathbf{b}-\mathbf{b_0} = \tilde{\mathbf{b}}$:

$$\chi^2(\mathbf{m},\mathbf{b}) = \chi^2_{\min} + \langle \tilde{\mathbf{m}}|\mathbf{A_M}|\tilde{\mathbf{m}}\rangle + 2\,\langle \tilde{\mathbf{m}}|\mathbf{A_{SM}}|\tilde{\mathbf{b}}\rangle + \langle \tilde{\mathbf{b}}|\mathbf{A_S}|\tilde{\mathbf{b}}\rangle\,. \tag{C.9}$$

To separate contributions from $\tilde{\mathbf{m}}$ and $\tilde{\mathbf{b}}$ in the term $2\,\langle \tilde{\mathbf{m}}|\mathbf{A_{SM}}|\tilde{\mathbf{b}}\rangle$, introduce a variable substitution $|\tilde{\mathbf{m}}'\rangle = |\tilde{\mathbf{m}}\rangle - \mathbf{X}\,|\tilde{\mathbf{b}}\rangle$:

$$\begin{aligned}\chi^2(\mathbf{m},\mathbf{b}) &= \chi^2_{\min} + \langle \tilde{\mathbf{m}}' + \tilde{\mathbf{b}}\mathbf{X}^T|\mathbf{A_M}|\tilde{\mathbf{m}}' + \mathbf{X}\tilde{\mathbf{b}}\rangle + 2\,\langle \tilde{\mathbf{m}}' + \tilde{\mathbf{b}}\mathbf{X}^T|\mathbf{A_{SM}}|\tilde{\mathbf{b}}\rangle + \langle \tilde{\mathbf{b}}|\mathbf{A_S}|\tilde{\mathbf{b}}\rangle \\ &= \chi^2_{\min} + \langle \tilde{\mathbf{m}}'|\mathbf{A_M}|\tilde{\mathbf{m}}'\rangle + \langle \tilde{\mathbf{b}}|\mathbf{A_S} + 2\mathbf{X}^T\mathbf{A_{SM}} + \mathbf{X}^T\mathbf{A_M}\mathbf{X}|\tilde{\mathbf{b}}\rangle + \langle \tilde{\mathbf{m}}'|2\mathbf{A_M}\mathbf{X} + 2\mathbf{A_{SM}}|\tilde{\mathbf{b}}\rangle\,,\end{aligned} \tag{C.10}$$

thus choosing $\mathbf{X} = -{\mathbf{A_M}}^{-1}\mathbf{A_{SM}}$:

$$\begin{aligned}\chi^2(\mathbf{m},\mathbf{b}) &= \chi^2_{\min} + \langle \tilde{\mathbf{m}}'|\mathbf{A_M}|\tilde{\mathbf{m}}'\rangle + \langle \tilde{\mathbf{b}}|\mathbf{A_S} - {\mathbf{A_{SM}}}^T{\mathbf{A_M}}^{-1}\mathbf{A_{SM}}|\tilde{\mathbf{b}}\rangle \\ &= \chi^2_{\min} + \langle \tilde{\mathbf{m}}'|\mathbf{A_M}|\tilde{\mathbf{m}}'\rangle + \langle \tilde{\mathbf{b}}|\mathbf{A'_S}|\tilde{\mathbf{b}}\rangle\,.\end{aligned} \tag{C.11}$$

Here $\mathbf{A_M} = (\mathbf{A_M})^T$, ${\mathbf{A_M}}^{-1} = ({\mathbf{A_M}}^{-1})^T$ were used.

Eq. C.11 allows interpretation of matrices $\mathbf{A_M}$ and $\mathbf{A'_S}$ in terms of uncertainties on $\tilde{\mathbf{m}}$ and $\tilde{\mathbf{b}}$. Since variation of χ^2-function of 1 corresponds to one standard deviation, diagonal elements of matrix $\mathbf{A_M}$ gives the uncertainty on $\tilde{\mathbf{m}}'$ and therefore the uncorrelated uncertainty on $\mathbf{m_0}$:

$$\delta^{\text{uncor}} m_{0i} = ([\mathbf{A_M}]_{ii})^{-1/2} = \left(\sum_{e=1}^{N_e} \frac{1}{\sigma_i^{e\,2}}\right)^{-1/2} \tag{C.12}$$

and diagonal elements of matrix $\mathbf{A'_S}$ gives the uncertainties on the fitted values of the nuisance parameter $\mathbf{b_0}$:

$$\delta b_{0i} = ([\mathbf{A'_S}]_{ii})^{-1/2}\,, \tag{C.13}$$

which are also referred to as the *reduction factors* of correlated uncertainties. Propagating them to $|\tilde{\mathbf{m}}\rangle = |\tilde{\mathbf{m}}'\rangle + \mathbf{X}\,|\tilde{\mathbf{b}}\rangle$ gives the correlated uncertainties on $\mathbf{m_0}$:

$$\delta^{\text{cor }j} m_{0i} = \left([-{\mathbf{A_M}}^{-1}\mathbf{A_{SM}}\mathbf{A'_S}]_{ij}\right)^{-1/2},\quad 1 \le i \le N_m,\quad 1 \le j \le N_s. \tag{C.14}$$

In Eq. C.11 variables $\tilde{\mathbf{b}}$ are still mixed because of the non-diagonal structure of matrix $\mathbf{A'_S}$, so the correlated uncertainties $\delta^{\text{cor }j} m_{0i}$ are not independent. It is possible to decompose them,

diagonilising this matrix

$$\mathbf{U}\mathbf{A}'_{\mathbf{S}}\mathbf{U}^{-1} = \mathbf{D}\mathbf{D} \tag{C.15}$$

and introducing new independent (diagonalised) correlated error sources, $\tilde{b}'$:

$$\tilde{\mathbf{b}}' = \mathbf{D}\mathbf{U}\tilde{\mathbf{b}}. \tag{C.16}$$

Here $\mathbf{U}$ is an orthogonal matrix, composed of the eigenvectors of $\mathbf{A}'_{\mathbf{S}}$, and $\mathbf{D}$ is a diagonal matrix, composed of the corresponding square roots of eigenvalues. Using C.15 and C.16, χ^2-function from Eq. C.11 can be written as:

$$\chi^2(\mathbf{m}, \mathbf{b}) = \chi^2_{\min} + \langle \tilde{\mathbf{m}}' | \mathbf{A}_{\mathbf{M}} | \tilde{\mathbf{m}}' \rangle + \langle \tilde{\mathbf{b}}' | \mathbf{I} | \tilde{\mathbf{b}}' \rangle \,, \tag{C.17}$$

where $\mathbf{I}$ is the unit matrix. Thus diagonalised correlated uncertainty sources are independent variables distributed according to the unit Gaussian distribution around zero. Propagating them to $\mathbf{m} = \mathbf{m}' + \mathbf{X}\tilde{\mathbf{b}}$ gives the correlated uncertainties on $\mathbf{m_0}$:

$$\delta^{\text{cor }j} m_{0i} = \left([-\mathbf{A_M}^{-1} \mathbf{A_{SM}} \mathbf{D}^{-1} \mathbf{U}^{-1}]_{ij} \right)^{-1/2}, \quad 1 \le i \le N_m, \quad 1 \le j \le N_s. \tag{C.18}$$

Summarising results of C.12 and C.18, averaged quantities can be written as:

$$m_i = m_{0i} + \delta^{\text{uncor}} m_{0i} a_i - \sum_{j=1}^{N_s} \delta^{\text{cor }j} m_{0i} b_j, \quad 1 \le i \le N_m \tag{C.19}$$

with a_i and b_j being independently distributed according to the unit Gaussian distribution around zero.

C.2 Iterative procedure

If some of the uncertainties are treated multiplicatively, the extremum conditions C.3 do not produce a system of linear equations, since $\Gamma_i^{e,j}$ are functions of unknown $\mathbf{m_0}$. In this case the averaging technique described in Section C.1 still can be used, but the average has to be found in an iterative procedure [240, 241]: first equation 6.10 is used to get an initial approximation for $\mathbf{m_0}$ and $\mathbf{b_0}$ which are used to recalculate the uncertainties as $\Gamma_i^{e,j} = \gamma_i^{e,j} m_{0i}$ and $\sigma_i^{e2} = \delta^e_{i,stat}{}^2 m_{0i}{}^2 + \delta^e_{i,uncor}{}^2 m_{0i}{}^2$. Then the determination of m_{0i} is repeated. Typically convergence is observed after two iterations and the iteration procedure is terminated.

Note that this iterative procedure does not give the exact minimum of the χ^2-function 6.14. Although there are arguments [216, 219] that the exact minimum of 6.14 is biased, while the iterative procedure described above gives an unbiased result.

APPENDIX D

Combination of visible D^{*+} cross sections: additional information

In this Appendix additional information on the combination of the visible D^{*+} cross sections (see Section 6.4) is provided.

Table D.1 gives information on the high-Q^2 swimming correction of the H1 HERA-II data (see Section 6.4.1.1).

Figs. D.1 to D.26 and Tables D.2 to D.4 summarise information on the swimming for the combination of double-differential D^{*+} cross sections (see Section 6.4.2.1).

Tables D.5 to D.12 present input data tables used for the combination.

Table D.13 provides information on the fitted nuisance parameters.

The combined data with all correlations are provided in Tables D.14 to D.16.

Figs. D.27 to D.31 show comparison of the combined data to the individual theoretical variations (see Section 6.4.1.4).

Fig. D.32 shows comparison of the combined data to the theoretical variations obtained with different PDFs (see Section 6.3).

$\mathrm{d}\sigma/\mathrm{d}p_T(D^{*+})$															
$p_T(D^{*+})$	C	δ^+_{mc}	δ^-_{mc}	δ^+_{mu}	δ^-_{mu}	δ^+_{as}	δ^-_{as}	δ^+_{ak}	δ^-_{ak}	δ^+_{bn}	δ^-_{bn}	δ^+_{kt}	δ^-_{kt}	δ^+_{tot}	δ^-_{tot}
[GeV]	[%]	[%]	[%]	[%]	[%]	[%]	[%]	[%]	[%]	[%]	[%]	[%]	[%]	[%]	[%]
1.50 : 1.88	1.0	−2.0	2.9	−2.1	4.6	0.3	0.4	−4.2	5.5	−1.5	3.7	−0.6	0.1	8.6	−5.3
1.88 : 2.28	1.2	−2.0	1.2	−2.8	5.0	0.1	−0.5	−4.2	5.5	−1.8	3.9	−0.3	0.2	8.5	−5.7
2.28 : 2.68	1.3	0.3	−0.1	−2.8	5.9	0.2	−0.5	−4.1	5.1	−2.8	5.0	0.1	0.3	9.3	−5.8
2.68 : 3.08	1.9	0.8	−0.6	−3.2	6.9	0.6	0.1	−3.7	5.3	−2.7	5.3	0.9	0.2	10.3	−5.6
3.08 : 3.50	2.3	1.1	−1.6	−3.2	6.2	−0.2	0.0	−4.2	4.8	−3.3	5.9	−0.1	−0.7	9.9	−6.5
3.50 : 4.00	3.2	1.0	−0.9	−2.6	5.0	0.4	0.0	−3.9	5.1	−3.4	6.1	0.1	0.2	9.4	−5.9
4.00 : 4.75	4.5	1.0	−1.9	−2.4	3.2	0.1	−0.3	−3.7	3.3	−3.2	5.0	−0.3	−0.2	6.9	−5.8
4.75 : 6.00	9.1	0.7	−0.4	0.1	1.1	−0.0	0.1	−1.8	2.1	−2.2	2.5	−0.3	0.1	3.5	−3.1
6.00 : 8.00	21.8	−0.3	0.4	2.1	−3.5	−0.1	0.1	1.5	−2.3	0.9	−3.3	−0.1	0.1	2.8	−5.3
8.00 : 11.00	37.8	−1.0	0.8	2.6	−5.3	−0.2	−0.0	5.0	−6.0	4.7	−7.2	0.2	−0.2	7.4	−10.8
11.00 : 20.00	54.0	0.4	0.1	1.7	−5.0	−0.2	0.3	7.3	−7.5	4.7	−4.6	0.7	−0.1	8.8	−10.1

$\mathrm{d}\sigma/\mathrm{d}\eta(D^{*+})$															
$\eta(D^{*+})$	C	δ^+_{mc}	δ^-_{mc}	δ^+_{mu}	δ^-_{mu}	δ^+_{as}	δ^-_{as}	δ^+_{ak}	δ^-_{ak}	δ^+_{bn}	δ^-_{bn}	δ^+_{kt}	δ^-_{kt}	δ^+_{tot}	δ^-_{tot}
	[%]	[%]	[%]	[%]	[%]	[%]	[%]	[%]	[%]	[%]	[%]	[%]	[%]	[%]	[%]
−1.50 : −1.25	2.5	−0.8	1.0	5.8	−7.3	−0.7	0.2	0.2	−0.5	−0.0	−0.2	−0.8	0.6	5.9	−7.4
−1.25 : −1.00	3.4	−0.4	0.3	4.6	−4.9	−0.1	0.5	0.0	−0.1	−0.1	−0.1	−0.7	0.1	4.7	−4.9
−1.00 : −0.75	3.8	−0.2	0.5	3.8	−3.8	0.1	0.7	0.0	0.2	−0.1	0.0	−0.0	0.4	3.9	−3.9
−0.75 : −0.50	4.2	−0.2	0.3	2.7	−3.0	−0.1	0.1	0.0	−0.2	−0.2	−0.1	−0.2	−0.0	2.8	−3.0
−0.50 : −0.25	4.9	−0.2	0.2	1.8	−1.9	−0.2	0.1	−0.0	0.1	−0.0	−0.3	−0.2	0.2	1.8	−1.9
−0.25 : 0.00	5.1	−0.3	0.1	0.9	−1.2	−0.1	−0.1	0.0	−0.2	−0.0	−0.2	−0.2	0.0	0.9	−1.3
0.00 : 0.25	5.1	−0.2	0.1	0.2	−0.2	0.1	0.1	−0.1	0.1	0.1	−0.2	0.0	0.1	0.3	−0.4
0.25 : 0.50	5.2	0.1	0.1	−0.8	1.1	0.0	0.1	−0.0	−0.0	0.1	0.0	0.2	0.1	1.1	−0.8
0.50 : 0.75	4.9	0.2	0.0	−1.5	1.8	0.2	−0.2	0.1	0.1	0.1	−0.0	0.2	0.1	1.8	−1.5
0.75 : 1.00	4.8	0.1	−0.5	−2.7	2.8	0.1	−0.1	0.1	0.2	0.1	0.2	0.1	−0.3	2.8	−2.8
1.00 : 1.25	3.9	0.4	−0.6	−3.3	3.4	0.1	−0.3	−0.3	−0.1	−0.1	0.3	0.1	−0.4	3.4	−3.4
1.25 : 1.50	4.3	0.7	−0.6	−4.5	5.0	0.2	−0.5	0.1	0.2	−0.0	0.3	0.8	−0.3	5.2	−4.6

$\mathrm{d}\sigma/\mathrm{d}z(D^{*+})$															
$z(D^{*+})$	C	δ^+_{mc}	δ^-_{mc}	δ^+_{mu}	δ^-_{mu}	δ^+_{as}	δ^-_{as}	δ^+_{ak}	δ^-_{ak}	δ^+_{bn}	δ^-_{bn}	δ^+_{kt}	δ^-_{kt}	δ^+_{tot}	δ^-_{tot}
	[%]	[%]	[%]	[%]	[%]	[%]	[%]	[%]	[%]	[%]	[%]	[%]	[%]	[%]	[%]
0.000 : 0.100	5.2	−2.9	2.5	−1.0	2.7	0.4	−0.1	−1.0	1.6	1.0	0.1	1.2	−0.7	4.4	−3.3
0.100 : 0.200	3.7	1.8	−1.6	−2.7	5.3	0.4	−0.3	−2.5	3.4	−1.2	1.7	0.2	−0.1	6.7	−4.2
0.200 : 0.325	3.1	2.0	−2.0	−4.6	8.2	0.3	−0.3	−4.2	5.2	−3.3	5.8	−0.1	0.0	11.5	−7.3
0.325 : 0.450	3.6	1.9	−1.9	−3.9	6.5	0.1	−0.3	−4.3	4.7	−4.2	7.0	−0.1	0.1	10.8	−7.4
0.450 : 0.575	4.0	1.0	−1.1	−1.2	1.7	−0.0	0.1	−1.9	1.5	−2.6	3.8	−0.2	0.1	4.6	−3.6
0.575 : 0.800	6.1	−1.4	1.3	4.1	−7.4	−0.3	0.2	4.6	−5.7	2.9	−6.3	−0.2	0.1	6.9	−11.4
0.800 : 1.000	7.0	−6.9	7.3	14.2	−24.3	−1.3	1.2	13.5	−13.6	15.2	−19.6	−0.1	0.1	25.9	−34.8

$\mathrm{d}\sigma/\mathrm{d}y$															
y	C	δ^+_{mc}	δ^-_{mc}	δ^+_{mu}	δ^-_{mu}	δ^+_{as}	δ^-_{as}	δ^+_{ak}	δ^-_{ak}	δ^+_{bn}	δ^-_{bn}	δ^+_{kt}	δ^-_{kt}	δ^+_{tot}	δ^-_{tot}
	[%]	[%]	[%]	[%]	[%]	[%]	[%]	[%]	[%]	[%]	[%]	[%]	[%]	[%]	[%]
0.02 : 0.05	0.5	−12.2	11.7	−4.8	2.5	0.5	−0.6	2.6	−3.5	2.3	−4.9	0.3	−0.1	12.4	−14.4
0.05 : 0.09	2.6	−4.4	4.0	−3.7	2.3	−0.2	−0.3	0.3	−0.4	−0.0	−0.5	−0.4	0.2	4.7	−5.8
0.09 : 0.13	3.4	−1.7	1.6	−2.4	1.7	−0.1	−0.2	−0.1	0.1	−0.2	0.1	−0.2	0.1	2.4	−2.9
0.13 : 0.18	4.0	−0.6	0.6	−1.2	0.9	0.0	0.0	−0.1	0.1	−0.2	0.0	−0.1	0.1	1.1	−1.4
0.18 : 0.26	4.2	0.1	−0.1	−0.1	0.1	−0.0	0.0	−0.1	0.1	−0.0	0.0	−0.1	0.0	0.2	−0.2
0.26 : 0.36	5.4	0.7	−0.6	0.8	−0.6	0.0	0.1	−0.1	0.1	0.0	0.1	0.0	−0.0	1.1	−0.9
0.36 : 0.50	6.6	1.1	−1.1	1.6	−1.2	−0.0	0.1	−0.0	0.1	0.0	0.1	0.1	−0.0	2.0	−1.7
0.50 : 0.70	8.1	1.9	−1.8	1.7	−0.9	0.1	0.0	0.0	−0.0	0.1	0.1	0.3	−0.2	2.5	−2.0

Table D.1: Contributions from the high-Q^2 region (C) and their uncertainties for high-Q^2 swimming for H1 HERA-II measurement (see Section 6.4.1.1 for more details).

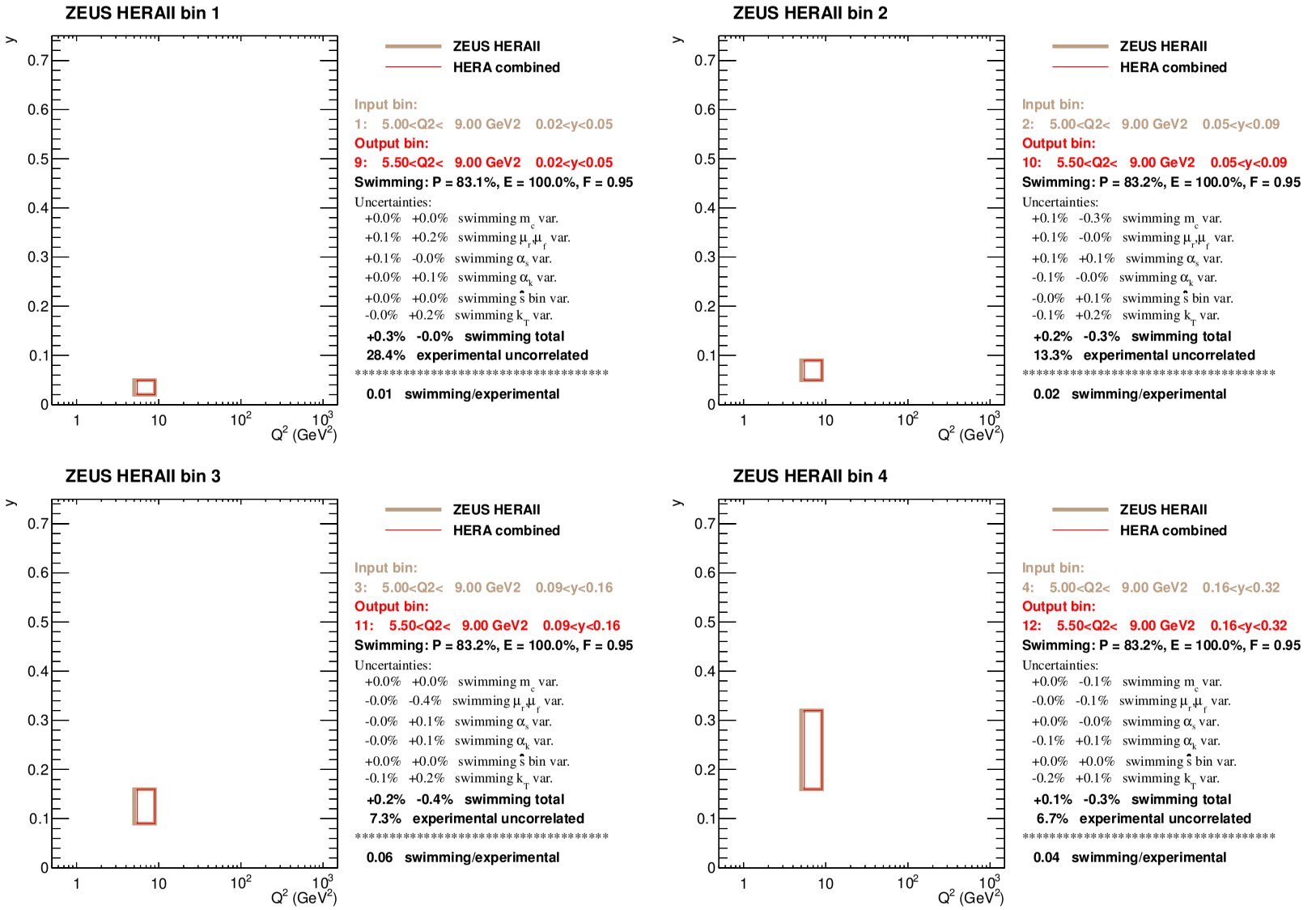

Figure D.1: Swimming corrections for the D^{*+} double-differential cross sections for datasets I–III (ZEUS HERA-II refers also to H1 HERA-II, which used the same binning scheme).

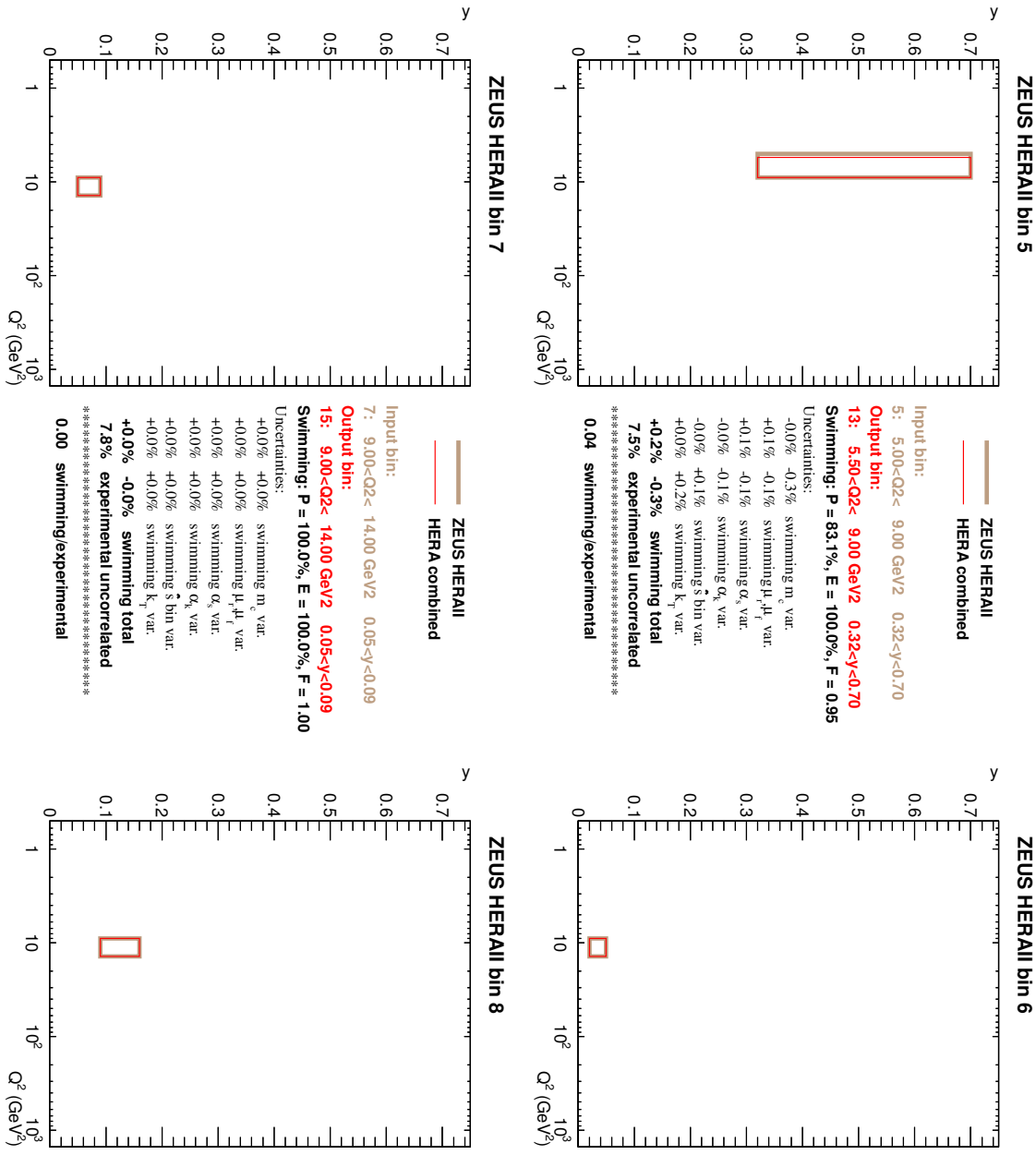

Figure D.2: The continuation of Fig. D.1.

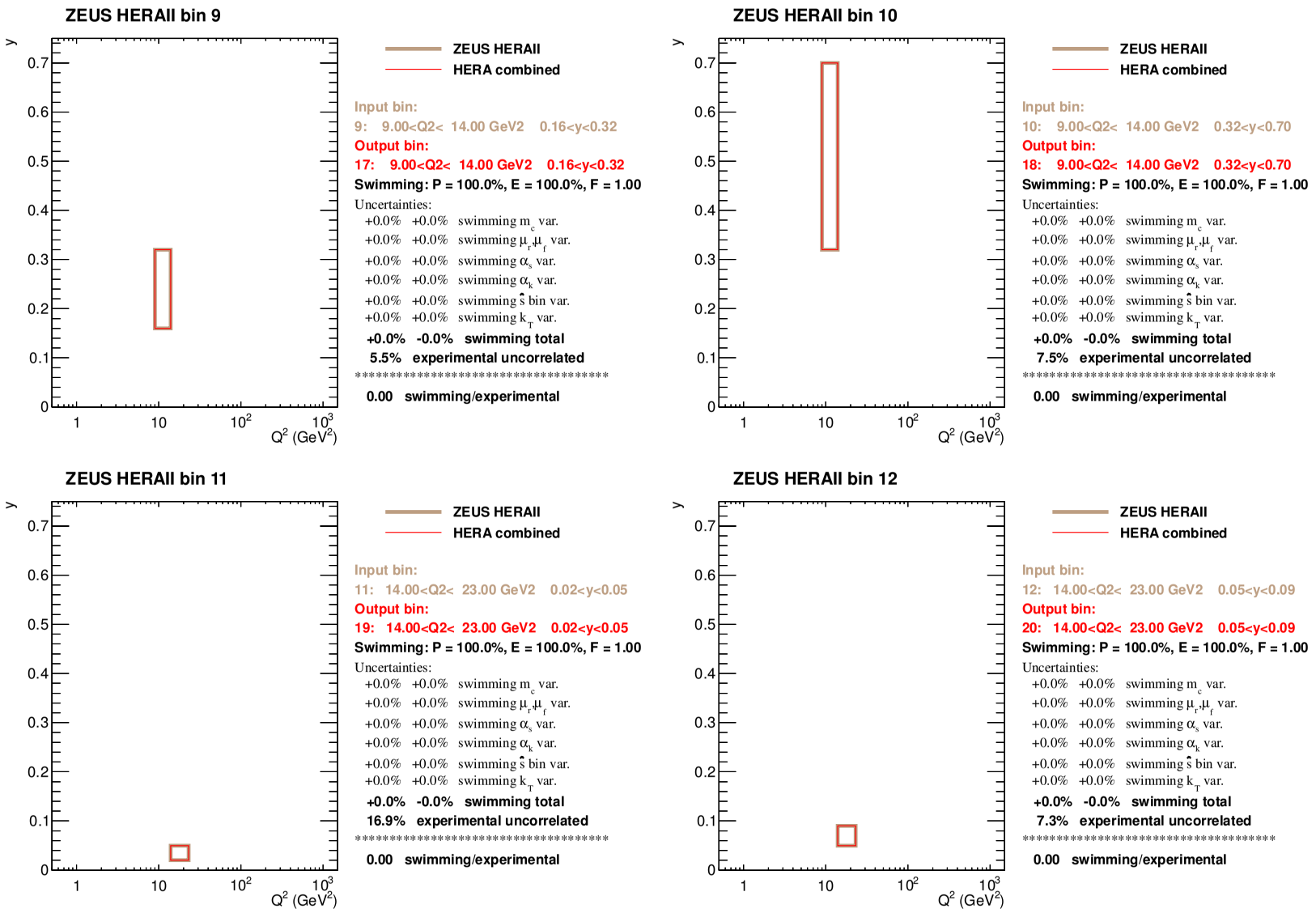

Figure D.3: The continuation of Fig. D.1.

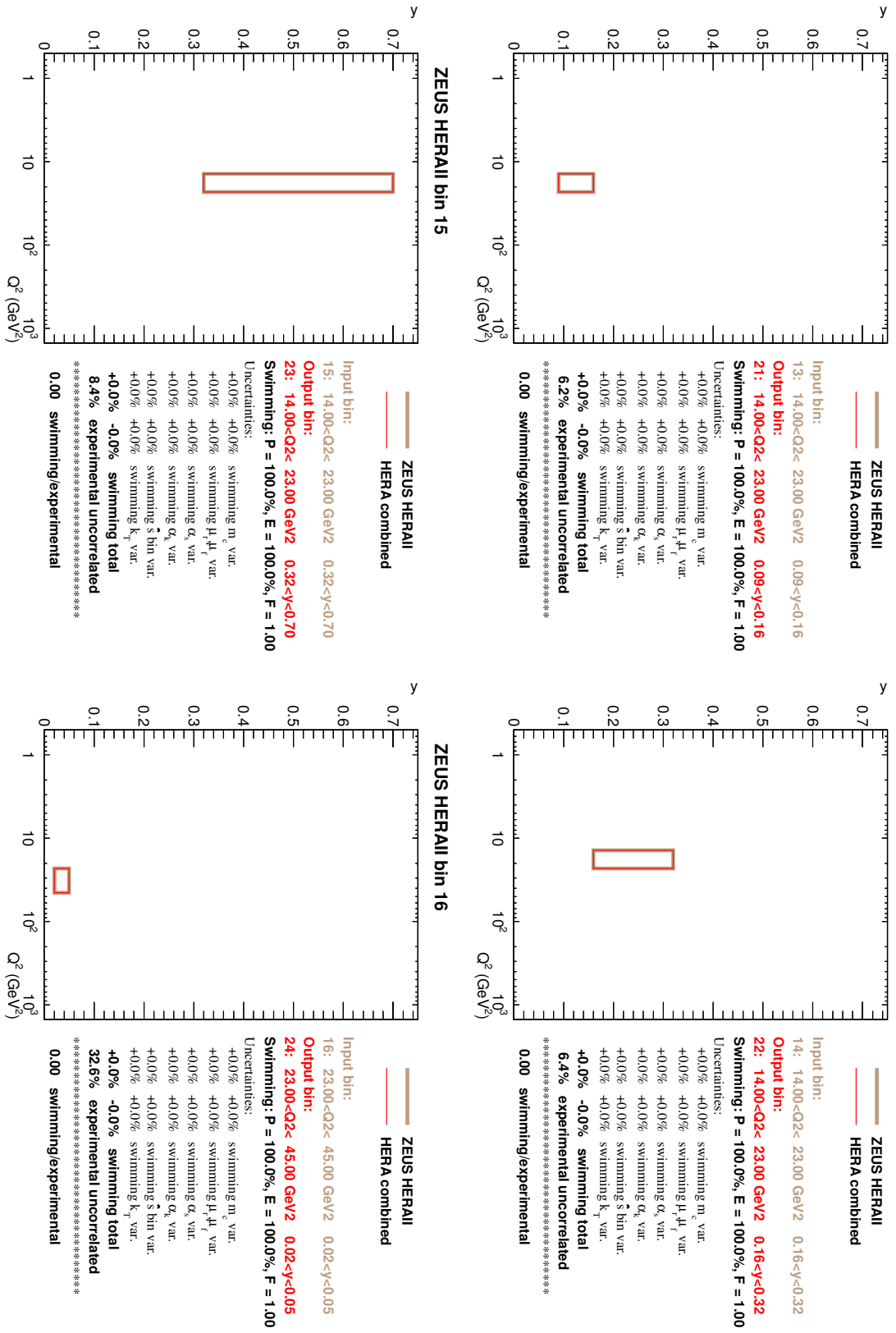

Figure D.4: The continuation of Fig. D.1.

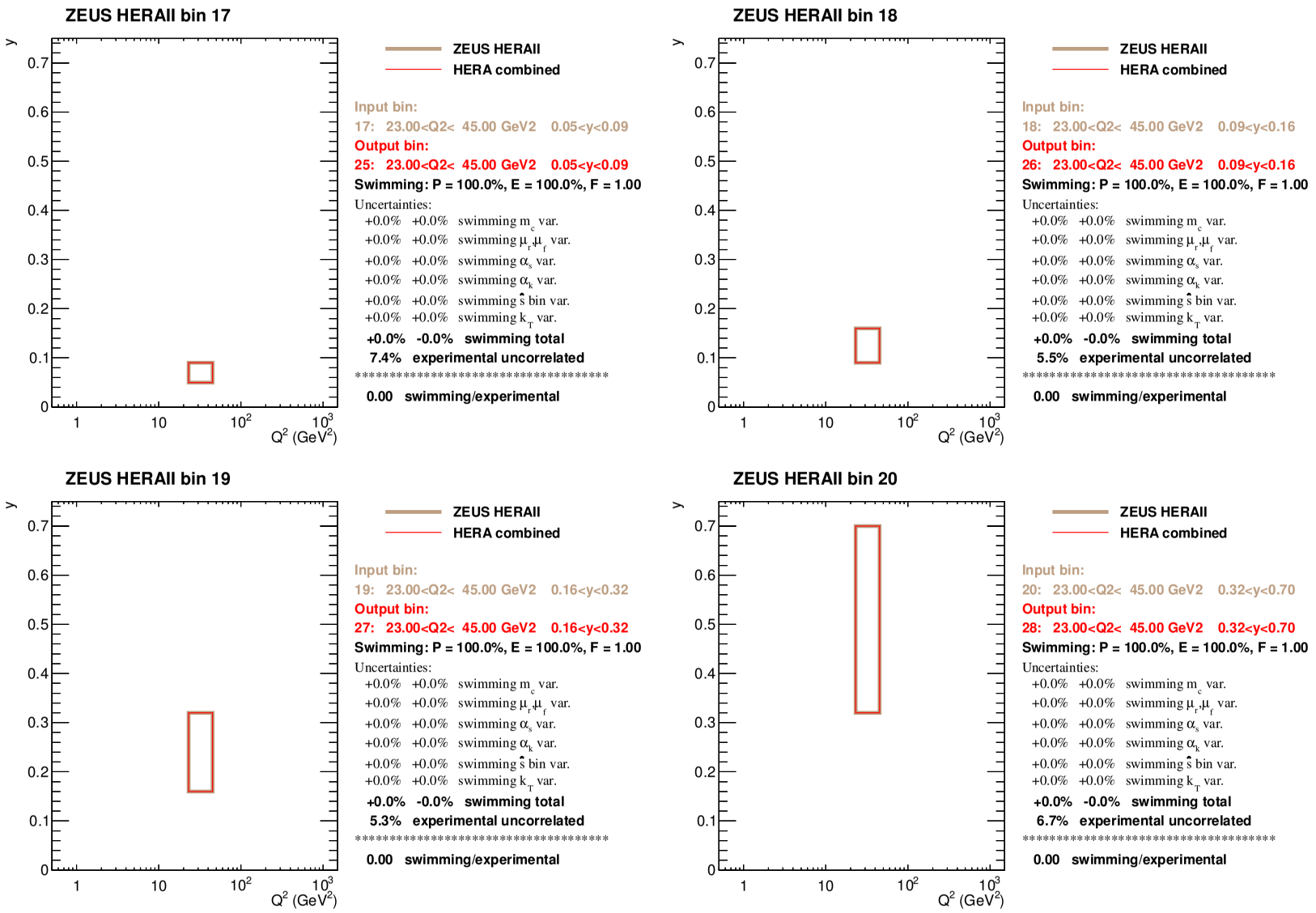

Figure D.5: The continuation of Fig. D.1.

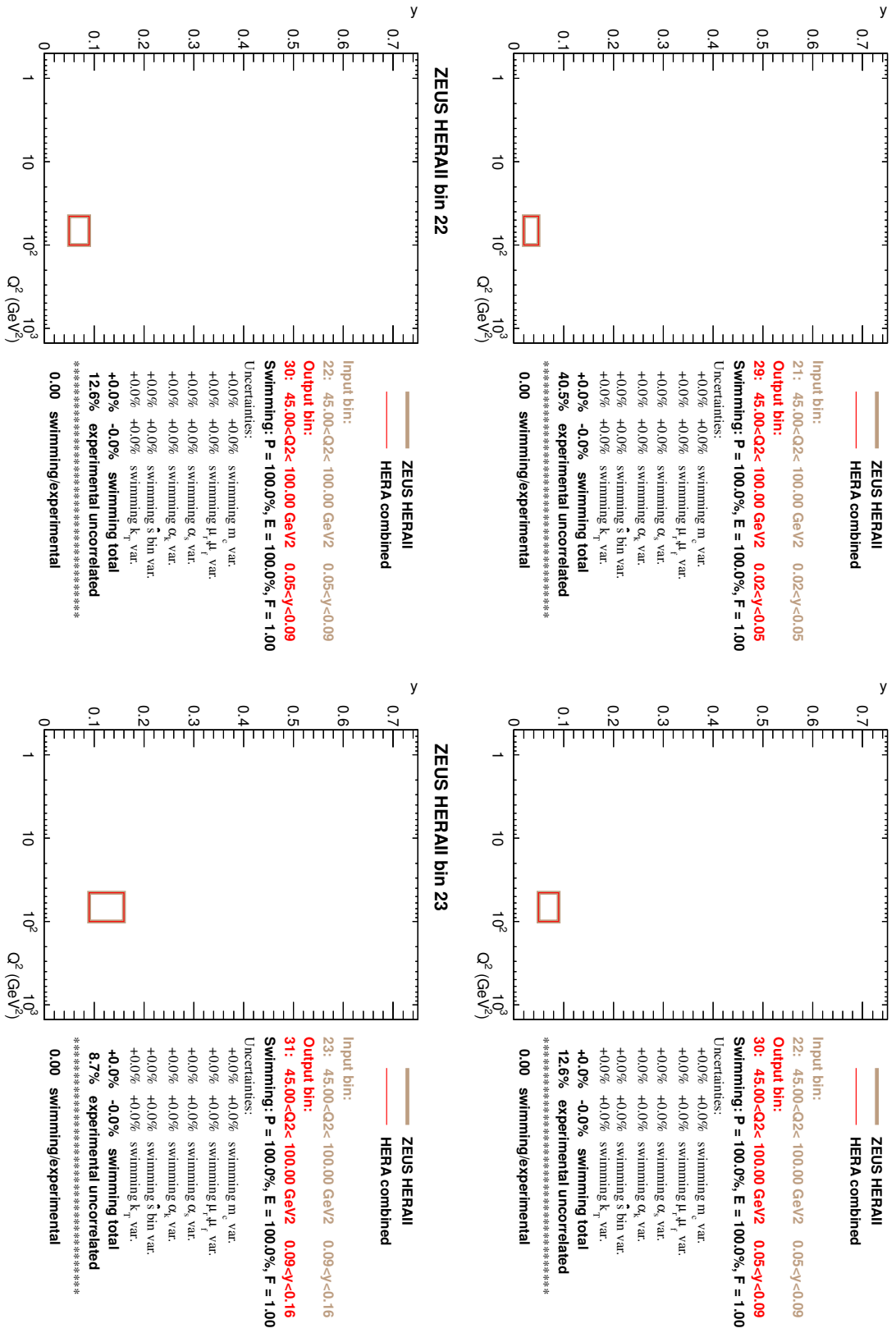

Figure D.6: The continuation of Fig. D.1.

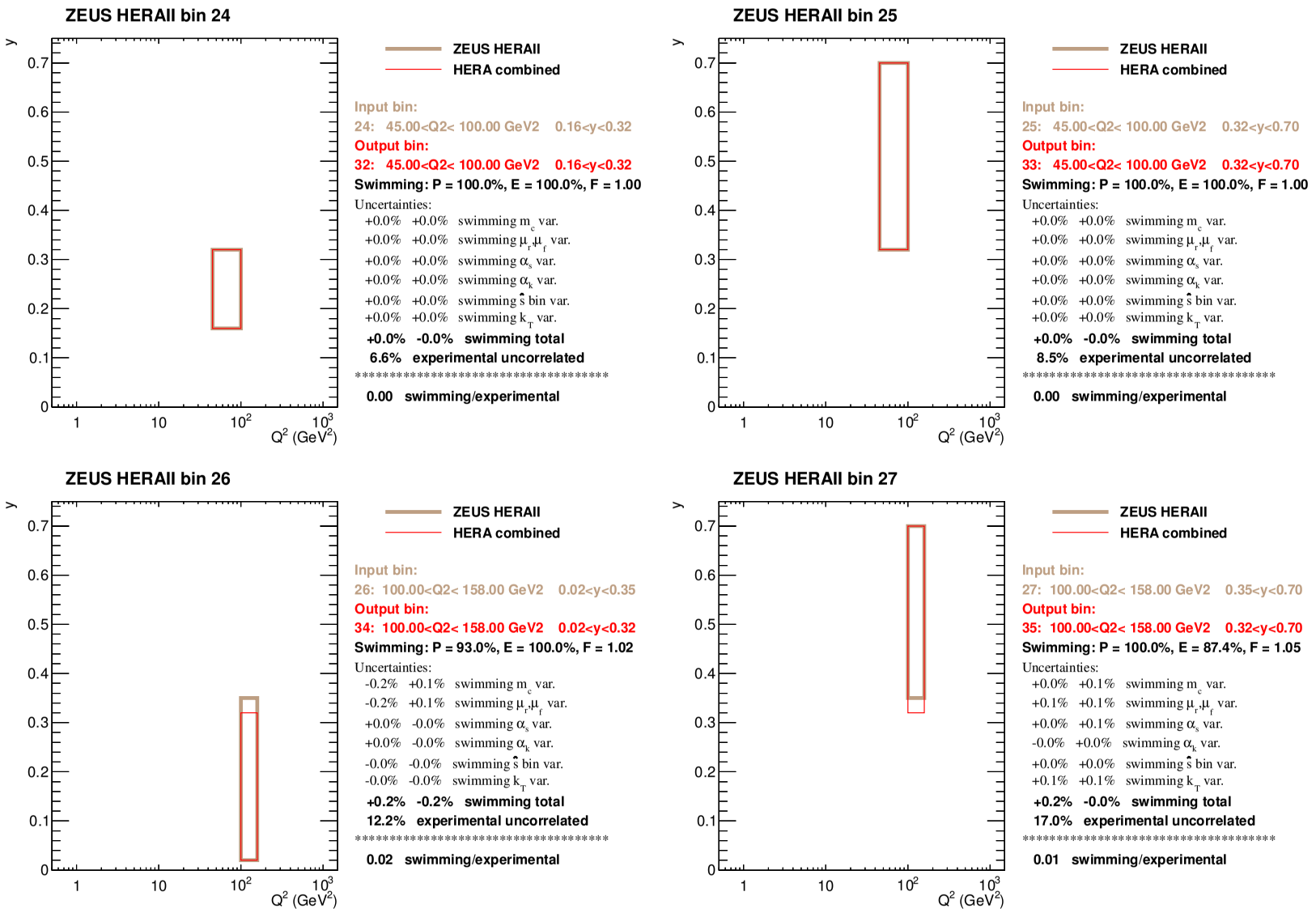

Figure D.7: The continuation of Fig. D.1.

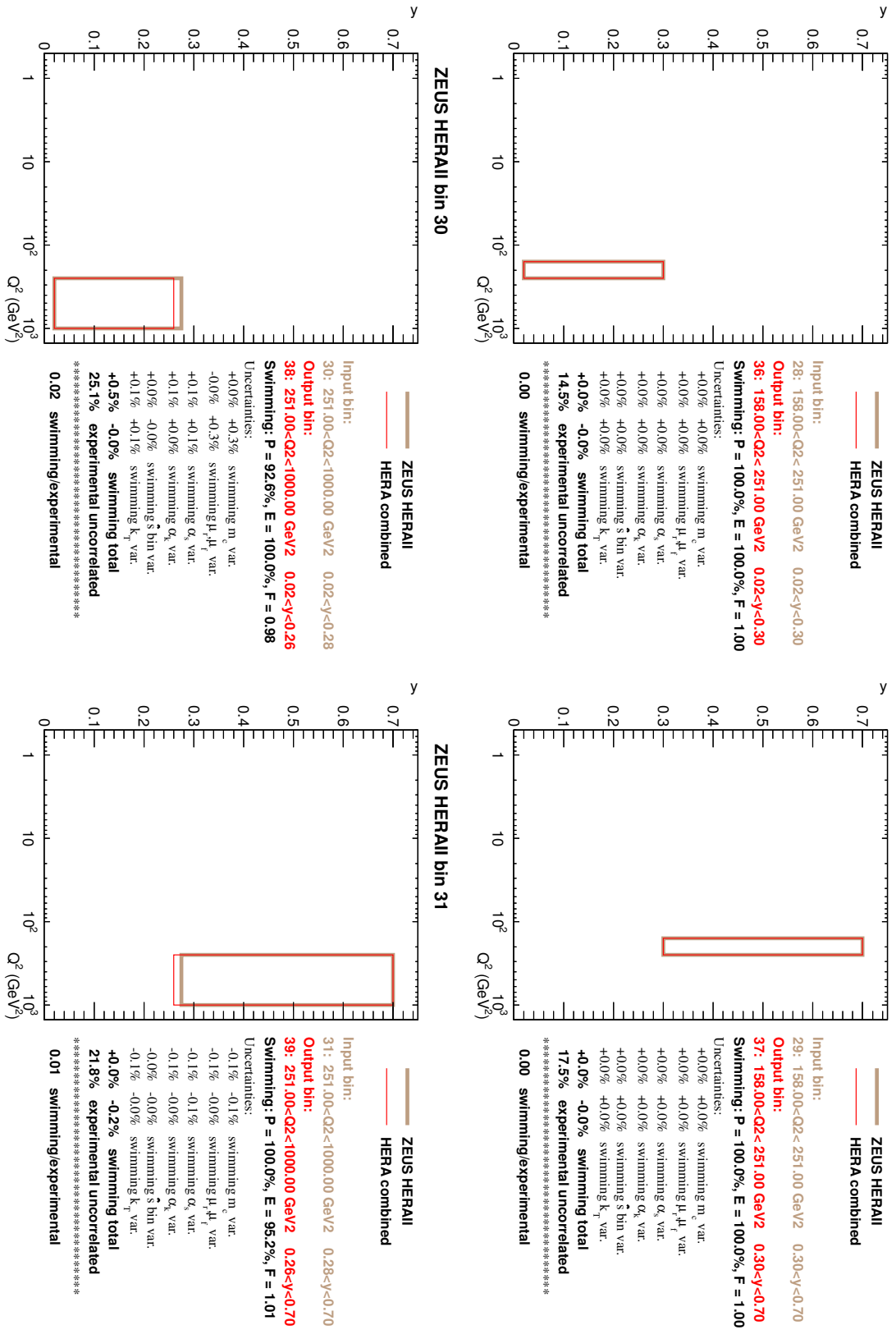

Figure D.8: The continuation of Fig. D.1.

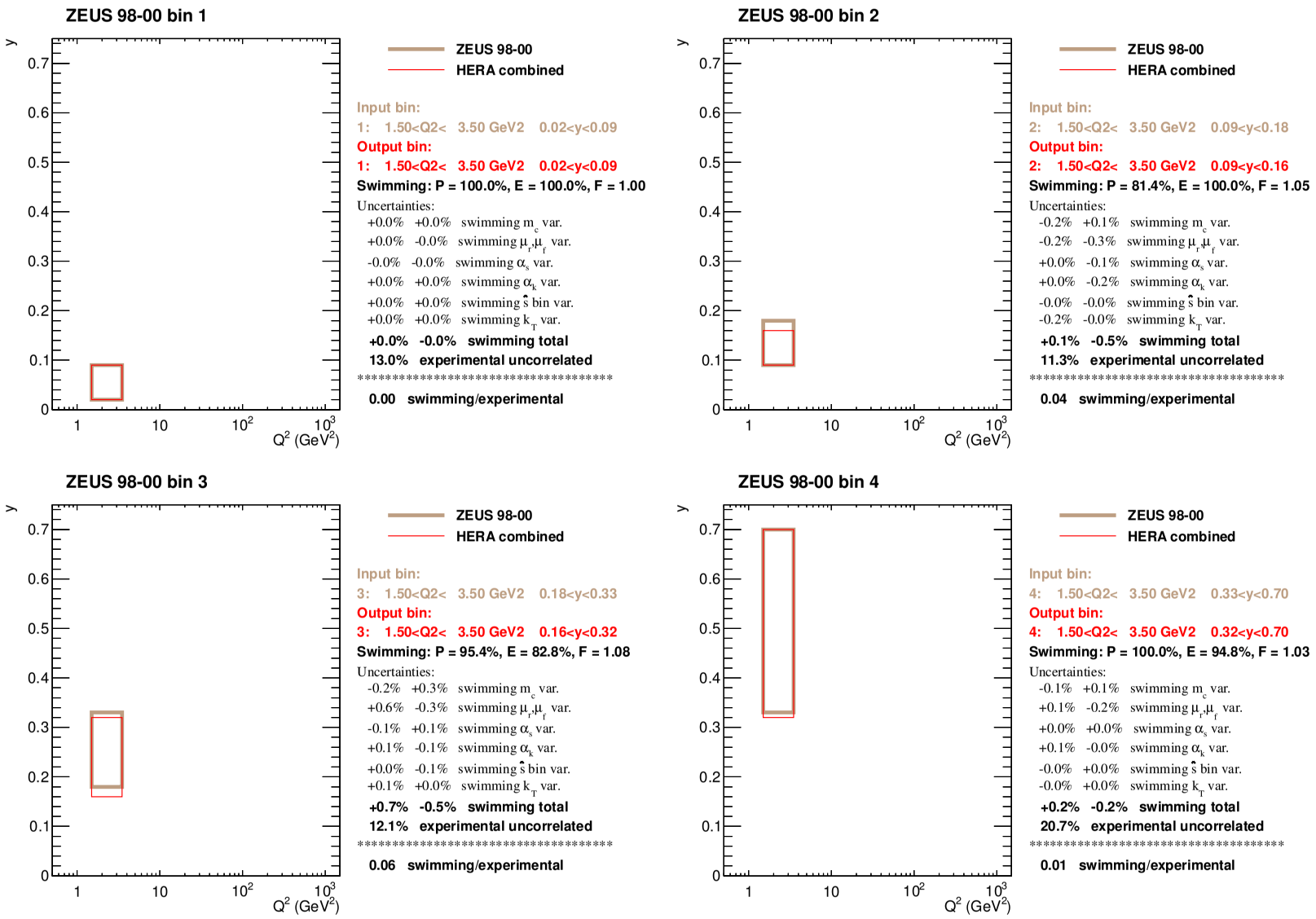

Figure D.9: Swimming corrections for the D^{*+} double-differential cross sections for dataset IV.

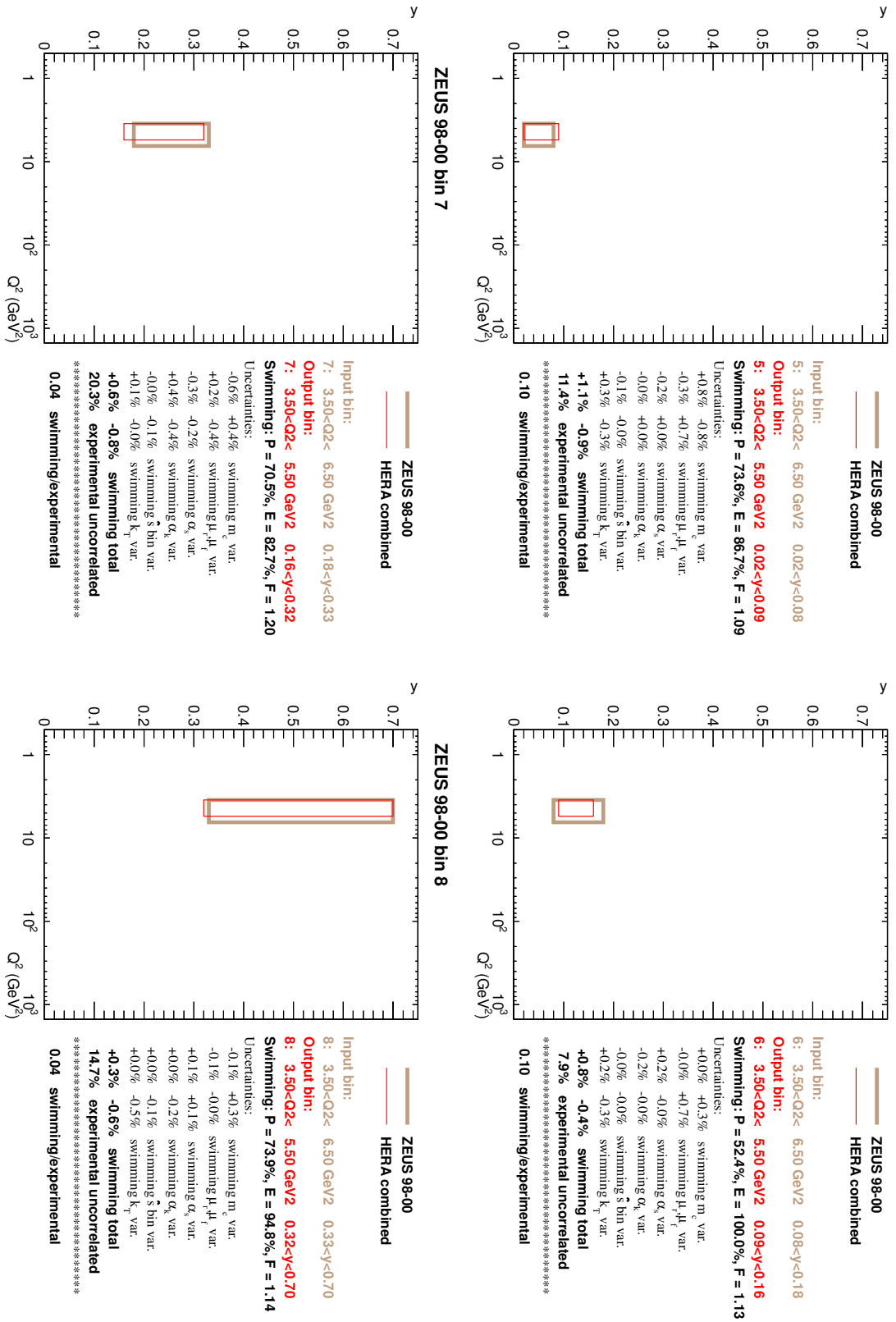

Figure D.10: The continuation of Fig. D.9.

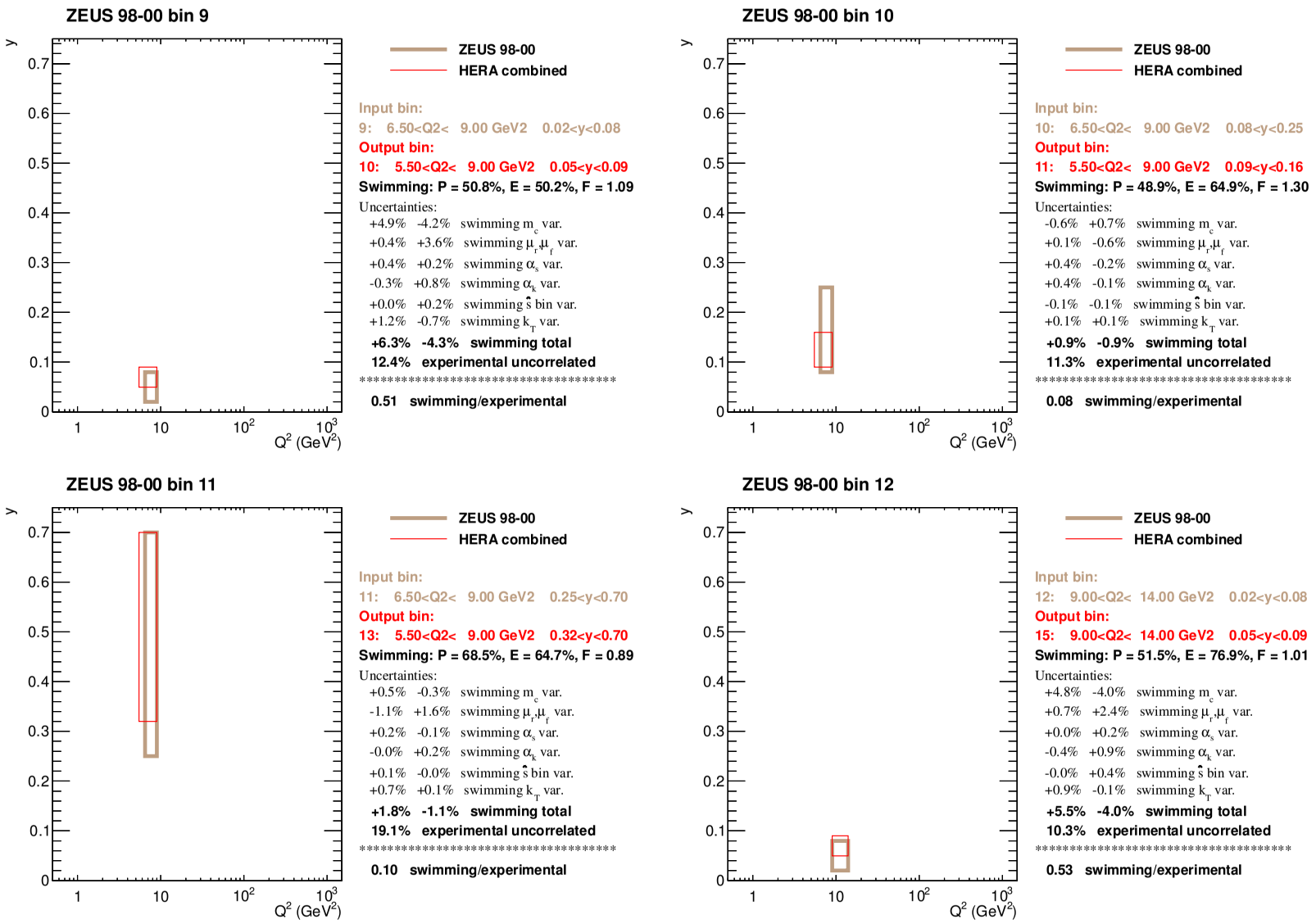

Figure D.11: The continuation of Fig. D.9.

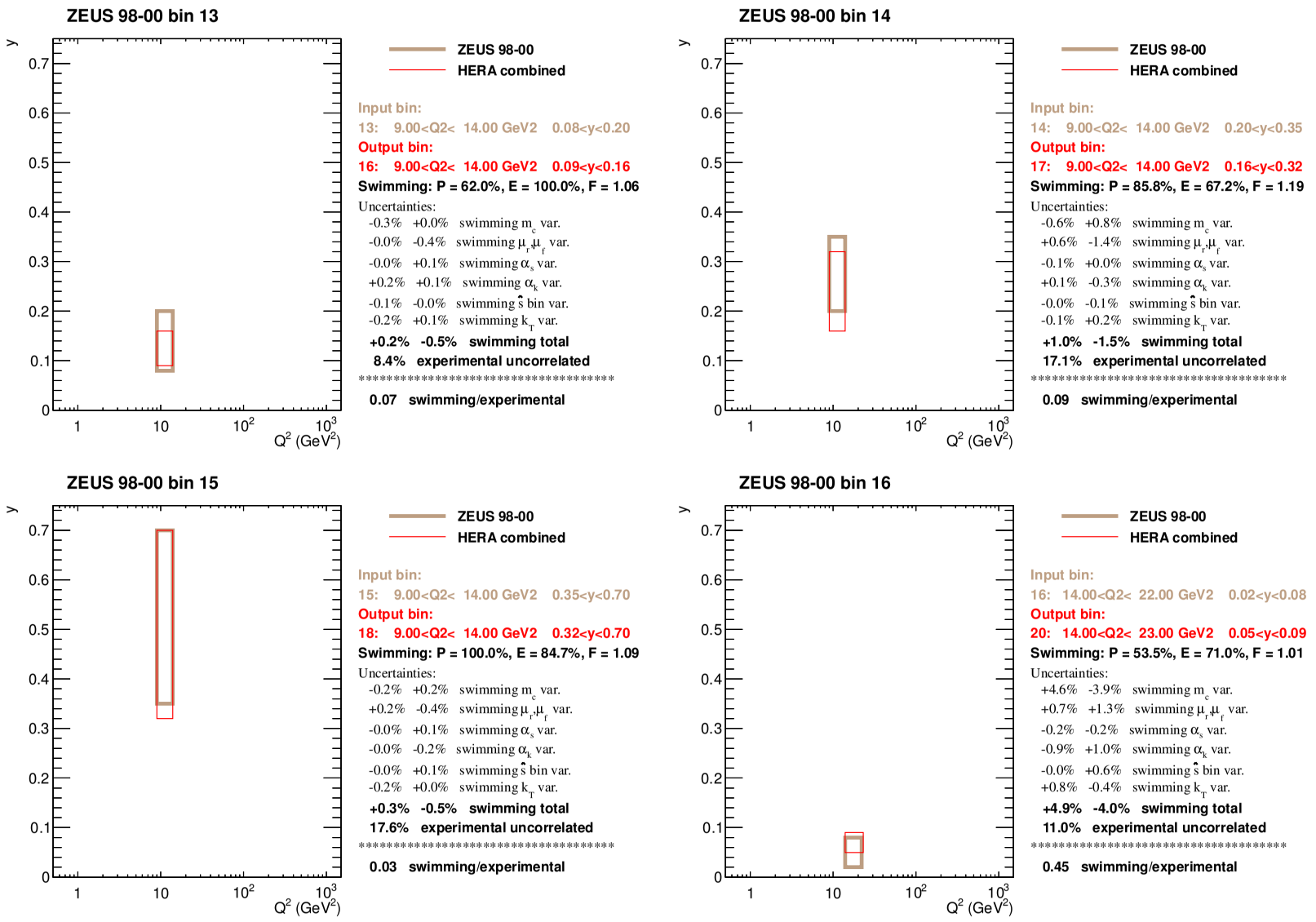

Figure D.12: The continuation of Fig. D.9.

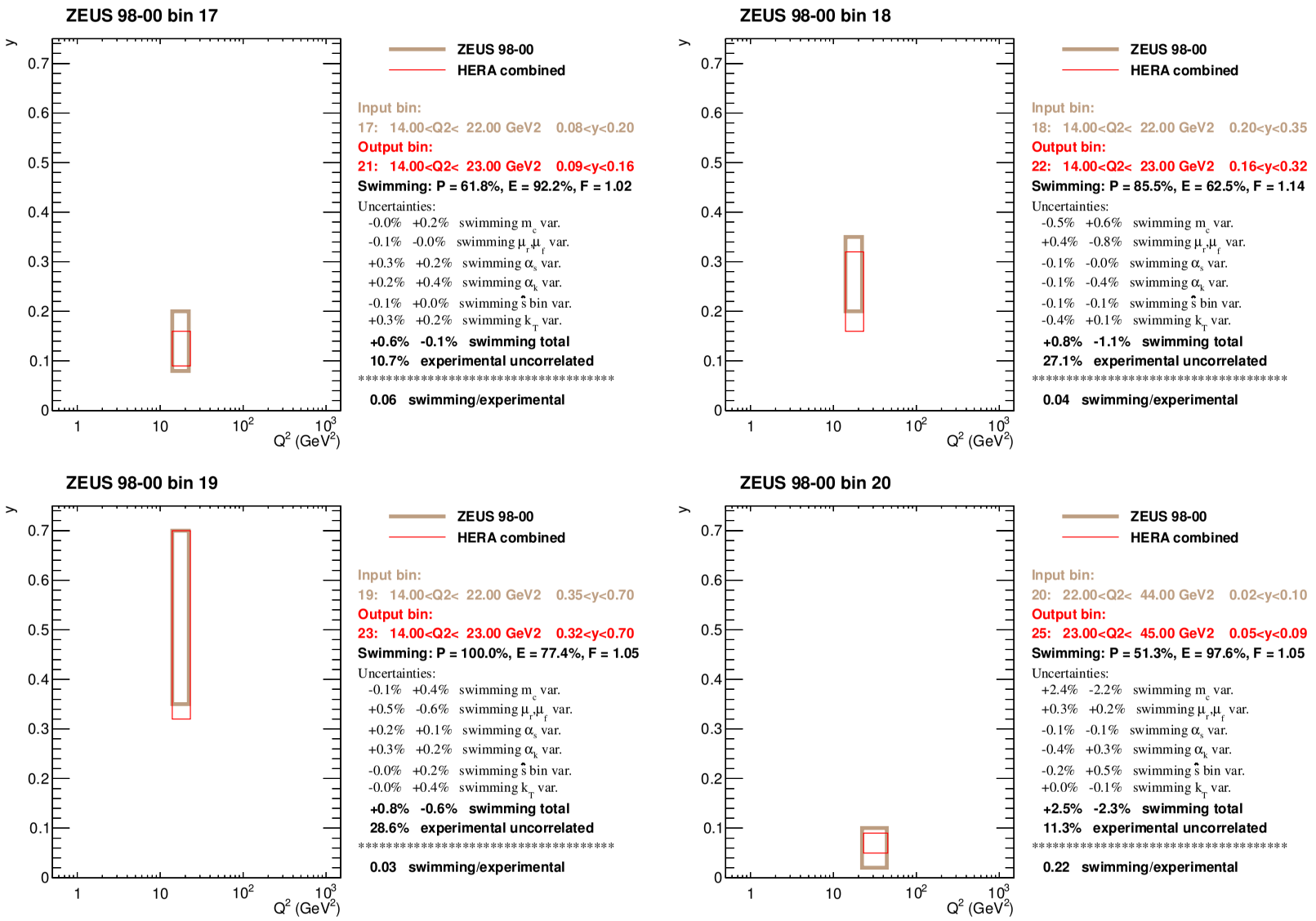

Figure D.13: The continuation of Fig. D.9.

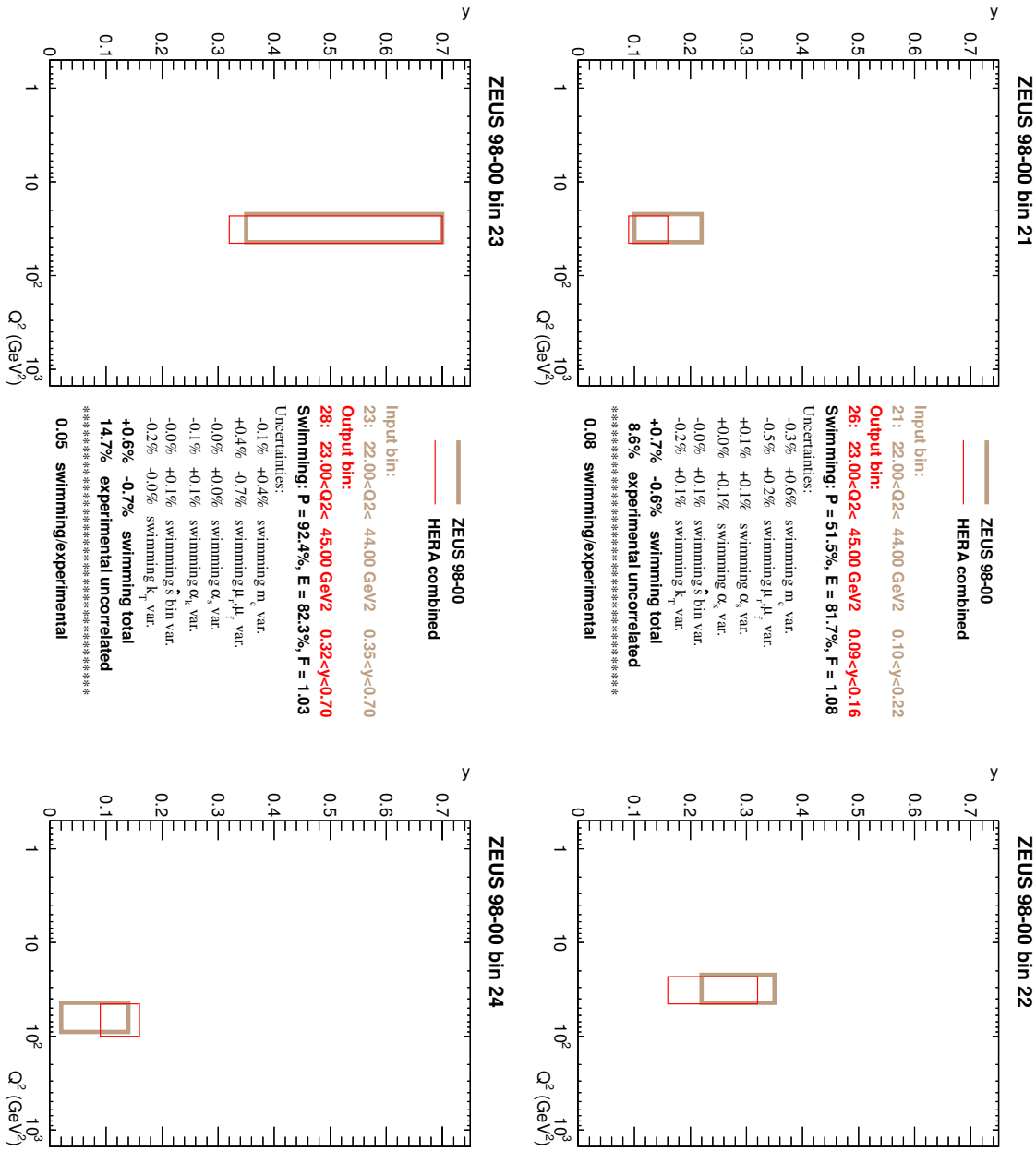

Figure D.14: The continuation of Fig. D.9.

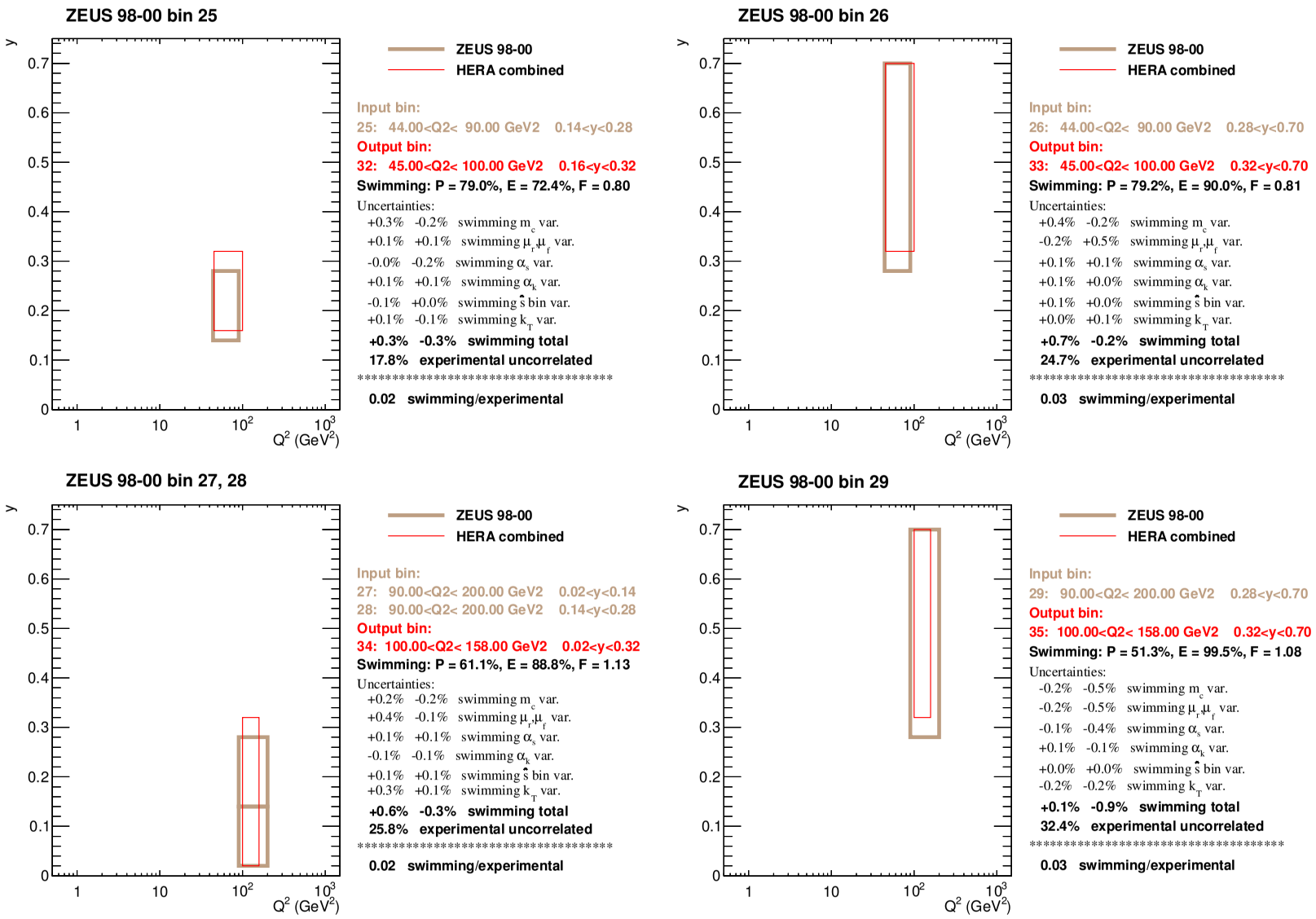

Figure D.15: The continuation of Fig. D.9.

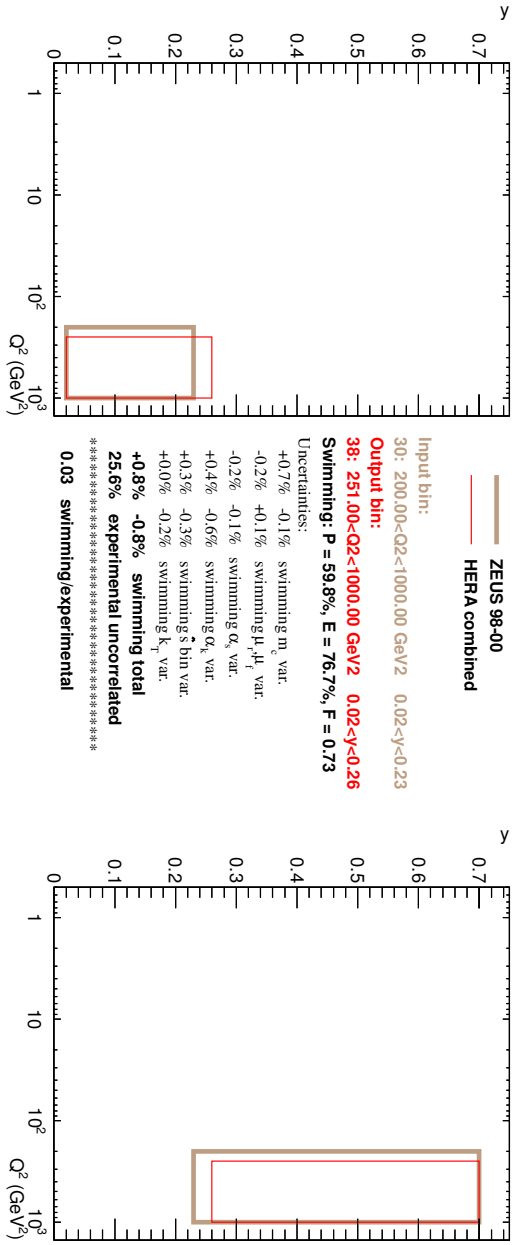

Figure D.16: The continuation of Fig. D.9.

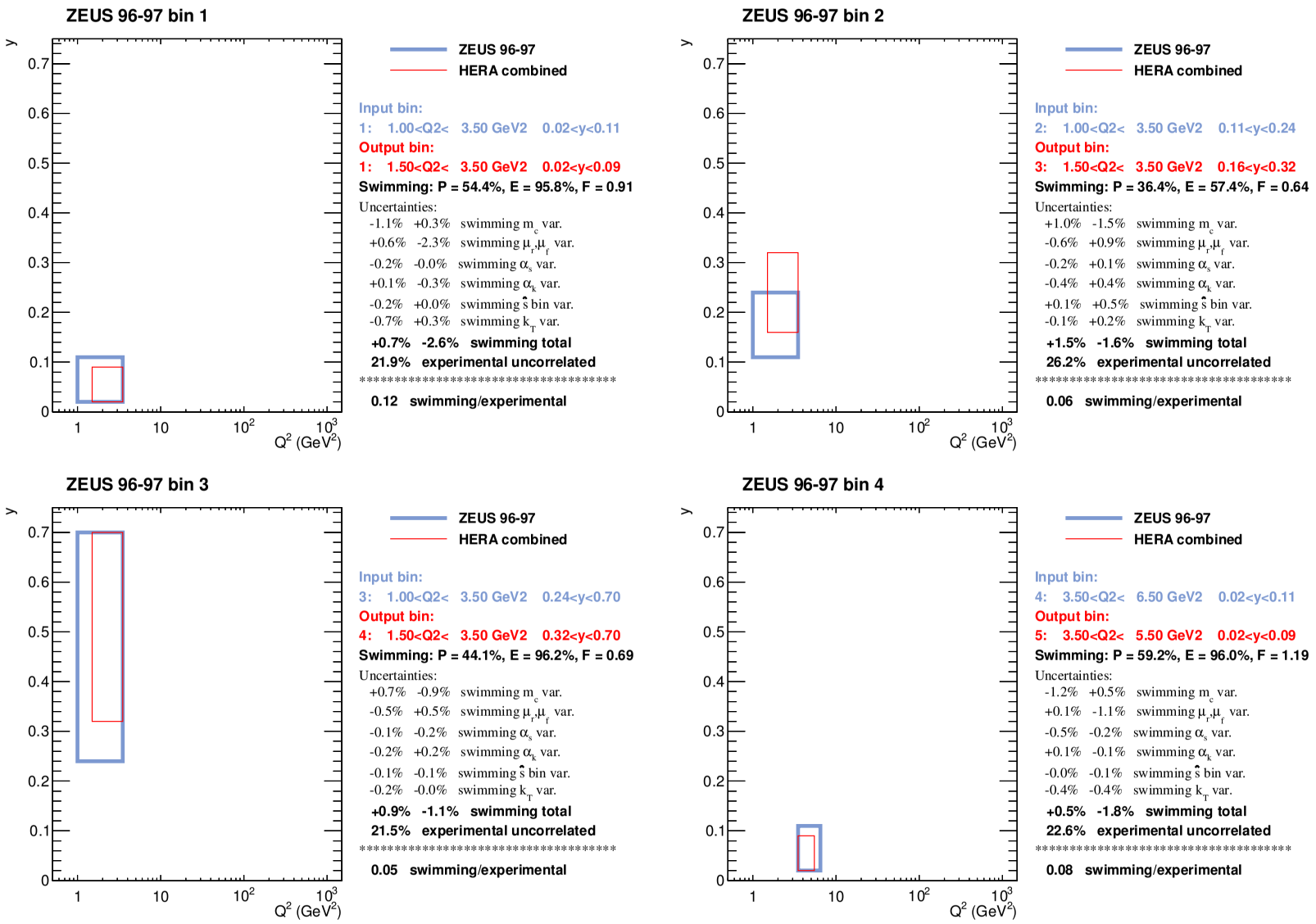

Figure D.17: Swimming corrections for D^{*+} double-differential cross sections for dataset V.

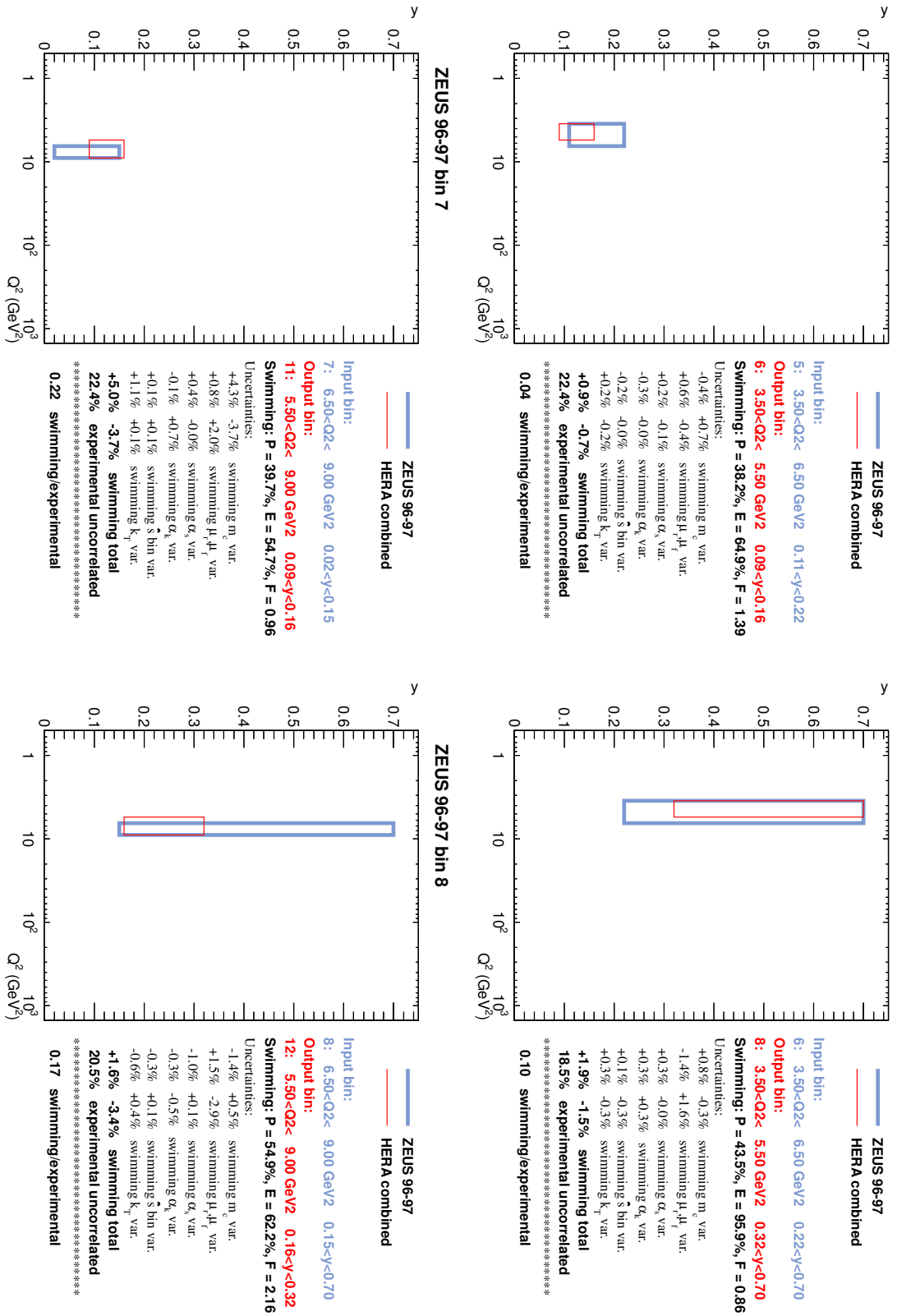

Figure D.18: The continuation of Fig. D.17.

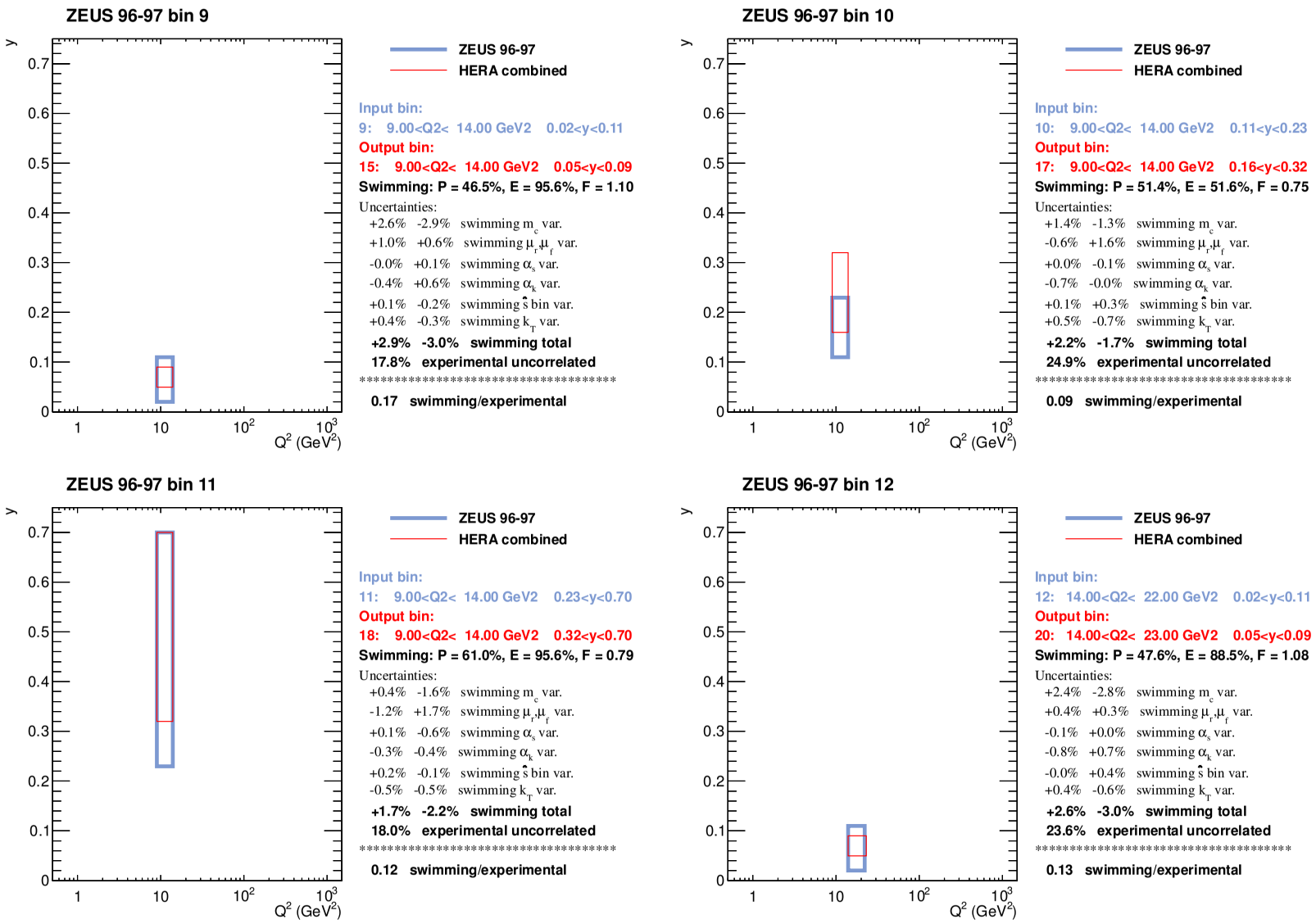

Figure D.19: The continuation of Fig. D.17.

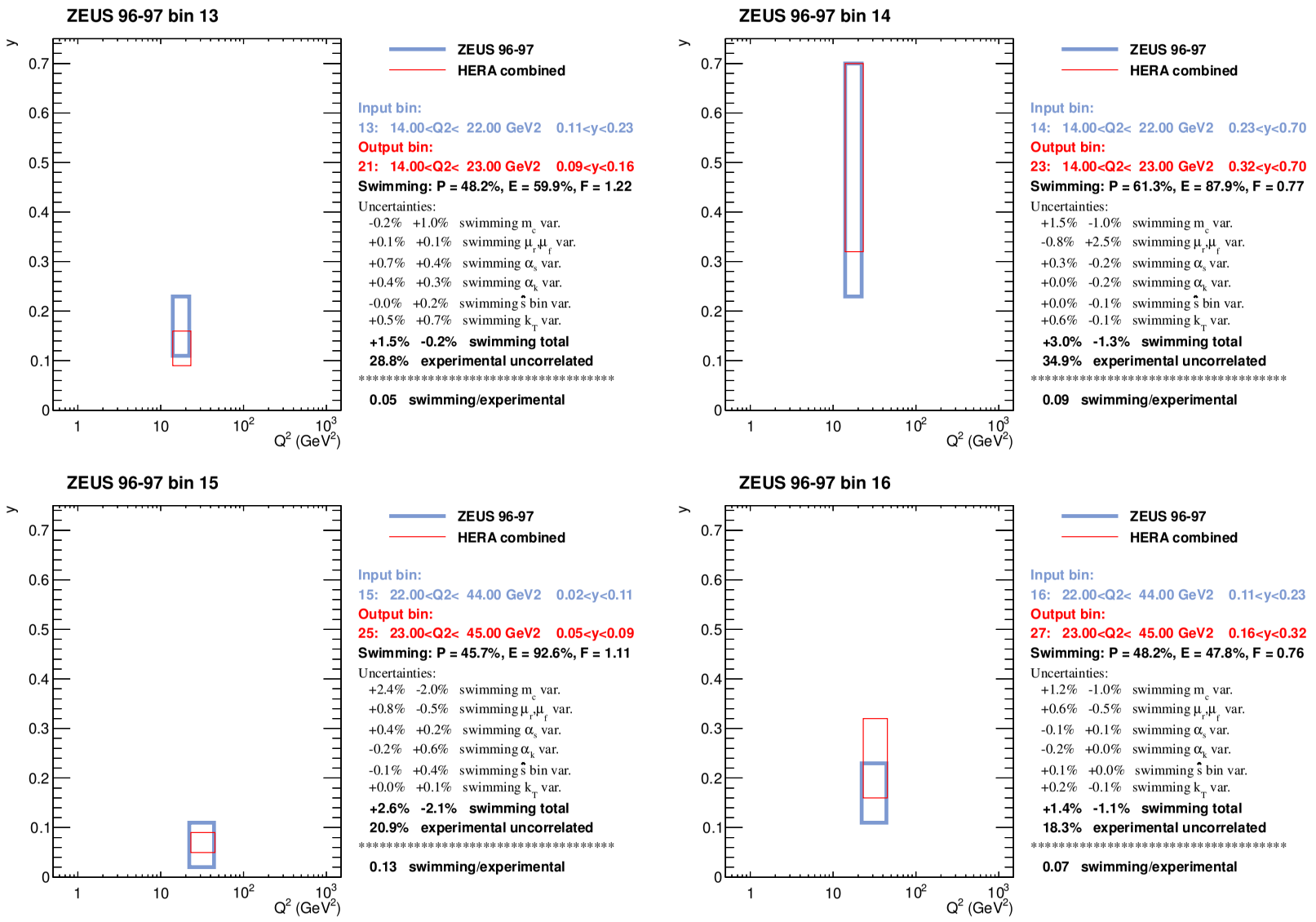

Figure D.20: The continuation of Fig. D.17.

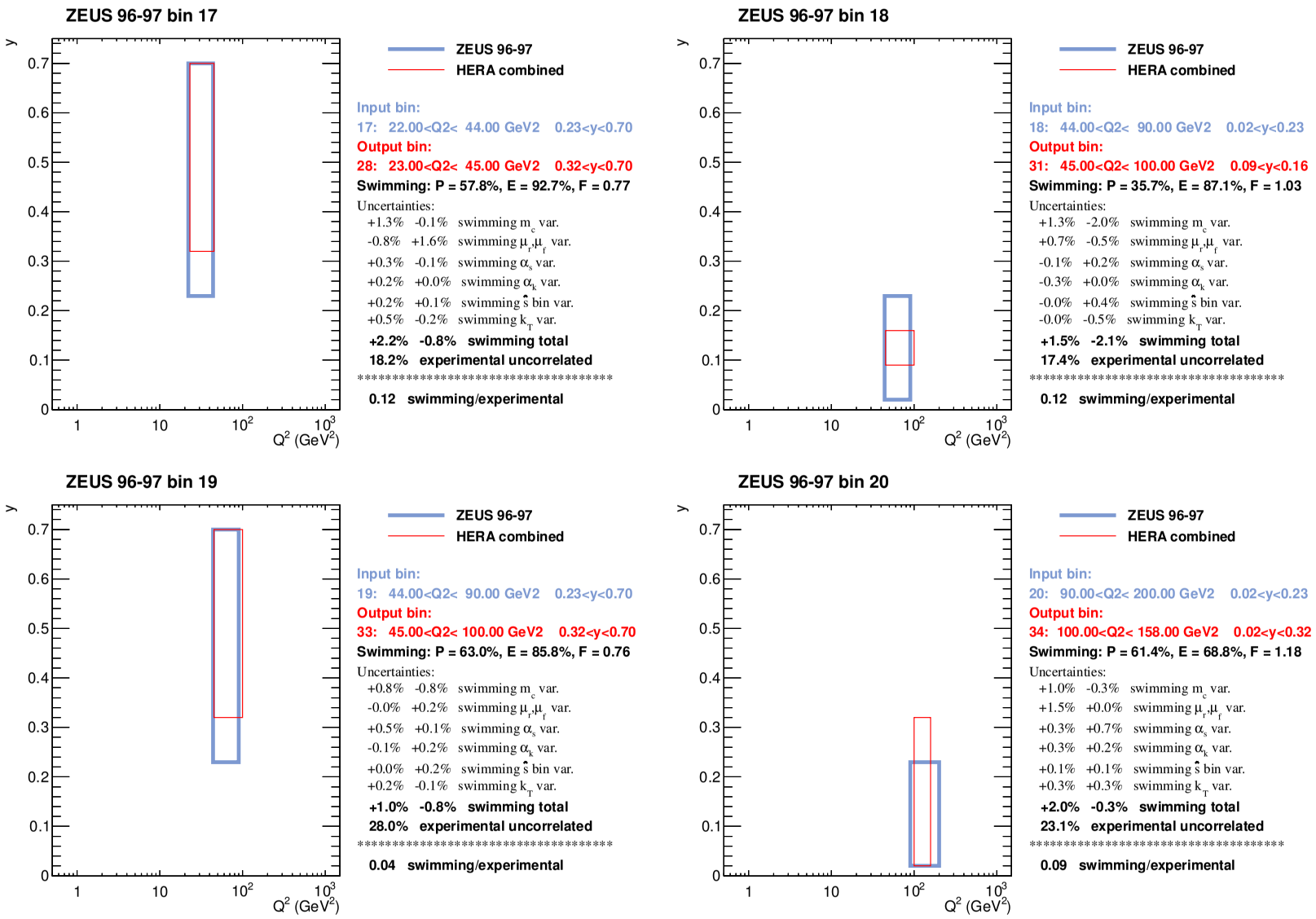

Figure D.21: The continuation of Fig. D.17.

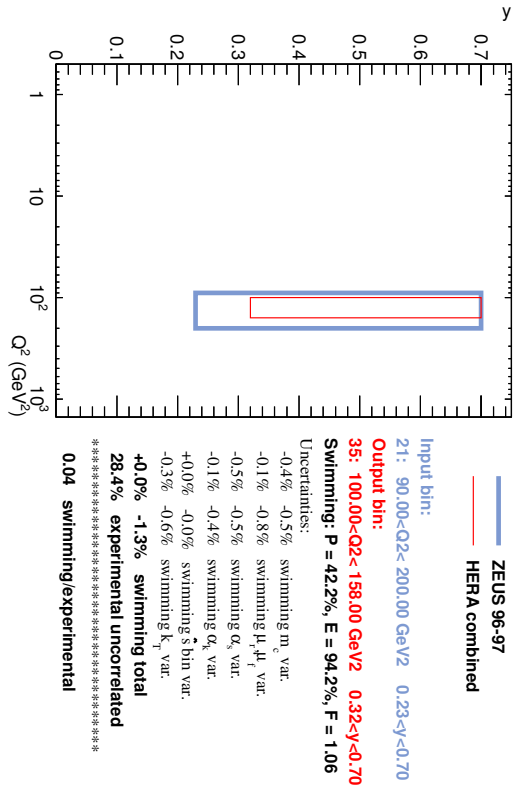

Figure D.22: The continuation of Fig. D.17.

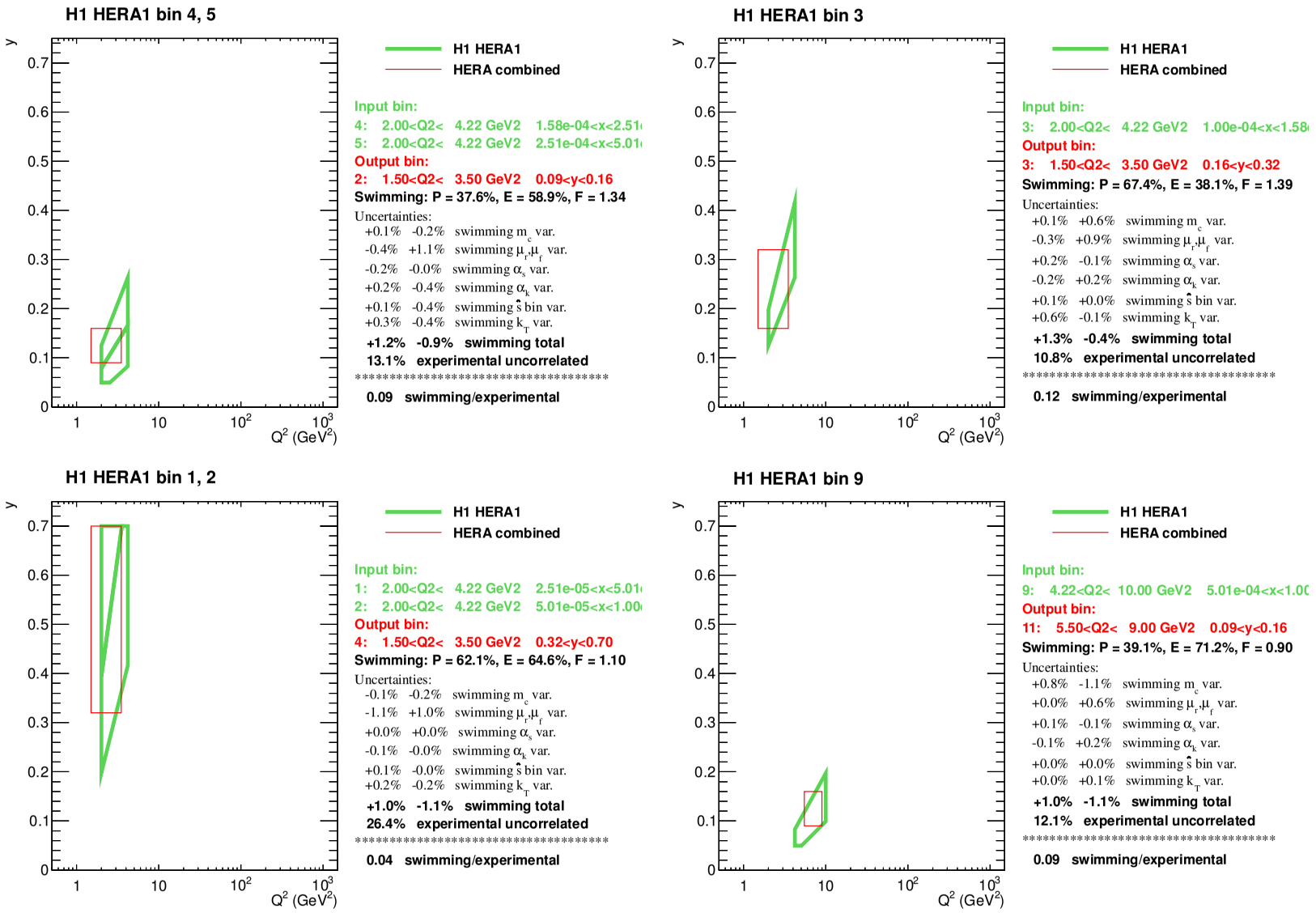

Figure D.23: Swimming corrections for D^{*+} double-differential cross sections for dataset VI.

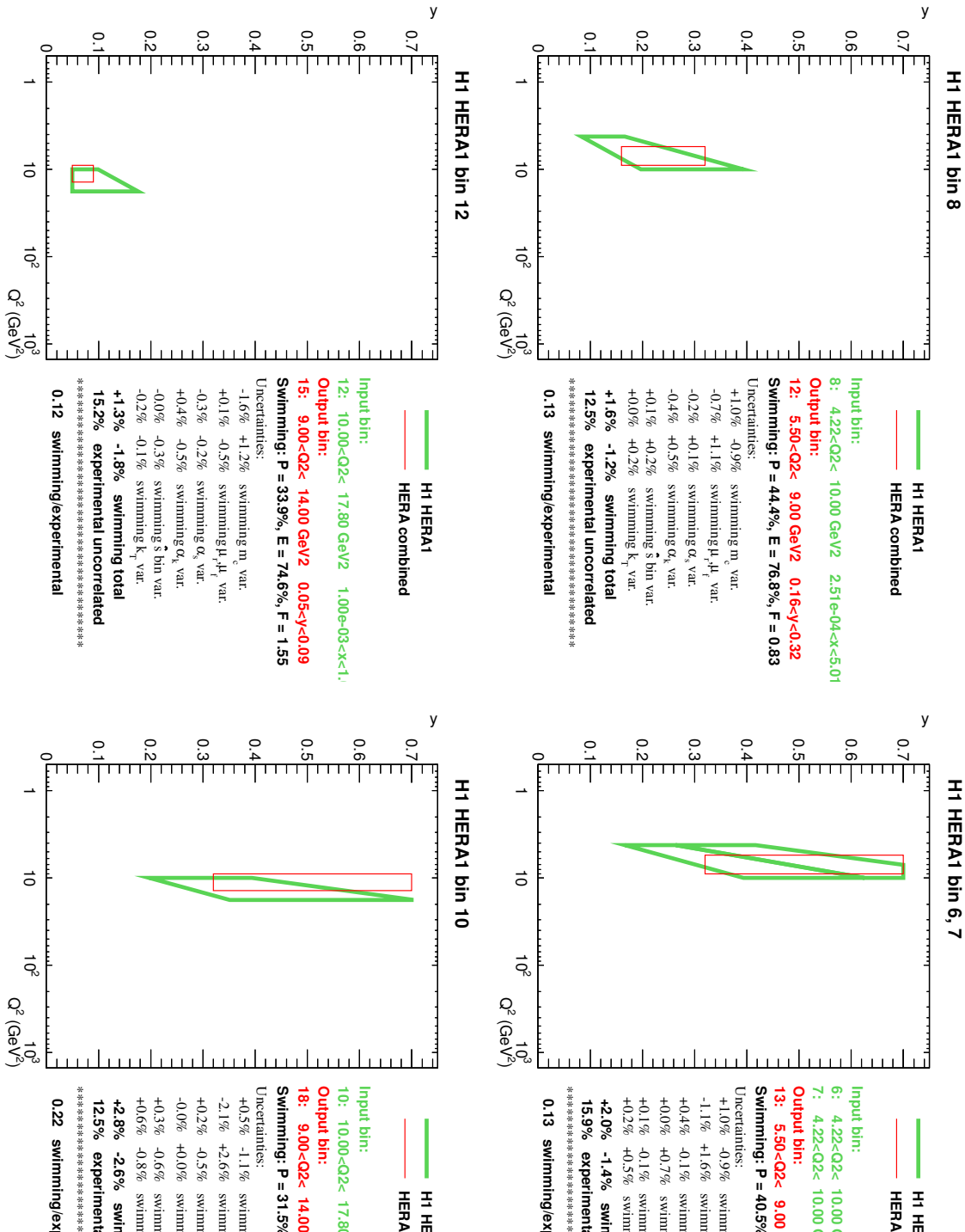

Figure D.24: The continuation of Fig. D.23.

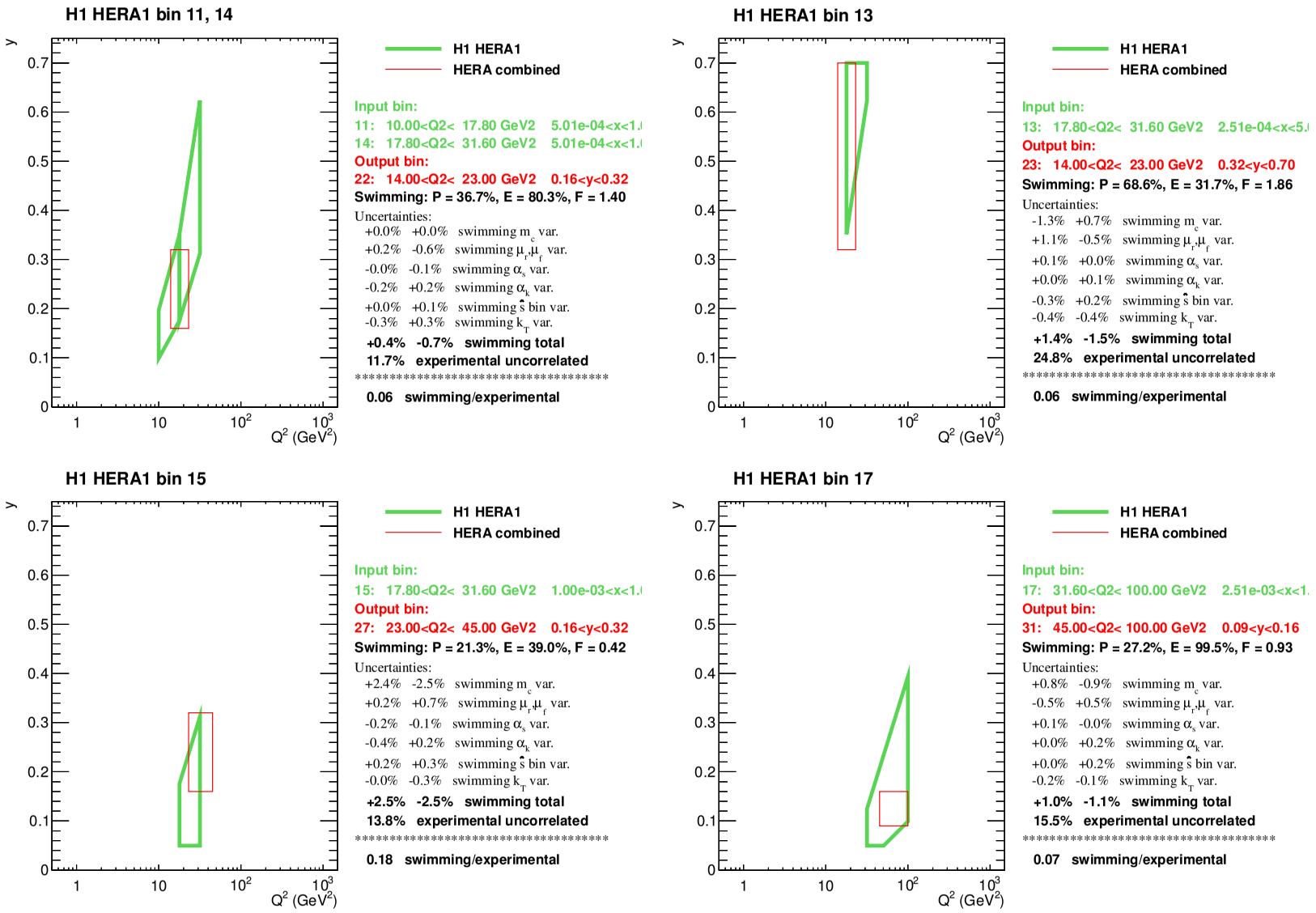

Figure D.25: The continuation of Fig. D.23.

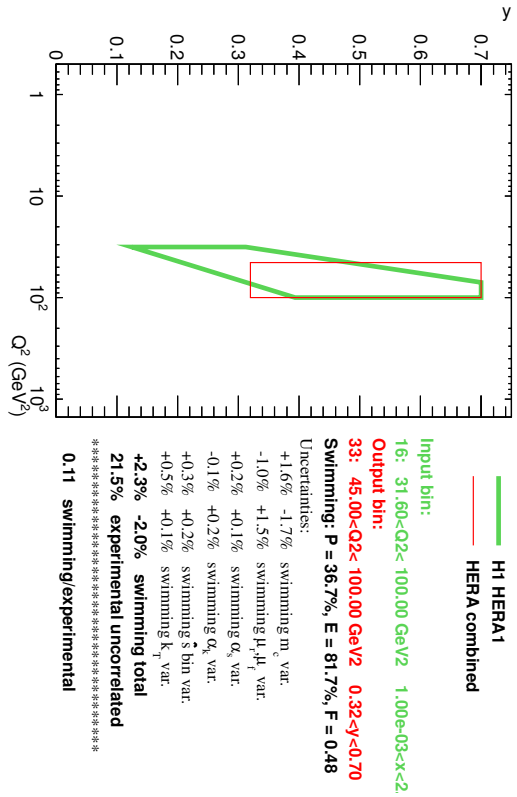

Figure D.26: The continuation of Fig. D.23.

Input bin	Output bin	P [%]	E [%]	F_{sw}	$\delta^{+}F_{\mathrm{sw}}$	$\delta^{-}F_{\mathrm{sw}}$ [%]	δ_{uncor} [%]	$\delta F_{\mathrm{sw}}/\delta_{uncor}$ [%]
1	9	83.1	100.0	0.948	0.3	−0.0	28.4	1.1
2	10	83.2	100.0	0.949	0.2	−0.3	13.3	2.3
3	11	83.2	100.0	0.949	0.2	−0.4	7.3	5.9
4	12	83.2	100.0	0.950	0.1	−0.3	6.7	4.4
5	13	83.1	100.0	0.948	0.2	−0.3	7.5	3.8
6	14	100.0	100.0	1.000	0.0	−0.0	16.1	0.0
7	15	100.0	100.0	1.000	0.0	−0.0	7.8	0.0
8	16	100.0	100.0	1.000	0.0	−0.0	6.4	0.0
9	17	100.0	100.0	1.000	0.0	−0.0	5.5	0.0
10	18	100.0	100.0	1.000	0.0	−0.0	7.5	0.0
11	19	100.0	100.0	1.000	0.0	−0.0	16.9	0.0
12	20	100.0	100.0	1.000	0.0	−0.0	7.3	0.0
13	21	100.0	100.0	1.000	0.0	−0.0	6.2	0.0
14	22	100.0	100.0	1.000	0.0	−0.0	6.4	0.0
15	23	100.0	100.0	1.000	0.0	−0.0	8.4	0.0
16	24	100.0	100.0	1.000	0.0	−0.0	32.6	0.0
17	25	100.0	100.0	1.000	0.0	−0.0	7.4	0.0
18	26	100.0	100.0	1.000	0.0	−0.0	5.5	0.0
19	27	100.0	100.0	1.000	0.0	−0.0	5.3	0.0
20	28	100.0	100.0	1.000	0.0	−0.0	6.7	0.0
21	29	100.0	100.0	1.000	0.0	−0.0	40.5	0.0
22	30	100.0	100.0	1.000	0.0	−0.0	12.6	0.0
23	31	100.0	100.0	1.000	0.0	−0.0	8.7	0.0
24	32	100.0	100.0	1.000	0.0	−0.0	6.6	0.0
25	33	100.0	100.0	1.000	0.0	−0.0	8.5	0.0
26	34	93.0	100.0	1.023	0.2	−0.2	12.2	1.9
27	35	100.0	87.4	1.052	0.2	−0.0	17.0	1.3
28	36	100.0	100.0	1.000	0.0	−0.0	14.5	0.0
29	37	100.0	100.0	1.000	0.0	−0.0	17.5	0.0
30	38	92.6	100.0	0.983	0.5	−0.0	25.1	1.9
31	39	100.0	95.2	1.015	0.0	−0.2	21.8	1.1

Table D.2: Purity (P), efficiency (E), swimming factors (F_{sw}), swimming uncertainties ($\delta^{+}F_{\mathrm{sw}}$, $\delta^{-}F_{\mathrm{sw}}$), uncorrelated experimental uncertainties (δ_{uncor}) and the ratio of the swimming uncertainty to the experimental uncorrelated one ($\delta F_{\mathrm{sw}}/\delta_{uncor}$) for the D^{*+} double-differential cross sections for datasets I–III. The bin numbering scheme is consistent with Figs. D.1 to D.26.

Input bin	Output bin	P [%]	E [%]	F_{sw}	$\delta^{+}F_{\mathrm{sw}}$	$\delta^{-}F_{\mathrm{sw}}$ [%]	δ_{uncor} [%]	$\delta F_{\mathrm{sw}}/\delta_{uncor}$ [%]
1	1	100.0	100.0	1.000	0.0	−0.0	13.0	0.0
2	2	81.4	100.0	1.046	0.1	−0.5	11.3	4.1
3	3	95.4	82.8	1.080	0.7	−0.5	12.1	5.6
4	4	100.0	94.8	1.027	0.2	−0.2	20.7	0.9
5	5	73.6	86.7	1.094	1.1	−0.9	11.4	9.6
6	6	52.4	100.0	1.127	0.8	−0.4	7.9	10.5
7	7	70.5	82.7	1.200	0.6	−0.8	20.3	4.1
8	8	73.9	94.8	1.145	0.3	−0.6	14.7	3.8
9	10	50.8	50.2	1.091	6.3	−4.3	12.4	50.5
10	11	48.9	64.9	1.304	0.9	−0.9	11.3	8.2
11	13	68.5	64.7	0.895	1.8	−1.1	19.1	9.7
12	15	51.5	76.9	1.007	5.5	−4.0	10.3	53.4
13	16	62.0	100.0	1.062	0.2	−0.5	8.4	6.5
14	17	85.8	67.2	1.194	1.0	−1.5	17.1	8.8
15	18	100.0	84.7	1.088	0.3	−0.5	17.6	3.1
16	20	53.5	71.0	1.007	4.9	−4.0	11.0	44.9
17	21	61.8	92.2	1.019	0.6	−0.1	10.7	5.6
18	22	85.5	62.5	1.137	0.8	−1.1	27.1	4.0
19	23	100.0	77.4	1.053	0.8	−0.6	28.6	2.8
20	25	51.3	97.6	1.053	2.5	−2.3	11.3	21.7
21	26	51.5	81.7	1.080	0.7	−0.6	8.6	7.9
22	27	75.2	53.7	1.137	0.1	−1.1	11.6	9.9
23	28	92.4	82.3	1.035	0.6	−0.7	14.7	4.9
24	31	43.1	67.5	0.915	3.2	−2.8	11.8	27.1
25	32	79.0	72.4	0.799	0.3	−0.3	17.8	1.8
26	33	79.2	90.0	0.812	0.7	−0.2	24.7	2.7
27,28	34	61.1	88.8	1.130	0.6	−0.3	25.8	2.2
29	35	51.3	99.5	1.082	0.1	−0.9	32.4	2.7
30	38	59.8	76.7	0.730	0.8	−0.8	25.6	3.1
31	39	62.1	95.1	0.746	0.4	−0.5	26.1	1.8

Table D.3: Purity (P), efficiency (E), swimming factors (F_{sw}), swimming uncertainties ($\delta^{+}F_{\mathrm{sw}}$, $\delta^{-}F_{\mathrm{sw}}$), uncorrelated experimental uncertainties (δ_{uncor}) and the ratio of the swimming uncertainty to the experimental uncorrelated one ($\delta F_{\mathrm{sw}}/\delta_{uncor}$) for the D^{*+} double-differential cross sections for dataset IV. The bin numbering scheme is consistent with Figs. D.9 to D.9.

ZEUS 9697 (dataset V)								
Input bin	Output bin	P [%]	E [%]	F_{sw}	$\delta^{+}F_{\mathrm{sw}}$	$\delta^{-}F_{\mathrm{sw}}$ [%]	δ_{uncor} [%]	$\delta F_{\mathrm{sw}}/\delta_{uncor}$ [%]
1	1	54.4	95.8	0.910	0.7	−2.6	21.9	11.9
2	3	36.4	57.4	0.642	1.5	−1.6	26.2	6.2
3	4	44.1	96.2	0.694	0.9	−1.1	21.5	5.1
4	5	59.2	96.0	1.195	0.5	−1.8	22.6	7.9
5	6	38.2	64.9	1.392	0.9	−0.7	22.4	4.0
6	8	43.5	95.9	0.862	1.9	−1.5	18.5	10.1
7	11	39.7	54.7	0.963	5.0	−3.7	22.4	22.2
8	12	54.9	62.2	2.157	1.6	−3.4	20.5	16.7
9	15	46.5	95.6	1.098	2.9	−3.0	17.8	16.9
10	17	51.4	51.6	0.753	2.2	−1.7	24.9	8.9
11	18	61.0	95.6	0.794	1.7	−2.2	18.0	12.2
12	20	47.6	88.5	1.083	2.6	−3.0	23.6	12.8
13	21	48.2	59.9	1.218	1.5	−0.2	28.8	5.2
14	23	61.3	87.9	0.767	3.0	−1.3	34.9	8.5
15	25	45.7	92.6	1.110	2.6	−2.1	20.9	12.6
16	27	48.2	47.8	0.756	1.4	−1.1	18.3	7.4
17	28	57.8	92.7	0.772	2.2	−0.8	18.2	12.2
18	31	35.7	87.1	1.033	1.5	−2.1	17.4	12.2
19	33	63.0	85.8	0.761	1.0	−0.8	28.0	3.6
20	34	61.4	68.8	1.182	2.0	−0.3	23.1	8.7
21	35	42.2	94.2	1.056	0.0	−1.3	28.4	4.5
H1 HERA-I (dataset VI)								
Input bin	Output bin	P [%]	E [%]	F_{sw}	$\delta^{+}F_{\mathrm{sw}}$	$\delta^{-}F_{\mathrm{sw}}$ [%]	δ_{uncor} [%]	$\delta F_{\mathrm{sw}}/\delta_{uncor}$ [%]
4, 5	2	37.6	58.9	1.338	1.2	−0.9	13.1	8.8
3	3	67.4	38.1	1.385	1.3	−0.4	10.8	11.9
1, 2	4	62.1	64.6	1.101	1.0	−1.1	26.4	4.1
9	11	39.1	71.2	0.898	1.0	−1.1	12.1	9.0
8	12	44.4	76.8	0.833	1.6	−1.2	12.5	12.6
6, 7	13	40.5	91.9	0.667	2.0	−1.4	15.9	12.9
12	15	33.9	74.6	1.551	1.3	−1.8	15.2	12.1
10	18	31.5	42.1	0.845	2.8	−2.6	12.5	22.1
11, 14	22	36.7	80.3	1.396	0.4	−0.7	11.7	6.3
13	23	68.6	31.7	1.865	1.4	−1.5	24.8	6.2
15	27	21.3	39.0	0.416	2.5	−2.5	13.8	18.4
17	31	27.2	99.5	0.929	1.0	−1.1	15.5	6.9
16	33	36.7	81.7	0.484	2.3	−2.0	21.5	10.7

Table D.4: Purity (P), efficiency (E), swimming factors (F_{sw}), swimming uncertainties ($\delta^{+}F_{\mathrm{sw}}$, $\delta^{-}F_{\mathrm{sw}}$), uncorrelated experimental uncertainties (δ_{uncor}) and the ratio of the swimming uncertainty to the experimental uncorrelated one ($\delta F_{\mathrm{sw}}/\delta_{uncor}$) for the D^{*+} double-differential cross sections for datasets V and VI. The bin numbering scheme is consistent with Figs. D.17 to D.23.

H1 HERA-II (datasets I+II)															
$p_T(D^{*+})$	$d\sigma/dp_T(D^{*+})$	δ_{stat}	δ_{uncor}	δ_1	δ_2	δ_3	δ_4	δ_5	δ_6	δ_7	δ_8	δ_9	δ_{10}	δ_{sw}	δ_{11}
[GeV]	[nb/GeV]	[%]	[%]	[%]	[%]	[%]	[%]	[%]	[%]	[%]	[%]	[%]	[%]	[%]	[%]
1.50 : 1.88	2.370403	6.5	5.0	2.9	3.2	1.0	−0.5	1.5	0.0	−0.0	−1.2	0.3	1.2	0.1	0.1
1.88 : 2.28	2.072862	4.6	5.0	2.9	3.2	1.0	−0.3	1.4	−0.0	−0.0	−0.9	−0.2	0.6	0.1	0.2
2.28 : 2.68	1.990029	3.6	5.0	2.9	3.2	1.0	−0.3	1.2	0.0	−0.0	−1.7	−0.2	0.2	0.1	0.2
2.68 : 3.08	1.414324	3.6	5.0	2.9	3.2	1.0	−0.2	1.1	−0.0	−0.0	−0.8	−0.2	0.5	0.2	0.3
3.08 : 3.50	1.181779	3.7	5.0	2.9	3.2	1.0	−0.2	0.9	0.0	−0.0	−0.5	−0.1	0.5	0.2	0.3
3.50 : 4.00	0.843302	3.5	5.0	2.9	3.2	1.0	−0.2	0.7	−0.0	−0.0	−0.7	−0.1	0.5	0.3	0.4
4.00 : 4.75	0.603741	3.1	5.0	2.9	3.2	1.0	−0.1	0.5	−0.0	−0.0	−0.8	−0.3	−0.3	0.3	0.6
4.75 : 6.00	0.299299	3.2	5.0	2.9	3.2	1.0	−0.1	0.3	0.0	−0.0	−0.7	−0.3	−1.0	0.4	1.2
6.00 : 8.00	0.109185	4.4	5.0	2.9	3.2	1.0	0.1	0.1	0.0	−0.0	−0.1	−0.4	−0.6	1.2	3.0
8.00 : 11.00	0.033956	7.1	5.0	2.9	3.2	1.0	0.1	0.2	−0.0	−0.0	−2.9	−0.4	−2.9	4.0	5.1
11.00 : 20.00	0.003892	15.8	5.0	2.9	3.2	1.0	0.1	−0.1	0.0	−0.0	−0.6	−0.7	−3.2	5.6	7.3

ZEUS HERA-II (datasets III)														
$p_T(D^{*+})$	$d\sigma/dp_T(D^{*+})$	δ_{stat}	δ_{uncor}	δ_{12}	δ_{13}	δ_{14}	δ_{15}	δ_{16}	δ_{17}	δ_{18}	δ_{19}	δ_{20}	δ_{21}	δ_{22}
[GeV]	[nb/GeV]	[%]	[%]	[%]	[%]	[%]	[%]	[%]	[%]	[%]	[%]	[%]	[%]	[%]
1.50 : 1.88	2.160000	9.9	4.5	11.1	0.7	−0.9	−0.2	1.2	−0.8	−0.3	3.4	3.0	1.4	1.9
1.88 : 2.28	2.300000	5.8	3.9	7.4	0.2	−0.6	−0.2	0.8	−1.0	−0.4	2.9	3.0	1.3	1.9
2.28 : 2.68	1.950000	4.4	1.8	5.0	0.2	−0.5	−0.2	0.7	−0.5	0.1	2.4	3.0	1.4	1.9
2.68 : 3.08	1.630000	4.0	1.2	2.6	−0.6	−0.4	−0.1	0.5	0.3	−0.3	2.0	3.0	1.5	1.9
3.08 : 3.50	1.220000	3.8	2.4	1.9	−0.0	−0.3	−0.1	0.5	0.2	−0.1	1.6	3.0	1.4	1.9
3.50 : 4.00	0.970000	3.4	1.5	2.1	0.0	−0.3	−0.1	0.3	0.5	0.1	1.4	2.9	1.2	1.9
4.00 : 4.75	0.630000	3.2	1.1	−1.3	−0.3	−0.4	−0.1	0.6	0.6	0.1	1.3	2.9	1.1	1.9
4.75 : 6.00	0.330000	3.0	1.8	1.1	−0.1	−0.4	−0.1	0.3	0.6	0.2	1.1	2.8	1.2	1.9
6.00 : 8.00	0.120000	3.8	2.3	−3.3	−0.0	−0.3	−0.2	0.4	0.4	0.4	1.1	2.7	1.3	1.9
8.00 : 11.00	0.033000	6.0	2.4	2.3	0.7	−0.3	−0.1	0.5	0.3	0.2	1.0	2.7	0.7	1.9
11.00 : 20.00	0.003600	12.3	5.1	13.5	1.3	0.3	0.0	0.3	0.5	0.2	1.0	2.6	0.4	1.9

Table D.5: Input data used for the combination of the D^{*+} single-differential cross section as a function of $p_T(D^{*+})$. The tables report for each bin the input differential cross section ($d\sigma/dp_T(D^{*+})$) together with its statistical (δ_{stat}), uncorrelated (δ_{uncor}) and all correlated (all other $\delta_{...}$) uncertainties; the theoretical uncertainties from the swimming procedure are shown separately (δ_{sw}).

H1 HERA-II (datasets I+II)															
$\eta(D^{*+})$	$d\sigma/d\eta(D^{*+})$	δ_{stat}	δ_{uncor}	δ_1	δ_2	δ_3	δ_4	δ_5	δ_6	δ_7	δ_8	δ_9	δ_{10}	δ_{sw}	δ_{11}
	[nb]	[%]	[%]	[%]	[%]	[%]	[%]	[%]	[%]	[%]	[%]	[%]	[%]	[%]	[%]
−1.50 : −1.25	1.264195	6.3	5.0	2.9	3.2	1.0	−0.6	1.2	0.0	−0.0	−1.0	−1.2	−1.6	0.2	0.3
−1.25 : −1.00	1.369066	4.7	5.0	2.9	3.2	1.0	−0.4	1.1	−0.0	−0.0	0.1	−1.2	−2.3	0.2	0.5
−1.00 : −0.75	1.564379	4.1	5.0	2.9	3.2	1.0	−0.4	1.1	−0.0	−0.0	0.2	−1.2	−2.6	0.2	0.5
−0.75 : −0.50	1.711417	4.0	5.0	2.9	3.2	1.0	−0.3	1.0	−0.0	−0.0	−0.5	−1.1	−1.6	0.1	0.6
−0.50 : −0.25	1.654022	4.0	5.0	2.9	3.2	1.0	−0.3	0.9	−0.0	−0.0	−0.1	−1.0	−1.4	0.2	0.7
−0.25 : 0.00	1.719374	4.0	5.0	2.9	3.2	1.0	−0.2	0.9	−0.0	−0.0	−1.0	−1.1	−1.7	0.1	0.7
0.00 : 0.25	1.761646	4.2	5.0	2.9	3.2	1.0	−0.2	0.9	−0.0	−0.0	−0.7	−0.7	−0.9	0.1	0.7
0.25 : 0.50	1.773855	4.4	5.0	2.9	3.2	1.0	−0.2	0.8	−0.0	−0.0	−1.0	−0.7	−1.7	0.1	0.7
0.50 : 0.75	1.851288	4.4	5.0	2.9	3.2	1.0	−0.2	0.9	0.0	−0.0	−0.7	−0.8	−1.6	0.2	0.7
0.75 : 1.00	1.838827	4.6	5.0	2.9	3.2	1.0	−0.2	0.8	0.0	−0.0	−1.3	−1.1	−2.4	0.1	0.6
1.00 : 1.25	2.112178	4.7	5.0	2.9	3.2	1.0	−0.2	0.8	−0.0	−0.0	−1.3	−0.9	−2.2	0.2	0.5
1.25 : 1.50	1.808955	7.1	5.0	2.9	3.2	1.0	−0.2	0.9	−0.0	−0.0	0.1	−1.1	−2.3	0.2	0.6

ZEUS HERA-II (datasets III)														
$\eta(D^{*+})$	$d\sigma/d\eta(D^{*+})$	δ_{stat}	δ_{uncor}	δ_{12}	δ_{13}	δ_{14}	δ_{15}	δ_{16}	δ_{17}	δ_{18}	δ_{19}	δ_{20}	δ_{21}	δ_{22}
	[nb]	[%]	[%]	[%]	[%]	[%]	[%]	[%]	[%]	[%]	[%]	[%]	[%]	[%]
−1.50 : −1.25	1.480000	7.5	3.5	1.7	1.8	−1.4	−0.2	1.3	0.1	−0.0	2.1	4.8	2.5	1.9
−1.25 : −1.00	1.660000	5.4	2.8	2.3	0.5	−0.9	−0.3	1.0	−0.0	0.2	2.0	3.8	1.2	1.9
−1.00 : −0.75	1.610000	4.9	4.1	3.8	0.8	−0.7	−0.3	1.0	0.1	−0.0	1.9	3.2	0.6	1.9
−0.75 : −0.50	1.850000	4.2	2.1	1.5	0.9	−0.6	−0.2	0.7	−0.1	0.0	1.9	2.7	0.7	1.9
−0.50 : −0.25	1.940000	4.2	1.9	−0.6	1.0	−0.5	−0.1	0.6	−0.1	0.2	1.8	2.4	0.7	1.9
−0.25 : 0.00	2.020000	4.0	2.2	3.8	0.9	−0.3	−0.0	0.6	−0.0	0.3	1.8	2.3	1.1	1.9
0.00 : 0.25	1.900000	4.4	2.3	−2.5	0.7	−0.4	−0.2	0.5	0.1	−0.1	1.8	2.2	1.1	1.9
0.25 : 0.50	1.970000	4.4	2.0	3.5	0.3	−0.3	−0.1	0.4	0.1	0.2	1.8	2.4	1.0	1.9
0.50 : 0.75	1.960000	4.7	2.2	2.3	0.8	−0.3	−0.1	0.4	0.1	0.1	1.8	2.7	0.5	1.9
0.75 : 1.00	2.000000	4.9	2.3	4.1	0.8	−0.2	−0.1	0.3	0.1	−0.5	1.8	3.2	0.6	1.9
1.00 : 1.25	2.000000	5.8	2.9	−3.6	0.9	−0.5	−0.1	0.4	−0.0	0.1	1.8	3.8	0.3	1.9
1.25 : 1.50	1.840000	7.7	4.8	7.8	1.1	−0.1	−0.0	0.4	0.0	−0.6	1.9	4.7	0.1	1.9

Table D.6: Input data used for the combination of the D^{*+} single-differential cross section as a function of $\eta(D^{*+})$. The tables report for each bin the input differential cross section ($d\sigma/d\eta(D^{*+})$) together with its statistical (δ_{stat}), uncorrelated (δ_{uncor}) and all correlated (all other $\delta_{...}$) uncertainties; the theoretical uncertainties from the swimming procedure are shown separately (δ_{sw}).

H1 HERA-II (datasets I+II)															
$z(D^{*+})$	$d\sigma/dz(D^{*+})$	δ_{stat}	δ_{uncor}	δ_1	δ_2	δ_3	δ_4	δ_5	δ_6	δ_7	δ_8	δ_9	δ_{10}	δ_{sw}	δ_{11}
	[nb]	[%]	[%]	[%]	[%]	[%]	[%]	[%]	[%]	[%]	[%]	[%]	[%]	[%]	[%]
0.000 : 0.100	3.479279	12.5	5.0	2.9	3.2	1.0	0.7	0.8	−1.4	−0.0	4.2	−0.7	−3.5	0.2	0.7
0.100 : 0.200	7.307088	6.2	5.0	2.9	3.2	1.0	0.9	0.9	−1.8	−0.0	0.6	−0.8	−4.1	0.2	0.5
0.200 : 0.325	8.506860	4.4	5.0	2.9	3.2	1.0	1.0	1.1	−1.9	−0.0	−3.7	−1.0	−2.5	0.4	0.4
0.325 : 0.450	7.895236	4.1	5.0	2.9	3.2	1.0	1.2	1.1	−2.5	−0.0	−3.6	−0.4	−2.3	0.4	0.5
0.450 : 0.575	7.723692	3.8	5.0	2.9	3.2	1.0	0.3	1.0	−1.1	−0.0	−3.8	0.1	−1.1	0.2	0.5
0.575 : 0.800	4.337003	3.1	5.0	2.9	3.2	1.0	−1.6	0.8	2.4	−0.0	−4.2	−0.7	−1.0	0.7	0.8
0.800 : 1.000	0.928485	7.4	5.0	2.9	3.2	1.0	−13.5	−0.4	21.1	−0.0	0.2	−2.7	−7.2	2.5	1.0

ZEUS HERA-II (datasets III)														
$z(D^{*+})$	$d\sigma/dz(D^{*+})$	δ_{stat}	δ_{uncor}	δ_{12}	δ_{13}	δ_{14}	δ_{15}	δ_{16}	δ_{17}	δ_{18}	δ_{19}	δ_{20}	δ_{21}	δ_{22}
	[nb]	[%]	[%]	[%]	[%]	[%]	[%]	[%]	[%]	[%]	[%]	[%]	[%]	[%]
0.000 : 0.100	3.000000	12.3	5.9	5.9	2.8	−1.4	−4.7	1.8	−0.0	0.2	2.4	3.4	2.4	1.9
0.100 : 0.200	6.800000	6.1	2.3	9.8	1.6	−0.8	−3.5	1.2	−0.4	0.2	2.2	2.9	1.3	1.9
0.200 : 0.325	8.180000	3.5	2.3	4.3	1.9	−0.5	−2.2	0.9	−0.2	0.1	2.0	2.9	0.9	1.9
0.325 : 0.450	9.100000	2.5	1.5	−0.3	1.3	−0.4	−0.6	0.4	0.1	−0.1	1.8	2.9	0.8	1.9
0.450 : 0.575	9.140000	1.3	1.3	1.1	0.6	−0.3	1.5	0.1	0.1	−0.1	1.7	2.9	1.5	1.9
0.575 : 0.800	5.120000	1.4	2.1	1.4	−1.6	−0.3	4.0	0.2	0.3	−0.1	1.5	2.9	2.5	1.9
0.800 : 1.000	0.630000	9.1	5.7	−1.0	−7.0	−0.2	5.6	0.0	1.1	0.3	1.4	3.1	2.7	1.9

Table D.7: Input data used for the combination of the D^{*+} single-differential cross section as a function of $z(D^{*+})$. The tables report for each bin the input differential cross section ($d\sigma/dz(D^{*+})$) together with its statistical (δ_{stat}), uncorrelated (δ_{uncor}) and all correlated (all other $\delta_{...}$) uncertainties; the theoretical uncertainties from the swimming procedure are shown separately (δ_{sw}).

H1 HERA-II (datasets I+II)													
Q^2	$d\sigma/dQ^2$	δ_{stat}	δ_{uncor}	δ_1	δ_2	δ_3	δ_4	δ_5	δ_6	δ_7	δ_8	δ_9	δ_{10}
[GeV^2]	[nb/GeV^2]	[%]	[%]	[%]	[%]	[%]	[%]	[%]	[%]	[%]	[%]	[%]	[%]
5 : 8	0.450491	3.4	5.0	2.9	3.2	1.0	−0.1	1.4	−0.0	−0.0	−2.3	−1.1	−3.0
8 : 10	0.278716	4.8	5.0	2.9	3.2	1.0	−0.1	0.4	−0.0	−0.0	−1.2	−1.0	−2.3
10 : 13	0.198811	4.4	5.0	2.9	3.2	1.0	−0.2	1.5	0.0	−0.0	−0.4	−1.2	−1.5
13 : 19	0.123919	3.4	5.0	2.9	3.2	1.0	−0.3	1.2	−0.0	−0.0	−0.6	−1.0	−1.3
19 : 28	0.068075	4.1	5.0	2.9	3.2	1.0	−0.3	0.9	0.0	−0.0	−0.1	−0.9	−1.3
28 : 40	0.037496	4.4	5.0	2.9	3.2	1.0	−0.5	1.2	−0.0	−0.0	−0.9	−1.0	−0.8
40 : 60	0.015640	6.1	5.0	2.9	3.2	1.0	−0.6	1.1	0.0	−0.0	1.0	−0.8	−1.6
60 : 100	0.007259	6.2	5.0	2.9	3.2	1.0	−0.7	0.9	−0.0	−0.0	0.9	−1.0	−1.8
100 : 158	0.001862	10.3	4.4	6.9	3.2	0.0	3.3	4.1	1.0	0.4	3.2	0.0	0.0
158 : 251	0.000777	9.8	4.8	6.9	3.2	0.0	1.7	1.0	1.3	0.5	4.1	0.0	0.0
251 : 1000	0.000058	15.6	6.0	6.9	3.2	0.0	1.5	1.3	1.4	0.4	7.3	0.0	0.0

ZEUS HERA-II (datasets III)														
Q^2	$d\sigma/dQ^2$	δ_{stat}	δ_{uncor}	δ_{12}	δ_{13}	δ_{14}	δ_{15}	δ_{16}	δ_{17}	δ_{18}	δ_{19}	δ_{20}	δ_{21}	δ_{22}
[GeV^2]	[nb/GeV^2]	[%]	[%]	[%]	[%]	[%]	[%]	[%]	[%]	[%]	[%]	[%]	[%]	[%]
5 : 8	0.499000	3.9	3.5	5.5	0.9	3.2	0.8	1.2	−0.6	−0.1	2.1	3.0	1.6	1.9
8 : 10	0.307000	4.3	3.5	−0.6	1.5	1.1	0.4	0.6	−1.0	−0.1	2.1	3.0	1.2	1.9
10 : 13	0.222000	4.0	2.2	3.3	0.4	−0.7	−0.3	0.5	−0.9	−0.1	2.1	3.0	1.1	1.9
13 : 19	0.125000	3.5	1.5	2.2	1.0	−0.9	−0.1	0.5	0.9	0.1	2.0	3.0	1.1	1.9
19 : 28	0.075200	3.7	1.9	1.6	0.6	−0.7	0.2	0.5	0.6	0.1	1.9	2.9	1.0	1.9
28 : 40	0.041500	3.9	1.8	3.9	0.1	−1.2	−0.1	0.5	0.2	0.1	1.7	2.9	1.1	1.9
40 : 60	0.016900	4.7	2.2	5.2	1.2	−1.4	−0.3	0.4	2.6	0.4	1.6	2.9	1.0	1.9
60 : 100	0.007470	5.0	4.8	0.4	−0.4	−2.8	−1.2	0.2	1.5	0.5	1.5	2.9	1.4	1.9
100 : 158	0.002160	9.1	3.9	2.0	0.0	−3.7	−0.8	0.3	−1.3	1.2	1.3	1.4	0.9	1.9
158 : 251	0.000937	10.8	2.8	2.0	0.6	−2.2	−0.7	0.5	−0.9	0.9	1.3	1.3	1.3	1.9
251 : 1000	0.000100	15.9	4.5	2.0	−0.7	−4.6	−1.8	0.9	−0.6	0.6	1.3	1.4	0.4	1.9

Table D.8: Input data used for the combination of the D^{*+} single-differential cross section as a function of Q^2. The tables report for each bin the input differential cross section ($d\sigma/dQ^2$) together with its statistical (δ_{stat}), uncorrelated (δ_{uncor}) and all correlated (all other $\delta_{...}$) uncertainties.

H1 HERA-II (datasets I+II)															
y	$d\sigma/dy$	δ_{stat}	δ_{uncor}	δ_1	δ_2	δ_3	δ_4	δ_5	δ_6	δ_7	δ_8	δ_9	δ_{10}	δ_{sw}	δ_{11}
	[nb]	[%]	[%]	[%]	[%]	[%]	[%]	[%]	[%]	[%]	[%]	[%]	[%]	[%]	[%]
0.02 : 0.05	12.304402	5.2	5.0	2.9	3.2	1.0	−3.9	0.5	7.0	−0.0	−5.6	−1.3	3.2	0.1	0.1
0.05 : 0.09	16.866968	4.2	5.0	2.9	3.2	1.0	−1.1	1.0	1.4	−0.0	−1.3	−0.9	−1.9	0.1	0.3
0.09 : 0.13	16.486118	4.5	5.0	2.9	3.2	1.0	−1.0	1.0	1.2	−0.0	−3.2	−1.0	−2.4	0.1	0.5
0.13 : 0.18	13.279848	4.8	5.0	2.9	3.2	1.0	−0.4	1.0	−0.4	−0.0	−1.0	−1.1	−1.8	0.1	0.5
0.18 : 0.26	11.401967	3.9	5.0	2.9	3.2	1.0	0.0	1.0	−0.8	−0.0	−2.1	−0.8	−2.5	0.0	0.6
0.26 : 0.36	7.258390	4.6	5.0	2.9	3.2	1.0	0.5	0.9	−1.7	−0.0	0.0	−1.2	−2.9	0.1	0.7
0.36 : 0.50	4.549839	5.1	5.0	2.9	3.2	1.0	1.0	0.9	−2.3	−0.0	1.5	−1.0	−4.2	0.1	0.9
0.50 : 0.70	2.324644	8.1	5.0	2.9	3.2	1.0	1.6	0.7	0.2	−0.0	4.2	−1.0	−4.6	0.2	1.1

ZEUS HERA-II (datasets III)														
y	$d\sigma/dy$	δ_{stat}	δ_{uncor}	δ_{12}	δ_{13}	δ_{14}	δ_{15}	δ_{16}	δ_{17}	δ_{18}	δ_{19}	δ_{20}	δ_{21}	δ_{22}
	[nb]	[%]	[%]	[%]	[%]	[%]	[%]	[%]	[%]	[%]	[%]	[%]	[%]	[%]
0.02 : 0.05	12.000000	7.9	5.5	−7.8	−5.9	−7.1	10.9	−0.0	0.3	0.0	2.1	4.2	1.9	1.9
0.05 : 0.09	20.700000	3.4	3.3	2.3	−0.8	−2.2	4.0	0.0	0.0	−0.0	2.0	3.4	−1.4	1.9
0.09 : 0.13	17.900000	3.4	1.5	3.6	0.8	−0.7	1.3	−0.0	−0.1	−0.0	1.9	2.9	−0.5	1.9
0.13 : 0.18	13.700000	3.6	2.2	2.5	1.4	−0.4	0.6	0.0	−0.1	0.0	1.9	2.6	−3.2	1.9
0.18 : 0.26	11.300000	3.3	2.3	1.0	1.1	0.2	−0.6	0.1	−0.1	0.1	1.8	2.7	1.3	1.9
0.26 : 0.36	8.030000	3.7	2.2	3.0	1.8	−0.5	−1.1	0.5	0.1	0.1	1.8	2.8	0.4	1.9
0.36 : 0.50	5.090000	4.2	1.9	5.6	1.1	0.9	−2.1	1.6	0.3	−0.2	1.8	3.1	0.9	1.9
0.50 : 0.70	2.900000	6.0	3.0	4.1	0.4	0.8	−5.1	2.5	0.2	0.6	1.7	3.2	5.8	1.9

Table D.9: Input data used for the combination of the D^{*+} single-differential cross section as a function of y. The tables report for each bin the input differential cross section ($d\sigma/dy$) together with its statistical (δ_{stat}), uncorrelated (δ_{uncor}) and all correlated (all other $\delta_{...}$) uncertainties; the theoretical uncertainties from the swimming procedure are shown separately (δ_{sw}).

H1 HERA-II (datasets I+II)																			
Q^2	y	$\frac{d^2\sigma}{dQ^2dy}$	δ_{stat}	δ_{uncor}	δ_1	δ_2	δ_3	δ_4	δ_5	δ_6	δ_7	δ_8	δ_9	δ_{10}	δ_{24}	δ_{25}	δ_{26}	δ_{27}	δ_{28}
[GeV^2]		[nb/GeV^2]	[%]	[%]	[%]	[%]	[%]	[%]	[%]	[%]	[%]	[%]	[%]	[%]	[%]	[%]	[%]	[%]	[%]
5.5 : 9.0	0.02 : 0.05	0.122771	11.7	5.0	2.9	3.2	1.0	−1.8	1.7	−0.5	−0.0	−4.6	−1.3	−0.9	0.0	−0.2	0.1	0.1	−0.2
5.5 : 9.0	0.05 : 0.09	0.208477	7.6	5.0	2.9	3.2	1.0	−2.8	1.6	−0.7	−0.0	−4.0	−2.3	−1.7	0.3	0.1	−0.1	0.1	−0.2
5.5 : 9.0	0.09 : 0.16	0.321166	5.6	5.0	2.9	3.2	1.0	−1.7	4.4	−0.3	−0.0	−1.3	−2.7	−4.0	−0.0	0.4	−0.1	0.1	−0.2
5.5 : 9.0	0.16 : 0.32	0.447618	4.7	5.0	2.9	3.2	1.0	−1.6	3.4	−0.4	−0.0	−3.4	−2.5	−4.8	0.1	0.1	0.0	0.1	−0.2
5.5 : 9.0	0.32 : 0.70	0.307615	7.2	5.0	2.9	3.2	1.0	3.1	3.7	−0.3	−0.0	1.5	−2.8	−6.4	0.3	0.1	0.1	0.1	−0.2
9.0 : 14.0	0.02 : 0.05	0.068712	18.0	5.0	2.9	3.2	1.0	−3.7	4.3	−1.2	−0.0	−4.1	0.9	3.5	−0.0	−0.0	−0.0	0.0	−0.0
9.0 : 14.0	0.05 : 0.09	0.149424	9.1	5.0	2.9	3.2	1.0	−3.3	3.6	−0.3	−0.0	−4.3	−2.5	−2.9	−0.0	−0.0	−0.0	0.0	−0.0
9.0 : 14.0	0.09 : 0.16	0.203839	7.6	5.0	2.9	3.2	1.0	−1.9	3.1	−0.1	−0.0	−2.8	−2.5	−3.0	−0.0	−0.0	−0.0	0.0	−0.0
9.0 : 14.0	0.16 : 0.32	0.331893	6.7	5.0	2.9	3.2	1.0	1.8	1.9	0.3	−0.0	−1.1	−2.3	−3.0	−0.0	−0.0	−0.0	0.0	−0.0
9.0 : 14.0	0.32 : 0.70	0.273543	7.7	5.0	2.9	3.2	1.0	2.9	2.5	0.1	−0.0	1.2	−2.8	−5.3	−0.0	−0.0	−0.0	0.0	−0.0
14.0 : 23.0	0.02 : 0.05	0.067376	13.0	5.0	2.9	3.2	1.0	−5.0	−0.8	−1.2	−0.0	−1.9	−1.5	3.5	−0.0	−0.0	−0.0	0.0	−0.0
14.0 : 23.0	0.05 : 0.09	0.129681	9.8	5.0	2.9	3.2	1.0	−1.7	2.7	−0.8	−0.0	−4.3	−2.0	−2.1	−0.0	−0.0	−0.0	0.0	−0.0
14.0 : 23.0	0.09 : 0.16	0.191319	7.0	5.0	2.9	3.2	1.0	−2.1	2.0	−0.8	−0.0	−6.4	−2.4	−3.1	−0.0	−0.0	−0.0	0.0	−0.0
14.0 : 23.0	0.16 : 0.32	0.301013	5.8	5.0	2.9	3.2	1.0	1.7	3.1	0.6	−0.0	−1.4	−2.6	−3.2	−0.0	−0.0	−0.0	0.0	−0.0
14.0 : 23.0	0.32 : 0.70	0.225959	8.4	5.0	2.9	3.2	1.0	2.7	3.1	0.3	−0.0	4.3	−2.9	−5.4	−0.0	−0.0	−0.0	0.0	−0.0
23.0 : 45.0	0.02 : 0.05	0.057502	13.3	5.0	2.9	3.2	1.0	−5.7	1.9	−3.1	−0.0	−12.9	0.7	1.8	−0.0	−0.0	−0.0	0.0	−0.0
23.0 : 45.0	0.05 : 0.09	0.105608	10.8	5.0	2.9	3.2	1.0	−2.5	3.0	−1.0	−0.0	−5.0	−2.4	−2.1	−0.0	−0.0	−0.0	0.0	−0.0
23.0 : 45.0	0.09 : 0.16	0.186974	7.8	5.0	2.9	3.2	1.0	−2.9	3.0	−0.1	−0.0	−4.7	−2.5	−2.5	−0.0	−0.0	−0.0	0.0	−0.0
23.0 : 45.0	0.16 : 0.32	0.262564	6.2	5.0	2.9	3.2	1.0	2.0	2.5	0.4	−0.0	−1.8	−2.5	−2.6	−0.0	−0.0	−0.0	0.0	−0.0
23.0 : 45.0	0.32 : 0.70	0.254796	7.9	5.0	2.9	3.2	1.0	2.7	2.2	0.4	−0.0	3.2	−2.9	−4.7	−0.0	−0.0	−0.0	0.0	−0.0
45.0 : 100.0	0.02 : 0.05	0.008933	47.8	5.0	2.9	3.2	1.0	−9.7	−0.5	−2.4	−0.0	−3.6	0.9	2.9	−0.0	−0.0	−0.0	0.0	−0.0
45.0 : 100.0	0.05 : 0.09	0.054921	16.6	5.0	2.9	3.2	1.0	−4.8	2.6	−0.5	−0.0	−4.9	−1.9	−0.6	−0.0	−0.0	−0.0	0.0	−0.0
45.0 : 100.0	0.09 : 0.16	0.082987	13.1	5.0	2.9	3.2	1.0	−1.5	2.3	−0.6	−0.0	−7.2	−2.1	−4.1	−0.0	−0.0	−0.0	0.0	−0.0
45.0 : 100.0	0.16 : 0.32	0.208217	7.9	5.0	2.9	3.2	1.0	−2.4	2.5	0.5	−0.0	−4.7	−3.2	−4.6	−0.0	−0.0	−0.0	0.0	−0.0
45.0 : 100.0	0.32 : 0.70	0.152967	11.7	5.0	2.9	3.2	1.0	3.1	2.7	0.2	−0.0	4.8	−2.2	−2.8	−0.0	−0.0	−0.0	0.0	−0.0
100.0 : 158.0	0.02 : 0.32	0.060493	14.0	6.1	6.9	3.2	0.0	5.2	6.8	0.5	0.2	4.7	0.0	0.0	−0.2	−0.2	0.0	0.0	−0.0
100.0 : 158.0	0.32 : 0.70	0.049052	15.0	6.1	6.9	3.2	0.0	1.4	0.7	1.8	0.6	0.9	0.0	0.0	−0.1	−0.1	−0.1	0.0	−0.1
158.0 : 251.0	0.02 : 0.30	0.042029	13.0	6.7	6.9	3.2	0.0	2.2	0.5	1.2	0.4	4.5	0.0	0.0	−0.0	−0.0	−0.0	0.0	−0.0
158.0 : 251.0	0.30 : 0.70	0.030206	15.0	6.7	6.9	3.2	0.0	1.0	1.8	1.7	0.7	3.6	−0.0	0.0	−0.0	−0.0	−0.0	0.0	−0.0
251.0 : 1000.0	0.02 : 0.26	0.016264	25.0	8.4	6.9	3.2	0.0	3.7	1.7	1.5	0.2	7.4	0.0	−0.0	−0.3	−0.3	−0.1	0.1	0.1
251.0 : 1000.0	0.26 : 0.70	0.027092	20.0	8.4	6.9	3.2	0.0	0.2	1.0	1.6	0.6	7.2	−0.0	−0.0	−0.1	−0.1	0.1	0.1	−0.1

Table D.10: Input data H1 HERA-II (datasets I+II) used for the combination of the D^{*+} double-differential cross section as a function of Q^2 and y. The table reports for each bin the input differential cross section ($\frac{d^2\sigma}{dQ^2dy}$) together with its statistical (δ_{stat}), uncorrelated (δ_{uncor}) and all correlated (all other $\delta_{...}$) uncertainties.

ZEUS HERA-II (dataset III)																				
Q^2	y	$\frac{d^2\sigma}{dQ^2dy}$	δ_{stat}	δ_{uncor}	δ_{12}	δ_{13}	δ_{14}	δ_{15}	δ_{16}	δ_{17}	δ_{18}	δ_{19}	δ_{20}	δ_{21}	δ_{22}	δ_{24}	δ_{25}	δ_{26}	δ_{27}	δ_{28}
[GeV^2]		[nb/GeV^2]	[%]	[%]	[%]	[%]	[%]	[%]	[%]	[%]	[%]	[%]	[%]	[%]	[%]	[%]	[%]	[%]	[%]	[%]
5.5 : 9.0	0.02 : 0.05	0.099573	23.0	16.6	2.0	−4.2	1.8	12.3	0.0	0.1	0.0	2.5	2.5	2.2	1.9	0.0	−0.2	0.1	0.1	−0.2
5.5 : 9.0	0.05 : 0.09	0.231647	10.0	8.8	2.0	−2.3	5.1	4.0	0.0	−0.8	−0.1	2.4	2.1	−1.6	1.9	0.3	0.1	−0.1	0.1	−0.2
5.5 : 9.0	0.09 : 0.16	0.349456	6.0	4.2	2.0	0.8	4.0	3.4	0.0	−1.5	0.1	2.3	1.8	−2.0	1.9	−0.0	0.4	−0.1	0.1	−0.2
5.5 : 9.0	0.16 : 0.32	0.457092	5.3	4.1	2.0	0.9	2.9	0.9	0.5	−1.8	0.0	2.2	1.8	0.7	1.9	0.1	0.1	0.0	0.1	−0.2
5.5 : 9.0	0.32 : 0.70	0.378328	6.8	3.1	2.0	0.4	1.9	1.7	2.4	−1.5	0.0	2.0	1.9	3.1	1.9	0.3	0.1	0.1	0.1	−0.2
9.0 : 14.0	0.02 : 0.05	0.108000	14.0	7.9	2.0	−4.7	−7.3	11.0	0.0	−0.7	0.1	2.2	2.4	1.4	1.9	−0.0	−0.0	−0.0	0.0	−0.0
9.0 : 14.0	0.05 : 0.09	0.178000	6.5	4.3	2.0	−1.5	−1.9	3.2	0.0	−1.2	0.0	2.2	2.0	−1.6	1.9	−0.0	−0.0	−0.0	0.0	−0.0
9.0 : 14.0	0.09 : 0.16	0.220000	5.8	2.8	2.0	−0.1	−0.3	−0.6	0.0	−1.7	−0.2	2.1	1.7	−2.0	1.9	−0.0	−0.0	−0.0	0.0	−0.0
9.0 : 14.0	0.16 : 0.32	0.352000	5.1	2.1	2.0	0.7	−0.5	−0.5	0.1	−1.9	−0.1	2.1	1.8	0.4	1.9	−0.0	−0.0	−0.0	0.0	−0.0
9.0 : 14.0	0.32 : 0.70	0.307000	7.2	2.0	2.0	−0.5	1.1	−3.8	1.6	−2.0	0.3	1.9	1.8	2.8	1.9	−0.0	−0.0	−0.0	0.0	−0.0
14.0 : 23.0	0.02 : 0.05	0.065100	15.0	7.7	2.0	−2.7	−6.4	11.5	0.0	−0.8	0.2	2.1	2.4	1.7	1.9	−0.0	−0.0	−0.0	0.0	−0.0
14.0 : 23.0	0.05 : 0.09	0.160000	6.4	3.5	2.0	−1.1	−3.8	3.9	0.0	−1.9	0.1	2.1	2.0	−1.7	1.9	−0.0	−0.0	−0.0	0.0	−0.0
14.0 : 23.0	0.09 : 0.16	0.205000	5.6	2.6	2.0	0.4	−0.8	1.3	0.0	−2.3	−0.1	2.0	1.7	−2.0	1.9	−0.0	−0.0	−0.0	0.0	−0.0
14.0 : 23.0	0.16 : 0.32	0.267000	5.9	2.5	2.0	1.3	−0.6	−0.9	0.3	−2.6	0.2	1.9	1.7	0.4	1.9	−0.0	−0.0	−0.0	0.0	−0.0
14.0 : 23.0	0.32 : 0.70	0.249999	7.4	3.9	2.0	0.4	1.7	−2.9	1.9	−2.7	0.2	1.9	1.8	2.9	1.9	−0.0	−0.0	−0.0	0.0	−0.0
23.0 : 45.0	0.02 : 0.05	0.037100	29.0	15.0	2.0	−0.4	−11.5	9.5	0.0	−0.6	−0.3	1.9	2.2	1.7	1.9	−0.0	−0.0	−0.0	0.0	−0.0
23.0 : 45.0	0.05 : 0.09	0.134000	7.0	2.3	2.0	−2.4	−4.8	4.6	0.0	−1.6	−0.3	1.8	1.9	−1.4	1.9	−0.0	−0.0	−0.0	0.0	−0.0
23.0 : 45.0	0.09 : 0.16	0.196000	5.3	1.5	2.0	−0.3	−1.8	1.1	0.0	−1.7	0.3	1.8	1.6	−2.1	1.9	−0.0	−0.0	−0.0	0.0	−0.0
23.0 : 45.0	0.16 : 0.32	0.275000	5.1	1.5	2.0	0.1	0.4	−1.2	0.2	−1.8	0.2	1.8	1.8	0.4	1.9	−0.0	−0.0	−0.0	0.0	−0.0
23.0 : 45.0	0.32 : 0.70	0.283998	6.1	2.8	2.0	0.2	−1.1	−3.5	1.3	−1.7	−0.2	1.8	1.8	2.4	1.9	−0.0	−0.0	−0.0	0.0	−0.0
45.0 : 100.0	0.02 : 0.05	0.014200	38.0	13.9	2.0	−3.4	18.2	26.2	0.0	−2.2	0.0	1.5	2.0	3.5	1.9	−0.0	−0.0	−0.0	0.0	−0.0
45.0 : 100.0	0.05 : 0.09	0.072101	11.6	5.0	2.0	−0.2	−4.0	4.2	0.0	−1.4	0.1	1.5	1.8	−1.6	1.9	−0.0	−0.0	−0.0	0.0	−0.0
45.0 : 100.0	0.09 : 0.16	0.086998	8.4	2.4	2.0	0.0	−2.4	1.1	0.0	−1.9	0.3	1.5	1.5	−2.1	1.9	−0.0	−0.0	−0.0	0.0	−0.0
45.0 : 100.0	0.16 : 0.32	0.182002	5.7	3.4	2.0	0.0	−1.9	−0.7	0.0	−2.3	0.7	1.6	1.5	0.2	1.9	−0.0	−0.0	−0.0	0.0	−0.0
45.0 : 100.0	0.32 : 0.70	0.174996	7.6	3.8	2.0	0.7	−0.8	−3.2	0.9	−2.7	0.7	1.7	1.6	2.9	1.9	−0.0	−0.0	−0.0	0.0	−0.0
100.0 : 158.0	0.02 : 0.32	0.074570	11.0	5.2	2.0	−0.2	−4.4	1.7	−0.2	−1.3	0.0	1.3	1.4	−0.2	1.9	−0.2	−0.2	0.0	0.0	−0.0
100.0 : 158.0	0.32 : 0.70	0.051533	16.0	5.6	2.0	0.4	−2.5	−5.3	1.1	−1.3	3.2	1.4	1.5	2.9	1.9	−0.1	−0.1	−0.1	0.0	−0.1
158.0 : 251.0	0.02 : 0.30	0.049788	14.0	3.8	2.0	0.6	−4.3	0.8	0.1	−0.9	1.0	1.2	1.3	0.1	1.9	−0.0	−0.0	−0.0	0.0	−0.0
158.0 : 251.0	0.30 : 0.70	0.037312	17.0	4.0	2.0	0.5	0.6	−2.6	1.0	−1.0	0.7	1.4	1.4	3.0	1.9	−0.0	−0.0	−0.0	0.0	−0.0
251.0 : 1000.0	0.02 : 0.26	0.026341	24.0	7.3	2.0	−1.0	−5.9	2.2	0.0	0.1	1.3	1.2	1.3	−0.3	1.9	−0.3	−0.3	−0.1	0.1	0.1
251.0 : 1000.0	0.26 : 0.70	0.049167	21.0	5.8	2.0	−0.5	−3.8	−4.3	1.4	−1.0	0.1	1.4	1.4	0.9	1.9	−0.1	−0.1	0.1	0.1	−0.1

Table D.11: Input data ZEUS HERA-II (dataset III) used for the combination of the D^{*+} double-differential cross section as a function of Q^2 and y. The table reports for each bin the input differential cross section ($\frac{d^2\sigma}{dQ^2dy}$) together with its statistical (δ_{stat}), uncorrelated (δ_{unc}) and all correlated (all other $\delta_{...}$) uncertainties.

ZEUS 9800 (dataset IV)										
Q^2	y	$\frac{d^2\sigma}{dQ^2dy}$	δ_{stat}	δ_{uncor}	δ_{23}	δ_{24}	δ_{25}	δ_{26}	δ_{27}	δ_{28}
[GeV^2]		[nb/GeV^2]	[%]	[%]	[%]	[%]	[%]	[%]	[%]	[%]
1.5 : 3.5	0.02 : 0.09	0.654477	7.4	10.7	2.2	−0.0	0.0	0.0	0.0	−0.0
1.5 : 3.5	0.09 : 0.16	0.755615	6.6	9.2	2.2	−0.2	0.3	0.1	0.2	−0.2
1.5 : 3.5	0.16 : 0.32	0.940910	8.3	8.8	2.2	−0.3	0.6	−0.1	0.1	0.1
1.5 : 3.5	0.32 : 0.70	0.687336	11.1	17.4	2.2	−0.1	0.2	−0.0	0.1	−0.0
3.5 : 5.5	0.02 : 0.09	0.305303	6.8	9.1	2.2	0.8	−0.7	−0.2	0.1	0.3
3.5 : 5.5	0.09 : 0.16	0.271557	6.5	4.6	2.2	−0.3	−0.7	0.2	0.2	0.3
3.5 : 5.5	0.16 : 0.32	0.342211	9.0	18.2	2.2	−0.6	0.4	−0.3	0.4	0.1
3.5 : 5.5	0.32 : 0.70	0.258784	12.1	8.4	2.2	−0.3	−0.1	0.1	0.2	0.5
5.5 : 9.0	0.32 : 0.70	0.296152	10.3	16.1	2.2	0.5	−1.6	0.2	0.2	0.7
9.0 : 14.0	0.09 : 0.16	0.187517	7.0	4.6	2.2	−0.3	0.4	−0.1	0.2	−0.2
9.0 : 14.0	0.16 : 0.32	0.312658	9.6	14.2	2.2	−0.8	1.4	−0.1	0.3	−0.2
9.0 : 14.0	0.32 : 0.70	0.265379	13.8	10.9	2.2	−0.2	0.4	−0.1	0.2	−0.2
14.0 : 23.0	0.09 : 0.16	0.171290	6.1	8.7	2.2	−0.2	−0.1	0.3	0.4	0.3
14.0 : 23.0	0.16 : 0.32	0.234964	11.0	24.8	2.2	−0.6	0.8	−0.1	0.4	−0.4
14.0 : 23.0	0.32 : 0.70	0.177335	16.9	23.1	2.2	−0.4	0.6	0.2	0.3	−0.4
23.0 : 45.0	0.05 : 0.09	0.097058	7.1	8.8	2.2	2.4	0.3	0.1	0.6	0.1
23.0 : 45.0	0.09 : 0.16	0.159526	6.9	5.1	2.2	−0.6	−0.5	−0.1	0.1	−0.2
23.0 : 45.0	0.16 : 0.32	0.265285	7.8	8.6	2.2	−0.8	0.7	0.3	0.2	−0.3
23.0 : 45.0	0.32 : 0.70	0.252602	11.5	9.2	2.2	−0.4	0.7	−0.0	0.2	−0.2
45.0 : 100.0	0.16 : 0.32	0.149621	9.8	14.8	2.2	0.3	0.1	0.2	0.1	0.1
45.0 : 100.0	0.32 : 0.70	0.129460	14.2	20.3	2.2	0.4	−0.5	0.1	0.1	−0.1
100.0 : 158.0	0.02 : 0.32	0.083083	11.3	13.9	2.2	0.2	0.4	0.1	0.1	0.3
100.0 : 158.0	0.32 : 0.70	0.032379	23.3	22.4	2.2	0.5	0.5	0.4	0.1	0.2
251.0 : 1000.0	0.02 : 0.26	0.037960	22.0	13.0	2.2	0.7	−0.2	−0.2	0.6	0.2
251.0 : 1000.0	0.26 : 0.70	0.052195	18.4	18.6	2.2	0.3	−0.3	−0.1	0.3	0.1

Table D.12: Input data ZEUS 98–00 (dataset IV) used for the combination of the D^{*+} double-differential cross section as a function of Q^2 and y. The table reports for each bin the input differential cross section ($\frac{d^2\sigma}{dQ^2dy}$) together with its statistical (δ_{stat}), uncorrelated (δ_{uncor}) and all correlated (all other $\delta_{...}$) uncertainties.

Descriptor	Dataset	Name	Type	Reference	$\frac{d\sigma}{dQ^2}$		$\frac{d\sigma}{dy}$		$\frac{d\sigma}{dp_T(D^{*+})}$		$\frac{d\sigma}{d\eta(D^{*+})}$		$\frac{d\sigma}{dz(D^{*+})}$		$\frac{d^2\sigma}{dQ^2dy}$	
					sh	red	sh	red	sh	red	sh	red	sh	red	sh	red
δ_1	I,II	H1 CJC efficiency	S	H1 Col.	0.8	0.9	0.3	0.9	0.5	0.9	0.5	0.9	0.4	0.9	0.6	0.8
δ_2	I,II	H1 luminosity	N	H1 Col.	0.5	0.9	0.4	0.9	0.6	0.9	0.6	0.9	0.4	0.9	0.1	0.9
δ_3	I,II	H1 MC PDF	S	H1 Col.	0.1	1.0	0.1	1.0	0.2	1.0	0.2	1.0	0.1	1.0	0.0	1.0
δ_4	I,II	H1 electron energy	S	H1 Col.	0.2	1.0	0.0	1.0	0.0	1.0	0.0	1.0	0.7	0.9	0.0	0.8
δ_5	I,II	H1 electron polar angle	S	H1 Col.	0.2	1.0	0.1	1.0	0.1	1.0	0.2	1.0	0.2	1.0	0.3	0.9
δ_6	I,II	H1 hadronic en. scale	S	H1 Col.	0.1	1.0	0.2	0.9	0.0	1.0	0.0	1.0	-1.0	0.7	0.0	1.0
δ_7	II	H1 frag. thres., high Q^2	S	H1 Col.	0.0	1.0									0.0	1.0
δ_8	I,II	H1 alternat. MC model	S	H1 Col.	0.4	0.9	0.4	0.9	0.1	1.0	0.0	1.0	−1.0	0.8	1.2	0.7
δ_9	I,II	H1 alternat. MC frag.	S	H1 Col.	0.0	1.0	0.0	1.0	0.0	1.0	−0.1	1.0	0.2	1.0	0.3	0.9
δ_{10}	I,II	H1 frag. thresh.	S	H1 Col.	0.0	1.0	−0.4	0.9	0.2	1.0	0.0	1.0	0.6	0.9	0.2	0.8
δ_{11}	I	H1 high Q^2 uncertainty	N	[64]			0.1	1.0	0.0	0.9	0.1	1.0	0.1	1.0		
δ_{12}	III	ZEUS hadron. en. scale	S	[137]	0.0	1.0	−0.1	0.8	0.0	1.0	0.0	1.0	−0.9	0.9	−0.5	0.7
δ_{13}	III	ZEUS electron en. scale	S	[137]	0.1	0.9	0.2	0.9	0.0	1.0	0.2	1.0	0.0	1.0	0.4	0.7
δ_{14}	III	ZEUS $p_T(\pi_s$ correction	S	[137]	−0.1	1.0	−0.1	1.0	−0.1	1.0	−0.3	1.0	0.0	1.0	−0.7	0.9
δ_{15}	III	ZEUS $M(K\pi)$ cut var.	S	[137]	−0.3	0.8	−0.7	0.8	0.4	0.6	−0.3	0.7	0.5	0.8	−0.7	0.9
δ_{16}	III	ZEUS track. efficiency	S	[137]	−0.2	0.9	−0.4	0.9	−0.4	0.9	−0.2	0.9	−0.2	0.9	−0.7	1.0
δ_{17}	III	ZEUS b MC norm.	S	[137]	0.0	1.0	0.0	1.0	0.0	1.0	0.0	1.0	0.1	1.0	0.0	1.0
δ_{18}	III	ZEUS PHP MC norm.	S	[137]	0.0	1.0	−0.1	1.0	0.0	1.0	−0.1	1.0	0.1	1.0	−0.3	1.0
δ_{19}	III	ZEUS diffr. MC norm.	S	[137]	0.0	1.0	0.1	0.9	0.2	1.0	0.0	1.0	0.0	1.0	0.7	0.9
δ_{20}	III	ZEUS MC rew. p_T, Q^2	S	[137]	0.3	0.9	0.0	1.0	−0.1	1.0	0.0	1.0	0.0	1.0	0.6	0.9
δ_{21}	III	ZEUS MC rew. η	S	[137]	0.0	1.0	0.0	0.8	−0.2	1.0	−0.3	1.0	−0.2	1.0	0.4	0.8
δ_{22}	III	ZEUS lum. (HERA-II)	N	[137]	−0.2	1.0	−0.1	1.0	−0.2	1.0	−0.2	1.0	−0.1	1.0	−0.7	0.9
δ_{23}	IV	ZEUS lum. (98-00)	N	[136]											0.8	0.9
δ_{24}	I-IV	Theory m_c variation	T	Theory											0.0	1.0
δ_{25}	I-IV	Theory μ_r, μ_f variation	T	Theory											0.0	1.0
δ_{26}	I-IV	Theory α_s variation	T	Theory											0.0	1.0
δ_{27}	I-IV	Theory longitud. frag.	T	Theory											0.1	1.0
δ_{28}	I-IV	Theory transverse frag.	T	Theory											0.0	1.0

Table D.13: Sources of bin-to-bin correlated uncertainties considered in the combination of the visible D^{*+} cross sections. For each source the affected datasets, name, type (see Section 6.2.2) and reference to the place, where information can be found, are given, together with the shift (sh) and reduction factor (red) in the combination obtained after the first iteration. For sources which do not affect the combination of a given differential cross section, no shifts and reductions are quoted.

$p_T(D^{*+})$ [GeV]	$\frac{d\sigma}{dp_T(D^{*+})}$ [nb/GeV]	δ_{unc} [%]	δ_1 [%]	δ_2 [%]	δ_3 [%]	δ_4 [%]	δ_5 [%]	δ_6 [%]	δ_7 [%]	δ_8 [%]	δ_9 [%]	δ_{10} [%]	δ_{11} [%]	δ_{12} [%]	δ_{13} [%]	δ_{14} [%]	δ_{15} [%]	δ_{16} [%]	δ_{17} [%]	δ_{18} [%]	δ_{19} [%]	δ_{20} [%]	δ_{21} [%]	δ_{22} [%]	δ_{br} [%]
1.50 : 1.88	2.358	6.4	−0.4	0.8	0.8	−1.0	0.4	0.0	−1.8	0.3	0.1	−1.0	0.6	1.0	−0.1	0.7	0.6	−0.4	−1.4	0.2	−0.5	−0.8	−2.7	0.4	1.5
1.88 : 2.28	2.227	4.8	−0.5	0.5	0.7	−0.9	0.3	0.0	−1.9	0.3	0.2	−1.0	0.6	0.8	−0.2	0.6	0.5	−0.4	−1.0	0.5	−0.3	−0.4	−2.1	0.3	1.5
2.28 : 2.68	1.984	3.7	−0.4	0.6	0.5	−0.9	0.3	0.0	−1.9	0.3	0.2	−1.0	0.7	1.0	−0.1	0.7	0.4	−0.3	−0.9	0.5	−0.5	−0.0	−1.7	0.6	1.5
2.68 : 3.08	1.559	3.5	−0.4	0.6	0.5	−0.8	0.3	0.0	−1.9	0.3	0.2	−1.0	0.6	1.0	−0.2	0.7	0.4	−0.8	−0.5	0.2	−0.2	0.2	−0.9	0.4	1.5
3.08 : 3.50	1.209	3.6	−0.4	0.6	0.5	−0.8	0.3	0.0	−1.8	0.2	0.1	−0.9	0.7	1.1	−0.3	0.5	0.3	−0.4	−0.4	0.3	−0.1	0.1	−0.7	0.3	1.5
3.50 : 4.00	0.9328	3.2	−0.4	0.7	0.3	−0.8	0.3	0.0	−1.7	0.2	0.0	−0.9	0.7	1.0	−0.2	0.6	0.3	−0.4	−0.3	0.0	−0.2	0.1	−0.7	0.4	1.5
4.00 : 4.75	0.6161	3.0	−0.4	0.6	0.3	−0.7	0.3	0.0	−1.7	0.1	−0.0	−0.9	0.8	1.1	−0.1	0.5	0.5	−0.4	−0.2	0.4	0.0	0.6	0.6	0.0	1.5
4.75 : 6.00	0.3204	3.0	−0.4	0.6	0.3	−0.7	0.3	0.0	−1.6	0.1	−0.1	−0.9	0.8	1.0	−0.2	0.6	0.3	−0.3	−0.0	0.1	−0.2	0.5	−0.4	0.3	1.5
6.00 : 8.00	0.1152	3.8	−0.3	0.7	0.2	−0.6	0.2	0.0	−1.6	0.1	−0.0	−0.9	0.6	1.1	−0.2	0.5	0.2	−0.0	−0.2	0.4	0.5	1.3	1.0	−0.3	1.5
8.00 : 11.00	0.03334	5.3	−0.3	0.7	0.3	−0.7	0.3	0.0	−1.5	0.1	−0.1	−0.9	0.7	1.0	−0.1	0.1	0.4	0.5	−0.3	−0.1	−0.6	1.4	−1.1	0.2	1.5
11.00 : 20.00	0.003819	10.3	−0.3	0.6	0.5	−0.8	0.4	0.0	−1.4	0.1	−0.0	−0.8	0.5	1.1	0.1	0.1	0.1	0.7	0.2	−1.6	−0.6	0.8	−5.1	1.4	1.5

$\eta(D^{*+})$	$\frac{d\sigma}{d\eta(D^{*+})}$ [nb]	δ_{unc} [%]	δ_1 [%]	δ_2 [%]	δ_3 [%]	δ_4 [%]	δ_5 [%]	δ_6 [%]	δ_7 [%]	δ_8 [%]	δ_9 [%]	δ_{10} [%]	δ_{11} [%]	δ_{12} [%]	δ_{13} [%]	δ_{14} [%]	δ_{15} [%]	δ_{16} [%]	δ_{17} [%]	δ_{18} [%]	δ_{19} [%]	δ_{20} [%]	δ_{21} [%]	δ_{22} [%]	δ_{br} [%]
−1.50 : −1.25	1.360	5.8	1.1	1.2	−0.5	−1.1	−0.9	−0.0	−0.6	−0.5	0.3	−0.2	−0.3	−0.0	−0.1	0.1	0.6	0.6	−0.9	−0.9	1.2	−2.5	−0.6	−0.1	1.5
−1.25 : −1.00	1.515	4.6	1.0	1.3	−0.4	−0.9	−0.7	−0.0	−0.4	−0.5	0.4	−0.2	−0.3	−0.2	0.4	0.5	0.7	0.8	−0.7	−1.1	0.9	−1.9	−0.8	0.0	1.5
−1.00 : −0.75	1.587	4.6	1.0	1.3	−0.4	−0.9	−0.7	−0.0	−0.4	−0.5	0.5	−0.3	−0.3	−0.2	0.4	0.7	0.7	0.6	−1.0	−1.1	0.8	−1.6	−1.3	0.0	1.5
−0.75 : −0.50	1.789	3.8	1.1	1.3	−0.3	−1.0	−0.6	−0.0	−0.4	−0.5	0.4	−0.2	−0.3	−0.1	0.2	0.4	0.5	0.4	−0.7	−0.7	0.6	−1.7	−0.6	0.2	1.5
−0.50 : −0.25	1.833	3.8	1.1	1.2	−0.3	−1.0	−0.6	−0.0	−0.3	−0.6	0.3	−0.1	−0.2	−0.1	0.1	0.3	0.5	0.2	−0.6	−0.7	0.5	−1.6	0.3	−0.0	1.5
−0.25 : 0.00	1.887	3.8	1.2	1.3	−0.2	−1.0	−0.5	−0.0	−0.3	−0.5	0.4	−0.1	−0.2	−0.1	0.0	0.2	0.6	0.4	−0.7	−0.6	0.9	−1.4	−1.5	0.3	1.5
0.00 : 0.25	1.857	4.0	1.2	1.3	−0.2	−1.0	−0.5	−0.0	−0.3	−0.6	0.4	−0.1	−0.1	−0.1	0.0	−0.0	0.1	0.4	−0.3	−0.5	0.5	−1.6	1.0	−0.1	1.5
0.25 : 0.50	1.879	4.0	1.1	1.3	−0.2	−1.0	−0.5	−0.0	−0.2	−0.5	0.5	−0.1	−0.1	−0.1	0.2	0.1	0.5	0.7	−0.6	−0.5	0.8	−1.4	−1.4	0.3	1.5
0.50 : 0.75	1.909	4.1	1.1	1.3	−0.2	−1.0	−0.5	−0.0	−0.3	−0.5	0.5	−0.1	−0.1	−0.1	0.2	0.3	0.5	0.4	−0.8	−0.6	0.5	−1.6	−0.9	0.2	1.5
0.75 : 1.00	1.920	4.3	1.1	1.3	−0.2	−1.0	−0.5	−0.0	−0.3	−0.5	0.4	−0.1	−0.1	−0.1	0.2	0.3	0.4	0.8	−1.3	−0.6	0.6	−1.8	−1.6	0.2	1.5
1.00 : 1.25	2.075	4.7	1.1	1.3	−0.2	−0.9	−0.5	−0.0	−0.3	−0.6	0.4	−0.2	−0.1	−0.2	0.2	0.2	0.7	0.7	−1.0	−0.4	0.3	−2.3	1.3	−0.3	1.5
1.25 : 1.50	1.813	6.3	1.0	1.4	−0.3	−0.9	−0.5	−0.0	−0.3	−0.5	0.4	−0.2	−0.2	−0.2	0.4	0.6	0.7	0.7	−1.4	−1.3	0.4	−2.0	−2.5	0.2	1.5

Table D.14: The combined single-differential D^{*+} cross sections as a function of $p_T(D^{*+})$ and $\eta(D^{*+})$, with their uncorrelated (δ_{unc}), correlated (δ_1 to δ_{22}) and external branching-ratio (δ_{br}) uncertainties.

$z(D^{*+})$	$\frac{d\sigma}{dz(D^{*+})}$	δ_{unc}	δ_1	δ_2	δ_3	δ_4	δ_5	δ_6	δ_7	δ_8	δ_9	δ_{10}	δ_{11}	δ_{12}	δ_{13}	δ_{14}	δ_{15}	δ_{16}	δ_{17}	δ_{18}	δ_{19}	δ_{20}	δ_{21}	δ_{22}	δ_{br}
	[nb]	[%]	[%]	[%]	[%]	[%]	[%]	[%]	[%]	[%]	[%]	[%]	[%]	[%]	[%]	[%]	[%]	[%]	[%]	[%]	[%]	[%]	[%]	[%]	[%]
0.000 : 0.100	3.277	9.5	1.7	1.9	−0.0	1.1	0.5	−1.0	1.0	0.5	−0.9	0.4	0.2	0.7	0.1	0.1	−0.1	−1.1	3.4	−2.0	1.1	−1.3	0.7	0.6	1.5
0.100 : 0.200	7.346	4.8	1.8	1.2	−0.2	1.1	0.2	−1.0	0.8	0.4	−0.7	0.1	0.3	0.7	0.4	0.1	0.3	−1.4	2.5	−1.5	2.9	−2.9	0.9	0.8	1.5
0.200 : 0.325	8.612	3.5	2.0	1.0	−0.1	0.9	0.2	−0.6	0.6	0.5	−0.2	0.1	0.3	0.5	0.6	0.1	0.3	−1.2	2.0	0.3	0.9	−2.0	0.6	0.5	1.5
0.325 : 0.450	8.918	2.7	2.1	1.0	−0.1	0.9	0.2	−0.4	0.4	0.5	−0.0	0.0	0.4	0.4	0.6	−0.0	0.3	−0.7	1.6	1.2	−0.7	−0.3	0.0	0.3	1.5
0.450 : 0.575	8.827	1.8	2.3	1.2	0.0	0.8	0.4	−0.0	0.3	0.5	0.3	0.0	0.4	0.3	0.4	−0.1	0.3	−0.4	0.7	1.6	0.9	−0.1	−0.1	0.8	1.5
0.575 : 0.800	4.785	2.4	2.2	1.4	0.1	0.9	0.6	−0.0	0.6	0.5	0.2	0.1	0.6	0.4	0.1	−0.1	0.2	0.8	−0.5	2.5	2.5	0.4	−0.5	0.7	1.5
0.800 : 1.000	0.6308	8.1	1.6	0.8	−0.3	2.4	1.0	−1.5	1.5	0.2	−1.3	−0.2	1.3	1.0	−0.3	−0.1	0.9	3.8	−2.8	3.8	4.4	4.0	3.1	−0.4	1.5
Q^2	$\frac{d\sigma}{dQ^2}$	δ_{unc}	δ_1	δ_2	δ_3	δ_4	δ_5	δ_6	δ_7	δ_8	δ_9	δ_{10}	δ_{11}	δ_{12}	δ_{13}	δ_{14}	δ_{15}	δ_{16}	δ_{17}	δ_{18}	δ_{19}	δ_{20}	δ_{21}	δ_{22}	δ_{br}
[GeV^2]	[nb/GeV^2]	[%]	[%]	[%]	[%]	[%]	[%]	[%]	[%]	[%]	[%]	[%]	[%]	[%]	[%]	[%]	[%]	[%]	[%]	[%]	[%]	[%]	[%]	[%]	[%]
5 : 8	0.4735	4.0	1.4	−1.4	−0.9	0.9	−0.9	0.6	−0.9	−0.3	1.1	−0.2	0.9	−1.3	0.7	0.7	0.8	1.5	−1.0	−0.6	0.7	−2.1	−1.2	0.3	1.5
8 : 10	0.2964	4.3	1.2	−1.3	−0.7	0.7	−1.0	0.8	−0.6	−0.4	1.0	0.0	0.8	−1.0	0.7	0.4	1.1	1.1	−0.2	−0.1	−0.1	0.5	−0.5	−0.1	1.5
10 : 13	0.2117	3.8	0.8	−1.9	−0.8	0.8	−0.6	0.8	−0.5	−0.6	1.0	−0.1	0.6	−0.6	0.4	−0.1	0.9	1.0	−0.9	0.7	−0.3	−1.2	−0.5	0.4	1.5
13 : 19	0.1236	3.2	0.8	−1.8	−0.8	0.8	−0.7	0.8	−0.4	−0.7	1.0	−0.1	0.6	−0.6	0.6	0.0	0.8	0.8	−0.0	0.0	−1.0	−0.9	−0.3	0.5	1.5
19 : 28	0.07263	3.5	0.8	−1.8	−0.7	0.7	−0.7	0.8	−0.3	−0.7	0.9	−0.1	0.6	−0.6	0.5	0.2	0.7	0.7	−0.0	0.2	−0.9	−0.6	−0.3	0.4	1.5
28 : 40	0.03970	3.7	0.7	−1.9	−0.8	0.8	−0.6	0.8	−0.3	−0.8	1.0	−0.2	0.5	−0.5	0.3	0.0	0.8	0.6	−0.6	0.5	−0.7	−1.7	−0.3	0.6	1.5
40 : 60	0.01635	4.4	0.7	−2.0	−0.8	0.8	−0.5	0.7	−0.3	−0.7	0.8	−0.3	0.6	−0.4	0.6	−0.4	0.5	0.9	0.5	−0.0	−1.5	−2.6	−0.6	0.7	1.5
60 : 100	0.007445	5.2	0.8	−1.9	−0.8	0.9	−0.5	0.7	−0.4	−0.6	0.9	−0.3	0.6	−0.4	0.7	−0.3	0.1	0.2	0.2	0.9	−1.6	−0.4	0.3	−0.0	1.5
100 : 158	0.002081	7.2	0.1	−2.3	−0.4	−0.6	−0.8	0.3	−0.2	−0.8	1.0	0.0	0.6	−0.0	−0.4	−1.3	0.7	0.8	−1.6	1.8	−2.5	−0.8	−1.3	−0.5	1.5
158 : 251	0.0008817	7.6	0.3	−1.8	−0.5	−0.4	−0.9	0.2	−0.4	−0.8	1.1	−0.0	0.7	−0.3	−0.0	−1.0	1.1	0.0	−0.2	2.1	−2.1	−0.8	−2.0	−0.6	1.5
251 : 1000	0.0000749	11.4	−0.1	−2.3	−0.6	−0.4	−0.5	0.2	−0.2	−0.9	0.9	−0.0	0.6	0.6	0.2	−1.6	0.3	−0.1	0.5	3.7	−2.9	−0.6	−3.1	−0.9	1.5
y	$\frac{d\sigma}{dy}$	δ_{unc}	δ_1	δ_2	δ_3	δ_4	δ_5	δ_6	δ_7	δ_8	δ_9	δ_{10}	δ_{11}	δ_{12}	δ_{13}	δ_{14}	δ_{15}	δ_{16}	δ_{17}	δ_{18}	δ_{19}	δ_{20}	δ_{21}	δ_{22}	δ_{br}
	[nb]	[%]	[%]	[%]	[%]	[%]	[%]	[%]	[%]	[%]	[%]	[%]	[%]	[%]	[%]	[%]	[%]	[%]	[%]	[%]	[%]	[%]	[%]	[%]	[%]
0.02 : 0.05	12.13	5.8	−0.6	0.6	−0.2	0.8	1.0	−0.6	−0.1	1.4	1.0	−0.1	0.0	−2.3	−0.2	0.8	−2.6	−0.7	5.4	4.8	2.7	1.4	0.4	−0.6	1.5
0.05 : 0.09	18.84	3.9	−1.3	1.5	0.2	0.4	1.0	0.4	−0.2	−0.1	−0.2	−0.2	−0.4	−1.9	−0.8	0.1	0.2	−0.7	1.6	0.4	2.2	−0.7	0.7	0.2	1.5
0.09 : 0.13	16.99	3.4	−1.3	1.7	0.2	0.4	0.8	0.8	−0.3	−0.5	−0.6	−0.1	−0.7	−1.7	−0.9	−0.2	0.4	−0.9	0.7	−0.3	1.9	−0.7	−0.1	0.7	1.5
0.13 : 0.18	13.35	3.7	−1.2	1.3	0.2	0.4	0.9	0.7	−0.4	0.1	−0.2	0.0	−0.6	−1.9	−0.7	0.0	0.4	−0.4	−0.5	0.1	1.4	−1.8	−0.0	0.5	1.5
0.18 : 0.26	11.19	3.4	−1.4	1.5	0.0	0.5	0.6	0.9	−0.4	−0.2	−0.5	0.1	−0.8	−1.7	−0.8	−0.3	0.2	−0.5	−0.2	−0.2	0.2	0.6	−0.2	0.3	1.5
0.26 : 0.36	7.649	3.7	−1.4	1.5	0.4	0.2	0.7	1.0	−0.5	−0.1	−0.5	0.0	−0.7	−1.9	−0.7	−0.4	1.0	−1.0	−0.5	−1.0	0.5	−0.1	−0.3	0.4	1.5
0.36 : 0.50	4.783	4.0	−1.7	1.7	0.6	0.2	0.7	1.1	−0.5	−0.6	−0.7	−0.1	−0.7	−1.8	−0.7	−0.6	2.1	−0.2	−0.4	−2.4	0.8	−0.2	−0.7	0.7	1.5
0.50 : 0.70	2.648	5.6	−2.2	1.7	0.9	−0.4	0.2	0.8	−0.4	−0.4	−1.0	−0.6	−0.5	−2.1	−0.5	−0.8	2.8	−0.4	0.3	−2.8	−1.4	1.7	−0.9	0.3	1.5

Table D.15: The combined single-differential D^{*+} cross sections as a function of $z(D^{*+})$, Q^2 and y, with their uncorrelated (δ_{unc}), correlated (δ_1 to δ_{22}) and external branching-ratio (δ_{br}) uncertainties.

Q^2 [GeV^2]	y	$\frac{d^2\sigma}{dQ^2dy}$ [nb/GeV^2]	δ_{unc} [%]	δ_1 [%]	δ_2 [%]	δ_3 [%]	δ_4 [%]	δ_5 [%]	δ_6 [%]	δ_7 [%]	δ_8 [%]	δ_9 [%]	δ_{10} [%]	δ_{11} [%]	δ_{12} [%]	δ_{13} [%]	δ_{14} [%]	δ_{15} [%]	δ_{16} [%]	δ_{17} [%]	δ_{18} [%]	δ_{19} [%]	δ_{20} [%]	δ_{21} [%]	δ_{22} [%]	δ_{23} [%]	δ_{24} [%]	δ_{25} [%]	δ_{26} [%]	δ_{27} [%]	δ_{28} [%]	δ_{br} [%]
1.5 : 3.5	0.02 : 0.09	4.761	12.9	0.0	−1.6	0.0	0.0	−0.1	−0.1	−0.1	−0.1	−0.2	0.1	0.8	0.0	0.1	0.3	−0.2	−0.0	−0.0	0.	50.0	−0.2	0.1	−0.0	0.1	−0.5	0.5	−0.3	0.0	0.0	1.5
1.5 : 3.5	0.09 : 0.16	5.498	11.3	0.0	−1.6	0.0	0.0	−0.1	−0.2	0.1	0.1	−0.2	0.1	0.7	−0.1	0.1	0.3	−0.3	0.3	0.2	0.5	0.0	−0.2	0.1	−0.0	0.1	−0.5	0.6	−0.3	0.0	0.0	1.5
1.5 : 3.5	0.16 : 0.32	2.994	12.0	0.0	−1.6	0.0	0.0	−0.1	−0.1	0.0	−0.3	−0.2	−0.1	0.7	−0.2	0.1	0.3	−0.3	0.4	0.3	0.5	0.0	−0.3	0.1	−0.0	0.1	−0.5	0.6	−0.3	0.0	0.0	1.5
1.5 : 3.5	0.32 : 0.70	0.9211	20.5	0.0	−1.6	0.0	0.0	−0.1	−0.2	0.0	−0.1	−0.2	0.0	0.7	−0.1	0.1	0.3	−0.2	0.1	0.1	0.5	0.0	−0.2	0.1	−0.0	0.1	−0.5	0.5	−0.3	0.0	0.0	1.5
3.5 : 5.5	0.02 : 0.09	2.2219	11.3	0.0	−1.6	0.0	0.0	−0.1	−0.1	0.1	−0.2	−0.2	0.2	0.8	0.3	−0.0	0.3	0.1	−0.5	−0.8	0.7	0.0	−0.0	0.0	−0.1	0.0	−0.5	0.5	−0.3	0.0	0.0	1.5
3.5 : 5.5	0.09 : 0.16	1.9759	7.9	0.0	−1.6	0.0	0.0	−0.1	−0.2	0.2	0.1	−0.1	−0.2	0.8	0.3	0.3	0.4	−0.2	−0.7	0.1	0.4	−0.0	−0.2	0.1	−0.0	0.1	−0.5	0.5	−0.3	0.0	0.0	1.5
3.5 : 5.5	0.16 : 0.32	1.0890	20.2	0.0	−1.6	0.0	0.0	−0.1	−0.2	0.4	−0.4	−0.2	−0.0	0.7	−0.2	0.2	0.3	−0.4	0.2	0.5	0.4	−0.0	−0.3	0.1	0.0	0.1	−0.5	0.6	−0.3	0.0	0.0	1.5
3.5 : 5.5	0.32 : 0.70	0.3468	14.6	0.0	−1.6	0.0	0.0	−0.1	−0.1	0.2	−0.2	−0.1	−0.4	0.8	0.1	0.2	0.4	−0.2	−0.2	0.1	0.5	−0.0	−0.2	0.1	−0.0	0.1	−0.5	0.5	−0.3	0.0	0.0	1.5
5.5 : 9.0	0.02 : 0.05	1.057	12.3	0.0	−1.6	0.0	0.0	−0.1	−0.4	0.3	0.3	−0.5	0.1	0.5	−0.0	−0.4	−0.2	0.6	−0.2	−0.0	0.0	−0.0	−0.3	0.4	1.5	0.5	2.6	0.8	1.5	0.4	−1.0	1.5
5.5 : 9.0	0.05 : 0.09	1.461	7.8	0.0	−1.6	0.0	0.0	−0.1	−0.3	0.3	0.1	−0.2	0.3	0.8	−0.1	−0.3	0.0	0.4	0.2	−0.2	0.0	−0.6	−0.3	−0.7	0.8	−0.6	2.5	0.1	0.9	0.6	−1.0	1.5
5.5 : 9.0	0.09 : 0.16	1.317	5.4	0.0	−1.6	0.0	0.0	−0.1	−0.2	0.3	−0.0	−0.3	0.2	0.8	−0.0	0.2	0.2	−0.3	0.5	0.1	0.5	0.5	−1.3	−1.3	−0.2	−0.7	2.6	−0.5	0.6	−0.3	−0.7	1.5
5.5 : 9.0	0.16 : 0.32	0.7733	4.9	0.0	−1.6	0.0	0.0	−0.1	−0.2	0.2	0.1	−0.3	0.1	0.7	0.1	0.1	0.1	−0.3	0.2	0.2	0.9	0.3	−0.4	−0.8	−0.8	−0.0	2.2	−0.7	0.9	0.3	−0.8	1.5
5.5 : 9.0	0.32 : 0.70	0.2509	5.6	0.0	−1.6	0.0	0.0	−0.2	−0.2	0.2	0.1	−0.2	0.0	0.8	0.7	−0.1	−0.0	−0.5	0.4	0.1	0.6	0.3	0.1	−0.5	−1.9	1.4	1.6	−1.1	0.5	−0.8	−0.6	1.5
9.0 : 14.0	0.02 : 0.05	0.5201	13.0	0.0	−1.6	0.0	0.0	−0.1	−0.3	0.2	0.1	−0.9	−0.1	0.3	0.0	−1.0	−0.4	1.2	−0.2	−0.6	−0.6	0.6	−2.4	0.9	4.0	1.6	1.6	0.8	2.5	−0.0	−0.2	1.5
9.0 : 14.0	0.05 : 0.09	0.7677	6.6	0.0	−1.6	0.0	0.0	−0.1	−0.2	0.2	0.0	−0.3	0.1	0.8	−0.0	0.1	0.1	−0.0	0.1	−0.3	0.3	−0.2	−1.0	−0.3	1.0	−0.4	1.6	−0.2	2.1	−0.1	−0.4	1.5
9.0 : 14.0	0.09 : 0.16	0.5686	4.6	0.0	−1.6	0.0	0.0	−0.1	−0.2	0.2	−0.0	−0.2	0.1	0.8	−0.1	0.2	0.3	−0.4	0.2	0.0	0.4	−0.2	−0.4	−0.1	0.1	−0.7	0.6	−0.7	0.7	0.1	−0.2	1.5
9.0 : 14.0	0.16 : 0.32	0.4121	4.6	0.0	−1.6	0.0	0.0	−0.1	−0.2	0.1	−0.0	−0.3	−0.1	0.7	−0.4	0.0	0.1	−0.4	0.1	0.2	0.5	0.3	0.3	0.1	−0.5	0.2	0.9	−1.3	0.8	−0.1	−0.1	1.5
9.0 : 14.0	0.32 : 0.70	0.1506	5.6	0.0	−1.6	0.0	0.0	−0.1	−0.2	0.1	−0.0	−0.2	−0.0	0.7	0.1	0.1	0.3	−0.4	0.3	0.3	0.4	−0.7	0.4	−0.1	−1.9	1.1	0.6	−2.0	0.2	0.0	−0.4	1.5
14.0 : 23.0	0.02 : 0.05	0.2289	11.4	0.0	−1.6	0.0	0.0	−0.1	−0.4	0.2	0.0	−0.4	0.1	0.9	−0.2	−1.0	−0.4	1.3	−0.2	−0.2	−1.3	0.4	0.1	−1.0	4.0	1.3	1.5	1.2	2.3	−0.3	0.1	1.5
14.0 : 23.0	0.05 : 0.09	0.3779	6.5	0.0	−1.6	0.0	0.0	−0.1	−0.3	0.2	0.0	−0.4	0.0	0.9	0.1	−0.2	0.2	0.2	0.1	−0.1	0.3	0.3	−0.5	0.3	1.4	−0.3	1.3	−0.2	2.5	−0.5	−0.2	1.5
14.0 : 23.0	0.09 : 0.16	0.2902	4.8	0.0	−1.6	0.0	0.0	−0.1	−0.2	0.2	0.0	−0.2	−0.1	0.8	0.1	−0.0	0.4	−0.2	0.1	0.1	0.6	0.3	−0.1	0.1	0.4	−0.9	1.2	−0.3	1.3	0.2	−0.2	1.5
14.0 : 23.0	0.16 : 0.32	0.1862	5.0	0.0	−1.6	0.0	0.0	−0.1	−0.3	0.1	0.0	−0.3	−0.0	0.7	−0.2	0.1	0.5	−0.4	0.1	0.2	0.6	0.8	0.2	0.1	−0.6	0.2	0.9	−1.6	0.9	−0.0	−0.2	1.5
14.0 : 23.0	0.32 : 0.70	0.06920	6.2	0.0	−1.6	0.0	0.0	−0.1	−0.2	0.2	0.0	−0.2	−0.0	0.7	0.3	−0.0	0.6	−0.6	0.4	0.4	0.4	−0.2	0.3	−0.9	−2.0	1.4	0.8	−2.3	−0.1	−0.4	−0.4	1.5
23.0 : 45.0	0.02 : 0.05	0.06911	14.8	0.0	−1.6	0.0	0.0	−0.1	−0.3	0.3	−0.0	−0.6	−0.1	0.6	0.4	−1.2	−1.2	1.3	−0.2	0.2	0.5	1.5	−0.8	2.2	4.2	−0.2	2.0	2.0	4.0	2.5	−0.9	1.5
23.0 : 45.0	0.05 : 0.09	0.1233	5.9	0.0	−1.6	0.0	0.0	−0.1	−0.3	0.2	0.0	−0.2	0.1	0.8	0.0	−0.5	0.2	0.4	0.3	−0.7	0.4	−0.1	−0.5	0.3	1.1	−0.0	0.6	0.2	2.0	−0.4	−0.1	1.5
23.0 : 45.0	0.09 : 0.16	0.1135	4.4	0.0	−1.6	0.0	0.0	−0.1	−0.2	0.2	0.0	−0.2	0.1	0.8	0.1	0.3	0.3	−0.1	−0.0	0.0	0.3	0.0	−0.4	0.0	0.6	−0.7	0.6	−0.4	1.2	−0.0	−0.1	1.5
23.0 : 45.0	0.16 : 0.32	0.07418	4.3	0.0	−1.6	0.0	0.0	−0.2	−0.3	0.1	0.0	−0.2	−0.0	0.6	−0.4	0.2	0.3	−0.2	0.1	0.2	0.3	−0.0	0.1	0.3	−0.6	0.1	0.9	−1.3	0.5	0.1	−0.1	1.5
23.0 : 45.0	0.32 : 0.70	0.03209	5.2	0.0	−1.6	0.0	0.0	−0.1	−0.2	0.1	−0.0	−0.2	−0.0	0.7	−0.1	0.0	0.1	−0.7	0.3	0.2	0.3	−0.3	0.5	−0.3	−1.3	1.2	−0.0	−2.1	0.5	−0.1	−0.2	1.5
45.0 : 100.0	0.02 : 0.05	0.006162	33.5	0.0	−1.6	0.0	0.0	0.0	−0.3	0.3	0.1	−0.4	−0.0	−0.1	1.0	−1.8	−0.0	2.3	−0.3	0.6	−0.3	0.1	−1.8	−4.1	3.8	1.0	7.3	4.3	−0.4	0.3	0.0	1.5
45.0 : 100.0	0.05 : 0.09	0.02703	11.0	0.0	−1.6	0.0	0.0	−0.1	−0.3	0.1	−0.0	−0.2	0.1	0.7	0.1	−0.0	0.1	0.2	0.1	−0.3	0.1	0.7	−0.7	−0.4	2.2	−0.4	1.2	0.1	2.4	0.1	−0.4	1.5
45.0 : 100.0	0.09 : 0.16	0.02051	8.0	0.0	−1.6	0.0	0.0	−0.1	−0.2	0.1	−0.0	−0.1	0.0	0.6	0.2	0.2	0.3	0.0	0.2	0.1	0.7	0.3	−0.2	0.5	0.6	−1.1	1.0	−0.7	2.1	0.0	−0.2	1.5
45.0 : 100.0	0.16 : 0.32	0.01995	5.4	0.0	−1.6	0.0	0.0	−0.1	−0.2	0.1	0.1	−0.2	0.0	0.7	−0.2	0.3	0.6	0.1	0.1	0.1	0.7	0.1	0.0	−0.2	−0.1	−0.0	0.6	−1.1	1.6	0.3	−0.2	1.5
45.0 : 100.0	0.32 : 0.70	0.007841	6.9	0.0	−1.6	0.0	0.0	−0.1	−0.2	0.1	0.0	−0.3	−0.0	0.6	−0.1	−0.0	0.5	−0.0	0.1	0.3	0.3	0.2	0.4	−0.3	−1.2	1.5	0.0	−2.4	0.2	−0.1	−0.0	1.5
100.0 : 158.0	0.02 : 0.32	0.004124	8.2	0.0	−1.6	0.0	0.0	−0.0	−0.2	0.1	−0.0	0.0	−0.0	0.6	−0.2	0.0	−0.1	0.0	−0.1	−0.0	0.5	0.8	−1.0	1.2	1.0	1.3	0.1	−1.9	0.4	−1.4	−0.3	1.5
100.0 : 158.0	0.32 : 0.70	0.002181	11.1	0.0	−1.5	0.0	0.0	−0.1	−0.2	−0.0	0.0	−0.2	−0.0	0.6	−0.2	1.3	0.0	0.7	0.3	0.2	0.7	−0.2	1.1	0.7	0.8	1.4	−0.1	−2.2	−0.1	0.1	−0.4	1.5
158.0 : 251.0	0.02 : 0.30	0.001788	10.2	0.0	−1.6	0.0	0.0	−0.0	−0.2	0.0	−0.0	0.0	−0.0	0.5	−0.1	0.6	−0.4	0.5	0.2	0.2	0.6	0.2	1.1	0.2	1.9	1.3	0.1	−2.2	0.1	−1.3	−0.3	1.5
158.0 : 251.0	0.30 : 0.70	0.0009276	11.6	0.0	−1.5	0.0	0.0	−0.2	−0.1	0.0	−0.0	−0.0	−0.1	0.3	−0.2	0.8	−0.2	0.2	0.2	0.1	0.8	−0.2	0.6	−0.2	1.3	2.0	0.7	−2.6	−0.9	−0.6	−0.5	1.5
251.0 : 1000.0	0.02 : 0.26	0.0001315	14.5	0.0	−1.5	0.0	0.0	0.1	−0.2	0.2	−0.1	−0.0	−0.0	0.5	0.0	0.6	−0.3	0.4	−0.1	0.1	0.3	−0.1	0.5	0.2	1.7	1.7	−0.3	−2.3	−0.6	−2.1	−0.3	1.5
251.0 : 1000.0	0.26 : 0.70	0.0001184	12.7	0.0	−1.5	0.0	0.0	−0.1	−0.1	0.2	0.1	−0.1	0.0	0.5	0.1	0.6	−0.2	0.1	0.2	−0.0	0.5	−0.7	0.6	−1.2	2.0	1.6	−0.4	−2.8	−1.0	−1.3	−0.4	1.5

Table D.16: The combined double-differential D^{*+} cross section as a function of Q^2 and y, with its uncorrelated (δ_{unc}), correlated (δ_1 to δ_{28}) and external branching-ratio (δ_{br}) uncertainties.

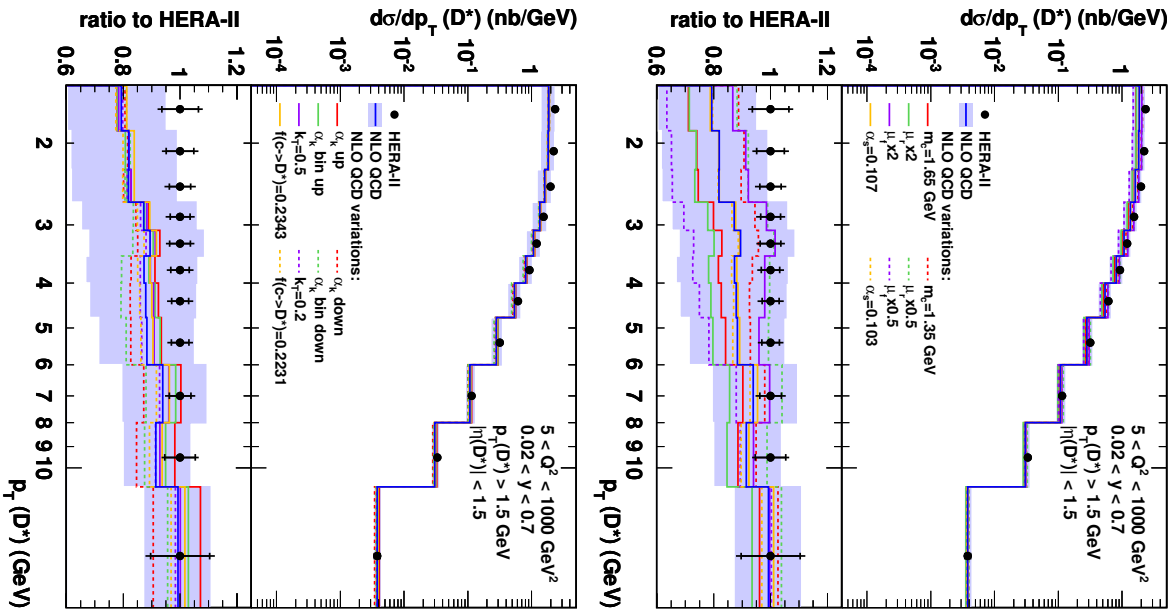

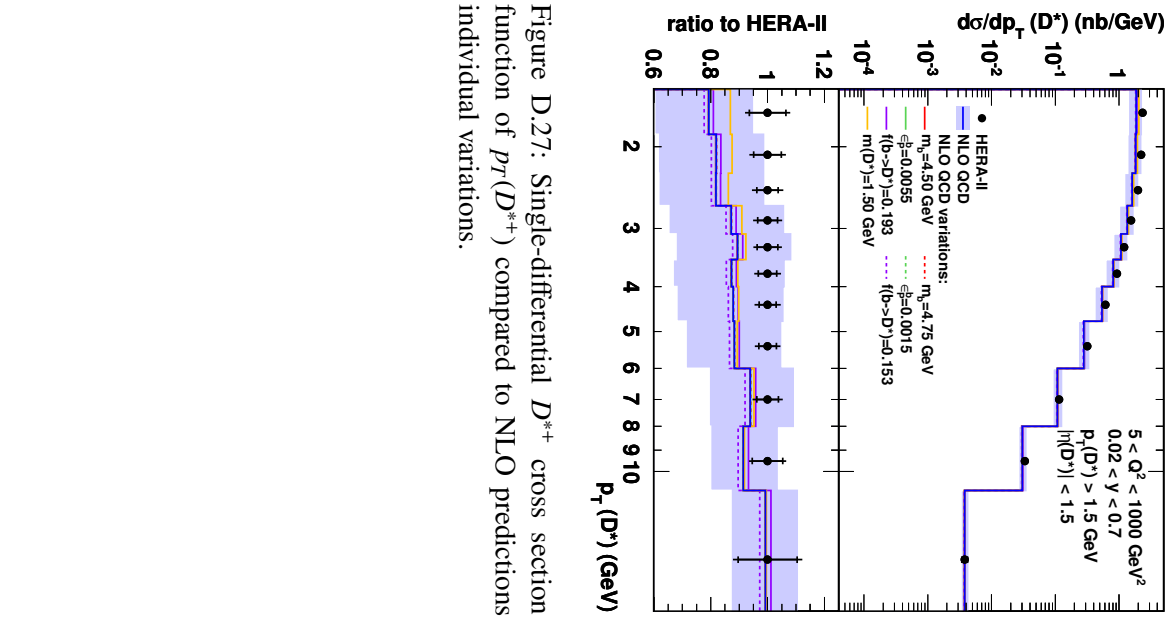

Figure D.27: Single-differential D^{*+} cross section as a function of $p_T(D^{*+})$ compared to NLO predictions with individual variations.

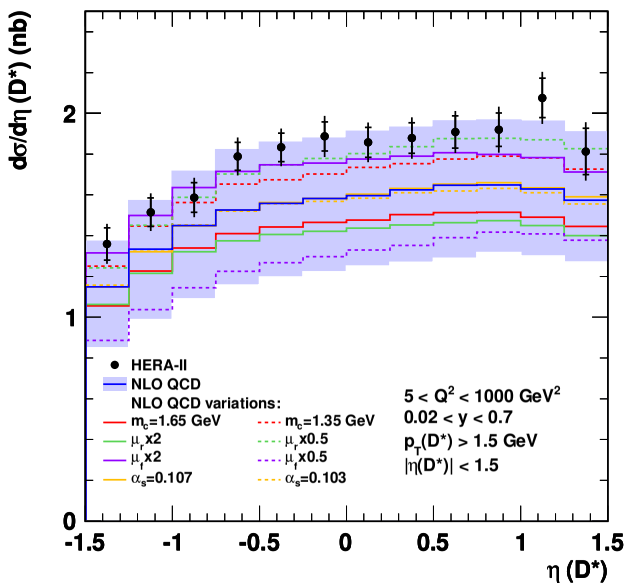

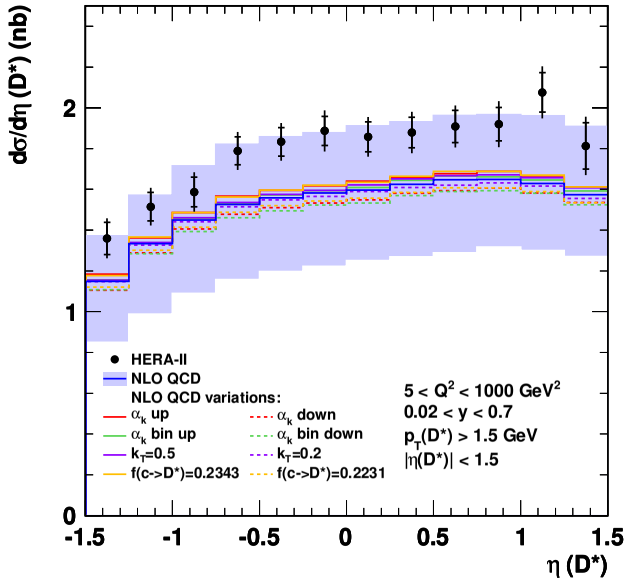

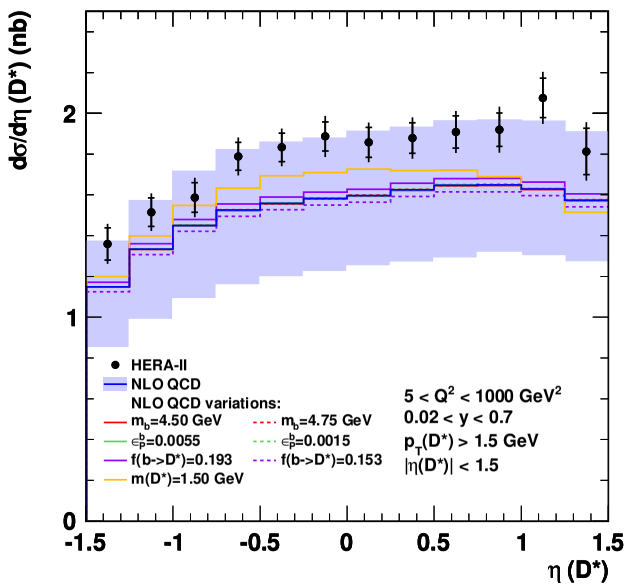

Figure D.28: Single-differential D^{*+} cross section as a function of $\eta(D^{*+})$ compared to NLO predictions with individual variations.

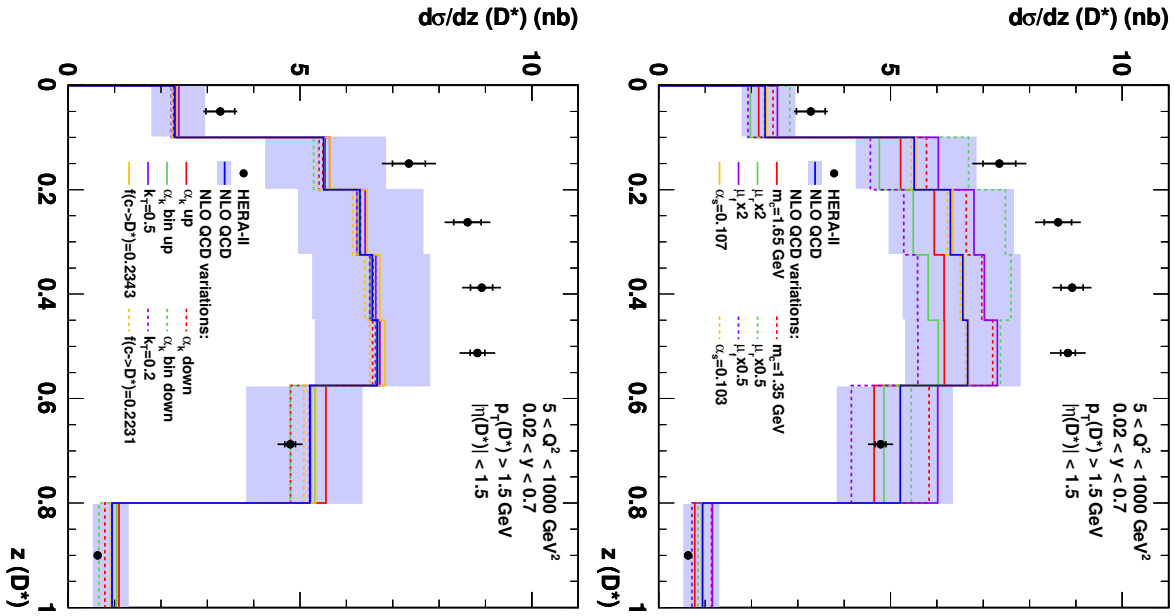

Figure D.29: Single-differential D^{*+} cross section as a function of $z(D^{*+})$ compared to NLO predictions with individual variations.

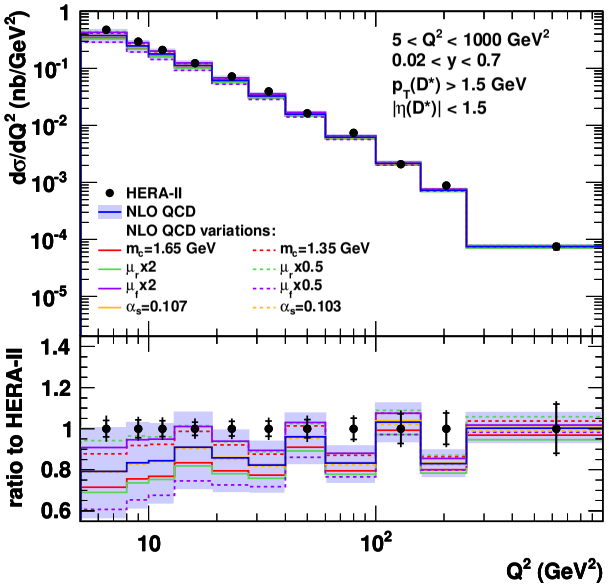

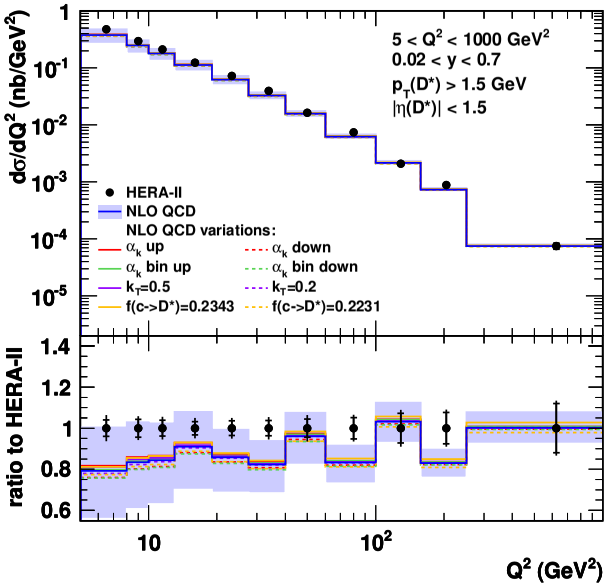

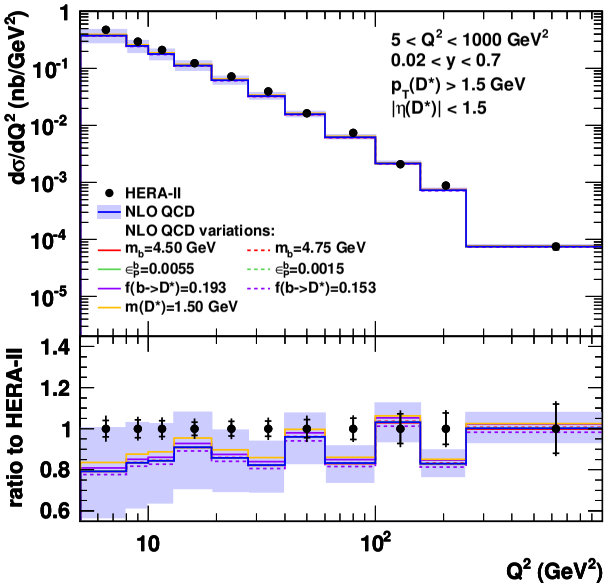

Figure D.30: Single-differential D^{*+} cross section as a function of Q^2 compared to NLO predictions with individual variations.

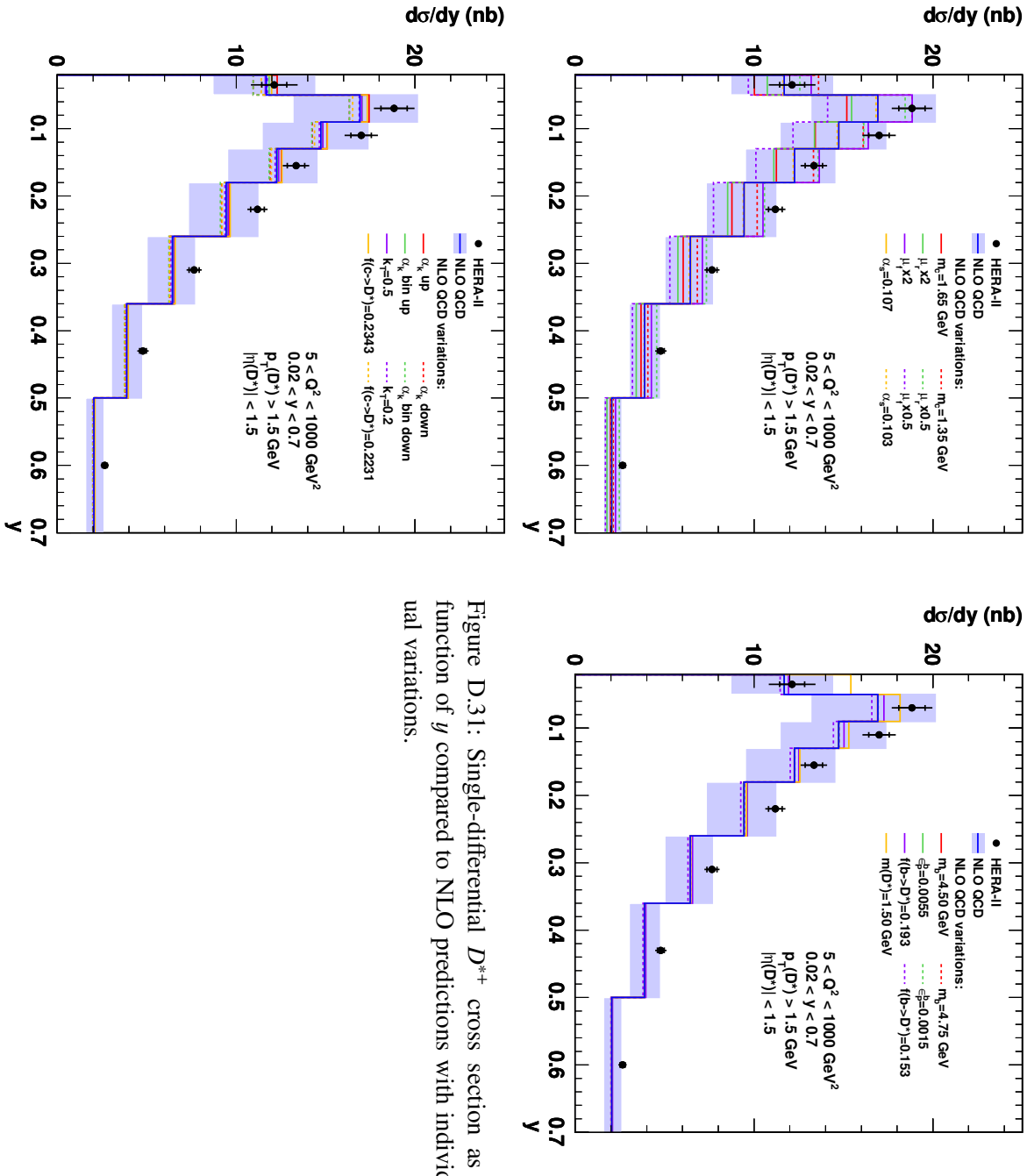

Figure D.31: Single-differential D^{*+} cross section as a function of y compared to NLO predictions with individual variations.

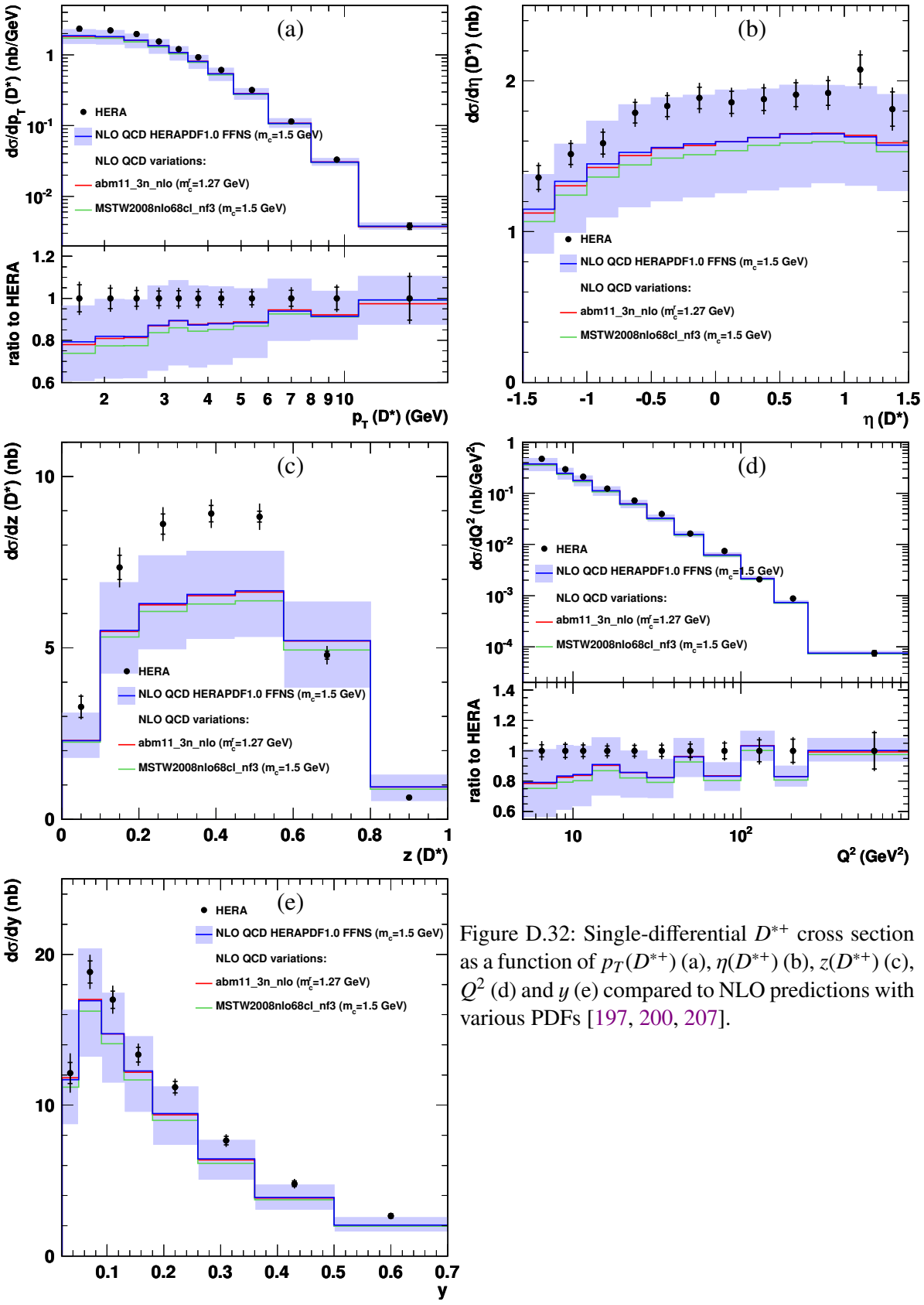

Figure D.32: Single-differential D^{*+} cross section as a function of $p_T(D^{*+})$ (a), $\eta(D^{*+})$ (b), $z(D^{*+})$ (c), Q^2 (d) and y (e) compared to NLO predictions with various PDFs [197, 200, 207].

APPENDIX E

Combination of charm reduced cross sections: additional information

In this Appendix additional information on the combination of the charm reduced cross sections (see Section 6.5) is provided.

Tables E.1 to E.2 provide information on the fitted nuisance parameters.

The combined data with all correlations are provided in Tables E.3 to E.4.

Figs. E.1 to E.12 show the combined data with the input measurements for individual values of Q^2.

Descriptor	Datasets	Name	Type	Reference	shift [%]	reduction [%]
δ_1	1	H1 VTX resolution	S	H1 Col.	−0.1	0.9
δ_2	1–4	H1 CJC efficiency	S	H1 Col.	0.2	0.8
δ_3	1	H1 CST efficiency	S	H1 Col.	0.1	1.0
δ_4	1	H1 B multiplicity	S	H1 Col.	−0.2	0.9
δ_5	1–11	NLO, c longitudinal fragmentation	T	Theory	−1.3	0.7
δ_6	1,3,4	H1 PHP background	S	H1 Col.	0.4	0.9
δ_7	1	H1 multiplicity D^+	S	H1 Col.	0.1	1.0
δ_8	1	H1 multiplicity D^0	S	H1 Col.	−0.1	1.0
δ_9	1	H1 multiplicity D_s	S	H1 Col.	0.1	1.0
δ_{10}	1	H1 VTX b frag.	S	H1 Col.	−0.1	1.0
δ_{11}	1	H1 VTX rew. x	S	H1 Col.	−0.1	0.9
δ_{12}	1	H1 VTX rew. p_T	S	H1 Col.	0.1	0.7
δ_{13}	1	H1 VTX rew. η	S	H1 Col.	−0.1	0.8
δ_{14}	1	H1 VTX uds background	S	H1 Col.	−0.5	0.4
δ_{15}	1	H1 VTX ϕ of c quark	S	H1 Col.	0.1	0.9
δ_{16}	1	H1 hadronic energy scale	S	H1 Col.	0.1	0.8
δ_{17}	1	H1 VTX F_2 normalisation	S	H1 Col.	−0.1	1.0
δ_{18}	3,4	H1 primary-vertex fit	S	H1 Col.	0.2	1.0
δ_{19}	2–4	H1 e energy	S	H1 Col.	0.3	0.7
δ_{20}	2–4	H1 e θ	S	H1 Col.	0.2	0.7
δ_{21}	3,4	H1 luminosity HERA-II	N	H1 Col.	−0.4	0.8
δ_{22}	3,4	H1 trigger HERA-II	S	H1 Col.	−0.1	1.0
δ_{23}	3,4	H1 MC fragmentation	S	H1 Col.	−0.2	0.9
δ_{24}	2–7,10	$br(D^{*+} \to K\pi\pi)$	N	[183]	0.4	1.0
δ_{25}	2–6,10	$ff(c \to D^{*+})$	T	[194]	0.6	0.9
δ_{26}	2,3	H1 MC efficiency	S	H1 Col.	0.3	0.7
δ_{27}	2–11	NLO, m_c	T	Theory	0.6	0.6
δ_{28}	2–11	NLO, scale	T	Theory	−0.9	0.4
δ_{29}	2–11	NLO, c transverse fragmentation	T	Theory	0.1	0.7
δ_{30}	2–4	NLO, PDF	T	Theory	0.9	0.9
δ_{31}	2–11	NLO, $\alpha_s(M_Z)$	T	Theory	−0.2	0.7
δ_{32}	2	H1 luminosity 96–97	N	H1 Col.	−0.0	1.0
δ_{33}	2	H1 trigger 96–97	S	H1 Col.	−0.0	0.9
δ_{34}	2	H1 MC alternative frag.	S	H1 Col.	−0.2	0.7
δ_{35}	8	ZEUS μ B/RMUON efficiency	S	[140]	−0.3	0.9
δ_{36}	8	ZEUS μ FMUON efficiency	S	[140]	0.2	1.0
δ_{37}	8	ZEUS μ energy scale	S	[140]	0.0	0.8
δ_{38}	8	ZEUS μ p_T^{miss} calibration	S	[140]	0.2	0.7
δ_{39}	8	ZEUS μ hadronic resolution	S	[140]	0.6	0.7

Table E.1: Sources of bin-to-bin correlated uncertainties considered in the combination of the charm reduced cross sections. For each source the affected datasets, name, type (see Section 6.2.2) and reference to the place, where information can be found, are given, together with the shift and reduction factor in the combination obtained after the first iteration.

Descriptor	Datasets	Name	Type	Reference	shift [%]	reduction [%]
δ_{40}	8	ZEUS μ IP resolution	S	[140]	−0.3	1.0
δ_{41}	8	ZEUS μ MC model	S	[140]	0.3	0.9
δ_{42}	8	$ff(c \to \mu)$	T	[183]	0.2	1.0
δ_{43}	7–11	ZEUS luminosity HERA-II	N	[19, 137, 139]	−0.6	0.9
δ_{44}	5	ZEUS luminosity 96–97	N	[59]	0.7	0.9
δ_{45}	6	ZEUS luminosity 98–00	N	[136]	0.9	0.9
δ_{46}	7	ZEUS D^0 lifetime significance	S	[138, 242]	0.9	0.5
δ_{47}	7	$ff(c \to D^0)$	T	[194]	0.2	1.0
δ_{48}	9	$ff(c \to D^+)$	T	[194]	−0.1	0.9
δ_{49}	9	ZEUS D^+ electron energy scale	S	[139]	0.3	1.0
δ_{50}	9	ZEUS D^+ hadronic energy scale	S	[139]	−0.1	1.0
δ_{51}	9	ZEUS D^+ trigger inefficiency	S	[139]	0.3	0.9
δ_{52}	9	ZEUS D^+ decay length smearing	S	[139]	0.2	1.0
δ_{53}	9	ZEUS D^+ MC b normalisation	S	[139]	0.1	0.9
δ_{54}	9	ZEUS D^+ MC rew. p_T–Q^2	S	[139]	−0.6	0.8
δ_{55}	9	ZEUS D^+ MC rew. η	S	[139]	0.5	0.7
δ_{56}	9	ZEUS D^+ tracking inefficiency	S	[139]	−0.2	1.0
δ_{57}	9	ZEUS D^+ MVD hit efficiency	S	[139]	−0.0	1.0
δ_{58}	9	ZEUS D^+ $\chi^2_{\text{sec.vtx.}}$ distribution	S	[139]	−0.1	1.0
δ_{59}	9	$br(D^+ \to K\pi\pi)$	N	[183]	−0.1	1.0
δ_{60}	10	ZEUS D^{*+} hadronic energy scale	S	[137]	0.1	0.5
δ_{61}	10	ZEUS D^{*+} electron energy scale	S	[137]	−0.3	0.6
δ_{62}	10	ZEUS D^{*+} $p_T(\pi_s)$	S	[137]	−1.0	0.9
δ_{63}	10	ZEUS D^{*+} tracking inefficiency	S	[137]	−0.8	0.9
δ_{64}	10	ZEUS D^{*+} PHP background	S	[137]	−0.4	1.0
δ_{65}	10	ZEUS D^{*+} diffractive backgr.	S	[137]	0.4	0.9
δ_{66}	10	ZEUS D^{*+} MC rew. p_T, Q^2	S	[137]	0.5	0.9
δ_{67}	10	ZEUS D^{*+} MC rew. η	S	[137]	0.4	0.8
δ_{68}	10	ZEUS D^{*+} MC b normalisation	S	[137]	−0.4	0.8
δ_{69}	11	ZEUS VTX trigger inefficiency	S	[19]	−0.3	0.9
δ_{70}	11	ZEUS VTX tracking inefficiency	S	[19]	0.3	1.0
δ_{71}	11	ZEUS VTX jet energy scale	S	[19]	0.6	0.7
δ_{72}	11	ZEUS VTX electron energy scale	S	[19]	0.1	1.0
δ_{73}	11	ZEUS VTX c MC rew. Q^2	S	[19]	0.3	0.9
δ_{74}	11	ZEUS VTX b MC rew. Q^2	S	[19]	−0.1	1.0
δ_{75}	11	ZEUS VTX c MC rew. η	S	[19]	0.0	1.0
δ_{76}	11	ZEUS VTX b MC rew. η	S	[19]	−0.5	1.0
δ_{77}	11	ZEUS VTX c MC rew. E_T	S	[19]	0.0	1.0
δ_{78}	11	ZEUS VTX b MC rew. E_T	S	[19]	−0.1	1.0

Table E.2: The continuation of Table E.1.

Table E.3: The combined charm reduced cross section, with its statistical (δ_{stat}),uncorrelated (δ_{unc}) and correlated (δ_1 to δ_{78}) uncertainties.

Q^2 (GeV^2)	x	$\sigma^{c\bar{c}}_{red}$	δ_{stat}	δ_{unc}	δ_1	δ_2	δ_3	δ_4	δ_5	δ_6	δ_7	δ_8	δ_9	δ_{10}	δ_{11}	δ_{12}	δ_{13}	δ_{14}	δ_{15}	δ_{16}	δ_{17}	δ_{18}	δ_{19}	δ_{20}	δ_{21}	δ_{22}	δ_{23}	δ_{24}	δ_{25}	δ_{26}	δ_{27}	δ_{28}	δ_{29}	δ_{30}	δ_{31}	δ_{32}	δ_{33}	δ_{34}	δ_{35}	δ_{36}	δ_{37}	δ_{38}
			[%]	[%]	[%]	[%]	[%]	[%]	[%]	[%]	[%]	[%]	[%]	[%]	[%]	[%]	[%]	[%]	[%]	[%]	[%]	[%]	[%]	[%]	[%]	[%]	[%]	[%]	[%]	[%]	[%]	[%]	[%]	[%]	[%]	[%]	[%]	[%]	[%]	[%]	[%]	[%]
2.5	0.00003	0.1215	0.0	0.0	−0.0	0.0	−0.0	0.0	−0.0	−0.0	−0.0	0.0	−0.0	−0.0	−0.1	−0.2	−0.1	−0.3	−0.0	0.4	0.4	0.2	0.3	−0.2	0.1	0.1	0.2	0.0	0.4	−0.3	0.8	0.2	−0.2	−0.2	0.4	0.1	0.9	−1.3	−0.9	0.3	0.4
2.5	0.00007	0.1144	0.0	0.0	−0.0	0.0	−0.0	0.0	−0.0	−0.0	−0.0	0.0	−0.0	−0.0	−0.1	−0.2	−0.1	−0.1	−0.3	0.0	0.3	0.4	0.2	0.3	−0.2	0.0	0.0	0.2	−0.1	0.4	−0.3	0.8	0.2	−0.1	−0.2	0.6	0.2	0.9	−1.6	−1.0	0.4	0.3
2.5	0.00013	0.0940	0.0	0.0	−0.0	0.0	−0.0	0.0	−0.0	−0.0	−0.0	0.0	−0.0	−0.0	−0.1	−0.2	−0.1	−0.3	−0.1	0.2	0.3	0.4	0.2	0.3	−0.2	0.1	−0.1	0.2	−0.1	0.4	−0.4	0.7	0.2	−0.2	−0.4	0.7	0.3	0.8	−1.3	−0.6	0.6	0.1
2.5	0.00018	0.0966	0.0	0.0	−0.0	0.0	−0.0	0.0	−0.0	−0.0	−0.0	0.0	−0.0	−0.0	−0.1	−0.2	−0.1	−0.3	−0.1	0.2	0.3	0.4	0.2	0.3	−0.2	0.1	−0.1	0.2	−0.2	0.4	−0.4	0.7	0.3	−0.2	−0.4	0.7	0.5	0.8	−1.3	−0.6	0.6	0.1
2.5	0.00035	0.0586	0.0	0.0	−0.0	0.0	−0.0	0.0	−0.0	−0.0	−0.0	0.0	−0.0	−0.0	−0.1	−0.2	−0.1	−0.3	−0.1	0.2	0.3	0.4	0.1	0.4	−0.2	0.2	−0.1	0.0	−0.3	0.3	−0.4	0.7	0.2	−0.3	−0.3	0.6	0.6	0.6	−1.0	−0.5	0.6	−0.1
5	0.00007	0.1568	0.0	0.0	−0.0	0.0	−0.0	0.0	−0.0	−0.0	−0.0	0.0	−0.0	−0.0	−0.1	−0.2	−0.1	−0.3	−0.0	0.4	0.4	0.2	0.2	0.3	0.0	0.1	0.2	0.2	−0.1	0.2	−0.2	0.6	0.1	−0.2	−0.2	0.3	0.2	0.6	−0.9	−0.3	0.2	−0.2
5	0.00018	0.1594	0.0	0.0	−0.0	0.0	−0.0	0.0	−0.0	−0.0	−0.0	0.0	−0.0	−0.0	−0.1	−0.3	−0.1	−0.3	−0.1	0.3	0.3	0.4	0.1	0.3	−0.4	0.1	0.1	0.2	−0.1	0.1	−0.4	0.6	0.2	−0.2	−0.3	0.5	0.1	0.6	−0.9	−0.3	0.2	−0.2
5	0.00035	0.1208	0.0	0.0	−0.0	0.0	−0.0	0.0	−0.0	−0.0	−0.0	0.0	−0.0	−0.0	−0.1	−0.3	−0.1	−0.3	−0.1	0.3	0.3	0.4	0.2	0.3	−0.3	0.1	0.0	0.1	−0.1	0.3	−0.4	0.7	0.1	−0.2	−0.2	0.5	0.3	0.5	−1.1	−0.6	0.3	0.1
5	0.00100	0.0839	0.0	0.0	−0.0	0.0	−0.0	0.0	−0.0	−0.0	−0.0	0.0	−0.0	−0.0	−0.1	−0.3	−0.1	−0.3	−0.1	0.3	0.3	0.4	0.2	0.4	−0.3	0.1	−0.0	0.0	−0.2	0.1	−0.3	0.8	0.0	−0.3	−0.2	0.3	0.4	0.3	−0.9	−0.7	0.4	0.0
7	0.00013	0.2333	0.0	0.0	−0.0	0.0	−0.0	0.0	−0.0	−0.0	−0.0	0.0	−0.0	−0.0	−0.1	−0.2	−0.1	−0.3	−0.1	0.2	0.3	0.4	0.2	0.3	−0.2	0.1	0.1	0.1	−0.1	0.3	−0.3	0.9	−0.1	−0.2	−0.1	0.2	0.1	0.8	−1.2	−0.5	0.3	−0.1
7	0.00018	0.2088	0.0	0.0	−0.0	0.0	−0.0	0.0	−0.0	−0.0	−0.0	0.0	−0.0	−0.0	−0.1	−0.3	−0.1	−0.3	−0.0	0.3	0.3	0.4	0.2	0.2	−0.3	0.1	0.0	0.2	−0.1	0.4	−0.2	0.6	0.1	−0.2	−0.2	0.4	0.2	0.8	−1.2	−0.4	−0.0	−0.3
7	0.00030	0.1833	0.0	0.0	−0.0	0.0	−0.0	0.0	−0.0	−0.0	−0.0	0.0	−0.0	−0.0	−0.1	−0.3	−0.1	−0.3	−0.1	0.3	0.3	0.4	0.2	0.2	−0.3	0.1	0.0	0.1	−0.1	0.3	−0.4	0.5	0.0	−0.2	0.1	0.5	0.1	0.5	−0.8	−0.3	0.3	−0.2
7	0.00050	0.1673	0.0	0.0	−0.0	0.0	−0.0	0.0	−0.0	−0.0	−0.0	0.0	−0.0	−0.0	−0.1	−0.3	−0.1	−0.3	−0.0	0.3	0.3	0.4	0.2	0.3	−0.3	0.1	0.0	0.1	−0.1	0.4	−0.3	0.6	−0.0	−0.3	0.0	0.5	0.3	0.6	−0.7	−0.3	0.3	−0.2
7	0.00080	0.1249	0.0	0.0	−0.0	0.0	−0.0	0.0	−0.0	−0.0	−0.0	0.0	−0.0	−0.0	−0.1	−0.3	−0.1	−0.3	−0.1	0.3	0.3	0.4	0.2	0.3	−0.3	0.1	0.0	0.0	−0.1	0.2	−0.4	0.5	0.0	−0.3	0.0	0.4	0.1	0.3	−0.5	−0.1	0.2	−0.2
7	0.00160	0.0958	0.0	0.0	−0.0	0.0	−0.0	0.0	−0.0	−0.0	−0.0	0.0	−0.0	−0.0	−0.1	−0.3	−0.1	−0.3	−0.1	0.3	0.3	0.4	0.2	0.3	−0.3	0.1	0.0	0.1	−0.0	0.1	−0.3	0.7	0.2	−0.3	−0.1	0.2	0.3	0.2	−0.3	−0.7	0.3	−0.0
12	0.00022	0.3279	0.0	0.0	−0.0	0.0	−0.0	0.0	−0.0	−0.0	−0.0	0.0	−0.0	−0.0	−0.1	−0.3	−0.1	−0.3	−0.1	0.3	0.3	0.4	0.3	0.2	−0.3	0.1	0.0	0.1	−0.1	0.3	−0.4	0.7	0.2	−0.1	−0.2	0.5	0.1	0.6	−0.9	−0.3	0.2	−0.1
12	0.00032	0.3041	0.0	0.0	−0.0	0.0	−0.0	0.0	−0.0	−0.0	−0.0	0.0	−0.0	−0.0	−0.1	−0.3	−0.1	−0.3	−0.0	0.3	0.3	0.4	0.3	0.2	−0.4	0.1	0.0	0.1	−0.1	0.3	−0.4	0.7	0.2	−0.1	−0.4	0.5	0.3	0.5	−0.7	−0.1	0.3	−0.0
12	0.00050	0.2470	0.0	0.0	−0.0	0.0	−0.0	0.0	−0.0	−0.0	−0.0	0.0	−0.0	−0.0	−0.1	−0.3	−0.1	−0.3	−0.1	0.3	0.3	0.4	0.2	0.2	−0.4	0.1	0.0	0.1	−0.0	0.2	−0.4	0.7	0.2	−0.1	−0.4	0.5	0.1	0.5	−0.8	−0.3	0.2	−0.2
12	0.00080	0.1882	0.0	0.0	−0.0	0.0	−0.0	0.0	−0.0	−0.0	−0.0	0.0	−0.0	−0.0	−0.1	−0.3	−0.1	−0.3	−0.1	0.3	0.3	0.4	0.2	0.2	−0.4	0.1	0.0	0.1	−0.0	0.2	−0.3	0.5	0.0	−0.2	−0.1	0.4	−0.0	0.4	−0.6	−0.3	0.2	−0.2
12	0.00150	0.1586	0.0	0.0	−0.0	0.0	−0.0	0.0	−0.0	−0.0	−0.0	0.0	−0.0	−0.0	−0.1	−0.3	−0.1	−0.3	−0.0	0.3	0.4	0.2	0.3	0.3	−0.3	0.1	0.1	0.1	−0.1	0.2	−0.3	0.6	−0.1	−0.3	−0.0	0.1	0.2	0.1	−0.6	−0.2	0.1	0.0
12	0.00300	0.1106	0.0	0.0	−0.0	0.0	−0.0	0.0	−0.0	−0.0	−0.0	0.0	−0.0	−0.0	−0.1	−0.3	−0.1	−0.3	−0.1	0.3	0.3	0.4	0.2	0.3	−0.3	0.1	0.1	0.1	−0.1	0.2	−0.3	0.7	0.0	−0.2	−0.1	0.2	0.2	0.2	−0.6	−0.2	0.1	0.0
18	0.00035	0.3306	0.0	0.0	−0.0	0.0	−0.0	0.0	−0.0	−0.0	−0.0	0.0	−0.0	−0.0	−0.1	−0.3	−0.1	−0.3	−0.0	0.3	0.3	0.4	0.3	0.2	−0.3	0.1	0.0	0.1	−0.1	0.2	−0.4	0.8	0.0	−0.3	0.0	0.3	0.1	0.4	−0.9	−0.5	0.1	0.0
18	0.00050	0.3030	0.0	0.0	−0.0	0.0	−0.0	0.0	−0.0	−0.0	−0.0	0.0	−0.0	−0.0	−0.1	−0.3	−0.1	−0.3	−0.0	0.3	0.3	0.4	0.3	0.2	−0.2	0.1	0.1	0.2	−0.0	0.3	−0.2	0.5	−0.1	−0.1	−0.1	0.7	0.2	0.5	−0.6	−0.1	0.4	0.1
18	0.00080	0.2685	0.0	0.0	−0.0	0.0	−0.0	0.0	−0.0	−0.0	−0.0	0.0	−0.0	−0.0	−0.1	−0.3	−0.1	−0.3	−0.1	0.3	0.3	0.4	0.3	0.2	−0.3	0.1	0.1	0.2	−0.1	0.2	−0.4	0.5	0.1	−0.2	−0.1	0.4	−0.1	0.3	−0.7	−0.3	0.1	−0.2
18	0.00135	0.2134	0.0	0.0	−0.0	0.0	−0.0	0.0	−0.0	−0.0	−0.0	0.0	−0.0	−0.0	−0.1	−0.3	−0.1	−0.3	−0.0	0.3	0.3	0.4	0.3	0.2	−0.3	0.1	0.1	0.2	−0.1	0.2	−0.4	0.6	0.0	−0.3	−0.1	0.4	−0.1	0.2	−0.6	−0.3	0.2	−0.1
18	0.00250	0.1723	0.0	0.0	−0.0	0.0	−0.0	0.0	−0.0	−0.0	−0.0	0.0	−0.0	−0.0	−0.1	−0.3	−0.0	−0.3	−0.1	0.3	0.3	0.4	0.3	0.3	−0.4	0.0	0.2	0.1	−0.1	0.2	−0.4	0.7	−0.1	−0.2	−0.2	0.3	−0.0	0.1	−0.5	−0.1	0.2	0.1
18	0.00450	0.1314	0.0	0.0	−0.0	0.0	−0.0	0.0	−0.0	−0.0	−0.0	0.0	−0.0	−0.0	−0.1	−0.3	−0.1	−0.3	−0.0	0.3	0.3	0.4	0.3	0.3	−0.3	0.0	0.2	0.1	−0.0	0.3	−0.3	0.6	−0.0	−0.2	−0.1	0.1	0.0	0.1	−0.5	−0.6	0.1	−0.0
32	0.00060	0.4348	0.0	0.0	−0.0	0.0	−0.0	0.0	−0.0	−0.0	−0.0	0.0	−0.0	−0.0	−0.2	−0.1	−0.1	−0.3	−0.0	0.2	0.3	0.4	0.3	0.2	−0.3	0.0	0.1	0.1	−0.1	0.3	−0.3	0.6	0.1	−0.1	−0.1	0.5	0.4	0.1	−0.8	−0.5	0.0	0.2
32	0.00080	0.3778	0.0	0.0	−0.0	0.0	−0.0	0.0	−0.0	−0.0	−0.0	0.0	−0.0	−0.0	−0.2	−0.1	−0.1	−0.3	−0.1	0.2	0.3	0.4	0.3	0.2	−0.3	0.0	0.1	0.2	−0.1	0.3	−0.4	0.6	0.1	−0.2	−0.1	0.4	−0.3	0.3	−0.7	−0.3	0.0	−0.1
32	0.00140	0.2874	0.0	0.0	−0.0	0.0	−0.0	0.0	−0.0	−0.0	−0.0	0.0	−0.0	−0.0	−0.2	−0.1	−0.1	−0.3	−0.0	0.2	0.3	0.4	0.3	0.2	−0.3	0.0	0.1	0.2	−0.1	0.3	−0.3	0.6	0.1	−0.2	−0.1	0.3	−0.1	0.3	−0.4	−0.1	0.1	−0.1
32	0.00240	0.2241	0.0	0.0	−0.0	0.0	−0.0	0.0	−0.0	−0.0	−0.0	0.0	−0.0	−0.0	−0.2	−0.1	−0.1	−0.3	−0.0	0.2	0.3	0.4	0.3	0.2	−0.3	0.0	0.2	0.1	−0.0	0.3	−0.3	0.6	0.1	−0.2	−0.1	0.3	0.1	0.4	−0.3	−0.1	0.1	−0.0
32	0.00320	0.2136	0.0	0.0	−0.0	0.0	−0.0	0.0	−0.0	−0.0	−0.0	0.0	−0.0	−0.0	−0.2	−0.1	−0.1	−0.3	−0.0	0.2	0.3	0.4	0.3	0.2	−0.3	0.0	0.2	0.2	−0.1	0.3	−0.3	0.6	0.1	−0.2	−0.1	0.3	0.2	0.2	−0.2	−0.3	0.3	0.1
32	0.00550	0.1610	0.0	0.0	−0.0	0.0	−0.0	0.0	−0.0	−0.0	−0.0	0.0	−0.0	−0.0	−0.3	−0.1	−0.1	−0.4	−0.0	0.3	0.3	0.4	0.3	0.2	−0.3	−0.0	0.2	0.2	−0.1	0.3	−0.4	0.6	0.1	−0.2	−0.2	0.3	0.1	0.0	−0.2	0.0	−0.1	0.2
32	0.00800	0.1022	0.0	0.0	−0.0	0.0	−0.0	0.0	−0.0	−0.0	−0.0	0.0	−0.0	−0.0	−0.3	−0.1	−0.1	−0.4	−0.0	0.3	0.3	0.4	0.3	0.2	−0.3	−0.0	0.2	0.2	−0.1	0.3	−0.4	0.7	0.1	−0.2	−0.2	0.3	0.1	0.0	−0.2	0.0	−0.1	0.2
60	0.00140	0.3380	0.0	0.0	−0.0	0.0	−0.0	0.0	−0.0	−0.0	−0.0	0.0	−0.0	−0.0	−0.3	−0.1	−0.1	−0.4	−0.0	0.3	0.4	0.4	0.3	0.2	−0.4	0.0	0.1	0.2	−0.1	0.4	−0.4	0.7	0.1	−0.2	−0.2	0.4	−0.1	0.1	−0.4	−0.1	0.1	0.0
60	0.00200	0.3440	0.0	0.0	−0.0	0.0	−0.0	0.0	−0.0	−0.0	−0.0	0.0	−0.0	−0.0	−0.3	−0.1	−0.1	−0.4	−0.0	0.3	0.4	0.4	0.3	0.2	−0.4	0.0	0.1	0.3	−0.2	0.4	−0.4	0.7	0.1	−0.2	−0.2	0.4	−0.1	0.2	−0.4	−0.1	0.1	0.0
60	0.00320	0.2709	0.0	0.0	−0.0	0.0	−0.0	0.0	−0.0	−0.0	−0.0	0.0	−0.0	−0.0	−0.3	−0.1	−0.1	−0.4	−0.0	0.3	0.4	0.4	0.3	0.2	−0.3	−0.0	0.2	0.2	−0.1	0.4	−0.4	0.7	0.1	−0.2	−0.2	0.4	−0.1	0.2	−0.4	−0.1	0.1	−0.1
60	0.00500	0.1993	0.0	0.0	−0.0	0.0	−0.0	0.0	−0.0	−0.0	−0.0	0.0	−0.0	−0.0	−0.2	−0.0	−0.1	−0.4	−0.0	0.3	0.4	0.4	0.3	0.2	−0.3	0.1	0.1	0.2	−0.0	0.4	−0.4	0.7	0.1	−0.2	−0.2	0.4	−0.1	0.2	−0.4	−0.1	0.2	0.1
60	0.00800	0.1712	0.0	0.0	−0.0	0.0	−0.0	0.0	−0.0	−0.0	−0.0	0.0	−0.0	−0.0	−0.3	−0.0	−0.0	−0.4	−0.0	0.3	0.3	0.4	0.3	0.2	−0.4	0.0	0.1	0.2	−0.0	0.4	−0.4	0.7	0.1	−0.2	−0.2	0.4	−0.1	0.2	−0.4	−0.1	0.2	0.1
60	0.01500	0.1014	0.0	0.0	−0.0	0.0	−0.0	0.0	−0.0	−0.0	−0.0	0.0	−0.0	−0.0	−0.3	−0.1	−0.1	−0.4	−0.0	0.3	0.3	0.4	0.3	0.2	−0.4	−0.0	0.2	0.2	−0.0	0.4	−0.4	0.7	0.1	−0.2	−0.2	0.4	−0.1	0.2	−0.4	−0.1	0.2	0.1
120	0.00200	0.3560	0.0	0.0	−0.0	0.0	−0.0	0.0	−0.0	−0.0	−0.0	0.0	−0.0	−0.0	−0.2	−0.1	−0.0	−0.3	−0.0	0.3	0.4	0.4	0.3	0.2	−0.4	−0.0	0.2	0.2	−0.0	0.4	−0.4	0.7	0.1	−0.2	−0.2	0.4	−0.1	0.2	−0.4	−0.1	0.2	0.1
120	0.00320	0.3619	0.0	0.0	−0.0	0.0	−0.0	0.0	−0.0	−0.0	−0.0	0.0	−0.0	−0.0	−0.3	−0.1	−0.1	−0.3	−0.1	0.3	0.4	0.4	0.3	0.2	−0.4	−0.0	0.2	0.2	−0.1	0.4	−0.4	0.7	0.1	−0.2	−0.2	0.4	−0.1	0.2	−0.4	−0.1	0.2	0.1
120	0.00550	0.2309	0.0	0.0	−0.0	0.0	−0.0	0.0	−0.0	−0.0	−0.0	0.0	−0.0	−0.0	−0.3	−0.1	−0.1	−0.3	−0.1	0.3	0.4	0.4	0.3	0.2	−0.4	−0.0	0.2	0.2	−0.1	0.4	−0.4	0.7	0.1	−0.2	−0.2	0.4	−0.1	0.2	−0.4	−0.1	0.2	0.1
120	0.01000	0.1605	0.0	0.0	−0.0	0.0	−0.0	0.0	−0.0	−0.0	−0.0	0.0	−0.0	−0.0	−0.2	−0.1	−0.1	−0.4	−0.0	0.3	0.4	0.4	0.3	0.2	−0.4	−0.0	0.2	0.2	−0.1	0.4	−0.4	0.7	0.1	−0.2	−0.2	0.4	−0.1	0.2	−0.4	−0.1	0.2	0.1
120	0.02500	0.0888	0.0	0.0	−0.0	0.0	−0.0	0.0	−0.0	−0.0	−0.0	0.0	−0.0	−0.0	−0.3	−0.1	−0.1	−0.4	−0.0	0.3	0.4	0.4	0.3	0.2	−0.4	−0.0	0.2	0.2	−0.1	0.4	−0.4	0.7	0.1	−0.2	−0.2	0.4	−0.1	0.2	−0.4	−0.1	0.2	0.1
200	0.00500	0.2510	0.0	0.0	−0.0	0.0	−0.0	0.0	−0.0	−0.0	−0.0	0.0	−0.0	−0.0	−0.2	−0.1	−0.1	−0.3	−0.0	0.2	0.3	0.4	0.3	0.2	−0.4	−0.0	0.2	0.2	−0.1	0.4	−0.4	0.7	0.1	−0.2	−0.2	0.4	−0.1	0.2	−0.4	−0.1	0.2	0.1
200	0.01300	0.1773	0.0	0.0	−0.0	0.0	−0.0	0.0	−0.0	−0.0	−0.0	0.0	−0.0	−0.0	−0.2	−0.1	−0.1	−0.4	−0.0	0.3	0.4	0.4	0.3	0.2	−0.4	−0.0	0.2	0.2	−0.1	0.4	−0.4	0.7	0.1	−0.2	−0.2	0.4	−0.1	0.2	−0.4	−0.1	0.2	0.1
350	0.01000	0.2264	0.0	0.0	−0.0	0.0	−0.0	0.0	−0.0	−0.0	−0.0	0.0	−0.0	−0.0	−0.2	−0.1	−0.1	−0.5	−0.0	0.3	0.4	0.4	0.3	0.2	−0.4	−0.0	0.2	0.2	−0.1	0.4	−0.4	0.7	0.1	−0.2	−0.2	0.4	−0.1	0.2	−0.4	−0.1	0.2	0.1
350	0.02500	0.1079	0.0	0.0	−0.0	0.0	−0.0	0.0	−0.0	−0.0	−0.0	0.0	−0.0	−0.0	−0.2	−0.1	−0.1	−0.4	−0.0	0.3	0.4	0.4	0.3	0.2	−0.4	−0.0	0.2	0.2	−0.1	0.4	−0.4	0.7	0.1	−0.2	−0.2	0.4	−0.1	0.2	−0.4	−0.1	0.2	0.1
650	0.01300	0.2124	0.0	0.0	−0.0	0.0	−0.0	0.0	−0.0	−0.0	−0.0	0.0	−0.0	−0.0	−0.2	−0.1	−0.1	−0.4	−0.0	0.3	0.4	0.4	0.3	0.2	−0.4	−0.0	0.2	0.2	−0.1	0.4	−0.4	0.7	0.1	−0.2	−0.2	0.4	−0.1	0.2	−0.4	−0.1	0.2	0.1
650	0.03200	0.0993	0.0	0.0	−0.0	0.0	−0.0	0.0	−0.0	−0.0	−0.0	0.0	−0.0	−0.0	−0.2	−0.1	−0.1	−0.4	−0.0	0.3	0.4	0.4	0.3	0.2	−0.4	−0.0	0.2	0.2	−0.1	0.4	−0.4	0.7	0.1	−0.2	−0.2	0.4	−0.1	0.2	−0.4	−0.1	0.2	0.1
2000	0.05000	0.0655	0.0	0.0	−0.0	0.0	−0.0	0.0	−0.0	−0.0	−0.0	0.0	−0.0	−0.0	−0.2	−0.1	−0.1	−0.4	−0.0	0.3	0.4	0.4	0.3	0.2	−0.4	−0.0	0.2	0.2	−0.1	0.4	−0.4	0.7	0.1	−0.2	−0.2	0.4	−0.1	0.2	−0.4	−0.1	0.2	0.1

Q^2 (GeV^2)	x	δ_{39} [%]	δ_{40} [%]	δ_{41} [%]	δ_{42} [%]	δ_{43} [%]	δ_{44} [%]	δ_{45} [%]	δ_{46} [%]	δ_{47} [%]	δ_{48} [%]	δ_{49} [%]	δ_{50} [%]	δ_{51} [%]	δ_{52} [%]	δ_{53} [%]	δ_{54} [%]	δ_{55} [%]	δ_{56} [%]	δ_{57} [%]	δ_{58} [%]	δ_{59} [%]	δ_{60} [%]	δ_{61} [%]	δ_{62} [%]	δ_{63} [%]	δ_{64} [%]	δ_{65} [%]	δ_{66} [%]	δ_{67} [%]	δ_{68} [%]	δ_{69} [%]	δ_{70} [%]	δ_{71} [%]	δ_{72} [%]	δ_{73} [%]	δ_{74} [%]	δ_{75} [%]	δ_{76} [%]	δ_{77} [%]	δ_{78} [%]
2.5	0.00003	−0.2	1.2	−1.0	0.4	−0.7	0.9	1.2	0.7	0.4	0.4	−1.3	−0.1	−2.0	2.4	1.0	1.8	0.2	−1.1	−2.2	−1.1	−1.5	−2.2	0.2	−0.0	−0.4	−2.4	−1.2	1.0	−1.7	0.3	1.7	−1.4	1.4	0.1	−0.7	0.3	1.1	0.7	−2.2	0.3
2.5	0.00007	0.0	1.3	−0.9	0.5	−0.9	0.7	1.0	0.8	0.6	0.2	−0.6	−0.1	−2.4	2.3	1.1	2.2	0.1	−1.2	−2.1	−1.2	−1.4	−2.2	0.3	0.1	−0.1	−2.2	−0.8	1.3	−2.4	1.2	0.1	−1.5	1.2	−0.4	−0.4	0.7	0.8	0.5	−1.7	0.1
2.5	0.00013	0.4	1.4	−0.8	0.7	−0.8	0.8	0.9	0.5	0.5	0.2	−0.5	0.3	−1.6	1.5	0.7	2.4	0.3	−1.2	−2.2	−0.5	−1.4	−2.6	0.4	0.4	−0.0	−2.1	−0.5	1.3	−2.4	1.6	−0.6	−1.7	1.3	−0.5	−0.4	0.7	0.6	0.3	−1.2	−0.1
2.5	0.00018	0.5	1.6	−0.7	0.8	−1.2	0.7	0.6	0.7	0.2	0.4	−0.1	0.1	−1.4	2.2	1.2	2.1	−0.1	−1.1	−1.2	−1.6	−1.1	−0.4	0.3	−0.2	−0.5	−1.7	−2.1	1.3	−2.4	0.8	0.2	−1.4	0.7	−0.7	−0.0	0.5	0.8	0.3	−0.2	−0.3
2.5	0.00035	0.8	1.5	−0.7	1.0	−1.1	1.1	0.5	0.3	0.1	0.3	−0.0	0.5	−0.2	1.6	0.6	2.3	0.1	−1.2	−1.1	−1.0	−0.6	−1.3	−0.6	0.3	−0.6	−1.1	−1.1	1.2	−2.3	1.0	0.3	−1.5	1.2	−0.6	−0.0	0.2	0.7	−0.0	0.8	−0.5
5.0	0.00007	−0.0	1.3	−0.8	0.4	−0.8	0.7	0.9	0.9	0.5	0.3	−0.5	−0.5	−2.5	2.5	1.0	2.1	−0.2	−1.1	−1.6	−1.8	−1.2	−1.5	−0.2	−0.2	−0.5	−2.1	−1.0	1.0	−1.9	0.5	1.1	−1.2	1.1	−0.2	−0.5	0.4	1.0	0.6	−1.8	0.2
5.0	0.00018	0.3	1.1	−0.9	0.7	−0.7	1.6	1.6	0.6	1.4	0.0	−0.2	−0.3	−1.4	0.9	0.1	2.4	−0.1	−1.1	−1.6	−0.9	−1.1	0.2	0.2	−0.1	0.3	−1.6	−0.9	0.2	−0.9	0.6	0.0	−0.2	0.9	−0.1	−0.1	0.1	0.5	0.3	0.5	0.9
5.0	0.00035	0.3	1.2	−0.8	0.9	−0.9	0.7	0.5	0.5	0.3	0.3	−0.2	0.1	−1.2	1.4	0.7	2.0	−0.2	−0.9	−1.1	−1.2	−0.5	−0.7	−0.2	−0.3	−0.6	−1.5	−0.7	0.7	−1.6	0.2	0.6	−1.2	0.6	−0.7	0.1	0.3	0.6	−0.0	0.5	−0.4
5.0	0.00100	0.5	1.2	−0.8	1.1	−1.0	0.9	0.2	0.1	−0.1	0.2	0.2	0.9	−0.1	0.9	0.7	1.3	−0.0	−0.6	−0.7	−0.6	0.0	−0.2	−0.3	−0.2	−0.8	−0.5	−0.3	0.7	−1.6	0.0	0.8	−1.1	0.8	−0.7	0.3	−0.1	0.4	−0.5	2.3	−0.7
7.0	0.00013	0.2	1.3	−0.7	0.7	−0.4	0.8	0.6	1.0	0.3	0.5	−0.6	−0.5	−1.9	1.6	−0.1	2.0	0.5	−0.7	−1.7	−1.7	−1.0	−1.1	1.2	0.0	−0.1	−1.9	−1.0	0.5	−0.7	1.2	0.1	−1.4	1.2	−0.4	−0.4	0.4	0.8	0.4	−1.6	0.1
7.0	0.00018	0.3	1.0	−0.5	0.6	−0.5	0.7	0.6	1.0	0.4	−0.2	−0.3	0.1	−1.6	1.1	0.8	2.3	0.5	−0.9	−2.8	−0.3	−1.1	−2.6	0.1	0.1	−0.0	−2.4	0.2	0.6	−1.2	0.6	0.2	−1.6	1.3	−0.1	−0.1	0.5	0.5	0.7	−1.1	−0.0
7.0	0.00030	0.4	1.1	−0.7	0.9	−0.5	0.8	0.6	0.4	0.4	0.3	−0.0	−0.0	−1.0	1.1	0.2	1.8	0.3	−0.7	−1.4	−1.1	−0.8	−0.3	0.7	−0.3	−0.2	−2.0	−0.7	0.3	−0.8	1.2	−0.3	−0.8	1.2	−0.3	−0.1	0.3	0.5	−0.0	0.3	0.2
7.0	0.00050	0.4	1.3	−0.6	1.0	−0.7	0.9	0.2	0.9	0.2	0.1	−0.1	0.0	−0.7	1.1	−0.1	1.7	−0.2	−0.8	−0.7	−0.4	−0.6	−0.1	0.1	−0.3	−0.2	−1.4	−1.0	0.2	−0.4	0.6	−0.2	−1.3	0.8	−0.4	0.2	0.2	0.4	0.1	0.8	0.2
7.0	0.00080	0.3	1.1	−0.6	1.0	−1.1	0.4	0.2	0.4	0.3	0.2	0.2	−0.2	0.7	−0.0	0.5	0.2	−0.3	−0.8	−0.6	−1.1	0.5	1.2	−0.4	−0.5	−1.2	−0.7	0.6	−0.9	0.9	−0.3	−1.6	0.7	−0.3	−0.0	0.2	0.2	−0.5	0.9	−0.5
7.0	0.00160	0.4	1.1	−0.7	1.0	−0.9	0.5	0.1	0.1	−0.0	−0.1	0.3	0.8	0.1	0.9	0.9	1.7	−0.3	−0.9	0.1	−0.3	0.4	−0.5	−0.2	0.4	−0.2	−0.3	−0.7	0.2	−0.5	0.4	0.3	−1.3	1.4	0.1	−0.0	−0.2	−0.1	−0.4	2.0	−0.7
12.0	0.00022	0.0	1.3	−0.7	0.6	−1.0	0.3	0.8	1.0	0.2	0.7	−0.4	−0.3	−1.5	1.4	0.5	1.4	0.4	−0.6	−1.4	−1.6	−1.2	−0.7	0.9	0.2	−0.1	−1.6	−1.1	0.3	−0.6	0.6	0.5	−0.9	1.9	−0.8	−0.2	0.5	0.7	0.2	−1.1	−0.0
12.0	0.00032	0.1	1.1	−1.0	0.8	−0.4	0.4	0.5	0.3	0.5	0.1	−0.2	−0.1	−0.9	1.2	0.6	2.0	0.6	−0.7	−1.9	−1.1	−0.9	−0.4	0.7	−0.3	−0.0	−2.4	−1.2	0.1	−1.0	0.8	0.1	0.2	1.1	0.2	−0.1	0.1	0.5	0.2	0.8	0.7
12.0	0.00050	0.3	1.2	−0.7	1.0	−0.3	0.6	0.2	0.8	0.2	0.3	−0.1	−0.1	−1.0	0.5	−0.0	1.3	0.0	−0.6	−1.0	−0.6	−0.7	−0.0	0.4	−0.1	0.0	−1.4	−0.8	0.0	−0.4	0.4	−0.3	−0.4	1.0	−0.3	0.0	0.1	0.5	−0.0	0.5	0.3
12.0	0.00080	0.3	1.1	−0.7	0.9	−0.8	0.4	0.3	0.5	0.3	0.2	0.2	0.4	−0.9	0.6	0.3	0.8	−0.0	−0.2	−0.5	−0.3	0.1	−0.3	0.2	−0.5	−0.8	−1.5	−0.8	0.2	−0.5	0.2	−0.5	−1.0	0.9	−0.5	0.0	0.1	0.4	−0.0	0.6	0.4
12.0	0.00150	0.0	1.2	−0.6	1.2	−0.9	0.5	0.2	0.1	0.0	0.2	0.3	0.6	0.2	0.7	0.1	1.2	−0.2	−0.5	−0.3	0.1	0.2	0.3	0.1	−0.6	−0.8	−0.7	−1.0	0.1	−0.3	−0.3	−0.5	−1.7	1.1	−0.4	−0.0	−0.2	0.4	−0.3	1.3	0.4
12.0	0.00300	0.3	0.9	−0.6	1.2	−0.9	0.5	−0.2	−0.0	−0.0	0.1	0.5	0.9	0.1	0.2	0.8	1.2	−0.2	−0.5	−0.2	−0.0	1.0	0.2	−0.4	0.1	−0.5	0.7	−0.4	0.5	−0.9	0.4	−0.5	−1.0	1.0	0.2	−0.1	−0.4	0.0	−1.1	2.5	−0.7
18.0	0.00035	−0.1	1.1	−0.7	0.7	−0.6	0.3	0.5	0.7	0.3	0.4	−0.3	−0.3	−1.4	1.1	0.7	1.7	0.3	−0.7	−1.4	−1.0	−0.7	−0.8	0.7	0.3	−0.0	−1.3	−1.7	−0.0	0.1	0.5	0.5	−0.8	1.7	−0.8	−0.1	0.4	0.5	−0.0	−0.7	−0.1
18.0	0.00050	0.2	0.8	−0.6	0.8	−0.9	0.9	0.4	0.5	−0.1	0.4	0.0	0.0	−1.3	1.1	0.6	1.8	0.7	−0.5	−1.9	−1.2	−0.6	−0.5	0.6	−0.3	0.0	−2.4	−1.3	0.1	−0.9	1.0	−0.2	0.1	1.3	0.4	−0.1	0.0	0.4	0.5	0.8	0.8
18.0	0.00080	0.3	1.0	−0.6	0.9	−0.2	0.5	0.0	0.5	0.2	0.2	−0.0	0.0	−0.8	0.5	−0.0	1.2	0.0	−0.5	−0.8	−0.3	−0.4	−0.0	0.3	−0.2	0.1	−1.1	−0.9	−0.0	−0.3	0.3	−0.3	−0.3	0.8	−0.4	0.1	0.1	0.4	−0.0	0.6	0.3
18.0	0.00135	0.2	1.0	−0.5	1.0	−0.6	0.6	0.0	0.4	0.1	0.1	0.1	0.2	−0.3	0.7	0.3	1.3	−0.1	−0.6	−0.6	−0.2	−0.2	0.4	0.1	−0.4	−0.1	−1.0	−0.5	0.1	−0.3	0.1	−0.6	−1.2	1.0	−0.2	0.5	0.1	0.2	0.3	1.0	0.1
18.0	0.00250	0.0	0.7	−0.8	0.9	−0.5	0.2	−0.1	0.1	0.0	0.1	0.3	0.4	0.2	1.0	0.2	1.1	−0.2	−0.5	−0.0	0.4	0.1	0.4	0.4	−0.3	−0.3	−0.2	−0.5	0.2	−0.5	−0.1	−0.4	−1.3	1.0	−0.4	−0.0	−0.2	0.1	0.1	1.3	0.3
18.0	0.00450	0.3	0.8	−0.6	1.2	−0.6	0.7	−0.2	−0.3	−0.2	0.1	0.1	0.8	0.5	0.1	1.3	0.8	−0.1	−0.3	−0.2	−0.4	0.7	0.5	0.3	0.2	−0.3	0.4	0.7	0.0	−0.1	−0.0	−0.8	−1.7	1.4	1.5	1.2	−0.3	0.5	−0.8	2.4	−0.7
32.0	0.00060	−0.2	0.9	−0.7	0.6	−0.6	0.4	0.4	0.8	0.4	0.2	−0.4	−0.5	−1.9	1.5	0.8	1.6	−0.2	−0.7	−1.1	−0.8	−0.1	−0.6	−0.1	−0.6	−0.5	−1.3	−0.6	0.6	−1.2	0.2	0.5	−0.8	0.5	−0.4	−0.1	0.2	0.5	0.1	−0.5	−0.1
32.0	0.00080	0.2	0.9	−0.3	0.7	−0.7	0.5	0.3	0.4	0.1	0.4	−0.1	−0.1	−1.2	0.8	0.4	1.4	0.3	−0.4	−1.3	−0.9	−0.4	−0.4	0.4	0.0	−0.1	−1.4	−1.0	−0.4	−0.9	0.5	−0.2	−0.3	1.3	−0.3	−0.1	0.2	0.5	0.2	0.3	0.3
32.0	0.00140	0.1	0.8	−0.5	0.8	−0.4	0.4	−0.2	0.4	0.3	0.3	0.0	−0.1	−0.6	0.3	−0.0	1.3	−0.1	−0.3	−0.8	−0.2	−0.1	0.3	0.1	−0.3	−0.3	−0.9	−0.7	0.1	−0.3	0.3	−0.2	−0.6	1.0	−0.3	−0.1	0.1	0.3	0.4	0.4	0.0
32.0	0.00240	0.2	0.7	−0.4	1.1	−0.7	0.8	−0.0	0.4	0.3	0.3	0.2	0.2	−0.3	0.2	−0.1	1.0	−0.6	−0.3	−0.5	0.1	−0.1	0.7	0.1	0.0	−0.5	−1.0	−0.5	0.1	−0.4	0.1	−0.3	−0.8	0.9	−0.1	−0.2	−0.0	0.5	0.1	0.3	0.3
32.0	0.00320	0.1	0.4	−1.3	0.6	−0.1	−0.5	−0.3	−0.4	0.8	0.0	−0.0	0.1	0.3	0.7	0.4	0.7	0.4	0.0	0.2	0.1	0.8	0.4	0.3	−0.1	−0.3	−0.7	−0.2	0.2	−0.3	−0.0	−0.2	−1.5	1.1	−0.5	−0.0	−0.2	−0.2	0.7	1.1	0.6
32.0	0.00550	0.4	0.7	−0.5	1.0	−0.7	0.5	−0.1	0.1	0.2	0.1	0.4	−0.1	0.2	−0.3	0.1	1.2	−0.7	−0.6	−0.3	−0.1	0.5	0.8	−0.2	−0.2	−1.0	−0.6	−0.7	0.5	−0.4	−0.4	−0.3	−0.7	1.0	0.6	−0.6	−0.3	1.0	−0.2	0.6	−0.3
32.0	0.00800	0.4	0.8	−0.6	1.2	0.1	1.1	−0.2	−0.2	−0.2	0.2	−0.5	0.4	1.2	0.6	0.5	0.4	0.7	0.1	−0.3	−0.4	1.0	0.7	0.5	−0.1	−0.5	0.3	2.2	0.4	−1.0	0.3	−0.5	−1.3	2.1	0.7	−0.6	−0.6	0.1	−1.2	1.7	−0.5
60.0	0.00140	−0.0	0.5	−0.2	1.0	−0.7	0.5	−0.4	0.3	−0.1	0.4	−0.1	−0.2	−1.1	0.3	0.4	0.7	0.4	−0.3	−0.8	−0.8	−0.2	−0.3	0.5	−0.1	−0.4	−1.3	−1.1	0.1	−0.2	0.2	−0.6	−0.5	1.2	−0.6	0.1	0.1	0.1	0.2	0.5	0.4
60.0	0.00200	0.0	0.4	−0.2	0.9	−0.4	0.4	−0.5	0.3	0.1	0.4	−0.0	−0.1	−0.6	−0.2	0.1	0.6	0.1	−0.2	−0.1	−0.3	−0.0	−0.2	0.1	−0.2	0.4	−0.8	−0.5	0.1	−0.3	0.1	−0.2	−0.5	0.4	−0.2	0.0	0.1	0.1	0.1	0.4	0.7
60.0	0.00320	0.1	0.6	−0.4	1.0	−0.4	0.5	−0.3	0.1	0.5	0.1	−0.0	−0.3	−0.3	0.2	0.0	1.2	−0.1	−0.3	−0.7	−0.1	−0.2	0.8	0.1	0.0	0.3	−0.6	−0.3	0.0	−0.2	−0.1	−0.5	−0.7	0.7	−0.6	0.1	−0.1	−0.0	0.3	0.7	−0.0
60.0	0.00500	0.2	0.3	−0.4	0.8	−0.6	0.7	−0.4	0.1	0.3	0.2	0.2	−0.0	−0.1	0.3	0.1	1.0	−0.0	−0.6	−0.3	0.6	0.0	0.8	0.1	0.4	−0.2	−0.5	−0.1	0.1	−0.2	−0.0	−0.6	−0.9	0.5	−0.5	0.1	0.0	0.2	−0.1	0.6	0.3
60.0	0.00800	0.0	0.6	−0.7	1.0	−0.3	0.5	−0.1	−0.6	0.5	0.6	0.1	0.1	−0.2	0.3	−0.0	0.2	−0.4	0.0	−0.2	0.1	0.1	0.4	0.2	−0.4	−0.0	−0.2	−0.3	0.1	−0.1	−0.4	−0.5	−0.8	0.7	0.1	−0.1	−0.6	−0.1	0.2	1.1	−0.4
60.0	0.01500	−0.2	0.3	−0.6	1.1	−0.3	0.6	−0.4	0.2	0.5	−0.2	0.1	−0.3	−0.2	0.1	0.1	1.0	−0.4	−0.2	−0.4	−0.2	0.8	0.4	0.1	−0.9	−1.1	0.3	0.2	0.2	0.1	0.9	0.2	−1.2	−0.5	−0.1	0.1	−0.4	0.0	−0.8	2.1	−0.6
120.0	0.00200	−0.3	0.5	−0.3	1.5	−0.5	0.3	−0.8	0.3	0.2	0.4	−0.0	−0.5	−0.9	0.1	0.3	1.3	0.9	0.5	−0.4	−0.3	−0.6	−0.1	0.4	0.3	0.1	−1.1	−0.9	−0.0	−0.6	0.2	−0.2	−0.2	1.0	−0.2	−0.3	0.7	0.6	0.1	0.7	0.2
120.0	0.00320	0.2	0.3	−0.7	1.0	−0.5	0.6	0.3	−0.4	−0.4	−0.4	0.2	−0.5	−0.2	−0.6	−0.2	0.7	−0.0	−0.7	0.1	−0.4	0.1	−0.1	−0.0	−0.7	−0.0	−0.5	−0.2	0.1	−0.2	0.0	−0.3	−0.2	−0.0	−0.1	0.3	0.2	0.1	0.2	−0.1	−0.1
120.0	0.00550	0.0	−0.3	−0.2	1.2	−0.5	0.6	−0.5	0.1	0.4	0.4	0.2	−0.4	−0.5	−0.4	0.2	0.7	0.1	0.2	0.0	0.1	0.5	0.4	0.0	0.4	0.2	−0.7	−0.4	0.1	−0.4	−0.0	−0.2	−1.2	0.6	−0.2	0.1	0.7	0.6	0.2	0.9	0.5
120.0	0.01000	0.2	0.1	−0.5	1.0	−0.5	0.6	−0.2	−0.2	0.6	−0.1	0.4	0.0	−0.3	−0.5	0.1	0.6	−0.0	0.0	0.0	−0.3	0.4	0.1	0.2	−0.3	0.4	−0.6	0.1	0.5	0.1	−0.1	−0.8	−0.7	0.6	−0.2	−0.4	0.6	0.4	0.0	0.7	−0.0
120.0	0.02500	0.2	0.3	−0.9	1.0	−0.4	0.5	0.5	−0.6	−0.7	−0.5	−0.3	−0.4	0.0	−0.8	−0.4	1.2	−0.7	0.1	−0.2	−0.0	0.1	0.4	−0.2	−0.4	−0.5	−0.4	−0.2	0.1	−0.3	−0.2	−0.6	−0.6	−0.1	−0.4	1.0	0.2	−0.0	−0.3	1.4	−0.5
200.0	0.00500	−0.3	0.1	−0.0	1.2	−0.3	0.4	−1.1	0.2	0.4	0.2	−0.1	−0.5	−0.8	−0.8	0.3	1.1	0.4	0.4	−0.7	0.2	1.0	1.1	0.7	−0.1	0.2	−1.0	−0.5	0.1	−0.2	0.4	−0.5	−0.6	0.9	−0.3	0.0	0.0	−0.2	0.1	0.7	0.4
200.0	0.01300	0.0	0.4	−0.8	0.8	−0.1	0.3	−0.1	−0.2	1.2	−0.1	−0.1	−0.4	−0.3	−0.2	0.4	0.6	0.2	0.1	−0.1	0.0	0.6	0.6	0.1	0.4	0.2	−0.6	−0.3	0.2	−0.3	−0.1	−0.3	−1.2	0.9	−0.4	−0.0	−0.1	−0.1	0.1	0.7	0.4
350.0	0.01000	−0.5	−0.1	−0.0	1.3	−0.5	0.9	−0.8	0.3	0.9	0.1	0.0	−1.2	−0.7	−1.0	0.4	1.0	−0.4	0.0	−0.3	−0.0	0.1	0.7	0.1	0.8	0.8	−0.8	−0.7	0.1	−0.1	−0.0	−0.4	−0.4	0.7	−0.3	0.1	0.2	−0.2	−0.5	0.5	0.2
350.0	0.02500	−0.1	−0.4	−0.6	0.9	−0.5	0.5	−0.6	−0.2	0.9	−0.0	0.1	−0.6	0.1	−0.3	0.7	1.1	0.2	0.2	0.1	0.0	1.1	0.4	−0.2	0.6	0.2	−0.8	−0.5	0.2	−0.2	−0.1	−0.7	−1.6	1.0	−0.4	−0.0	0.1	−0.1	−0.5	0.7	0.5
650.0	0.01300	−0.5	−0.1	0.6	1.8	−0.8	1.7	−0.7	0.1	1.7	0.9	0.5	−1.0	−1.0	−1.4	0.3	0.3	0.8	−0.4	0.2	0.1	0.8	0.5	0.2	1.4	0.7	−1.6	−0.6	0.5	−0.6	0.3	0.1	−0.8	0.3	−0.3	0.1	−0.0	0.1	0.1	0.5	0.9
650.0	0.03200	−0.9	1.0	0.0	1.9	−1.4	2.2	−0.1	−0.6	2.3	0.3	0.9	−0.3	−0.4	−0.6	0.8	2.2	1.1	1.8	1.5	0.9	0.8	1.5	−0.3	0.6	0.2	−0.7	−0.3	0.4	−0.5	−0.5	−0.3	−3.1	1.0	−1.3	−0.2	0.9	0.9	0.4	1.4	1.4
2000.0	0.05000	−1.5	1.4	2.9	2.7	−1.5	4.6	2.2	−0.6	4.6	0.0	0.8	−2.4	−2.5	−3.4	0.5	0.5	0.3	1.2	1.2	0.6	2.6	1.7	−0.0	2.9	2.1	−2.0	−1.0	1.1	−1.1	0.1	0.6	−2.9	0.9	−1.2	0.4	−0.1	0.3	0.1	1.2	2.0

Table E.4: The continuation of Table E.3.

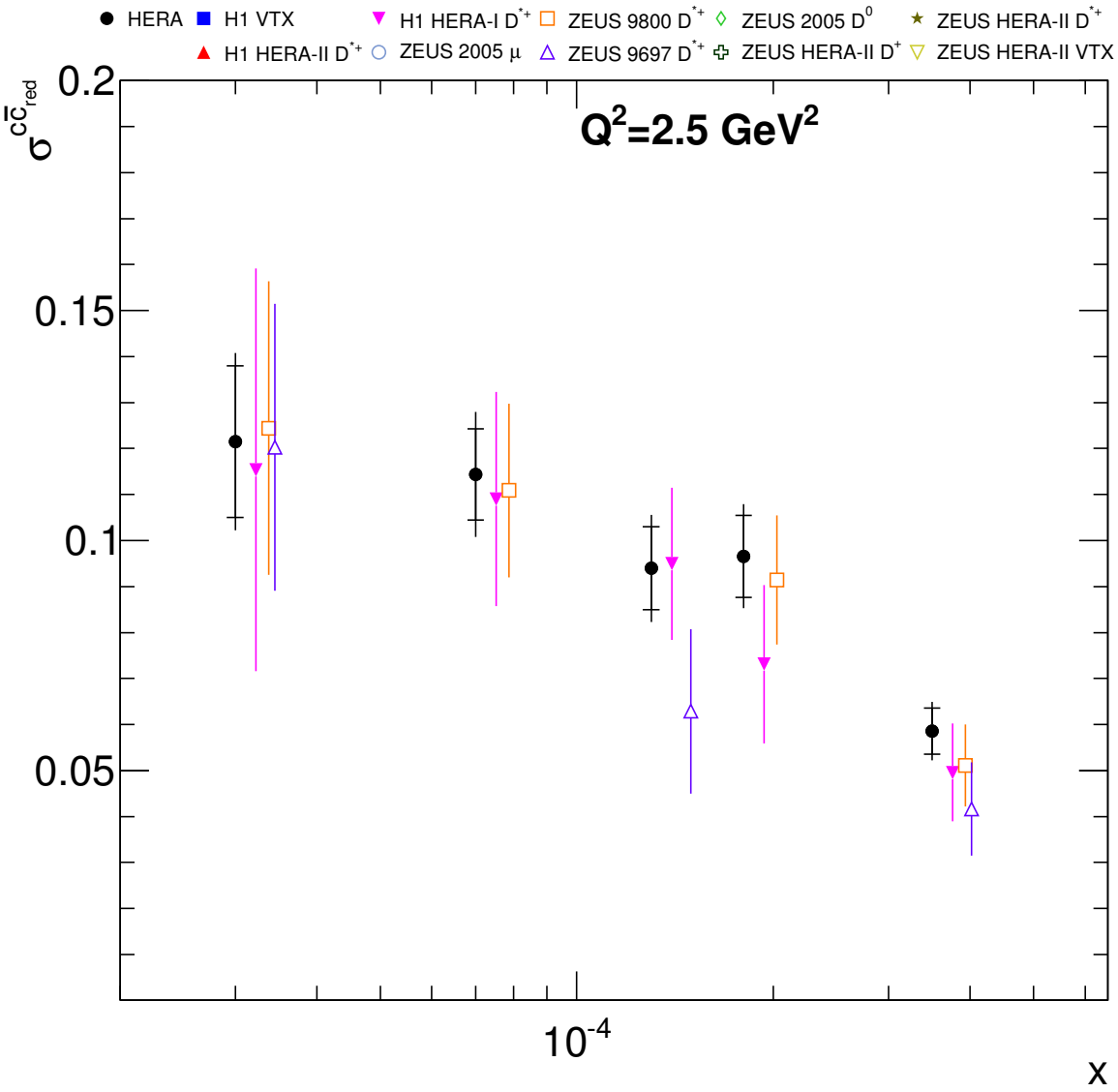

Figure E.1: Combined measurements of $\sigma_{red}^{c\bar{c}}$ (closed circles) shown as a function of x for $Q^2 = 2.5\,\mathrm{GeV}^2$. The input measurements are also shown with different markers. For the combined data, the inner error bars indicate the uncorrelated part of the uncertainties and the outer error bars represent the total uncertainties. For presentation purposes each individual measurement is shifted in x.

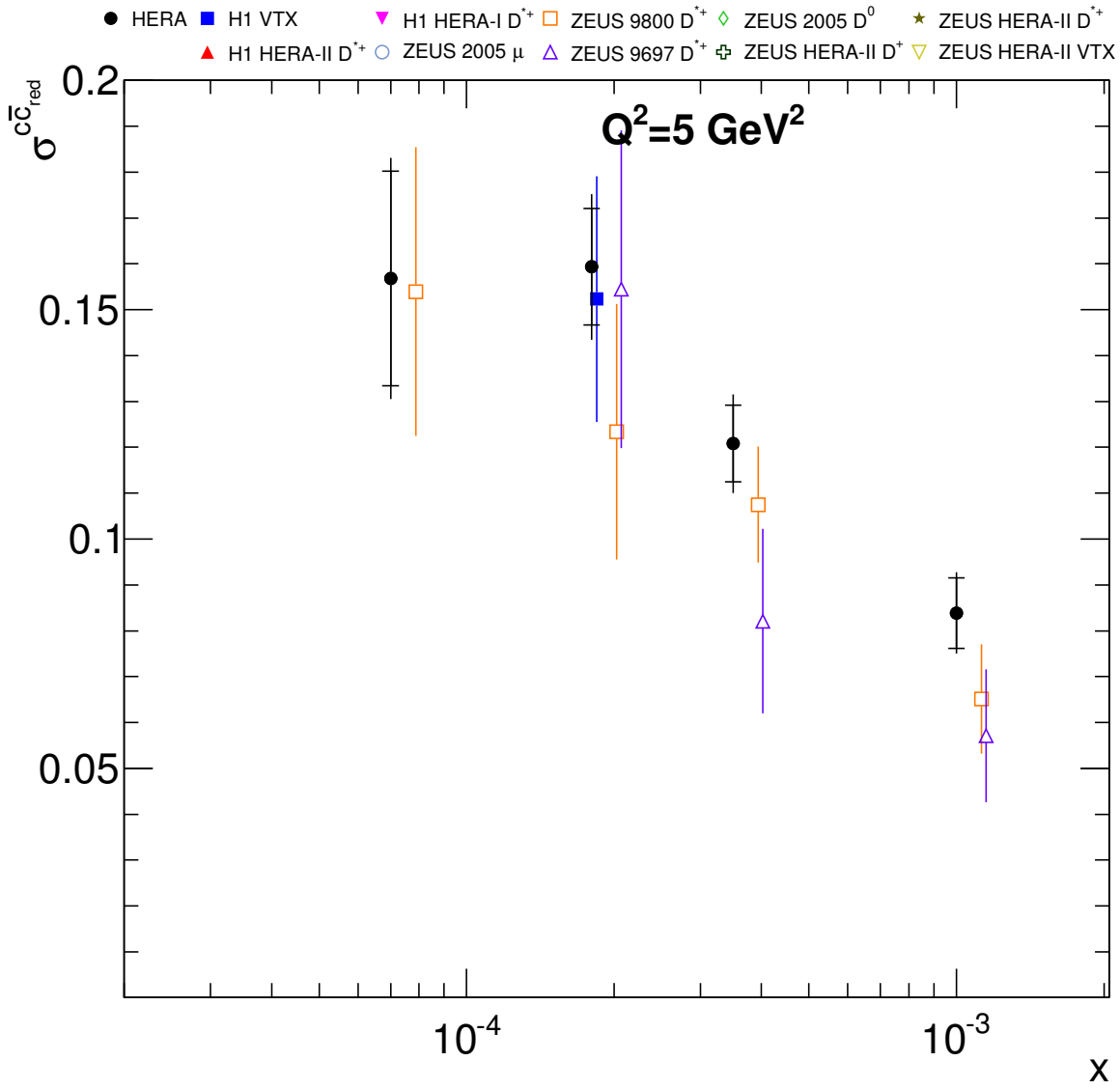

Figure E.2: Combined measurements of $\sigma_{red}^{c\bar{c}}$ (closed circles) shown as a function of x for $Q^2 = 5\,\mathrm{GeV}^2$. The input measurements are also shown with different markers. For the combined data, the inner error bars indicate the uncorrelated part of the uncertainties and the outer error bars represent the total uncertainties. For presentation purposes each individual measurement is shifted in x.

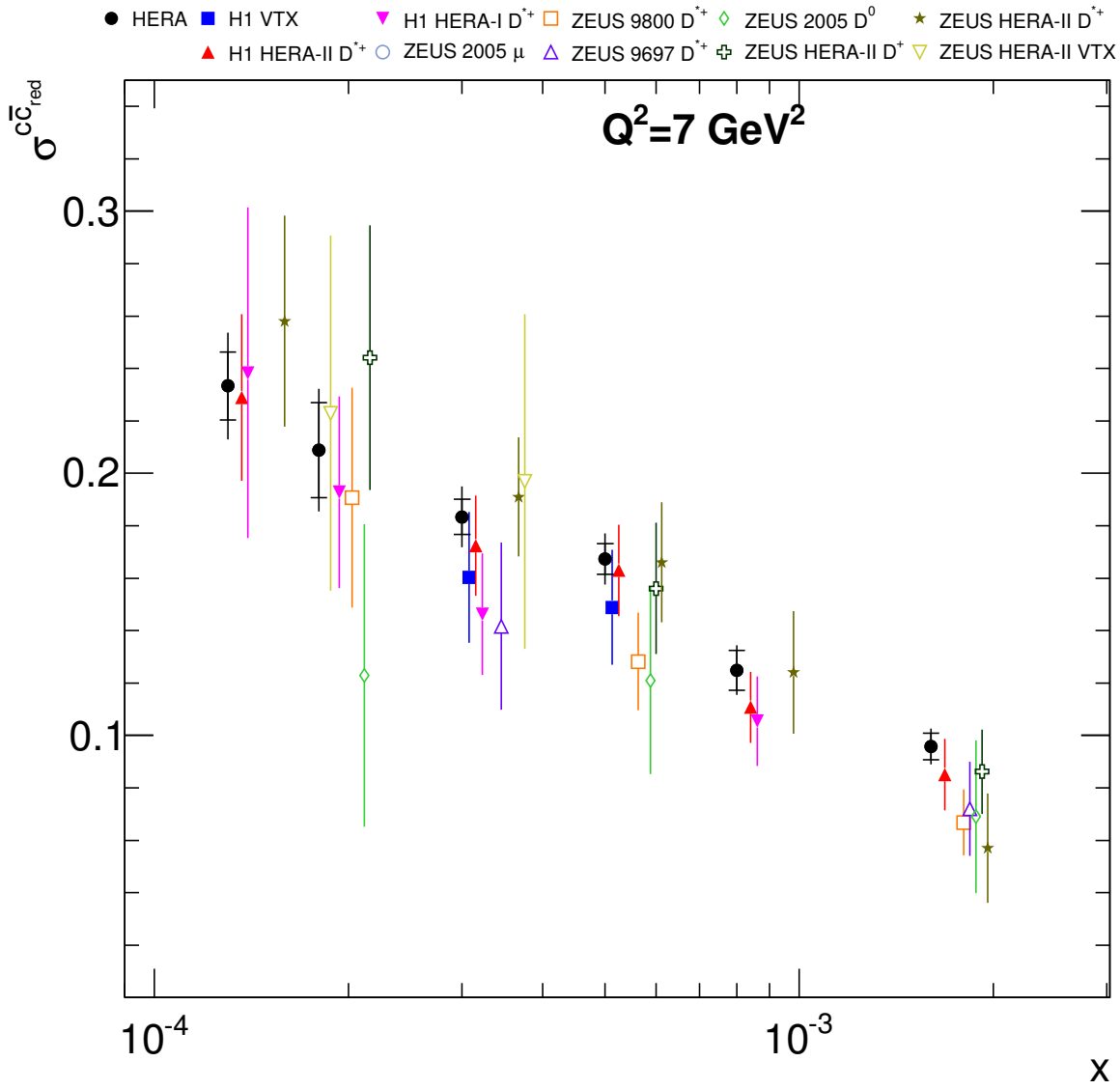

Figure E.3: Combined measurements of $\sigma_{red}^{c\bar{c}}$ (closed circles) shown as a function of x for $Q^2 = 7\,\mathrm{GeV}^2$. The input measurements are also shown with different markers. For the combined data, the inner error bars indicate the uncorrelated part of the uncertainties and the outer error bars represent the total uncertainties. For presentation purposes each individual measurement is shifted in x.

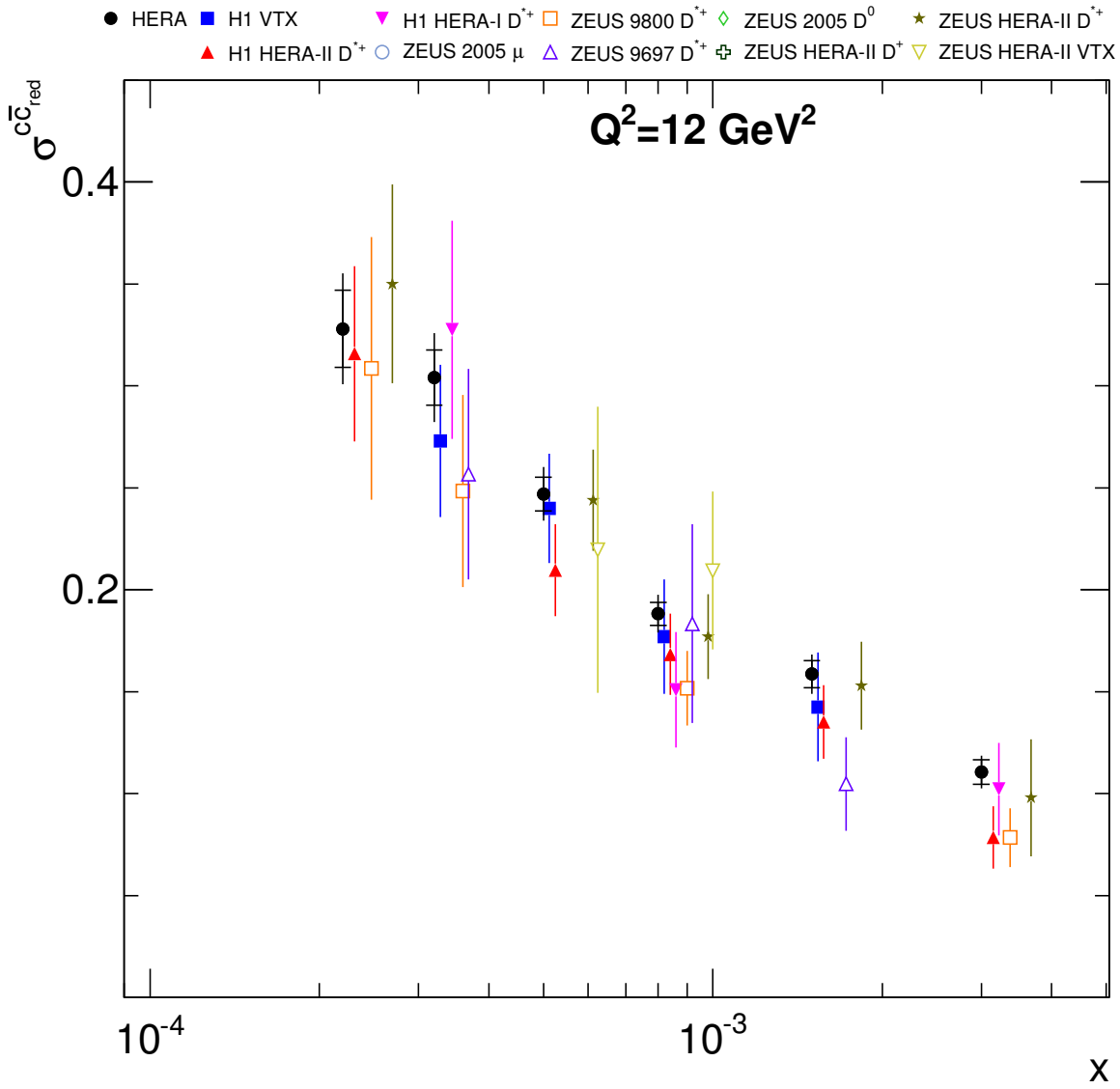

Figure E.4: Combined measurements of $\sigma_{red}^{c\bar{c}}$ (closed circles) shown as a function of x for $Q^2 = 12\,\mathrm{GeV}^2$. The input measurements are also shown with different markers. For the combined data, the inner error bars indicate the uncorrelated part of the uncertainties and the outer error bars represent the total uncertainties. For presentation purposes each individual measurement is shifted in x.

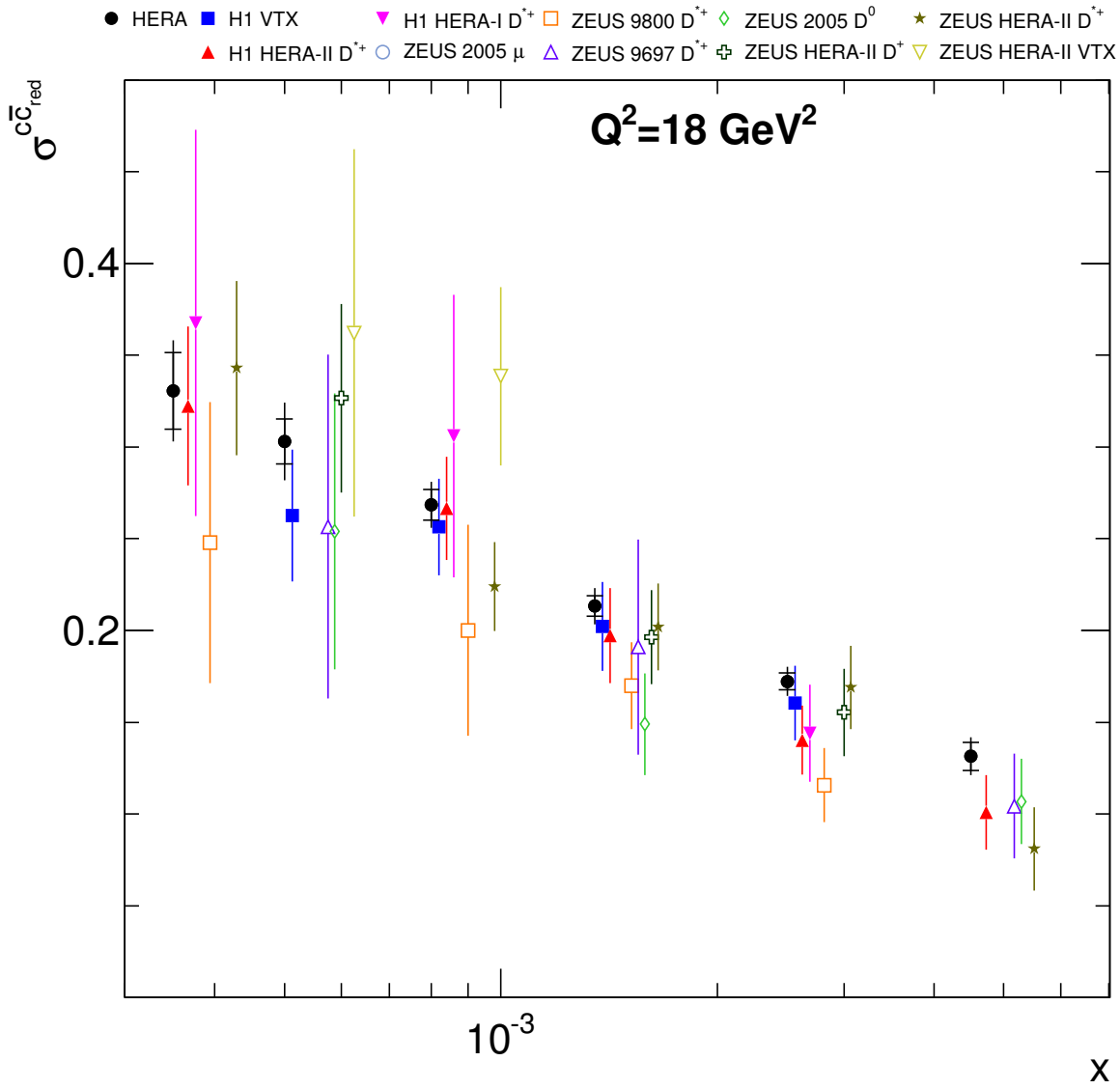

Figure E.5: Combined measurements of $\sigma_{red}^{c\bar{c}}$ (closed circles) shown as a function of x for $Q^2 = 18\,\mathrm{GeV}^2$. The input measurements are also shown with different markers. For the combined data, the inner error bars indicate the uncorrelated part of the uncertainties and the outer error bars represent the total uncertainties. For presentation purposes each individual measurement is shifted in x.

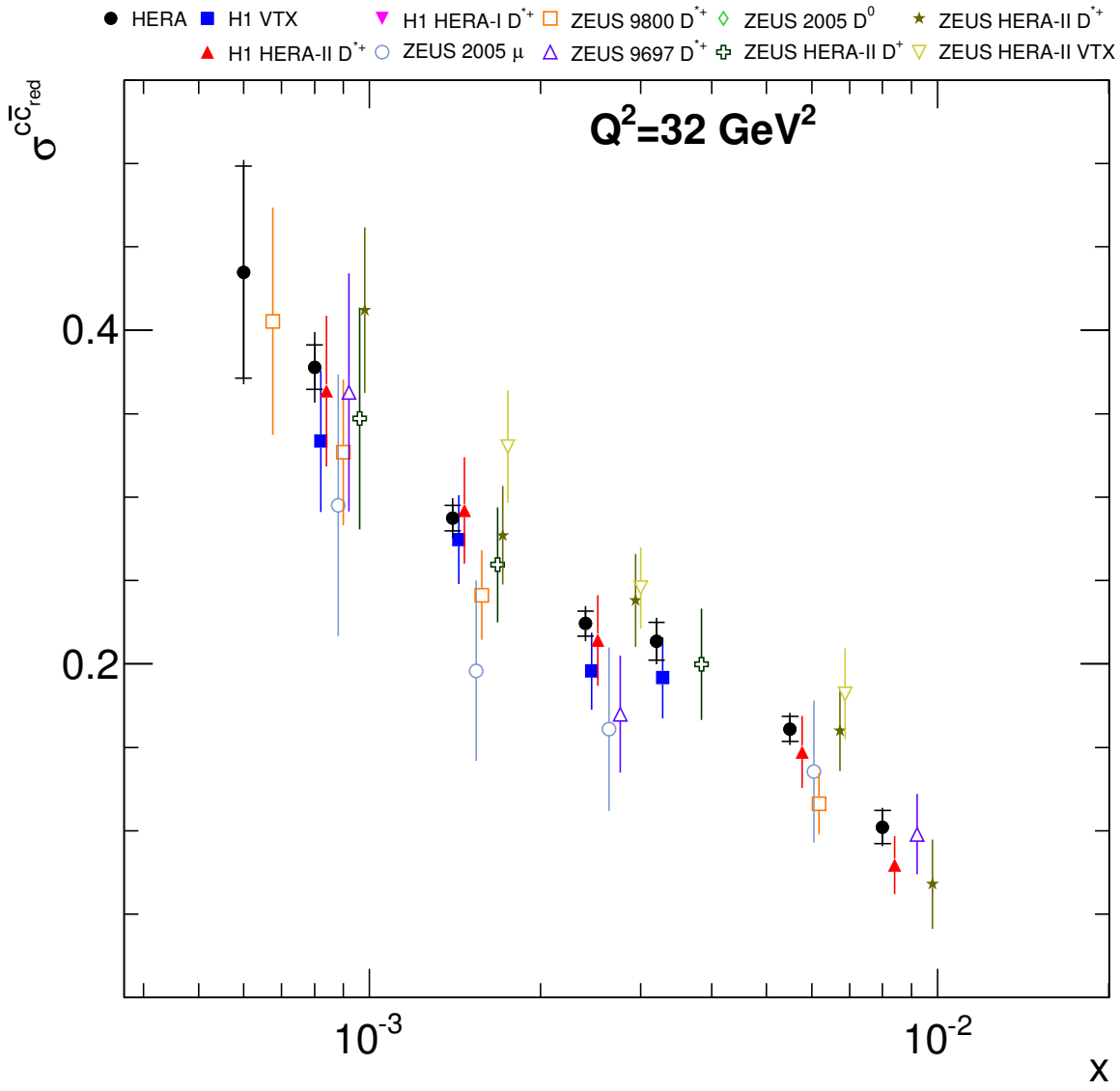

Figure E.6: Combined measurements of $\sigma_{red}^{c\bar{c}}$ (closed circles) shown as a function of x for $Q^2 = 32\,\mathrm{GeV}^2$. The input measurements are also shown with different markers. For the combined data, the inner error bars indicate the uncorrelated part of the uncertainties and the outer error bars represent the total uncertainties. For presentation purposes each individual measurement is shifted in x.

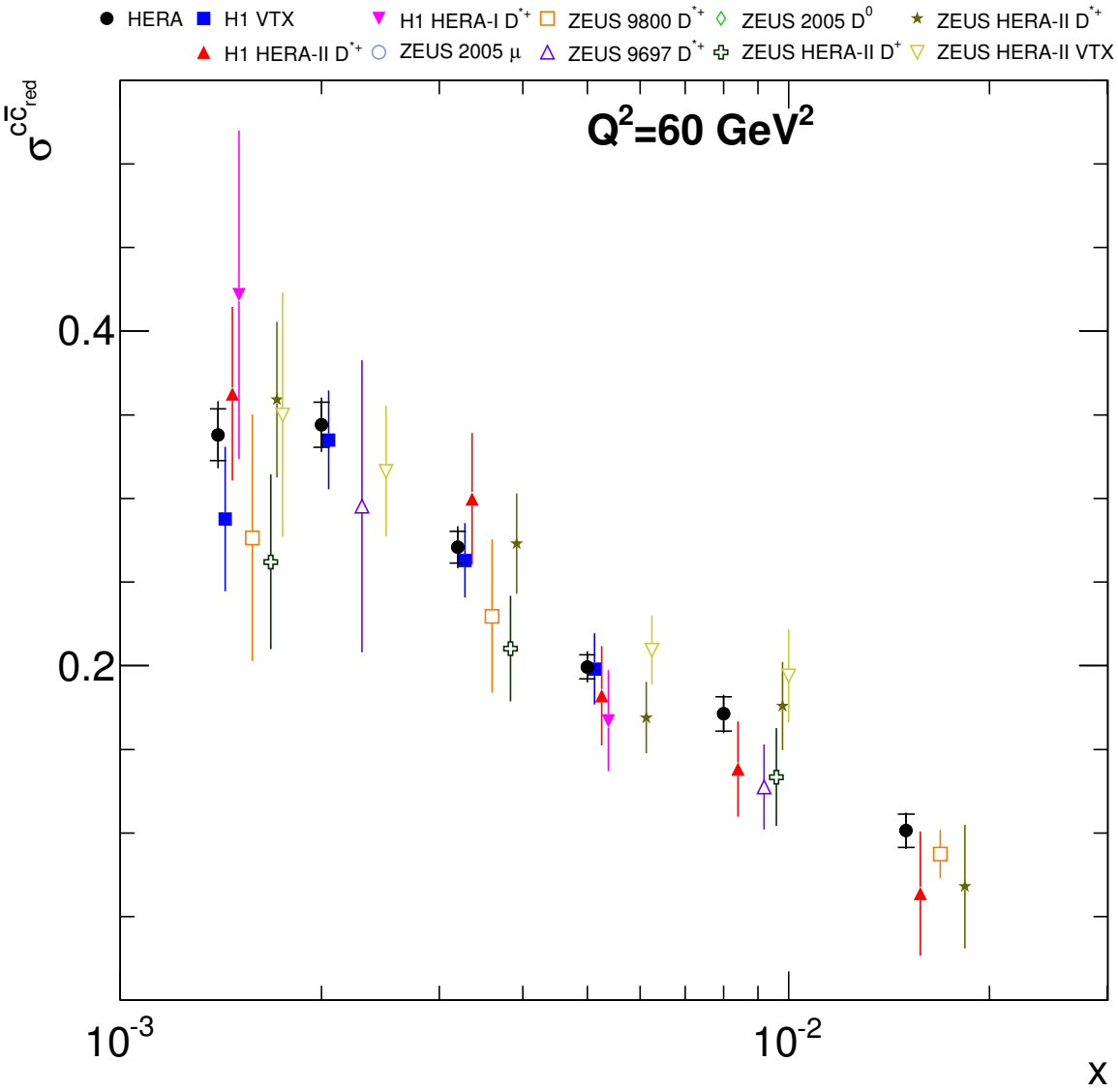

Figure E.7: Combined measurements of $\sigma_{red}^{c\bar{c}}$ (closed circles) shown as a function of x for $Q^2 = 60\,\mathrm{GeV}^2$. The input measurements are also shown with different markers. For the combined data, the inner error bars indicate the uncorrelated part of the uncertainties and the outer error bars represent the total uncertainties. For presentation purposes each individual measurement is shifted in x.

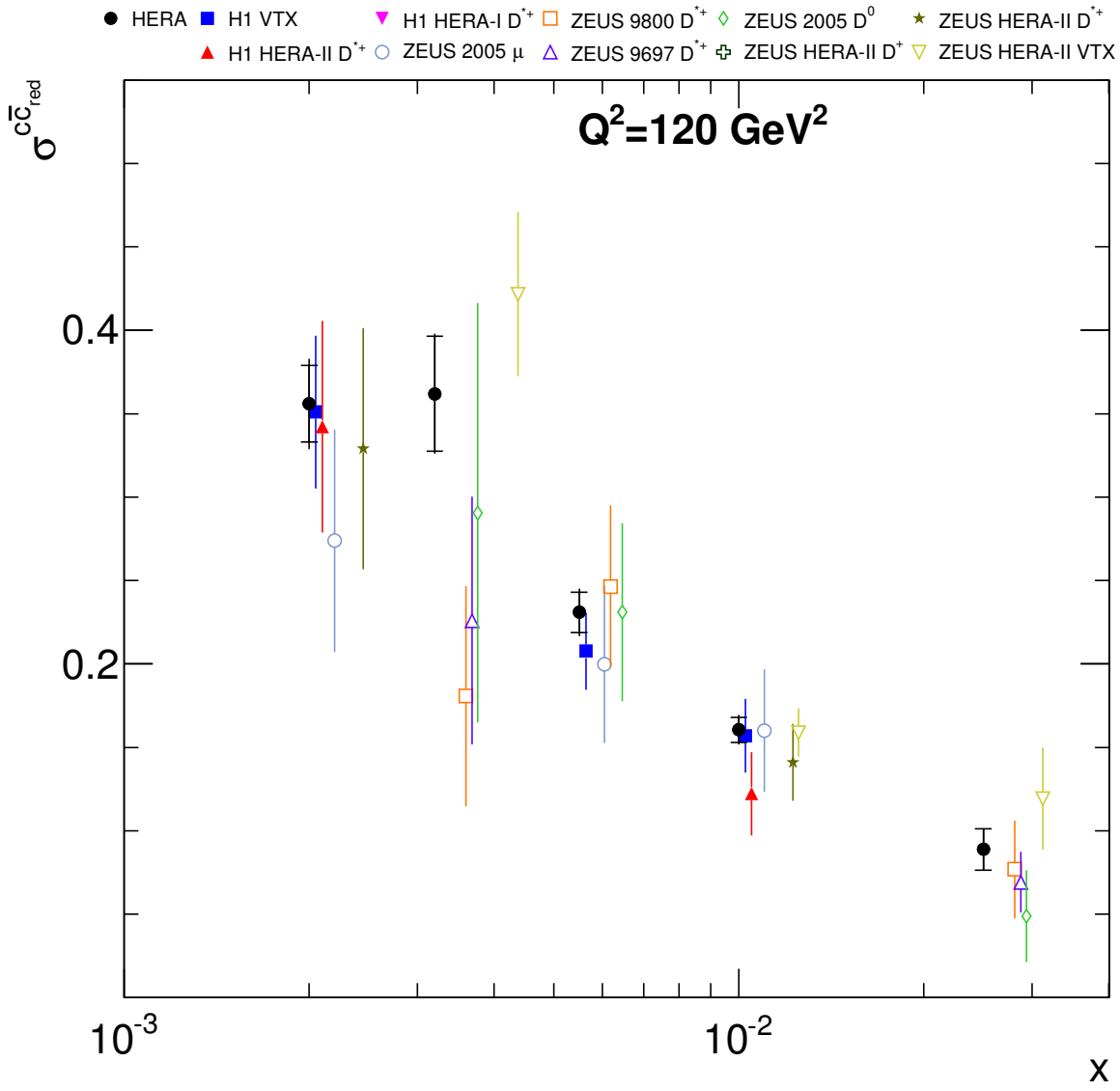

Figure E.8: Combined measurements of $\sigma_{red}^{c\bar{c}}$ (closed circles) shown as a function of x for $Q^2 = 120\,\mathrm{GeV}^2$. The input measurements are also shown with different markers. For the combined data, the inner error bars indicate the uncorrelated part of the uncertainties and the outer error bars represent the total uncertainties. For presentation purposes each individual measurement is shifted in x.

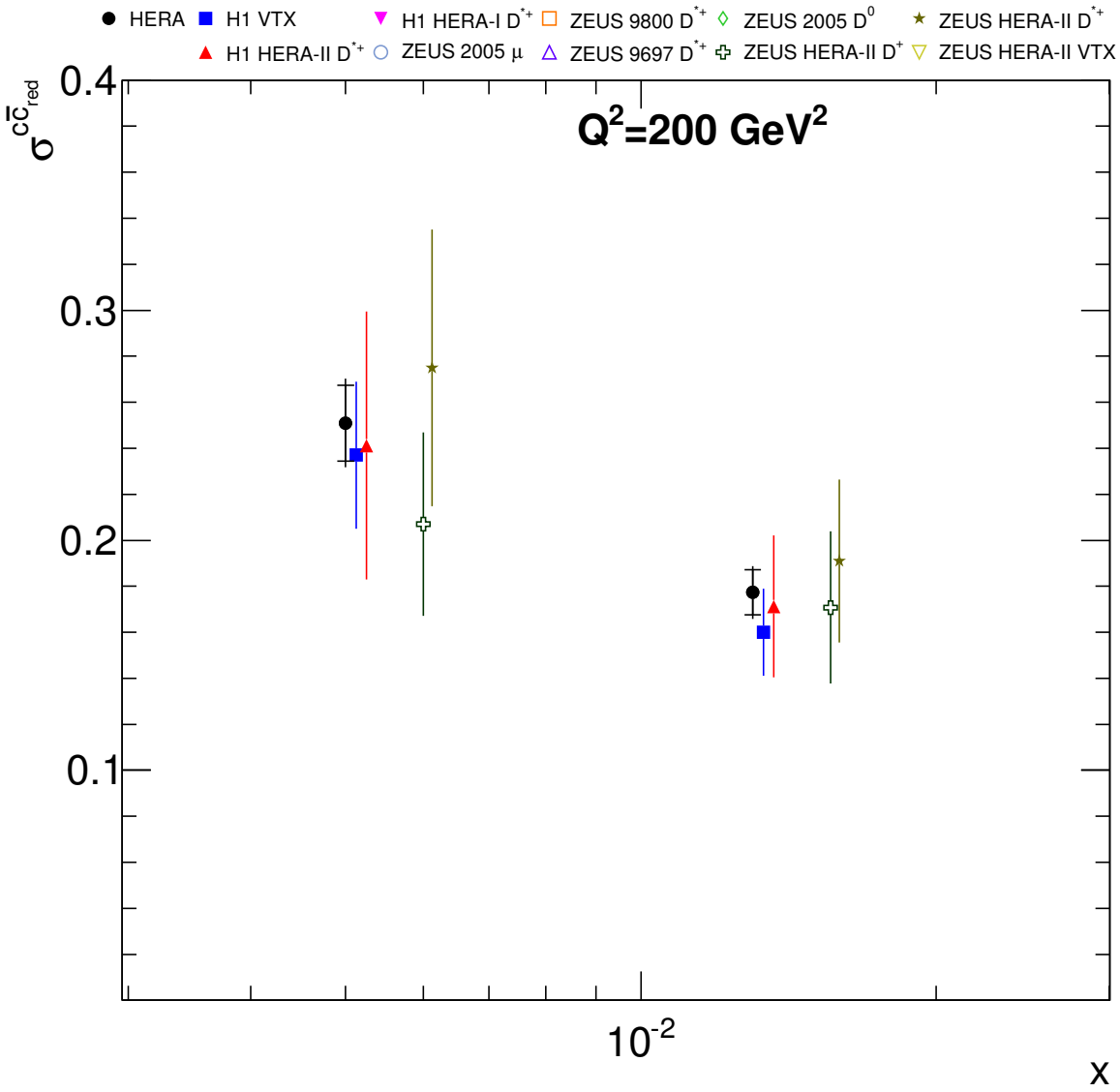

Figure E.9: Combined measurements of $\sigma_{red}^{c\bar{c}}$ (closed circles) shown as a function of x for $Q^2 = 200\,\mathrm{GeV}^2$. The input measurements are also shown with different markers. For the combined data, the inner error bars indicate the uncorrelated part of the uncertainties and the outer error bars represent the total uncertainties. For presentation purposes each individual measurement is shifted in x.

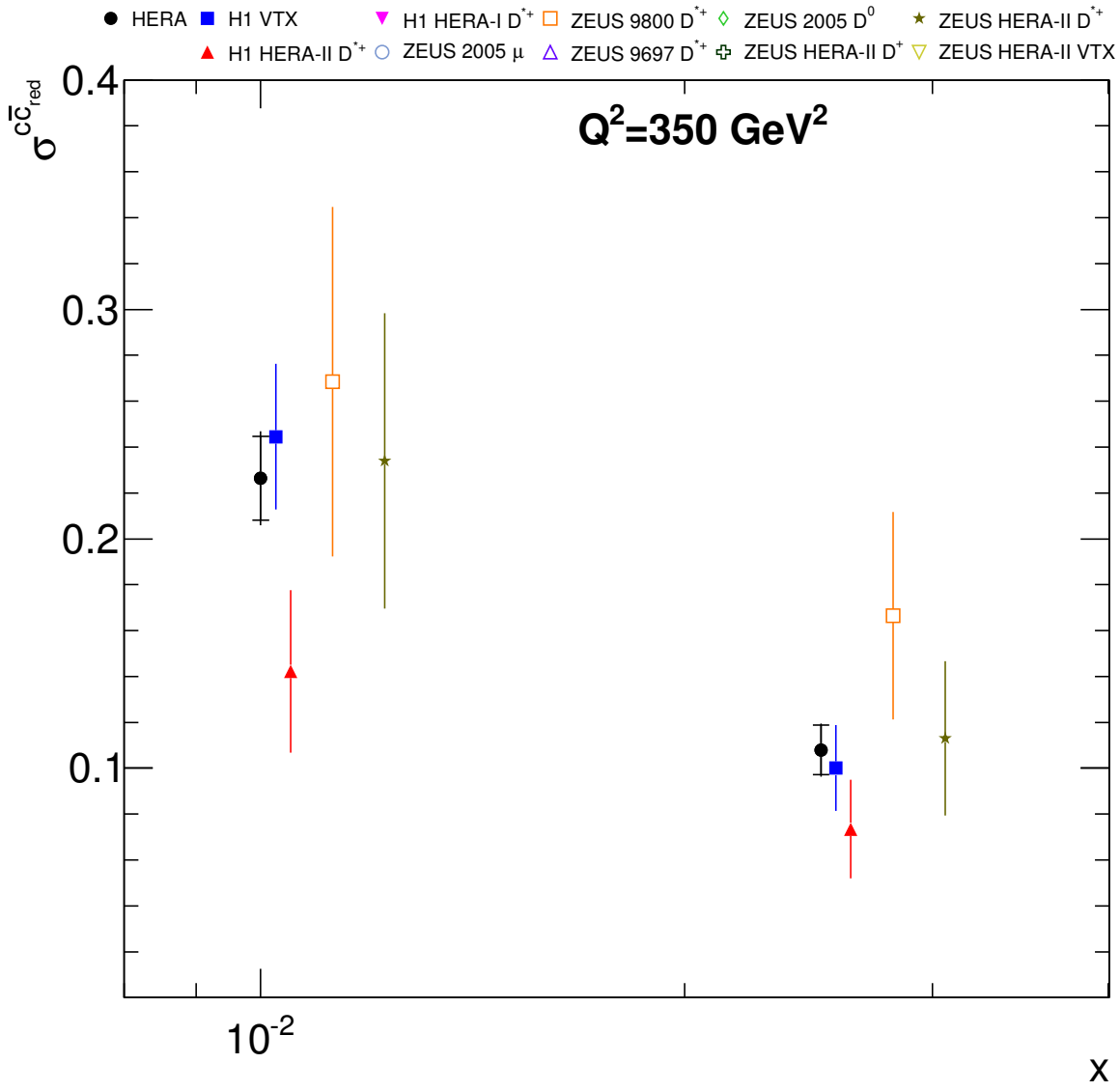

Figure E.10: Combined measurements of $\sigma_{red}^{c\bar{c}}$ (closed circles) shown as a function of x for $Q^2 = 350\,\mathrm{GeV}^2$. The input measurements are also shown with different markers. For the combined data, the inner error bars indicate the uncorrelated part of the uncertainties and the outer error bars represent the total uncertainties. For presentation purposes each individual measurement is shifted in x.

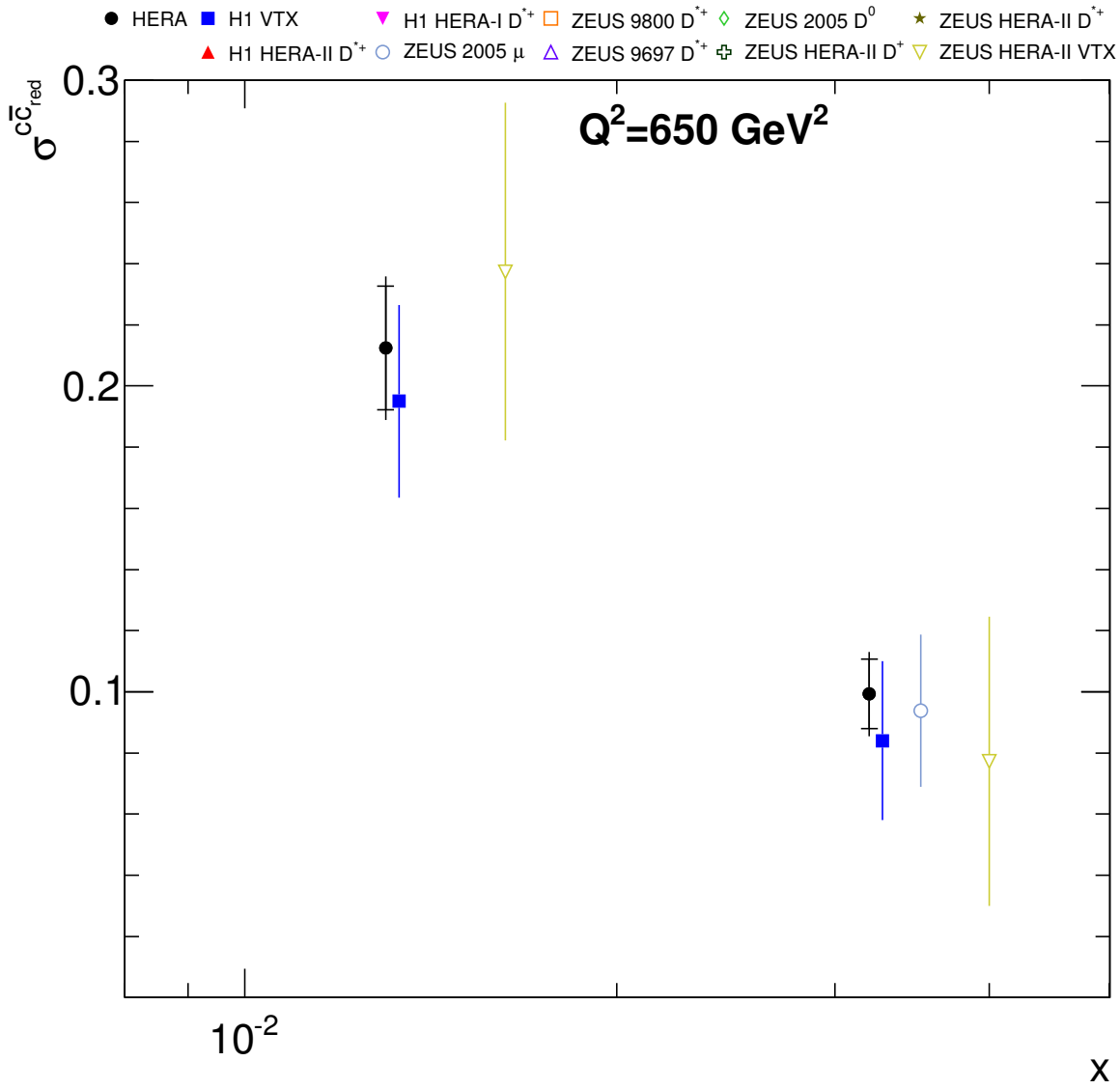

Figure E.11: Combined measurements of $\sigma_{red}^{c\bar{c}}$ (closed circles) shown as a function of x for $Q^2 = 650\,\mathrm{GeV}^2$. The input measurements are also shown with different markers. For the combined data, the inner error bars indicate the uncorrelated part of the uncertainties and the outer error bars represent the total uncertainties. For presentation purposes each individual measurement is shifted in x.

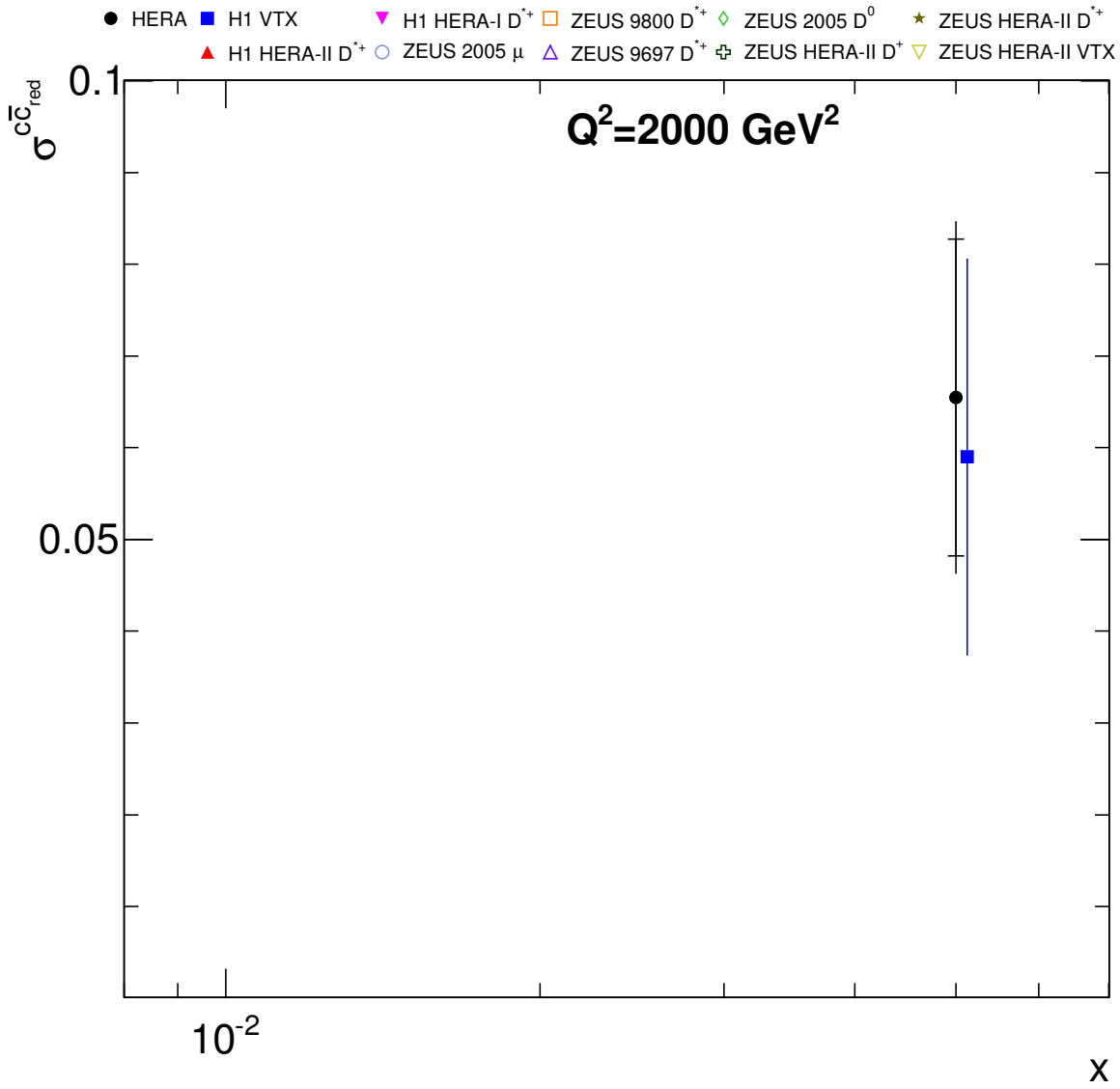

Figure E.12: Combined measurements of $\sigma_{red}^{c\bar{c}}$ (closed circles) shown as a function of x for $Q^2 = 2000\,\mathrm{GeV}^2$. The input measurements are also shown with different markers. For the combined data, the inner error bars indicate the uncorrelated part of the uncertainties and the outer error bars represent the total uncertainties. For presentation purposes each individual measurement is shifted in x.

APPENDIX F

PDF fit with LHCb heavy-flavour data: additional information

In this Appendix additional information on the PDF fit with the LHCb heavy-flavour data (Section 7) is provided.

F.1 MNR calculations in HERAFitter: details of implementation

A PDF fit in the framework described in Section 7.3.2 typically requires several thousands of iterations to converge. In each iteration the theoretical predictions for each dataset must be recomputed. Since computation of the NLO predictions is usually very time consuming, this requires a "smart" implementation of the calculations with separating the bottleneck parts from the iterative procedure. Another popular solution is to use "fast" techniques, such as K-factors or precomputed perturbative grids (see, e.g. [243–247]). Although "fast" techniques are widely used by modern PDF groups, they usually have shortcomings, since they do not allow changing parameters of the calculations, like the factorisation and renormalisation scales or heavy-quark masses.

The MNR calculations (one-particle inclusive variant) as implemented originally in the FORTRAN code [229] require about several hours to calculate one set of the predictions for one of the considered LHCb datasets.[1] Numerical multi-dimensional integration over the phase space is done with the MC method using the VEGAS algorithm [248]. The main advantage of the MC integration is that it can be suitably performed for any configuration of the phase space; the only number to be adjusted to reach the desired accuracy is the total number of iterations. The disadvantage is that all parts of the calculations have to be repeated in each iteration.

Therefore in HERAFitter numerical multi-dimensional integration for the MNR calculations

[1] The timing depends on the number of bins, desired accuracy of the predictions and CPU; the quoted one is for 40 bins from [135], 1% inaccuracy and Intel Core i7-3520M.

was implemented as nested loops using the trapezoidal rule for each one-dimensional integration. This allows for separation of the most time consuming parts in the top loop(s). The one-particle inclusive variant of the calculations was used. All flexibility of the original MNR code was retained: the factorisation and renormalisation scales, heavy-quark mass, strong coupling constant, fragmentation function and PDFs may be changed in each iteration (in other words, may be treated as fit parameters). The typical timing to calculate one set of the predictions for the considered LHCb datasets is $\sim$ 1 s and the inaccuracy of the predictions is less than 1% comparing to the results obtained with the original MNR code. This allows a PDF fit with these data to converge typically within a few hours. Additionally the results were cross checked with the NLO predictions as calculated by the (semi)independent FONLL program, using the public web interface [79][2], and differences were found to be within 1–3%.

However note that the integration loops were adjusted for this particular configuration; another phase space and/or binning will need their readjustment.

F.2 Study of charm fragmentation function

In the 'LHCb Abs' fit the following tendency was observed: the LHCb charm data prefer a harder fragmentation function than was measured at HERA, since the variation of α_k to upper values results in better χ^2. This can be seen even from the nominal fit: predictions for the bins $1 < p_T < 3$ GeV are on average above the data, while the bins with higher p_T are below; this non-perfect description of the p_T shape actually explains the somewhat large χ^2 values for the LHCb charm datasets in Table 7.2.

In order to investigate this further the fragmentation-function parameter for charm was released in the fit. The fit converged to a very large α_k value which corresponds to an almost $z \simeq 1$ parton to hadron transition. Another check was done by using the BCFY fragmentation function [249] with $r = 0.1$ extracted from e^+e^- colliders within the FONLL approach [231], which corresponds approximately to $\alpha_k = 12$. A much better description of the charm data was found than with the fragmentation function derived from the HERA data. This study qualitatively confirms the recipe for heavy-flavour fragmentation provided in [43]: since FONLL resummations of NLL provide evolution of the perturbative part of the fragmentation function to the scale $\sim m_Q$, with NLO QCD predictions for hadro- and electroproduction of heavy flavours for the p_T region close to the threshold it would be more appropriate to use a fragmentation function extracted at FONLL (e.g. those from e^+e^- at the Z^0 resonance), while for the high-p_T region it is more appropriate to use a fragmentation function extracted at the NLO approach. However such a study is beyond the purpose of this thesis, so the QCD analysis was limited to the usage of the fragmentation function measured at HERA.

For beauty no tendencies were observed: the LHCb data clearly prefer the value $\alpha_k \approx 11$ similar to that extracted from the LEP data.

[2] The 'NLO' option of the FONLL program was used.

F.3 Prospects of usage of approximate NNLO calculations

Recently a novel public code for the calculation of the one particle inclusive differential cross sections for heavy-quark pair production at hadron colliders has become available in the DiffTop package [233]. The cross sections are calculated at approximate NNLO $O(\alpha_s^4)$, by using methods of threshold resummation (for more details see [250] and references therein). Since in the current study the dominant uncertainties on the impact of the heavy-flavour LHCb data on the PDFs come from the scale variations, changing the perturbative order from NLO to NNLO should give a great improvement of the results.

In this Section a short prospect of a possible extension of the current QCD analysis with these calculations is given in the form of a list of things to do and to study:

- currently the DiffTop package [233] provides either single-differential cross sections as a function of p_T for the full y phase space or single-differential cross sections as a function of y for the full p_T phase space. Though calculations of the double-differential cross sections as a function of p_T and y is possible in principle, they should be implemented in the package;

- the contribution from the qg channel currently is not implemented in the DiffTop package [233] and should be added separately;

- the partial NNLO calculations are even more time consuming than the NLO ones (MNR), so their direct implementation in HERAFitter might not be realistic. Thus a workaround based on "fast" techniques, e.g. FastNLO [243–245][3] has to be adopted and grids for the charm and beauty LHCb data should be prepared;

- the treatment of the inclusive and heavy-flavour HERA data, as well as the PDF evolution, also should be moved to NNLO. For the light flavours and the PDF evolution it is rather straightforward and the NNLO option is already available in HERAFitter, while for the heavy quarks approximate NNLO calculations [63] are available only in the standalone OPENQCDRAD package [218], thus this should be implemented and tested in HERAFitter;

- the fragmentation functions for charm and beauty should be rederived (reestimated) at NNLO, which has never been done before.

F.4 Additional tables and plots

Table F.1 presents the fitted parameters.

Figs. F.1, F.2 show the scale dependence of the NLO QCD predictions for the absolute and normalised LHCb cross sections.

[3] The FastNLO technique might not allow for the adjustment of the scales used in the 'LHCb Abs' approach, although with the NNLO predictions it might not be need.

Figs. F.3 to F.8 show individual contributions to the uncertainties and individual relative uncertainties for the distributions at $Q^2 = 100\,\text{GeV}^2$, obtained in the 'HERA only', 'LHCb Abs' and 'LHCb Norm' fits.

The PDFs obtained obtained in the 'HERA only', 'LHCb Abs' and 'LHCb Norm' fits are compared using the linear x scale at $Q^2 = 10\,\text{GeV}^2$ and $Q^2 = 100\,\text{GeV}^2$ in Figs. F.9 and F.10, respectively. Their relative uncertainties are compared in Figs. F.11 and F.12.

Parameter	HERA only	LHCb Abs	LHCb Norm
B_g	-0.08 ± 0.14	-0.135 ± 0.069	-0.075 ± 0.095
C_g	7.3 ± 1.1	6.83 ± 0.31	5.23 ± 0.34
A'_g	1.99 ± 0.60	1.74 ± 0.22	1.29 ± 0.32
B'_g	-0.15 ± 0.11	-0.194 ± 0.044	-0.155 ± 0.050
B_{u_v}	0.688 ± 0.025	0.668 ± 0.020	0.649 ± 0.021
C_{u_v}	4.75 ± 0.24	4.99 ± 0.23	4.98 ± 0.23
E_{u_v}	10.1 ± 2.4	12.2 ± 2.4	13.5 ± 2.7
B_{d_v}	0.86 ± 0.10	0.928 ± 0.093	0.959 ± 0.088
C_{d_v}	4.95 ± 0.53	5.50 ± 0.56	5.59 ± 0.55
$C_{\overline{U}}$	1.79 ± 0.35	1.63 ± 0.21	1.63 ± 0.24
$A_{\overline{D}}$	0.1466 ± 0.0088	0.1727 ± 0.0068	0.1579 ± 0.0073
$B_{\overline{D}}$	-0.1663 ± 0.0081	-0.1462 ± 0.0058	-0.1551 ± 0.0067
$C_{\overline{D}}$	4.6 ± 1.8	10.4 ± 2.5	15.1 ± 4.2
m_c [GeV]	1.344 ± 0.055	1.709 ± 0.024	1.257 ± 0.014
m_b [GeV]	4.31 ± 0.16	4.673 ± 0.079	4.19 ± 0.13
A_f^c		0.659 ± 0.020	1.0
A_f^b		0.262 ± 0.007	1.0
A_r^c		0.444 ± 0.021	1.0
A_r^b		0.335 ± 0.024	1.0

Table F.1: The fitted parameters for the QCD analysis. The listed uncertainties are the fitting uncertainties only. Uncertainties are not quoted for parameters that are fixed.

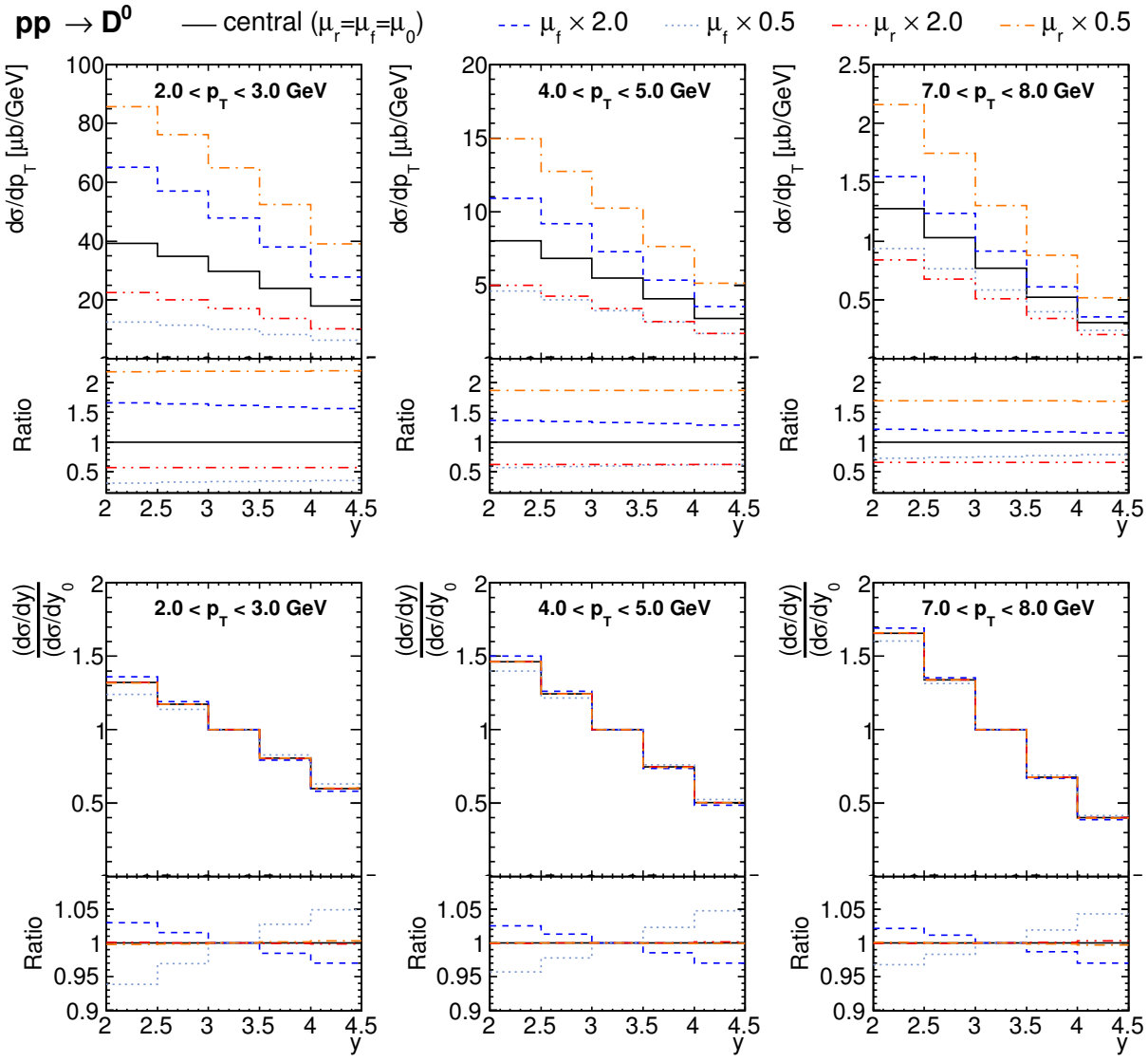

Figure F.1: NLO QCD predictions for charm LHCb data with different scale choices for absolute (top) and normalised (bottom) cross sections. Bottom parts indicate the ratio of predictions to the central scale choice. The predictions were obtained by using the FFNS variant of MSTW 2008 PDFs [200] with $n_f = 3$; the charm mass was set to $m_c = 1.5$ GeV.

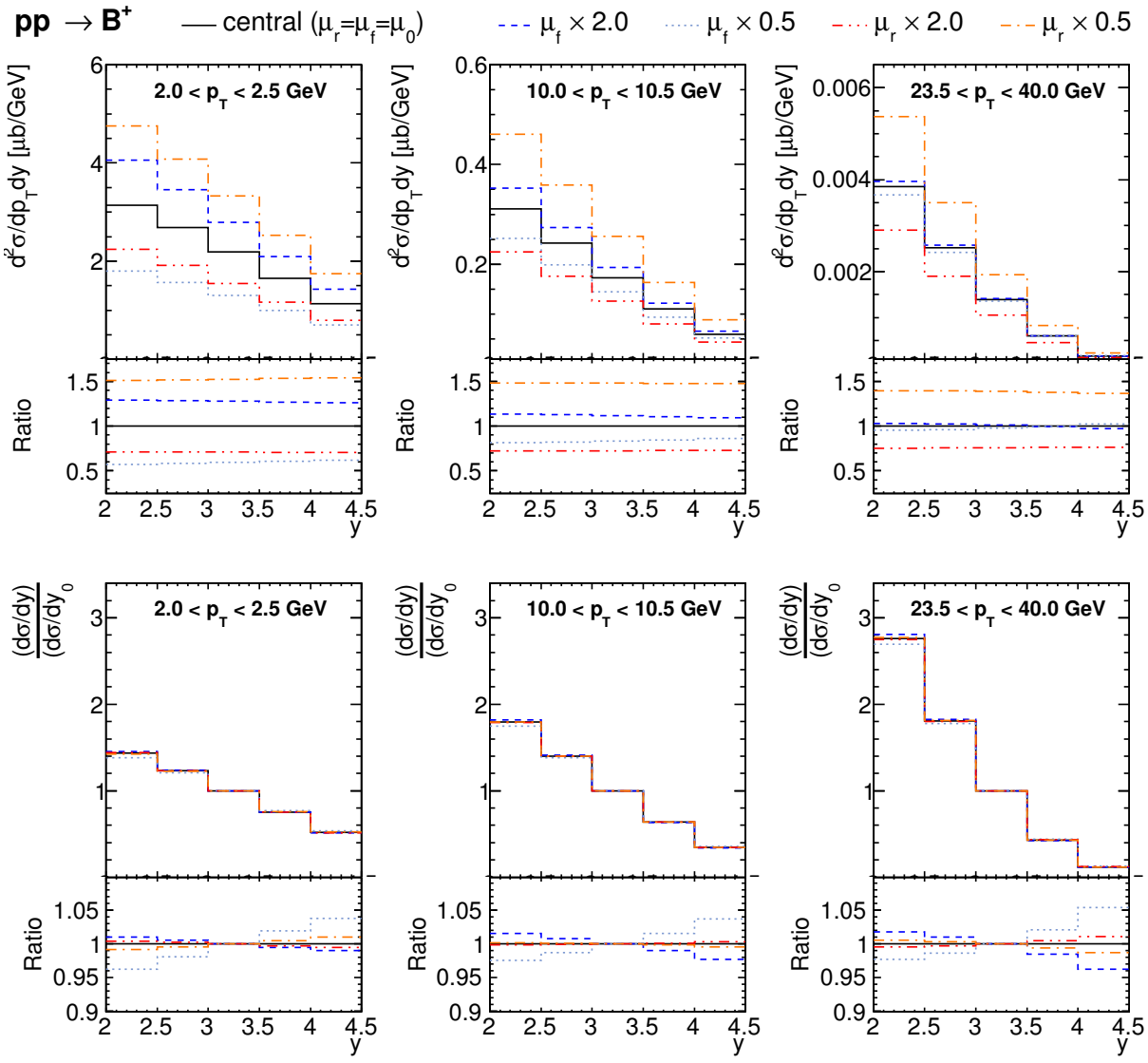

Figure F.2: NLO QCD predictions for beauty LHCb data with different scale choices for absolute (top) and normalised (bottom) cross sections. Bottom parts indicate the ratio of predictions to the central scale choice. The predictions were obtained by using the FFNS variant of MSTW 2008 PDFs [200] with $n_f = 3$; the beauty mass was set to $m_b = 4.5$ GeV.

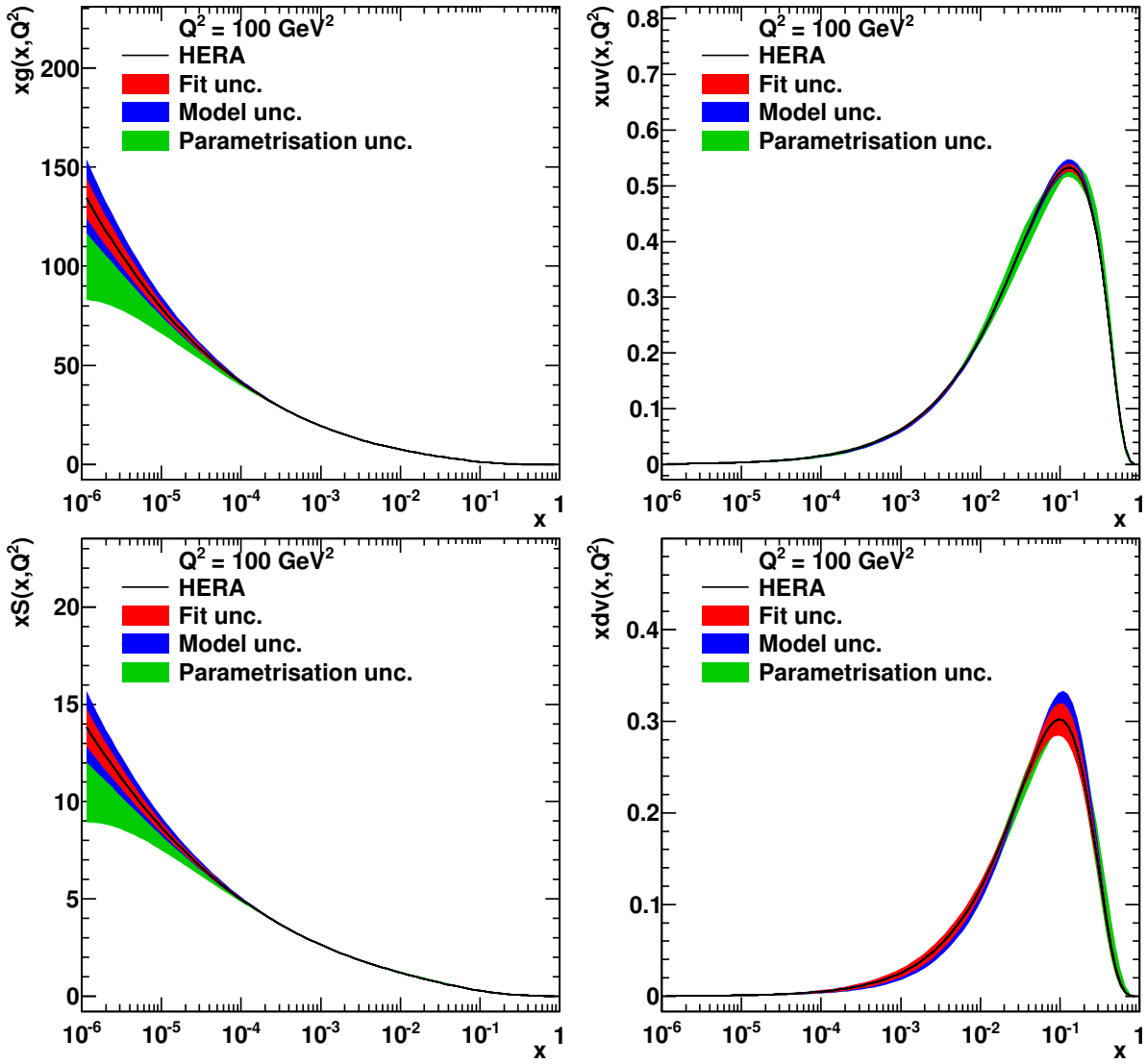

Figure F.3: The individual contributions to the uncertainties of the gluon (top left), u-valence (top right), sea (bottom left) and d-valence (bottom right) distributions at $Q^2 = 100\,\mathrm{GeV}^2$ obtained in the fit with the HERA-only data.

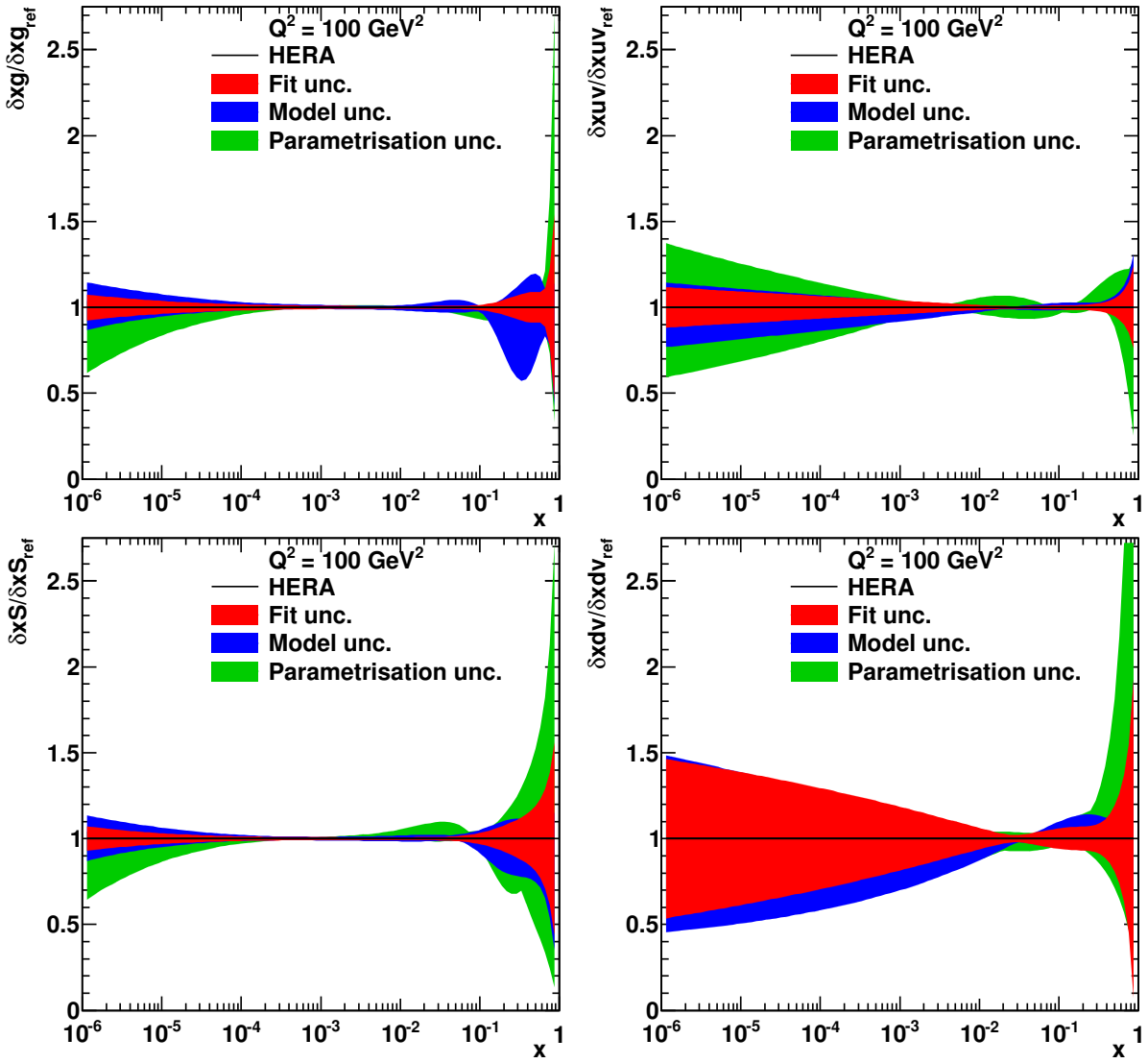

Figure F.4: The individual contributions to the relative uncertainties of the gluon (top left), u-valence (top right), sea (bottom left) and d-valence (bottom right) distributions at $Q^2 = 100\,\text{GeV}^2$ obtained in the fit with the HERA-only data.

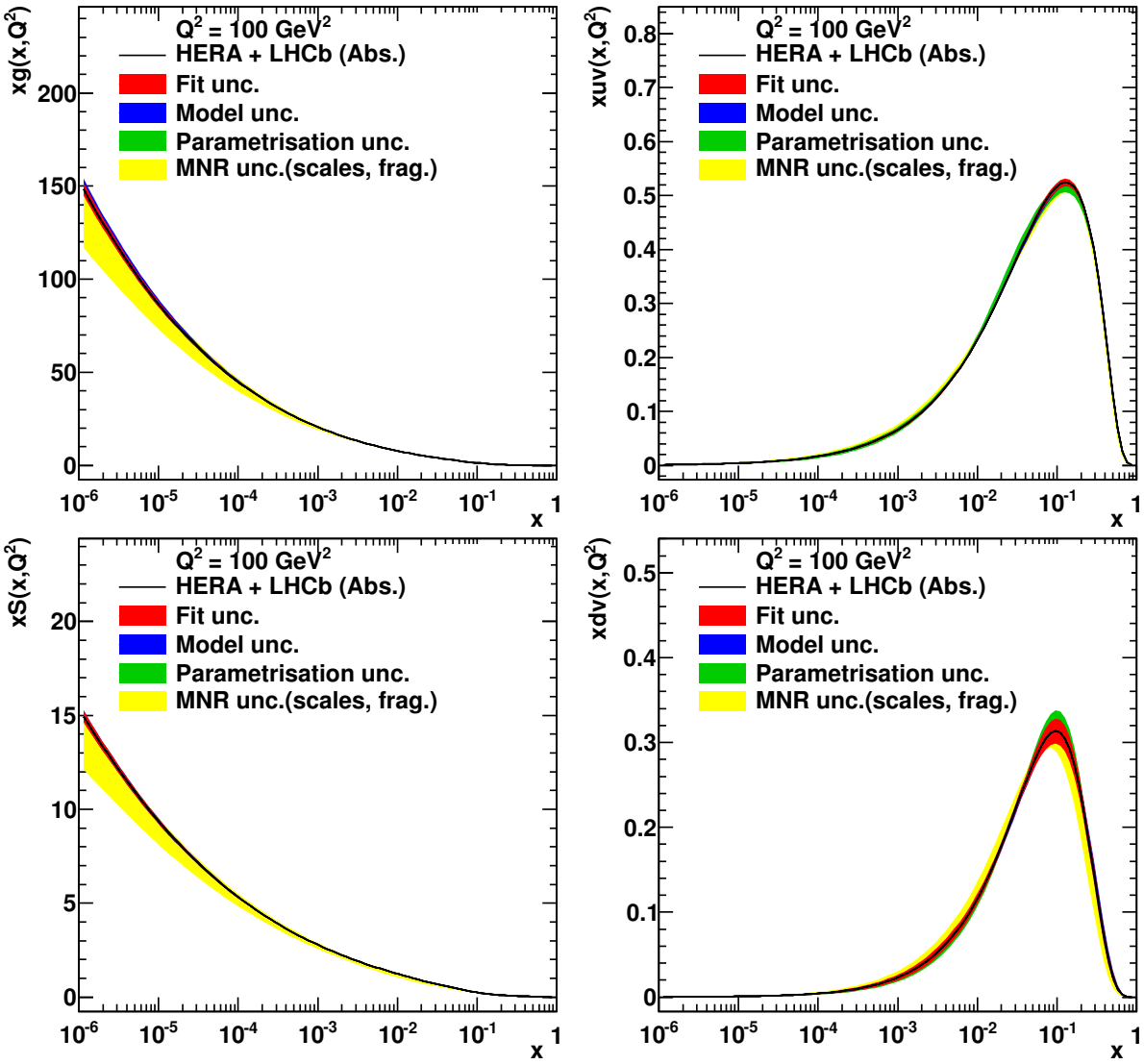

Figure F.5: The individual contributions to the uncertainties of the gluon (top left), u-valence (top right), sea (bottom left) and d-valence (bottom right) distributions at $Q^2 = 100\,\text{GeV}^2$ obtained in the fit with the HERA and LHCb data using the 'LHCb Abs' approach.

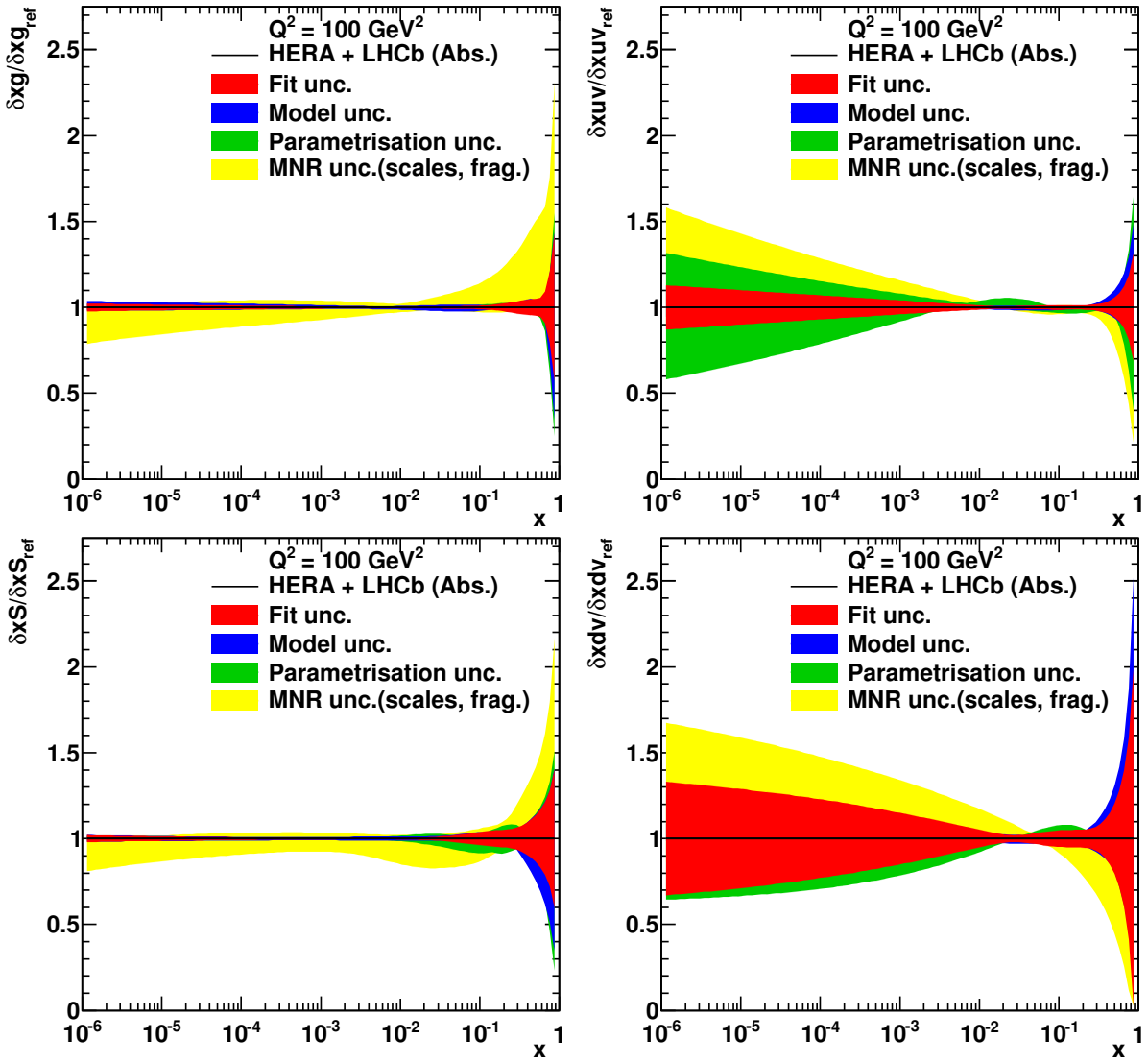

Figure F.6: The individual contributions to the relative uncertainties of the gluon (top left), u-valence (top right), sea (bottom left) and d-valence (bottom right) distributions at $Q^2 = 100\,\text{GeV}^2$ obtained in the fit with the HERA and LHCb data using the 'LHCb Abs' approach.

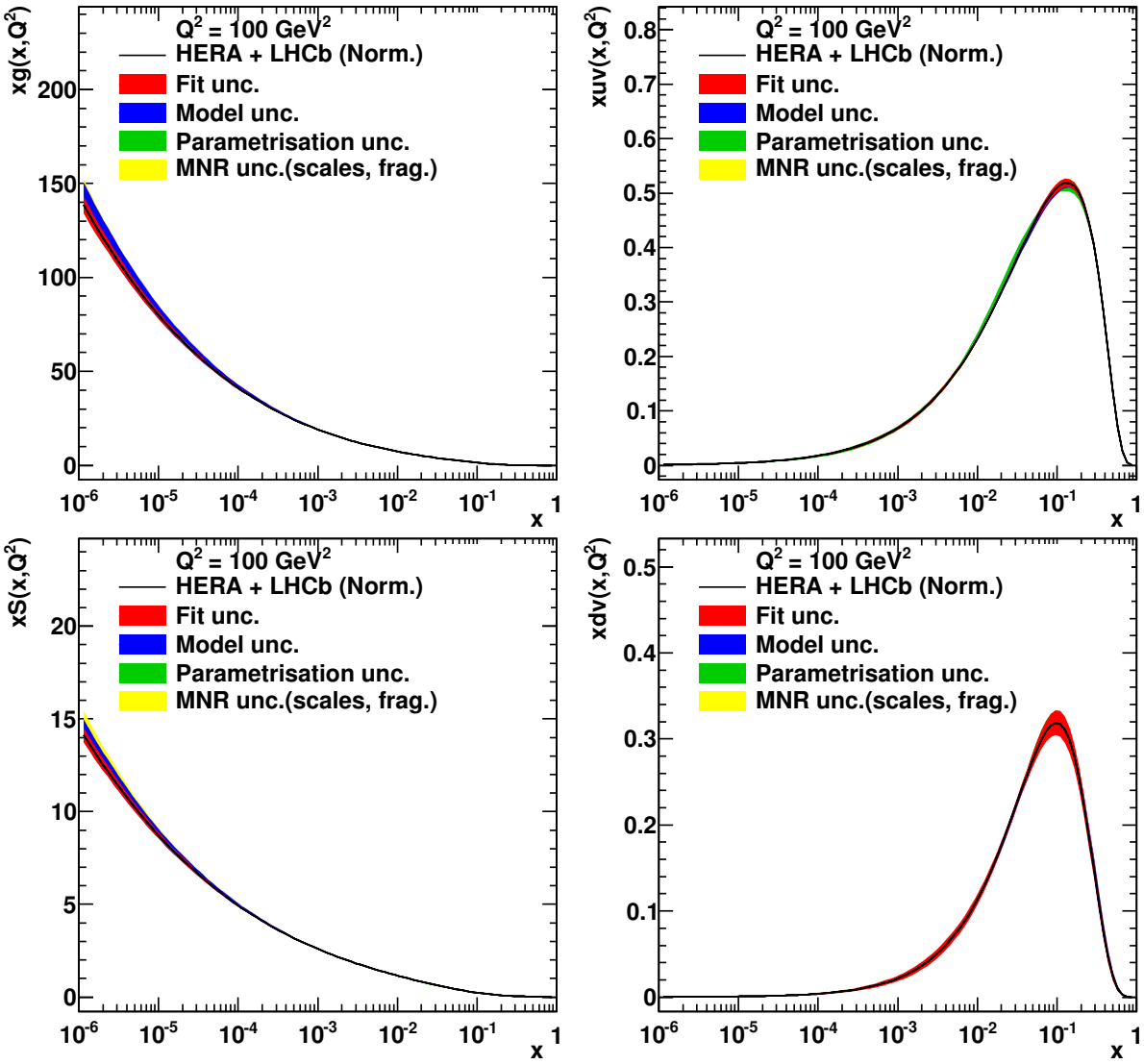

Figure F.7: The individual contributions to the uncertainties of the gluon (top left), u-valence (top right), sea (bottom left) and d-valence (bottom right) distributions at $Q^2 = 100\,\text{GeV}^2$ obtained in the fit with the HERA and LHCb data using the 'LHCb Norm' approach.

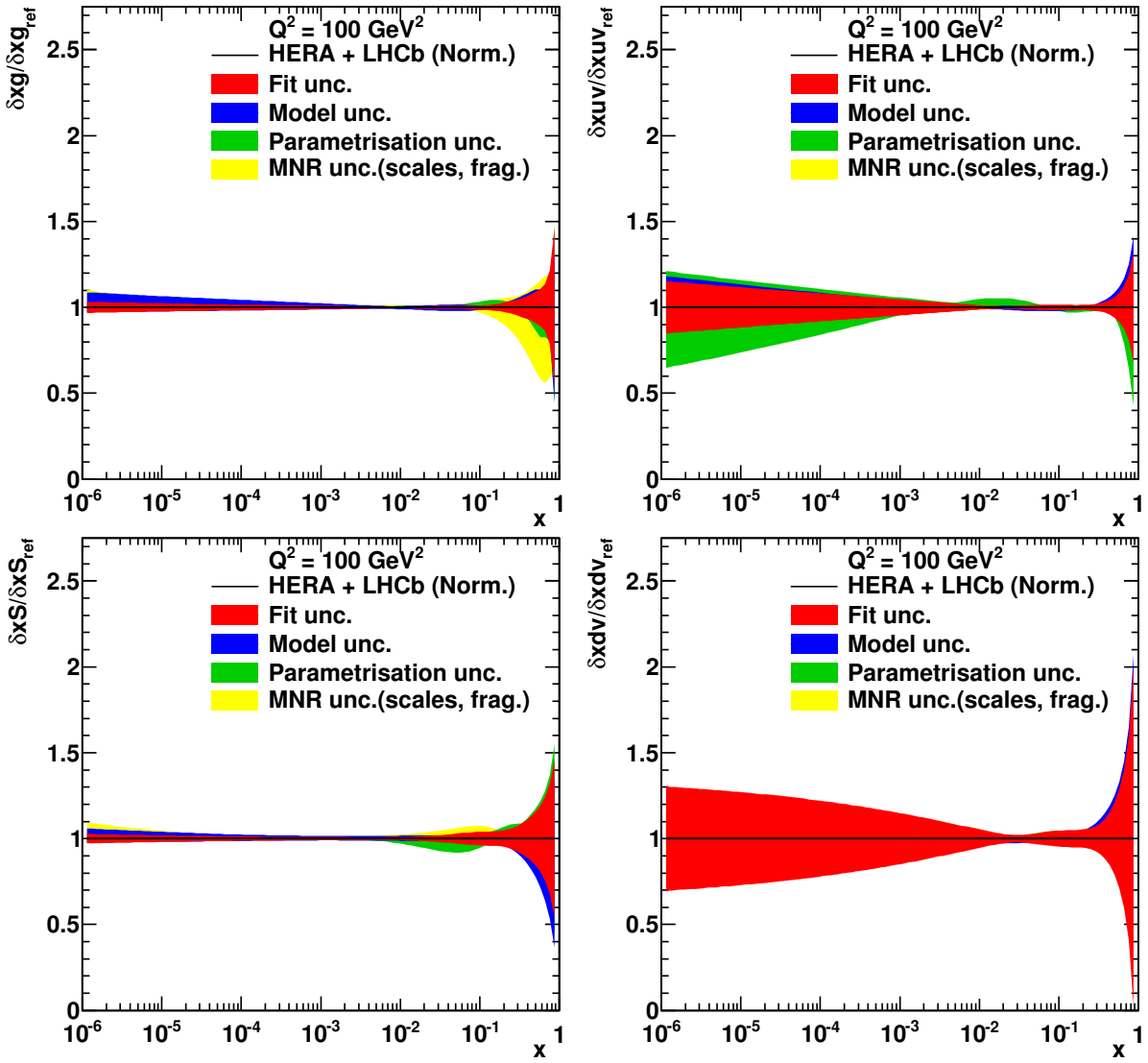

Figure F.8: The individual contributions to the relative uncertainties of the gluon (top left), u-valence (top right), sea (bottom left) and d-valence (bottom right) distributions at $Q^2 = 100\,\text{GeV}^2$ obtained in the fit with the HERA and LHCb data using the 'LHCb Norm' approach.

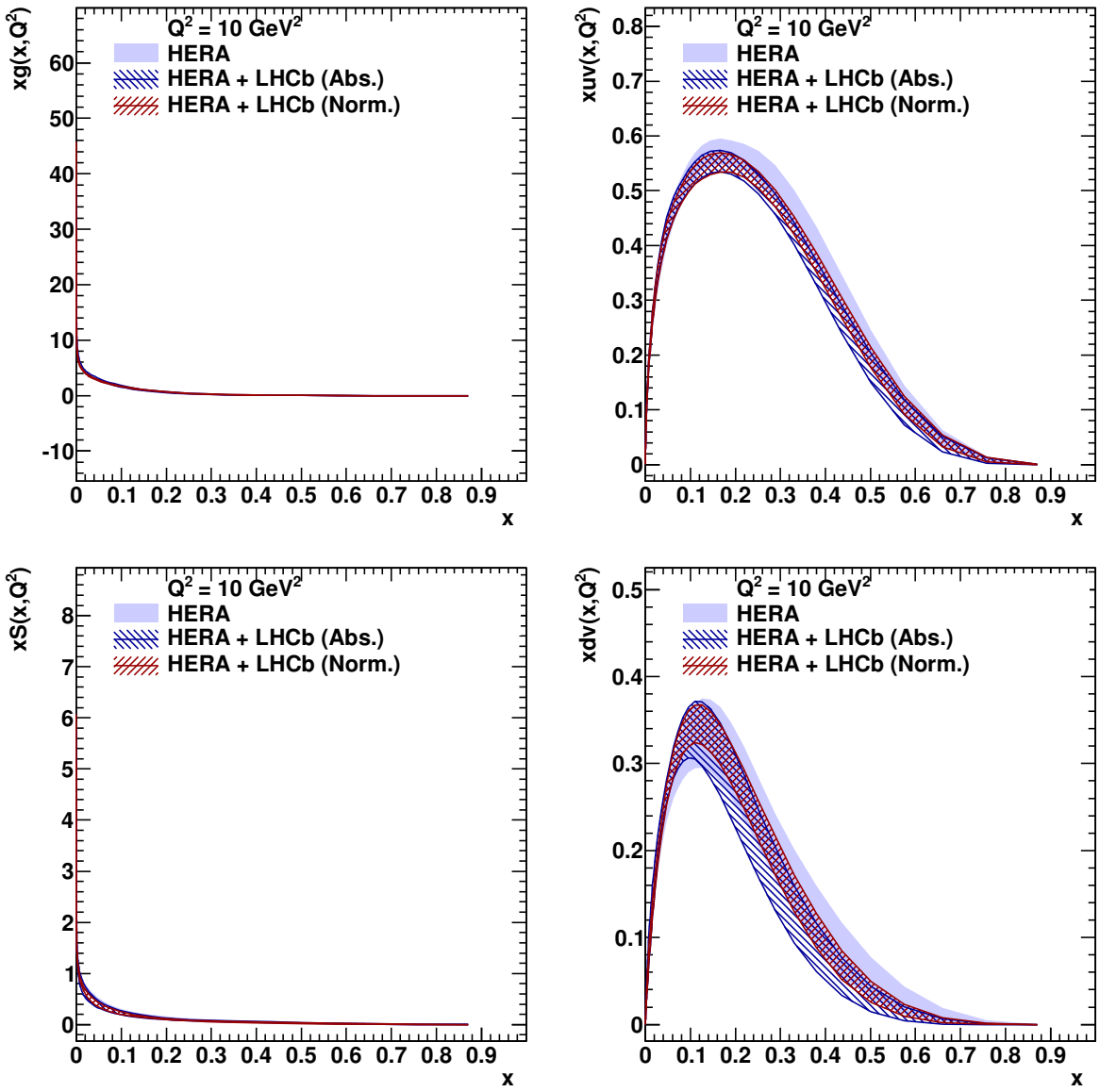

Figure F.9: The gluon (top left), u-valence (top right), sea (bottom left) and d-valence (bottom right) distributions at $Q^2 = 10\,\text{GeV}^2$ obtained in the fit with the HERA-only, HERA and LHCb absolute, and HERA and LHCb normalised data. The widths of the bands represent the total uncertainties.

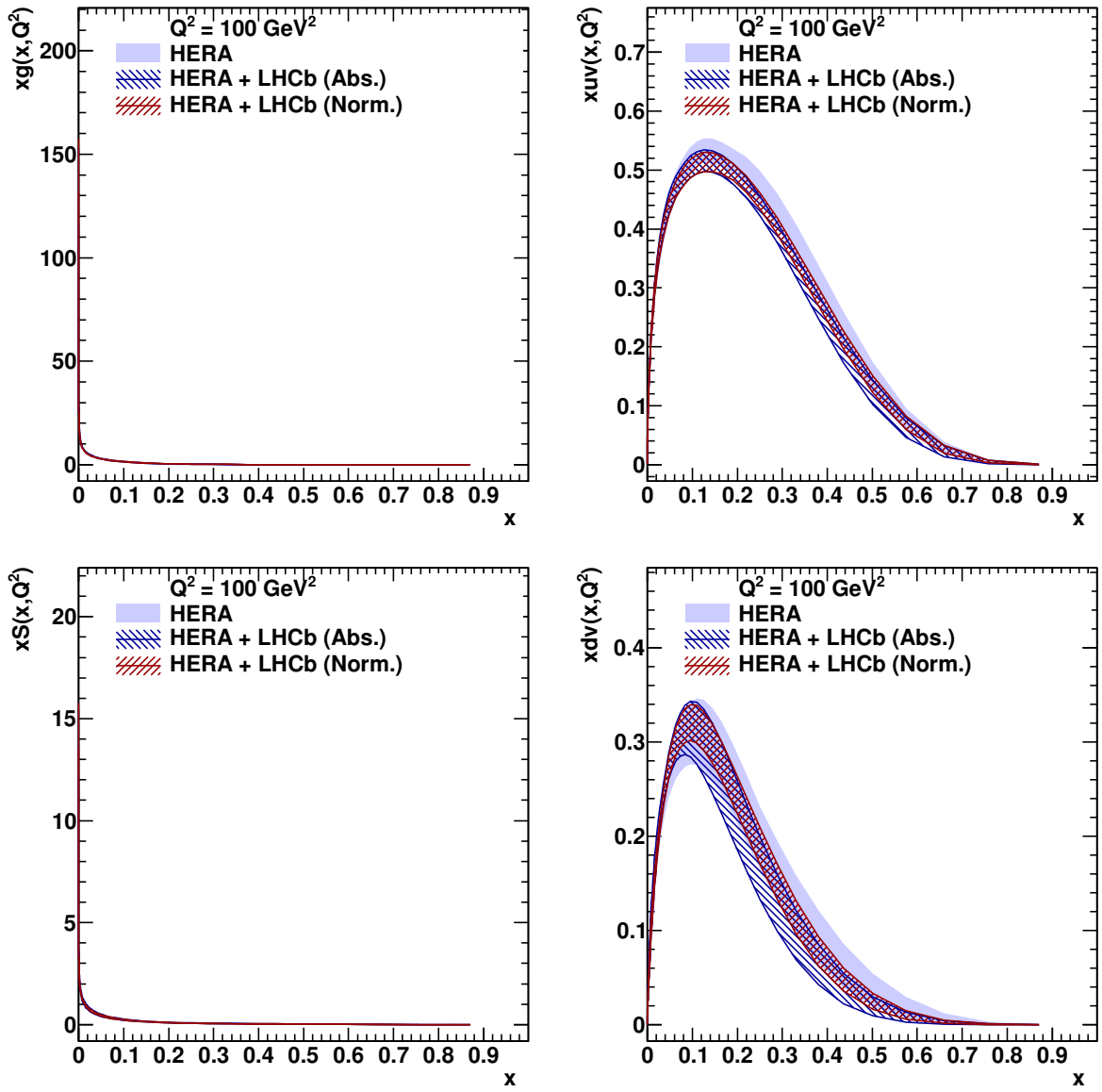

Figure F.10: The gluon (top left), u-valence (top right), sea (bottom left) and d-valence (bottom right) distributions at $Q^2 = 100\,\mathrm{GeV}^2$ obtained in the fit with the HERA-only, HERA and LHCb absolute, and HERA and LHCb normalised data. The widths of the bands represent the total uncertainties.

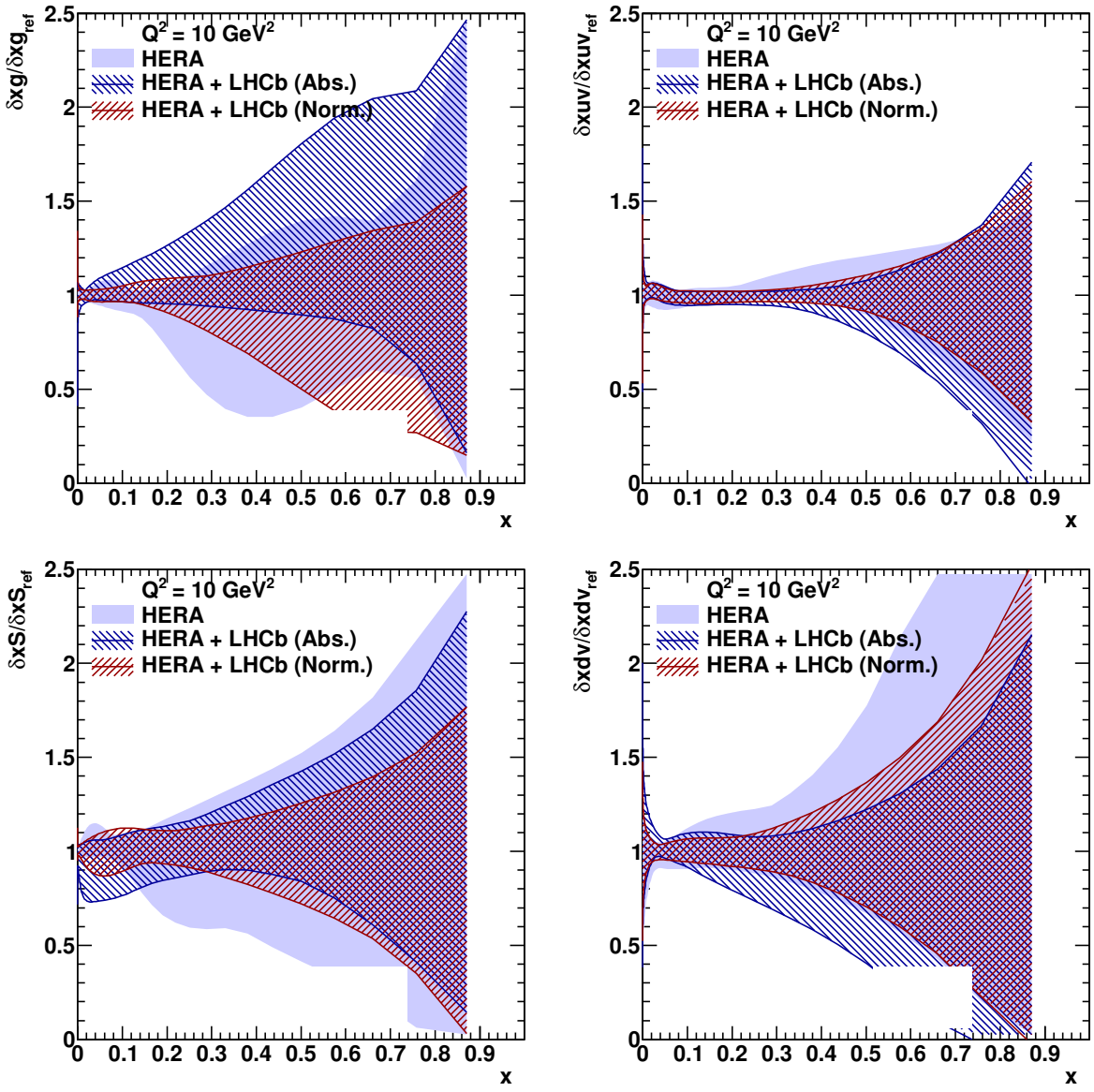

Figure F.11: The gluon (top left), u-valence (top right), sea (bottom left) and d-valence (bottom right) distributions at $Q^2 = 10\,\mathrm{GeV}^2$ obtained in the fit with the HERA-only, HERA and LHCb absolute, and HERA and LHCb normalised data, normalised to one for a direct comparison of the uncertainties. The widths of the bands represent the total uncertainties.

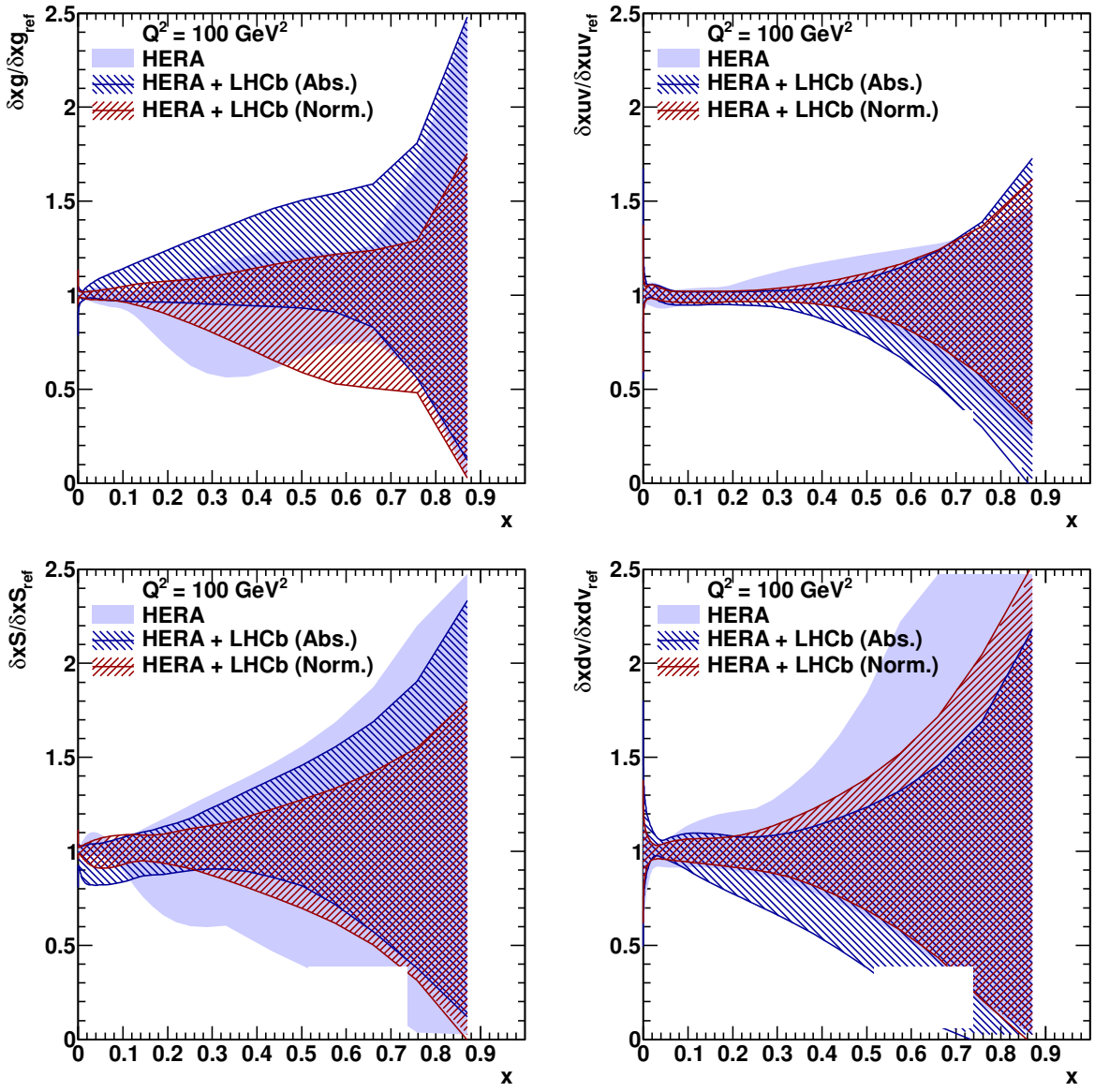

Figure F.12: The gluon (top left), u-valence (top right), sea (bottom left) and d-valence (bottom right) distributions at $Q^2 = 100\,\text{GeV}^2$ obtained in the fit with the HERA-only, HERA and LHCb absolute, and HERA and LHCb normalised data, normalised to one for a direct comparison of the uncertainties. The widths of the bands represent the total uncertainties.

Bibliography

[1] A. M. Cooper-Sarkar, R. Devenish and A. De Roeck,
"Structure functions of the nucleon and their interpretation",
Int.J.Mod.Phys. A13 (1998) 3385–3586, DOI: 10.1142/S0217751X98001670,
arXiv: hep-ph/9712301 [hep-ph].

[2] "NC and CC inclusive cross section as function of Q^2",
H1 + ZEUS compilation plots, URL: https://www.desy.de/h1zeus/combined_results/index.php?do=proton_structure.

[3] R. Ciesielski, "Charged and neutral current cross sections from HERA",
J.Phys.Conf.Ser. 110 (2008) 042007, DOI: 10.1088/1742-6596/110/4/042007.

[4] J. Bjorken, "Asymptotic Sum Rules at Infinite Momentum",
Phys.Rev. 179 (1969) 1547–1553, DOI: 10.1103/PhysRev.179.1547.

[5] G. Miller et al., "Inelastic Electron-Proton Scattering at Large Momentum Transfers",
Phys.Rev. D5 (1972) 528, DOI: 10.1103/PhysRevD.5.528.

[6] M. Gell-Mann, "A Schematic Model of Baryons and Mesons",
Phys.Lett. 8 (1964) 214–215, DOI: 10.1016/S0031-9163(64)92001-3.

[7] K. Olive et al., "Review of Particle Physics", *Chin.Phys.* C38 (2014) 090001,
DOI: 10.1088/1674-1137/38/9/090001.

[8] T. Eichten et al.,
"Measurement of the Neutrinonucleon Antineutrino-Nucleon Total Cross-sections",
Phys.Lett. B46 (1973) 274–280, DOI: 10.1016/0370-2693(73)90702-8.

[9] T. Muta, *Foundations of Quantum Chromodynamics: An Introduction to Perturbative Methods in Gauge Theories*, World Scientific Publishing Co., 1987.

[10] G. 't Hooft, "Dimensional regularization and the renormalization group",
Nucl.Phys. B61 (1973) 455–468, DOI: 10.1016/0550-3213(73)90376-3.

[11] W. A. Bardeen et al., "Deep Inelastic Scattering Beyond the Leading Order in Asymptotically Free Gauge Theories", *Phys.Rev.* D18 (1978) 3998,
DOI: 10.1103/PhysRevD.18.3998.

[12] P. M. Stevenson, "Optimized Perturbation Theory", *Phys.Rev.* D23 (1981) 2916,
DOI: 10.1103/PhysRevD.23.2916.

[13] G. Grunberg, "Renormalization Group Improved Perturbative QCD", *Phys.Lett.* B95 (1980) 70, DOI: 10.1016/0370-2693(80)90402-5.

[14] P. M. Stevenson, "Resolution of the Renormalization Scheme Ambiguity in Perturbative QCD", *Phys.Lett.* B100 (1981) 61, DOI: 10.1016/0370-2693(81)90287-2.

[15] P. Stevenson, "Optimization of QCD Perturbation Theory: Results for $R_{e^+e^-}$ at fourth order", *Nucl.Phys.* B868 (2013) 38–64, DOI: 10.1016/j.nuclphysb.2012.11.005, arXiv: 1210.7001 [hep-ph].

[16] I. I. Bigi et al., "The pole mass of the heavy quark. Perturbation theory and beyond", *Phys.Rev.* D50 (1994) 2234–2246, DOI: 10.1103/PhysRevD.50.2234, arXiv: hep-ph/9402360 [hep-ph].

[17] S. Alekhin and S. Moch, "Heavy-quark deep-inelastic scattering with a running mass", *Phys.Lett.* B699 (2011) 345–353, DOI: 10.1016/j.physletb.2011.04.026, arXiv: 1011.5790 [hep-ph].

[18] J. Abdallah et al., "Study of b-quark mass effects in multijet topologies with the DELPHI detector at LEP", *Eur.Phys.J.* C55 (2008) 525–538, DOI: 10.1140/epjc/s10052-008-0631-5, arXiv: 0804.3883 [hep-ex].

[19] H. Abramowicz et al., "Measurement of beauty and charm production in deep inelastic scattering at HERA and measurement of the beauty-quark mass", *JHEP* 1409 (2014) 127, DOI: 10.1007/JHEP09(2014)127, arXiv: 1405.6915 [hep-ex].

[20] "Determination of Charm Mass Running from an Analysis of Combined HERA Charm Data", H1-prelim-14-071, ZEUS-prel-14-006.

[21] N. Gray et al., "Three Loop Relation of Quark $\overline{\text{MS}}$ and Pole Masses", *Z.Phys.* C48 (1990) 673–680, DOI: 10.1007/BF01614703.

[22] D. J. Broadhurst, N. Gray and K. Schilcher, "Gauge invariant on-shell Z_2 in QED, QCD and the effective field theory of a static quark", *Z.Phys.* C52 (1991) 111–122, DOI: 10.1007/BF01412333.

[23] K. Chetyrkin and M. Steinhauser, "Short distance mass of a heavy quark at order α_s^3", *Phys.Rev.Lett.* 83 (1999) 4001–4004, DOI: 10.1103/PhysRevLett.83.4001, arXiv: hep-ph/9907509 [hep-ph].

[24] K. Melnikov and T. v. Ritbergen, "The three loop relation between the $\overline{\text{MS}}$ and the pole quark masses", *Phys.Lett.* B482 (2000) 99–108, DOI: 10.1016/S0370-2693(00)00507-4, arXiv: hep-ph/9912391 [hep-ph].

[25] J. C. Collins, D. E. Soper and G. F. Sterman,
"Factorization of Hard Processes in QCD",
Adv.Ser.Direct.High Energy Phys. 5 (1988) 1–91,
arXiv: hep-ph/0409313 [hep-ph].

[26] G. Altarelli, R. K. Ellis and G. Martinelli,
"Large Perturbative Corrections to the Drell-Yan Process in QCD",
Nucl.Phys. B157 (1979) 461, DOI: 10.1016/0550-3213(79)90116-0.

[27] V. Gribov and L. Lipatov, "Deep inelastic ep scattering in perturbation theory",
Sov.J.Nucl.Phys. 15 (1972) 438–450.

[28] G. Altarelli and G. Parisi, "Asymptotic Freedom in Parton Language",
Nucl.Phys. B126 (1977) 298, DOI: 10.1016/0550-3213(77)90384-4.

[29] G. Curci, W. Furmanski and R. Petronzio,
"Evolution of Parton Densities Beyond Leading Order: The Nonsinglet Case",
Nucl.Phys. B175 (1980) 27, DOI: 10.1016/0550-3213(80)90003-6.

[30] W. Furmanski and R. Petronzio, "Singlet Parton Densities Beyond Leading Order",
Phys.Lett. B97 (1980) 437, DOI: 10.1016/0370-2693(80)90636-X.

[31] S. Moch, J. Vermaseren and A. Vogt,
"The Three-Loop Splitting Functions in QCD: The Nonsinglet Case",
Nucl.Phys. B688 (2004) 101–134, DOI: 10.1016/j.nuclphysb.2004.03.030,
arXiv: hep-ph/0403192 [hep-ph].

[32] A. Vogt, S. Moch and J. Vermaseren,
"The Three-Loop Splitting Functions in QCD: The Singlet Case",
Nucl.Phys. B691 (2004) 129–181, DOI: 10.1016/j.nuclphysb.2004.04.024,
arXiv: hep-ph/0404111 [hep-ph].

[33] E. A. Kuraev, L. N. Lipatov and V. S. Fadin,
"Multi-Reggeon Processes in the Yang-Mills Theory",
Sov.Phys.JETP 44 (1976) 443–450.

[34] E. Kuraev, L. Lipatov and V. S. Fadin,
"The Pomeranchuk Singularity in Nonabelian Gauge Theories",
Sov.Phys.JETP 45 (1977) 199–204.

[35] I. Balitsky and L. Lipatov,
"The Pomeranchuk Singularity in Quantum Chromodynamics",
Sov.J.Nucl.Phys. 28 (1978) 822–829.

[36] M. Aguilar-Benitez et al., "Charm Hadron Properties in 400 GeV/c pp Interactions",
Z.Phys. C40 (1988) 321, DOI: 10.1007/BF01548848.

[37] S. Catani, F. Fiorani and G. Marchesini, "QCD Coherence in Initial State Radiation",
Phys.Lett. B234 (1990) 339, DOI: 10.1016/0370-2693(90)91938-8.

[38] S. Catani, F. Fiorani and G. Marchesini,
"Small x Behavior of Initial State Radiation in Perturbative QCD",
Nucl.Phys. B336 (1990) 18, DOI: 10.1016/0550-3213(90)90342-B.

[39] G. Marchesini,
"QCD coherence in the structure function and associated distributions at small x",
Nucl.Phys. B445 (1995) 49–80, DOI: 10.1016/0550-3213(95)00149-M,
arXiv: hep-ph/9412327 [hep-ph].

[40] W. van Neerven,
"Production of heavy quarks in deep inelastic lepton hadron scattering" (2001) 40–59,
arXiv: hep-ph/0107193 [hep-ph].

[41] M. L. Mangano, "Two lectures on heavy quark production in hadronic collisions"
(1997), arXiv: hep-ph/9711337 [hep-ph].

[42] M. Klasen et al., "NLO Monte Carlo predictions for heavy-quark production at the
LHC: pp collisions in ALICE", *JHEP* 1408 (2014) 109,
DOI: 10.1007/JHEP08(2014)109, arXiv: 1405.3083 [hep-ph].

[43] J. Baines et al., "Heavy quarks (Working Group 3): Summary Report for the
HERA-LHC Workshop Proceedings" (2006), arXiv: hep-ph/0601164 [hep-ph].

[44] M. Gluck, E. Reya and M. Stratmann, "Heavy quarks at high-energy colliders",
Nucl.Phys. B422 (1994) 37–56, DOI: 10.1016/0550-3213(94)00131-6.

[45] M. Botje, "QCDNUM: Fast QCD Evolution and Convolution",
Comput.Phys.Commun. 182 (2011) 490–532, DOI: 10.1016/j.cpc.2010.10.020,
arXiv: 1005.1481 [hep-ph].

[46] J. C. Collins and W.-K. Tung, "Calculating Heavy Quark Distributions",
Nucl.Phys. B278 (1986) 934, DOI: 10.1016/0550-3213(86)90425-6.

[47] M. Aivazis, F. I. Olness and W.-K. Tung,
"Leptoproduction of heavy quarks. 1. General formalism and kinematics of charged
current and neutral current production processes", *Phys.Rev.* D50 (1994) 3085–3101,
DOI: 10.1103/PhysRevD.50.3085, arXiv: hep-ph/9312318 [hep-ph].

[48] M. Aivazis et al., "Leptoproduction of heavy quarks. 2. A unified QCD formulation of
charged and neutral current processes from fixed target to collider energies",
Phys.Rev. D50 (1994) 3102–3118, DOI: 10.1103/PhysRevD.50.3102,
arXiv: hep-ph/9312319 [hep-ph].

[49] M. Buza et al., "Heavy quark coefficient functions at asymptotic values $Q^2 > m^2$",
Nucl.Phys. B472 (1996) 611–658, DOI: 10.1016/0550-3213(96)00228-3,
arXiv: hep-ph/9601302 [hep-ph].

[50] J. C. Collins, "Hard scattering factorization with heavy quarks: a general treatment",
Phys.Rev. D58 (1998) 094002, DOI: 10.1103/PhysRevD.58.094002,
arXiv: hep-ph/9806259 [hep-ph].

[51] M. Kramer, F. I. Olness and D. E. Soper,
"Treatment of heavy quarks in deeply inelastic scattering",
Phys.Rev. D62 (2000) 096007, DOI: 10.1103/PhysRevD.62.096007,
arXiv: hep-ph/0003035 [hep-ph].

[52] W.-K. Tung, S. Kretzer and C. Schmidt, "Open heavy flavor production in QCD: conceptual framework and implementation issues", *J.Phys.* G28 (2002) 983–996, DOI: 10.1088/0954-3899/28/5/321, arXiv: hep-ph/0110247 [hep-ph].

[53] R. Thorne, "A variable-flavor number scheme for NNLO", *Phys.Rev.* D73 (2006) 054019, DOI: 10.1103/PhysRevD.73.054019, arXiv: hep-ph/0601245 [hep-ph].

[54] A. Martin et al., "Parton distributions for the LHC", *Eur.Phys.J.* C63 (2009) 189–285, DOI: 10.1140/epjc/s10052-009-1072-5, arXiv: 0901.0002 [hep-ph].

[55] S. Forte et al., "Heavy quarks in deep-inelastic scattering", *Nucl.Phys.* B834 (2010) 116–162, DOI: 10.1016/j.nuclphysb.2010.03.014, arXiv: 1001.2312 [hep-ph].

[56] R. D. Ball et al., "Impact of Heavy Quark Masses on Parton Distributions and LHC Phenomenology", *Nucl.Phys.* B849 (2011) 296–363, DOI: 10.1016/j.nuclphysb.2011.03.021, arXiv: 1101.1300 [hep-ph].

[57] R. D. Ball et al., "Unbiased global determination of parton distributions and their uncertainties at NNLO and at LO", *Nucl.Phys.* B855 (2012) 153–221, DOI: 10.1016/j.nuclphysb.2011.09.024, arXiv: 1107.2652 [hep-ph].

[58] R. Thorne, "Effect of changes of variable flavor number scheme on parton distribution functions and predicted cross sections", *Phys.Rev.* D86 (2012) 074017, DOI: 10.1103/PhysRevD.86.074017, arXiv: 1201.6180 [hep-ph].

[59] J. Breitweg et al., "Measurement of $D^{*\pm}$ production and the charm contribution to F_2 in deep inelastic scattering at HERA", *Eur.Phys.J.* C12 (2000) 35–52, DOI: 10.1007/s100529900244, arXiv: hep-ex/9908012 [hep-ex].

[60] E. Laenen et al., "Complete $O(\alpha_s)$ corrections to heavy flavor structure functions in electroproduction", *Nucl.Phys.* B392 (1993) 162–228, DOI: 10.1016/0550-3213(93)90201-Y.

[61] E. Laenen et al., "$O(\alpha_s)$ corrections to heavy flavor inclusive distributions in electroproduction", *Nucl.Phys.* B392 (1993) 229–250, DOI: 10.1016/0550-3213(93)90202-Z.

[62] B. Harris and J. Smith, "Charm quark and $D^{*\pm}$ cross-sections in deeply inelastic scattering at HERA", *Phys.Rev.* D57 (1998) 2806–2812, DOI: 10.1103/PhysRevD.57.2806, arXiv: hep-ph/9706334 [hep-ph].

[63] H. Kawamura et al., "On the next-to-next-to-leading order QCD corrections to heavy-quark production in deep-inelastic scattering", *Nucl.Phys.* B864 (2012) 399–468, DOI: 10.1016/j.nuclphysb.2012.07.001, arXiv: 1205.5727 [hep-ph].

[64] F. Aaron et al., "Measurement of the $D^{*\pm}$ Meson Production Cross Section and $F_2^{c\bar{c}}$, at High Q^2, in ep Scattering at HERA", *Phys.Lett.* B686 (2010) 91–100, DOI: 10.1016/j.physletb.2010.02.024, arXiv: 0911.3989 [hep-ex].

[65] F. Aaron et al., "Measurement of $D^{*\pm}$ Meson Production and Determination of $F_2^{c\bar{c}}$ at low Q^2 in Deep-Inelastic Scattering at HERA", *Eur.Phys.J.* C71 (2011) 1769, DOI: 10.1140/epjc/s10052-011-1769-0,10.1140/epjc/s10052-012-2252-2, arXiv: 1106.1028 [hep-ex].

[66] H. Abramowicz et al., "Combination and QCD Analysis of Charm Production Cross Section Measurements in Deep-Inelastic ep Scattering at HERA", *Eur.Phys.J.* C73 (2013) 2311, DOI: 10.1140/epjc/s10052-013-2311-3, arXiv: 1211.1182 [hep-ex].

[67] P. Nason, S. Dawson and R. K. Ellis, "The Total Cross-Section for the Production of Heavy Quarks in Hadronic Collisions", *Nucl.Phys.* B303 (1988) 607, DOI: 10.1016/0550-3213(88)90422-1.

[68] W. Beenakker et al., "QCD Corrections to Heavy Quark Production in $p\bar{p}$ Collisions", *Phys.Rev.* D40 (1989) 54–82, DOI: 10.1103/PhysRevD.40.54.

[69] P. Nason, S. Dawson and R. K. Ellis, "The One Particle Inclusive Differential Cross-Section for Heavy Quark Production in Hadronic Collisions", *Nucl.Phys.* B327 (1989) 49–92, DOI: 10.1016/0550-3213(89)90286-1.

[70] W. Beenakker et al., "QCD corrections to heavy quark production in hadron-hadron collisions", *Nucl.Phys.* B351 (1991) 507–560, DOI: 10.1016/S0550-3213(05)80032-X.

[71] R. K. Ellis and P. Nason, "QCD Radiative Corrections to the Photoproduction of Heavy Quarks", *Nucl.Phys.* B312 (1989) 551, DOI: 10.1016/0550-3213(89)90571-3.

[72] J. Smith and W. van Neerven, "QCD corrections to heavy flavor photoproduction and electroproduction", *Nucl.Phys.* B374 (1992) 36–82, DOI: 10.1016/0550-3213(92)90476-R.

[73] M. L. Mangano, P. Nason and G. Ridolfi, "Heavy quark correlations in hadron collisions at next-to-leading order", *Nucl.Phys.* B373 (1992) 295–345, DOI: 10.1016/0550-3213(92)90435-E.

[74] S. Frixione et al., "Heavy quark correlations in photon-hadron collisions", *Nucl.Phys.* B412 (1994) 225–259, DOI: 10.1016/0550-3213(94)90501-0, arXiv: hep-ph/9306337 [hep-ph].

[75] M. Cacciari, M. Greco and P. Nason, "The p_T spectrum in heavy flavor hadroproduction", *JHEP* 9805 (1998) 007, DOI: 10.1088/1126-6708/1998/05/007, arXiv: hep-ph/9803400 [hep-ph].

[76] M. Cacciari, S. Frixione and P. Nason, "The p_T spectrum in heavy flavor photoproduction", *JHEP* 0103 (2001) 006, DOI: 10.1088/1126-6708/2001/03/006, arXiv: hep-ph/0102134 [hep-ph].

[77] B. Mele and P. Nason, "The Fragmentation function for heavy quarks in QCD", *Nucl.Phys.* B361 (1991) 626–644, DOI: 10.1016/0550-3213(91)90597-Q.

[78] M. Cacciari et al.,
"Theoretical predictions for charm and bottom production at the LHC",
JHEP 1210 (2012) 137, DOI: 10.1007/JHEP10(2012)137,
arXiv: 1205.6344 [hep-ph].

[79] *Program to calculate heavy quark transverse momentum and rapidity distributions in hadron-hadron and photon-hadron collisions*,
URL: http://cacciari.web.cern.ch/cacciari/fonll.

[80] B. Kniehl et al., "Collinear subtractions in hadroproduction of heavy quarks",
Eur.Phys.J. C41 (2005) 199–212, DOI: 10.1140/epjc/s2005-02200-7,
arXiv: hep-ph/0502194 [hep-ph].

[81] A. H. Mueller,
"Cut Vertices and their Renormalization: A Generalization of the Wilson Expansion",
Phys.Rev. D18 (1978) 3705, DOI: 10.1103/PhysRevD.18.3705.

[82] J. C. Collins and G. F. Sterman, "Soft Partons in QCD", *Nucl.Phys.* B185 (1981) 172,
DOI: 10.1016/0550-3213(81)90370-9.

[83] J. C. Collins, D. E. Soper and G. F. Sterman,
"Factorization for Short Distance Hadron-Hadron Scattering",
Nucl.Phys. B261 (1985) 104, DOI: 10.1016/0550-3213(85)90565-6.

[84] J. C. Collins, D. E. Soper and G. F. Sterman, "Soft Gluons and Factorization",
Nucl.Phys. B308 (1988) 833, DOI: 10.1016/0550-3213(88)90130-7.

[85] G. T. Bodwin, "Factorization of the Drell-Yan Cross-Section in Perturbation Theory",
Phys.Rev. D31 (1985) 2616,
DOI: 10.1103/PhysRevD.34.3932,10.1103/PhysRevD.31.2616.

[86] J. Bjorken,
"Properties of Hadron Distributions in Reactions Containing Very Heavy Quarks",
Phys.Rev. D17 (1978) 171–173, DOI: 10.1103/PhysRevD.17.171.

[87] M. Suzuki, "Fragmentation of Hadrons from Heavy Quark Partons",
Phys.Lett. B71 (1977) 139, DOI: 10.1016/0370-2693(77)90761-4.

[88] R. Jaffe and L. Randall, "Heavy quark fragmentation into heavy mesons",
Nucl.Phys. B412 (1994) 79–105, DOI: 10.1016/0550-3213(94)90495-2,
arXiv: hep-ph/9306201 [hep-ph].

[89] P. Nason and B. Webber,
"Nonperturbative corrections to heavy quark fragmentation in e^+e^- annihilation",
Phys.Lett. B395 (1997) 355–363, DOI: 10.1016/S0370-2693(97)00129-9,
arXiv: hep-ph/9612353 [hep-ph].

[90] M. Cacciari and E. Gardi, "Heavy quark fragmentation",
Nucl.Phys. B664 (2003) 299–340, DOI: 10.1016/S0550-3213(03)00435-8,
arXiv: hep-ph/0301047 [hep-ph].

[91] V. Kartvelishvili, A. Likhoded and V. Petrov,
"On the Fragmentation Functions of Heavy Quarks Into Hadrons",
Phys.Lett. B78 (1978) 615, DOI: 10.1016/0370-2693(78)90653-6.

[92] M. Bowler, "e^+e^- Production of Heavy Quarks in the String Model",
Z.Phys. C11 (1981) 169, DOI: 10.1007/BF01574001.

[93] C. Peterson et al., "Scaling Violations in Inclusive e^+e^- Annihilation Spectra",
Phys.Rev. D27 (1983) 105, DOI: 10.1103/PhysRevD.27.105.

[94] P. Collins and T. Spiller, "The Fragmentation of Heavy Quarks",
J.Phys. G11 (1985) 1289, DOI: 10.1088/0305-4616/11/12/006.

[95] F. Aaron et al., "Study of Charm Fragmentation into $D^{*\pm}$ Mesons in Deep-Inelastic Scattering at HERA", *Eur.Phys.J.* C59 (2009) 589–606,
DOI: 10.1140/epjc/s10052-008-0792-2, arXiv: 0808.1003 [hep-ex].

[96] M. Cacciari and P. Nason,
"Is there a significant excess in bottom hadroproduction at the Tevatron?",
Phys.Rev.Lett. 89 (2002) 122003, DOI: 10.1103/PhysRevLett.89.122003,
arXiv: hep-ph/0204025 [hep-ph].

[97] M. Klein and R. Yoshida, "Collider Physics at HERA",
Prog.Part.Nucl.Phys. 61 (2008) 343–393, DOI: 10.1016/j.ppnp.2008.05.002,
arXiv: 0805.3334 [hep-ex].

[98] *ZEUS Analysis Primer: Introduction to ZEUS analysis*, ZEUS internal,
URL: http://www-zeus.desy.de/ZEUS_ONLY/analysis/primer.

[99] "HERA - A Proposal for a Large Electron Proton Colliding Beam Facility at DESY",
tech. rep. DESY-HERA-81-10, 1981.

[100] *Pictures Database on the Verena Schönberg's ZEUS Homepage*,
URL: http://www-zeus.desy.de/~vschoenb/.

[101] I. Abt et al., "The H1 detector at HERA", *Nucl.Instrum.Meth.* A386 (1997) 310–347,
DOI: 10.1016/S0168-9002(96)00893-5.

[102] ZEUS Coll., "The ZEUS Detector. Status Report", tech. rep., 1993,
URL: http://www-zeus.desy.de/bluebook/bluebook.html.

[103] HERMES Coll., "HERMES technical design report", tech. rep. DESY-PRC-93-06,
1993.

[104] E. P. Hartouni et al., "HERA-B: An experiment to study CP violation in the B system using an internal target at the HERA proton ring. Design report",
tech. rep. DESY-PRC-95-01, 1995.

[105] U. Schneekloth, "The HERA luminosity upgrade", tech. rep. DESY-HERA-98-05,
July 1998.

[106] I. Abt et al.,
"The tracking, calorimeter and muon detectors of the H1 experiment at HERA",
Nucl.Instrum.Meth. A386 (1997) 348–396,
DOI: 10.1016/S0168-9002(96)00894-7.

[107] B. Andrieu et al., "The H1 liquid argon calorimeter system",
Nucl.Instrum.Meth. A336 (1993) 460–498, DOI: 10.1016/0168-9002(93)91257-N.

[108] R. Appuhn et al., "The H1 lead/scintillating fiber calorimeter",
Nucl.Instrum.Meth. A386 (1997) 397–408,
DOI: 10.1016/S0168-9002(96)01171-0.

[109] D. Pitzl et al., "The H1 silicon vertex detector",
Nucl.Instrum.Meth. A454 (2000) 334–349,
DOI: 10.1016/S0168-9002(00)00488-5, arXiv: hep-ex/0002044 [hep-ex].

[110] M. Derrick et al., "Design and construction of the ZEUS barrel calorimeter.",
Nucl.Instrum.Meth. A309 (1991) 77–100, DOI: 10.1016/0168-9002(91)90094-7.

[111] A. Andresen et al.,
"Construction and beam test of the ZEUS forward and rear calorimeter",
Nucl.Instrum.Meth. A309 (1991) 101–142, DOI: 10.1016/0168-9002(91)90095-8.

[112] A. Caldwell et al., "Design and implementation of a high precision readout system for the ZEUS calorimeter", *Nucl.Instrum.Meth.* A321 (1992) 356–364,
DOI: 10.1016/0168-9002(92)90413-X.

[113] A. Bernstein et al., "Beam tests of the ZEUS barrel calorimeter",
Nucl.Instrum.Meth. A336 (1993) 23–52, DOI: 10.1016/0168-9002(93)91078-2.

[114] N. Harnew et al., "Vertex Triggering Using Time Difference Measurements in the ZEUS Central Tracking Detector", *Nucl.Instrum.Meth.* A279 (1989) 290–296,
DOI: 10.1016/0168-9002(89)91096-6.

[115] B. Foster et al., "The performance of the ZEUS central tracking detector z-by-timing electronics in a transputer based data acquisition system",
Nucl.Phys.Proc.Suppl. 32 (1993) 181–188, DOI: 10.1016/0920-5632(93)90023-Y.

[116] B. Foster et al., "The design and construction of the ZEUS central tracking detector",
Nucl.Instrum.Meth. A338 (1994) 254–283, DOI: 10.1016/0168-9002(94)91313-7.

[117] E. Acerbi et al., "Thin and compensating solenoids for ZEUS detector"
(1987), In "Boston 1987, Proceedings, Magnet technology" 1354–1357.

[118] Hall-Wilton et al., "The CTD Tracking Resolution",
ZEUS Internal Note ZEUS-IN-99-024.

[119] A. Polini et al., "The design and performance of the ZEUS Micro Vertex detector",
Nucl.Instrum.Meth. A581 (2007) 656–686, DOI: 10.1016/j.nima.2007.08.167,
arXiv: 0708.3011 [physics.ins-det].

[120] *Transverse momentum resolution at the ZEUS Homepage*, Internal ZEUS,
URL: https://www-zeus-data.desy.de/tracking/ZEUS_ONLY/info/resolution.html.

[121] S. Fourletov, "Straw tube tracking detector (STT) for ZEUS", *Nucl.Instrum.Meth.* A535 (2004) 191–196, DOI: 10.1016/j.nima.2004.07.212.

[122] A. Bamberger et al., "The small angle rear tracking detector of ZEUS", *Nucl.Instrum.Meth.* A401 (1997) 63–80, DOI: 10.1016/S0168-9002(97)01029-2.

[123] G. Abbiendi et al., "The ZEUS barrel and rear muon detector", *Nucl.Instrum.Meth.* A333 (1993) 342–354, DOI: 10.1016/0168-9002(93)91176-N.

[124] H. Bethe and W. Heitler, "On the stopping of fast particles and on the creation of positive electrons", *Proc.Roy.Soc.Lond.* A146 (1934) 83–112, DOI: 10.1098/rspa.1934.0140.

[125] J. Andruszkow et al., "Luminosity measurement in the ZEUS experiment", *Acta Phys.Polon.* B32 (2001) 2025–2058.

[126] M. Helbich et al., "The spectrometer system for measuring ZEUS luminosity at HERA", *Nucl.Instrum.Meth.* A565 (2006) 572–588, DOI: 10.1016/j.nima.2006.06.049, arXiv: physics/0512153 [physics].

[127] W. Smith et al., "The ZEUS calorimeter first level trigger", *Nucl.Instrum.Meth.* A355 (1995) 278–294, DOI: 10.1016/0168-9002(94)01163-X.

[128] G. Heath et al., "The ZEUS first level tracking trigger", *Nucl.Instrum.Meth.* A315 (1992) 431–435, DOI: 10.1016/0168-9002(92)90741-L.

[129] A. Quadt et al., "The design and performance of the ZEUS central tracking detector second level trigger", *Nucl.Instrum.Meth.* A438 (1999) 472–501, DOI: 10.1016/S0168-9002(99)00826-8.

[130] S. Bhadra et al., "The ZEUS third level trigger system", *Comput.Phys.Commun.* 57 (1989) 321–324, DOI: 10.1016/0010-4655(89)90236-1.

[131] S. Nussinov, "On Possible Effects of Decays of Charmed Particle Resonances", *Phys.Rev.Lett.* 35 (1975) 1672, DOI: 10.1103/PhysRevLett.35.1672.

[132] G. Feldman et al., "Observation of the Decay $D^{*+} \to D^0\pi^+$", *Phys.Rev.Lett.* 38 (1977) 1313, DOI: 10.1103/PhysRevLett.38.1313.

[133] L. Gibbons et al., "The Inclusive decays $B \to DX$ and $B \to D^*X$", *Phys.Rev.* D56 (1997) 3783–3802, DOI: 10.1103/PhysRevD.56.3783, arXiv: hep-ex/9703006 [hep-ex].

[134] A. Aktas et al., "Production of $D^{*\pm}$ Mesons with Dijets in Deep-Inelastic Scattering at HERA", *Eur.Phys.J.* C51 (2007) 271–287, DOI: 10.1140/epjc/s10052-007-0296-5, arXiv: hep-ex/0701023 [hep-ex].

[135] R. Aaij et al., "Prompt charm production in pp collisions at $\sqrt{s} = 7$ TeV", *Nucl.Phys.* B871 (2013) 1–20, DOI: 10.1016/j.nuclphysb.2013.02.010, arXiv: 1302.2864 [hep-ex].

[136] S. Chekanov et al.,
"Measurement of $D^{*\pm}$ production in deep inelastic $e^{\pm}p$ scattering at HERA",
Phys.Rev. D69 (2004) 012004, DOI: 10.1103/PhysRevD.69.012004,
arXiv: hep-ex/0308068 [hep-ex].

[137] H. Abramowicz et al.,
"Measurement of $D^{*\pm}$ production in deep inelastic scattering at HERA",
JHEP 1305 (2013) 097, DOI: 10.1007/JHEP05(2013)097,
arXiv: 1303.6578 [hep-ex].

[138] S. Chekanov et al., "Measurement of $D^{\pm}$ and D^0 production in deep inelastic scattering using a lifetime tag at HERA", *Eur.Phys.J.* C63 (2009) 171–188,
DOI: 10.1140/epjc/s10052-009-1088-x, arXiv: 0812.3775 [hep-ex].

[139] I. Abt et al., "Measurement of $D^{\pm}$ production in deep inelastic ep scattering with the ZEUS detector at HERA", *JHEP* 1305 (2013) 023,
DOI: 10.1007/JHEP05(2013)023, arXiv: 1302.5058 [hep-ex].

[140] S. Chekanov et al., "Measurement of charm and beauty production in deep inelastic ep scattering from decays into muons at HERA", *Eur.Phys.J.* C65 (2010) 65–79,
DOI: 10.1140/epjc/s10052-009-1193-x, arXiv: 0904.3487 [hep-ex].

[141] F. Aaron et al., "Measurement of the Charm and Beauty Structure Functions using the H1 Vertex Detector at HERA", *Eur.Phys.J.* C65 (2010) 89–109,
DOI: 10.1140/epjc/s10052-009-1190-0, arXiv: 0907.2643 [hep-ex].

[142] A. Aktas et al.,
"Measurement of $F_2^{c\bar{c}}$ and $F_2^{b\bar{b}}$ at high Q^2 using the H1 vertex detector at HERA",
Eur.Phys.J. C40 (2005) 349–359, DOI: 10.1140/epjc/s2005-02154-8,
arXiv: hep-ex/0411046 [hep-ex].

[143] A. Aktas et al.,
"Measurement of $F_2^{c\bar{c}}$ and $F_2^{b\bar{b}}$ at low Q^2 and x using the H1 vertex detector at HERA",
Eur.Phys.J. C45 (2006) 23–33, DOI: 10.1140/epjc/s2005-02415-6,
arXiv: hep-ex/0507081 [hep-ex].

[144] L. R. Evans and P. Bryant, "LHC Machine", *J. Instrum.* 3 (2008), This report is an abridged version of the LHC Design Report (CERN-2004-003) S08001. 164 p,
DOI: 10.1088/1748-0221/3/08/S08001.

[145] J. Alves A. Augusto et al., "The LHCb Detector at the LHC",
J. Instrum. 3.LHCb-DP-2008-001. CERN-LHCb-DP-2008-001 (2008), Also published by CERN Geneva in 2010 S08005,
DOI: 10.1088/1748-0221/3/08/S08005.

[146] M. Adinolfi et al., "Performance of the LHCb RICH detector at the LHC",
Eur.Phys.J. C73 (2013) 2431, DOI: 10.1140/epjc/s10052-013-2431-9,
arXiv: 1211.6759 [physics.ins-det].

[147] J. Pumplin, H. Lai and W. Tung, "The Charm Parton Content of the Nucleon", *Phys.Rev.* D75 (2007) 054029, DOI: 10.1103/PhysRevD.75.054029, arXiv: hep-ph/0701220 [hep-ph].

[148] R. Aaij et al., "Measurement of B meson production cross-sections in proton-proton collisions at $\sqrt{s} = 7$ TeV", *JHEP* 1308 (2013) 117, DOI: 10.1007/JHEP08(2013)117, arXiv: 1306.3663.

[149] J. Malka and K. Wichmann, "The ZEUS data preservation project", *J.Phys.Conf.Ser.* 396 (2012) 022033, DOI: 10.1088/1742-6596/396/2/022033.

[150] *ZeVis: Zeus Event Visualisation*, URL: http://www-zeus.desy.de/~zevis.

[151] S. Chekanov et al., "Multi-lepton production at high transverse momentum at HERA", *Phys.Lett.* B680 (2009) 13–23, DOI: 10.1016/j.physletb.2009.08.026, arXiv: 0906.1504 [hep-ex].

[152] S. Chekanov et al., "Isolated tau leptons in events with large missing transverse momentum at HERA", *Phys.Lett.* B583 (2004) 41–58, DOI: 10.1016/j.physletb.2003.12.054, arXiv: hep-ex/0311028 [hep-ex].

[153] *LAZE: Logical Access to ZEUS Events*, URL: http://www-zeus.desy.de/ZEUS_MANUALS/laze.ps.

[154] *ROOT: Data Analysis Framework*, URL: http://root.cern.ch.

[155] H. Abramowicz et al., "Production of Z^0 bosons in elastic and quasi-elastic ep collisions at HERA", *Phys.Lett.* B718 (2013) 915–921, DOI: 10.1016/j.physletb.2012.11.051, arXiv: 1210.5511 [hep-ex].

[156] *ICFA Study Group on Data Preservation and Long Term Analysis in High Energy Physics*, URL: http://dphep.org.

[157] R. Mount et al., "Data Preservation in High Energy Physics" (2009), arXiv: 0912.0255 [hep-ex].

[158] O. Zenaiev, "Measurement of total and differential cross sections of D^+ meson production in deep inelastic scattering with the ZEUS detector at HERA", in Ukrainian, MA thesis: National Taras Shevchenko University of Kyiv, June 2011.

[159] M. Lisovyi, "Measurement of charm production in deep inelastic scattering using lifetime tagging for $D^\pm$ meson decays with the ZEUS detector at HERA", PhD thesis: Hamburg University, Oct. 2011.

[160] R. Kalman, "A New Approach to Linear Filtering and Prediction Problems", *Trans. ASME J. Basic Engineering* D82 (1960) 35.

[161] A. Spiridonov, "Mathematical Framework for Fast and Rigorous Track Fit for the ZEUS Detector", ZEUS Internal Note ZEUS-IN-08-003.

[162] G. Hartner, "VCTRAK Briefing: Program and Math",
ZEUS Internal Note ZEUS-IN-98-058.

[163] P. Avery, "Applied Fitting Theory V: Track Fitting Using the Kalman Filter",
unpublished, 1992, URL: www.phys.ufl.edu/~avery/fitting/fitting5.pdf.

[164] G. Hartner and C. Catterall, "VCTRAK for HERA II",
ZEUS Internal Note ZEUS-IN-12-001.

[165] A. Verbytskyi, "Production of the excited charm mesons D_1 and D_2^* at HERA",
PhD thesis: Hamburg University, Feb. 2013.

[166] R. Frühwirth and A. Strandlie, "Track fitting with ambiguities and noise: A study of elastic tracking and nonlinear filters",
Comput.Phys.Commun. 120.2-3 (1999) 197–214,
DOI: 10.1016/S0010-4655(99)00231-3.

[167] R. Mankel, "ZEUS Tracking Tutorial", ZEUS Internal Report,
URL: http://www-zeus.desy.de/lectures/tracking_lecture.ppt.

[168] N. Tuning, "ZUFOs: Hadronic final state reconstruction with calorimeter, tracking and backsplash correction", ZEUS Internal Note ZEUS-IN-01-021.

[169] H. Abramowicz, A. Caldwell and R. Sinkus,
"Neural network based electron identification in the ZEUS calorimeter",
Nucl.Instrum.Meth. A365 (1995) 508–517, DOI: 10.1016/0168-9002(95)00612-5,
arXiv: hep-ex/9505004 [hep-ex].

[170] A. Kappes, "Measurement of $e^- p \to e^- X$ differential cross-sections at high Q^2 and of the structure function xF_3 with ZEUS at HERA", PhD thesis: Bonn University, 2001.

[171] F. Jacquet and A. Blondel,
"Study of an ep Facility for Europe DESY, Hamburg, April 2-3, 1979",
ed. by U. Amaldi, DESY-79-48.

[172] S. Bentvelsen et al., "Physics at HERA. Proceedings, Workshop, Hamburg, Germany, October 29-30, 1991. Vol. 1, p.23", ed. by W. Buchmuller and G. Ingelman, 1992.

[173] K. Hoeger, "Physics at HERA. Proceedings, Workshop, Hamburg, Germany, October 29-30, 1991. Vol. 1, p.43", ed. by W. Buchmuller and G. Ingelman, 1992.

[174] *Description of ZEUS trigger bits*, ZEUS internal,
URL: http://www-zeus.desy.de/ZEUS_ONLY/analysis/primer/Trigger/.

[175] N. Metropolis and S. Ulam, "The Monte Carlo method",
Jour. of the Amer. Stat. Assoc. 44 (1949) 335–341.

[176] T. Sjostrand, L. Lonnblad and S. Mrenna, "PYTHIA 6.2: Physics and manual" (2001),
arXiv: hep-ph/0108264 [hep-ph].

[177] L. Lonnblad, "ARIADNE version 4: A program for simulation of QCD cascades implementing the color dipole model", *Comput.Phys.Commun.* 71 (1992) 15–31,
DOI: 10.1016/0010-4655(92)90068-A.

[178] H. Jung, "Hard diffractive scattering in high-energy ep collisions and the Monte Carlo generator RAPGAP", *Comput.Phys.Commun.* 86 (1995) 147–161, DOI: 10.1016/0010-4655(94)00150-Z.

[179] R. Shehzadi, "Measurement of beauty production in deep inelastic scattering at HERA using decays into electrons", PhD thesis: Bonn University, Jan. 2011.

[180] R. Brun et al., "GEANT3", CERN-DD-EE-84-1, 1987.

[181] A. Kwiatkowski, H. Spiesberger and H. Mohring, "Heracles: An Event Generator for ep Interactions at HERA Energies Including Radiative Processes: Version 1.0", *Comput.Phys.Commun.* 69 (1992) 155–172, DOI: 10.1016/0010-4655(92)90136-M.

[182] H. Lai et al., "Global QCD analysis of parton structure of the nucleon: CTEQ5 parton distributions", *Eur.Phys.J.* C12 (2000) 375–392, DOI: 10.1007/s100529900196, arXiv: hep-ph/9903282 [hep-ph].

[183] J. Beringer et al., "Review of Particle Physics (RPP)", *Phys.Rev.* D86 (2012) 010001, DOI: 10.1103/PhysRevD.86.010001.

[184] F. James and M. Roos, "Minuit: A System for Function Minimization and Analysis of the Parameter Errors and Correlations", *Comput.Phys.Commun.* 10 (1975) 343–367, DOI: 10.1016/0010-4655(75)90039-9.

[185] F. James, "CERN Program Library Long Writeup D506. MINUIT Reference Manual. Version 94.1", URL: http://wwwasdoc.web.cern.ch/wwwasdoc/minuit/minmain.html.

[186] S. Chekanov et al., "Measurement of charm and beauty production in deep inelastic ep scattering from decays into muons at HERA", *Eur.Phys.J.* C65 (2010) 65–79, DOI: 10.1140/epjc/s10052-009-1193-x, arXiv: 0904.3487 [hep-ex].

[187] H. Abramowicz et al., "Measurement of beauty production in DIS and $F_2^{b\bar{b}}$ extraction at ZEUS", *Eur.Phys.J.* C69 (2010) 347–360, DOI: 10.1140/epjc/s10052-010-1423-2, arXiv: 1005.3396 [hep-ex].

[188] H. Abramowicz et al., "Measurement of beauty production in deep inelastic scattering at HERA using decays into electrons", *Eur.Phys.J.* C71 (2011) 1573, DOI: 10.1140/epjc/s10052-011-1573-x, arXiv: 1101.3692 [hep-ex].

[189] V. Libov, "Measurement of Charm and Beauty Production in Deep Inelastic Scattering at HERA and Test Beam Studies of ATLAS Pixel Sensors", PhD thesis: Hamburg University, Dec. 2012.

[190] S. Chekanov et al., "A ZEUS next-to-leading-order QCD analysis of data on deep inelastic scattering", *Phys.Rev.* D67 (2003) 012007, DOI: 10.1103/PhysRevD.67.012007, arXiv: hep-ex/0208023 [hep-ex].

[191] S. Chekanov et al., "Measurement of the charm fragmentation function in $D^{*\pm}$ photoproduction at HERA", *JHEP* 0904 (2009) 082, DOI: 10.1088/1126-6708/2009/04/082, arXiv: 0901.1210 [hep-ex].

[192] M. Cacciari, P. Nason and C. Oleari, "A study of heavy flavored meson fragmentation functions in e^+e^- annihilation", *JHEP* 0604 (2006) 006, DOI: 10.1088/1126-6708/2006/04/006, arXiv: hep-ph/0510032 [hep-ph].

[193] R. Seuster et al., "Charm hadrons from fragmentation and B decays in e^+e^- annihilation at $\sqrt{s}$ = 10.6 GeV", *Phys.Rev.* D73 (2006) 032002, DOI: 10.1103/PhysRevD.73.032002, arXiv: hep-ex/0506068 [hep-ex].

[194] E. Lohrmann, "A Summary of Charm Hadron Production Fractions" (2011), arXiv: 1112.3757 [hep-ex].

[195] A. Glazov, "Averaging of DIS cross section data", *AIP Conf.Proc.* 792 (2005) 237–240, DOI: 10.1063/1.2122026.

[196] R. D. Ball et al., "Parton distributions with LHC data", *Nucl.Phys.* B867 (2013) 244–289, DOI: 10.1016/j.nuclphysb.2012.10.003, arXiv: 1207.1303 [hep-ph].

[197] S. Alekhin, J. Blumlein and S. Moch, "Parton Distribution Functions and Benchmark Cross Sections at NNLO", *Phys.Rev.* D86 (2012) 054009, DOI: 10.1103/PhysRevD.86.054009, arXiv: 1202.2281 [hep-ph].

[198] H.-L. Lai et al., "New parton distributions for collider physics", *Phys.Rev.* D82 (2010) 074024, DOI: 10.1103/PhysRevD.82.074024, arXiv: 1007.2241 [hep-ph].

[199] R. Thorne et al., "Questions on uncertainties in parton distributions", *J.Phys.* G28 (2002) 2717–2722, DOI: 10.1088/0954-3899/28/10/315, arXiv: hep-ph/0205233 [hep-ph].

[200] A. Martin et al., "Heavy-quark mass dependence in global PDF analyses and 3- and 4-flavour parton distributions", *Eur.Phys.J.* C70 (2010) 51–72, DOI: 10.1140/epjc/s10052-010-1462-8, arXiv: 1007.2624 [hep-ph].

[201] H.-L. Lai et al., "New parton distributions for collider physics", *Phys.Rev.* D82 (2010) 074024, DOI: 10.1103/PhysRevD.82.074024, arXiv: 1007.2241 [hep-ph].

[202] M. Botje, "Error estimates on parton density distributions", *J.Phys.* G28 (2002) 779–790, DOI: 10.1088/0954-3899/28/5/305, arXiv: hep-ph/0110123 [hep-ph].

[203] *HERAverager: an averaging tool developed for the H1 and ZEUS data combination (version 0.0.2)*, URL: https://wiki-zeuthen.desy.de/HERAverager.

[204] J. Pumplin et al., "Uncertainties of predictions from parton distribution functions. 2. The Hessian method", *Phys.Rev.* D65 (2001) 014013, DOI: 10.1103/PhysRevD.65.014013, arXiv: hep-ph/0101032 [hep-ph].

[205] R. Barlow, *Statistics: a guide to use of statistical methods in the physical sciences*, Manchester Physics Series, 1989.

[206] D. Stump et al., "Uncertainties of predictions from parton distribution functions. 1. The Lagrange multiplier method", *Phys.Rev.* D65 (2001) 014012, DOI: 10.1103/PhysRevD.65.014012, arXiv: hep-ph/0101051 [hep-ph].

[207] F. Aaron et al., "Combined Measurement and QCD Analysis of the Inclusive $e^{\pm}p$ Scattering Cross Sections at HERA", *JHEP* 1001 (2010) 109, DOI: 10.1007/JHEP01(2010)109, arXiv: 0911.0884 [hep-ex].

[208] N. Adam et al., "Absolute Branching Fraction Measurements for D^+ and D^0 Inclusive Semileptonic Decays", *Phys.Rev.Lett.* 97 (2006) 251801, DOI: 10.1103/PhysRevLett.97.251801, arXiv: hep-ex/0604044 [hep-ex].

[209] S. Chekanov et al., "Measurement of beauty production in deep inelastic scattering at HERA", *Phys.Lett.* B599 (2004) 173–189, DOI: 10.1016/j.physletb.2004.08.048, arXiv: hep-ex/0405069 [hep-ex].

[210] D. Lange, "The EvtGen particle decay simulation package", *Nucl.Instrum.Meth.* A462 (2001) 152–155, DOI: 10.1016/S0168-9002(01)00089-4.

[211] H. Albrecht et al., "Two measurements of $B^0\bar{B}^0$ mixing using kaon tagging", *Phys.Lett.* B374 (1996) 256–264, DOI: 10.1016/0370-2693(96)00206-7.

[212] P. Nason and C. Oleari, "A phenomenological study of heavy quark fragmentation functions in e^+e^- annihilation", *Nucl.Phys.* B565 (2000) 245–266, DOI: 10.1016/S0550-3213(99)00673-2, arXiv: hep-ph/9903541 [hep-ph].

[213] K. Lipka, "Combination and QCD Analysis of Charm Production Measurements in Deep-Inelastic ep Scattering at HERA", *PoS* EPS-HEP2013 (2013) 440.

[214] H. Abramowicz et al., "Combination of Differential $D^{*\pm}$ Cross-Section Measurements in Deep-Inelastic ep Scattering at HERA" (2015), arXiv: 1503.06042 [hep-ex].

[215] S. Alekhin et al., "The 3, 4, and 5-flavor NNLO Parton from Deep-Inelastic-Scattering Data and at Hadron Colliders", *Phys.Rev.* D81 (2010) 014032, DOI: 10.1103/PhysRevD.81.014032, arXiv: 0908.2766 [hep-ph].

[216] *HERAFitter: an open source QCD fit framework (version 1.0.0)*, URL: https://wiki-zeuthen.desy.de/HERAFitter.

[217] S. Alekhin et al., "HERAFitter, Open Source QCD Fit Project" (2014), arXiv: 1410.4412 [hep-ph].

[218] *S. Alekhin, "OPENQCDRAD-1.5"*, URL: http://www-zeuthen.desy.de/~alekhin/OPENQCDRAD/.

[219] F. Aaron et al., "Inclusive Deep Inelastic Scattering at High Q^2 with Longitudinally Polarised Lepton Beams at HERA", *JHEP* 1209 (2012) 061, DOI: 10.1007/JHEP09(2012)061, arXiv: 1206.7007 [hep-ex].

[220] J. Gao, M. Guzzi and P. M. Nadolsky, "Charm quark mass dependence in a global QCD analysis", *Eur.Phys.J.* C73 (2013) 2541, DOI: 10.1140/epjc/s10052-013-2541-4, arXiv: 1304.3494 [hep-ph].

[221] S. Alekhin et al., "Precise charm-quark mass from deep-inelastic scattering", *Phys.Lett.* B720 (2013) 172–176, DOI: 10.1016/j.physletb.2013.02.010, arXiv: 1212.2355 [hep-ph].

[222] V. Radescu, "Combination and QCD analysis of the HERA inclusive cross sections", *PoS* ICHEP2010 (2010) 168, URL: http://www.desy.de/h1zeus/combined_results/index.php?do=proton_structure.

[223] P. Nadolsky et al., "Progress in CTEQ-TEA PDF Analysis" (2012), DOI: 10.3204/DESY-PROC-2012-02/301, arXiv: 1206.3321 [hep-ph].

[224] J. Pumplin, D. Stump and W. Tung, "Multivariate fitting and the error matrix in global analysis of data", *Phys.Rev.* D65 (2001) 014011, DOI: 10.1103/PhysRevD.65.014011, arXiv: hep-ph/0008191 [hep-ph].

[225] "Impact of the LHCb measurements of forward charm and beauty production on PDFs", PROSA 14-001, URL: https://prosa.desy.de/Proton_Structure_Analyses_in_Hadronic_Collisions_(PROSA):Recent_results.

[226] O. Zenaiev et al., "Impact of heavy-flavour production cross sections measured by the LHCb experiment on parton distribution functions at low x" (2015), arXiv: 1503.04581 [hep-ph].

[227] M. Gluck, P. Jimenez-Delgado and E. Reya, "Dynamical parton distributions of the nucleon and very small-x physics", *Eur.Phys.J.* C53 (2008) 355–366, DOI: 10.1140/epjc/s10052-007-0462-9, arXiv: 0709.0614 [hep-ph].

[228] V. Bertone, S. Carrazza and J. Rojo, "APFEL: A PDF evolution library with QED corrections", *Comput.Phys.Commun.* 185 (2014) 1647–1668, DOI: 10.1016/j.cpc.2014.03.007, arXiv: 1310.1394 [hep-ph].

[229] *A package of FORTRAN routines for the computation of heavy quark cross sections and distributions in hadron-hadron collisions in QCD at next-to-leading order*, URL: http://www.ge.infn.it/~ridolfi/hvqlibx.tgz.

[230] M. Cacciari and M. Greco, "D^* production from e^+e^- to ep collisions in NLO QCD", *Phys.Rev.* D55 (1997) 7134–7143, DOI: 10.1103/PhysRevD.55.7134, arXiv: hep-ph/9702389 [hep-ph].

[231] M. Cacciari, P. Nason and C. Oleari,
"A study of heavy flavored meson fragmentation functions in e^+e^- annihilation",
JHEP 0604 (2006) 006, DOI: 10.1088/1126-6708/2006/04/006,
arXiv: hep-ph/0510032 [hep-ph].

[232] M. Cacciari and P. Nason, "Charm cross-sections for the Tevatron Run II",
JHEP 0309 (2003) 006, DOI: 10.1088/1126-6708/2003/09/006,
arXiv: hep-ph/0306212 [hep-ph].

[233] *The Fortran-based package, which allows the user to calculate the differential and total cross section for heavy-quark pair production at hadron colliders in one-particle inclusive kinematics*, URL: http://difftop.hepforge.org/.

[234] B. Abelev et al., "Measurement of charm production at central rapidity in proton-proton collisions at $\sqrt{s} = 7$ TeV", *JHEP* 1201 (2012) 128,
DOI: 10.1007/JHEP01(2012)128, arXiv: 1111.1553 [hep-ex].

[235] G. Aad et al., "Measurement of the differential cross-section of B^+ meson production in pp collisions at $\sqrt{s} = 7$ TeV at ATLAS", *JHEP* 1310 (2013) 042,
DOI: 10.1007/JHEP10(2013)042, arXiv: 1307.0126 [hep-ex].

[236] H. Abramowicz et al.,
"Measurement of D^+ and Λ_c^+ production in deep inelastic scattering at HERA",
JHEP 1011 (2010) 009, DOI: 10.1007/JHEP11(2010)009,
arXiv: 1007.1945 [hep-ex].

[237] S. Chekanov et al.,
"Measurement of D mesons production in deep inelastic scattering at HERA",
JHEP 0707 (2007) 074, DOI: 10.1088/1126-6708/2007/07/074,
arXiv: 0704.3562 [hep-ex].

[238] P. Billoir and S. Qian, "Fast vertex fitting with a local parametrization of tracks",
Nucl.Instrum.Meth. A311 (1992) 139–150, DOI: 10.1016/0168-9002(92)90859-3.

[239] H. Abramowicz et al.,
"Scaled momentum distributions for K_S^0 and $\Lambda/\bar{\Lambda}$ in DIS at HERA",
JHEP 1203 (2012) 020, DOI: 10.1007/JHEP03(2012)020,
arXiv: 1111.3526 [hep-ex].

[240] F. Aaron et al., "Measurement of the Inclusive ep Scattering Cross Section at Low Q^2 and x at HERA", *Eur.Phys.J.* C63 (2009) 625–678,
DOI: 10.1140/epjc/s10052-009-1128-6, arXiv: 0904.0929 [hep-ex].

[241] P. Belov, "Combination of the H1 and ZEUS inclusive cross-section measurements at proton beam energies of 460 GeV and 575 GeV and tests of low Bjorken-x phenomenological models", PhD thesis: Hamburg University, May 2013.

[242] D. Nicholass, "The study of $D^\pm$ and D^0 meson production in deep inelastic scattering at HERA II with the ZEUS detector",
PhD thesis: University Coll. London, Aug. 2008,
DOI: 10.3204/DESY-THESIS-2008-046.

[243] T. Kluge, K. Rabbertz and M. Wobisch,
"FastNLO: Fast pQCD calculations for PDF fits" (2006),
arXiv: hep-ph/0609285 [hep-ph].

[244] M. Wobisch et al.,
"Theory-Data Comparisons for Jet Measurements in Hadron-Induced Processes"
(2011), arXiv: 1109.1310 [hep-ph].

[245] D. Britzger et al., "New features in version 2 of the fastNLO project" (2012),
DOI: 10.3204/DESY-PROC-2012-02/165, arXiv: 1208.3641 [hep-ph].

[246] T. Carli et al., "A posteriori inclusion of parton density functions in NLO QCD
final-state calculations at hadron colliders: The APPLGRID Project",
Eur.Phys.J. C66 (2010) 503–524, DOI: 10.1140/epjc/s10052-010-1255-0,
arXiv: 0911.2985 [hep-ph].

[247] V. Bertone et al., "aMCfast: automation of fast NLO computations for PDF fits",
JHEP 1408 (2014) 166, DOI: 10.1007/JHEP08(2014)166,
arXiv: 1406.7693 [hep-ph].

[248] G. P. Lepage, "A New Algorithm for Adaptive Multidimensional Integration",
J.Comput.Phys. 27 (1978) 192, DOI: 10.1016/0021-9991(78)90004-9.

[249] E. Braaten et al., "Perturbative QCD fragmentation functions as a model for heavy
quark fragmentation", *Phys.Rev.* D51 (1995) 4819–4829,
DOI: 10.1103/PhysRevD.51.4819, arXiv: hep-ph/9409316 [hep-ph].

[250] M. Guzzi, K. Lipka and S.-O. Moch, "Top-quark pair production at hadron colliders:
differential cross section and phenomenological applications with DiffTop",
JHEP 1501 (2015) 082, DOI: 10.1007/JHEP01(2015)082,
arXiv: 1406.0386 [hep-ph].

List of Figures

List of Tables

Acknowledgements

First of all I must thank all the physicists who whenever contributed to the development of science. These are people without whom this work will never appear. Thank you very much!

Concerning personal contributions, most of all I thank my supervisor Achim Geiser. It was a great pleasure to work with you during these years, and I learned and understood a lot of things. I thank Brian Foster very much for carefully reading the manuscript and suggesting many important corrections.

The next part of the acknowledgements I will give in a historical sequence. I thank all my school teachers and especially Tariel Sanikidze. I will never meet another so talented mathematician who would be able to explain complicated things so easily. I thank my lectures from the Physics Faculty of the Taras Shevchenko National University of Kyiv for inspiration to be a physicist.

Next, I thank Volodymyr Aushev, who opened for me a door of modern particle physics. I thank my friend Maksym Zolko, who was helping me a lot in the very beginning; I remember very well how we spent a whole night writing a code for D^+ 'pre-selection', and in the morning I saw a peak in the mass spectrum. I thank many other Ukrainian colleagues who later helped me to get more experience and who were always open for questions. My special acknowledgement goes to Misha Lisovyi with whom I continued to work on the D^+ measurement, since during this work I started to understand what I am doing and why. At this point, I also thank all members of the ZEUS Collaboration for their interest, questions, comments, discussions and encouragement. All of you, who were attending meetings, asking questions, sending comments and sharing your ideas on the physics analises or just complaining that ZeVis does not work, contributed a lot. I thank Katerina Lipka for sharing the work on the H1ZEUS D^{*+} combination and the later support of the PROSA analysis. And at this point I cannot hold back and again want to thank Achim for sharing with me his so simple and so nice idea of this analysis! I thank the members of the PROSA Collaboration for their feedback, comments, questions, criticism and even original skepticism to this study, because it motivated me to think harder.

Finally, I thank my parents for their love and support. I thank Inna for being the light of my life. I might forget something or someone important — please do not be offended.